Repeated partial melting events in the polymetamorphic Carlos Chagas batholith: implications for the tectono-metamorphic evolution of the Araçuaí orogen (southeastern Brazil)

by

Marilane Gonzaga de Melo

Dissertation presented for the joint-Degree of *Doctor of Geology in the Faculty of Science at Stellenbosch University (South Africa) and Universidade Federal de Ouro Preto (Brazil)*

Supervisor: Prof. Cristiano de Carvalho Lana
Co-supervisor: Prof. Gary Stevens
Co-supervisor: Prof. Fernando Flecha de Alkmin

March 2017

DECLARATION

By submitting this dissertation electronically, I declare that the entirety of the work contained therein is my own, original work, that I am the sole author thereof (save to the extent explicitly otherwise stated), that reproduction and publication thereof by Stellenbosch University will not infringe any third party rights and that I have not previously in its entirety or in part submitted it for obtaining any qualification. This dissertation has also been presented at Universidade Federal de Ouro Preto in terms of a joint-/double-degree agreement.

Signature: . . . . . .
M. G. Melo

March 2017
Date: . . . . . .

ABSTRACT

The Araçuaí orogen (AO), located in the southeastern Brazil, and its African counterpart, the West Congo belt, is part of the Pan-African-Brasiliano orogenic system developed between the Congo and São Francisco paleocontinents. From the earliest (ca. 630 Ma) pre-collisional plutons to the latest (ca. 480 Ma) post-collisional intrusions, the Araçuaí orogen records an outstanding succession of granite production events in space and time.

This study investigates the petrogenesis of the Carlos Chagas batholith (CCB), a very large body (~ 14,000 km^2) composed of S-type granites ascribed to the collisional plutonism (G2 supersuite) in the back-arc region of the AO, to the east of the Rio Doce magmatic arc. CCB extends in a N-S direction between latitudes 17°S and 19°30'S in the states of Espírito Santo, Minas Gerais and Bahia. The CCB includes a dominant granite richer in garnet than in biotite, in which three mineral assemblages can be identified: 1) Qz + Pl + Kfs + Bt + Grt + Ilm ± Rt; 2) Qz + Pl + Kfs + Bt + Grt + Ilm + Sil; and 3) Qz + Pl + Kfs + Bt + Grt + Ilm + Sil + Spl. Rocks which contain mineral assemblage 2 and 3 all contain two generations of garnet. Textural evidence for the presence of former melt, recognized in all studied CCB samples, includes: silicate melt inclusions in poikiloblastic garnet, pseudomorphed thin films of melt surrounding both generations of garnet, pseudomorphed melt pools adjacent to garnet and biotite, and plagioclase and quartz with cuspate-lobate shapes occurring among matrix grains. Both generations of garnet crystals (Grt_1 and Grt_2) are unzoned in terms of major element concentration, contain small rounded inclusions of Ti-rich biotite and, in addition, the Grt_2 crystals also contain inclusions of remnant sillimanite needles. Microstructural evidence, in combination with mineral chemistry, indicates that the garnet crystals grew during two distinct metamorphic-anatectic events, as the peritectic products of fluid-absent melting reactions which consumed biotite, quartz and plagioclase, in the case of Grt_1, and which consumed biotite, quartz, plagioclase and sillimanite in the case of Grt_2.

P-T pseudosections calculated via Theriak-Domino, in combination with U-Pb monazite and zircon dating, provide new constraints on the thermal evolution of the back-arc region of the Araçuaí orogen. Data from assemblage 1 suggests *P-T* conditions for the first granulite-facies metamorphic event (M1) at 790-820 ºC and 9.5-10.5 kbar, while the assemblage 2 records *P-T* conditions for a second granulite-facies metamorphism (M2) of around 770 ºC and 6.6 kbar. Ti-in-zircon thermometry is consistent with the phase equilibrium modelling, indicating that the two metamorphic events in the batholith reached granulite facies conditions.

A wide range of monazite and zircon ages (> 825 Ma to ca. 490 Ma) have been found in CCB rocks, recording a complex history of crustal recycling and inheritance, magmatic crystallization and anateksis during the evolution of the AO. 582 Ma magmatic zircons are marked by similar Hf isotope compositions and REE patterns to those of inherited cores (ca. 825-600 Ma), indicating that the chemical signature of these crystals has likely been inherited from the source.

The U-Pb ages and initial $^{176}Hf/^{177}Hf$ ratios from anatectic and/or metamorphic zircon domains are consistent with a two-stage metamorphic evolution marked by contrasting mechanisms of zircon growth and recrystallization during the orogeny. The oldest metamorphic episode (ca. 570-550 Ma) is recorded by development of thin anatectic overgrowths on older cores and by growth of new anatectic zircon crystals. Both domains have higher initial $^{176}Hf/^{177}Hf$ values compared to relict cores and display REE patterns typical of zircon that grew contemporaneously with peritectic Grt_1 through biotite-absent fluid partial melting. U-Pb ages obtained in monazite and zircon (ca. 569-552 Ma) included in Grt_1, further support the interpretation that the Grt_1 crystals grew during the first anatectic episode.

Hf isotopic and chemical evidences indicate that a second anatectic episode (ca. 535-500 Ma) is only recorded in part from the CCB rocks (assemblage 2 and 3). In these rocks, the growth of new anatectic zircon and/or overgrowth is marked by high initial $^{176}Hf/^{177}Hf$ values and also by generation of Grt_2, as indicated by petrographic observations and REE patterns. On the other hand, some rocks have zircon grains formed by solid-state recrystallization of pre-existing zircon, which exhibit similar Hf isotope composition those to inherited/magmatic core domains.

The M1 event likely corresponds to the striking crustal thickening and widespread anateksis in the CCB. The M2 event can be associated to asthenosphere upwelling during extensional thinning and gravitational collapse of the orogen, this produced anateksis in parts from the CCB that had been re-fertilized by retrogression along shear zones following the first granulite facies event.

OPSOMMING

Die Araçuaí orogen (AO), geleë in die suidooste van Brasilië, en sy Afrikaanse eweknie, die Weste Kongo-gordel, is deel van die Pan-Afrika-Brasiliano orogenetiese stelsel ontwikkelde tussen die Kongo en São Francisco kratons. Van die vroegste (ongeveer 630 Ma) pre-botsing plutone om die nuutste (ongeveer 480 Ma) post-botsing rotse, die Araçuaí orogen rekords 'n uitstekende opvolging van graniet produksie gebeure in ruimte en tyd.

Hierdie studie ondersoek die petrogenese van die Carlos Chagas batoliet (CCB), 'n baie groot liggaam (~ 14.000 km^2) bestaan uit S-tipe graniet toegeskryf word aan die botsing plutonism in die back-boog streek van die AO, om die oos van die Rio Doce magmatiese boog. CCB strek in 'n N-S rigting tussen breedtegrade 17°S en 19°30'S in die state van Espírito Santo, Minas Gerais en Bahia. Die BSB sluit 'n dominante graniet ryker in granaat as in biotiet, waarin drie mineraal samestellings kan geïdentifiseer word: 1) Qz + Pl + Kfs + Bt + Grt + Ilm ± Rt; 2) Qz + Pl + Kfs + Bt + Grt + Ilm + Sil; en 3) Qz + Pl + Kfs + Bt + Grt + Ilm + Sil + Spl. Tekstuur bewyse vir die teenwoordigheid van die voormalige smelt, erken in al bestudeer CCB monsters, sluit in: silikaat smelt insluitings in granaat, pseudomorphed dun films van smelt omliggende beide generasies van granaat, pseudomorphed smelt poele aanliggend aan Garnet en biotite, en plagioklaas en kwarts met cuspate-lobate vorms voorkom tussen matriks korrels. Beide geslagte van granaat kristalle (Grt_1 en Grt_2) is unzoned in terme van belangrike element konsentrasie, bevat klein ronde insluitings van Ti-ryk biotiet en, benewens, die Grt_2 kristalle bevat insluitings van oorblyfsel sillimanite naalde. Mikrostrukturele bewyse, in kombinasie met minerale chemie, dui daarop dat die granaat kristalle gegroei gedurende twee afsonderlike metamorfiese-anatectic gebeure, soos die peritektiese produkte van vloeistof-afwesig smelting reaksies wat verbruik biotiet, kwarts en plagioklaas, in die geval van Grt_1, en wat verbruik biotiet, kwarts, plagioklaas en sillimanite in die geval van Grt_2.

P-T bereken deur Theriak-Domino, in kombinasie met die U-Pb monasiet en sirkoon dating, verskaf nuwe beperkings op die termiese evolusie van die back-boog streek van die Araçuaí orogen. Data van mineraal samestellings 1 dui PT toestande vir die eerste granulietterreine-fasies metamorfiese gebeurtenis (M1) by 790â820 ºC en 9.5â10.5 kbar, terwyl die mineraal samestellings 2 rekords PT toestande vir 'n tweede granulietterreine-fasies metamorfose (M2) van sowat 770 ºC en 6.6 kbar. Ti-in-sirkoon thermometry is in ooreenstemming met die fase-ewewig modellering, wat daarop dui dat die twee metamorfe gebeurtenisse in die batoliet bereik granulietterreine fasies voorwaardes.

'N Wye verskeidenheid van monasiet en sirkoon ouderdomme (> 825 Ma tot ongeveer 490 Ma) is gevind in CCB rotse, opname van 'n komplekse geskiedenis van kors herwinning, magmatiese kristallisasie en anateksis gedurende die evolusie van die AO. 582 Ma magmatiese sirkone is gekenmerk deur soortgelyke Hf isotoop komposisies en REE patrone aan dié van geërf kern (ongeveer 825-600 Ma), wat aandui dat die chemiese ondertekening van hierdie kristalle het waarskynlik geërf uit die bron.

Die U-Pb ouderdomme en aanvanklike ^{176}Hf / ^{177}Hf verhoudings van anatectic en / of metamorfiese sirkoon domeine is in ooreenstemming met 'n twee-stadium metamorfiese evolusie gekenmerk deur kontrasterende meganismes van groei sirkoon en dekristallisatie gedurende die orogenie. Die oudste metamorfiese episode (ongeveer 570-550 Ma) is aangeteken deur die ontwikkeling van dun anatectic oorgroei op ouer gebiede en deur groei van nuwe anatectic sirkoon kristalle. Beide gebiede hoër aanvanklike ^{176}Hf / ^{177}Hf waardes in vergelyking met oorblyfsel cores en vertoon REE patrone tipies van sirkoon wat gelyktydig gegroei met peritektiese Grt_1 deur vloeistof-vrye biotiet smelting. U-Pb ouderdomme verkry in monasiet en sirkoon (ongeveer 569-552 Ma) ingesluit in Grt1, verder te ondersteun die interpretasie dat die Grt_1 kristalle gegroei gedurende die eerste anatectic episode.

HF isotope en chemiese bewyse dui daarop dat 'n tweede anatectic episode (ongeveer 535-500 Ma) is slegs aangeteken in sommige CCB rotse (mineraal samestellings 2 en 3). In hierdie rotse, is die groei van nuwe anatectic sirkoon en / of oorgroei word gekenmerk deur 'n hoë aanvanklike ^{176}Hf / ^{177}Hf waardes en ook deur die opwekking van Grt_2, soos aangedui deur petrografiese waarnemings en REE patrone. Aan die ander kant, sommige rotse het sirkoon korrels gevorm deur vastetoestand dekristallisatie van voorafbestaande sirkoon, met 'n soortgelyke Hf isotoop komposisie diegene te geërf / magmatiese domeine.

Die M1 gebeurtenis waarskynlik ooreenstem met die treffende kors verdikking en wydverspreide anateksis in die CCB. Die M2 gebeurtenis geassosieer kan word om opwelling astenosfeer gedurende extensieve dunner en gravitasie ineenstorting van die orogen, hierdie geproduseer anateksis in dele van die CCB wat was weer bevrug deur agteruitgang saam skuifskeursones na aanleiding van die eerste granulietterreine-fasies metamorfiese.

RESUMO

O orógeno Araçuaí (OA) localizado no sudeste do Brasil e sua contraparte africana (cinturão Congo Ocidental) constituem o sistema orogênico Brasiliano Pan Africano desenvolvido entre as paleocontinentes Congo e São Francisco. O orógeno Araçuaí registra uma notável sucessão de eventos de produção de granitos no espaço e no tempo, que engloba desde os primeiros plútons pré-colisionais (~ 630 Ma) até as mais recentes intrusões pós-colisionais (~ 480 Ma).

Este estudo investiga a petrogênese do batólito Carlos Chagas (BCC), um enorme corpo (~ 14.000 km^2) composto por granitos do tipo S atribuídos ao plutonismo colisional (supersuíte G2) na região de retro arco do OA, a leste do arco magmático Rio Doce. BBC estende-se em uma direção N-S entre as latitudes 17 ° S e 19°30'S, nos estados de Espírito Santo, Minas Gerais e Bahia. BBC inclui predominantemente granitos ricos em granada, em que três assembleias minerais podem ser identificadas: 1) Qz + Pl + KFS + Bt + Grt + Ilm ± Rt; 2) Qz + Pl + KFS + Bt + Grt + Ilm + Sil; e 3) Qz + Pl + KFS + Bt + Grt + Ilm + Sil + Spl. As rochas que contêm as assembleias 2 e 3 contêm duas gerações de granadas. Evidências microestruturais para a presença de melt são identificadas em todas as amostras estudadas, tais como: inclusões de melt silicático em granadas poiquiloblásticas, finos filmes de melt pseudomorfizados ao redor de ambas gerações de granada, "piscinas" de melt adjacentes a granada e biotita, além de plagioclásio e quartzo com formas cuspade a lobulados que ocorrem entre os grãos da matriz. Ambas gerações de granada (Grt_1 e Grt_2) não apresentam zoneamento em termos de elementos maiores e contêm pequenas inclusões arredondadas de biotita rica em Ti. Além disso, os cristais Grt_2 também contêm inclusões de remanescentes agulhas de sillimanita. Evidências microestruturais, em combinação com a química mineral, indicam que os cristais de granada cresceram durante dois eventos metamórficos/anatéticos distintos, como produtos peritéticos de reações de fusão parcial em regime de fluido ausente que consumiram biotita, quartzo e plagioclásio, no caso de Grt_1, e que consumiram biotita, quartzo, plagioclásio e silimanita, no caso de Grt_2. Pseudoseções calculadas via Theriak-Domino forneceram novas condições metamórficas para a região do retro arco do OA. Dados da assembleia mineral 1 sugerem que o primeiro evento metamórfico de fácies granulito (M1) ocorreu a temperaturas de 790-820 ºC e pressões de 9.5-10.5 kbar, enquanto a assembleia mineral 2 registra condições PT para um segundo metamorfismo de fácies granulito (M2) a aproximadamente 770 ºC e 6.6 kbar. Dados do geotermômetro Ti em zircão são consistentes com modelamento metamórfico, indicando que os dois eventos metamórficos no batólito atingiram condições de fácies granulito.

Variadas idades foram encontradas em grãos de monazita e zircão (> 825 Ma a 490 Ma) das rochas do BCC, registrando uma complexa história de reciclagem crustal e herança, cristalização magmática e anatexia durante a evolução do OA. Os zircões magmáticos (~ 582 Ma) mostram composição isotópica de Hf e padrões de ETR similar aos dos núcleos herdados (825-600 Ma), indicando que a assinatura química destes cristais provavelmente foi herdada da fonte.

Idades U-Pb e razões iniciais $^{176}Hf/^{177}Hf$ dos domínios de zircões anatéticos e/ou metamórficos são consistentes com dois estágios metamórficos caracterizados por processos de crescimento/sobrecrescimento e recristalização de grãos de zircão durante a orogenia. O episódio metamórfico mais antigo (570-550 Ma) é caracterizado pelo sobrecrescimento anatético em núcleos mais velhos e pelo crescimento de novos cristais de zircão anatético. Ambos os domínios têm elevados valores iniciais de $^{176}Hf/^{177}Hf$ em comparação com núcleos mais antigos e exibem padrões de ETR típicos de zircão que cresceu simultaneamente com granada peritética (Grt_1) através de reações de fusão parcial em regime de fluido ausente. Idades U-Pb obtidas em grãos de monazita e zircão (569-552 Ma) inclusos na Grt_1, corroboram a interpretação de que os cristais Grt_1 cresceram durante o primeiro episódio anatético.

Composição isotópica de Hf e evidências químicas indicam que um segundo episódio anatético (535-500 Ma) é registrado em parte das rochas do batólito (assembleias 2 e 3). Nestas rochas, o crescimento e/ou sobrecrescimento de novos zircões anatéticos é marcado por elevada razão inicial de $^{176}Hf/^{177}Hf$ e também pela geração da Grt_2, como indicado pelas observações petrográficas e padrões de ETR. Por outro lado, algumas rochas têm grãos de zircão formados por processos de recristalização no estado sólido de zircão pré-existente, que exibem composição isotópica de Hf similar àqueles domínios magmáticos/herdados.

O evento M1 é associado ao espessamento crustal e anatexia no batólito. O evento M2 pode ser associado a ascensão da astenosfera durante o colapso gravitacional do orógeno. Isto produziu anatexia em partes do BCC que tinham sido refertilizado ao longo de zonas de cisalhamento após o primeiro evento de fácies granulito.

ACKNOWLEDGEMENTS

Firstly, I would like to express my special appreciation and thanks to my supervisor Dr. Cristiano de Lana, you have been a tremendous mentor for me. I would like to thank you for encouraging my research and for allowing me to grow as a research scientist. Your advice on both research as well as on my career have been priceless.

I would also like to express my gratitude to my other supervisor Prof. Gary Stevens for the useful comments, remarks and engagement through the learning processes of this thesis. Furthermore I would like to thank Dr. Fernando Alkmim and Antônio Carlos Pedrosa Soares for introducing me to the topic as well for the support on the way.

I would like to thank the many graduate and undergraduate students I have worked with in Applied Isotope Research Group: Leonardo Alkmim, Guilherme Gonçalves, Hugo Moreira, Fabiana Richter, Francesco Narduzzi, Capucine Albert, Mathias Schannor, Kathryn Cutts, Federico Farina, Carmen Aguilar, Carmen Dopico, Lorena, Maristella Santos, Lynthener Takenaka, Viviane Coelho, Tiago Ribeiro, Livia Teixeira, Ariela Mazoz, Camila Fadul, Camila Schuch, Rosana Oliveira, João Paulo Silva and Guilherme Silveira. I would also like to thank my many friends and colleagues in the Universidade Federal de Ouro Preto: Alice Costa, Gabriela Fonseca, Kássia Medeiros, Taynara D'Angelo, Ana Alkmim and Ramón Messias.

I also thank all the people from the Department of Geology (Stellenbosch University), the staff: Ian Buick, Dirk Frei, Anton du Plessis, Loxie Conradie, George Oliver, Dorothy Stevens, Cynthia Sanchez-Garrido, Madelaine Frazenburg, Riana Rossouw, Theo Pauw, Stephan le Roux, Lize Engelbrecht, but also all the postgrad students and postdoctorates: Gautier Nicoli, Valby van Schijndel, Marcos García-Arias, Tolene Kruger, Duncan Hall, Corne Koegelenberg and many other people.

Finally, I must express my very profound gratitude to my family and to my husband Rafael for providing me with unfailing support and continuous encouragement throughout my years of study and through the process of researching and writing this thesis. This accomplishment would not have been possible without them. Thank you for all.

TABLE OF CONTENTS

LIST OF FIGURES

LIST OF FIGURES IN ATTACHED PUBLICATIONS

LIST OF TABLES

LIST OF TABLES IN ATTACHED PUBLICATIONS

CHAPTER 1

INTRODUCTION

1.1. PREFACE

Crustal differentiation is an important process for the production and stabilization of the continental crust. It takes place along orogenic belts where older continental rocks are recycled in the mid to lower crust and melted to produce more evolved granitic magmas. During heating in the granulite facies (> 800 ºC), the lower crust melts to produce a mobile, water under-saturated granitoid magma that is capable of intruding into the upper crust. These magmas are produced by fluid-absent partial melting reactions involving the breakdown of mica and amphibole (e.g., Brown, 1994; 2010). These magmas migrate upwards in the crust to build middle- to high-level granitic plutons and volcanic complexes. This results in an upper crust that is enriched in SiO_2, K_2O, Na_2O and heat producing elements, leaving the lower crust dehydrated, more refractory and enriched in Al_2O_3, FeO, MgO and CaO (Petford *et al.*, 2000; Brown & Rushmer, 2006; Brown, 2013).

Orogenic events drive crustal differentiation by introducing material that is fertile for the production of granitic magma into the deep crust, as well as inducing heat onto this fertile deep crust via mechanisms such as: (i) reestablishment of disrupted isotherms in the thickened crust; (ii) burial of radiogenic heat producing layers; and (iii) transfer of mantle heat to the crust. In more vigorous, long-lived orogenic systems some sedimentary and volcanic rocks (caught in the orogenic cycle) may record more than one cycle of tectonic burial with partial melting at depth (Jeon *et al.*, 2012). Likewise, early stage granites, emplaced into the upper crust, may be buried together with overlying sedimentary and volcanic sequences to lower crustal levels, and recycled in the lower crust as the orogeny evolves.

Despite this broad understanding, some very important aspects of how crustal differentiation occurs are poorly understood, particularly in the case of orogens, which produce a substantial volume of peraluminous magma, implying the melting of metasedimentary rocks in the deep crust. In this case, rock sequences derived from weathered continental crust must be a major component of the deep crust. This recurring process of partial melting may have contributed to the formation of vast amounts of S-type granites and has been documented in a number of orogenic systems, such as the Lachlan fold belt (Chappell & White, 1974), the Araçuaí Orogen (Pedrosa-Soares *et al.*, 2001, 2011), and the Tasmanide orogenic system (Collins & Richards, 2008).

1.2. MAIN GOALS

This study has investigated the petrogenesis of the Carlos Chagas batholith, a very large body (~ 14,000 km^2) composed of peraluminous, -type granites formed during the collisional stage of the Araçuaí orogen. The rocks of the intended study area provide unique opportunities to better understanding of the crustal recycling processes during a long-lived orogeny. Few studies have investigated the potential anatectic recycling of collisional granites through detailed study of their mineralogy, mineral textures, mineral chemistry, geochronology, and isotope composition (Vauchez *et al.* 2007; Roncato, 2009; Gradim, 2013; Gradim *et al.*, 2014). Thus, the aims in this study are:

- ✓ To investigate the origin of garnet crystals through the textures and mineral chemistry;
- ✓ To detail the time interval of magmatic crystallization of the batholith;
- ✓ To investigate the isotopic evolution of this granitoid from crystallization through to the anatectic episodes;
- ✓ To constrain the metamorphic evolution of the batholith and its relation to the paragneisses (Nova Venécia complex).

1.3. LOCALITY AND MAIN ACCESS ROADS

The studied area extends roughly between latitudes 17ºS and 19º30'S, encompassing the states of Espírito Santo, Minas Gerais and Bahia. The field work took place in the regions of Carlos Chagas, Nanuque, Ataléia, Montanha, Ecoporanga, Barra de São Francisco, Nova Venécia, Colatina, among others. This area comprises the geologic maps of the Padre Paraíso (SE-24-V-C-II), Águas Formosas (SE-24-V-C-III), Medeiros Neto (SE-24-V-D-I), Mucuri (SE-24-V-C-V), Carlos Chagas (SE-24-V-C-VI), Nanuque (SE-24-V-D-IV), Ataléia (SE-24-Y-A-II), Ecoporanga (SE-24-Y-A-III), Montanha (SE-24-Y-B-I), Itabirinha de Mantena (SE-24-Y-A-V), Mantena (SE-24-Y-A-VI), Nova Venécia (SE-24-Y-B-IV), Conselheiro Pena (SE-24-Y-C-II), São Gabriel da Palha (SE-24-Y-C-III) e Linhares (SE-24-Y-D-I) Sheets, carried out by the Brazilian Geological Survey (CPRM), Companhia de Desenvolvimento Econômico de Minas Gerais (CODEMIG) and Universidade Federal de Minas Gerais (UFMG). Figure 1.1 shows the main access roads in the studied area.

1.4. METHODOLOGY

The methods employed during this study are summarized as following:

- ✓ Field work was carried out in two stages: (i) between March 24 and March 29 of 2013; and (ii) between May 26 and May 29 of 2014. Representative samples were collected over an extensive area of the batholith, most samples being sourced from large quarries (e.g., Pedreira Toledo, Stone Mineração, Mineração Vale du Granito, Plêiades Mineração, Pedreira Monte Horeb and Gramil Granitos) and

road cuts. Table 1.1 reports the location of the samples collected for petrography, geochemical, geochronology and isotopic studies during the field work.

- ✓ Petrographic investigation was carried out on seventy-one thin sections, including the thirty-five thin sections previously studied by Castañeda *et al*. (2006), Gradim *et al.* (2007), Queiroga *et al.* (2012a) and Roncato *et al*. (2012). The identification of microstructures indicative of the former of melt in high-grade metamorphic rocks was based on studies of Sawyer (1999, 2001, 2008), Waters (2001), Holness (2006), Holness & Sawyer (2008), Holness *et al.* (2011), Vernon (2011) and Ferrero *et al.* (2012). Mineral abbreviations are according to Whitney & Evans (2010) for rock forming minerals.
- ✓ Mineral compositional analysis was performed using a Leo® 1430VP Scanning Electron Microscope at the Department of Earth Sciences, Stellenbosch University (South Africa). The mineral phases analyzed were garnet, biotite, feldspar, spinel, ilmenite, rutile and carbonate (see description of the analytical method in Appendix A).
- ✓ Garnet trace element compositions were analyzed via laser ablation-inductively-coupled-mass spectrometry (LA-ICP-MS) using an Agilent 7500ce quadrupole ICP-MS coupled to a 213 nm New Wave laser at the Department of Earth Sciences, Stellenbosch University (South Africa). For more details, see description of the analytical method in Appendix A.
- ✓ Whole-rock major element compositions (SiO_2, TiO_2, Al_2O_3, Fe_2O_3, MnO, MgO, CaO, Na_2O, K_2O, Cr_2O_3 e P_2O_5) were carried out at the Department of Earth Sciences, Stellenbosch University (South Africa), using X-ray fluorescence spectrometer on a Philips 1404 Wavelength Dispersive spectrometer (see description of the analytical method in Appendix A).

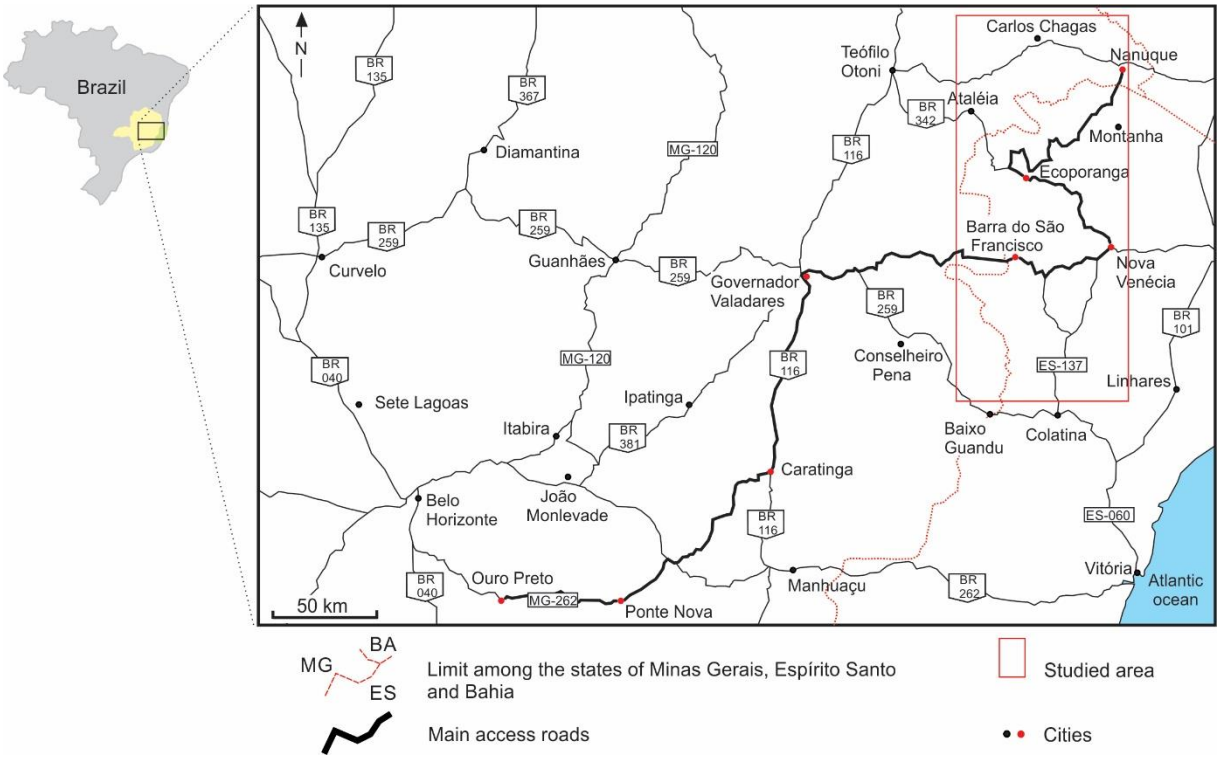

Figure 1.1 – Map showing main access roads for the studied area (Modified from Google Maps).

Table 1.1 - Location of the samples collected for petrological, geochronological and isotopic studies.

Sample	X	Y	MP	MC	WR	MM	MD	ZD	IA
CC10	18º46'9.5"	41º01'47.1"							
CC12	18º45'47"	41º7'49.3"	x					x	x
CC13	18º45'47"	41º7'49.3"	x						
CC14	18º45'36.2"	41º9'28.4"	x		x	x			
CC15	18º41'36.7"	41º3'8.6"	x						
CC16	18º42'5.9"	40º50'59"	x						
CC17	18º40'44.1"	40º47'1.5"	x						
CC18	18º41'1.2"	40º45'44.4"	x					x	x
CC21	18º43'34"	40º43'41.5"	x	x			x	x	
CC22	18º43'34"	40º43'41.5"	x						
CC24	18º45'44.4"	40º43'59.5"	x						
CC25	18º46'52.4"	40º42'24.5"	x						
CC26	18º46'1.6"	40º51'52.6"	x						
CC28	18º50'16.1"	40º46'45.2"	x	x	x	x			
CC29	18º49'46"	40º45'8.2"	x						
CC30	18º55'54.4	40º45'17.3"	x		x	x		x	x
CC31	19º30.6"	40º43'57.9"	x	x	x	x	x	x	
CC32	18º33'40.9"	40º57'35"							
CC33	18º33'10.7"	40º58'35.5"	x		x	x			
CC34	18º33'17.9"	40º58'13.6"	x					x	x
CC35a	18º41'26.4	40º54'22.4"	x					x	x
CC35b	18º41'26.4	40º54'22.4"	x						
CC36	18º20'19.3"	40º47'59.7"	x					x	x
CC37	18º17'29.9"	40º43'17.6	x	x		x	x	x	
CC39	18º16'30.4"	40º40'18.3"	x						
CC40	18º14'43"	40º43'47.5"	x					x	x
CC41	18º12'16.6"	40º39'31.6"	x						
CC42	18º3'59"	40º46'28.8"	x					x	x
CC45	18º10'13.4"	40º44'52"	x						
CC46	18º53'44.3"	40º39'7.2"	x						
CC47	18º53'4.2"	40º37'48.3"	x					x	
CC48	18º56'11.4"	40º34'36.4"	x						
CC49	18º35'19.5"	40º32'19"	x						
CC50	18º19'2.7"	40º52'56.6"	x						
CC51	18º7'22.04"	40º22'10.2"	x						
CC52	18º0'49"	40º23'52.7"	x						
CC53	17º49'19"	40º20'35"	x						
CC55	17º49'52,7"	40º56'16,7"	x						

MP = microscopic petrography; MC = mineral chemistry; WR = whole-rock chemistry; MM = metamorphic modelling; MD = U-Pb monazite dating; ZD = U-Pb zircon dating; IA = Lu-Hf isotopic analysis.

- ✓ Phase equilibrium modeling was performed in the chemical system NCKFMASHTO (Na_2O-CaO-K_2O-FeO-MgO-Al_2O_3-SiO_2-H_2O-TiO_2-Fe_2O_3) using Theriak-Domino software (De Capitani & Petrakakis, 2010), in combination with the updated tc2td.exe converted Holland & Powell (1998) database created by Tinkham (see detailed description in Chapter 3 - section 3.6). The melt-reintegrated pseudosections were calculated using the method of White *et al.* (2004).
- ✓ In situ monazite and zircon U-Pb dating were carried out in three thin sections in the Stellenbosch University Central analytical facility (CAF) ICP-MS unit using an Agilent 7500ce quadrupole ICP-MS coupled to a 213 nm New Wave laser. Prior to analysis, back-scattered electron (BSE) and cathodoluminescence imaging were used to determine the microstructural location of monazite and zircon grains, as well as its internal structures. See description of the analytical method in Appendix A.
- ✓ U-Pb zircon analysis for seven rock samples were performed using an Agilent 7700x quadrupole ICP-MS coupled to a 213 NdYAG laser (New Wave Research UP-213) and for two samples were carried out using a Thermo-Finnigan Element 2 sector field ICP-MS coupled to a CETAC ultraviolet laser system (LA-SF-ICP-MC), both at Geology Department, Universidade Federal de Ouro Preto (Brazil). For more details, see description of the analytical method in Appendix B.
- ✓ Lu-Hf analyses were performed on zircons of eight samples using a Thermo-Scientific Finnigan Neptune LA-MC-ICP-MS, at the Institut für Petrologie, Geochemie und Lagerstättenkunde, Universität Frankfurt (Germany). For more details, see description of the analytical method in Appendix B.
- ✓ Trace element analysis of zircon (two samples) was performed using a Thermo-Scientific Finnigan Element 2 SF-ICP-MS, at the LOPAG, Universidade Federal de Ouro Preto (Brazil). See detailed description of the analytical method in Appendix B.

1.5. STRUCTURE OF THE THESIS

This thesis presents detailed aspects of the petrogenesis from the Carlos Chagas batholith. It includes petrographic, mineral chemistry, geochronology and isotopic data, as well as metamorphic modelling. Results from this study provide a valuable contribution for understanding of the partial melting processes involving of S-type granites during an orogeny. The thesis is laid out as follows:

Chapter 1 described the nature of the study, the main goals, location of studied area and methodology employed during the development this thesis.

Chapter 2 provides valuable information about tectonic setting from the Araçuaí orogen based on previous stratigraphy, geochemical and geochronological studies.

Chapter 3 presents the manuscript "Two cryptic anatectic events within a syn-collisional granitoid from the Araçuaí orogen (southeastern Brazil): evidence from the polymetamorphic Carlos Chagas batholith" accepted for publication in Lithos. This manuscript describes two generations of garnet formed by two separate partial melting within of the Carlos Chagas batholith during the single orogeny. The P-T conditions and timing for these events are constrained using phase equilibria modelling and in situ U-Pb monazite and zircon dating, respectively. The findings of this paper explain how the granitic bodies can undergone more than one cycle of mid- to lower crystal tectonic recycling during a long-lived orogenic event.

Chapter 4 reports the manuscript "Assessing the isotopic evolution of S-type granites of the Carlos Chagas batholith, SE Brazil: clues from U-Pb, Hf isotopes, Ti geothermometry and trace element composition of zircon" submitted to Lithos. This manuscript discusses the processes of new zircon growth (or overgrowths) and recrystallization of zircon based on U-Pb ages and Hf isotope composition, as well as the petrological conditions of formation of the distinct zircon domains by rare earth elements and Ti-in-zircon thermometry.

Chapter 5 reports preliminary data on the melt inclusions, which were trapped into peritectic garnet crystals. Microstructure evidence show the coexistence of immiscible silicate and carbonate melts during the first anatectic event in the batholith.

Chapter 6 describes the major conclusions of the research and the questions that remain unresolved which may be investigated in future studies.

Appendix includes the detailed description of the analytical methods used in this study, as well as data tables of mineral chemistry, U-Pb monazite and zircon geochronology, Hf isotope composition and rare earth element composition of garnet and zircon.

References

Brown M. 1994. The generation, segregation, ascent and emplacement of granite magma: the migmatite-to-crustally-derived granite connection in thickened orogens. *Earth-Science Reviews*, **36:**83-130.

Brown M. 2010. Melting of the continental crust during orogenesis: the thermal, rheological, and compositional consequences of melt transport from lower to upper continental crust. *Canadian Journal of Earth Sciences*, **47:**655-694.

Brown M. 2013. Granite: From genesis to emplacement. *Geological Society of America Bulletin*, **125:** 1079–1113.

Brown M. & Rushmer T. 2006. *Evolution and Differentiation of the Continental Crust*. Cambridge, UK, Cambridge University Press, 562 p.

Castañeda C., Pedrosa-Soares A. C., Belém J., Gradim D., Dias P. H. A., Medeiros S. R., Oliveira L. 2006. *Mapa Geológico e Nota Explicativa da Folha Ecoporanga, 1:100.000. In*: *Folha Ecoporanga*. Programa Geologia do Brasil, CPRM–UFMG (geobank.sa.cprm.gov.br), 50 p.

Chappell B. W. & White A. J. R. 1974. Two contrasting granite types. *Pacific Geology***, 8**:173–174.

Collins W. J. & Richards S. W. 2008. Geodynamic significance of S-type granites in circum-Pacific orogens. *Geology*, **36:**559-562

De Capitani C. & Petrakakis K. 2010. The computation of equilibrium assemblage diagrams with Theriak/Domino software. *American Mineralogist*, **95:** 1006–1016.

Ferrero S., Bartoli O., Cesare B., Salvioli-Mariani E., Acosta-Vigil A., Cavallo A., Groppo C., Battiston S., 2012. Microstructures of melt inclusions in anatectic metasedimentary rocks. *Journal of Metamorphic Geology*, **30**:303-322.

Gradim C. T. 2013. *Complexo Nova Venécia e magmatismo associado, Orógeno Araçuaí, Estado do Espírito Santo.* Departamento de Geologia, Universidade Federal de Minas Gerais, Belo Horizonte, MSc dissertation, 96p.

Gradim C. T., Queiroga G. N., Roncato J. G., Novo T. A., Pedrosa-Soares A. C. 2007. *Folha Mantena, SE.24-Y-A-VI, escala 1:100.000.* Minas Gerais/Espírito Santo, UFMG/CPRM.

Gradim C., Roncato J., Pedrosa-Soares A.C., Cordani U., Dussin I., Alkmim F.F., Queiroga G., Jacobssohn T., Silva L.C., Babinski M. 2014. The hot back-arc zone of the Araçuaí orogen, Eastern Brazil: from sedimentation to granite generation. *Brazilian Journal of Geology*, **44**, 155-180.

Holland T. J. B. & Powell R. 1998. An internally consistente thermodynamic data set for phases of petrological interest. *Journal of Metamorphic Geology*, **16:** 309–343.

Holness M. B. 2006. Melt solid dihedral angles of common minerals in natural rocks. *Journal of Petrology*, **47:**791-800.

Holness M. B. & Sawyer E. W. 2008. On the pseudomorphing of melt-filled pores during the crystallization of migmatites. *Journal of Petrology*, **49:**1343-1363.

Holness M. B., Cesare B., Sawyer E. W. 2011. Melted rocks under the microscope: microstructures and their interpretation. *Elements*, **7**:247-252.

Jeon H., Williams I. S., Chappell B. W. 2012. Magma to mud to magma: Rapid crustal recycling by Permian granite magmatism near the eastern Gondwana margin. *Earth and Planetary Science Letters*, **319-320:**104–117.

Pedrosa-Soares A. C., Noce C. M., Wiedemann C. M., Pinto C. P. 2001. The Araçuaí-West-Congo Orogen in Brazil: an overview of a confined orogen formed during Gondwanaland assembly. *Precambrian Research*, **110:**307-323.

Pedrosa-Soares A. C., De Campos C. P., Noce C., Silva L. C., Novo T., Roncato J., Medeiros S., Castañeda C., Queiroga G., Dantas E., Dussin I., Alkmim F. 2011. Late Neoproterozoic–Cambrian granitic magmatism in the Araçuaí orogen (Brazil), the Eastern Brazilian Pegmatite Province and related mineral resources. *Geological Society of London, Special Publications*, **350**:25–51.

Petford N., Cruden A. R., McCaffrey K. J. W., Vigneresse J. L. 2000. Granite magma formation, transport and emplacement in the Earth's crust. *Nature*, **408:**669-673.

Roncato J. G. 2009. *As suítes graníticas tipo-S do norte do Espírito Santo na região das folhas Ecoporanga, Mantena, Montanha e Nova Venécia*. Instituto de Geociências, Universidade Federal de Minas Gerais, Minas Gerais, Masters dissertation,102p.

Roncato J. G., Pedrosa-Soares A. C., Mascarenhas T. F., Fornero S. A., Galinari L. M., Gonçalves L. T., Queiroga G. N., Braga F. C. S., Novo T. A. 2012. *Geologia e recursos minerais da folha Montanha, SE.24-Y-B-I, escala 1:100.000: nota explicativa*. Minas Gerais/Espírito Santo, UFMG/CPRM. 64p.

Sawyer E. W. 1999. Criteria for the recognition of partial melting. *Physics and Chemistry of the Earth*, Part A: Solid Earth and Geodesy, **24**:269-279.

Sawyer E. W. 2001. Melt segregation in the continental crust: distribution and movement of melt in anatectic rocks. *Journal of Metamorphic Geology*, **19:**291-309.

Sawyer E. W. 2008. *Atlas of migmatites*. The Canadian Mineralogist. In: Special Publication vol. 9. NRC Research Press, Ottawa, Ontario, 371 p.

Vauchez A., Egydio Silva M., Babinski M., Tommasi A., Uhlein A., Liu D. 2007. Deformation of a pervasely molten middle crust: insights from the neoproterozoic Ribeira-Araçuaí orogen (SE Brazil). *Terra Nova*, **19:** 278-286.

Vernon R. H. 2011. Microstructures of melt-bearing regional metamorphic rocks. *The Geological Society of America Memoir*, **207**:1-11.

Waters D. J. 2001. The significance of prograde and retrograde quartz-bearing intergrowth microstructures in partially melted granulite-facies rocks. *Lithos*, **56**:97-110.

White R. W., Powell R., Halpin J. A. 2004. Spatially-focussed melt formation in aluminous metapelites from Broken Hill, Australia. *Journal of Metamorphic Geology*, **22:**825-845.

Whitney D. L. & Evans B. W. 2010. Abbreviations for names of rock-forming minerals. *American Mineralogist*, **95**:185-187.

CHAPTER 2

GENERAL ASPECTS OF THE ARAÇUAÍ OROGEN (BRAZIL)

The Araçuaí orogen corresponds to the Neoproterozoic orogenic domain located among the São Francisco craton, Ribeira belt and continental margin in eastern Brazil (Figure 2.1). This orogenic system has continuity in the african continent (designated as West Congo belt) and covers the coastal zone of Gabon, Congo and Angola. The Araçuaí orogen and its african counterpart (West Congo belt) constitutes the Araçuaí-West Congo orogen, which was formed by amalgamation of the West Gondwana from Neoproterozoic to Cambrian (Alkmim *et al*., 2006, 2007) during the closure of the Adamastor-Brazilide ocean (Daziel, 1997). The São Francisco and Congo cratons remained connected since the Amazonian-Eburnian cycle (ca. 2300-1900 Ma) by the so-called Bahia-Gabão cratonic bridge (Porada, 1989). The Araçuaí- West Congo orogen was split by the Cretaceous South Atlantic rifting into two complementary counterparts (Araçuaí and West Congo orogens).

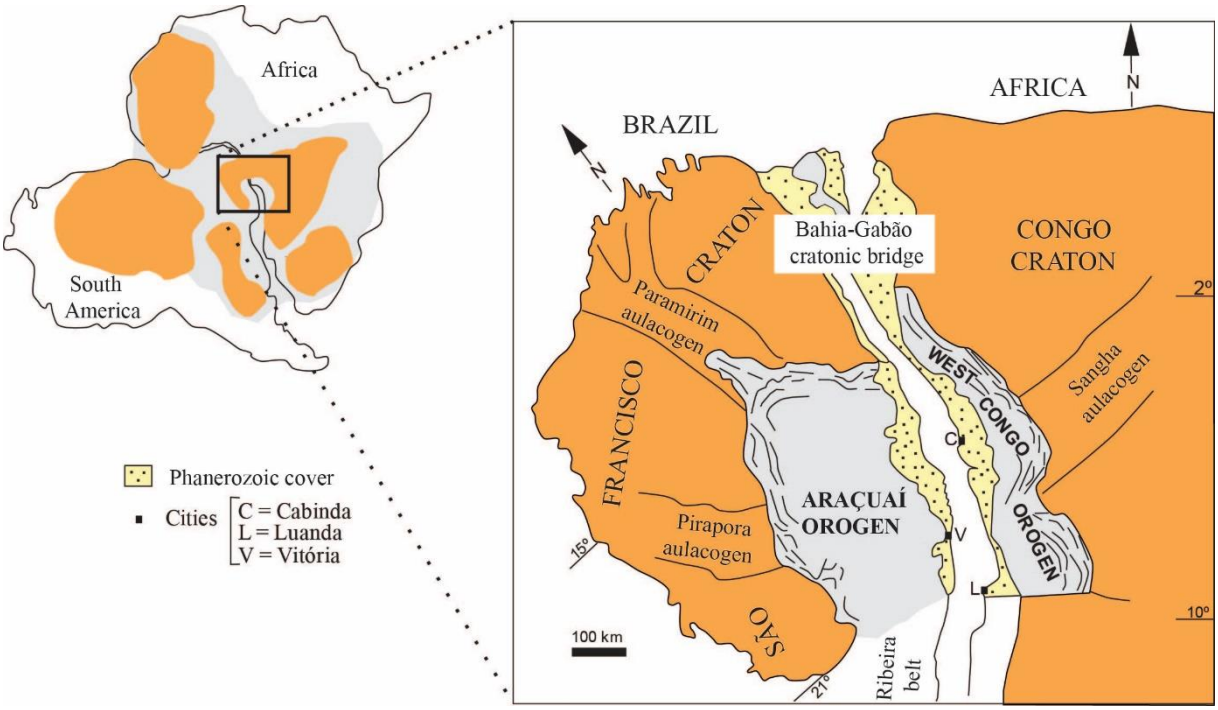

Figure 2.1 – Araçuaí- West Congo orogen and the adjacent São Francisco-Congo craton in the context of West Gondwana (modified from Alkmim *et al.*, 2006).

The Braziliano-Pan African orogenic system comprises the Araçuaí, Ribeira and Dom Feliciano belts in Brazil and the Kaoko, Damara, Gariep and Saldania belts in Africa (Pedrosa-Soares & Wiedemann-Leonardos, 2000). In the Araçuaí- West Congo, the external zone is characterized by the Araçuaí belt and one

third of the West Congo belt. The internal zone is represented by the crystalline core that comprises high-grade metamorphic rocks and granitic supersuites (Trompette, 1994).

In the last decades, several stratigraphic, geochemical and geochronology studies were carried out in units belonging to Araçuaí orogen, providing important information about its evolution. The following sections present a synthesis of the major studies related to tectonic evolution of the Araçuaí orogen.

2.1. STRATIGRAPHY

The tectonic evolution and development of the Araçuaí orogen is recorded by major lithostratigraphic units that comprise this orogenic system. The figure 2.2 shows a simplified geological map of the Araçuaí orogen.

2.1.1. Basement

The basement comprises the Guanhães, Gouveia, Porteirinha, Mantiqueira and Juiz de Fora complexes (Alkmim *et al*., 2006, 2007; Noce *et al.*, 2007a,b). These units correspond to segments of a Rhyacian orogen developed between 2.2 and 2.05 Ga, and reworked during the Brasiliano orogeny (Noce *et al.*, 2007b). The Guanhães complex is composed by Archean tonalite–trondhjemite–granodiorite (TTG) gneisses, migmatites and metavolcano-sedimentary sequences. U-Pb zircon dating of TTG gneisses range from 2867± 10 Ma to 2711 ± 11 Ma (Silva *et al.*, 2002) and leucogranite intrusion yield an age of magmatic crystallization of 2710 ± 6 Ma (Silva *et al.*, 2002). The Gouveia complex consists of migmatitic-gneiss, granitoids and greenstone belt sequence. The granitoids were crystallized at 2839 ± 14 Ma, whilst the metarhyolites of the greenstone belt yield an age of 2971 ± 16 Ma (Machado *et al.*, 1989). TTG gneisses of the Porteirinha complex dated at 3371 ± 6 Ma record two metamorphic overprinting events with ages of 3146 ± 24 Ma and 698 ± 85 Ma (Silva *et al.*, 2015). Whole-rock Sm-Nd data (epsilon Nd = - 0.78 and T_{DM} = 3500 Ma) indicate that the protholiths of these gneisses were mainly derived from the melting of a tholeiitic source (Silva *et al.*, 2015). The Mantiqueira complex consists predominantly of biotite-amphibole orthogneisses, whose U-Pb crystallization ages range from 2220 ± 52 Ma to 2041 ± 7 Ma (Silva *et al.*, 2002; Noce *et al.*, 2007a; Heilbron *et al.*, 2010). These rocks display strongly negative εNd (- 9.6 to - 13) with T_{DM} model ages ranging from 2.9 to 3.2 Ga, suggesting an Archean crust as the main source for magmas generated from of the gneiss protholiths (Noce *et al.*, 2007a). The Juiz de Fora complex comprises orthogneisses crystallized from 2199 ± 17 Ma to 1966 ± 38 Ma and metamorphosed (ca. 633-574 Ma) during the Brasiliano orogeny (Silva *et al.*, 2002; Noce *et al.*, 2007a; Heilbron *et al.*, 2010). The Nd signature of the gabbro-dioritic rocks (εNd = - 0.4 and T_{DM} = 2.3 Ga) and enderbitic gneiss (εNd = - 3.5 and T_{DM} = 2.6 Ga) indicate a mixed source of Paleoproterozoic juvenile material with contribution of Archean crust material (Noce *et al.*, 2007a).

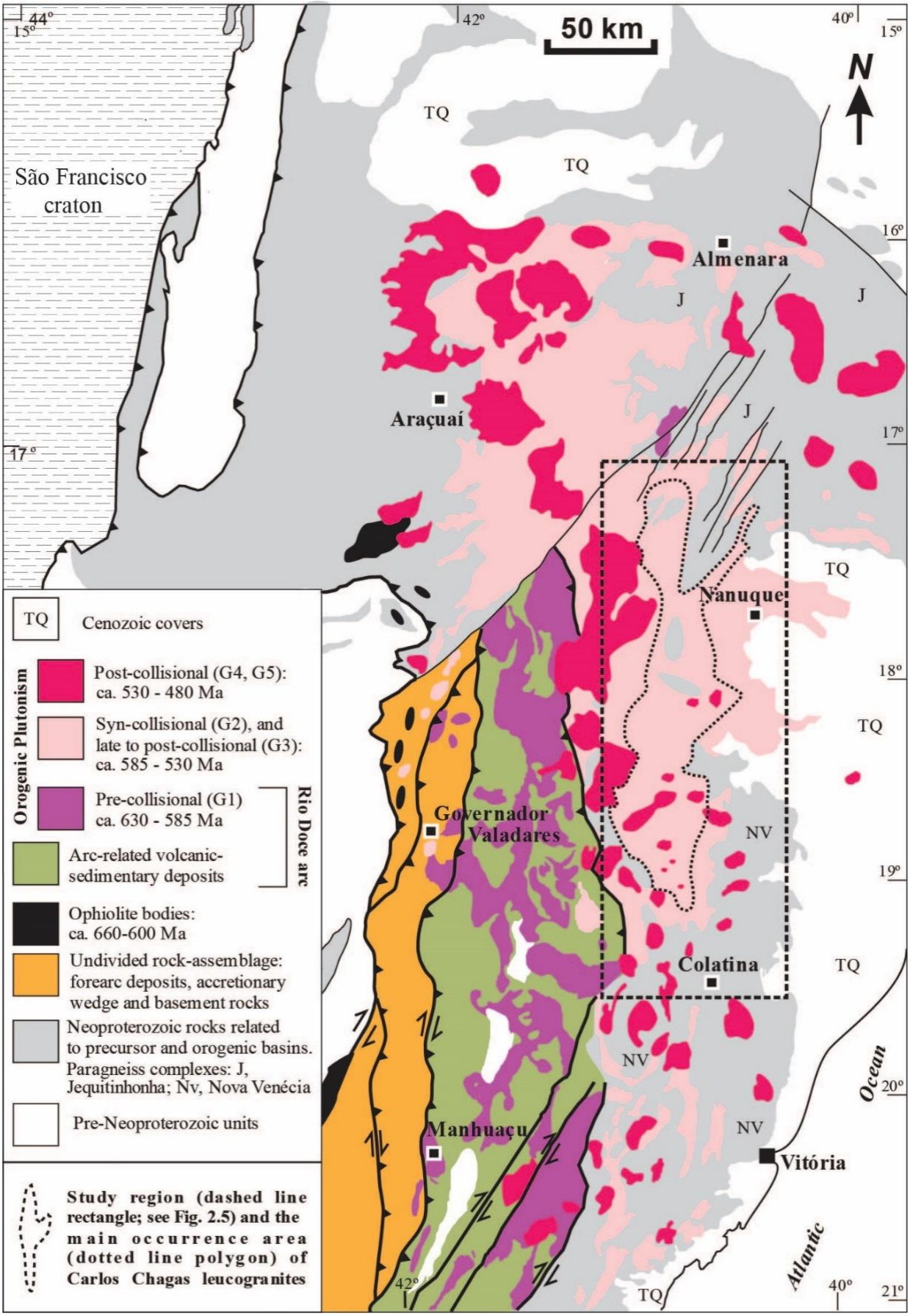

Figure 2.2 - Simplified geological map of the Araçuaí orogen (modified from Pedrosa-Soares *et al*., 2011) showing the location of the studied area (dashed line rectangle).

2.1.2. Rift-related rocks

The development of the Araçuaí- West Congo orogen was preceded by at least six events of rifting and/or anorogenic magmatism, namely as Statherian E1 (ca. 1.77-1.7 Ga), Calymmian E2 (ca. 1.57-1.5 Ga), Early Stenian E3 (ca. 1.18 - ? Ga), Stenian-Tonian E4 (ca. 1 Ga), Tonian E5 (ca. 930-850 Ma) and Cryogenian E6 (ca. 750-670 Ga) (Pedrosa-Soares & Alkmim, 2011).

The E1 event (ca. 1.77-1.7 Ga) is recorded by rift-related sedimentary and volcanic rocks of the basal section of the Espinhaço Supergroup and also by Borrachudos and Lagoa Real suites. The Borrachudos Suite consists of anorogenic alkaline granites, dated from 1770 ± 30 to 1670 ± 32 Ma (Chemale Jr. *et al.*, 1998; Fernandes, 2001; Silva *et al.*, 2002), which occur as intrusive bodies within the basement (Guanhães complex). Available U-Pb data from the Lagoa Real suite indicate that the granitoids were emplaced at 1746 ± 5 Ma (Lobato *et al.*, 2015).

The E2 event (ca. 1.57 Ga) is recorded in the northern Espinhaço and Chapada Diamantina by sediments and volcanic material from the middle portion of the Espinhaço Supergroup. In the northern Espinhaço, this episode is characterized by alluvial and aeolian sandstones and acid to intermediate volcanic rocks of the Bomba formation. The zircon U-Pb ages of 1582 ± 8 Ma and 1569 ± 14 Ma are considered as the extrusion age of the volcanic rocks (Danderfer *et al.*, 2009). In the Chapada Diamantina, the record of E2 is represented by deposition of alluvial and aeolian sediments of the Tombador formation (Chapada Diamantina group) and intrusion of dykes and sills with U-Pb ages of 1514 ± 22 Ma (Babinski *et al.*, 1999). The E3 event (ca. 1.18 - ? Ga) is recorded by syn-rift deposition of the Sopa-Brumadinho formation (Espinhaço supergroup) around 1.18. The E4 event (ca. 1 Ga) is represented by emplacement of anorogenic Noqui granites (999 ± 7 Ma; Tack *et al.*, 2001) in Africa during the opening of the Sangha aulacogen. In Brazil, this event is recorded by intrusion of mafic dykes in southern Bahia region (Renne *et al.*, 1990).

The record of the E5 event (ca. 930-850 Ma) in the West Congo belt is represented by the thick bimodal volcanic pile of the Zadinian and Mayumbian groups, as well as the intrusions of monzo-syenogranite and alkali-feldspar granite. The volcanic rocks (Mayumbian group) yield ages of 920 ± 8 Ma and 912 ± 7 Ma (Tack *et al.*, 2001), whilst gabbros and anorogenic granites exposed in the Gabon sector of the West Congo belt have ages of 904 ± 6 Ma and 867 ± 4 Ma, respectively (Thieblemont *et al.*, 2011). Mafic dykes, anorogenic granites and the deposition of the pre-glacial formation of the Macaúbas basin are the record of the E5 event in the Araçuaí orogen and São Francisco craton. A-type Salto da Divisa suite yields age of 875 ± 9 (Silva *et al.*, 2008), whilst mafic dikes (e.g., Pedro Lessa suite) give ages from 946 ± 46 Ma to 906 ± 7 Ma (Machado *et al.*, 1989; Queiroga *et al.*, 2012b; Souza, 2016). Recently, other two Tonian magmatic events have been characterized in the Macaúbas basin, corresponding to the anphibolites of the Capelinha formation (957 ± 14 Ma; Castro, 2014) and basaltic greenschists of the Planalto de Minas formation (889 ± 10 Ma; Souza, 2016).

The E6 event (ca. 750-670 Ga) is characterized by intrusions of alkaline rocks of the Southern Bahia alkaline province and deposition of diamictites of the Macaúbas Group. Pb-Pb zircon and U-Pb titanite dating of the anorogenic intrusions yield ages between 732 ± 8 Ma and 696 ± 3 Ma (Rosa *et al.*, 2007, 2015). In the West Congo belt, this event can be represented by felsic volcanism that includes rhyolites and rhyolitic tuffs (La Louila formation) with a maximum age of 713 ± 49 Ma (Thieblemont *et al*., 2011).

2.1.3. Macaúbas Group and correlative units

The Macaúbas Basin is the precursor Neoproterozoic basin of the Araçuaí orogen (Pedrosa-Soares & Akmim, 2011; Pedrosa-Soares *et al.*, 2011). This basin was partially floored by a Cryogenian oceanic crust and inverted during the Neoproterozoic Brasiliano-Pan African orogeny. The type-unit of the precursor basin is represented by the Macaúbas Group that consists of glaciogenic to siliciclastic-carbonatic deposits. These rocks record the basin evolution that includes the pre-rift, rift, transitional and passive margin stages (Pedrosa-Soares *et al.*, 2001, 2008; Alkmim & Martins-Neto, 2012). Detrital zircon U-Pb geochronology indicates maximum depositional age of the glacial diamictites around 900 Ma (Pedrosa-Soares *et al.*, 2000; Babisnski *et al.*, 2012). In contrast, detrital zircon extracted from metasandstones yield maximum depositional age for the Upper Chapada Acauã formation at ca.750 Ma (Kuchenbecker *et al.*, 2015). Dismembered ophiolite sections were found in the Ribeirão da Folha formation, consisting of ocean-floor sediments tectonically imbricated with mafic/ultramafic rocks (Pedrosa-Soares *et al.*, 1990, 1998, 2001, 2008). U-Pb zircon dating of plagiogranite patches associated with ophiolitic section give age an of 660 ± 29 Ma (Queiroga *et al.*, 2007).

2.1.4. Accretionary wedge

A suture-related accretionary wedge was described by Peixoto *et al.* (2015) in the region of São José da Safira, located to the west of the Rio Doce magmatic arc. The suture zone (30 km x 100 km) comprises pelitic schists intercalated with quartzites, metaultramafic schists and diopsidites, intruded by collisional granites of the G2 supersuite. U-Pb ages of detrital zircons to constrain the maximum deposition age of the lower succession are at 819 ± 21 Ma, similar to the passive margin deposits of the precursor basin. The youngest zircon ages (ca. 640-580 Ma) of the upper succession suggest the Rio Doce magmatic arc as the main sediment source (Peixoto *et al.*, 2015).

Thermobarometric estimates indicate that the western base of the sediment pile was metamorphosed at 700 ºC and 7.5 kbar, whilst the top of the package record lowest PT conditions (550 ºC and 5.5 kbar). Zircons extracted of the Guanhães basement gneiss yield a metamorphic age of 560 ± 20 Ma, which is within analytical uncertainties of the crystallization age of the Santa Rosa granite (544 ± 10 Ma) (Peixoto *et al.*, 2015). As this granite cut all the sequence of the accretionary wedge, Peixoto *et al.* (2015) have interpreted that the basin closure during the assembly of Western Gondwanaland occurred 20 Ma later than previously suggested in literature.

2.1.5. Orogenic magmatism

Based on field relationships, structural features and geochemical and geochronological data, the orogenic magmatism has been grouped into five supersuites (G1 to G5; Pedrosa-Soares *et al.*, 2011). The G1 supersuite (ca. 630-585 Ma) mainly comprises arc-related I-type granitoids, whilst the G2 (ca. 585-545 Ma), G3 (ca. 545-530 Ma) and G4 (ca. 530-500 Ma) supersuites included S-type granites formed from sin- to post-collisional period of the orogeny. The G5 supersuite (ca. 530-480 Ma) consist of post-collisional I- to A-type granitoids. The arc-related supracrustal sequences comprise metavolcano-sedimentary successions of the Rio Doce Group (Vieira, 2007; Novo *et al.*, 2015), which were mainly deposited during the Ediacaran period (Pedrosa-Soares *et al*., 2007a; Vieira, 2007; Queiroga *et al.*, 2012a). The sedimentation of the Tumiritinga and Palmital do Sul formations occurred in intra-arc and fore-arc zones, respectively, whilst the São Tomé formation covers the previous formations and represents the proximal part of the back-arc basin (Vieira, 2007).

2.1.6. Metamorphic complexes

The Jequitinhonha and Nova Venécia complexes mainly consist of migmatitic paragneiss derived from pelites, whose protoliths were deposited in the distal passive margin and in the back-arc basin, respectively (Noce *et al*., 2004; Pedrosa-Soares *et al.*, 2007a; Vieira, 2007; Gonçalves-Dias *et al.*, 2011; Gradim, 2013; Gradim *et al.*, 2014; Moraes *et al.*, 2015; Richter *et al.*, 2016).

The Jequitinhonha Complex is exposed in the northeast portion of the Araçuaí orogen (Figure 2.2). It comprises migmatitic paragneisses intercalated with quartzite, graphite gneiss and calc-silicate rocks. The paragneisses were metamorphosed under high-grade conditions, reaching amphibolite to granulite facies (Belém, 2006; Moraes *et al.*, 2015). PT conditions (AvPT method by THERMOCALC) for sillimanite-garnet-cordierite-biotite gneiss indicate that metamorphism reached temperatures of 791 ± 42 ºC and pressures of 5 ± 0.5 kbar (Belém, 2006). Thermobarometric estimated performed by Moraes *et al*. (2015) indicate metamorphic peak conditions of 850 ºC and 7 kbar. Detrital zircon U-Pb data of the quartzites indicates five main peaks at ca. 1.0, 1.2, 1.5, 1.8, and 2.2 Ga, indicating as sediment sources: the São Francisco-Congo craton basement, the Espinhaço-Chapada Diamantina system, and the Noqui-Zadinian-Mayumbian-Salto da Divisa rift system (Gonçalves-Dias *et al.*, 2011, 2016). The youngest zircon population indicate maximum sedimentation age around 900 Ma (Gonçalves-Dias *et al.*, 2011, 2016). Based on similar U-Pb detrital zircon age spectra and Sm-Nd isotope, Gonçalves-Dias *et al.* (2016) proposed a correlation between Jequitinhonha Complex and upper units of the Macaúbas Group.

The Nova Venécia Complex occurs in the southern portion of the Araçuaí orogen (Figure 2.2). It consists of migmatitic and granulitic paragneisses rich in biotite, garnet, cordierite and/or sillimanite, and calc-silicate rocks (Roncato, 2009; Gradim *et al.*, 2014; Richter *et al.*, 2016). Some studies have reported that the

paragneisses record the PT conditions in the transition from the amphibolite to granulite facies (Munhá *et al.*, 2005; Gradim, 2013; Gradim *et al.*, 2014; Richter *et al.*, 2016). Detrital zircons extracted of the paragneisses indicate seven populations with ages of ca. 609-612 Ma, ca. 649-652 Ma, ca.715-698 Ma, ca. 746 Ma, ca. 789–781 Ma, ca. 807-822 Ma and ca. 903–877 Ma (Richter *et al.*, 2016). An oldest detrital population is reported by Noce *et al*. (2004) and Gradim *et al.* (2014), with peak between 2086 and 2124 Ma. The peak metamorphism is recorded in monazite and zircon from the paragneisses at ca. 575-560 Ma (Richter *et al.*, 2016).

2.1.7. Salinas Formation

The Salinas formation includes metagraywackes, metapelites and clast-supported metaconglomerates with maximum depositional age of 588 Ma, and metamorphosed under greenschist to amphibolite conditions at 500 Ma (Lima *et al.*, 2002; Pedrosa-Soares *et al.*, 2008). This unit records the development of a syn-orogenic basin (flysch) between a passive margin and an orogenic front (Santos *et al*., 2009).

2.2. KINEMATIC ANATOMY OF THE ARAÇUAÍ- WEST CONGO OROGEN

Based on synthesis from previous studies, Alkmim *et al.* (2006, 2007) described the general kinematic that took place in the orogen during the Brasiliano- Pan African orogeny. At least ten major structural domains (Figure 2.3) can be recognized in the Araçuaí- West Congo orogen, which differ from each other in terms of style, orientation, shear sense and deformation history: (i) Serra do Espinhaço fold-trust belt; (ii) Chapada Acauã shear zone; (iii) Minas Novas corridor; (iv) Rio Pardo salient; (v) Paramirim aulacogen; (vi) Guanhães block; (vii) Dom Silvério shear zone; (viii) Itapebi shear zone; (ix) crystalline core; and (x) West- Congo belt.

The Serra do Espinhaço fold-trust belt (700 km) is characterized by NS-trending and west-verging system of faults and folds developed on eastern edge of the São Francisco craton. It encompasses the Archean basement, units from the Espinhaço Supergroup and Macaúbas Group, as well as mafic intrusions (Alkmim *et al*., 2007).

Chapada Acauã shear zone is a long plateau (50 x 150 km) located on the east side of the Serra do Espinhaço and north of the parallel 18ºS. This plateau is underlain by metasedimentary sequence of the Macaúbas Group. These rocks comprise the hanging wall of a regional east-dipping shear zone (Alkmim *et al*., 2007).

Minas Novas corridor (Pedrosa-Soares, 1995) is considered as dextral strike-slip shear zone (30 x 150 km) that involves the metasediments of the Macaúbas group and Salinas formation (Alkmim *et al*., 2007).

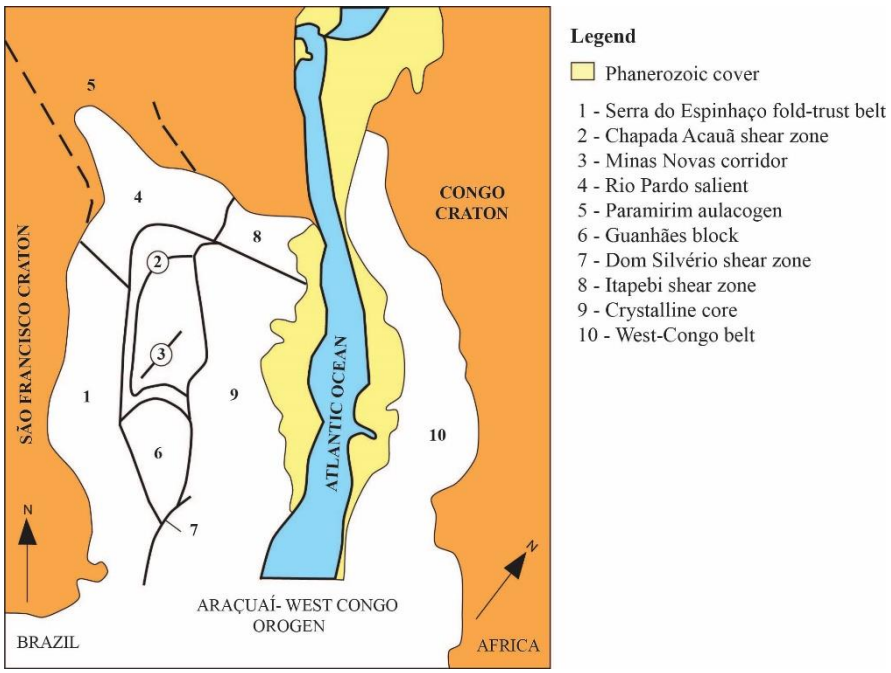

Figure 2.3 – Major structural domains of the Araçuaí- West Congo orogen (modified from Alkmim *et al.*, 2006).

The Rio Pardo salient was traced out by the internal trend-lines of the Serra do Espinhaço fold-thrust belt in a regional-scale convex-to-the-foreland curve (Cruz & Alkmim, 2006). This structure comprises rocks of the Espinhaço supergroup and Macaúbas group (Alkmim *et al.*, 2006). Cruz & Alkmim (2006) interpreted that the Rio Pardo salient was generated during an early stage of closure of the Neoproterozoic rift system.

The NNW-trending Paramirim aulacogen marks the limit between the northeast and the southeast lobe of the São Francisco Craton. This structure was initially generated by the Espinhaço rifting and reactivated during the Macaúbas rifting. In the Brasiliano- Pan African orogeny, the aulacogen was partially inverted, reactivating pre-existing normal and transfer faults (Danderfer & Dardenne, 2002).

The Guanhães Block (250 km x 140 km) is exposed southeast of the Serra do Espinhaço fold-thrust belt. It includes Archean TTG gneisses (ca. 2.9-2.7 Ga; Silva *et al.*, 2002), migmatites and Paleoproterozoic metavolcano-sedimentary sequences. This block was intruded by anorogenic granite stocks of the Borrachudos suite (1.75-1.67 Ga; (Chemale Jr. *et al.*, 1998; Fernandes, 2001; Silva *et al.*, 2002), related to the opening of the Espinhaço rift. The margins of the Guanhães Block are delineated by shear zones. In its southeastern margin, the Dom Silvério shear zone juxtaposes Rio Doce metapelites against the basement. The western margin of the block is characterized by foreland-west-verging thrust, which placed the Guanhães basement lying onto the Espinhaço Supergroup strata and over supracrustal sequences of the Quadrilátero Ferrífero. In the northern margin of the Guanhães block, a shallowly dipping shear zone juxtaposes units of the Macaúbas group against the basement, recording reverse-sinistral and normal-dextral motions (Peres *et al.*, 2004).

The Dom Silvério shear zone (100 km x 4 km) is a NNE-trending, steeply dipping belt of mylonitic rock. This structure terminates against the dextral strike-slip Abre Campo shear zone at its northern end (Alkmim *et al*., 2006, 2007).

NW-trending Itapebi shear zone is the main structure within dextral transpressive system developed at the northern edge of the Araçuaí orogen (Alkmim *et al*., 2006, 2007). This shear zone involves the Archean basement, the Salto da Divisa suite and the Jequitinhonha complex.

The crystalline core of the Araçuaí orogen is composed by paragneiss complexes (Jequitinhonha and Nova Venécia) and granitic supersuites (G1 to G5). Two distinct structural sub-domains are recognized within the crystalline core: (i) the northern sub-domain (between 16ºS and 18º30') that comprises west- and east-verging thrust-sense shear zones; and (ii) the southern sub-domain (south of 18º30') that contains a system of dextral-transpressional shear zones (Alkmim *et al*., 2006, 2007).

The West- Congo belt (900 km) is located in the west margin of the Congo craton between latitude 1º S and 10º S. It corresponds to an ENE-verging fold-thrust belt that involved the Neoproterozoic metavolcanic and metasedimentary rocks of the West Congo Supergroup and also Archaean/Paleoproterozoic basement (Alkmim *et al*., 2006).

2.3. TECTONIC EVOLUTION OF THE ARAÇUAÍ-WEST CONGO OROGEN

The Araçuaí and West Congo belts were considered counterparts of an ensialic orogen by several authors (e.g., Hasui *et al.*, 1978; Porada, 1989; Trompette, 1994; Brito-Neves & Cordani, 1991). This model was supported by the presence of a cratonic bridge in Bahia and Gabon regions (Porada, 1989), which did not allow the opening of the basin and the generation of oceanic lithosphere. However, this model was questioned by Pedrosa-Soares *et al.* (1990) based on the description of volcano-sedimentary sequences (typical of an ocean-floor environment) tectonically imbricated with slabs of mafic/ultramafic rocks (Ribeirão da Folha formation). The discovery of the oceanic crust remnants (Pedrosa-Soares *et al*., 1990, 1992) and the description of the Neoproterozoic magmatic arc (Nalini, 1997) allowed a better understanding of the evolution of the Araçuaí- West Congo orogen.

Based on these previous data, Pedrosa-Soares *et al*. (2001) proposed the concept of "confined orogen". This model suggests that the precursor basin remained ensialic in its northern portion by presence of the Bahia-Gabon cratonic bridge (Porada, 1989), whilst in southern sector occurred the oceanic opening (characterized by ophiolitic remnants) and generation of the magmatic arc. Currently, the kinematic model called "tectonic Nutcracker" (Alkmim et al., 2006, 2007) demonstrates that the tectonic evolution of the Araçuaí- West Congo orogen comprises five major stages (Pedrosa-Soares *et al.*, 2007a, 2008, Alkmim *et al*., 2006, 2007), which are described below:

2.3.1. Stage 1: Opening of the Macaúbas basin

The stage 1 corresponds to the opening of the precursor Neoproterozoic basin of the Araçuaí orogen (Macaúbas basin) by a rift event between São Francisco and Congo cratons around 880 Ma (Silva *et al.*, 2008). This basin evolved into two passive margins that remain connected by Bahia-Gabon cratonic bridge (Porada, 1989). The sedimentary record related to continental rift phase of the basin (ca. 906-880 Ma) is characterized by basal and proximal units of the Macaúbas Group. On the hand other, the magmatic record is represented by mafic dikes from the south Bahia (ca. 1.0 Ga; Renné *et al.*, 1990), amphibolites from the Capelinha formation (957 ± 14 Ma; Castro, 2014); metagabbros/metadiabases from the Pedro Lessa suite (946 ± 46 Ma to 906 ± 7 Ma; Machado *et al.*, 1989; Queiroga *et al.*, 2012b; Souza, 2016); basaltic greenschists of the Planalto de Minas formation (889 ± 10 Ma; Souza, 2016); and anorogenic granites from the Salto da Divisa suite (875 ± 9 Ma; Silva *et al.*, 2008). According to Pedrosa-Soares *et al.* (1992), the opening of the Macaúbas basin was accommodated in the north of the orogen by a transfer fault (Figure 2.4a).

The passive margin phase of the basin is recorded by deposition of deep-sea sediments and occurrence of ophiolitic remnants (Pedrosa-Soares *et al.*, 1990, 1992, 1998; Queiroga *et al.*, 2007). The U-Pb age of 660 ± 29 Ma (LA-ICP-MS) obtained in zircon from plagiogranite patches associated to ophiolitic sections (Ribeirão da Folha formation), indicates that the Macaúbas basin was probably in development in this time (Queiroga *et al.*, 2007). The long-lived basin (~ 220 Ma) may be related to low lateral expansion rates of the Macaúbas gulf due to the basin being surrounded by cratonic domains (Alkmim *et al.*, 2007).

2.3.2. Stage 2: Initial closure of the Macaúbas basin

The stage 2 involved the tectonic convergence on both passive margins from the Macaúbas basin around 630 Ma (Pedrosa-Soares *et al.*, 2001; Silva *et al.*, 2005). The closure of the basin has been interpreted as a consequence of the collision between the southwestern margin of the São Francisco craton and the Paranapanema block (Seer *et al.*, 2001; Valeriano *et al.*, 2004). According to the "Nutcracker tectonic model" proposed by Alkmim *et al.* (2006), the southern edge of the São Francisco craton rotated counterclockwise leading to the closure of the Macaúbas basin. This compressive event induced the subduction of the oceanic crust beneath the Congo craton, which led to the formation of a magmatic arc (Figure 2.4b). The arc-related plutonic magmatism is characterized by the emplacement of I-type granitoids of the G1 supersuite (ca. 630-585 Ma; Pedrosa-Soares & Wiedemann-Leonardos, 2000; Pedrosa-Soares *et al.*, 2011), whilst the explosive volcanism is represented by metavulcano-sedimentary sequence from the Rio Doce Group (Vieira, 2007).

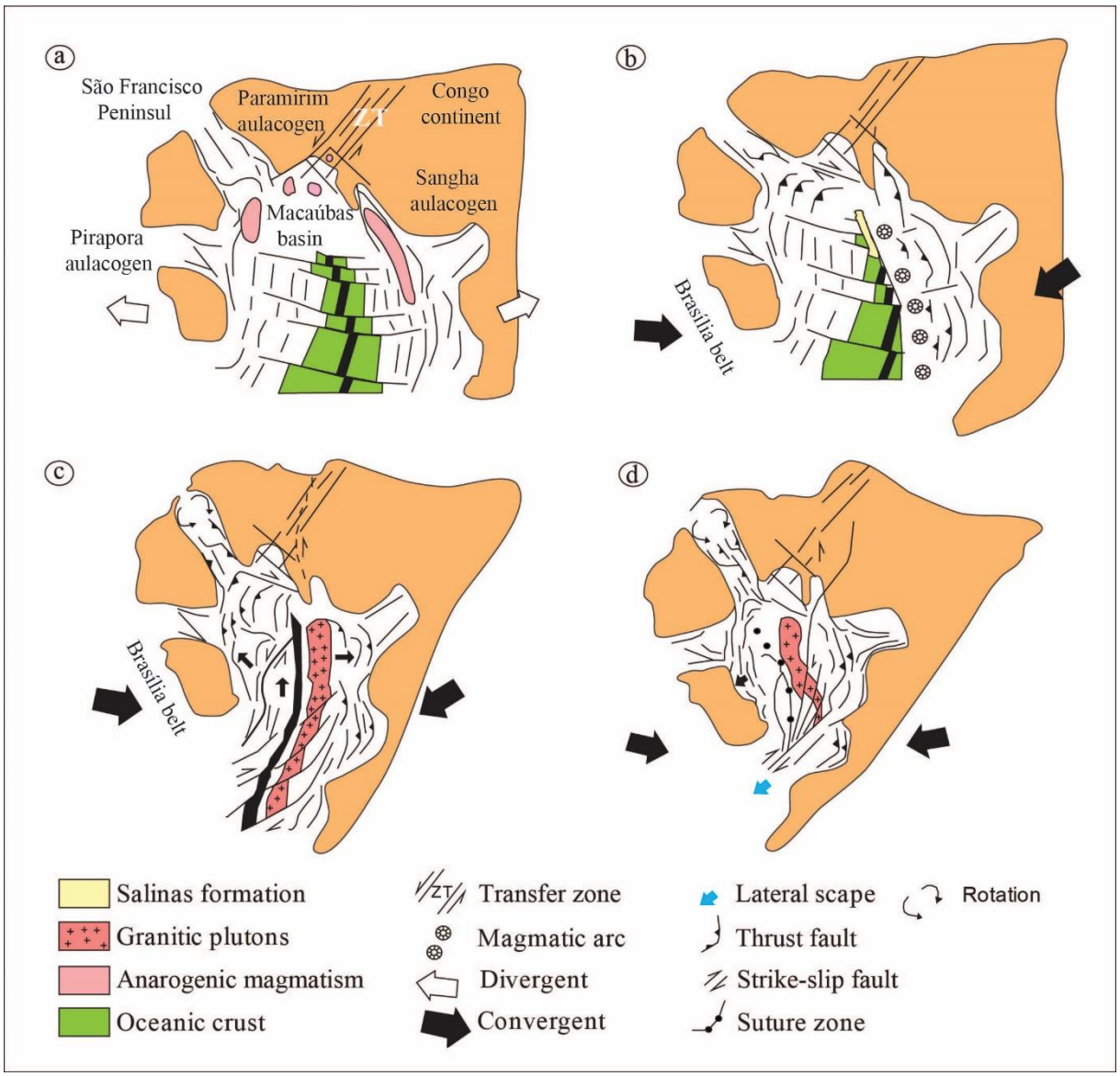

Figure 2.4 – Tectonic nutcracker model proposed for evolution of the Araçuaí- West Congo orogen (modified from Alkmim *et al.*, 2006 and Vieira, 2007). (a) Macaúbas basin at ca. 800 Ma. (b) Initial convergence of the Macaúbas basin margins (~ 630 Ma) as consequence of the interaction between São Francisco craton and Paranapanema block, causing the formation of the magmatic arc in eastern margin. (c) Collisional stage of the orogen (~ 590 Ma) and generation of the G2 supersuite. (d) Lateral scape of the southern Araçuaí- West Congo orogen and gravitational collapse.

2.3.3. Stage 3: Full closure of the Macaúbas basin

The stage 3 corresponds to the full closure of the Macaúbas basin (~ 580 Ma) that led to the development of the Araçuaí- West Congo orogen. The collision of the passive margins generated fold-trust belts toward the cratons, as well as uplift mountain at ca. 580-560 Ma (Alkmim *et al.*, 2007; Pedrosa-Soares *et al.*, 2007a). The magmatic record of this stage is characterized by the emplacement of S-type granites of the

G2 supersuite (Figure 2.4c) (ca. 585-545 Ma; Pedrosa-Soares & Wiedemann-Leonardos, 2000; Pedrosa-Soares *et al.*, 2007a, 2011). These bodies are considered to be the product of anatexis of aluminous metasedimentary rocks (Pedrosa-Soares *et al*, 2007b). The collisional stage probably occurred between 590 and 560 Ma, which is interval ages correspond to G2 production and regional metamorphism (Nalini *et al*., 2000; Noce *et al*., 2000; Silva *et al.*, 2002, 2011; Vauchez *et al*., 2007; Roncato, 2009; Pedrosa-Soares *et al.*, 2011; Gradim *et al*., 2014; Gonçalves *et al.*, 2015; Richter *et al*., 2016).

2.3.4. Stage 4: Southward scape of the Southern Araçuaí- West Congo orogen

In the stage 4 (ca. 560-535 Ma), the crustal thickening associated to continuous convergence led to lateral scape of the southern part of the orogen towards Ribeira orogen (Figure 2.4d). The tectonic record of this stage corresponds to dextral strike-slip faults system exposed in southward crystalline core of the orogen (Alkmim *et al.*, 2006, 2007). The G3 supersuite (ca. 545-530 Ma) is interpreted to have formed during the late- to post-collisional stage of the orogeny (Noce *et al.*, 2004; Silva *et al.*, 2005; Silva *et al*., 2007; Pedrosa-Soares *et al*., 2011; Gradim *et al.*, 2014). It consists of garnet- and/or cordierite-bearing leucogranites veins and patches that overprinting the regional foliation. These rocks are interpreted as anatectic product of the G2 granites and paragneiss complexes (Pedrosa-Soares *et al.*, 2001, 2006, 2007b, 2011; Gradim *et al.*, 2014).

2.3.5. Stage 5: Orogenic collapse

The stage 5 (ca. 520-490 Ma) corresponds to gravitational collapse of the central part of the orogen, induced by orogenic overload. Extensional structures related to tectonic collapse, such as normal shear zones (e.g., Chapada Acauã shear zone) and fracture systems, are typical for the whole orogen (Alkmim *et al*., 2006, 2007; De Campos *et al.*, 2016). The asthenosphere upwelling in response to thinning crustal during the gravitational collapse provide the partial melting of the mid- to lower crust (Pedrosa-Soares & Wiedemann-Leonardos, 2000; Alkmim *et al.*, 2006, 2007) and generation of the post-collisional G4 (ca. 530-500 Ma) and G5 (ca. 525-480 Ma) Ma supersuites (Noce *et al*., 2000; De Campos *et al*., 2004, 2016; Mendes *et al.*, 2005; Silva *et al.*, 2007; Petitgirard *et al*., 2009; Baltazar *et al.*, 2010; Gradim *et al.*, 2014).

2.4. INTERNAL ZONE OF THE ARAÇUAÍ OROGEN

The studied area is located in the eastern portion of the Araçuaí orogen that comprises high-grade metamorphic rocks and granitic supersuites generated during the pre- to post-collisional stages of the orogeny (Figure 2.5). The most important units for this study are: (i) paragneisses and migmatites of the Nova Venécia complex, whose protholiths were deposited in a back-arc basin (Noce *et al.*, 2004; Gradim *et al.*, 2014; Richter *et al.*, 2016); (ii) metavulcano-sedimentary sequences of the Rio Doce group (Vieira, 2007; Novo, 2013); and (iii) G1 to G5 supersuites (Pedrosa-Soares *et al*., 2011).

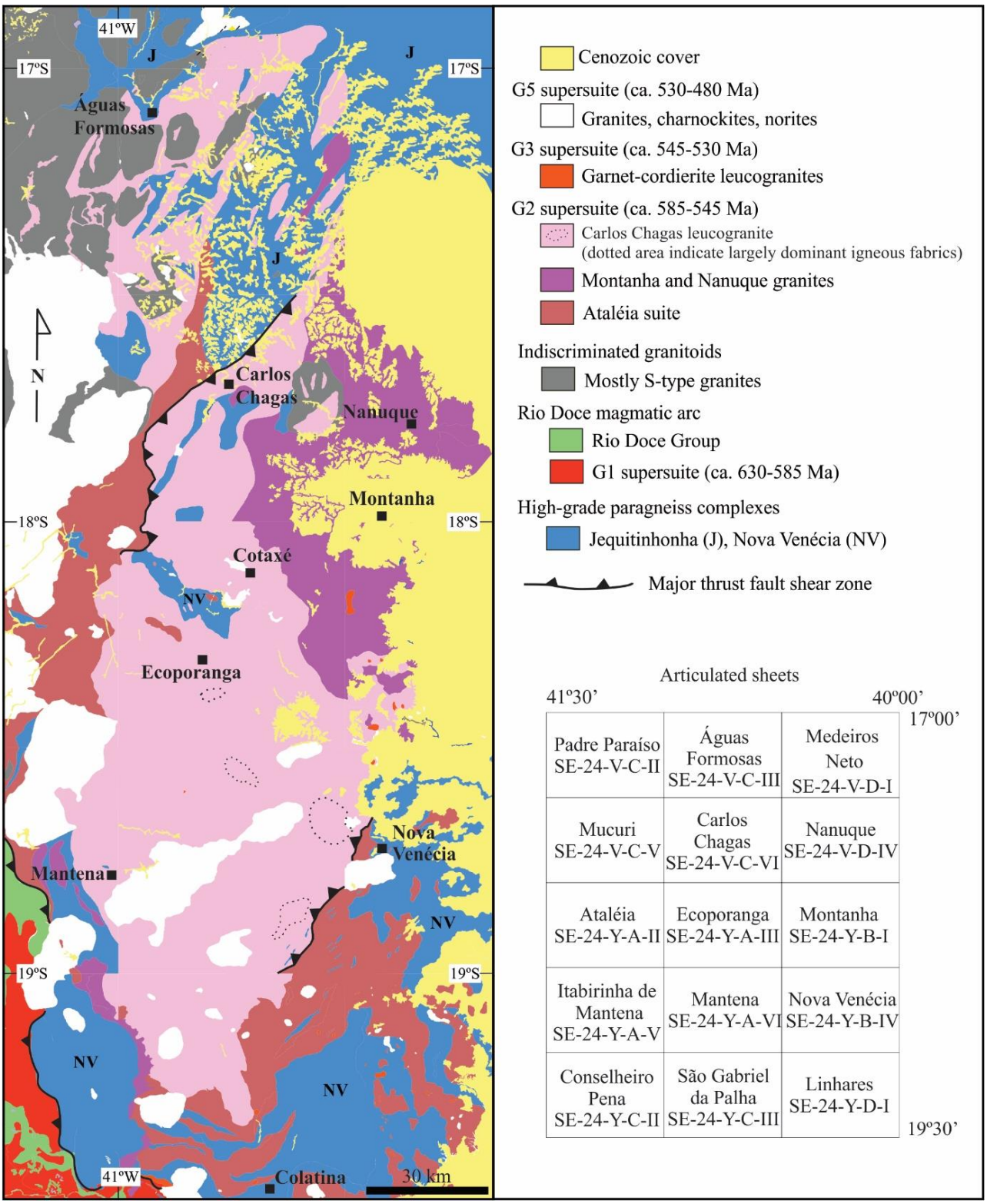

Figure 2.5 - Simplified geological map for the study region (compiled from 1:100.000 scale maps published by Pinto *et al.*, 2001; Castañeda *et al.*, 2006; Gradim *et al.*, 2007; Baltazar *et al.*, 2010; Queiroga *et al.*, 2012a; Roncato *et al.*, 2012), showing the area covered by the Carlos Chagas batholith.

2.4.1. Nova Venécia complex

The Nova Venécia Complex (Pedrosa-Soares *et al*., 2007b, 2008) consists of migmatitic paragneisses, granulites and calcsilicate rocks. The migmatites commonly show stromatic structure, where leucosomes and melanosomes are spaced regularly and oriented parallel to the foliation defined by biotite; subordinately there is the occurrence of ptygmatic folds, schlieren and flebitic structures (Roncato, 2009; Queiroga *et al*., 2012a; Gradim *et al*., 2014; Richter *et al.*, 2016). Leucosomes locally cross-cut the foliation, forming a network of interconnected felsic segregations. The presence of calc-silicate rock lenses is interpreted as relicts of the sedimentary layering (Roncato, 2009). Both cordierite-bearing granulite and migmatitic paragneisses record the foliation developed during regional deformational event (Roncato, 2009; Gradim, 2013).

The contact of the Nova Venécia complex with Ataléia suite is gradational, marked by an increase of migmatization intensity until the Ataléia granite is predominant, with xenoliths of paragneisses and calcsilicate rocks (Roncato, 2009; Gradim *et al*., 2014). Based on field observations, some studies have been interpreted the Ataléia suite (G2 supersuite – ca. 585-545 Ma) as an anatectic product from the paragneisses (Pedrosa-Soares *et al*., 2007b; Gradim *et al.*, 2014). The Nova Venécia complex was intruded by post-collisional granitic rocks (G5 supersuite – ca. 525-480 Ma), which produced contact metamorphism aureoles. The Nova Venécia complex protholiths were probably greywackes enriched in clay and silt components, deposited in back-arc basin (Pedrosa-Soares *et al*., 2008; Roncato, 2009; Roncato *et al*., 2012; Gradim *et al.*, 2014; Richter *et al*., 2016).

U-Pb ages of detrital zircon in paragneisses indicate at least eight populations, with peak at: (i) 609-631 Ma; (ii) 641-652 Ma; (iii) 698-715 Ma; (iv) 746 Ma; (v) 774-789 Ma; (vi) 807-822 Ma; (vii) 77-903 Ma; and (viii) 2086-2124 Ma (Noce *et al*., 2004; Gradim *et al.*, 2014; Richter *et al.*, 2016). These ages may correlate to reported ages of the Rio Doce magmatic arc, southern Rio Negro arc and Serra da Bolívia complex (ca. 585-650 Ma; Heilbron & Machado, 2003; Noce *et al*., 2004; Pedrosa-Soares *et al.*, 2011; Heilbron *et al.*, 2013; Novo, 2013; Gonçalves *et al.*, 2014, 2015; Tedeschi *et al.*, 2016), rocks associated with ophiolitic remnants (ca. 660 Ma; Queiroga *et al.*, 2007), rift-related Southern Bahia Alkaline Province (ca. 696-732 Ma; Rosa *et al*., 2007, 2015), early portions of the Rio Negro magmatic arc in the Ribeira belt (ca. 790 Ma; Tupinambá *et al.*, 2012); Salto da Divisa and Pedro Lessa suites (ca. 887-906 Ma; Machado *et al.*, 1989; Silva *et al.*, 2008) and Paleoproterozoic basement (Noce *et al.*, 2007a). However, the provenance of the populations with ages at ca. 807-822 is uncertain. The maximum sedimentation age of the Nova Venécia complex is 606 Ma (Richter *et al.*, 2016).

Based on the mineral paragenesis of the paragnaisses (cordierite + garnet + sillimanite + hercynite + biotite), some studies have considered that the metamorphism took place at amphibolite to granulite facies conditions (Castañeda *et al.*, 2006; Pedrosa-Soares *et al*., 2007b). Semi-quantitative thermobarometric estimates indicate temperatures of 712-930º and pressures of 5-6.1 kbar (Gradim, 2013). According to Munhá

et al. (2005), the metamorphism peak was reached at 820 ± 30 ºC and 6.5 ± 0.5 kbar. Phase equilibrium modelling carried out by Richter *et al.* (2016) indicates that the metamorphism peak took place at temperatures of 750-850 °C and pressures 5.3-7.5 kbar, followed by high-temperature retrograde evolution at 640-800 ºC and 4.5-6 kbar. The high-grade metamorphic peak is recorded in monazite and zircon grains of the Nova Venécia complex between 575 and 560 Ma (Söllner *et al.*, 2000; Gradim *et al.*, 2014; Richter *et al.*, 2016). A second metamorphic event (ca. 495-513 Ma) is recorded in monazites from the paragneisses, being associated with emplacement of the G5 supersuite (Richter *et al.*, 2016).

2.4.2. Rio Doce Group

The Rio Doce group consists of arc-related metavolcano-sedimentary sequence which includes, from the base to the top, the Palmital do Sul, Tumiritinga, São Tomé and João Pinto formations (Vieira, 2007) (Figure 2.6).

The Palmital do Sul formation consists of pelitic schists to paragneisses with intercalations of quartzites and metavolcanic rocks (Vieira, 2007; Gonçalves, 2009). The pyroclastic volcanic rocks have lapilli and bomb fractions that are indicative of deposition relatively close to volcanic edifice (Vieira, 2007). P-T conditions calculated from the garnet-bearing schists (via conventional thermobarometry) show that the garnet grew with increasing temperature (from ca. 450°C up to 580°C) under decompression conditions (from ca. 8 to 5.8 kbar) (Novo, 2013). The zircon U-Pb ages of 584 ± 5 Ma to 595 ± 13 Ma (TIMS and SHRIMP methods) of the pyroclastic tuff of dacitic to rhyolitic composition are interpreted as the timing of the formation of volcanic edifices in the Araçuaí orogen (Vieira, 2007; Gonçalves, 2009; Novo, 2013) (Table 2.1). At least five distinct populations of detrital zircon are identified in the schists, with peak ages of: (i) 3252 ± 72 Ma; (ii) 2493 ± 18; (iii) 1980 ± 16; (iv) 1325 ± 16; and (v) 766 ± 4 Ma (Novo, 2013). The age of 665 ± 25 Ma (LA-ICP-MS) obtained from the youngest detrital zircon grains is interpreted to represent the maximum sedimentation age of the metapelitic rocks (Novo, 2013).

The Tumiritinga formation mainly comprises calc-silicate rocks, marbles and quartz- biotite schists (Gonçalves, 2009), whose protoliths were deposited in marine environment. Metavolcanoclastic rocks of dacitic composition have high ash content, indicating distal deposition regard to pyroclastic rocks of the Palmital do Sul formation (Vieira, 2007). Based on average PT method by THERMOCALC, the metamorphism recorded in these rocks ranges from greenschist (468 ± 50 ºC and 4.96 ± 1 kbar) to upper amphibolite (638 ± 76 ºC and 4.56 ± 1 kbar) facies (Castañeda *et al.*, 2006). The U/Pb age of 585 ± 4 Ma (LA-ICP-MS) obtained in zircon from the metavolcanoclastic sequence is interpreted as the age of magmatic crystallization (Vieira, 2007) (Table 2.1).

The São Tomé formation comprises mica schist and metasandstones with intercalations of marbles and calc-silicate rocks, which were deposited in a deep-marine slope environment (Vieira, 2007; Gonçalves, 2009).

These rocks were metamorphosed at amphibolite facies conditions. Detrital zircon grains extracted from the metasandstone indicate as provenance the Paleoproterozoic basement (ca. 2.0-2.2 Ga), rift-related rocks (996 ± 5 Ma) and rocks from the magmatic arc (643± 3 Ma and 594 ± 3 Ma) (Table 2.1). The maximum age of sedimentation is 594 ± 3 Ma (LA-ICP-MS) (Vieira, 2007).

Table 2.1 - Zircon U-Pb ages (Ma) from the Rio Doce group.

Formation	Rock	Method	Crystallization age	Detrital population	Maximum age of sedimentation	Reference
	Dacitic tuff	TIMS	584 ± 5			Vieira (2007)
Palmital do Sul	Schist	LA-ICP-MS		3252 ± 72 2493 ± 18 1980 ± 16 1325 ± 16 766 ± 4	665 ± 25	Novo (2013)
	Metavolcanic	SHRIMP	595 ± 13			Novo (2013)
Tumiritinga	Metavolcanoclastic	LA-ICP-MS	585 ± 4			Vieira (2007)
São Tomé	Metasandstone	LA-ICP-MS		2200-2000 996 ± 5 643 ± 3	594 ± 3	Vieira (2007)
João Pinto	Quartzite	LA-ICP-MS		2976 ± 62 2087 ± 12 1824 ± 21 1201 ± 24	619 ± 19	Novo (2013)

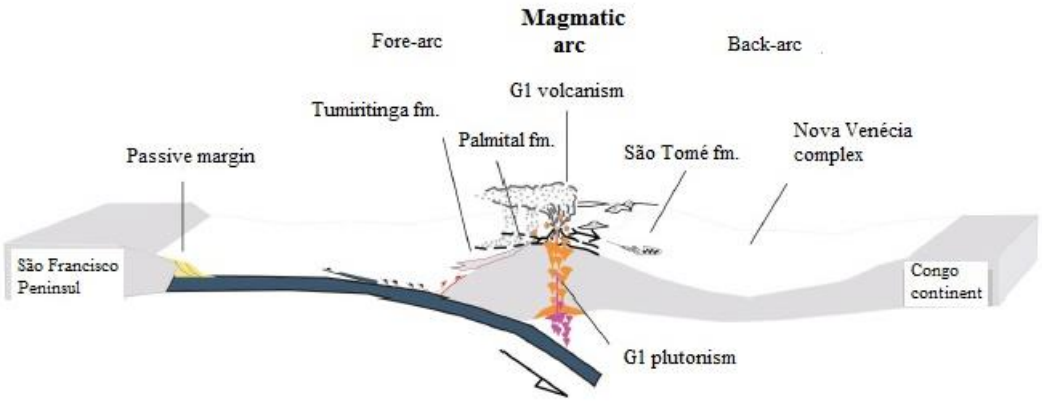

Figure 2.6 – Paleoenvironmental model proposed by Vieira (2007) for deposition of the metavulcano-sedimentary sequences (Rio Doce group) and emplacement of arc-related granitoids (G1 supersuite).

The João Pinto formation consists of quartzites with rare interbedded schists and calcsilicate rocks (Vieira, 2007). Detrital zircon ages spectrum of the quartzites shows peaks at 1201 ± 24 Ma, 1824 ± 21 Ma, 2087 ± 12 Ma and 2976 ± 62 Ma (Table 2.1). According to Novo (2013), the potential sources of the detrital zircons are the magmatic rocks of the Espinhaço-Chapada Diamantina system (ca. 1.2 Ga, ca. 1.5 Ga, ca. 1.75 Ga; Pedrosa-Soares & Alkmim, 2011; Chemale-Jr *et al*., 2012), Rhyacian-Orosirian basement (Noce *et al*., 2007a; Heilbron *et al.*, 2010) and possibly Arquean rocks from the São Francisco and Congo cratons (Teixeira *et al*., 2000; Tack *et al.*, 2001). The maximum age of sedimentation of the quartzites is 619 ± 19 Ma, indicating Rio Doce magmatic arc as major provenance of these grains (Novo, 2013).

2.4.3. Granitic Supersuites

The granitic magmatism in the Araçuaí orogen was initially described by Guimarães & Barbosa (1934) during the geological mapping of Minas Gerais. In the last two decades, several studies have reported new petrological, structure features, geochemical signature and geochronological data about granitic suites in the Araçuaí orogen. Based on these data, the granitic magmatism was divided into six suites named of G1, G2, G3S, G3I, G4 e G5 (Pedrosa-Soares & Wiedemann-Leonardos, 2000; Pedrosa-Soares *et al*., 1999, 2001; Silva *et al.* 2005). Posteriorly, these huge intrusive bodies were regrouped into five suites (G1, G2, G3, G4 and G5) based on additional data obtained by De Campos *et al.* (2004) and Pedrosa-Soares *et al*. (2008). Pedrosa-Soares *et al.* (2011) proposed the substitution from the term suite for supersuite due to innumerous names given locally to different plutons. The main features of the supersuites (G1 to G5) are synthetized in Table 2.2.

G1 Supersuite (ca. 630-585 Ma)

The G1 supersuite consists of metaluminous to slightly peraluminous, medium- to high-K, calc-alkaline, I-type granitoids generated during the pre-collisional stage of the Araçuaí orogen (Novo *et al.*, 2010; Gonçalves *et al.*, 2014, 2015; Tedeschi *et al.*, 2016). G1 mainly comprises tonalitic to granitic bodies (including orthopyroxene-bearing equivalents) and subordinately gabbroic to enderbitic facies (Pedrosa-Soares *et al.*, 2001; Gonçalves, 2009; Novo, 2013; Gonçalves *et al.*, 2014, 2015; Tedeschi *et al.*, 2016). These rocks were deformed and metamorphosed during the Brasiliano orogeny, being that some bodies show evidences for migmatization. Locally, some rocks are free of solid-state foliation with preserved igneous features (Pedrosa-Soares *et al*., 2011; Novo, 2013; Gonçalves *et al*., 2014, 2015; Tedeschi *et al.*, 2016).

Based on geochemical signature, several studies have interpreted that the most G1 granitic rocks are related to continental magmatic arcs (Nalini, 1997; Pedrosa-Soares & Wiedemann-Leonardos, 2000; Pedrosa-Soares *et al*., 2001, 2011; De Campos *et al*., 2004; Silva *et al*., 2005; Vieira, 2007; Novo, 2013; Gonçalves *et al.*, 2014, 2015; Tedeschi *et al.*, 2016). Nalini (1997) reported the presence of calcic garnet and anorthite-rich plagioclase in enclaves from the Galiléia suite as indicative of mantle contributions to granite genesis.

Table 2.2 - Orogenic magmatism from the Araçuaí orogen (Compilation from Pedrosa-Soares *et al.*, 2011; Gradim *et al*., 2014; Gonçalves *et al*., 2015 and Tedeschi *et al.*, 2016).

Supersuites	Age (Ma)	Tectonic stage	Main rock types*	Geochemical signature	Origin
G1	630 - 585	Pre-collisional	Tonalite to granite and minor gabbro to enderbite	I-type, metaluminous to slighly peraluminous, medium- to high-K, calc-alkaline	Plutonism related to the Rio Doce magmatic-arc
G2	585 - 545	Sin-collisional	Syenogranite to tonalite and syenogranite to granodiorite	Mostly S-type, peraluminous, sub- to calc-alkaline	Generated mostly from anatexis of metassedimentary rocks
G3	545 - 530	Late- to post-collisional	Leucogranite (alkali-granite to syenogranite)	S-type, peraluminous, subalkaline	Generated mostly from anatexis of G2 granites
G4	530 - 500	Post-collisional	Two-mica granites, pegmatites and minor biotitegranites	Mostly S-type, mostly peraluminous sub-alkaline	S-type event of granite genesis related to the orogenic gravitational collapse
G5	530 -480	Post-collisional	Syenogranite to granodiorite and minor norite to enderbite	I- to A-types, metaluminous to slightly peraluminous, high K-Fe calc-alkaline to alkaline	Predominant mantle contribution, partial re-melting from a mainly metaluminous continental crust, and dehydration melting from slightly peraluminous rocks

* G1, G2 and G5 can included orthopyroxene-bearing granites.

However, Rb/Sr, Sm/Nd and Lu-Hf isotope data from the G1 rocks indicate significant crustal contribution during their genesis, implying interaction of mantle magma and continental crust material (Nalini, 1997; Gonçalves *et al.*, 2015). Sm-Nd isotopic data from the gabbro-norite to diorite facies (epsilon Nd = -6.9 to -9.1 and T_{DM} = 1.62 to 2.09 Ga) further support the interpretation of involvement of Neoproterozoic mantle magma during the melting of the Paleoproterozoic basement (Pedrosa-Soares *et al.*, 2011).

Zircon U-Pb ages indicate that most of the G1 rocks crystallized between 630 and 585 Ma (Table 2.3; Söllner *et al.*, 1991; Nalini, 1997; Paes, 1999; Noce *et al*., 2000; Silva *et al.*, 2005, 2011; Figueiredo, 2009; Novo, 2009, 2013; Petitgirard *et al*., 2009; Baltazar *et al.*, 2010; Pedrosa-Soares *et al.*, 2011; Mondou *et al*., 2012; Gonçalves *et al*., 2014, 2015; Gradim *et al.*, 2014; Tedeschi *et al.*, 2016). However, some studies have reported youngest ages for late plutonism in the western arc region (~ 575 Ma; Noce *et al*., 2000; Gonçalves *et al*., 2015; Tedeschi *et al.*, 2016). The oldest G1 rocks (ca. 630-590 Ma) underwent by a migmatization event at ca. 585 Ma, as indicated by U-Pb analyses carried out on metamorphic overgrowths (Gonçalves *et al.*, 2015; Tedeschi *et al.*, 2016).

Table 2.3 - Zircon U-Pb ages (Ma) from the G1 supersuite.

Batholith/Stocks	Method	Magmatic crystallization	Metamorphism	Inherited	Reference
Cuité Velho	SHRIMP	630 ± 3			Silva *et al.* (2005)
Chapada do Bueno	Pb/Pb	625 ± 11			Paes (1999)
Rancho Alegre	LA-ICP-MS	622 ± 24			Silva *et al.* (2011)
	LA-MC-ICP-MS	618 ± 9	589 ± 7		Gonçalves *et al*. (2015)
	LA-MC-ICP-MS	607 ± 9	587 ± 10		Gonçalves *et al*. (2015)
	LA-MC-ICP-MS	595 ± 13	576 ± 7		Gonçalves *et al*. (2015)
Baixo Guandu	SHRIMP	621 ± 5		835 ± 15	Novo (2013)
	SHRIMP	621 ± 5		835 ± 15	Tedeschi *et al.* (2016)
	SHRIMP	589 ± 14			Gradim *et al*. (2014)
Pedra do Sino	LA-MC-ICP-MS	616 ± 12	555 ± 7		Gonçalves *et al*. (2015)
	LA-MC-ICP-MS	584 ± 13			Gonçalves *et al*. (2015)
Serra do Valentim	LA-MC-ICP-MS	605 ± 8	590 ± 7		Tedeschi *et al.* (2016)
Chaves	SHRIMP	599 ± 15			Tedeschi *et al*. (2016)
Mascarenhas	LA-ICP-MS	590			Baltazar *et al.* (2010)
Brasilândia	Pb-Pb evaporation	595 ± 3			Noce *et al*. (2000)
	SHRIMP	581 ± 11			Tedeschi *et al*. (2016)

Divino	LA-ICP-MS	595 ± 4 592 ± 7			Novo (2009)
Galiléia	TIMS	594 ± 6			Nalini (1997)
	LA-ICP-MS	585 ± 4			Mondou *et al*. (2012)
	LA-ICP-MS	583 ± 4			Mondou *et al*. (2012)
	LA-ICP-MS	582 ± 7			Mondou *et al*. (2012)
	LA-ICP-MS	581 ± 4			Mondou *et al*. (2012)
	LA-ICP-MS	579 ± 4			Mondou *et al*. (2012)
Muriaé	LA-ICP-MS	593 ± 4			Figueiredo (2009)
	SHRIMP	592 ± 4			Figueiredo (2009)
	LA-ICP-MS	582 ± 8			Figueiredo (2009)
	SHRIMP	620 ± 3	592 ± 4		Tedeschi *et al*. (2016)
Complexo Quirino	SHRIMP	586 ± 7		2012 ± 16 2029 ± 5 2132 ± 7	Novo (2013)
Manhuaçu	LA-ICP-MS	597 ± 3			Pedrosa-Soares *et al.* (2011)
	SHRIMP	585 ± 5			Silva *et al.* (2011)
	LA-ICP-MS	584 ± 5			Silva *et al*. (2011)
Estrela-Muniz Freire	LA-ICP-MS	588 ± 4			Pedrosa-Soares *et al.* (2011)
	TIMS	580 ± 6			Söllner *et al*. (1991)
Conceição da Boa Vista	SHRIMP	586 ± 7			Tedeschi *et al.* (2016)
Derribadinha	LA-ICP-MS	580 ± 8			Petitgirard *et al.* (2009)
		597 ± 4		~ 2100	Gonçalves *et al*. (2014)
São Vítor	LA-ICP-MS	585 ± 7			Mondou *et al*. (2012)
	LA-ICP-MS	583 ± 4			Mondou *et al*. (2012)
	LA-ICP-MS	582 ± 6			Mondou *et al*. (2012)
	Pb-Pb evaporation	576 ± 4			Noce *et al.* (2000)
Bom Jesus da Vitória	LA-MC-ICP-MS	575 ± 6			Gonçalves *et al.* (2015)
Guarataia	Pb-Pb evaporation	574 ± 2			Noce *et al.* (2000)
	SHRIMP	576 ± 9			Tedeschi *et al.* (2016)
Topázio	LA-MC-ICP-MS	574 ± 7			Gonçalves *et al*. (2015)

This supersuite comprises batholiths and stocks locally named as Alto Capim, Baixo Guandu, Bom Jesus da Vitória, Brasilândia, Chapada do Bueno, Chaves, Conceição da Boa Vista, Cuieté Velho, Derribadinha, Divino, Estrela-Muniz Freire, Galiléia, Guarataia, Manhuaçu, Mascarenhas, Muriaé, Pedra do Sino, Rancho Alegre, São Vitor, Serra do Valentim, Teófilo Otoni and Topázio (Pedrosa-Soares & Wiedemann-Leonardos, 2000; Pedrosa-Soares *et al.*, 2001, 2011; Vieira, 2007; Gonçalves, 2009; Novo, 2013).

G2 Supersuite (ca. 585-545 Ma)

The G2 rocks were initially included in the Barbacena-Paraíba do Sul complex (Fontes *et al.*, 1978), and later in the Medina and Montanha complexes (Silva, 1987). Based on field relation, structural features, petrography, geochemical signature and geochronological data, Pedrosa-Soares & Wiedemann-Leonardos (2000) proposed the inclusion of these granitic bodies within the G2 supersuite. It consists of peraluminous, subalkaline to calc-alkaline, S-type granites formed during the sin-collisional stage of the orogeny (Pedrosa-Soares & Wiedemann-Leonardos, 2000; Pedrosa-Soares *et al.*, 2006, 2007a; Roncato, 2009; Nalini *et al.*, 2015).

G2 occurs as batholiths, stocks and tabular bodies that show ductile deformational structures related to compressive tectonic event. Locally, some bodies display preserved igneous features (Pedrosa-Soares & Wiedemann-Leonardos, 2000; Pedrosa-Soares *et al*., 2007b; Castañeda *et al.*, 2006; Roncato, 2009). The generation of large amounts of S-type granites in the Araçuaí orogen is interpreted as consequence of the upwelling asthenosphere beneath the back-arc zone (Pedrosa-Soares *et al*., 2006). This process associated with crustal thickening generated sufficient heat for the anatexis of the metasedimentary rocks (Nova Venécia complex) and subsequent generation of G2 granitoids. Zircon and monazite U/Pb and Pb/Pb evaporation ages constrained the magmatic crystallization of the G2 supersuite from ca. 590 to ca. 560 Ma (Table 2.4; Nalini *et al*., 2000; Noce *et al*., 2000; Silva *et al.*, 2002, 2011; Vauchez *et al*., 2007; Roncato, 2009; Gradim, 2013; Novo, 2013; Gradim *et al.*, 2014). Based on metamorphic monazite and zircon ages, the metamorphism took place at ca. 571-549 Ma and ca. 508-497 Ma (Silva *et al.*, 2002; Gradim, 2013; Gradim *et al.*, 2014). Rb/Sr data indicate that the granitic melt crystallized at a depth above 30 km (Roncato, 2009).

This supersuite comprises batholiths and stocks locally so-called as Ataléia, Bom Jesus do Galho, Buranhém, Cananéia, Carlos Chagas, Faísca, Fazenda Cachoeira, Iriri, José Rodrigues, Maranhão, Montanha, Nanuque, Palmital, Pau-de-Óleo, Pescador, Santa Maria do Baixio, Santo Antônio, São Paulino, Tromba, Urucum and Wolf, (Pedrosa-Soares & Wiedemann-Leonardos, 2000; Pedrosa-Soares *et al.*, 2001, 2007a, 2007b, 2011; Castañeda *et al*., 2006; Gonçalves, 2009; Roncato, 2009; Paes *et al*., 2010). This thesis focuses in the Carlos Chagas batholith and therefore is presented below an overview of the main studies on this batholith. Further details on the others intrusive bodies belonging to G2 supersuite can be seen in the following works: Nalini (1997), Nalini *et al*. (2000), Noce *et al.* (2000), Ferreira *et al*. (2005), Paes *et al*. (2010), Silva *et al.* (2011), Novo (2013), Gradim *et al.* (2014); Gonçalves *et al.*, (2015); and Richter *et al.* (2016).

Tabela 2.4 - U-Pb ages (Ma) obtained in zircon and monazite from the G2 supersuite.

Batholith/ Stocks	Method	Magmatic crystallization	Metamorphism	Inherited	Reference
Ataléia	LA-ICP-MS (Zrn)	576 ± 3			Roncato (2009)
	Pb/Pb evaporation (Zrn)	591 ± 5			Noce *et al.* (2000)
	LA-ICP-MS (Zrn)	590 ± 7	571 ± 5		Gradim *et al.* (2014)
	SHRIMP (Zrn)	587 ± 9			Gradim *et al*. (2014)
Carlos Chagas	SHRIMP (Zrn)	576 ± 2			Roncato (2009)
	TIMS (Zrn)		557 ± 5		Gradim (2013)
	TIMS (Mnz)		497 ± 10		Gradim (2013)
	LA-ICP-MS (Zrn)	576 ± 5			Roncato (2009)
	SHRIMP (Zrn)	575 ± 3			Vauchez *et al*. (2007)
	LA-ICP-MS (Zrn)	568 ± 5	563 ± 13		Gradim *et al.* (2014)
	SHRIMP (Zrn)		549 ± 28		Gradim *et al.* (2014)
no identified	SHRIMP (Zrn)	579 ± 4		2169 ± 10	Novo (2013)
Nanuque	LA-ICP-MS (Zrn)	573 ± 4			Silva *et al*. (2011)
	SHRIMP (Zrn)	573 ± 5	508 ± 8		Silva *et al*. (2002)
Pangarito	SHRIMP (Zrn)	577 ± 5			Novo (2013)
Urucum	TIMS (Zrn) TIMS (Mnz)	582 ± 2 576-573 ± 3			Nalini *et al*. (2000)
Wolf	Pb/Pb evaporation (Zrn)	582 ± 5			Noce *et al*. (2000)
	LA-ICP-MS (Zrn)	563 ± 9			Gonçalves *et al*. (2015)
no identified	SHRIMP (Zrn)	565 ± 31			Silva *et al*. (2002)
	SHRIMP (Zrn)	561 ± 7			Silva *et al*. (2002)

Mnz = monazite and Zrn = zircon

Carlos Chagas batholith

The Carlos Chagas batholith extends in the N-S direction between latitudes 17°S and 19°30'S in the states of Espírito Santo, Minas Gerais and Bahia. Cropping out over an area around 14,000 km^2, it is one of the largest bodies of S-type granite in the world. The first characterization and delimitation of such a large amount of S-type granites resulted from systematic geological mapping covering the whole area of the batholith (Pinto *et al*., 2001; Pedrosa-Soares *et al.*, 2001, 2007b; Sampaio *et al.*, 2004; Castañeda *et al.*, 2006; Roncato, 2009; Queiroga *et al.*, 2012a; Roncato *et al.*, 2012; Gradim *et al.*, 2014). These publications also

characterized the CCB lithotypes, and describe their main field, petrographic, structural and lithochemical features.

The typical CCB rocks are coarse-grained S-type granites rich in K-feldspar megacrysts and relatively poor in mafic minerals. In most of the CCB, garnet is the dominant ferromagnesian mineral with subordinate biotite (the Carlos Chagas leucogranite), whilst granites with biotite as the dominant ferromagnesian mineral are subordinate (the Montanha and Nanuque granites). The Carlos Chagas leucogranite mostly occurs along the southern and central parts of the batholith, whereas the Montanha and Nanuque granites are mainly found along the northern outer zones of the CCB (Figure 2.5). These lithotypes grade into one another by variation of the garnet:biotite ratio. The mineralogy consists of quartz, plagioclase, k-feldspar, plagioclase, biotite, garnet and minor sillimanite and hercynite. CCB rocks occur predominantly deformed, recording the regional ductile foliation (S_n), grading to granites with apparent well-preserved igneous fabrics and free from S_n (Pedrosa-Soares *et al.*, 2011; Cavalcante *et al.*, 2013; Gradim *et al.*, 2014). The deformed CCB granites commonly show leucosomes of garnet- and/or cordierite-bearing leucogranite (G3) in the form of veins and patches (Pedrosa-Soares *et al.*, 2011; Gradim *et al.*, 2014). G3 generally show gradational contacts in relation to the host G2 granite, suggesting an autochthonous origin for the G3 melt. Locally, sharp contacts between G3 veins and the host G2 granite can occur, suggesting some allochthone of the G3 melt. The G3 leucogranites show many remnants of the host G2 granite, in the form of paleosome (restites) and biotite-sillimanite-rich schlieren.

Foliated peraluminous granites of the G2 Ataléia suite (ca. 590 - 570 Ma) and granulite facies paragneiss complexes (Jequitinhonha and Nova Venécia; Gradim *et al.*, 2014; Moraes *et al.*, 2015; Richter *et al.*, 2016) surround and underlie the CCB, and also appear as isolated massifs in erosional windows within the batholith (Figure 2.5). The contact of the CCB with its host rocks varies from intrusive to gradational, with the Nova Venécia and Jequitinhonha paragneisses, to gradational or sharp, with the Ataléia foliated granites, and is defined by shear zones in some places. The CCB is relatively poor in xenoliths of the host rocks, which tend to be more common along the batholith borders. The batholith was intruded by km-scale plutons and thin dykes/veins composed of granitic, charnockitic and gabbroic rocks (G5 supersuite). These intrusions cut the regional and local structures of the CBB, and locally imposed high-grade metamorphic recrystallization on their host rocks (Pedrosa-Soares *et al.*, 2011; Queiroga *et al.*, 2012a; Roncato *et al.*, 2012; Belém, 2014; De Campos *et al.*, 2016).

U-Pb zircon dating (SHRIMP and LA-ICP-MS) of CCB rocks indicate crystallization ages of 576 ± 8 to 568 ± 10 Ma (Table 2.4; Silva *et al.*, 2002; Vauchez *et al.*, 2007; Roncato, 2009; Gradim, 2013; Gradim *et al.*, 2014). Additionally, Gradim *et al.* (2014) reported ages of 563 ± 13 Ma and 549 ± 28 Ma for metamorphic zircons extracted from foliated granite and sillimanite- and garnet-bearing ultramylonite, respectively. The oldest age is similar, within analytical error, to the magmatic zircon age (568 ± 5 Ma) from the same sample, leading the authors to consider that the emplacement of the granite was followed by solid-state deformation at

elevated metamorphic temperatures within a short time of crystallization. The youngest age (549 ± 28 Ma) was interpreted to mark the final collisional processes. A youngest metamorphic age is recorded in monazite (TIMS) from the CCB at 497 ± 10 Ma (Gradim, 2013).

G3 Supersuite (ca. 545-530 Ma)

The G3 supersuite comprises subalkaline, peraluminous, S-type granites generated during the late- to post-collisional stage of the Araçuaí orogen (De Campos *et al.,* 2004; Castañeda *et al.,* 2006; Pedrosa-Soares *et al.,* 2007b, 2011; Queiroga *et al.,* 2009; Roncato, 2009; Gradim *et al.,* 2014). It consists of garnet- and/or cordierite-bearing leucogranites that are free of the regional solid-state foliation (Pedrosa-Soares *et al.,* 2001, 2007b, 2011). Leucogranite veins and patches are frequently associated with G2 granitoids (e.g., Ataléia, Carlos Chagas and Montanha) (Pedrosa-Soares *et al.,* 2007b, 2011; Gradim *et al.,* 2014). G3 commonly shows gradational and irregular contacts with host G2 granites apparently without evidence of injection, suggesting an autochthonous origin for the G3 melts. The mineralogy consists of quartz, plagioclase, k-feldspar, sillimanite, cordierite and/or garnet and minor hercynite. The accessory phases commonly found are apatite, zircon, monazite, sulfides and opaque minerals (Roncato, 2009; Gradim *et al.,* 2014).

Some G3 rocks display partial replacement of garnet by cordierite that can be associated to decompression processes. Geothermobarometric data indicates that the G3 leucogranites crystallized at 815°C and 5 kbar (Pedrosa-Soares *et al.,* 2011). Pedrosa-Soares *et al.* (2001, 2007b, 2011) have interpreted the G3 leucogranites as product of the anatexis of G2 granitoids. U-Pb geochronological data of zircon and monazite in G3 yields crystallization ages between 545 and 530 Ma (Noce *et al.,* 2004; Silva *et al.*, 2005, 2007; Castañeda *et al.,* 2006; Pedrosa-Soares *et al.,* 2011; Gradim, 2013; Gradim *et al.,* 2014) (Table 2.5). The G3 rocks are locally known as Água Branca, Água Boa, Almenara, Barro Branco, Campo Queimado, Córrego do Brejo, Córrego do Chapéu, Itaobim, Ponto dos Volantes, Poranga, São Joanico, Teste and Timorante (Paes *et al.,* 2010; Pedrosa-Soares *et al.,* 2001, 2011).

G4 Supersuite (ca. 530-500 Ma)

The G4 supersuite consists of peraluminous to slightly metaluminous, sub-alkaline, S-type granites related to the gravitational collapse of the Araçuaí orogen (Pedrosa-Soares & Wiedemann-Leonardos, 2000). G4 includes two-mica granites, pegmatites and subordinately biotite granites (Pedrosa-Soares & Wiedemann-Leonardos, 2000; Pedrosa-Soares *et al.*, 2001; Roncato *et al.*, 2012). The G4 granites generally display xenoliths and roof-pendants of the country rocks. U-Pb zircon data constrain the magmatic crystallization age of the G4 supersuite from 530 to 500 Ma (Table 2.6; Whittington *et al.,* 2001; Paes *et al.,* 2008; Silva *et al.,* 2005, 2007).

Table 2.5 - Monazite and zircon U-Pb ages of the G3 supersuite.

Plutons/veins/ patches	Lithotype	Method	Magmatic crystallization	Reference
Timorante	granite	LA-ICP-MS (Zrn)	541 ± 5	Silva *et al.* (2007)
Itaobim	granite	LA-ICP-MS (Zrn)	531 ± 4	Silva *et al.* (2007)
Água Branca	granite	LA-ICP-MS (Zrn)	527 ± 3	Silva *et al.* (2007)
no identified	Grt- Cdr leucogranite	LA-ICP-MS (Zrn)	546 ± 7	Gradim *et al.* (2014)
	Sil-Grt leucogranite	TIMS (Zrn)	546 ± 5	Gradim (2013)
		TIMS (Mnz)	546 ± 10	Gradim (2013)
	Grt leucogranite	TIMS (Mnz)	541 ± 3	Castañeda *et al.* (2006)
	Leucogranite	SHRIMP (Zrn)	532 ± 10	Silva *et al.* (2005)
	Grt-Cdr leucogranite	TIMS (Zrn)	532 ± 11	Pedrosa-Soares *et al.* (2011)
	granite	SHRIMP (Mnz)	530 ± 5	Noce *et al.* (2004)

Cdr = cordierite, Grt = garnet, Mnz = monazite, Sil = sillimanite and Zrn = zircon.

The G4 intrusive bodies are locally named as Caraí, Córrego da Chuva, Córrego do Fogo, Fazenda Areão, Itaporé, Laje Velha, Malacacheta, Mangabeiras, Murici, Piauí, Quati, Santa Rosa, Soturno and Teixeirinha (Pedrosa-Soares *et al.*, 2001, 2011; Paes *et al.*, 2010; Gonçalves *et al.*, 2015). In addition, small bodies formed by residual silicate liquid are known as Lagoa da Espera, Córrego Taquaral and Campestre (Paes *et al.*, 2010).

Table 2.6 - Summary of ages from the literature for the G4 superuite.

Plutons	Method	Magmatic crystallization	Metamorphism	Inherited	Reference
Caraí	LA-ICP-MS (Zrn)	538 ± 8			Gonçalves *et al.* (2015)
Córrego do Fogo	Pb/Pb evaporation (Zrn)	537 ± 8			Basílio *et al.* (2000)
Ibiturama	SHRIMP (Zrn)	534 ± 5		606 ± 6 585 ± 8 576 ± 6 572 ± 9	Petitgirard *et al.* (2009)
	^{40}Ar-^{39}Ar (Amp)		495 ± 4		
Teixeirinha	LA-ICP-MS (Zrn)	523 ± 19			Paes *et al.* (2008, 2010)

Amp = amphibole and Zrn = zircon

G5 Supersuite (ca. 530-480 Ma)

The G5 supersuite consists of A- and I-type, tholeiitic, high-K calc-alkaline, alkaline to peralkaline granitoids, ranging in composition from gabbro-norite to granite with minor enderbite to charnockite facies (Mendes *et al.*, 1997, 2002; 2005; Pedrosa-Soares *et al.*, 2011; Gradim *et al.*, 2014; De Campos *et al.*, 2016). Granitic plutons are generally surrounded by noritic to charnockitic outer rings, although some plutons show an inversely zoned structure with a core consisting of gabbro and norite enveloped by syeno-monzonite, monzonite and granite. These bodies cut and disturb the regional tectonic trend, and intruded the Nova Venécia complex, as well as G2 and G3 supersuites (De Campos *et al*., 2004, 2016; Pedrosa-Soares *et al*., 2011; Mendes & De Campos, 2012). Migmatization evidence (e.g., formation of cordierite- and garnet-bearing leucogranitic neosomes) can be observed in aureoles of contact metamorphism close to G5 rocks (Pedrosa-Soares *et al.*, 2011).

Evidence of mingling is attested by presence of enclaves, xenocrysts and pillow-like structures at the contact between the gabbro/norite and syeno-monzonite (Pedrosa-Soares *et al.*, 2011; Mendes & De Campos, 2012; Queiroga *et al*., 2012a). On the other hand, the whole rock geochemical and isotopic (Sm/Nd and Rb/Sr) data indicates mixing process (Wiedemann-Leonardos *et al*., 2000; Wiedemann *et al*. 2002; De Campos *et al*., 2004). This G5 supersuite correspond to the last regional magmatic event related to the gravitational collapse of the Araçuaí orogen. Geochronological data constrains the magmatic crystallization of the G5 supersuite between 530 and 480 Ma (Table 2.7; Machado *et al.*, 1996; Medeiros, 1999; Noce *et al.*, 2000; Söllner *et al.*, 2000; De Campos *et al.*, 2004, 2016; Mendes *et al.*, 2005; Silva *et al.*, 2005; Baltazar *et al.*, 2010; Gradim, 2013; Gradim *et al.*, 2014; Gonçalves *et al*., 2015).

The G5 supersuite comprises suites, batholiths, complex zoned plutons, sills and dikes named as Aimorés, Barra do São Francisco, Caladão, Castelo, Conceição de Muqui, Córrego do Volta, Cotaxé, Iconha, Itaoca, Fazenda Liberdade, Guaratinga, Jacutinga, Lagoa Preta, Lajinha, Medina, Padre Paraíso, Pedra Azul, Pedra do Elefante, Rubim, Santa Angélica, Salomão, Santo Antônio do Jacinto, Várzea Alegre, Venda Nova and Torre (Wiedemann-Leonardos *et al*., 2000, Pedrosa-Soares *et al.*, 2001, 2011, Wiedemann *et al*., 2002, De Campos *et al*., 2004, Queiroga *et al*., 2012a).

Table 2.7 - Summary of ages from the literature for the G5 superuite.

Batholith/Pluton	Method	Magmatic crystallization	Reference
Fazenda Liberdade	LA-ICP-MS (Zrn)	526 ± 5	Gonçalves *et al.* (2015)
Caladão	Pb/Pb evaporation (Zrn)	520 ± 2	Noce *et al.* (2000)
Padre Paraíso	Pb/Pb evaporation (Zrn)	519 ± 2	Noce *et al.* (2000)
Santa Angélica	U/Pb (Zrn)	513 ± 8	De Campos *et al.* (2004)

	U/Pb (Zrn)	492 ± 15	De Campos *et al.* (2004)
	TIMS (Zrn)	513 ± 8	Machado *et al*. (1996)
Aimorés	LA-ICP-MS (Zrn)	513-502	Baltazar *et al.* (2010)
Barra de São Francisco	SHRIMP (Zrn)	504 ± 5	Gradim *et al*. (2014)
Várzea Alegre	U/Pb (Zrn)	499 ± 5	De Campos *et al.* (2004)
	Rb/Sr (whole rock)	507 ± 3	Medeiros (1999)
	TIMS (Zrn)	498 ± 5	Mendes *et al.* (2005)
Cotaxé	U/Pb (Zrn)	492 ± 9	De Campos *et al.* (2004)
	TIMS (Zrn)	502 ± 9	Gradim (2013)
	TIMS (Zrn)	503 ± 3	De Campos *et al*. (2016)
Mimoso do Sul	U/Pb (zircão)	480 ± 4	De Campos *et al.* (2004)
	TIMS (Zrn)	498 ± 5	Söllner *et al*. (2000)
Pedra do Elefante	LA-ICP-MS (Zrn)	531 ± 3	De Campos *et al*. (2016)
	LA-ICP-MS (Zrn)	487 ± 7	De Campos *et al*. (2016)
Montanha	TIMS (Zrn)	500 ± 2	De Campos *et al*. (2016)
No identified	Pb/Pb evaporation (Zrn)	503 ± 9	Noce *et al*. (2000)
	SHRIMP (Zrn)	500 ± 4	Silva *et al*. (2005)
	LA-ICP-MS (Zrn)	499 ± 8	Baltazar *et al.* (2010)

Zrn = zircon

References

Alkmim F. F. & Martins-Neto M. A. 2012. Proterozoic first-order sedimentary sequences of the São Francisco craton, eastern Brazil. *Marine and Petroleum Geology*, **33**:127-139.

Alkmim F. F., Marshak S., Pedrosa-Soares A. C., Peres G. G., Cruz S. C. P., Whittingyon A. 2006. Kinematic evolution of the Araçuaí-West Congo orogen in Brazil and Africa: Nutcracker tectonics during the Neoproterozoic assembly of Gondwana. *Precambrian Research*, **149**:43-64.

Alkmim F. F., Pedrosa-Soares A. C., Noce C. M., Cruz S. C. P. 2007. Sobre a evolução tectônica do Orógeno Araçuaí-Congo Ocidental. *Geonomos*, **15**(1):25-43.

Babinski M., Pedreira A. J., Brito Neves B. B., Van Schmus W. R. 1999. Contribuição à geocronologia da Chapada Diamantina. In: *Anais*, VII Simpósio Nacional de Estudos Tectônicos-SNET, Lençóis-BA, SBG, ABGP, sessão 2, p.118-120.

Babinski M., Pedrosa-Soares A. C., Trindade R. I. F., Martins M., Noce C. M. Liu D. 2012. Neoproterozoic glacial deposits from the Araçuaí orogen, Brazil: Age, provenance and correlations with the São Francisco craton and West Congo belt. *Gondwana Research*, **21**:451-465.

Baltazar O. F., Zucchetti M., Oliveira S. A. M., Scandolara J., Silva L. C. 2010. *Folhas São Gabriel da Palha e Linhares, SE.24-Y-C-III/ SE.24-Y-D-I, escala 1:100.000: nota explicativa*. Espírito Santo e Minas Gerais, CPRM. 144p.

Basílio M. S., Pedrosa-Soares A. C., Jordt-Evangelista H. 2000. Depósitos de alexandrita de Malacacheta, Minas Gerais. *Geonomos*, **8**(1):47-54.

Belém J. 2006. Caracterização Mineralógica, Física e Termobarométrica de Minérios de Grafita da Província Grafítica Bahia-Minas. Instituto de Geociências, Universidade Federal de Minas Gerais, Belo Horizonte, Masters dissertation, 165p.

Belém J. 2014. *Geoquímica, geocronologia e contexto geotectônico do magmatismo máfico associado ao feixe de fraturas Colatina, Estado do Espírito Santo*. Instituto de Geociências, Universidade Federal de Minas Gerais, Belo Horizonte, PhD thesis, 134p.

Brito Neves B. B. & Cordani U. G. 1991. Tectonic evolution of South America duing the late Proterozoic. *Precambrian Research*, **53**:23-40.

Castañeda C., Pedrosa-Soares A. C., Belém J., Gradim D., Dias P. H. A., Medeiros S. R., Oliveira L. 2006. *Mapa Geológico e Nota Explicativa da Folha Ecoporanga, 1:100.000. In*: *Folha Ecoporanga*. Programa Geologia do Brasil, CPRM–UFMG (geobank.sa.cprm.gov.br), 50 p.

Castro M. P. 2014. *Caracterização geológica da Formação Capelinha como uma unidade basal do Grupo Macaúbas em sua área tipo, Minas Gerais*. Departamento de Geologia, Universidade Federal de Ouro Preto, Ouro Preto, Dissertação de Mestrado, 146p.

Cavalcante G. C. G., Egydio-Silva M., Vauchez A., Campos P., Oliveira E. 2013. Strain distribution across a partially molten middle crust: Insights from the AMS mapping of the Carlos Chagas Anatexite, Araçuaí belt (East Brazil). *Journal of Structural Geology*, **55:** 79-100.

Chemale-Jr F., Quade H., Van Schmus W. R. 1998. Petrography, geochemistry and geochronology of the Borrachudos and Santa Bárbara metagranites, Quadrilátero Ferrífero, Brazil. Zbl. *Geol. Paläont*., 739-750.

Chemale Jr F., Dussin I. A., Martins M. S., Alkmim F. F., Queiroga G. 2012. Unravelling a Proterozoic basin history through detrital zicon geochronology: The case of Espinhaço Supergroup, Minas Gerais, Brazil. *Gondwna Research,* **22**:200-206.

Cruz S. C. P. & Alkmim F. F. 2006. The Tectonic interaction between the Paramirim Aulacogen and the Araçuaí Belt, São Francisco craton region, Eastern Brazil. *Anais da Academia Brasileira de Ciências*, **78**(1):151-173.

Dalziel I. W. D. 1997. Neoproterozoic-Proterozoic geography and tectonics: review, hypothesis, environmental speculation. *The Geological Society of American Bulletin,* **109**(1):16-42.

Danderfer A. & Dardenne M.A. 2002. Tectonoestratigrafia da Bacia Espinhaço na porcção centro-norte do Cráton do São Francisco: Registro de uma evolução poli-histórica descontínua. *Revista Brasileira de Geociências,* **32:** 449-460.

Danderfer A., Waele B., Pedreira A. J., Nalini H. A. 2009. New geochronological constraints on the geological evolution of Espinhaço basin within the São Francisco Craton Brazil. *Precambrian Research*, **170**:116-128.

De Campos C. M., Mendes J. C., Ludka I. P., Medeiros S. R., Moura J. C., Wallfass C. 2004. A review of the Brasiliano magmatism in southern Espírito Santo, Brazil, with emphasis on postcollisional magmatism. Journal of the Virtual Explorer, **17**(1). http://virtualexplorer.com.au/journal/2004/17/campos.

De Campos C. P., Medeiros S. R., Mendes J. C., Pedrosa-Soares A. C., Dussin I., Ludka I. P., Dantas E. L. 2016. Cambro-Ordovician Magmatism in the Araçuaí Belt (SE Brazil): snapshots from a post-collisional event. *Journal of South American Earth Sciences*, **68**:248-268.

Fernandes M. L. S. 2001. *O Granito Borrachudos na região entre Guanhães e Dores de Guanhães, MG (Plutonito Morro do Urubu): gênese e evolução.* Universidade Federal do Rio de Janeiro, Rio de Janeiro, PhD thesis, 110 p.

Ferreira M. S. F., Fonseca M. A., Pires F. R. M. 2005. Pegmatitos mineralizados em água-marinha e topázio do Ponto do Marambaia, Minas Gerais: tipologia e relações com o Granito Caladão. *Revista Brasileira de Geociências*, **35**(4):463-473.

Figueiredo C. M. S. 2009. *O Arco Magmático Brasiliano na Conexão entre os Orógenos Araçuaí e Ribeira, Região de Muriaé – MG.* Instituto de Geociências, Universidade Federal de Minas Gerais, Minas Gerais, Masters dissertation, 88p.

Fontes C. Q., Netto C., Costa M. R. A., Baltazar O. F., Silva S. L., Vieira V. S. 1978. *Projeto Jequitinhonha*. Ministério das Minas e Energia. DNPM/CPRM. 543p.

Gonçalves L. E. S. 2009. *Características gerais e história deformacional da Suíte Granítica G1, entre Governador Valadares e Ipanema, MG*. Departamento de Geologia, Universidade Federal de Ouro Preto, Ouro Preto, Masters dissertation, 112p.

Gonçalves L., Farina F., Lana C., Pedrosa-Soares A. C., Alkmim F., Nalini Jr H. A. 2014. New U-Pb ages and lithochemical attributes of the Ediacaran Rio Doce magmatic arc, Araçuaí confined orogen, southeastern Brazil. *Journal of South American Earth Sciences*, **52:**129-148.

Gonçalves L., Alkmim F. F., Pedrosa-Soares A. C., Dussin I. A., Valeriano C. M., Lana C., Tedeschi M. 2015. Granites of the intracontinental termination of a magmatic arc: An example from the Ediacaran Araçuaí Orogen, Southeastern Brazil. *Gondwana Research*, **36**:439-458.

Gonçalves-Dias T., Pedrosa-Soares A. C., Dussin I. A., Alkmim F. F., Caxito F. A., Silva L. C., Noce C. M. 2011. Idade máxima de sedimentação e proveniência do Complexo Jequitinhonha na área tipo (Orógeno Araçuaí): primeiros dados U–Pb (LA-ICP-MS) de grãos detríticos de zircão. *Geonomos*, **19**(2):121-130.

Gonçalves-Dias T., Caxito F. A., Pedrosa-Soares A. C., Stevenson R., Dussin I., Silva L. C., Alkmim F., Pimentel M. 2016. Age, provenance and tectonic setting of the high-grade Jequitinhonha Complex, Araçuaí Orogen, eastern Brazil. *Brazilian Journal of Geology*, **46**(2):199-219.

Gradim C. T. 2013. *Complexo Nova Venécia e magmatismo associado, Orógeno Araçuaí, Estado do Espírito Santo.* Departamento de Geologia, Universidade Federal de Minas Gerais, Belo Horizonte, MSc dissertation, 96p.

Gradim C. T., Queiroga G. N., Roncato J. G., Novo T. A., Pedrosa-Soares A. C. 2007. *Folha Mantena, SE.24-Y-A-VI, escala 1:100.000.* Minas Gerais/Espírito Santo, UFMG/CPRM.

Gradim C., Roncato J., Pedrosa-Soares A.C., Cordani U., Dussin I., Alkmim F.F., Queiroga G., Jacobssohn T., Silva L.C., Babinski M. 2014. The hot back-arc zone of the Araçuaí orogen, Eastern Brazil: from sedimentation to granite generation. *Brazilian Journal of Geology*, **44**, 155-180.

Guimarães D. & Barbosa O.1934. Mapa Geológico do Estado de Minas Gerais, escala 1:1.000.000. Serviço Geológico do Estado de Minas Gerais, Belo Horizonte, MG.

Hasui Y., Almeida F. F. M., Brito-Neves B. B. 1978. As estruturas brasilianas. *Anais*, XXX Congresso Brasileiro de Geologia, Recife, 6:2423-2437.

Heilbron M. & Machado N. 2003. Timing of terrane accretion in the Neoproterozoic-Eopaleozoic Ribeira Orogen (SE Brazil). *Precambrian Research*, **125:** 87–112.

Heilbron M., Duarte B., Valeriano C., Simonetti A., Machado N., Nogueira J. 2010. Evolution of reworked Paleoproterozoic basement rocks within the Ribeira belt (Neoproterozoic), SE-Brazil, based on U Pb geochronology: Implications for paleogeographic reconstructions of the São Francisco-Congo paleocontinent. *Precambrian Research*, **178**:136-148.

Heilbron M., Tupinambá M., Valeriano C.D.M., Armstrong R., Do Eirado Siva L.G., Melo R.S., Simonetti A., Pedrosa Soares A.C., Machado N. 2013. The Serra da Bolívia complex: The record of a new Neoproterozoic arc-related unit at Ribeira belt. *Precambrian Res.*, **238:** 158-175.

Kuchenbecker M., Pedrosa-Soares A. C., Babinski M., Fanning M. 2015. Detrital zircon age patterns and provenance assessment for pre-glacial to post-glacial successions of the Neoproterozoic Macaúbas Group, Araçuaí orogen, Brazil. *Precambrian Research*, **266**:12-26.

Lima S. A. A., Martins-Neto M. A., Pedrosa-Soares A. C., Cordani U. G., Nutman A. 2002. A Formação Salinas na área-tipo, NE de Minas Gerais: Uma proposta de revisão da estratigrafia da Faixa Araçuaí

com base em evidências sedimentares, metamórficas e idades U-Pb SHRIMP. *Revista Brasileira de Geociências*, **32**:491-500.

Lobato L. M., Pimentel M. M., Cruz S. C. P., Machado N., Noce C. M., Alkmim F. F. 2015. U-Pb geochronology of the Lagoa Real uranium district, Brazil: Implications for the age of the uranium mineralization. *Journal of South American Earth Sciences*, **58**:129-140.

Machado N., Schrank A., Abreu F. R., Knauer L. G., Almeida-Abreu P. A. 1989. Resultados preliminares da geocronologia U/Pb na Serra do Espinhaço Meridional. In: V Simpósio de Geologia de Minas Gerais, Belo Horizonte: SBG, *Anais*, 171-174.

Machado N., Valladares C., Heilbron M., Valeriano C. 1996. UPb geochronology of the central Ribeira belt (Brazil) and implications for the evolution of the Brazilian Orogeny. *Precambrian Research.*, **69**:347-361.

Medeiros S. R. 1999. *Estudo Mineralógico, petrográfico, geoquímico e isotópico do Complexo Intrusivo de Varzea Alegre - ES*. Instituto de Geociências, Universidade Federal do Rio de Janeiro, Rio de Janeiro. PhD thesis, 174 p.

Mendes J. C. & De Campos C. M. P. 2012. Norite and charnockites from the Venda Nova Pluton, SE Brazil: Intensive parameters and some petrogenetic constraints. *Geoscience Frontiers*, **3**(6): 789-800.

Mendes J. C., Mcreath I., Wiedemann C. M., Figueiredo M. C. H. 1997. Charnoquitóides do maciço de Várzea Alegre: um novo exemplo do magmatismo Ca-alcalino de alto K no arco magmático do Espírito Santo. *Revista Brasileiro de Geociências*, **27**(1):13-24.

Mendes J. C., Wiedemann C. M., McReath I. 2002. Norito e Charnoenderbitos da Borda do Maciço Intrusivo de Venda Nova, Espírito Santo. *Anuário do Instituto de Geociências*, **25**:99-124.

Mendes J. C., Medeiros S. R., McReath I., Campos C. M. P. 2005. Cambro-Ordovician Magmatism in SE Brazil: U-Pb and Rb-Sr Ages, Combined with Sr and Nd Isotopic Data of Charnockitic Rocks from the Varzea Alegre Complex. *Gondwana Research*, **8**(3):337-345.

Mondou M., Egydio-Silva M., Vauchez A., Raposo M. I. B., Bruguier O., Oliveira A. F. 2012. Complex, 3D strain patterns in a synkinematic tonalite batholith from the Araçuaí Neoproterozoic orogen (Eastern Brazil): evidence from combined magnetic and isotopic chronology studies. *Journal of Structural Geology*, **39**:158-179.

Moraes R., Nicollet C., Barbosa J. H. F., Fuck R. A., Sampaio A. R. 2015. Applications and limitations of thermobarometry in migmatites and granulites using as an example rocks of the Araçuaí Orogen in southern Bahia, including a discussion on the tectonic meaning of the current results. *Brazilian Journal of Geology*, **45**(4):517-539.

Munhá J. M. U., Cordani U. G., Tassinari C. C. G., Palácios T. 2005. Petrologia e termocronologia de gnaisses migmatíticos da faixa de dobramentos Araçuaí (Espírito Santo, Brasil). *Revista Brasileira de Geociências*, **35**(1):123-134.

Nalini H. A. 1997. *Caractérisation des suites magmatiques néoprotérozoïques de la region de Conselheiro Pena et Galiléia (Minas Gerais, Brésil). Etude géochimique et structurale des suitesGaliléia et Urucum et relations avec les pegmatites à éléments rares associées.* Ecole des Mines de Saint Etienne et Ecole des Mines de Paris, PhD thesis, 237p.

Nalini H. A., Bilal E., Neves J. M. C. 2000. Syn-collisional peraluminous magmatism in the Rio Doce region: mineralogy, geochemistry and isotopic data of the Neoproterozoic Urucum Suite (Eastern Minas Gerais State, Brazil). *Revista Brasileira de Geociências*, **30**(1):120-125.

Nalini H. A., Machado R., Bilal E. 2015. Petrogenesis and tectonic of the Urucum granitic suite, Rio Doce Valley (Minas Gerais - Brazil): an example of syn to late collisional peraluminous magmatism associated with high-angle transcurrent shear zone. *Brazilian Journal of Geology*, **45**(1): 127-141.

Noce C. M., Macambira M. J. B., Pedrosa-Soares A. C. 2000. Chronology of Neoproterozoic-Cambrian Granitic magmatism in the Araçuaí Belt, eastern Brazil, based on single zircon evaporation dating. *Revista Brasileira de Geociências*, **30**(1):25-29.

Noce C. M, Pedrosa-Soares A. C., Piuzana D., Armstrong R., Laux J. H. Campos C. M., Medeiros S. R. 2004. Ages of sedimentation of the kinzigitic complex and of a late orogenic thermal episode in the Araçuaí orogen, northern Espírito Santo State, Brazil: Zircon and monazite U-Pb SHRIMP and ID-TIMS data. *Revista Brasileira de Geociências*, **34**:587-592.

Noce C. M., Pedrosa-Soares A. C., Silva L. C., Armstrong R., Piuzana D. 2007a. Evolution of polycyclic basement complexes in the Araçuaí Orogen, based on U-Pb SHRIMP data: Implications for Brazil-Africa links in Paleoproterozoic time. *Precambrian Research*, **159**: 60-78.

Noce C. M., Pedrosa-Soares A. C., Silva L. C., Alkmim F. F. 2007b. O embasamento Arqueano e Paleoproterozóico do Orógeno Araçuaí. *Geonomos*, **15**(1):17-23.

Novo T. A. 2009. *Significado geotectônico das rochas charnockíticas da região de Carangola: implicações para a conexão Araçuaí-Ribeira*. Instituto de Geociências, Universidade Federal de Minas Gerais, Belo Horizonte, Dissertação de Mestrado, 87p.

Novo T. A. 2013. *Caracterização do Complexo Pocrane, magmatismo básico Mesoproterozóico e unidades neoproterozóicas do Sistema Araçuaí-Ribeira, com ênfase em geocronologia U-Pb (SHRIMP e LA-ICP-MS).* Instituto de Geociências, Universidade Federal de Minas Gerais, Belo Horizonte, Phd thesis. 193p.

Novo T. A., Pedrosa-Soares A. C., Noce C. M., Alkmim F. F., Dussin I. A. 2010. Rochas charnockíticas do sudeste de Minas Gerais: a raiz granulítica do arco magmático do Orógeno Araçuaí. *Revista Brasileira de Geociências*, **40**(4):573-592.

Novo T. A., Pedrosa-Soares A. C., Degler R., Schulz B. 2015. Termobarometria de metapelitos granadíferos do Grupo Rio Doce, Orógeno Araçuaí. *Geonomos*, **23**(1):18-25.

Paes V. J. C. 1999. *Geologia e geoquímica de rochas metamáficas e meta-ultramáficas da região de Alvarenga-MG e suas implicações geotectônicas*. Instituto de Geociências, Universidade Federal de Minas Gerais, Belo Horizonte, Masters dissertation, 153p.

Paes V. C., Heineck C., Malouf R. 2008. *Folha Itaobim. Programa Geologia do Brasil*. Rio de Janeiro, CPRM–Serviço Geológico do Brasil.

Paes V. J. C., Raposo F. O., Pinto C. P. Oliveira F. A. R. 2010. Projeto Jequitinhonha, Estados de Minas Gerais e Bahia: Geologia e Recursos Minerais das folhas Comercinho, Jequitinhonha, Almenara, Itaobim, Joaíma e Rio do Prado. Belo Horizonte, CPRM. 376p.

Pedrosa-Soares A.C. 1995. *Potencial Aurífero do Vale do Araçuaí, MG: História da Exploração, Geologia e Controle Tectono- Metamórfico.* Instituto de Geociências, Universidade de Brasília, Brasília, Phd thesis, 125p.

Pedrosa-Soares A. C. & Alkmim F. F. 2011. How many rifting events preceded the development of the Araçuaí–West Congo orogen? *Geonomos*, **19**:244-251.

Pedrosa-Soares A. C. & Wiedemann-Leonardos C. M. 2000. Evolution of the Araçuaí Belt and its connection to the Ribeira Belt, eastern Brazil. In: U. G. Cordani, Milani E. J., Thomaz-Filho A, Campos D. A (eds). *Tectonic evolution of South America*. São Paulo, Sociedade Brasileira de Geologia, 265-285.

Pedrosa- Soares A. C., Monteiro R. L. B. P., Noce C. M., Freitas e Silva F. H., Oliveira M. J. R., Schettino A. 1990. Caracterização de uma sequência vulcano-sedimentar distal na Faixa Araçuaí, MG: bacia oceânica restrita? *Boletim de Resumos*, XXXVI Congresso Brasileiro de Geologia, Natal, 308.

Pedrosa-Soares A. C., Noce C. M., Vidal Ph., Monteiro R. L. B. P., Leonardos O. H. 1992. Toward a new tectonic model for the Late Proterozoic Araçuaí (SE Brazil) – West Congolian (SW Africa) Belt. Journal of *South American Earth Sciences*, **6**(1/2):33-47.

Pedrosa-Soares A. C., Vidal P., Leonardos O. H., Brito-Neves B. B. 1998. Neoproterozoic oceanic remnants in eastern Brazil:Further evidence and refutation of an exclusively ensialic evolution for the Araçuaí–West Congo orogen. *Geology*, **26**(6):519-522.

Pedrosa-Soares A. C., Wiedemann C. M., Fernandes M. L. S., Faria L. F., Ferreira J. C. H. 1999. Geotectonic significance of the Neoproterozoic granitic magmatism in the Araçuaí belt, Eastern Brazil: a model and pertinent questions. *Revista Brasileira de Geociências*, **29**:57-64.

Pedrosa-Soares A. C., Cordani U. G., Nutman A. 2000. Constraining the age of Neoproterozoic glaciation in eastern Brazil: First U-Pb SHRIMP data of detrital zircons. *Revista Brasileira de Geociências*, **30:**58-61.

Pedrosa-Soares A. C., Noce C. M., Wiedemann C. M., Pinto C. P. 2001. The Araçuaí-West-Congo Orogen in Brazil: an overview of a confined orogen formed during Gondwanaland assembly. *Precambrian Research*, **110:**307-323.

Pedrosa-Soares A. C., Castañeda C, Queiroga G., Gradim C., Belém J., Roncato J., Novo T., Dias P., Gradim D., Medeiros S., Jacobsohn T., Babinski M., Vieira V. 2006. Magmatismo e tectônica do Orógeno Araçuaí no extremo leste de Minas e norte do Espírito Santo (18°-19°S, 41°-40°30'W). *Geonomos*, **14**(1/2):97-111.

Pedrosa-Soares A. C., Noce C. M., Alkmim F. F., Silva L. C., Babinski M., Cordani U., Castañeda C. 2007a. Orógeno Araçuaí: síntese do conhecimento 30 anos após Almeida 1977. *Geonomos*, **15**(1):1-16.

Pedrosa-Soares A. C., Queiroga G. N., Gradim C. T., Roncato J. G., Novo T. A., Jacobsohn T., Silva K. L. 2007b. Geologia da Folha Mantena (SE-24-Y-A-VI). Programa Geologia do Brasil, CPRM, 82p. (http://geobank.cprm.gov.br)

Pedrosa-Soares A. C., Alkmim F. F., Tack L., Noce C. M., Babinski M., Silva L. C., Martins-Neto M. 2008. Similarities and differences between the Brazilian and African counterparts of the Neoproterozoic Araçuaí-West Congo Orogen. In: Pankhurst J. R., Trouw R. A. J., Brito Neves B. B., De Wit M. J.(eds) West

Gondwana: Pre-Cenozoic Correlations across the South Atlantic Region. Geological Society of London, Special Publications, **294**:153-172.

Pedrosa-Soares A. C., De Campos C. P., Noce C., Silva L. C., Novo T., Roncato J., Medeiros S., Castañeda C., Queiroga G., Dantas E., Dussin I., Alkmim F. 2011. Late Neoproterozoic–Cambrian granitic magmatism in the Araçuaí orogen (Brazil), the Eastern Brazilian Pegmatite Province and related mineral resources. *Geological Society of London, Special Publications*, **350**:25–51.

Peixoto E., Pedrosa-Soares A. C., Alkmim F. F., Dussin I. A. 2015. A suture-related accretionary wedge formed in the Neoproterozoic Araçuaí Orogen (SE Brazil) during Western Gondwanaland assembly. *Gondwana Research*, **27**:878-896

Peres G. G., Alkmim F. F., Jordt-Evangelista H. 2004. The southern Araçuaí belt and the Dom Silvério Group: geologic architecture and tectonic significance. *Anais da Academia Brasileira de Ciências*, **76**(4):771-790.

Petitgirard S., Vauchez A., Egydio-Silva M., Bruguier O., Camps P., Monié P., Babinsky M., Mondou M. 2009. Conficting structural and geochronological data from the Ibiturana quartz-syenite (SE Brazil): Effect of protracted "hot" orogeny and slow cooling rate? *Tectonophysics*, **477:**174-196.

Pinto C. P., Drumond J. B. V., Féboli W. L. 2001. Projeto Leste. Belo Horizonte: CPRM/CODEMIG, CD-ROM.

Porada H. 1989. Pan-African Rifting and Orogenesis in Southern to Equatorial Africa and Eastern Brazil. *Precambrian Research*, **44**:103-136.

Queiroga G. N., Pedrosa-Soares A. C., Noce C. M., Alkmim F. F., Pimentel M. M., Dantas E., Martins M., Castañeda C., Suita M. T. F., Prichard H. 2007. Age of the Ribeirão da Folha ophiolite, Araçuaí Orogen: the U-Pb zircon (LA-ICPMS) dating of a plagiogranite. *Geonomos*, **15**(1):61-65.

Queiroga G.N., Pedrosa-Soares A.C., Roncato J.G., Dias P.H.A., Guimarães H.A., Coutinho M.O.G., Freitas N.C., Gradim C.T., Braga F.C.S., Novo T.A. 2009. *Mapa Geológico da Folha Nova Venécia 1: 100.000.* Belo Horizonte, Programa Geologia do Brasil, CPRM-UFMG.

Queiroga G. N., Pedrosa-Soares A. C., Roncato Júnior G. G., Dias P. H. A., Guimarães H. A., Coutinho M. O. G., Freitas N. C., Gradim C. T., Braga F. C. S., Novo T. A. 2012a. *Geologia e recursos minerais da folha Nova Venécia SE.24-Y-B-IV, estado do Espírito Santo, escala 1:100.000*. Belo Horizonte, CPRM. 76p.

Queiroga G. N., Dussin I.A., Martins M., Machado M.C., Kawashita K., Chemale F. 2012b. Roteiro de Campo – Rochas Ígneas. In: Dussin I.A. & Chemale F. (ed). Geologia Estrutural e Estratigrafia do Sistema Espinhaço – Chapada Diamantina e sua Aplicação nas Bacias Mesocenozóicas da Margem Passiva Brasileira. Belo Horizonte, FUNDEP/PETROBRÁS, 170-195.

Renné P. R., Onstott T. C., D'AgrelaFilho M. S., Pacca I. G., Teixeira W. 1990. $^{40}Ar/^{39}Ar$ dating of l .0 -1.l Ga magnetizations from the São Francisco and Kalahari Cratons: Tectonic implications for Pan-African and Brasiliano Mobile Belts. *Earth and Planetary Sciences Letters*, **101**(2-4):349-366

Richter F., Lana C., Stevens G., Buick I., Pedrosa-Soares A. C., Alkmim F. F., Cutts K. 2016. Sedimentation, metamorphism and granite generation in a back-arc region: Records from the Ediacaran Nova Venécia Complex (Araçuaí Orogen, Southeastern Brazil). *Precambrian Research*, **272**:78-100.

Roncato J. G. 2009. *As suítes graníticas tipo-S do norte do Espírito Santo na região das folhas Ecoporanga, Mantena, Montanha e Nova Venécia*. Instituto de Geociências, Universidade Federal de Minas Gerais, Minas Gerais, Masters dissertation,102p.

Roncato J. G., Pedrosa-Soares A. C., Mascarenhas T. F., Fornero S. A., Galinari L. M., Gonçalves L. T., Queiroga G. N., Braga F. C. S., Novo T. A. 2012. *Geologia e recursos minerais da folha Montanha, SE.24-Y-B-I, escala 1:100.000: nota explicativa*. Minas Gerais/Espírito Santo, UFMG/CPRM. 64p.

Rosa M. de L. S., Conceição H., Macambira M. J. B., Galarza M. A., Cunha M. P., Menezes R. C. L., Marinho M. M., Filho B. E. C., Rios D. C. 2007. Neoproterozoic anorogenic magmatism in the Southern Bahia Alkaline Province of NE Brazil: U-Pb and Pb-Pb ages of the blue sodalite syenites. *Lithos*, **97:** 88–97.

Rosa M. L. S., Oliveira J. A., Conceição H., Conceição J. A., Macambira M. J. B., Galarza M. A. 2015. Idade Pb-Pb do Stock Nefelina Sienítico Serra da Gruta, Província Alcalina do Sul do Estado da Bahia. *Scientia Plena*, **11**(3):1-5.

Sampaio A. R., Martins A. M., Loureiro H. C., Arcanjo J. B., Moraes Filho J. C., Souza J. D., Pereira L. H., Couto P. A., Santos R. A., Melo R. C., Bento R. V., Borges V. P. 2004. Extremo Sul da Bahia: Geologia e Recursos Minerais. Arquivos Abertos. CBPM e CPRM.

Santos R. F., Alkmim F. F., Pedrosa-Soares A. C. 2009. A Formação Salinas, Orógeno Araçuaí, MG: História deformacional e significado tectônico. *Revista Brasileira de Geociências*, **39**(1):81-100.

Seer H. J., Brod J. A., Fuck R. A., Pimentel M. M., Boaventura G. R., Dardenne M. A. 2001. Grupo Araxá em sua área tipo: um fragmento de crosta oceânica neoproterozóica na Faixa de Dobramento Brasília. *Revista Brasileira de Geociências*, **31**:396-924.

Silva J. M. R. 1987. *Projeto RadamBrasil. Folha SE.24 Rio Doce.* Levantamento de Recursos Naturais, Rio de Janeiro.

Silva L. C., Armstrong R., Noce C. M., Carneiro M. A., Pimentel M., Pedrosa-Soares A. C., Leite C. A., Vieira V. S., Silva M. A., Paes V. J. C., Filho J. M. C. 2002. Reavaliação da evolução geológica em terrenos Pré-cambrianos brasileiros com base em novos dados U-Pb SHRIMP, parte II: Orógeno Araçuaí, Cinturão Mineiro e Cráton São Francisco Meridional. *Revista Brasileira de Geociências*, **32**(4):513-528.

Silva L. C., McNaughton N. J., Armstrong R., Hartmann L. A., Fletcher I. R. 2005. The neoproterozoic Mantiqueira Province and its African connections: a zircon-based U-Pb geochronologic subdivision for the Brasiliano/Pan-African systems of orogens. *Precambrian Research*, **136**:203-240.

Silva L. C., Pedrosa-Soares A. C., Teixeira L. R., Armstrong R. 2007. Tonian rift-related, A-type continental plutonism in the Araçuaí Orogen, eastern Brazil: New evidence for the breakup stage of the São Francisco–Congo Paleocontinent. *Gondwana Research*, **13**(4):527-537.

Silva L. C., Pedrosa-Soares A. C., Teixeira L. R., Armstrong R. 2008. Tonian rift-related, A-type continental plutonism in the Araçuaí Orogen, eastern Brazil: New evidence for the breakup stage of the São Francisco-Congo Paleocontinent. *Gondwana Research*, **13**: 527–537.

Silva L. C., Pedrosa-Soares A. C., Armstrong R., Noce C. M. 2011. Determinando a duração do período colisional do Orógeno Araçuaí com base em geocronologia U-Pb de alta resolução em zircão: uma contribuição para a história da amalgamação do Gondwana Ocidental. *Geonomos*, **19**(2):180-197.

Silva L. C., Pedrosa-Soares A. C., Armstrong R., Pinto C. P., Magalhães J. T. R., Pinheiro M. A. P., Santos G. G. 2015. Disclosing the Paleoarchean to Ediacaran history of the São Francisco craton basement: The Porteirinha domain (northern Araçuaí orogen, Brazil). *Journal of South American Earth Sciences*, **68**:50-67.

Söllner H. S., Lammerer B., Weber-Diefenbach K. 1991. Die Krustenentwicklung in der Küstenregion nördlich von Rio de Janeiro, Brasilien. *Müncher Geologische Hefte*, **4**:1–100.

Söllner H. S., Lammerer B., Wiedemann-Leonardos C. 2000. Dating the Araçuaí–Ribeira mobile belt of Brazil. *Sonderheft, Zeitschrift Angewandte Geologie*, **1**:245-255.

Souza M. E. S. 2016. *Caracterização Litoestrutural e Geocronológica dos Xistos Verdes e Metagabros do Grupo Macaúbas na Faixa Terra Branca - Planalto de Minas, Minas Gerais*. Departamento de Geologia, Universidade Federal de Ouro Preto, Ouro Preto, Masters dissertation, 215p.

Tack L., Wingate M.T.D., Liégeois J.-P., Fernandez-Alonso M., Deblond A. 2001. Early Neoproterozoic magmatism (1000-910 Ma) of the Zadinian and Mayumbian groups (Bas-Congo): onset of Rodinia at the western edge of the Congo craton. *Precambrian Research*, **110**:277-306.

Tedeschi M., Novo T., Pedrosa-Soares A. C., Dussin I., Tassinari C., Silva L. C., Gonçalves L., Alkmim F., Lana C., Figueiredo C., Dantas E., Medeiros S., De Campos C., Corrales F., Heilbron M. 2016. The Ediacaran Rio Doce magmatic arc revisited (Araçuaí-Ribeira orogenic system, SE Brazil). *Journal of South American Earth Sciences*, **68**:167-186.

Teixeira W., Sabaté P., Barbosa J., Noce C. M., Carneiro M. A. 2000. Archean and Paleoproterozoic tectonic evolution of the São Francisco Craton. *In*: U.G. Cordani, E.J. Milani, A. Thomaz-Filho, D.A. Campos, D. A. (eds.) Tectonic Evolution of South America. Rio de Janeiro, 101-138.

Thiéblemont D., Prian J. P., Goujou J. C., Boulingui B., Ekogha H., Kassadou A. B., Simo-Ndounze S., Walemba A., Préat A., Theunissen K., Cocherie A., Guerrot C. 2011. Timing and characteristics of Neoproterozoic magmatism in SW-Gabon: First geochronogical and geochemical data on the West-Congolian orogen in Gabon (SYSMIN project, Gabon 2005-2009). *In*: 23 Colloquium of African Geology, posters and abstracts.

Trompette R. 1994. *Geology of Western Gondwana (2000-500Ma). Pan-African-Brasiliano Aggregation of South America and Africa.* Balkema, Rotterdam. 350p.

Tupinambá M., Heilbron M., Valeriano C., Júnior R. P., Dios F. B., Machado N., Silva L. G. E., Almeida J. C. H. 2012. Juvenile contribution of the Neoproterozoic Rio Negro Magmatic Arc (Ribeira Belt, Brazil): Implications for Western Gondwana amalgamation. *Gondwana Research,* **21**:422–438.

Valeriano, C.M., Machado, N., Simonetti, A., Valladares, C.S., Seer, H.J., Simões, L.S.A., 2004. U–Pb geochronology of the southern Brasília belt (SE-Brazil): Sedimentary Provenance, Neoproterozoic orogeny and assembly of West-Gondwana. *Precambrian Research,* **130** (1/4), 27–55.

Vauchez A., Egydio Silva M., Babinski M., Tommasi A., Uhlein A., Liu D. 2007. Deformation of a pervasely molten middle crust: insights from the neoproterozoic Ribeira-Araçuaí orogen (SE Brazil). *Terra Nova,* **19:** 278-286.

Vieira V. S. 2007. *Significado do Grupo Rio Doce no contexto do Orógeno Araçuaí*. Instituto de Geociências, Universidade Federal de Minas Gerais, Belo Horizonte, PhD thesis, 117p.

Wiedemann-Leonardos C. M., Ludka I. P., Medeiros S. R., Mendes J. C., Costa-de-Moura J. 2000. Arquitetura de plútons zonados da Faixa Araçuaí-Ribeira. *Geonomos*, **8**(1):25-38.

Wiedemann C. M., Medeiros S. R., Ludka I. P., Mendes J. C., Costa-de-Moura. 2002. Architecture of Late Orogenic Plutons in the Araçuaí-Ribeira Fold Belt, Southeast Brazil. *Gondwana Research*, **5**(2):381-399.

Whittington A. G., Connelly J., Pedrosa-Soares A. C., Marshak S., Alkmim F. F. 2001. Collapse and melting in a confined orogenic belt: preliminary results from the Neoproterozoic Araçuaí belt of eastern Brazil. AGU Fall Meeteing, *Abstract T32B-0895,* American Geophysical Union, 82:1181-1182.

CHAPTER 3

TWO CRYPTIC ANATECTIC EVENTS WITHIN A SYN-COLLISIONAL GRANITOID FROM THE ARAÇUAÍ OROGEN (SOUTHEASTERN BRAZIL): EVIDENCE FROM THE POLYMETAMORPHIC CARLOS CHAGAS BATHOLITH

PRESENTATION OF THE PUBLICATION

This paper[1], first authored by Marilane Gonzaga Melo, was accepted for publication in the journal Lithos. The following aspects of the research were done independently by Marilane Gonzaga Melo while receiving standard supervision by his supervisors Gary Stevens, Cristiano Lana and Fernando Flecha de Alkmim. I did the sampling in the field, acquisition of mineral chemical data on the SEM, mineral separation for zircon geochronology, monazite and zircon imaging by SEM, petrography and mineral equilibria modelling in Theriak-Domino. I was also responsible for the literature review and the majority of the written work. Professor Pedrosa-Soares contributed to the field work and regional concepts and tectonics. Zircon and monazite U-Pb (LA-ICP-MS) and trace element in garnet data reduction were done by Dirk Frei. Alkmin assisted me with the use of the Theriak-Domino and pseudosection development.

Marilane Gonzaga Melo[a,b]
Gary Stevens[b]
Cristiano Lana[a]
Antônio Carlos Pedrosa-Soares[c]
Dirk Frei[b]
Fernando Flecha de Alkmim[a]
Leonardo Azevedo Alkmin[a]

a: Applied Isotope Research Group, Departamento de Geologia, Escola deMinas, Universidade Federal de Ouro Preto, Campus UniversitárioMorro do Cruzeiro s/n, 35400-000 Ouro Preto,MG, Brazil
b: Centre for Crustal Petrology, Department of Earth Sciences, Stellenbosch University, Private Bag X1, Matieland 7602, South Africa
c: Universidade Federal de Minas Gerais, IGC–CPMTC, Campus Pampulha, 31270-901 Belo Horizonte, MG, Brazil

[1]Melo, M.G, Stevens, G., Lana, C., Pedrosa-Soares, A.C., Frei, D., Alkmim, F.F., Alkmin, L.A. 2016. Two cryptic anatectic events within a syn-collisional granitoid from the Araçuaí orogen (southeastern Brazil): Evidence from the polymetamorphic Carlos Chagas batholiths. Lithos, doi: 10.1016/j.lithos.2016.10.012

Lithos xxx (2016) xxx–xxx

Contents lists available at ScienceDirect

Lithos

journal homepage: www.elsevier.com/locate/lithos

Two cryptic anatectic events within a syn-collisional granitoid from the Araçuaí orogen (southeastern Brazil): Evidence from the polymetamorphic Carlos Chagas batholith

M.G. Melo [a,b,*], G. Stevens [b], C. Lana [a,1], A.C. Pedrosa-Soares [c,1], D. Frei [b], F.F. Alkmim [a,1], L.A. Alkmin [a]

[a] Applied Isotope Research Group, Departamento de Geologia, Escola de Minas, Universidade Federal de Ouro Preto, Campus Universitário Morro do Cruzeiro s/n, 35400-000 Ouro Preto, MG, Brazil
[b] Centre for Crustal Petrology, Department of Earth Sciences, Stellenbosch University, Private Bag X1, Matieland 7602, South Africa
[c] Universidade Federal de Minas Gerais, IGC–CPMTC, Campus Pampulha, 31270-901 Belo Horizonte, MG, Brazil

ARTICLE INFO

Article history:
Received 15 February 2016
Accepted 9 October 2016
Available online xxxx

Keywords:
Multiple anatectic event
Garnet
Granulite facies metamorphism
Monazite and zircon dating
Araçuaí orogen

ABSTRACT

From the earliest (ca. 630 Ma) pre-collisional plutons to the latest (ca. 480 Ma) post-collisional intrusions, the Araçuaí orogen (SE Brazil) records an outstanding succession of granite production events in space and time. The Carlos Chagas batholith (CCB) is the largest (~14,000 km^2) granitic body ascribed to the collisional plutonism (G2 supersuite) in the back-arc region of the Araçuaí orogen, to the east of the Rio Doce magmatic arc. A wide range of monazite and zircon ages (>725 Ma to ca. 490 Ma) have been found in CCB granites, recording a rich history of crustal recycling and inheritance, magmatic crystallization and anatexis. The CCB includes a dominant granite richer in garnet than in biotite, in which three mineral assemblages can be identified: 1) Qz + Pl + Kfs + Bt + Grt + Ilm ± Rt; 2) Qz + Pl + Kfs + Bt + Grt + Ilm + Sil; and 3) Qz + Pl + Kfs + Bt + Grt + Ilm + Sil + Spl. Rocks which contain mineral assemblage 2 and 3 all contain two generations of garnet. Textural evidence for the presence of former melt, recognized in all studied CCB samples, includes: silicate melt inclusions in poikiloblastic garnet, pseudomorphed thin films of melt surrounding both generations of garnet, pseudomorphed melt pools adjacent to garnet and biotite, and plagioclase and quartz with cuspate-lobate shapes occurring among matrix grains. Both generations of garnet crystals (Grt_1 and Grt_2) are unzoned in terms of major element concentration, contain small rounded inclusions of Ti-rich biotite and, in addition, the Grt_2 crystals also contain inclusions of remnant sillimanite needles. Microstructural evidence, in combination with mineral chemistry, indicates that the garnet crystals grew during two distinct metamorphic-anatectic events, as the peritectic products of fluid-absent melting reactions which consumed biotite, quartz and plagioclase, in the case of Grt_1, and which consumed biotite, quartz, plagioclase and sillimanite in the case of Grt_2. *P–T* pseudosections calculated via Theriak-Domino, in combination with in situ U–Pb monazite and zircon dating, provide new constraints on the thermal evolution of the back-arc region of the Araçuaí orogen. Data from assemblage 1 suggests *P–T* conditions for the first granulite-facies metamorphic event (M1) at 790–820 °C and 9.5–10.5 kbar, while the assemblage 2 records *P–T* conditions for a second granulite-facies metamorphism (M2) of around 770 °C and 6.6 kbar. Monazite and zircon within garnets from the different assemblages give age peaks at 570–550 Ma (M1) and 535–515 Ma (M2), recording two anatectic events in the CCB during a single orogenic cycle. The PT conditions for these metamorphic events can be related to: i) M1, striking crustal thickening, probably involving thrusting of the magmatic arc onto the back-arc region; and ii) M2, decompression related to the gravitational collapse of the Araçuaí orogen.

1. Introduction

Crustal differentiation is an important process in the stabilization of the continental crust. There is widespread consensus that the rocks forming the lower continental crust record at least one cycle of partial melting (>800 °C; e.g. Brown, 1994, 2010). The resultant granitic magmas migrate upwards, enriching the upper crust in SiO_2, K_2O and Na_2O, and leaving the lower crust dehydrated, more refractory and enriched in Al_2O_3, FeO, MgO and CaO (Brown, 2013; Brown and Rushmer, 2006; Petford et al., 2000).

* Corresponding author at: Applied Isotope Research Group, Departamento de Geologia, Escola de Minas, Universidade Federal de Ouro Preto, Campus Universitário Morro do Cruzeiro s/n, 35400-000 Ouro Preto, MG, Brazil.
E-mail addresses: marilanegonzaga@hotmail.com (M.G. Melo), pedrosasoares@ufmg.br (A.C. Pedrosa-Soares).
[1] Fellow of the Brazilian Research Council (CNPq).

http://dx.doi.org/10.1016/j.lithos.2016.10.012
0024-4937/

In long-lived orogenic systems some rocks may record more than one cycle of tectonic burial with partial melting at depth (Jeon et al., 2012; Richter et al., 2016). Likewise, early orogenic granites (sensu lato), emplaced into the upper crust, may be buried together with overlying sedimentary and volcanic sequences to lower crustal levels, and recycled in the lower crust as the orogeny evolves. This recurring process of partial melting may have contributed to the formation of vast amounts of S-type granite and has been documented in a number of orogenic systems, such as the Lachlan fold belt (Chappell and White, 1974), the Aracuaí Orogen (Pedrosa-Soares et al., 2001, 2011), and the Tasmanide orogenic system (Collins and Richards, 2008).

In the Ediacaran-Cambrian Araçuaí orogen, there is evidence of at least three regional anatectic events that formed the S-type granites included in the G2 (ca. 585–545 Ma), G3 (ca. 545–530 Ma) and G4 supersuites (ca. 530–500 Ma) (De Campos et al., 2004, 2016; Gradim et al., 2014; Pedrosa-Soares et al., 2001, 2011; Richter et al., 2016; Tedeschi et al., 2016). No previous studies have investigated the potential anatectic recycling of older granites through detailed study of their mineralogy, mineral textures, mineral chemistry and geochronology. This study investigates the petrogenesis of the Carlos Chagas batholith (CCB), a very large body (~14,000 km^2) composed of peraluminous, S-type granites that formed during the syn-collisional stage of the Araçuaí orogen, with a view to better understanding crustal recycling during a long-lived orogeny. We present new petrographic evidence, as well as major and trace element mineral chemistry which documents garnet growth during two separate partial melting episodes in the CCB. U–Pb in situ monazite and zircon dating allow the timing of the high-grade metamorphic events that produced the garnet crystals to be constrained. In addition, P–T–t paths for the two successive metamorphic events are quantified in order to explain how granitic bodies, possibly initially intruded into the upper crust, can experience more than one cycle of mid- to lower crustal tectonic recycling.

2. Geotectonic and regional setting

The Araçuaí orogen of southeastern Brazil together with its counterpart located in southwestern Africa, the West Congo belt (Fig. 1), form an orogenic system that developed during the Brasiliano–Pan-African orogeny between the São Francisco and Congo cratons (Alkmim et al., 2006; Pedrosa-Soares et al., 2001, 2008). Formed during the amalgamation of Western Gondwana in Ediacaran to Cambrian time, the Araçuaí-West Congo orogenic system was split into two distinct belts by the opening of the South Atlantic Ocean in the Cretaceous (Fig. 1). The West Congo belt inherited important rift to proximal passive margin sequences of the precursor basins, which show low grade metamorphism and no orogenic igneous rocks (Tack et al., 2001). On the other hand, the Araçuaí orogen inherited two thirds of the orogenic system, including rift-related to distal passive margin and oceanic sequences with ophiolitic bodies of the precursor basin system, and the Rio Doce magmatic arc, as well as the collisional and post-collisional igneous suites (Pedrosa-Soares et al., 2001, 2008, 2011). The huge quantity of orogenic granites in the Araçuaí orogen can be grouped into five regional supersuites based on field relationships, structural features and geochemical and geochronological data. These are: G1 (Rio Doce magmatic arc, ca. 630–585 Ma), G2 (ca. 585–545 Ma), G3 (ca. 545–530 Ma), G4 (ca. 530–500 Ma), and G5 (ca. 525–480 Ma) (see synthesis, and updated geochemical and geochronological data in Belém, 2014; De Campos et al., 2016; Gradim et al., 2014; Pedrosa-Soares et al., 2011; Peixoto et al., 2015; Richter et al., 2016; Silva et al., 2011; Tedeschi et al., 2016). Most collisional peraluminous granites ascribed to the G2 supersuite, like the Carlos Chagas batholith, occur in the northern back-arc region to the east of the Rio Doce arc (G1 supersuite), and along the northeastern sector of the Araçuaí orogen (Figs. 1 and 2).

The Carlos Chagas batholith, extends in a N-S direction between latitudes 17°S and 19°30′S in the states of Espírito Santo, Minas Gerais and Bahia. Cropping out over an area of approximately 14,000 km^2, it is one of the largest bodies of S-type granite in the world. The first characterization and delimitation of such a large amount of S-type granite resulted from systematic geological mapping covering the whole area of the batholith (Castañeda et al., 2006; Gradim et al., 2014; Pedrosa-Soares et al., 2001, 2006, 2007; Pinto et al., 2001; Queiroga et al., 2012; Roncato, 2009; Roncato et al., 2012; Sampaio et al., 2004). These publications also characterize the CCB lithotypes, and describe their main field, petrographic, structural and lithochemical features (see below).

The typical CCB rocks are coarse-grained S-type granites rich in K-feldspar megacrysts and relatively poor in mafic minerals, the so-called Carlos Chagas leucogranite. Macroscopically, the batholith shows striking structural variations from non-deformed granites with well-preserved igneous fabrics to increasingly deformed varieties showing the regional ductile foliation (Cavalcante et al., 2013; Gradim et al., 2014; Pedrosa-Soares et al., 2011). The deformed CCB granites frequently show post-kinematic leucosomes of garnet- and cordierite-bearing leucogranite (G3) in the form of veins and patches, overprinting the regional foliation Sn (Gradim et al., 2014; Pedrosa-Soares et al., 2011). The G3 leucosomes generally show gradational contacts in relation to the host G2 granite, suggesting an autochthonous origin for the G3 melt. Locally, sharp contacts between G3 veins and the host G2 granite can occur, indicating mobility of the G3 melt (Gradim et al., 2014; Pedrosa-Soares et al., 2011; Roncato, 2009). The G3 leucogranites show many remnants of the host G2 granite, in the form of paleosome (restites) and biotite-sillimanite-rich schlieren (Pedrosa-Soares et al., 2006; Roncato, 2009). The U–Pb ages of G2 and G3 from the same outcrops (Fig. 2) show that G3 leucogranites (ca. 545–530 Ma) are 40 Ma to 50 Ma younger than the older Carlos Chagas and Ataléia granites (Gradim et al., 2014; Pedrosa-Soares et al., 2011; Silva et al., 2002, 2011).

Foliated peraluminous granites of the G2 Ataléia suite (ca. 590–570 Ma) and granulite facies paragneiss complexes (Jequitinhonha and Nova Venécia; Gradim et al., 2014; Moraes et al., 2015; Richter et al., 2016) surround and underlie the CCB, and also appear as isolated massifs in erosional windows within the batholith (Fig. 2). The contact of the CCB with its host rocks varies from intrusive to gradational, with the Nova Venécia and Jequitinhonha paragneisses, to gradational or sharp, with the Ataléia foliated granites, and is defined by shear zones in some places. However, no evidence of large displacements along the CCB contacts has been described. Regionally, the CCB is relatively poor in xenoliths of the host rocks, which tend to be more common along the batholith borders.

The batholith was intruded by a number of plutons, dikes and veins composed of granitic, charnockitic and gabbroic rocks of the post-collisional (525 Ma–490 Ma) G5 supersuite (Belém, 2014; De Campos et al., 2004, 2016; Gradim et al., 2014). G5 intrusions cut the regional and local structures of the CCB rocks, and locally imposed high-grade metamorphic recrystallization on their host rocks (Belém, 2014; De Campos et al., 2016; Pedrosa-Soares et al., 2011; Queiroga et al., 2012; Roncato et al., 2012).

Ages of magmatic crystallization from 576 ± 8 Ma to 568 ± 5 Ma (uncertainties reported as 2σ) for the CCB have been constrained by several SHRIMP and LA-ICP-MS zircon U–Pb studies (Gradim et al., 2014; Silva et al., 2002, 2011; Vauchez et al., 2007). The youngest metamorphic age (549 ± 28 Ma) from the ultramylonite, together with the age (546 ± 7 Ma) of a garnet-cordierite granite (G3) forming leucosomes that overprint a foliated Carlos Chagas leucogranite were suggested to constrain the end of the collisional stage (Gradim et al., 2014). However, Noce et al. (2004), Pedrosa-Soares et al. (2011), and Silva et al. (2002, 2011) reported ages as young as 532 ± 11 to 531 ± 10 Ma for G3 granites. To some extent, the uncertainties on some of the age data from these previous studies make the interpretations of the timing of crystallization, metamorphism and possible anatexis speculative.

Please cite this article as: Melo, M.G., et al., Two cryptic anatectic events within a syn-collisional granitoid from the Araçuaí orogen (southeastern Brazil): Evidence from the..., Lithos (2016), http://dx.doi.org/10.1016/j.lithos.2016.10.012

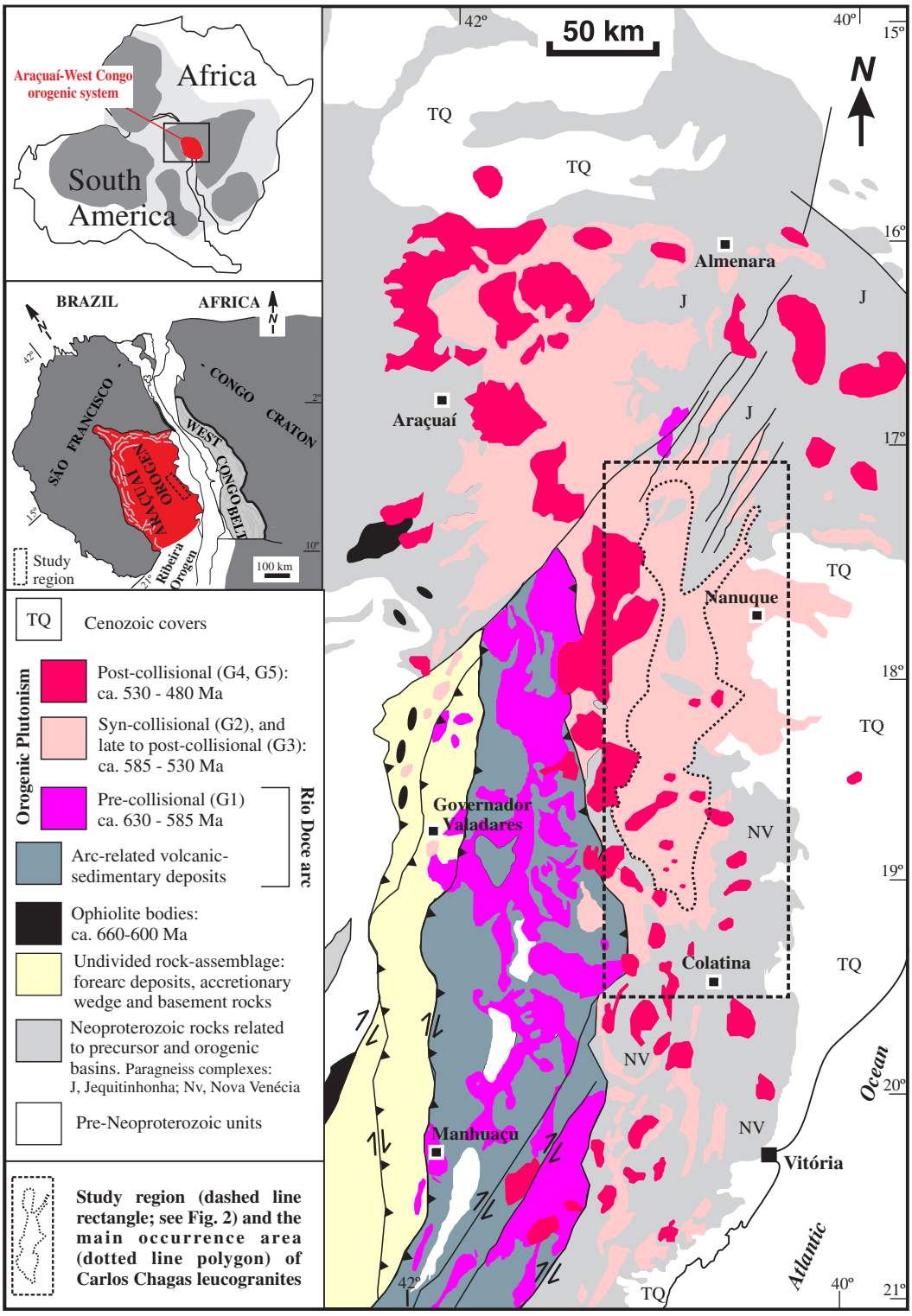

Fig. 1. Simplified geological map of the Araçuaí orogen (modified from Pedrosa-Soares et al., 2011), showing location of the study region (dashed rectangle) and the main occurrence area (dotted polygon) of the Carlos Chagas leucogranites.

3. Sampling and petrography

Representative samples were collected over an extensive area of the CCB (Fig. 2), with most samples being sourced from large dimension stone quarries and road cuts. Petrographic studies were carried out on sixty-four thin sections, including the thirty-five thin sections previously studied by Castañeda et al. (2006), Gradim et al. (2007), Queiroga et al. (2012) and Roncato et al. (2012). Three different mineral assemblages characterize the Carlos Chagas leucogranite from the G2 supersuite (mineral abbreviation after Whitney and Evans, 2010):

Assemblage 1: Qz + Pl + Kfs + Bt + Grt + Ilm ± Rt
Assemblage 2: Qz + Pl + Kfs + Bt + Grt + Ilm + Sil
Assemblage 3: Qz + Pl + Kfs + Bt + Grt + Ilm + Sil + Spl

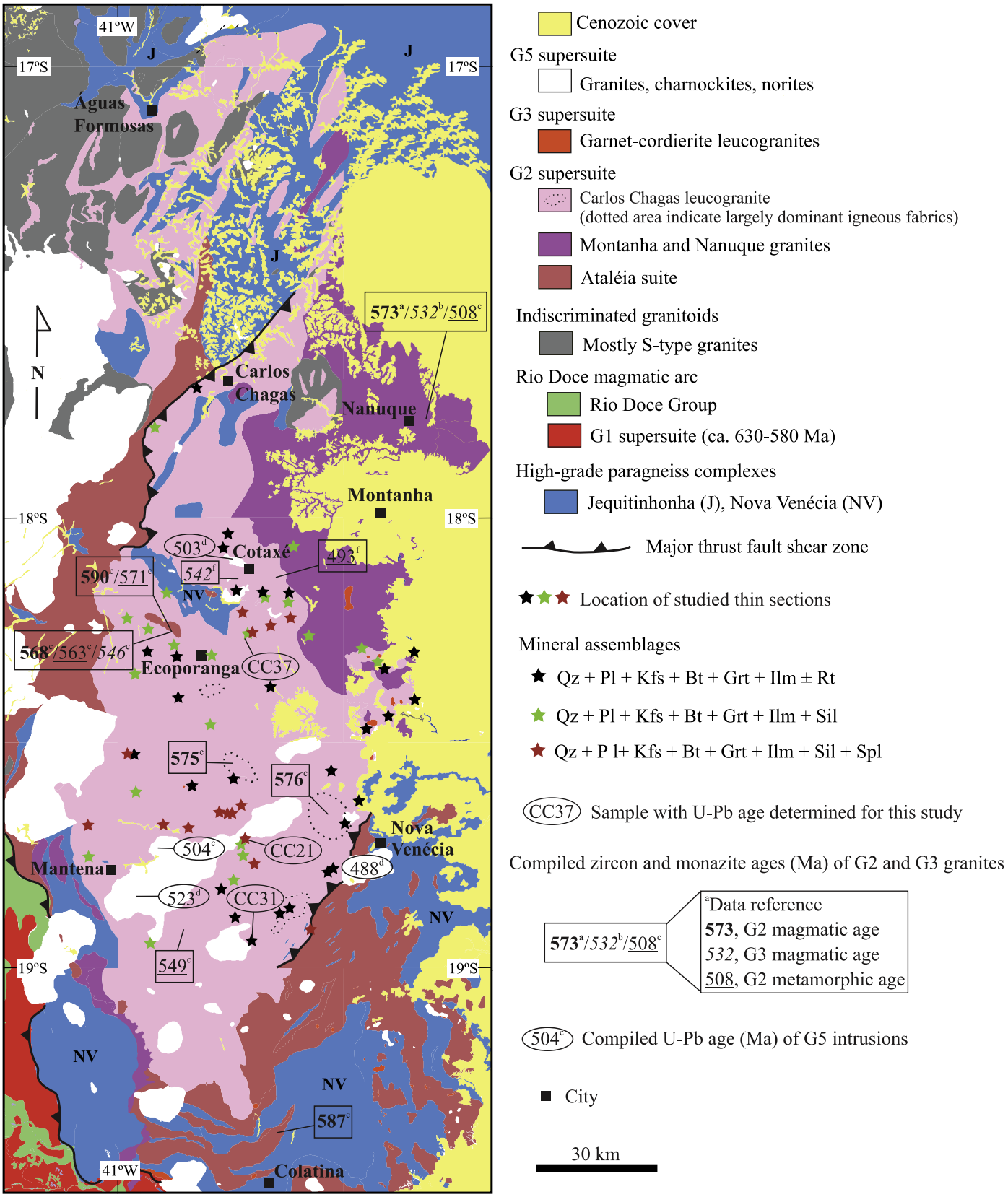

Fig. 2. Simplified geological map for the study region (compiled from 1:100.000 scale maps published by Baltazar et al., 2010; Castañeda et al., 2006; Gradim et al., 2007; Pinto et al., 2001; Queiroga et al., 2012; Roncato et al., 2012), showing the area covered by Carlos Chagas leucogranites, location of samples (CC) analyzed in this study, and compiled U–Pb geochronological data from: a, Silva et al. (2002, 2011); b, Pedrosa-Soares et al. (2011); c, Gradim et al. (2014); d, De Campos et al. (2016); e, Vauchez et al. (2007); f, Pedrosa-Soares et al. (2006).

Please cite this article as: Melo, M.G., et al., Two cryptic anatectic events within a syn-collisional granitoid from the Araçuaí orogen (southeastern Brazil): Evidence from the..., Lithos (2016), http://dx.doi.org/10.1016/j.lithos.2016.10.012

Table 1
Mineral modal proportions (in vol.%) based on the thin sections.

Assemblages	Qz	Pl	Kfs	Bt	Grt	Sil	Hc
1	29–45	8–15	22–43	2–5	4–18	–	–
2	22–37	15–22	17–28	1–4	3–15	1–5	–
3	25–41	17–24	28–39	0.5–3	4–10	0.5–2	<1

Scanned images of the thin sections were used in conjunction with the software programme ImageJ (Rasband, 1997–2012) to determine the modal proportions of the minerals which are presented in Table 1.

Fig. 3 shows the macroscopic features of representative rock samples from each mineral assemblage type.

3.1. Assemblage 1

The samples comprise foliated and non-foliated, very coarse- to coarse grained granites with abundant euhedral K-feldspar megacrysts (Fig. 3a,b). Many large outcrops show that the non-deformed facies with macroscopically well-preserved igneous fabrics progressively grade into the deformed facies. The mineral assemblage in both foliated and non-foliated varieties is characterized by large garnet porphyroblasts

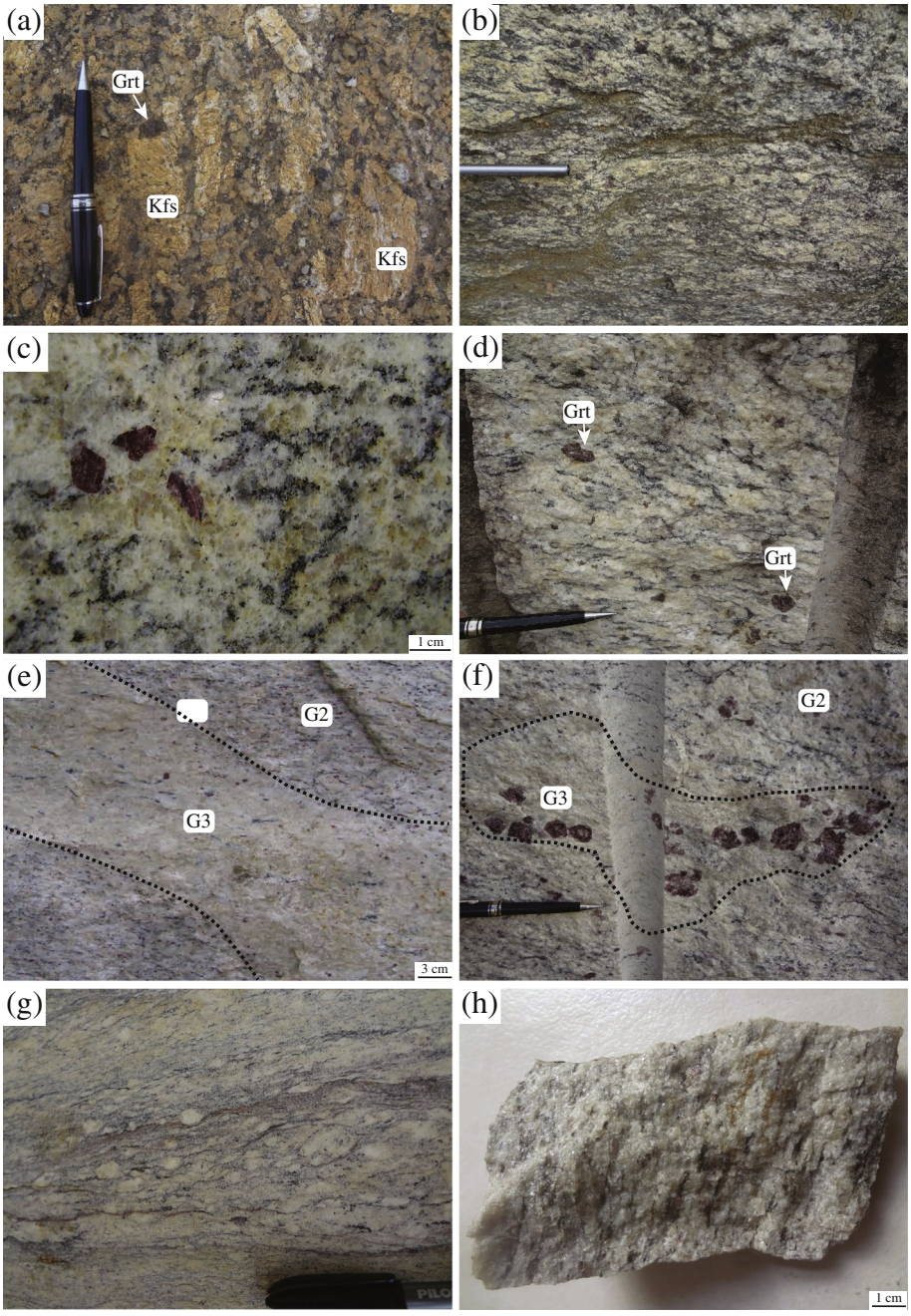

Fig. 3. Macroscopic features in rocks from mineral assemblages 1 (a,b), 2 (c–f) and 3 (g,h). Note that most examples are deformed to some degree. (a) Very coarse-grained granite showing fabrics interpreted to record a transition from magmatic deformation marked by the alignment of K-feldspar megacrysts, to solid-state recrystallization of interstitial quartz and K-feldspar. (b) Regional foliation (S_n) marked by biotite in the granite. (c) Weakly deformed leucogranite showing euhedral to subhedral garnet crystals. (d) Sigma shape of K-feldspar grains in sillimanite- and garnet-bearing leucogranite. (e) G3 leucogranite vein (dashed line) cutting the G2 granite. (f) Dashed lined delimited G3 garnet-bearing leucogranite patches. (g) Mylonite showing feldspar porphyroclasts surrounded by a quartz-rick matrix. (h) Highly deformed mylonitic leucogranite, with foliation marked by sillimanite needles, greenish spinel and quartz ribbons.

Please cite this article as: Melo, M.G., et al., Two cryptic anatectic events within a syn-collisional granitoid from the Araçuaí orogen (southeastern Brazil): Evidence from the..., Lithos (2016), http://dx.doi.org/10.1016/j.lithos.2016.10.012

crystals in a coarse- to very coarse-grained biotite-bearing quartz-feldspathic matrix (Fig. 4a). The accessory assemblage is dominated by rutile, ilmenite, zircon, monazite and apatite, followed in abundance by sulfide phases (e.g. pyrite, chalcopyrite and sphalerite). The majority of garnet porphyroblasts (Grt_1, 5–35 mm) are poikiloblastic and contain numerous inclusions (40–380 μm) of rounded biotite, lobate and rounded quartz (Fig. 4b,c), as well as the accessory minerals (ilmenite, rutile, apatite, zircon and monazite). Thin films of quartz and plagioclase occur along the boundaries of garnet and euhedral rutile crystals (Fig. 4d). Additionally, thin films of quartz are also observed between plagioclase grains in the matrix (Fig. 4e).

Three textural varieties of biotite are recognized in these samples. The first type is characterized by rounded inclusions in poikiloblastic garnet, as mentioned above (Fig. 4b,c). Matrix biotite consists of small single crystals and/or clots of crystals (0.1–1.7 mm) aligned with the regional foliation (Fig. 4a,e). Zircon is a common inclusion in these biotite crystals and some grains show rims that have been partially altered to ilmenite. The last type (0.16–1.2 mm) occasionally occurs at the margins of the larger garnet crystals (Fig. 4a,c).

Plagioclase and quartz in the matrix commonly have sutured boundaries typical of grain boundary migration at high-temperature (Fig. 4f). K-feldspar occurs mainly as megacrysts in the matrix (up to 12 cm) and surrounding garnet crystals. Euhedral K-feldspar crystals are common in all but the most strongly deformed granites, presumably due to strain partitioning preferentially into the surrounding quartz-bearing matrix.

3.2. Assemblages 2 and 3

Mineral assemblages 2 and 3 are only found in the deformed Carlos Chagas leucogranite that vary progressively from foliated granites with an incipient augen structure to mylonitic granites (Fig. 3c–h). The foliation around sigmoidal porphyroclasts of K-feldspar and garnet are a result of anastomosing foliation and form augen structure. Moreover, the ductile deformation is attested by presence of quartz ribbons, recrystallization tails around (rotated or not) garnet and feldspar porphyroclasts, and mineral trails of sillimanite needles and green spinel. Generally, the biotite content decreases (from 5 vol.% to <1 vol.%) with increasing deformation. Deformed granites exhibiting the regional foliation Sn largely predominates in the Carlos Chagas batholith.

The samples differ from assemblage 1 by the presence of sillimanite in a foliation that wraps around the biotite-bearing garnet porphyroblasts (Grt_1) and by formation of a second generation of garnet (Grt_2) (Fig. 5a,b). In these samples, matrix sillimanite forms prismatic aggregates with inclusions of rounded plagioclase. In addition, corroded plagioclase occurs adjacent to sillimanite prisms. Grt_2 occurs as smaller euhedral/subhedral crystals (0.1–0.6 mm) with inclusions of sillimanite needles that are aligned with foliated matrix sillimanite (Fig. 5a).

Distinct textural types of biotite are also identified in assemblages 2 and 3. Matrix biotite commonly shows evidence of having formed through reactions between melt and ferromagnesian minerals in that it commonly occurs in symplectites with quartz (Fig. 5c). The

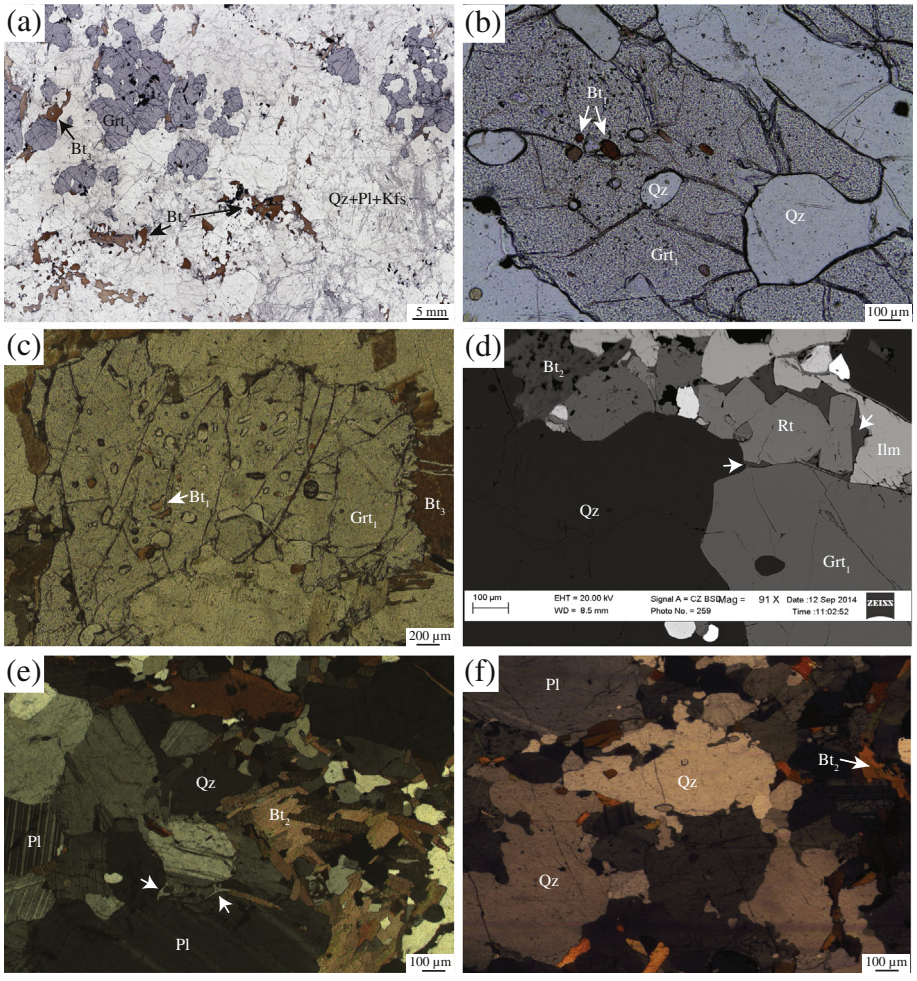

Fig. 4. Photomicrographs of microstructures in rocks from assemblage 1. (a) Scanned thin section showing garnet porphyroblasts in a biotite-bearing quartz-feldspathic matrix. (b) Garnet porphyroblasts (Grt_1) in the foliated granite, showing rounded biotite and quartz inclusions. (c) Multiple rounded and quartz biotite inclusions in garnet, which are likely to be the consequence of a biotite melting reaction. (d) BSE image showing thin films of plagioclase (white arrows) along garnet boundaries and surrounding euhedral rutile crystals. (e) Quartz films (white arrows) between plagioclase grains in matrix. Foliation marked by biotite. (f) Sutured boundaries in quartz formed by grain-boundary bulging.

Please cite this article as: Melo, M.G., et al., Two cryptic anatectic events within a syn-collisional granitoid from the Araçuaí orogen (southeastern Brazil): Evidence from the..., Lithos (2016), http://dx.doi.org/10.1016/j.lithos.2016.10.012

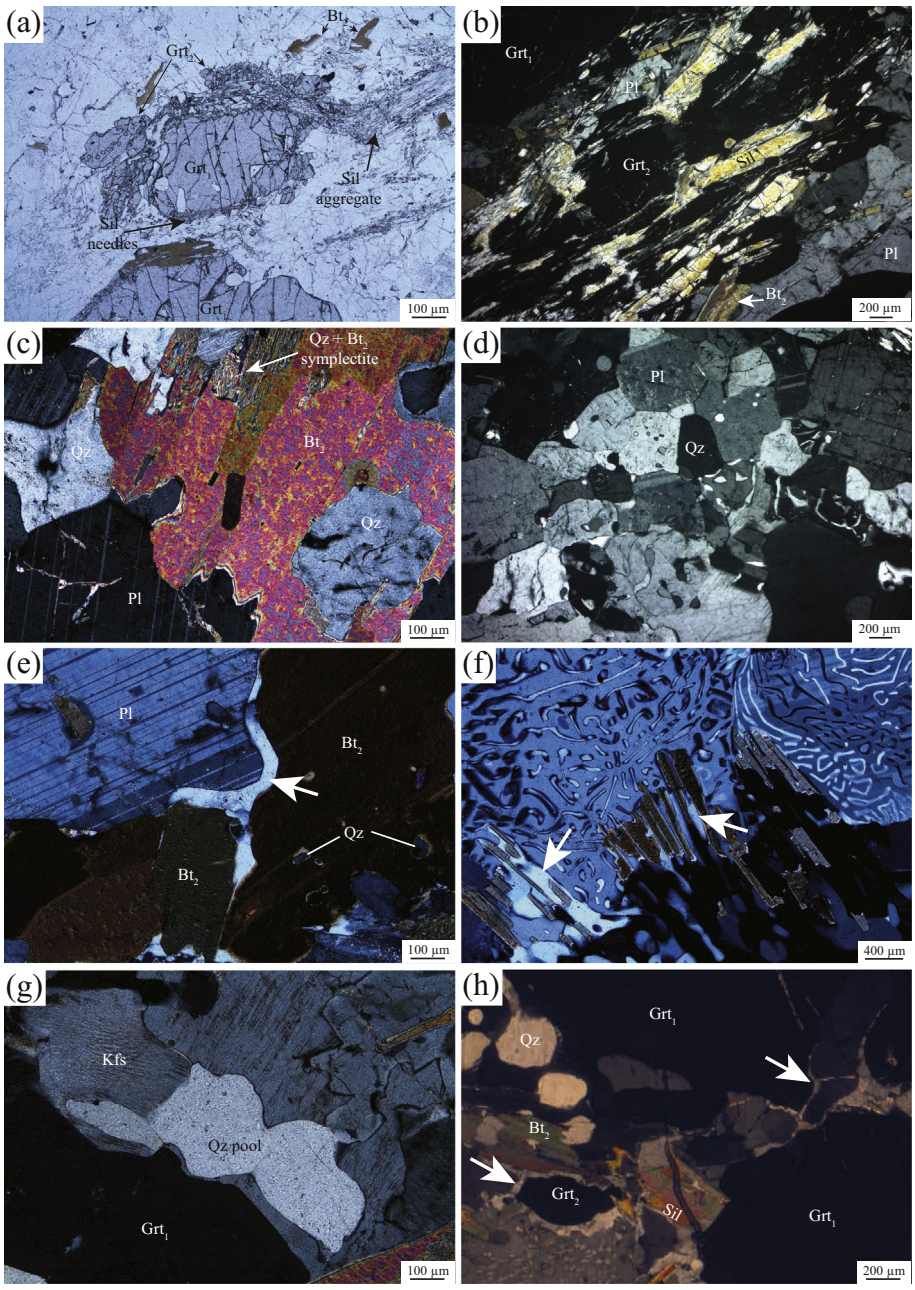

Fig. 5. Photomicrographs of microstructures observed in rocks from assemblages 2 and 3. (a) Two different textural varieties of garnet and their relationships with the biotite-sillimanite fabric. Mineral inclusion suites in both garnet generations are consistent with their production as peritectic products of incongruent melting reactions, which consumed biotite. Sillimanite needles wrap around Grt_1, but are overgrown by Grt_2. (b) An aggregate of garnet crystals (Grt_2) which overprint the biotite-sillimanite foliation. (c) Quartz and biotite symplectite in the matrix. (d) Development of polygonal grains in the quartzofeldspathic matrix. (e) Cuspate quartz (white arrow) along the grain boundaries of biotite and plagioclase in the matrix. (f) Quartz-filled melt pools (white arrow) around biotite grains. Intergrowth myrmekite. (g) Quartz-filled melt pools adjacent to garnet. (h) Films of quartz (white arrow) in garnet boundaries.

quartzofeldspathic matrix generally shows evidence for high temperature intracrystalline deformation and recrystallization, such as undulose extinction and development of subgrains in quartz, irregular twinning in plagioclase and polygonal grains of quartz and plagioclase (Fig. 5d). Intergrowths of myrmekite and albite in K-feldspar are common. Plagioclase and quartz with cuspate-lobate shapes occur as interstitial phases (Fig. 5e). Quartz-filled former melt pools are observed adjacent to garnet and biotite (Fig. 5f,g). Pseudomorphed thin melt films commonly occur surrounding both generations of garnet crystals (Fig. 5h).

In contrast to assemblage 2, the assemblage 3 shows spinel as dark-green, elongated, subhedral to rounded grains typically surrounded garnet and occasionally included in sillimanite and garnet.

4. Mineral chemistry

The mineral chemistry of garnet, biotite, plagioclase, K-feldspar, spinel and ilmenite is listed in Supplementary data (Table 1); the analytical methodology is reported in Supplementary material. The end-member concentrations were calculated as: $X_{Alm} = Fe^{2+}/(Fe^{2+}+Mg + Mn + Ca)$, $X_{Py} = Mg/(Fe^{2+}+Mg + Mn + Ca)$, $X_{Spss} = Mn/(Fe^{2+}+Mg + Mn + Ca)$, $X_{Grs} = Ca/(Fe^{2+}+Mg + Mn + Ca)$, $Mg\# = Mg/(Mg + Fe^{2+})$, $X_{An} = Ca/(Ca + Na + K)$, $X_{Ab} = Na/(Ca + Na + K)$, $X_{Or} = K/(Ca + Na + K)$ and $X_{Ghn} = Zn/(Zn + Mg + Fe^{2+})$. Fe^{3+} concentration in garnet, ilmenite and spinel was calculated using the general equation of Droop (1987).

Please cite this article as: Melo, M.G., et al., Two cryptic anatectic events within a syn-collisional granitoid from the Araçuaí orogen (southeastern Brazil): Evidence from the..., Lithos (2016), http://dx.doi.org/10.1016/j.lithos.2016.10.012

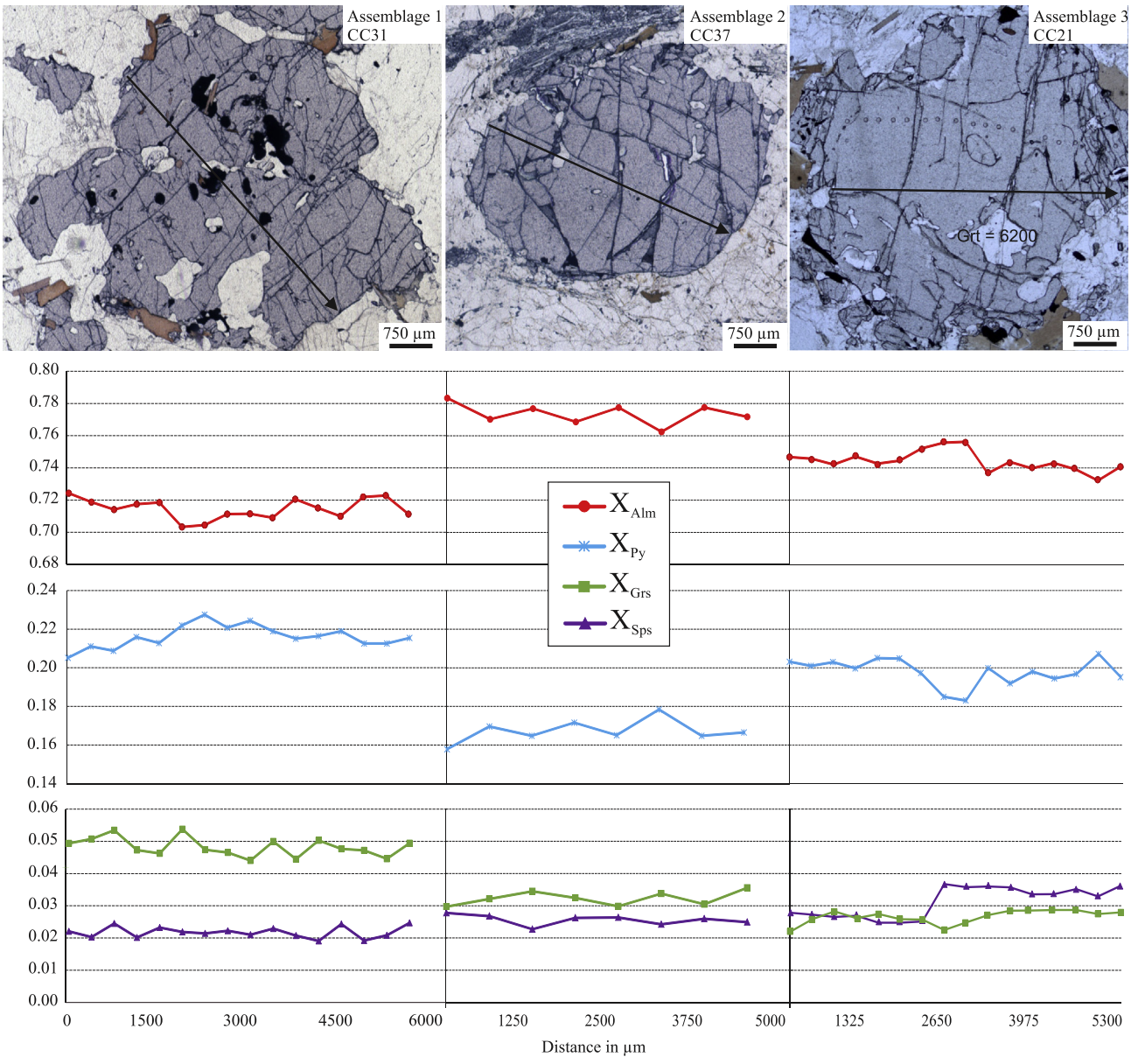

Fig. 6. Compositional profile of representative poikiloblastic garnet (Grt_1) analyzed in each mineral assemblage.

Both generations of garnet are almandine-rich with subordinate pyrope, and minor grossular and spessartine. Individual crystals do not display any significant major element zonation (Figs. 6 and 7a, see more details in Supplementary data – Table 1). The Grt_1 crystals have X_{Alm} and X_{Py} ranging of 0.70 to 0.79 and 0.15 to 0.23, respectively (Figs. 6 and 7a). X_{Grs} is higher in Grt_1 from assemblage 1 (X_{Grs} = 0.04–0.06) than Grt_1 from assemblages 2 and 3 (X_{Grs} ~ 0.03) (Figs. 6 and 7a). Spessartine component in Grt_1 is similar in all assemblages (X_{Spss} = 0.02–0.03) and Mg# varies between 0.16 and 0.25. Grt_2 is characterized by slightly different compositions to Grt_1, which is indicated by an increase in Fe-content (X_{Alm} = 0.78–0.82) and decrease in Mg-content (X_{Py} = 0.12–0.17) (Fig. 7a). For Grt_2, its Mg# varies between 0.13 and 0.18. Spessartine and grossular contents are homogeneous in the Grt_2 crystals (X_{Spss} ~ 0.03 and X_{Grs} ~ 0.02).

As shown in Fig. 7b, biotite displays variable composition depending on its microstructural position. Biotite inclusions in Grt_1 present high Ti (0.48–0.74) and Mg# (0.50–0.69) values compared to matrix biotite (Ti = 0.39–0.63 and Mg# = 0.40–0.52). Retrograde biotite around garnet is characterized by low Ti and intermediate Mg# values (Ti = 0.25–0.58 and Mg# = 0.48–0.59).

Matrix plagioclase is unzoned and displays X_{An} values of 0.22–0.33 (Supplementary data – Table 1). Plagioclase adjacent to garnet has the same composition as the matrix crystals, whereas inclusions in garnet have X_{An} values ranging from 0.25 to 0.29, and inclusions in sillimanite have X_{An} of ~0.26. Matrix K-feldspar has X_{Or} values of 0.71 to 0.92. Spinel crystals have relatively high Zn-content with X_{Ghn} of 0.10–0.20.

5. Rare earth element composition of garnet

Rare earth element (REE) concentrations in garnet were measured by LA-ICP-MS (Supplementary data - Table 2, see methodology in Supplementary material) from the same three thin sections representing assemblages 1, 2 and 3 from which major element compositions were reported.

The Grt_1 crystals from all assemblages are enriched in HREE, with ΣGd-Lu of 86–467 ppm. They have lower Gd_N/Lu_N ratios in the rim (0.21–2.91) than in the cores (0.08–0.42) (Fig. 8). If the small number of samples studied can be considered to be representative, the garnet rims also display a larger negative Eu anomaly in assemblages 2 and 3 (Eu/Eu^* = 0.01–0.02) than the assemblage 1

Please cite this article as: Melo, M.G., et al., Two cryptic anatectic events within a syn-collisional granitoid from the Araçuaí orogen (southeastern Brazil): Evidence from the..., Lithos (2016), http://dx.doi.org/10.1016/j.lithos.2016.10.012

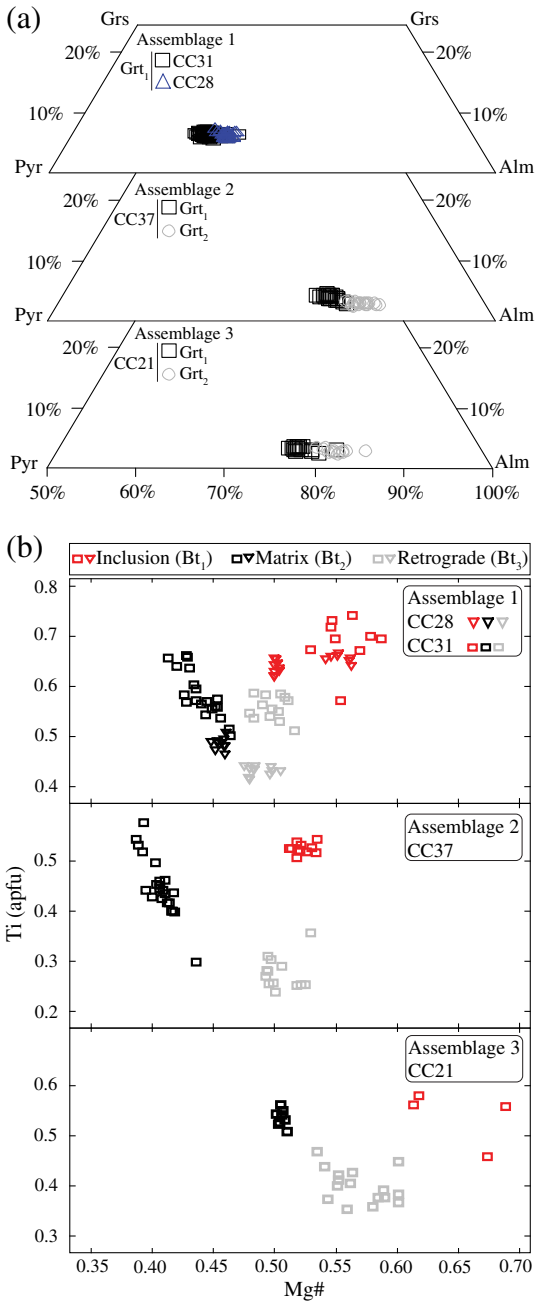

Fig. 7. Mineral chemistry for all mineral assemblages from CCB. (a) Grs-Alm-Py garnet diagram. (b) Biotite compositions plotted on a Ti (apfu) v. Mg#.

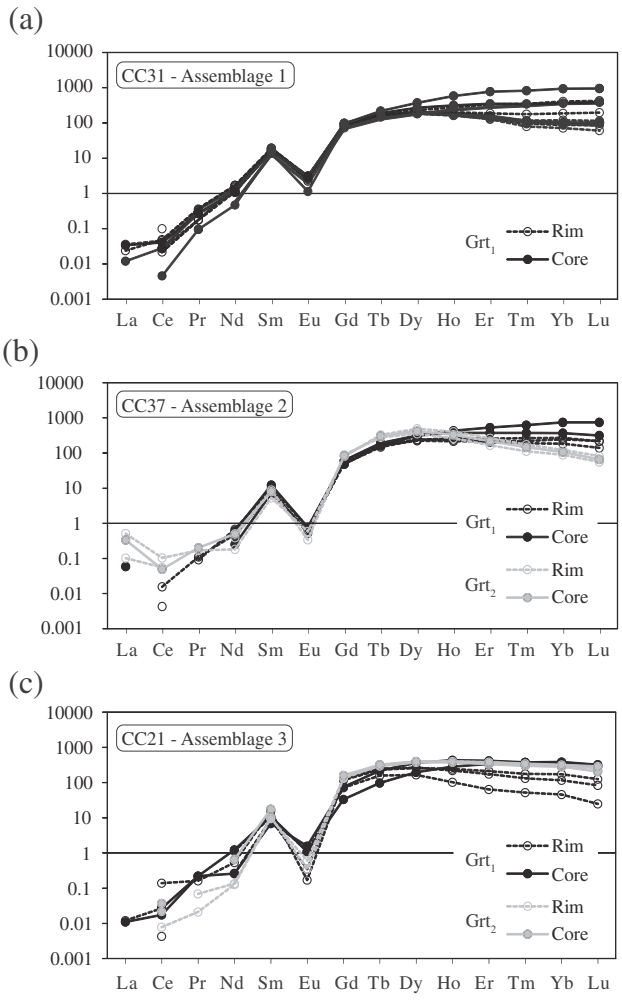

Fig. 8. Chondrite-normalized (McDonough and Sun, 1995) REE patterns in garnet from Carlos Chagas leucogranite. (a) Grt_1 from assemblage 1 are enriched in HREE, have flat HREE patterns and negative Eu anomalies. (b) Grt_1 are richer in Gd-Dy than Grt_2 from assemblage 2. (c) Both garnet generations from assemblage 3 display flat HREE patterns and pronounced negative Eu anomalies.

rocks ($Eu/Eu^* = 0.04–0.07$) (Fig. 8). The Grt_2 crystals have ΣGd-Lu of 175–290 ppm that is within the range of Grt_1. In assemblage 2, both the cores and rims vary from slightly positive to slightly negative HREE ratios ($Gd_N/Lu_N = 0.69–1.60$) (Fig. 8b). Grt_2 crystals from assemblage 3 have slightly positive slope HREE patterns ($Gd_N/Lu_N = 0.51–0.71$, Fig. 8c). Both samples show broadly similar negative Eu anomalies ($Eu/Eu^* = 0.01$) (Fig. 8b,c).

6. *P–T* conditions

Phase equilibrium modeling was performed in the chemical system NCKFMASHTO (Na_2O-CaO-K_2O-FeO-MgO-Al_2O_3-SiO_2-H_2O-TiO_2-Fe_2O_3) using Theriak-Domino software (De Capitani and Petrakakis, 2010), in combination with the updated tc2td.exe converted Holland and Powell (1998) database created by Tinkham. The modeling used the a-x relationships of White et al. (2007) for silicate melt, garnet and biotite; White et al. (2002) for orthopyroxene and spinel; White et al. (2000) for ilmenite; Coggon and Holland (2002) for white mica; and Holland and Powell (2003) for plagioclase and alkali feldspar. Pseudosections were calculated using the bulk composition from foliated Grt-bearing (samples CC28 and CC31 – assemblage 1) and Sil-Grt-bearing granites (sample CC37 – assemblage 2) (Table 2). Phase equilibrium modeling could not be successfully conducted for the Spl-Sil-Grt-bearing samples (assemblage 3) because the available a-x models for spinel do not include Zn and the Zn content of the spinel in these samples is too high to be ignored (7.20 wt.% - Supplementary data – Table 1). CCB rocks record textural and mineral chemical evidence of partial melting (Figs. 4d,e and 5c,e,f,g,h). In addition, the peritectic garnet produced by partial melting is well preserved, which necessitates substantial melt loss prior to cooling (White and Powell, 2002). Consequently, the prograde evolution of the CCB cannot be constrained by phase equilibrium modeling in these melt-depleted bulk compositions (White and Powell, 2002). However, the unretrogressed nature of the rocks does allow for detailed investigation peak metamorphic conditions recorded by assemblage 1 and 2.

Appropriate values for water content were investigated on T-X pseudosections and the bulk H_2O values were chosen according to the methodology of White et al. (2001), such that the solidus was located just below the lowest temperature of occurrence of the interpreted

Table 2
Bulk composition used for metamorphic modeling and normalized to 100%. H_2O and Fe_2O_3 content.

Samples	SiO_2	Al_2O_3	TiO_2	FeO	Fe_2O_3	MgO	CaO	Na_2O	K_2O	H_2O	Total
CC28	74.57	12.78	0.38	2.69	0.03	0.59	1.08	2.16	5.50	0.22	100.00
CC31	66.81	15.82	1.06	5.33	0.15	1.32	2.00	2.82	4.40	0.29	100.00
CC37	60.69	24.44	0.22	9.03	0.00	0.90	1.47	2.51	0.61	0.12	100.00

peak assemblage (CC28 = 0.22%, CC31 = 0.28% and CC37 = 0.12%). The Fe_2O_3 content for all compositions were determined using P-X pseudosections with T fixed at 800 °C (CC28 and CC31) and 760 °C (CC37). This is consistent with experimental studies which document that these are the approximate minimum temperatures for garnet formation by absent-fluid melting reactions consuming biotite, quartz and plagioclase, and biotite, sillimanite, quartz and plagioclase, respectively (e.g. Castro et al., 1999; Patiño Douce and Harris, 1998; Patiño Douce and Johnston, 1991; Pickering and Johnston, 1998; Stevens et al., 1997). The value chosen for Fe^{3+} concentration in each bulk composition results in modeled Fe^{3+} concentrations in ilmenite and garnet, within the field of the relevant peak assemblage, that are in agreement with measured values in these minerals in the specific sample.

6.1. Assemblage 1

Five samples were modeled to evaluate the *P–T* conditions of the assemblage 1 (Pl + Kfs + Grt + Bt + Qz + Rt + Ilm + melt). The modeling of two representative samples is presented below (samples CC28 and CC31). The results from another three samples are presented in Supplementary material (Figure SM1), indicating that the assemblage 1 is stable between 770 and 900 °C and 9.5–13 kbar.

6.1.1. Sample CC28

In this sample, the assemblage 1 is stable between 780 and 860 °C and 9.2–12.6 kbar (Fig. 9a), with a melt fraction <5 vol.% (Fig. 9b). Within this field, the amount of garnet (3–6 vol.%) and biotite (<3 vol.%) (Fig. 9c,e) is consistent with the quantities estimated in thin section (~4% and ~2%, respectively). The modeling shows an increase in the mode of Grt, melt and rutile, coupled with a decrease in the mode of Bt as temperature increases over the range defined by the peak assemblage (Fig. 9c,e). This is consistent with the occurrence of fluid-absent melting reactions consuming biotite.

Modeled garnet composition shows Mg# of 0.19–0.30, X_{Grs} of 0.04–0.10 and X_{Alm} of 0.64–0.77 in the peak assemblage field (Fig. 9c,d). These values encompass those of measured in Grt_1, showing Mg#, X_{Grs} and X_{Alm} values of 0.20–0.22, 0.04–0.06 and 0.72–0.74, respectively (Supplementary data - Table 1). Mg# values for the modeled biotite range from 0.46 to 0.61 in the peak field (Fig. 9e) and measured values for biotite inclusions (Bt_1) in garnet range from 0.50 to 0.56 (Supplementary data - Table 1). The use of X_{Grs}, X_{Alm}, Grt Mg# and Bt_1 Mg# values help to more tightly constrain the *P–T* conditions of the peak assemblage to 790–820 °C and 9.5–10.5 kbar (Fig. 9f).

6.1.2. Sample CC31

The peak assemblage Pl + Kfs + Grt + Bt + Qz + Rt + Ilm + melt occurs at P–T conditions between 800 and 870 °C and 8.9–13.4 kbar (Fig. 10a). Within this field the maximum amount of melt is <6 vol.% (Fig. 10b). This is consistent with the mineral assemblage observed in the assemblage 1 rocks that commonly show ilmenite and rutile as inclusions in Grt_1 and also associated pseudomorphed thin films of melt along the garnet boundaries (Fig. 4d). In the peak assemblage field, the garnet mode ranges from 8 to 13 vol.% (Fig. 10c), while biotite is <5 vol.% (Fig. 10e). These modes are consistent with the garnet and biotite proportions estimated in thin section (~12% and ~4.5%, respectively) and outcrop (5–10% and 1–4%, respectively).

Modeled garnet and biotite compositions record Mg# of 0.23–0.35 (Fig. 10c) and 0.54–0.64 (Fig. 10e) in the assemblage field, respectively. The values of Mg# number measured in Grt_1 range from 0.21 to 0.25, while the biotite inclusions in garnet have values of 0.55–0.59 (Supplementary data - Table 1). Within the peak assemblage field, the garnet and melt proportions increase with increasing temperature while biotite proportion decreases (Fig. 10b,c,e), consistent with biotite-breakdown via incongruent melting reactions. X_{Grs} and X_{Alm} values are increased by increasing pressure and temperature, respectively. Measured Grt_1 composition yield X_{Grs} and X_{Alm} values that range from 0.04–0.05 and 0.70–0.72, respectively (Fig. 10d). *P–T* conditions of equilibration are further constrained by compositional isopleths of X_{Grs}, X_{Alm}, Grt Mg# and Bt_1 Mg# at 800–820 °C and 10–11 kbar (Fig. 10f).

6.2. Assemblage 2

Small domains of the garnet and sillimanite-bearing assemblage in the thin section CC37 are potentially useful to constrain the peak metamorphic conditions of the second metamorphic event. Rastered electron beam analyses of these areas were used to constrain the new bulk composition relevant to formation of the second generation of garnet. An average of the compositions of ten ~0.1 cm^2 size areas dominated by this assemblage is presented in Table 2. Using this bulk composition, the assemblage Pl + Kfs + Grt + Bt + Ilm + Qz + Sil + melt is stable between 755 and 770 °C and 4.8–9.0 kbar (Fig. 11a). In this field the amount of melt is below 3 vol.% (Fig. 11b); garnet between 16 and 17 vol.% and biotite below 2 vol.% (Fig. 11c,d). This is consistent with the mineral proportions estimated in this area of the thin section (garnet: ~17 vol.% and biotite: <1 vol.%). The lower pressure limit of the assemblage is bounded by the stability of cordierite at 5 kbar (Fig. 11a).

In the peak assemblage field, the modeled Mg# number and X_{Grs} for garnet are 0.14–0.15 and 0.01–0.04 (Fig. 11c,d), respectively. The values measured in Grt_2 are Mg # = 0.13–0.16 and X_{Grs} ~ 0.02 (Supplementary data - Table 1). The use of Grt Mg# and X_{Grs} isopleths allow the estimate of *PT* conditions of equilibration to be further constrained to approximately 770 °C and 6.6 kbar (Fig. 11e).

6.3. Melt production

As mentioned above, the excellent preservation of the garnet crystals within the metamorphosed CCB rocks necessitates significant melt loss prior to the cooling (White and Powell, 2002). To constrain the amount of melt produced in the CCB during the metamorphic events, we performed melt reintegration on samples CC31 and CC37 following the methodology of White et al. (2004).

The pseudosection modeling of the melt-reintegrated bulk composition (CC31) indicates that muscovite is stable over a substantial PT range in the protolith. During prograde metamorphism the rock underwent muscovite breakdown at ~650 °C producing 8 vol.% of melt, followed by biotite melting at 780–800 °C (Fig. 12a), with the

Fig. 9. *P–T* pseudosection calculated using the bulk composition from sample CC28 (assemblage 1). (a) *P–T* fields of peak assemblage Pl-Kfs-Grt-Bt-Ilm-Qz-Rt-Liq (bold line). (b) Plots of melt vol.%. (c) Plots of Grt Mg# and Grt vol.%. (d) Plots of X_{Grs} and X_{Alm}. (e) Plots of Bt Mg# and Bt vol.%. (f) *P–T* conditions of equilibrium based on the use of overlapping ranges of phase composition and abundance.

Please cite this article as: Melo, M.G., et al., Two cryptic anatectic events within a syn-collisional granitoid from the Araçuaí orogen (southeastern Brazil): Evidence from the..., Lithos (2016), http://dx.doi.org/10.1016/j.lithos.2016.10.012

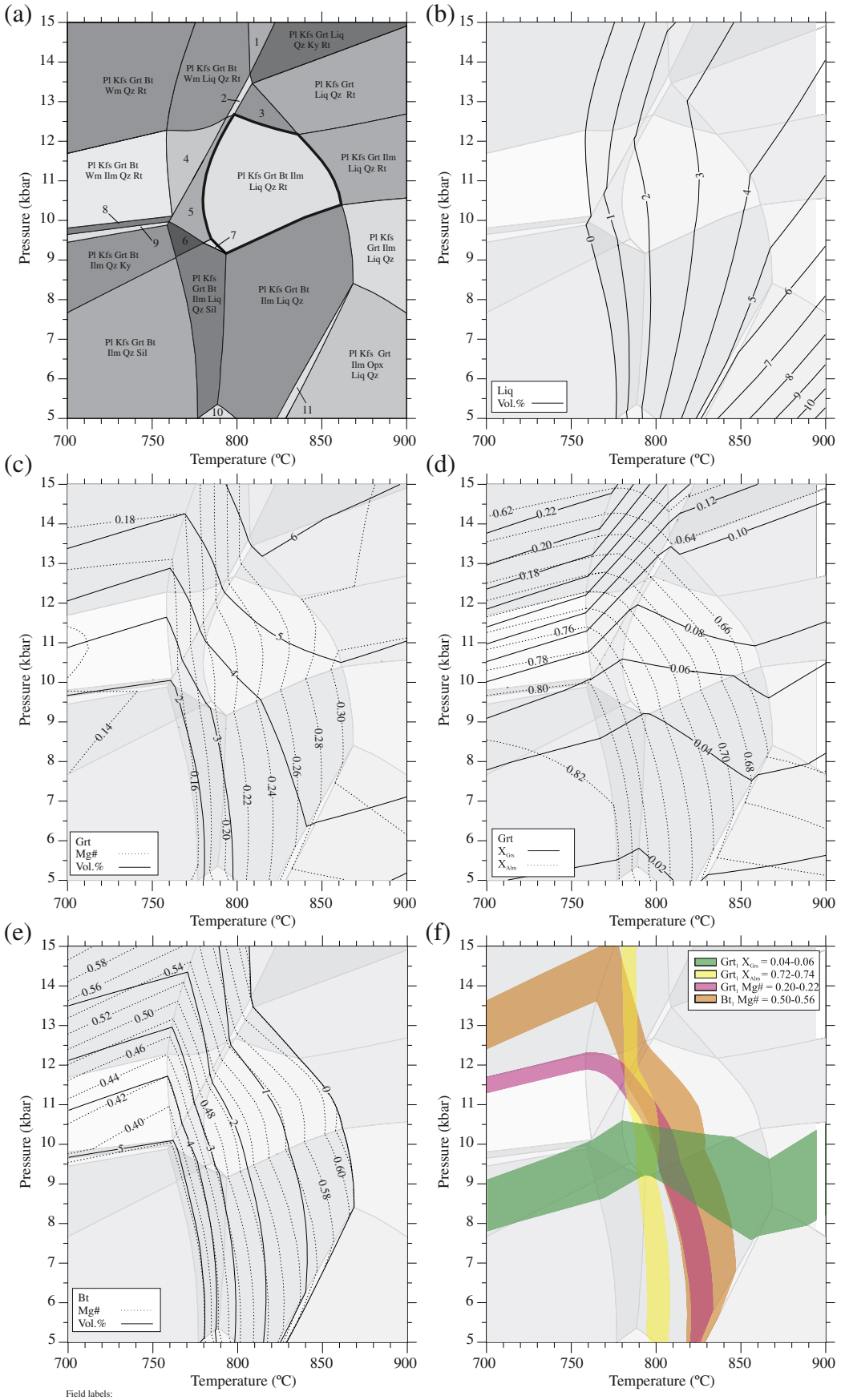

Field labels:

1 - Pl Kfs Grt Wm Liq Qz Rt, 2 - Pl Kfs Grt Bt Liq Ky Qz Rt, 3 - Pl Kfs Grt Bt Liq Qz Rt, 4 - Pl Kfs Grt Bt Wm Ilm Liq Qz Rt, 5 - Pl Kfs Grt Bt Ilm Liq Qz Ky Rt, 6 - Pl Kfs Grt Bt Ilm Liq Qz Ky, 7 - Pl Kfs Grt Bt Ilm Liq Qz Sil Rt, 8 - Pl Kfs Grt Bt Wm Ilm Qz Ky Rt, 9 - Pl Kfs Grt Bt Wm Ilm Qz Ky, 10 - Pl Kfs Grt Bt Ilm Cdr Liq Qz and 11 - Pl Kfs Grt Bt Ilm Opx Liq Qz

Please cite this article as: Melo, M.G., et al., Two cryptic anatectic events within a syn-collisional granitoid from the Araçuaí orogen (southeastern Brazil): Evidence from the..., Lithos (2016), http://dx.doi.org/10.1016/j.lithos.2016.10.012

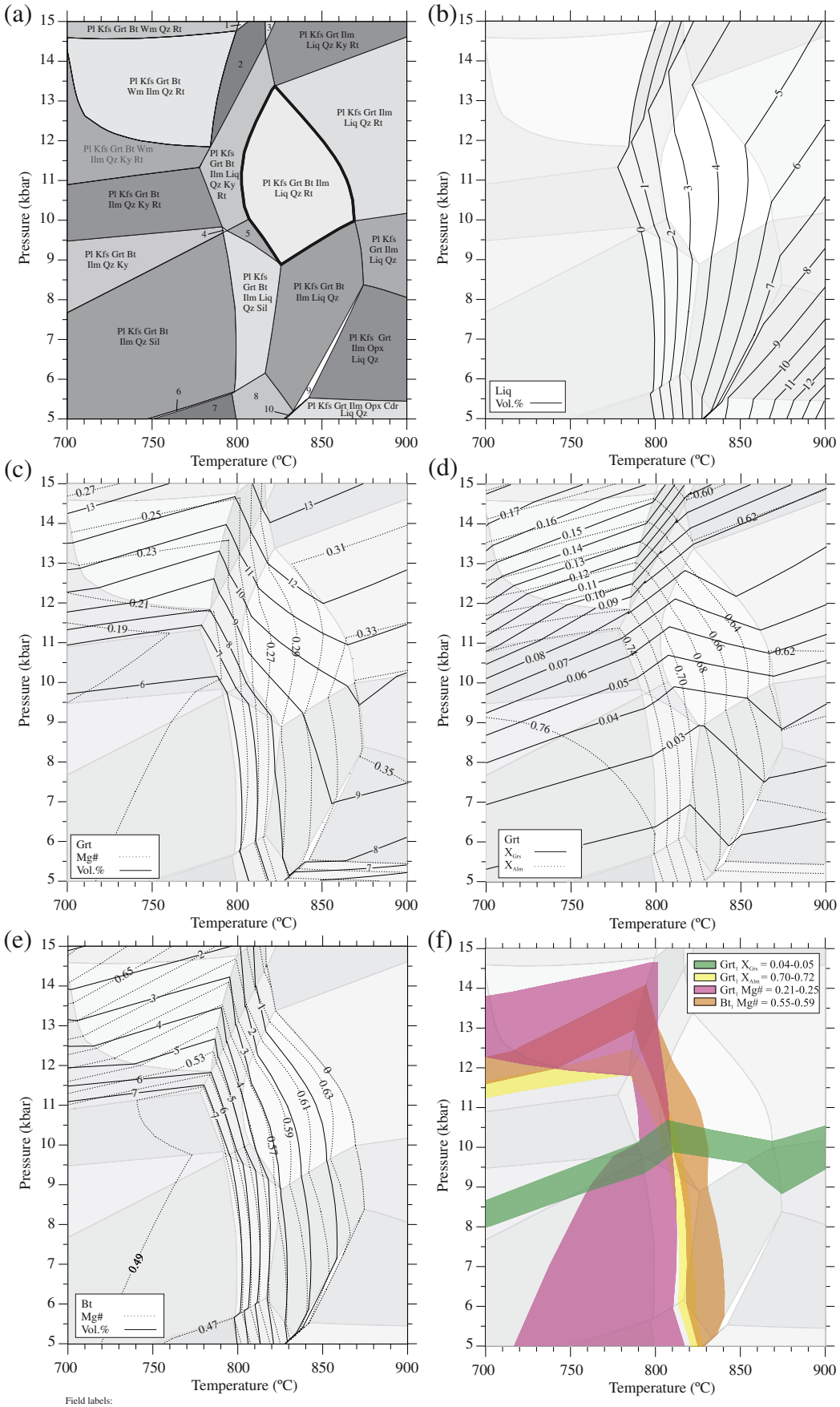

Field labels:

1 - Pl Kfs Grt Bt Wm Liq Qz Rt, 2 - Kfs Grt Bt Wm Ilm Liq Qz Rt, 3 - Kfs Grt Bt Wm Ilm Liq Qz Ky Rt, 4 - Pl Kfs Grt Bt Ilm Liq Qz Ky, 5 - Pl Kfs Grt Bt Ilm Liq Qz Sil Rt, 6 - Pl Kfs Grt Bt Ilm Cdr Qz Sil, 7 - Pl Kfs Grt Bt Ilm Cdr Qz, 8 - Pl Kfs Grt Bt Ilm Cdr Liq Qz, 9 - Pl Kfs Grt Bt Ilm Opx Liq Qz and 10 - Pl Kfs Grt Bt Ilm Opx Cdr Liq Qz

Please cite this article as: Melo, M.G., et al., Two cryptic anatectic events within a syn-collisional granitoid from the Araçuaí orogen (southeastern Brazil): Evidence from the..., Lithos (2016), http://dx.doi.org/10.1016/j.lithos.2016.10.012

addition of 26 vol.% of melt (Fig. 12b). Under the peak metamorphic conditions (bold line in Fig. 12a), peritectic phases (garnet and rutile) and melt are produced by fluid-absent melting reactions (Bt + Pl + Qz = Grt + Rt ± Kfs + melt). The pseudosection modeling predicts that 12–34 vol.% of melt was produced as the rock progressed to the peak conditions through partial melting reactions consuming biotite.

Applying the same approach to sample CC37, muscovite and sillimanite were present just below the wet solidus in the pre-melting assemblage (Pl + Bt + Wm + Qz + Sil + H_2O) at 650 ± 20 °C and 5 ± 1 kbar (Fig. 12a). During prograde metamorphism, garnet and melt were produced by incongruent melting of biotite and sillimanite via reaction Bt + Sil + Qz + Pl = Grt + melt, as indicated by increase in mode of garnet and melt (Fig. 12b). The modeling indicates that 16–30 vol.% of melt was produced on the evolution to peak metamorphism conditions via absent-fluid melting reactions.

7. LA-ICP-MS monazite geochronology

To better constrain the timing of the two partial melting episodes that have affected the CCB, we selected a separate thin section representing each of the three assemblages from the CCB for in situ LA-ICP-MS dating of monazite. Monazite grains in the samples commonly occur as: a) inclusions in Grt_1 crystals; b) adjacent to garnet boundaries; c) within the quartzo-feldspathic matrix; d) rarely as inclusions within Grt_2 crystals. The results of all monazite analyses are presented in Supplementary data (Table 3) and the analytical methods are described in Supplementary material. Spot analyses that were more than 5% discordant were discarded in the calculation of weighted mean $^{206}Pb/^{238}U$ ages. A summary with the monazite ages is presented in Table 3.

7.1. Sample CC31 – assemblage 1

Monazite grains are euhedral to subhedral, elongated and subrounded, and are 70–190 μm in diameter. Backscattered electron (BSE) imaging displays unzoned internal structure to weakly zoned grains (Fig. 13a).

Two spot analyses of monazite included in a Grt_1 core have Th/U values of 83–85 and show a mean $^{206}Pb/^{238}U$ age of 617 ± 12 Ma (95% conf., MSWD = 0.54). Six additional spot analyses on monazite included in Grt_1, which have Th/U values of 40–134, show a mean $^{206}Pb/^{238}U$ age of 560 ± 9 Ma (95% conf., MSWD = 1.8). One spot analysis in a monazite crystal that occur along microcracks in the Grt_1 core yields a younger $^{206}Pb/^{238}U$ age of 519 ± 14 Ma (Th/U = 20). This age is within error of the age of monazite included in the rim of Grt_1 crystals ($^{206}Pb/^{238}U$ = 521 ± 14 Ma, Th/U = 27), which also displays fractures.

Matrix monazite spot analyses range from 612 to 485 Ma. Two spot analyses in the core of matrix grains, with Th/U values of 60–61, have a mean $^{206}Pb/^{238}U$ age of 562 ± 11 Ma (95% conf., MSWD = 0.68) and other spots show a concordant age of 612 ± 17 Ma and a Th/U value of 98. Four spot analyses in the rims of matrix grains, with Th/U values between 36 and 43, display a mean $^{206}Pb/^{238}U$ age of 492 ± 16 Ma (95% conf., MSWD = 2.2).

7.2. Sample CC37 – assemblage 2

Monazite occurs as euhedral to subhedral, elongated, subrounded to oval-shaped grains of 50–90 μm of diameter. BSE imaging revealed that most grains are unzoned and a few crystals display a fine brighter rim (Fig. 13b).

Four spot analyses in monazite included within Grt_1 core, with Th/U values of 9–18, generate a mean $^{206}Pb/^{238}U$ age of 557 ± 7 Ma (95% conf., MSWD = 1.03). Two spot analyses on monazite included within the rim of Grt_1 crystals show $^{206}Pb/^{238}U$ ages of 569 ± 14 and 528 ± 14 (Th/U = 13 and 15, respectively). Eight spot analyses from matrix monazite, with Th/U values between 8 and 21, produced a mean $^{206}Pb/^{238}U$ age of 558 ± 10 Ma (95% conf., MSWD = 2.5). One spot analysis presents younger $^{206}Pb/^{238}U$ age of 484 ± 13 Ma, with Th/U value of 8.

7.3. Sample CC21 – assemblage 3

Monazite occurs in many grain shapes that vary from euhedral/subhedral, rounded/subrounded to oval, ranging from 30 to 120 μm in size. BSE images display unzoned grains as well as complex, patchy zonation in some examples (Fig. 13c).

Two spot analyses on monazite cores within the cores of Grt_1 crystals show $^{206}Pb/^{238}U$ ages of 566 ± 16 and 552 ± 15, with Th/U values of 81 and 24, respectively. Two spot analysis in monazite rims that occur along microcracks in the Grt_1 core display younger ages of 535 ± 14 (Th/U = 42) and 516 ± 14 Ma (Th/U = 15). One spot analysis on a monazite included in a Grt_2 core shows age of 515 ± 14 Ma and Th/U value of 10.

Eight spot analyses on matrix monazite, with Th/U values between 18 and 117, display a mean $^{206}Pb/^{238}U$ age of 562 ± 5 Ma (95% conf., MSWD = 1.11). Two spot analyses on matrix monazite have Th/U values of 5–25 and show a mean $^{206}Pb/^{238}U$ age of 485 ± 9 Ma (95% conf., MSWD = 0.098). One spot analysis shows an intermediate $^{206}Pb/^{238}U$ age of 527 ± 14 Ma (95% of concordance, Th/U = 20).

8. LA-ICP-MS zircon geochronology

U–Pb zircon dating can be used in combination with monazite geochronology to constrain the metamorphic history from CCB. The samples CC31 and CC21 were chosen for in situ LA-ICP-MS dating of zircon due to the common presence of zircon within and in close proximity to garnet. In addition a zircon separate was extracted from sample CC37 to investigate possible inheritance and constrain the timing of crystallization and metamorphism. The results of all zircon analyses are reported in Supplementary Data (Table 4) and the analytical methods are described in Supplementary material. Spot analyses that were more than 5% discordant were excluded from the calculation of the mean $^{206}Pb/^{238}U$ ages. A summary with the zircon ages is presented in Table 3.

8.1. Sample CC31 – assemblage 1

This sample contains 80–400 μm, prismatic, subhedral/euhedral to subrounded shaped zircon grains. Cathodoluminescence (CL) imaging displays different internal structures such as concentric and convolute zoning and some grains show isometric intergrowth (Fig. 14a).

Zircon grains included within a Grt_1 core display convolute zoning (Fig. 14a), typical of high-grade metamorphic zircon (e.g., Vavra et al., 1999). Two spot analyses, with Th/U values of 1.3–1.5, show a mean $^{206}Pb/^{238}U$ age of 563 ± 9 Ma (95% conf., MSWD = 0.094). Two spot analyses on zircon included in the rim of the same garnet crystal have Th/U values of 0.2–1.3 and yielded a mean $^{206}Pb/^{238}U$ age of 543 ± 9 Ma (95% conf., MSWD = 0.21).

We distinguished three different types of zircon in the matrix. The first variety displays magmatic oscillatory zoning in CL and is characterized by a high Th/U ratio (0.88–1.29). Four spot analyses in these domains generated a mean $^{206}Pb/^{238}U$ age of 577 ± 6 Ma (95% conf., MSWD = 0.105). The second type is characterized by structureless or convolute zoning under CL imaging and low to high Th/U ratios (0.01–

Fig. 10. *P–T* pseudosection calculated using the bulk composition from sample CC31 (assemblage 1). (a) *P–T* fields of peak assemblage Pl-Kfs-Grt-Bt-Ilm-Qz-Rt-Liq (bold line). (b) Plot of melt vol.%. (c) Plot of Grt Mg# and Grt vol.%. (d) Plot of X_{Grs} and X_{Alm}. (e) Plot of Bt Mg# and Bt vol.%. (f) *P–T* conditions of equilibration estimated based on overlapping ranges of phase composition and abundance.

Please cite this article as: Melo, M.G., et al., Two cryptic anatectic events within a syn-collisional granitoid from the Araçuaí orogen (southeastern Brazil): Evidence from the..., Lithos (2016), http://dx.doi.org/10.1016/j.lithos.2016.10.012

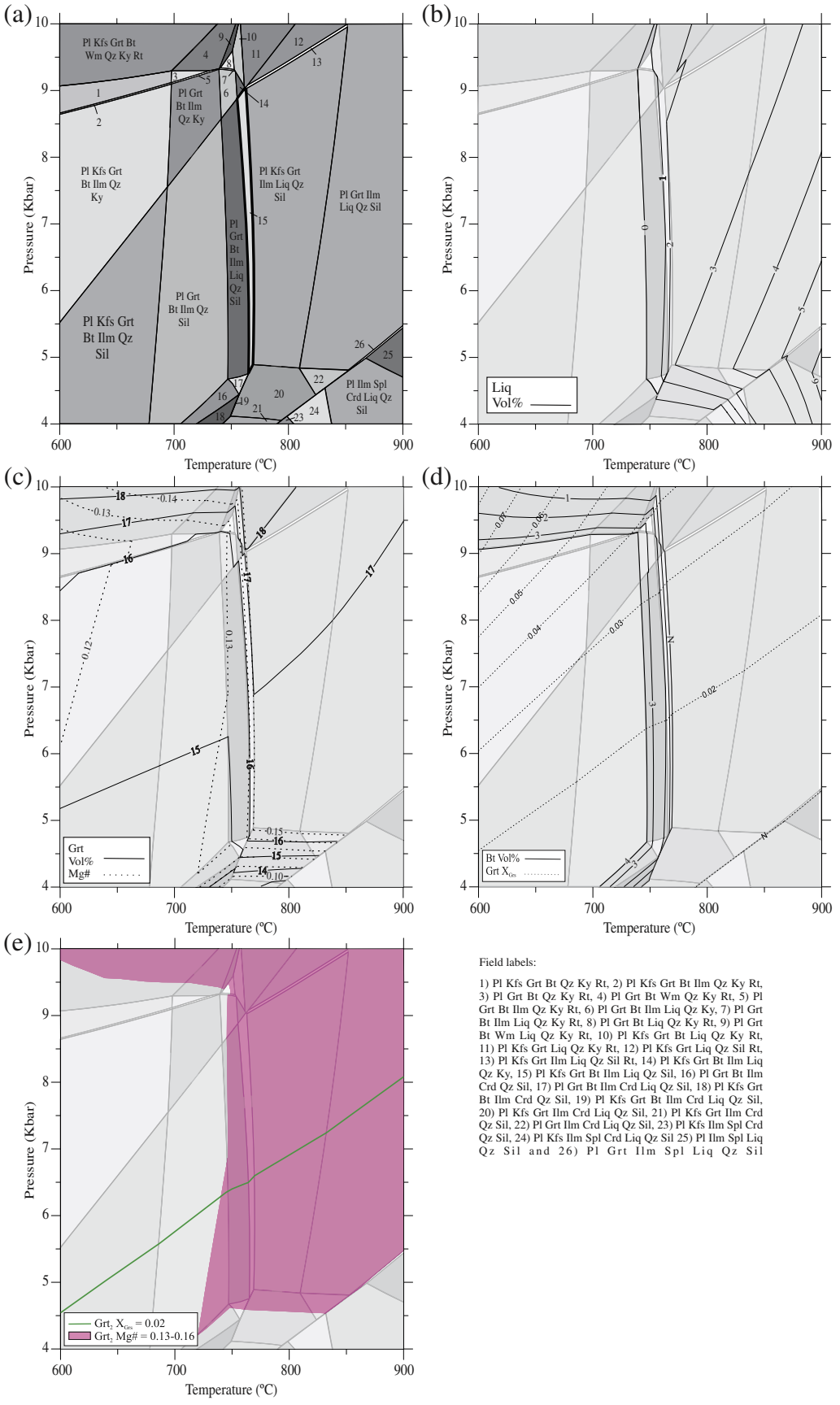

Field labels:

1) Pl Kfs Grt Bt Qz Ky Rt, 2) Pl Kfs Grt Bt Ilm Qz Ky Rt, 3) Pl Grt Bt Qz Ky Rt, 4) Pl Grt Bt Wm Qz Ky Rt, 5) Pl Grt Bt Ilm Qz Ky Rt, 6) Pl Grt Bt Ilm Liq Qz Ky, 7) Pl Grt Bt Ilm Liq Qz Ky Rt, 8) Pl Grt Bt Liq Qz Ky Rt, 9) Pl Grt Bt Wm Liq Qz Ky Rt, 10) Pl Kfs Grt Bt Liq Qz Ky Rt, 11) Pl Kfs Grt Liq Qz Ky Rt, 12) Pl Kfs Grt Liq Qz Sil Rt, 13) Pl Kfs Grt Ilm Liq Qz Sil Rt, 14) Pl Kfs Grt Bt Ilm Liq Qz Ky, 15) Pl Kfs Grt Bt Ilm Liq Qz Sil, 16) Pl Grt Bt Ilm Crd Qz Sil, 17) Pl Grt Bt Ilm Crd Liq Qz Sil, 18) Pl Kfs Grt Bt Ilm Crd Qz Sil, 19) Pl Kfs Grt Bt Ilm Crd Liq Qz Sil, 20) Pl Kfs Grt Ilm Crd Liq Qz Sil, 21) Pl Kfs Grt Ilm Crd Qz Sil, 22) Pl Grt Ilm Crd Liq Qz Sil, 23) Pl Kfs Ilm Spl Crd Qz Sil, 24) Pl Kfs Ilm Spl Crd Liq Qz Sil 25) Pl Ilm Spl Liq Qz Sil and 26) Pl Grt Ilm Spl Liq Qz Sil

Fig. 11. *P–T* pseudosection calculated with bulk composition from sample CC37 (assemblage 2). (a) P–T fields of peak assemblage Pl-Kfs-Grt-Bt-Ilm-Qz-Sil-Liq (bold line). (b) Plots of melt vol.%. (c) Plots of Grt Mg# and Grt vol.%. (d) Plots of X_{Grs} and Bt vol.%. (e) *P–T* conditions of equilibration further constrained by information on garnet composition.

Please cite this article as: Melo, M.G., et al., Two cryptic anatectic events within a syn-collisional granitoid from the Araçuaí orogen (southeastern Brazil): Evidence from the..., Lithos (2016), http://dx.doi.org/10.1016/j.lithos.2016.10.012

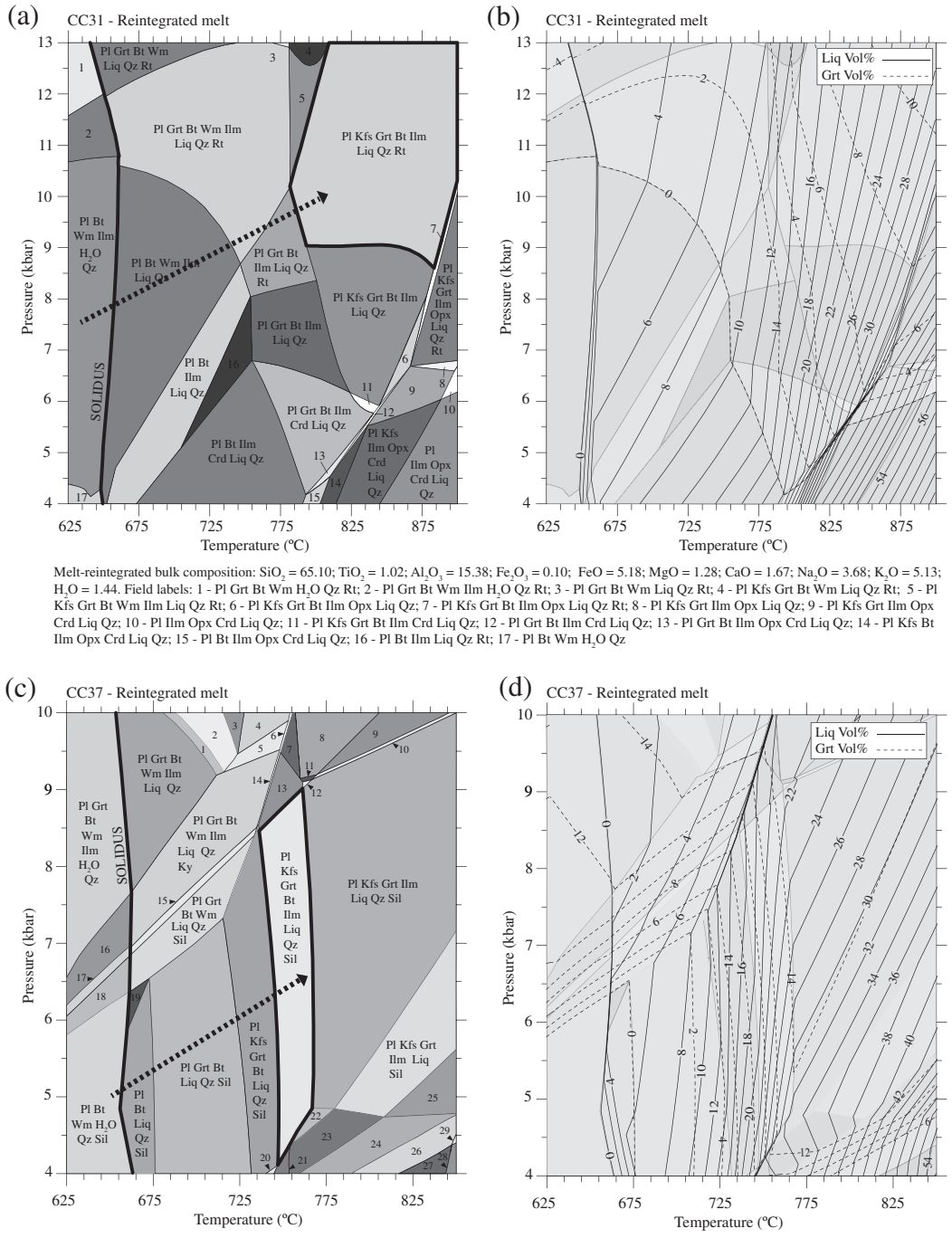

Melt-reintegrated bulk composition: SiO_2 = 65.10; TiO_2 = 1.02; Al_2O_3 = 15.38; Fe_2O_3 = 0.10; FeO = 5.18; MgO = 1.28; CaO = 1.67; Na_2O = 3.68; K_2O = 5.13; H_2O = 1.44. Field labels: 1 - Pl Grt Bt Wm H_2O Qz Rt; 2 - Pl Grt Bt Wm Ilm H_2O Qz Rt; 3 - Pl Grt Bt Wm Liq Qz Rt; 4 - Pl Kfs Grt Bt Wm Liq Qz Rt; 5 - Pl Kfs Grt Bt Wm Ilm Liq Qz Rt; 6 - Pl Kfs Grt Bt Ilm Opx Liq Qz; 7 - Pl Kfs Grt Bt Ilm Opx Liq Qz Rt; 8 - Pl Kfs Grt Ilm Opx Liq Qz; 9 - Pl Kfs Grt Ilm Opx Crd Liq Qz; 10 - Pl Ilm Opx Crd Liq Qz; 11 - Pl Kfs Grt Bt Ilm Crd Liq Qz; 12 - Pl Grt Bt Ilm Crd Liq Qz; 13 - Pl Grt Bt Ilm Opx Crd Liq Qz; 14 - Pl Kfs Bt Ilm Opx Crd Liq Qz; 15 - Pl Bt Ilm Opx Crd Liq Qz; 16 - Pl Bt Ilm Liq Qz Rt; 17 - Pl Bt Wm H_2O Qz

Melt-reintegrated bulk composition: SiO_2 = 57.69; TiO_2 = 0.20; Al_2O_3 = 22.88; Fe_2O_3 = 0.00; FeO = 8.39; MgO = 0.83; CaO = 1.42; Na_2O = 4.06; K_2O = 3.06; H_2O = 1.45. Field labels: 1 - Pl Grt Bt Wm Ilm Liq Qz Rt; 2 - Pl Grt Bt Wm Liq Qz Rt; 3 - Pl Grt Wm Liq Qz Rt; 4 - Pl Grt Wm Liq Qz Ky Rt; 5 - Pl Grt Bt Wm Liq Qz Ky Rt; 6 - Pl Kfs Grt Bt Wm Liq Qz Ky Rt; 7 - Pl Kfs Grt Bt Liq Qz Ky Rt; 8 - Pl Kfs Grt Liq Qz Ky Rt; 9 - Pl Kfs Grt Liq Qz Sil Rt; 10 - Pl Kfs Grt Ilm Liq Qz Sil Rt; 11 - Pl Kfs Grt Ilm Liq Qz Ky Rt; 12 - Pl Kfs Grt Ilm Liq Qz Ky; 13 - Pl Kfs Grt Bt Ilm Liq Qz Ky; 14 - Pl Kfs Grt Bt Wm Ilm Liq Qz Ky; 15 - Pl Grt Bt Wm Liq Qz Ky; 16 - Pl Grt Bt Wm Ilm H_2O Qz Ky;17 - Pl Grt Bt Wm H_2O Qz Ky; 18 - Pl Grt Bt Wm H_2O Qz Sil; 19 - Pl Bt Wm Liq Qz Sil; 20 - Pl Kfs Grt Bt Crd Liq Qz Sil; 21 - Pl Kfs Grt Bt Crd Ilm Liq Qz Sil; 22 - Pl Kfs Grt Ilm Crd Liq Qz Sil; 23 - Pl Kfs Grt Ilm Crd Liq Sil; 24 - Pl Kfs Grt Ilm Spl Crd Liq Sil; 25 - Pl Kfs Grt Ilm Spl Liq Sil; 26 - Pl Kfs Grt Ilm Spl Crd Liq Qz; 27 - Pl Kfs Grt Ilm Spl Crd Liq; 28 - Pl Grt Ilm Spl Crd Liq; 29 - Pl Grt Ilm Spl Crd Liq Qz.

Fig. 12. Melt-reintegrated *P–T* pseudosection for samples CC31 (a,b) and CC37 (c,d) following the method of White et al. (2004). (a) The arrow shows the prograde path from the subsolidus assemblage (Pl-Bt-Wm-Ilm-H_2O-Qz) towards peak metamorphism indicated by bold line (Pl-Kfs-Grt-Bt-Ilm-Qz-Rt-Liq). (b) Plots of Melt vol.% and Grt vol.%. (c) The arrow indicates the prograde path from the subsolidus assemblage (Pl-Bt-Wm-H_2O-Qz-Sil) towards peak metamorphism assemblage (Pl-Kfs-Grt-Bt-Ilm-Qz-Sil-Liq) indicated by bold line. (d) Plots of Melt vol.% and Grt vol.%.

2.51). Ten spot analyses yield a mean $^{206}Pb/^{238}U$ age of 562 ± 4 Ma (95% conf., MSWD = 0.64). The last variety presents brighter cores and fine darker rims in CL imaging, moderate to high Th/U ratios (1.06–1.53) and it occurs together with ilmenite, adjacent to the poikiloblastic garnet crystals. Five spot analyses in brighter domains produced a mean $^{206}Pb/^{238}U$ age of 528 ± 5 Ma (95% conf., MSWD = 0.37).

8.2. Sample CC37 – assemblage 2

This sample yielded 50 to 280 μm, prismatic, subhedral/euhedral to subrounded zircon grains. CL imaging displays strongly luminescent or oscillatory-zoned to irregular zoning cores truncated by darker structureless overgrowths and convoluted zoning (Fig. 14c).

Table 3
Summary of geochronological data showing inherited, crystallization and metamorphism ages for the Carlos Chagas batholith.

Samples	Textural context	Inherited age (Ma)	Crystallization age (Ma)	Metamorphism age (Ma)		
Monazite						
CC31	Grt_1(c)	617 ± 12 (n = 25)		560 ± 9 (n = 6)	521 ± 14 (n = 1)	
	ad_Grt_1				519 ± 14 (n = 1)	
	M	612 ± 17 (n = 1)		562 ± 11 (n = 2)		492 ± 16 (n = 4)
CC37	Grt_1(c)			557 ± 7 (n = 4)		
	Grt_1(r)			569 ± 14 (n = 1)	528 ± 14 (n = 1)	
	M			558 ± 10 (n = 8)		484 ± 13 (n = 1)
CC21	Grt_1(c)			566 ± 16 (n = 1)	535 ± 14 (n = 1)	
	Grt_1(c)			552 ± 15 (n = 1)	516 ± 14 (n = 1)	
	Grt_2(c)				515 ± 14 (n = 1)	
	M			562 ± 5 (n = 8)	527 ± 14 (n = 1)	485 ± 9 (n = 2)
Zircon						
CC31	Grt_1(c)			563 ± 9 (n = 2)		
	Grt_1(r)			543 ± 9 (n = 2)		
	M		577 ± 6 Ma (n = 4)	562 ± 4 (n = 10)	528 ± 5 Ma (n = 5)	
CC37		706 ± 15 (n = 1)	576 ± 3 Ma (n = 14)	562 ± 5 (n = 6)	530 ± 4 Ma (n = 8)	
		607 ± 4 (n = 10)				
CC21	Grt_1(c)			564 ± 4 (n = 7)		

Textural context of the monazite and zircon: Grt_1(c), monazite/zircon grain included in poikiloblastic garnet core; Grt_1(r), monazite/zircon grain included in poikiloblastic garnet rim; Grt_2(c), monazite grain included in smaller garnet core; ad_Grt_1, monazite grain adjacent or touching poikiloblastic garnet rim; M, monazite/zircon grain in the matrix. n = number of analyses.

Ten spot analyses on CL-defined inherited cores (strongly luminescent cores) have variable Th/U values of 0.03–0.49 and yield a mean $^{206}Pb/^{238}U$ age of 607 ± 4 Ma (95% conf., MSWD = 0.90). One spot has an older inherited $^{206}Pb/^{238}U$ age of 706 ± 15 Ma and a Th/U ratio of 0.10. Based on the Th/U ratio obtained in fourteen analyses from the brighter zircon cores with oscillatory to irregular zoning, two

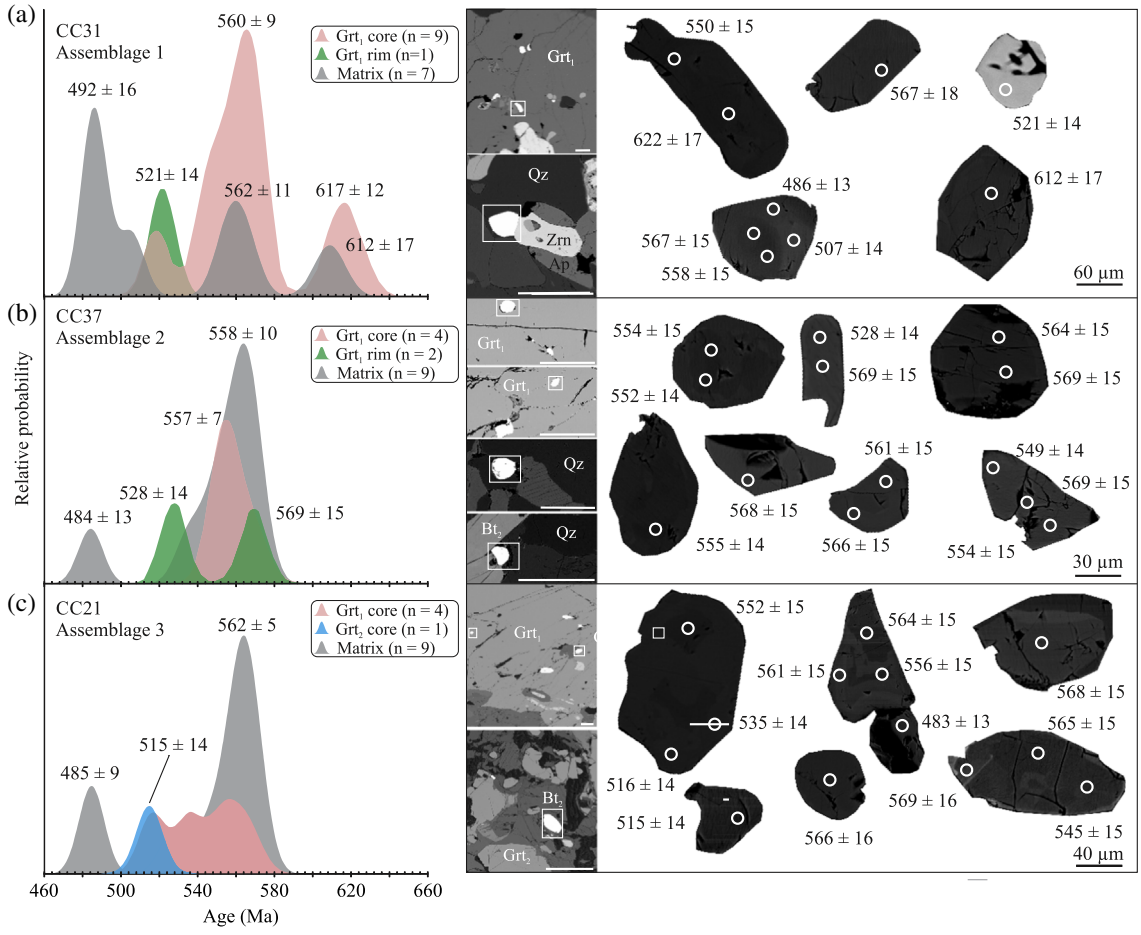

Fig. 13. Histogram of monazite age data using the mean $^{206}Pb/^{238}U$ age and representative BSE images for monazite grains analyzed in this study. The microstructure position of monazite analyzed in each sample is indicated by white rectangles. (a) Histogram of inherited and metamorphic monazite grains obtained from sample CC31 (assemblage 1). BSE images display unzoned internal structure to weakly zoned grains. (b) Histogram of metamorphic monazite included in Grt_1 and matrix from sample CC37 (assemblage 2). Some grains show darker core surrounded by fine brighter rim in BSE images (c) Histogram showing metamorphic monazite age obtained in the matrix and Grt_1 and Grt_2 crystals from sample CC21 (assemblage 3). Matrix monazite displays patchy zoning via BSE images. Scale bar is equal to 200 µm for the textural position of analyzed grains.

Please cite this article as: Melo, M.G., et al., Two cryptic anatectic events within a syn-collisional granitoid from the Araçuaí orogen (southeastern Brazil): Evidence from the..., Lithos (2016), http://dx.doi.org/10.1016/j.lithos.2016.10.012

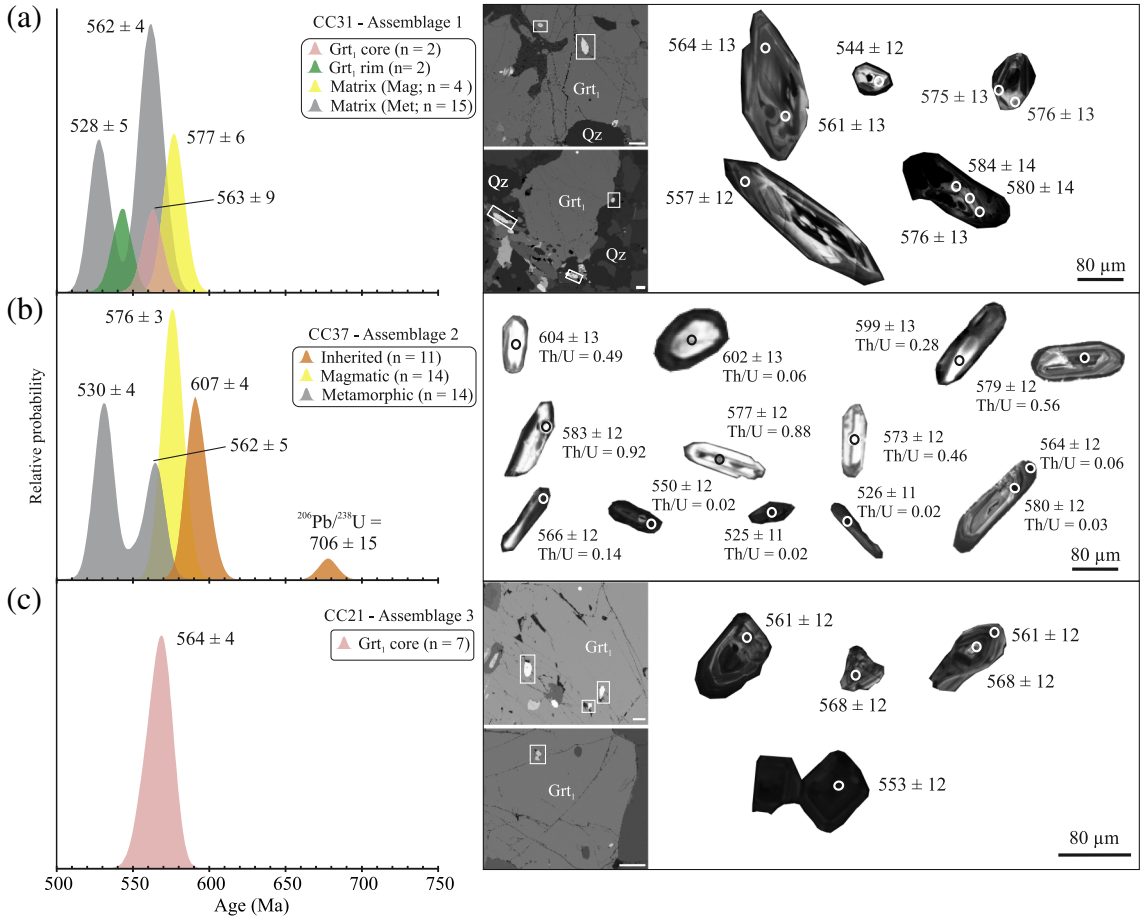

Fig. 14. Histogram and representative cathodoluminescence images of zircons from CCB. The microstructure position of zircon analyzed in each sample is indicated by white rectangles. (a) Histogram displaying $^{206}Pb/^{238}U$ age of zircon included in Grt_1 and matrix from sample CC31 (assemblage 1). Zircon show convoluted zonation typical of high-grade metamorphism. (b) Histogram showing main $^{206}Pb/^{238}U$ age of inherited, magmatic and metamorphic zircons from sample CC37 (assemblage 2). Zircon comprising strongly luminescent inherited core and irregular zoning magmatic core truncated by darker rim. (c) Histogram showing main $^{206}Pb/^{238}U$ age of zircon included in Grt_1 from sample CC21 (assemblage 3). Zircon displays irregular zoning. Scale bar is equal to 200 µm for the textural position of analyzed grains.

different populations were distinguished: low (0.02–0.06) and high Th/U (0.28–0.92) ratios. However, both populations are age equivalent within analytical uncertainties and provide a mean $^{206}Pb/^{238}U$ age of 576 ± 3 Ma (95% conf., MSWD = 0.35). Six out of fourteen spot analyses performed on the darker and structureless zircon grains, with Th/U values between 0.02 and 0.14, yielded a mean $^{206}Pb/^{238}U$ age of 562 ± 5 Ma (95% conf., MSWD = 1.15). Eight additional analyses on the structureless zircon grains also have low Th/U ratio (0.02–0.16) and show a mean $^{206}Pb/^{238}U$ age of 530 ± 4 Ma (95% conf., MSWD = 0.38).

8.3. Sample CC21 – assemblage 3

Zircon grains are prismatic, subhedral to euhedral, ranging from 25 to 150 µm. CL images reveal recrystallization features typical of granulite facies zircon, such as convoluted zoning and darker cores truncated by irregular zoning (Fig. 14b). Seven spot analyses from zircon within Grt_1 core, with Th/U values between 0.03 and 0.39, yield a mean $^{206}Pb/^{238}U$ age of 564 ± 4 Ma (95% conf., MSWD = 1.01).

9. Discussion and conclusions

This work has uncovered two previously unrecognized anatectic events that have affected the entire Carlos Chagas batholith. This polymetamorphic anatectic history has not been identified by previous regional geological investigations due to the fact that the ubiquitous megacrystic K-feldspar crystals that characterize the CCB were not involved in the melting processes which, in both events, primarily consumed biotite, quartz and plagioclase in the matrix interstitial to the megacrysts. The reason for this is that biotite fluid-absent melting reactions are close to degeneracy with regard to K-feldspar and either produce or consume only small amounts of K-feldspar, depending on the specifics of pressure of melting and bulk composition (e.g. Carrington and Watt, 1995). In the CCB this results in anatectic events that are not obvious without detailed textural and quantitative mineral chemical analysis. The evidence for anatexis of the CCB, the timing of anatexis and the P–T paths relevant to the anatectic events are discussed below.

9.1. U–Pb ages of monazite and zircon from the Carlos Chagas batholith

The ages of 577 ± 6 Ma (CC31) and 576 ± 3 Ma (CC37) obtained from oscillatory-zoned or irregular zoned cores of zircon, with variable Th/U ratios (0.02–1.29), are interpreted as best representing the crystallization age of the batholith (Fig. 14a,b; Table 3). This is in agreement with previous studies which have demonstrated that the syn-collisional granites in the Araçuaí orogen were emplaced between 585 and 545 Ma, with the dominant magmatic age being ca. 575 Ma (Gradim et al., 2014; Pedrosa-Soares et al., 2011; Richter et al., 2016; Roncato, 2009; Silva et al., 2002, 2005; Vauchez et al., 2007).

U–Pb ages of some monazite cores found within Grt_1 and in the matrix (CC31) give ages of 617 ± 12 Ma and 612 ± 17 Ma (Fig. 13a; Table 3), respectively. These grains can be interpreted as inherited

monazite from the source of the CCB. This interpretation is consistent with other studies in granulitic rocks worldwide (e.g. Hermann and Rubatto, 2003; Montel et al., 2000) and experimental studies (e.g. Cherniak et al., 2000), which demonstrate that monazite can persist during high-grade metamorphism and anatexis. As illustrated by CL-images in Fig. 14b, some zircon grains show strongly luminescent cores with low to moderate Th/U ratios (0.03–0.49) rimmed by darker and structureless domains. These zircon cores are interpreted as inherited and present a dominant age peak at 607 ± 4 Ma (Fig. 14b), which is similar, within analytical error, to the inherited monazite age (Fig. 13a). The NVC records a peak in the age distribution of detrital zircon and monazite grains at ca. 606–612 Ma (Richter et al., 2016), which is similar to the age of inherited grains from the CCB, possibly indicating the Rio Doce (Pedrosa-Soares et al., 2011) and/or Rio Negro (Heilbron and Machado, 2003) magmatic arcs as representing material similar to the source of the CCB. A single zircon grain with the oldest recorded age in this study (706 ± 15 Ma; Fig. 14b) may correlate with reported ages from the Southern Bahia Alkaline Province (ca. 696–732 Ma; Rosa et al., 2007), which is related to the rift episode along the southern part of the São Francisco craton.

Geochronology on monazite and zircon inclusions in Grt_1 yielding ages from 569 ± 14 to 552 ± 15 Ma (Table 3) and are interpreted as age of peak of the first metamorphic event (M1) in the CCB. This age interval is equal, within analytical error, to the oldest monazite (from 562 ± 11 to 558 ± 10 Ma; Table 3) and zircon (562 ± 4 Ma; Table 3) ages found in the matrix, implying that these grains were formed at peak metamorphism. Zircon crystals handpicked from the whole rock aliquot of CC37 also revealed a similar age of 562 ± 5 Ma (Fig. 14b; Table 3) and are interpreted to be metamorphic because of their lack of zonation (Fig. 14b) and low Th/U ratios (0.02–0.14). Metamorphic ages such as these have also found in NVC (ca. 575–560 Ma; Gradim et al., 2014; Richter et al., 2016).

The second metamorphic event (M2) affected all the CCB rocks (assemblages 1, 2 and 3) at ca. 535–515 Ma, as indicated by monazite and zircon ages in this study (Figs. 13 and 14). Monazite inclusions within Grt_2 which clearly texturally post-dates Grt_1, give an age of 515 ± 14 Ma (CC21), defining the age of M2. In addition, zircon rims that are relatively dark in CL images (Fig. 14a,b) yielded ages of 528 ± 5 Ma (n = 5; CC31 – Fig. 14a) and 530 ± 4 Ma (n = 8; CC37 - Fig. 14b), which are within analytical uncertainties of those monazite ages included in Grt_2. We interpreted the monazite ages ranging from 535 ± 14 Ma to 516 ± 14 Ma (Table 3) obtained from the rims of Grt_1 to be metamorphic ages produced due to interaction with fluid/melt along microcracks in the garnet during the second metamorphic event (M2).

The M2 age is not widely documented in the Araçuaí orogen and some studies have interpreted the youngest metamorphic ages as Pb-loss disturbance due to post-collisional intrusions (Silva et al., 2002). Richter et al. (2016) have also reported metamorphic ages of ca. 523–495 Ma for monazite and zircon from the NVC and G2 granites.

The youngest ages recorded in this study of 492 ± 16 Ma (n = 4; CC31), ca. 484 ± 13 Ma (n = 1; CC37) and ca. 485 ± 9 Ma (n = 2; CC21) were found in matrix monazite (Fig. 13) and can be attributed to later fluid–rock interaction contemporaneous with gravitational collapse of the Araçuaí orogen (Gradim et al., 2014; Pedrosa-Soares et al., 2011). Fluid movement through the crust at this time is supported by hydrothermal gem deposits (e.g., emerald, alexandrite and/or aquamarine) from districts of the Eastern Pegmatite Province in the Araçuaí orogen (Pedrosa-Soares et al., 2011).

9.2. First period of garnet growth (Grt_1)

The PT conditions of formation indicated by the peak assemblage 1 (Pl-Kfs-Grt-Bt-Ilm-Qz-Rt-Liq; Figs. 10 and 11) are consistent with the occurrence of incongruent melting reactions consuming biotite, as constrained by experiments and studies of peraluminous metasedimentary migmatitic granulites (Johnson et al., 2008; Nicoli et al., 2015; Patiño Douce and Beard, 1996; Richter et al., 2016; Stevens et al., 1997; Vielzeuf and Montel, 1994). Therefore, the poikiloblastic garnet crystals (Grt_1) in all parts of the CCB (assemblages 1, 2 and 3) are interpreted as a product of partial melting reactions that consumed high-Ti biotite, quartz and plagioclase at granulite facies conditions and produced peritectic phases (garnet and rutile) and melt. Microstructures such as, films and pools of plagioclase and/or quartz occur both in the matrix and surrounding Grt_1 crystals (Figs. 4d,e and 5e,f,g,h). These microstructures are typically interpreted to represent melt pseudomorphs. Further to that, abundant rounded inclusions of Ti-biotite in Grt_1 indicate that garnet grew at the expense of Bt and corroborate the interpretation that melting was ongoing (Fig. 4b,c).

Grt_1 is unzoned in terms of major elements (Supplementary data - Table 1; Figs. 6 and 7a), yet displays a slight zoning of HREE (Supplementary data - Table 2, Fig. 8). Its negative Eu anomaly (Fig. 8) indicates that garnet was in equilibrium with K-feldspar, as expected from the phase equilibrium modeling.

In addition to the grossular content of Grt_1 (assemblage 1), the peak pressure of this event can be constrained by the presence of ilmenite and rutile. Taken into consideration the phase equilibrium modeling for samples CC28 and CC31 (Figs. 9a and 10a), the field of the peak assemblage 1 is stable between 780 and 870 °C and 8.9–13.4 kbar. Based on the $X_{Grs} + X_{Alm} + Grt_{Mg\#} + Bt_{Mg\#}$ isopleths, we infer that M1 event reached 790–820 °C and 9.5–10.5 kbar (Figs. 9f and 10f). Assuming the average density of the crust to be 2.75 g/cm^3 these conditions translate to depths of 26–29 km with a geothermal gradient up to 28–30 °C km^{-1} (Fig. 15).

The CCB records higher pressure conditions than the adjacent paragneisses complexes which record peak pressures below 8 kbar (e.g. Gradim, 2013; Munhá et al., 2005; Richter et al., 2016). According to Richter et al. (2016) rocks of the nearby NVC sediments were buried to at least 25 km at ca. 570 Ma suggesting that the currently exposed units in the core of the AO were buried to varied depths and were differentially exhumed during cooling, with the CCB representing rocks that at the time of peak metamorphism were below the paragneiss complexes that now surround the batholith. In the Araçuaí orogen, east–west verging shear zones developed along the major lithological contacts appear to have accommodated the differential motion of blocks (Alkmim

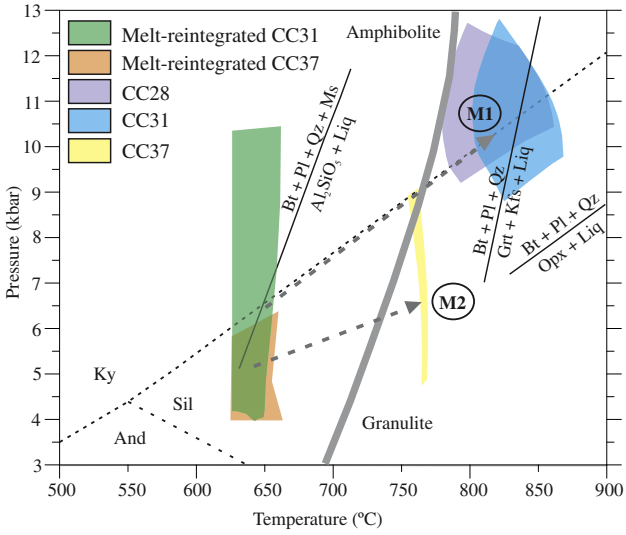

Fig. 15. Suggested *P–T* conditions for Carlos Chagas batholith. Peak metamorphism in studied samples was attained at granulite conditions and both generations of garnet were produced by biotite absent-fluid melting reactions. Reaction curves after partial melting experiments (Patiño Douce and Johnston, 1991; Stevens et al., 1997; Vielzeuf and Montel, 1994).

Please cite this article as: Melo, M.G., et al., Two cryptic anatectic events within a syn-collisional granitoid from the Araçuaí orogen (southeastern Brazil): Evidence from the..., Lithos (2016), http://dx.doi.org/10.1016/j.lithos.2016.10.012

et al., 2006; Castañeda et al., 2006; Pinto et al., 2001; Queiroga et al., 2012).

M1 is interpreted to be a consequence of the collisional stage of orogeny, where crustal thickening probably involved thrusting of the magmatic arc onto the back-arc region (Gradim et al., 2014; Pedrosa-Soares et al., 2011). This event produced most of the garnet in the CCB and the almost complete lack of retrogression of these crystals to biotite indicates that melt loss after this first melting event efficiently removed H_2O from the rock. Pseudosection modeling of the melt-reintegrated bulk composition (Fig. 12a,b) indicates that 12–34 vol.% of melt had been produced by the time peak conditions were attained. Less than 3 vol.% of melt (Figs. 9b and 10b) is inferred to have remained in the rock. This minor remnant melt volume produced the microstructures which corroborate the presence of melt, showing films of melt along garnet boundaries and between plagioclase grains in matrix (Fig. 4d,e). It is also aligned with recent models of melt extractions in which excess melt is drained away and does not leave significant imprint (Yakymchuk and Brown, 2014).

9.3. Second period of garnet growth (Grt_2)

As discussed above, a substantial amount of melt must be removed from the residuum before cooling in order to preserve the peak assemblage. After the M1 event, the CCB was relatively anhydrous with the remnant M1 biotite being the only source of water in the assemblage. Thus, the rocks were unfertile for the further production of melt. This situation was changed along shear zones where fluids were able to infiltrate, most likely under amphibolite to greenschist facies conditions and rehydrate the sheared rocks. This most likely occurred through hydration of K-feldspar and possibly also some minor fraction of Grt_1 along the shear fabric to produce an anastomosing muscovite-biotite fabric. These hydrated domains were the only portions of the CCB that were susceptible to further anatexis during the M2 event, which resulted in muscovite breakdown to produce sillimanite on the second metamorphic event (M2) prograde path. The presence of sillimanite and the locally higher water activity allowed a second melting reaction to occur which consumed biotite, sillimanite, plagioclase and quartz, and which produced peritectic Grt_2 (Figs. 3g and 5a,b).

Indeed, the microstructures show that Grt_1 crystals produced during M1 melting are free of sillimanite inclusions (e.g., Fig. 4b,c) and therefore it is very unlikely that the CCB contained sillimanite during M1. Thus, sillimanite was a product of deformation and metamorphism associated with M2, in the previously rehydrated rocks (assemblages 2 and 3). Sillimanite occurs in such rocks as prismatic aggregates in the matrix and also as needles inclusions in the 2nd generation of garnet (Fig. 5a,b). These petrographic observations indicate that this Grt_2 is likely to have formed as a consequence fluid-absent melting reaction at the expense of biotite and sillimanite during M2 event. In addition, pseudomorphed thin melt films are documented surrounding of Grt_2 crystals (Fig. 5h), implying that garnet grew in the presence of melt.

Phase equilibrium modeling using the bulk compositions of small domains (e.g. CC37 – assemblage 2) indicate that the inferred peak metamorphic mineral assemblage (Pl-Kfs-Grt-Bt-Ilm-Qz-Sil-Liq) equilibrated at 770 °C and 6.6 kbar (Fig. 11e). These conditions correspond to depths of ~18 km with a geothermal gradient up to 42 °C km^{-1} (Fig. 15). The M2 peak metamorphic estimates are in agreement with garnet formation via an incongruent melting reaction that consumed biotite and sillimanite. This is confirmed by comparison with previous experimental studies (Patiño Douce and Harris, 1998; Patiño Douce and Johnston, 1991; Pickering and Johnston, 1998) and studies of peraluminous metasedimentary migmatites (Richter et al., 2016). Furthermore, the absence of composition zonation and enrich in HREE (Figs. 7 and 9) support that garnet has grown at granulite-facies conditions. Pedrosa-Soares et al. (2011) published temperatures of 642–683 °C (average T method by THERMOCALC) for the Qz + Kfs + Pl + Grt + Bt + Sil assemblage from the CCB. However, these temperatures conditions are inconsistent with mineral compositions documented in this study and with the microtextures indicating the coexistence of melt and Grt_2. The pseudosection modeling melt-reintegrated indicates 16–30 vol.% of melt was produced at peak conditions (Fig. 12d).

M2 heating is probably related to asthenosphere ascendance during the extensional thinning and gravitational collapse of the orogen (De Campos et al., 2016; Gradim et al., 2014; Moraes et al., 2015; Pedrosa-Soares et al., 2011), which provided sufficient heat to induce a second anatectic event in the CCB. The G5 supersuite (ca. 525–480 Ma) was emplaced during this extensional episode along pre-existing structures at depths of ~20 km (Baltazar et al., 2010; De Campos et al., 2004, 2016; Gradim et al., 2014; Mendes and De Campos, 2012; Mendes et al., 2005; Noce et al., 2000; Silva et al., 2005).

9.4. Regional implications

The evolution and development of the Araçuaí orogen is marked by a long history of granite production between 630 and 480 Ma (G1 to G5 Supersuites - Pedrosa-Soares et al., 2011). The evidence described in this work indicates three episodes of crustal recycling in the Araçuaí orogeny. In the first event, source rocks with a volume substantially larger than that of the CCB melted to produce a hydrous, peraluminous granitic melt that intruded at presumably higher crustal level within the orogenic belt at ca. 575 Ma. At least part of the water in this hydrous magma was trapped due to biotite crystallization producing a fertile granite. Thickening and further evolution of the orogen buried the CCB producing a second process of crustal melting, some 15 Ma after the first. Melting and melt extraction produced an almost completely anhydrous and refractory rock. The third and final episode occurred only where hydration due to shearing had refertilized the CCB for melt generation and produced relatively minor melt volumes, which were lost leaving the CCB dry and refractory. Recognizing repeated partial melting events involving granites during an orogeny provides the key for understand the mid- to lower crustal tectonic recycling in an exhumed orogenic belt and interpreting complex zircon and monazite age distributions.

Acknowledgements

This work was carried out as part of the Brazil-South Africa scientific collaboration and was supported by CNPq, (Grant No. 401334/2012-0, 402852/2012-5 and 302058/2015-0), FAPEMIG (APQ03943, RPQ-0067-10 and RDP 00063-10) and by NRF funding to Gary Stevens via the SARChI programme. This work is part of the doctoral research of the first author. We thank Editor Ed Sawyer and two referees Roberto Weinberg and Tim Johnson for their constructive and helpful suggestions which greatly improved our manuscript.

Appendix A. Supplementary data

Supplementary data to this article can be found online at http://dx.doi.org/10.1016/j.lithos.2016.10.012.

References

Alkmim, F.F., Marshak, S., Pedrosa-Soares, A.C., Peres, G.G., Cruz, S.C.P., Whittingyon, A., 2006. Kinematic evolution of the Araçuaí-West Congo orogen in Brazil and Africa: nutcracker tectonics during the Neoproterozoic assembly of Gondwana. Precambrian Research 149, 43–64.

Baltazar, O.F., Zuchetti, M., Oliveira, S.A.M., Scandolara, J., Silva, L.C., 2010. Folhas São Gabriel Da Palha e Linhares. Nota Explicativa. Programa Geologia do Brasil, CPRM-BH (144 pp.).

Belém, J., 2014. Geoquímica, Geocronologia e Contexto geotectônico Do Magmatismo máfico Associado Ao Feixe de Fraturas Colatina, Estado Do Espírito Santo. Instituto de Geociências, Universidade Federal de Minas Gerais, Belo Horizonte (Phd Thesis, 134 pp.).

Brown, M., 1994. The generation, segregation, ascent and emplacement of granite magma: the migmatite-to-crustally-derived granite connection in thickened orogens. Earth-Science Reviews 36, 83–130.

Brown, M., 2010. Melting of the continental crust during orogenesis: the thermal, rheological, and compositional consequences of melt transport from lower to upper continental crust. Canadian Journal of Earth Sciences 47, 655–694.

Brown, M., 2013. Granite: from genesis to emplacement. Geological Society of America Bulletin 125, 1079–1113.

Brown, M., Rushmer, T., 2006. Evolution and Differentiation of the Continental Crust. Cambridge University Press, Cambridge, UK (562 pp.).

Carrington, D.P., Watt, G.R., 1995. A geochemical and experimental study of the role of K-feldspar during water-undersaturated melting of metapelites. Chemical Geology 122, 59–76.

Castañeda, C., Pedrosa-Soares, A.C., Belém, J., Dias, P.H.A., Gradim, D.T., Medeiros, S.R., Oliveira, F.F., 2006. Folha Ecoporanga, SE.24-Y-A-III, escala 1:100.000: nota explicativa Espírito Santo, UFMG/CPRM 80 pp.

Castro, A., Patiño Douce, A.E., Corretgé, L.G., De la Rosa, J.D., El-Biad, M., El-Hmidi, H., 1999. Origin of peraluminous granites and granodiorites, Iberian massif, Spain: and experimental test of granite petrogenesis. Contributions to Mineralogy and Petrology 135, 255–276.

Cavalcante, G.C.G., Egydio-Silva, M., Vauchez, A., Camps, P., Oliveira, E., 2013. Strain distribution across a partially molten middle crust: insights from the AMS mapping of the Carlos Chagas Anatexite, Araçuaí belt (East Brazil). Journal of Structural Geology 55, 79–100.

Chappell, B.W., White, A.J.R., 1974. Two contrasting granite types. Pacific Geology 8, 173–174.

Cherniak, D.J., Watson, B.E., Harrison, M.T., Grove, M., 2000. Pb diffusion in monazite: a progress report on a combined RBS/SIMS study. Eos Transactions 41 (19), S25.

Coggon, R., Holland, T.J.B., 2002. Mixing properties of phengitic micas and revised garnet–phengite thermobarometers. Journal of Metamorphic Geology 20, 683–696.

Collins, W.J., Richards, S.W., 2008. Geodynamic significance of S-type granites in circum-Pacific orogens. Geology 36, 559–562.

De Campos, C.P., Mendes, J.C., Ludka, I.P., Medeiros, S.R., Moura, J.C., Wallfass, C., 2004. A review of the Brasiliano magmatism in southern Espírito Santo, Brazil, with emphasis on post-collisional magmatism. Journal of the Virtual Explorer 17.

De Campos, C.P., Medeiros, S.R., Mendes, J.C., Pedrosa-Soares, A.C., Dussin, I., Ludka, I.P., Dantas, E.L., 2016. Cambro-Ordovician magmatism in the Araçuaí Belt (SE Brazil): snapshots from a post-collisional event. Journal of South American Earth Sciences 68, 248–268.

De Capitani, C., Petrakakis, K., 2010. The computation of equilibrium assemblage diagrams with Theriak/Domino software. American Mineralogist 95, 1006–1016.

Droop, G.T.R., 1987. A general equation for estimating Fe^{3+} concentrations in ferromagnesian silicates and oxides from microprobe analyses, using stoichiometric criteria. Mineralogical Magazine 51, 431–435.

Gradim, C.T., 2013. Complexo Nova Venécia e Magmatismo Associado, Orógeno Araçuaí, Estado Do Espírito Santo. Instituto de Geociências, Universidade Federal de Minas Gerais, Belo Horizonte (MSc Dissertation, 96 pp.).

Gradim, C.T., Queiroga, G.N., Roncato, J.G., Novo, T.A., Pedrosa-Soares, A.C., 2007. Mapa Geológico da Folha Mantena 1: 100.000 Belo Horizonte, Programa Geologia do Brasil, CPRM-UFMG.

Gradim, C., Roncato, J., Pedrosa-Soares, A.C., Cordani, U., Dussin, I., Alkmim, F.F., Queiroga, G., Jacobssohn, T., Silva, L.C., Babinski, M., 2014. The hot back-arc zone of the Araçuaí orogen, Eastern Brazil: from sedimentation to granite generation. Brazilian Journal of Geology 44, 155–180.

Heilbron, M., Machado, N., 2003. Timing of terrane accretion in the Neoproterozoic-Eopaleozoic Ribeira Orogen (SE Brazil). Precambrian Research 125, 87–112.

Hermann, J., Rubatto, D., 2003. Relating zircon and monazite domains to garnet growth zones: age and duration of granulite facies metamorphism in the Val Malenco lower crust. Journal of Metamorphic Geology 21, 833–852.

Holland, T.J.B., Powell, R., 1998. An internally consistent thermodynamic data set for phases of petrological interest. Journal of Metamorphic Geology 16, 309–343.

Holland, T., Powell, R., 2003. Activity–composition relations for phases in petrological calculations: an asymmetric multicomponent formulation. Contributions to Mineralogy and Petrology 145, 492–501.

Jeon, H., Williams, I.S., Chappell, B.W., 2012. Magma to mud to magma: rapid crustal recycling by Permian granite magmatism near the eastern Gondwana margin. Earth and Planetary Science Letters 319-320, 104–117.

Johnson, T.E., White, R.W., Powell, R., 2008. Partial melting of metagreywacke - a calculated mineral equilibria study. Journal of Metamorphic Geology 26, 837–853.

McDonough, W.F., Sun, S.S., 1995. The composition of the Earth. Chemical Geology 120, 223–253.

Mendes, J.C., De Campos, C.M.P., 2012. Norite and charnockites from the Venda Nova Pluton, SE Brazil: intensive parameters and some petrogenetic constraints. Geoscience Frontiers 3, 789–800.

Mendes, J.C., Medeiros, S.R., McReath, I., De Campos, C.M.P., 2005. Cambro-Ordovician magmatism in SE Brazil: U–Pb ages, combined with Sr and Nd isotopic data of charnockitic rocks from the Varzea Alegre complex. Gondwana Research 8, 337–345.

Montel, J.M., Kornprobst, J., Vielzeuf, D., 2000. Preservation of U-Th-Pb ages in shielded monazite: example from the Beni Bousera Hercynian Kinzigites (Morocco). Journal of Metamorphic Geology 18, 335–342.

Moraes, R., Nicollet, C., Barbosa, J.S.F., Fuck, R.A., Sampaio, A.R., 2015. Applications and limitations of thermobarometry in migmatites and granulites using as an example rocks of the Araçuaí Orogen in southern Bahia, including a discussion on the tectonic meaning of the current results. Brazilian Journal of Geology 45, 517–539.

Munhá, J.M.U., Cordani, U.G., Tassinari, C.C.G., Palácios, T., 2005. Petrologia e termocronologia de gnaisses migmatíticos da faixa de dobramentos Araçuaí (Espirito Santo, Brasil). Revista Brasileira de Geociencias 35, 123–134.

Nicoli, G., Stevens, G., Moyen, J.F., Frei, D., 2015. Rapid evolution from sediment to anatectic granulite in an Archean continental collision zone: the example of the Bandelierkop Formation metapelites, South Marginal Zone, Limpopo Belt, South Africa. Journal of Metamorphic Geology 33, 177–202.

Noce, C.M., Macambira, M.J.B., Pedrosa-Soares, A.C., 2000. Chronology of Neoproterozoic-Cambrian granitic magmatism in the Araçuaí Belt, eastern Brazil, based on single zircon evaporation dating. Revista Brasileira de Geociencias 30, 25–29.

Noce, C.M., Pedrosa-Soares, A.C., Piuzana, D., Armstrong, R., Laux, J.H., De Campos, C.M., Medeiros, S.R., 2004. Ages of sedimentation of the kinzigitic complex and of a late orogenic thermal episode in the Araçuaí orogen, northern Espírito Santo state, Brazil: zircon and monazite U–Pb SHRIMP and IDTIMS data. Revista Brasileira de Geociencias 34, 587–592.

Patiño Douce, A.E., Beard, J.S., 1996. Effects of P, $f(O_2)$ and Mg/Fe ratio on dehydration melting of model metagreywackes. Journal of Petrology 37, 999–1024.

Patiño Douce, A.E., Harris, N., 1998. Experimental constraints on Himalayan anatexis. Journal of Petrology 39, 689–710.

Patiño Douce, A.E., Johnston, A.D., 1991. Phase equilibria and melt productivity in the pelitic system: implications for the origin of peraluminous granitoids and aluminous granulites. Contributions to Mineralogy and Petrology 107, 202–218.

Pedrosa-Soares, A.C., Noce, C.M., Wiedemann, C., Pinto, C.P., 2001. The Araçuaí-West-Congo Orogen in Brazil: an overview of a confined orogen formed during Gondwanaland assembly. Precambrian Research 110, 307–323.

Pedrosa-Soares, A.C., Queiroga, G.N., Gradim, C.T., Roncato, J.G., Novo, T.A., Jacobsohn, T., Silva, K.L., 2006. Geologia Da Folha Mantena (SE-24-Y-A-VI). Programa Geologia do Brasil, CPRM (82pp. http://geobank.cprm.gov.br).

Pedrosa-Soares, A.C., Noce, C.M., Alkmim, F.F., Silva, L.C.S., Babinski, M., Cordani, U., Castañeda, C., 2007. Orógeno Araçuaí: síntese do conhecimento 30 anos após Almeida 1977. Geonomos 15, 1–16.

Pedrosa-Soares, A.C., Alkmim, F.F., Tack, L., Noce, C.M., Babinski, M., Silva, L.C., Martins-Neto, M., 2008. Similarities and differences between the Brazilian and African counterparts of the Neoproterozoic Araçuaí West Congo Orogen. In: Pankhurst, J.R., Trouw, R.A.J., Brito Neves, B.B., De Wit, M.J. (Eds.), West Gondwana: Pre-Cenozoic Correlations across the South Atlantic Region. Geological Society of London, Special Publications vol. 294, pp. 153–172.

Pedrosa-Soares, A.C., De Campos, C.P., Noce, C., Silva, L.C., Novo, T., Roncato, J., Medeiros, S., Castañeda, C., Queiroga, G., Dantas, E., Dussin, I., Alkmim, F., 2011. Late Neoproterozoic–Cambrian granitic magmatism in the Araçuaí orogen (Brazil), the Eastern Brazilian Pegmatite Province and related mineral resources. Geological Society of London, Special Publication 350, 25–51.

Peixoto, E., Pedrosa-Soares, A.C., Alkmim, F.F., Dussin, I.A., 2015. A suture-related accretionary wedge formed in the Neoproterozoic Araçuaí orogen (SE Brazil) during Western Gondwanaland assembly. Gondwana Research 27, 878–896.

Petford, N., Cruden, A.R., McCaffrey, K.J.W., Vigneresse, J.L., 2000. Granite magma formation, transport and emplacement in the Earth's crust. Nature 408, 669–673.

Pickering, J.M., Johnston, A.D., 1998. Fluid-absent melting behavior of a two-mica metapelite: experimental constraints on the origin of Black Hills granite. Journal of Petrology 39, 1787–1804.

Pinto, C.P., Drumond, J.B.V., Féboli, W.L., 2001. Projeto Leste. CPRM/CODEMIG, CD-ROM, Belo Horizonte.

Queiroga, G.N., Pedrosa-Soares, A.C., Roncato, J.G., Dias, P.H.A., Guimarães, H.A., Coutinho, M.O.G., Freitas, N.C., Gradim, C.T., Braga, F.C.S., Novo, T.A., 2012. Geologia e recursos minerais da Folha Nova Venécia SE-24-Y-B-IV Escala 1:100.000, Estado do Espírito Santo Programa Geologia do Brasil, CPRM-UFMG.

Rasband, W.S., 1997–2012. ImageJ. U.S. National Institutes of Health, Bethesda, MD Available at: http://imagej.nih.gov/ij/ (last accessed on May 2014).

Richter, F., Lana, C., Stevens, G., Buick, I., Pedrosa-Soares, A.C., Alkmim, F.F., Cutts, K., 2016. Sedimentation, metamorphism and granite generation in a back-arc region: records from the Ediacaran Nova Venécia Complex (Araçuaí Orogen, Southeastern Brazil). Precambrian Research 272, 78–100.

Roncato, J.G., 2009. As suítes graníticas Tipo-S Do Norte Do Espírito Santo na região Das Folhas Ecoporanga, Mantena, Montanha e Nova Venécia. Instituto de Geociências, Universidade Federal de Minas Gerais, Minas Gerais (MSc Dissertation 102pp.).

Roncato, J.G., Pedrosa-Soares, A.C., Mascarenhas, T.F., Fornero, S.A., Galinari, L.M., Gonçalves, L.T., Queiroga, G.N., Braga, F.C.S., Novo, T.A., 2012. Geologia e recursos mineras da Folha Montanha SE-24-Y-B-I Escala 1:100.000, Estado do Espírito Santo Programa Geologia do Brasil, CPRM-UFMG.

Rosa, M.L.S., Conceição, H., Macambira, M.J.B., Galarza, M.A., Cunha, M.P., Menezes, R.C.L., Marinho, M.M., Filho, B.E.C., Rios, D.C., 2007. Neoproterozoic anorogenic magmatism in the Southern Bahia Alkaline Province of NE Brazil: U–Pb and Pb–Pb ages of the blue sodalite syenites. Lithos 97, 88–97.

Sampaio, A.R., Martins, A.M., Loureiro, H.C., Arcanjo, J.B., Moraes Filho, J.C., Souza, J.D., Pereira, L.H., Couto, P.A., Santos, R.A., Melo, R.C., Bento, R.V., Borges, V.P., 2004. Extremo Sul Da Bahia: Geologia e Recursos Minerais. Arquivos Abertos. CBPM e CPRM.

Silva, L.C., Armstrong, R., Noce, C.M., Carneiro, M.A., Pimentel, M., Pedrosa-Soares, A.C., Leite, C.A., Vieira, V.S., Silva, M.A., Paes, V.J.C., Filho, J.M.C., 2002. Reavaliação da evolução geológica em terrenos Pré-cambrianos brasileiros com base em novos dados U–Pb SHRIMP, parte II: Orógeno Araçuaí, Cinturão Mineiro e Cráton São Francisco meridional. Revista Brasileira de Geociencias 32, 513–528.

Silva, L.C., McNaughton, N.J., Armstrong, R., Hartmann, L.A., Fletcher, I.R., 2005. The neoproterozoic Mantiqueira Province and its African connections: a zircon-based U–Pb geochronologic subdivision for the Brasiliano/Pan-African systems of orogens. Precambrian Research 136, 203–240.

Silva, L.C., Pedrosa-Soares, A.C., Armstrong, R., Noce, C.M., 2011. Determinando a duração do período colisional do Orógeno Araçuaí com base em geocronologia U–Pb de Alta

Please cite this article as: Melo, M.G., et al., Two cryptic anatectic events within a syn-collisional granitoid from the Araçuaí orogen (southeastern Brazil): Evidence from the..., Lithos (2016), http://dx.doi.org/10.1016/j.lithos.2016.10.012

resolução em zircão: uma contribuição Para a história da amalgamação do Gondwana Ocidental. Geonomos 19, 180–197.
Stevens, G., Clemens, J.D., Droop, G.T.R., 1997. Melt production during granulite-facies anatexis: experimental data from "primitive" metasedimentary protholiths. Contributions to Mineralogy and Petrology 128, 352–370.
Tack, L., Wingate, M.T.D., Liégeois, J.P., Fernandez-Alonso, M., Deblond, A., 2001. Early Neoproterozoic magmatism (1000–910 Ma) of the Zadinian and Mayumbian Groups (Bas-Congo): onset of Rodinian rifting at the western edge of the Congo craton. Precambrian Research 110, 277–306.
Tedeschi, M., Novo, T., Pedrosa-Soares, A.C., Dussin, I., Tassinari, C., Silva, L.C., Gonçalves, L., Alkmim, F., Lana, C., Figueiredo, C., Dantas, E., Medeiros, S., De Campos, C., Corrales, F., Heibron, M., 2016. The Ediacaran Rio Doce magmatic arc revisited (Araçuaí-Ribeira orogenic system, SE Brazil). Journal of South American Earth Sciences 68, 248–268.
Vauchez, A., Egydio Silva, M., Babinski, M., Tommasi, A., Uhlein, A., Liu, D., 2007. Deformation of a pervasely molten middle crust: insights from the Neoproterozoic Ribeira-Araçuaí orogen (SE Brazil). Terra Nova 19, 167–186.
Vavra, G., Schmid, R., Gebauer, D., 1999. Internal morphology, habitat and U-Th-Pb microanalysis of amphibolite-to-granulite facies zircons: geochronology of the Ivrea Zone (Southern Alps). Contributions to Mineralogy and Petrology 134, 380–404.
Vielzeuf, D., Montel, J.M., 1994. Partial melting of metagreywackes. Part I. Fluid-absent experiments and phase relationships. Contributions to Mineralogy and Petrology 117, 375–393.
White, R.W., Powell, R., 2002. Melt loss and the preservation of granulite facies mineral assemblages. Journal of Metamorphic Geology 20, 621–632.
White, R.W., Powell, R., Holland, T.J.B., Worley, B.A., 2000. The effect of TiO_2 and Fe_2O_3 on metapelitic assemblages at greenschist and amphibolite facies conditions: mineral equilibria calculations in the system K_2O–FeO–MgO–Al_2O_3–SiO_2–H_2O–TiO_2–Fe_2O_3. Journal of Metamorphic Geology 18, 497–511.
White, R.W., Powell, R., Holland, T.J.B., 2001. Calculation of partial melting equilibria in the system Na_2O-CaO-K_2O-FeO-MgO-Al_2O_3-SiO_2-H_2O (NCKFMASH). Journal of Metamorphic Geology 19, 139–153.
White, R.W., Powell, R., Clarke, G.L., 2002. The interpretation of reaction textures in Fe-rich metapelite granulites of the Musgrave Block, Central Australia: constraints from mineral equilibria calculations in the system K_2O–FeO–MgO–Al_2O_3–SiO_2–H_2O–TiO_2–Fe_2O_3. Journal of Metamorphic Geology 20, 41–55.
White, R.W., Powell, R., Halpin, J.A., 2004. Spatially-focussed melt formation in aluminous metapelites from Broken Hill, Australia. Journal of Metamorphic Geology 22, 825–845.
White, R.W., Powell, R., Holland, T.J.B., 2007. Progress relating to calculation of partial melting equilibria for metapelites. Journal of Metamorphic Geology 25, 511–527.
Whitney, D.L., Evans, B.W., 2010. Abbreviations for names of rock-forming minerals. American Mineralogist 95, 185–187.
Yakymchuk, C., Brown, M., 2014. Consequences of open-system melting in tectonics. Journal of the Geological Society 171, 21–40.

Please cite this article as: Melo, M.G., et al., Two cryptic anatectic events within a syn-collisional granitoid from the Araçuaí orogen (southeastern Brazil): Evidence from the..., Lithos (2016), http://dx.doi.org/10.1016/j.lithos.2016.10.012

CHAPTER 4

ASSESSING THE ISOTOPIC EVOLUTION OF S-TYPE GRANITES OF THE CARLOS CHAGAS BATHOLITH, SE BRAZIL: CLUES FROM U-Pb, Hf ISOTOPES, Ti GEOTHERMOMETRY AND TRACE ELEMENT COMPOSITION OF ZIRCON

PRESENTATION OF THE PUBLICATION

This paper[1], first authored by Marilane Gonzaga Melo, was submitted to Lithos. The following aspects of the research were done independently by Marilane Gonzaga Melo while receiving standard supervision by his supervisors Gary Stevens, Cristiano Lana and Fernando Flecha de Alkmim. I did the sampling in the field, mineral separation for zircon geochronology, zircon imaging by SEM, zircon U-Pb analysis (LA-Q-ICP-MS and LA-SF-ICP-MS) and trace element analysis of zircon (LA-SF-ICP-MS). I was also responsible for the literature review and the majority of the written work. Professor Pedrosa-Soares contributed to the fieldwork and regional concepts. Axel Gerdes was responsible for Lu-Hf analyses and processing of the data. Professor Nalini Jr. contributed to the zircon U-Pb analyses (LA-Q-ICP-MS) and Leonardo Alkmin helped with the Ti-thermometry calculations.

Marilane Gonzaga Melo[a,b]

Cristiano Lana[a]

Gary Stevens[b]

Antônio Carlos Pedrosa-Soares[c]

Axel Gerdes[d]

Leonardo Azevedo Alkmin[a]

Hermínio Arias Nalini Júnior[a]

Fernando Flecha de Alkmim[a]

a: Applied Isotope Research Group, Departamento de Geologia, Escola deMinas, Universidade Federal de Ouro Preto, Campus UniversitárioMorro do Cruzeiro s/n, 35400-000 Ouro Preto,MG, Brazil
b: Centre for Crustal Petrology, Department of Earth Sciences, Stellenbosch University, Private Bag X1, Matieland 7602, South Africa
c: Universidade Federal de Minas Gerais, IGC–CPMTC, Campus Pampulha, 31270-901 Belo Horizonte, MG, Brazil
d: Institut für Geowissenschaften, Johann Wolfgang Goethe-Universität Frankfurt, Altenhöferallee 1, Frankfurt am Main 60438, Germany

[1]Melo, M.G, Lana, C., Stevens, G., Pedrosa-Soares, A.C., Gerdes, A., Alkmin, L.A., Nalini Jr., H.A., Alkmim, F.F. Assessing the isotopic evolution of S-type granites of the Carlos Chagas Batholith, SE Brazil: clues from U-Pb, Hf isotopes, Ti geothermometry and trace element composition of zircon. Submitted to Lithos.

Manuscript submitted to Lithos - manuscript number: LITHOS6233

Assessing the isotopic evolution of S-type granites of the Carlos Chagas Batholith, SE Brazil: clues from U-Pb, Hf isotopes, Ti geothermometry and trace element composition of zircon

M.G. Melo[a,b], C. Lana[a], G. Stevens[b], Pedrosa-Soares[c], A.C., Gerdes, A[d]., L.A. Alkmin[a], H.A. Nalini Jr[a]., F.F. Alkmim[a]

[a]Applied Isotope Research Group, Departamento de Geologia, Universidade Federal de Ouro Preto, Morro do Cruzeiro, 35400-000, Ouro Preto, MG, Brazil
[b]Centre for Crustal Petrology, Department of Earth Sciences, Stellenbosch University, Private Bag X1, Matieland 7602, South Africa
[c]Universidade Federal de Minas Gerais, IGC–CPMTC, Campus Pampulha, 31270-901 Belo Horizonte, MG, Brazil
[d]Institut für Geowissenschaften, Johann Wolfgang Goethe-Universität Frankfurt, Altenhöferallee 1, Frankfurt am Main 60438, Germany

ABSTRACT

The Carlos Chagas batholith (CCB) is a very large (~14,000 km^2) S-type granitic body formed during the syn-collisional stage of the Araçuaí orogen (southeastern Brazil). Zircons extracted from the CCB record a wide range of U-Pb ages (from 825 to 490 Ma), indicating a complex history of inheritance, magmatic crystallization and partial melting during the evolution of the orogeny. 582 Ma magmatic zircons are marked by similar Hf isotope compositions and REE patterns to those of inherited cores (ca. 825-600 Ma), indicating that these aspects of the chemical signature of the magmatic zircons has likely been inherited from the source. The U-Pb ages and initial $^{176}Hf/^{177}Hf$ ratios from anatectic and metamorphic zircon domains are consistent with a two-stage metamorphic evolution marked by contrasting mechanisms of zircon growth and recrystallization during the orogeny. Ti-in-zircon thermometry is consistent with the findings of previous metamorphic work and indicates that the two metamorphic events in the batholith reached granulite facies conditions (> 800 ºC) producing two generations of garnet via fluid-absent partial melting reactions. The oldest metamorphic episode (ca. 570-550 Ma) is recorded by development of thin anatectic overgrowths on older cores and by growth of new anatectic zircon crystals. Both domains have higher initial $^{176}Hf/^{177}Hf$ values compared to relict cores and display REE patterns typical of zircon that grew contemporaneously with peritectic garnet through biotite-absent fluid partial melting reactions. Hf isotopic and chemical evidences indicate that a second anatectic episode (ca. 535-500 Ma) is only recorded in parts from the CCB. In these rocks, the growth of new anatectic zircon and/or overgrowths is marked by high initial $^{176}Hf/^{177}Hf$ values and also by formation of second generation of garnet, as indicated by petrographic observations and REE patterns. In addition, some rocks contain zircon crystals formed by solid-state recrystallization of pre-existing zircon, which exhibit similar Hf isotope composition to those to inherited/magmatic core domains. The first anatectic event is interpreted as result of the crustal thickening, which introduced the batholith at deeper crust level and produced a widespread anatexis in these rocks. The second event can be associated with asthenospheric upwelling during extensional

thinning and gravitational collapse of the orogen, this produced anatexis in parts from the CCB that had been re-fertilized by retrogression along shear zones following the first granulite facies event.

Key words: U-Pb dating, Hf isotope, REE zircon, Ti-in-zircon thermometer, repeated partial melting, crustal recycling

1. INTRODUCTION

The low diffusivity of trace elements in zircon (Cherniak et al., 1997) allows the preservation of isotopic and chemical variations within distinct growth zones within individual zircon crystals. Thus, such growth zones have the potential to provide valuable insights about geological processes that affected the magma or rock within which the zircon grew. Early studies have shown that metamorphic zircons can be formed by different processes, such as: (i) new zircon growth related to dissolution and re-precipitation of pre-existing zircon in anatectic melts or fluids (e.g., Williams et al., 1996; Schaltegger et al., 1999; Vavra et al., 1999; Flowerdew et al., 2006; Geisler et al., 2007; Wu et al., 2007; Zheng, 2009; Taylor et al., 2014); (ii) growth associated with metamorphic reactions that release sufficient Zr (e.g., Vavra et al., 1996; Fraser et al., 1997; Liermann et al., 2002; Slamá et al., 2007); and (iii) solid-state recrystallization of pre-existing zircon grains (e.g., Hoskin & Black, 2000). Each of these processes affects zircon trace element chemistry and Hf isotope composition in different ways (Xia et al., 2009; Ge et al., 2013b; Chen et al., 2015).

Due to inheritance, recrystallized zircons often display Hf isotope compositions similar to those of relict cores (Ge et al., 2013a), whereas new zircon growth or overgrowth zones derived from melts and/or external fluid interaction generally has elevated initial $^{176}Hf/^{177}Hf$ values relative to their relict cores (Xia et al., 2009; Ge et al., 2013b; Chen et al., 2015). Likewise, the behavior of rare earth element (REE) compositions in zircon and other major metamorphic mineral phases (especially garnet) reflect specific processes of metamorphic growth (e.g., Rubatto, 2002; Whitehouse & Platt, 2003; Rubatto et al., 2006; Harley & Kelly, 2007; Rubatto & Hermman, 2007; Taylor et al., 2015). For example, coexisting zircon and garnet are enriched in heavy-REE with respect to chondrite values and exhibits variable REE patterns, reflecting equilibrium with different assemblages and with the bulk composition. The experimental study carried out by Rubatto & Hermman (2007) demonstrates that zircon incorporates more HREE than garnet crystals at 800-850 ºC (P = 20 kbar) and partitioning values are temperature-dependent. On the other hand, some studies (Whitehouse & Platt, 2003; Taylor et al., 2015) have reported different partitioning values between zircon and garnet, which can possibly be related to pressure of equilibration and/or chemical composition of garnet. In other words, partitioning of HREE between garnet and zircon is likely to be dependent on these parameters in addition to temperature.

Interest in zircon trace element geochemistry has been renewed with the development of the Ti-in-zircon thermometer (Watson et al., 2006; Ferry & Watson, 2007), which provides a valuable link between

temperature of zircon growth/equilibration and age of crystallization (Clark et al., 2009; Ewing et al., 2013; Liu et al., 2015). Thus, the combination of U-Pb age data, Hf isotope compositions, mineral trace element compositions and Ti-in-zircon thermometry provides a powerful tool for documenting the evolution of crustal processes. The various contributions of inheritance, magmatic crystallization and metamorphic resetting in zircon from polymetamorphic granites remains, however, poorly understood. For instance, recent studies suggest that zircons from S-type granites inherit much of the isotopic signature from the source (Villaros et al., 2012; Farina et al., 2014), whereas other studies seem to indicate that the Hf contributions from minerals other than zircon is important for producing the Hf isotope variation in S-type granites and migmatites (Tang et al., 2014; Chen et al., 2015).

In this study, we investigate the isotopic and trace element composition of zircon crystals from the Carlos Chagas Batholith (CCB), a >200 km-scale, S-type granite batholith that was emplaced during the collisional stage of the Araçuaí orogen in southeastern Brazil (Pedrosa-Soares et al., 2011). The CCB is ideal for such a study because it show an uniform geochemistry, recording nearly identical U-Pb crystallization ages at ca. 580-570 Ma (Roncato, 2009; Pedrosa-Soares et al., 2011; Gradim et al., 2014) and yet, a recent study by Melo et al. (2016) has demonstrated that the batholith underwent partial melting and melt loss during two high-grade metamorphic events. By combining U-Pb dating with Hf isotopic information from different growth zones of the complexly crystallized zircon grains, we were able investigate the isotopic evolution of this granitoid from crystallization through to the anatectic episodes. In addition, analysis of rare earth element (REE) compositions and Ti geothermometry on distinct domains of zircon provide important information about petrologic conditions that affected the batholith at different times of its history.

2. GEOLOGICAL SETTING

The Araçuaí orogen, situated in southeastern Brazil, and its African counterpart, the West Congo belt, constitute a confined orogenic system developed between the São Francisco and Congo cratons (Alkmim et al., 2006) (Fig.1). Araçuaí-West Congo orogen is considered to be the result of Adamastor-Brazilide ocean (Dalziel, 1997) closure during the amalgamation of Western Gondwana in late Proterozoic time. This orogenic system was divided into two parts by the Cretaceous South Atlantic rifting. The evolution of the Araçuaí orogen is recorded in rift-related to distal passive margin and oceanic, Rio Doce magmatic arc-related rocks and collisional to post-collisional igneous supersuites.

Based on field relationships, structural features, geochemical and geochronological data, the granitic magmatism produced during this orogenic episode has been grouped into five supersuites (G1 to G5 - Pedrosa-Soares et al., 2011), which are currently exposed over an area of 350,000 Km^2 (Fig. 1). G1 supersuite (ca. 630-580 Ma, pre-collisional stage) represents the plutonic part of the Rio Doce magmatic arc, consisting of I-type, metaluminous to slightly peraluminous, calc-alkaline granites (Nalini et al., 2005; Vieira, 2007; Gonçalves et al., 2014, 2015; Tedeschi et al., 2016). The arc-related supracrustal sequences comprise metavolcano-

sedimentary successions of the Rio Doce group (Vieira, 2007), as well as metasedimentary sequences deposited in the back-arc (Nova Venécia complex - Gradim et al., 2014; Richter et al., 2016) and fore-arc (Peixoto et al., 2015) zones. G2 supersuite (ca. 585 – 545 Ma, syn-collisional stage) mostly includes S-type, peraluminous, sub-to calc-alkalines granites (Pedrosa-Soares et al., 2011; Gradim et al., 2014). G3 supersuite (ca. 545-530 Ma, late collisional stage) consists of S-type, peraluminous, high-K alkaline granites which are considered to the result of the anatexis of paragneisses complexes and G2 rocks (Silva et al., 2002, 2011; Noce et al., 2004; Roncato, 2009; Pedrosa-Soares et al., 2011; Gradim et al., 2014). G4 supersuite (ca. 530-500 Ma, post-collisional stage) mostly comprises S-type, peraluminous, sub-alkaline granites (Pedrosa-Soares et al., 2011). G5 supersuite (ca. 525-480 Ma, post-collisional stage) consists of I-to A-types, metaluminous to slightly peraluminous, high K-Fe calc-alkaline to alkaline granites (De Campos et al., 2004, 2016; Pedrosa-Soares et al., 2011; Gradim et al., 2014).

2.1. Carlos Chagas batholith

The ca. 580-565 Ma Carlos Chagas batholith (CCB), is the largest S-type granitoid batholith of the Araçuaí orogen. CCB covers a large area, extending for about 260 km N-S and 60 km W-E, in the core of the orogen (Fig. 2). Most exposures of the CCB rocks occurs along the southern and central parts of the batholith (Carlos Chagas leucogranite), whereas subordinate lithotypes are mainly found along the northern outer zones of the CCB (Montanha and Nanuque granites) (Fig. 2). Migmatitic paragneisses (Nova Venécia and Jequitinhonha complexes) and Ataléia suite occur around CCB and also as isolated massifs within the batholith (Fig. 2). The Ataléia suite comprises garnet-sillimanite-orthopyroxene-bearing S-type granites that occur in association with migmatitic paragneisses, being interpreted as anatectic product of the Nova Venécia complex (Gradim et al., 2014). Cordierite- and/or garnet-bearing leucogranites (G3 supersuite) form vein- to irregular-shaped leucosomes generally associated with Ataléia suite and CCB (Pedrosa-Soares et al., 2011; Gradim et al., 2014). CCB was intruded by several post-collisional igneous bodies from the G5 supersuite (ca. 525-480 Ma) during the gravitational collapse of the orogen (Noce et al., 2000; Pedrosa-Soares et al., 2011; Gradim et al., 2014; De Campos et al., 2016) (Fig. 2).

Melo et al. (2016) showed that the CCB underwent at least two granulite facies metamorphic events. The earlier high-grade metamorphic event produced a first generation of garnet via fluid-absent partial melting of an assemblage consisting of high-Ti biotite, plagioclase, K-feldspar and quartz. Based on the peak assemblage Qz-Pl-Kfs-Bt-Grt-Ilm-Rt-Liq, the P-T conditions are estimated to be 790-820 ºC and 9.5-10.5 kbar (Melo et al., 2016), which can be related to crustal thickening caused by contractional thrusting and folding during the collisional stage of orogeny (Pedrosa-Soares et al., 2011; Gradim et al., 2014). The later granulite facies metamorphism is manifested by the formation of the second generation of garnet through incongruent melting of a muscovite + quartz + plagioclase assemblage, with subsequent biotite + sillimanite + quartz + plagioclase melting to produce the second generation of peritectic garnet. The P-T conditions of equilibrium for the assemblage Qz-Pl-Kfs-Bt-Grt-Sil-Ilm-Liq is 770 ºC and 6.6 kbar (Melo et al., 2016), which is attributed

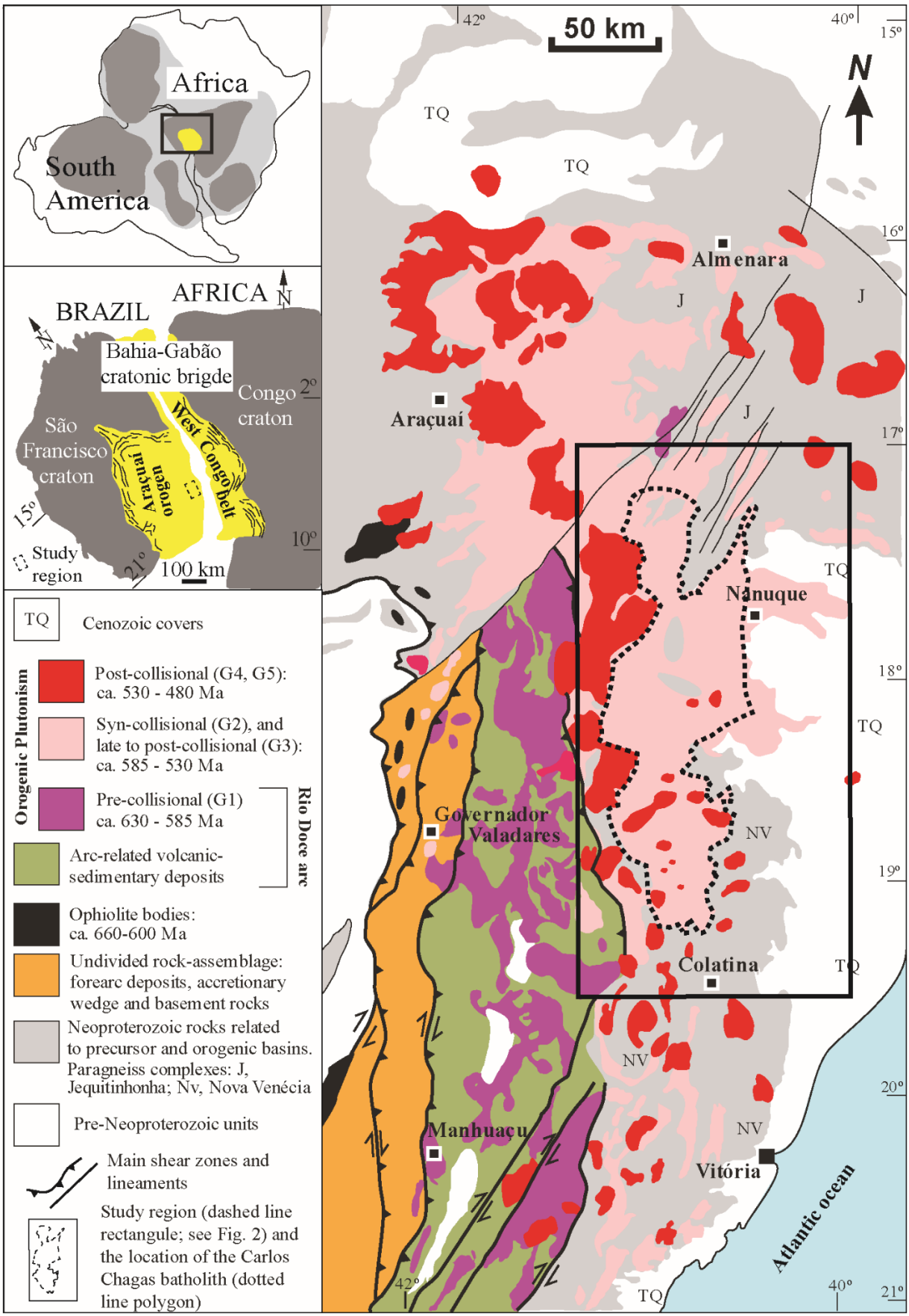

Figure 1. The Araçuaí-West Congo orogen in the context of West Gondwana (after Alkmim et al. 2006). Simplified geological map from Araçuaí orogen (modified from Pedrosa-Soares et al. 2011) showing location of the study area (dashed rectangle) and occurrence area of Carlos Chagas batholith (dotted polygon).

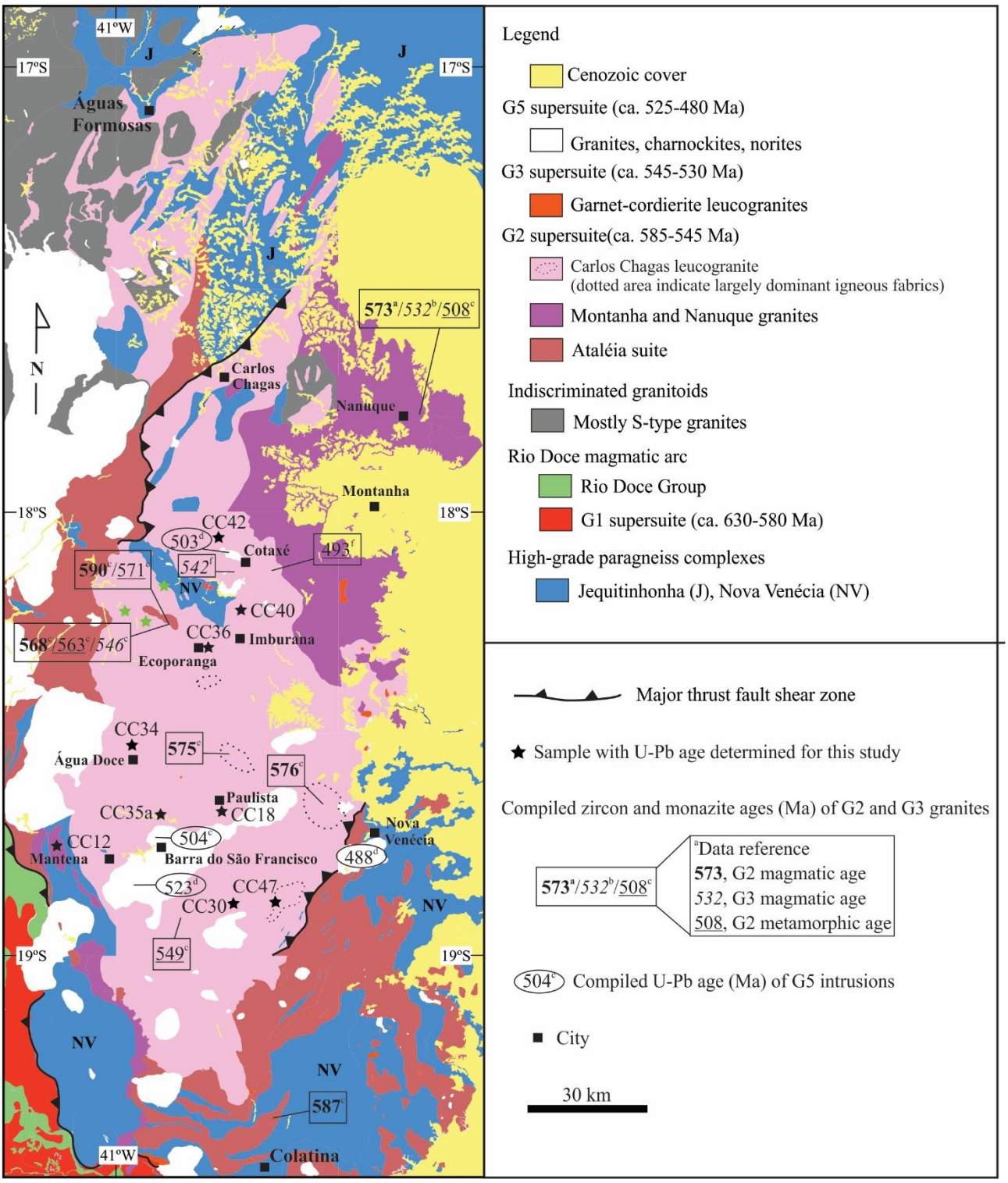

Figure 2. Simplified geological map for the study area (compiled from 1:100.000 scale maps published by Pinto et al., 2001; Castañeda et al., 2006; Gradim et al., 2007; Baltazar et al., 2010; Queiroga et al., 2012; Roncato et al., 2012), showing the area covered by Carlos Chagas batholith, location of samples (CC) analyzed in this study, and compiled U-Pb geochronological data from: a, Silva et al. (2002, 2011); b, Pedrosa-Soares et al. (2011); c, Gradim et al. (2014); d, De Campos et al. (2016); e, Vauchez et al. (2007); f, Pedrosa-Soares et al. (2007).

to the gravitational collapse of the orogen (Pedrosa-Soares et al., 2011; Gradim et al., 2014; De Campos et al., 2016). This second partial melting event only affected portions of the CCB that were previously rehydrated along shear zones, with subsequent formation of retrograde muscovite.

Previous SHRIMP and LA-ICP-MS zircon U-Pb studies have constrained the age of crystallization of the CCB to between ca. 577 and 565 Ma (Silva et al., 2002; Vauchez et al., 2007; Roncato, 2009; Gradim et al., 2014) and the age of metamorphism to between ca. 563-549 Ma (Gradim et al., 2014). In situ U-Pb monazite and zircon geochronology reveals two ages of metamorphism: ca. 570-550 Ma and ca. 535-515 Ma (Melo et al., 2016). The oldest metamorphic age is contemporaneous with peak metamorphism recorded in Nova Venécia complex and Ataléia suite (ca. 575-560 Ma; Gradim et al., 2014; Richter et al., 2016), whilst the younger metamorphic event overlaps in age with veins and patches of the G3 supersuite (ca. 545-530 Ma; Silva et al., 2002, 2011; Noce et al., 2004; Pedrosa-Soares et al., 2011; Gradim et al., 2014) within the CCB, which the work of Mello et al. (2016) has demonstrated are produced by anatexis of the CCB during the 2nd anatectic event.

3. SAMPLING AND PETROGRAPHY

Representative rock samples were collected from the Carlos Chagas batholith for geochronology studies; these included eight samples of the Carlos Chagas leucogranite and one of the Nanuque granite (Fig. 2). Field features, sample location and mineral assemblages of each sample are presented in Table 1. The petrography of the CCB is discussed in detail by Melo et al. (2016); therefore, only a brief summary is presented here. Mineral abbreviations are after Whitney and Evans (2010).

Table 1. Descriptions and localities of geochronology samples from the Carlos Chagas batholith.

	Sample	Location	Field features	Main mineralogy	Accessory mineralogy
Carlos Chagas leucogranite	CC18	18º41'1.2''S/40º45'44.4''W	Strongly foliated	Qz + Kfs +Pl +Bt + Grt + Sil	Ilm + Hc + Zrn + Mnz + Ap + Rt
	CC30	18º55'54.4"S/41º45'17.3"W	Weakly foliated	Qz + Kfs +Pl +Bt + Grt	Ilm + Zrn + Mnz + Ap + Rt
	CC34	18º33'17.9''S/40º58'13.6''W	Moderately foliated	Qz + Kfs +Pl +Bt + Grt + Sil	Ilm + Zrn + Mnz + Ap + Rt
	CC35a	18º41'26.4"S/40º54'22.4"W	Strongly foliated	Qz + Kfs +Pl +Bt + Grt + Sil	Ilm + Zrn + Mnz + Ap + Rt
	CC36	18º20'19.3''S/40º47'59.7"W	Moderately foliated	Qz + Kfs +Pl +Bt + Grt + Sil	Ilm + Zrn + Mnz + Ap + Rt
	CC40	18º14'43"S/41º43'47.5"W	Strongly foliated	Qz + Kfs +Pl +Bt + Grt + Sil	Ilm + Hc + Zrn + Mnz + Ap + Rt
	CC42	18º3'59"S/40º46'28.8"W	Strongly foliated	Qz + Kfs +Pl +Bt + Grt	Ilm + Zrn + Mnz + Ap + Rt
	CC47	18º53'4.2"S/40º37'48.3"W	Incipient foliation	Qz + Kfs +Pl +Bt + Grt	Ilm + Zrn + Mnz + Ap + Rt
Nanuque granite	CC12	18º45'47''S/ 41º7'49.3''W	Strongly foliated	Qz + Kfs +Pl +Bt + Grt	Ilm + Zrn + Mnz + Ap

3.1. Carlos Chagas leucogranite (Samples CC18, CC30, CC34, CC35a, CC36, CC40, CC42 and CC47)

The Carlos Chagas leucogranite is white to light pink, medium to very coarse-grained and some samples contain K-feldspar megacrysts up to 15 cm long. These leucogranites were deformed to different degrees, ranging from weakly to strongly foliated, with local preserved igneous features (Fig. 3a,b,c). Garnet- and/or cordierite-bearing leucogranite patches and veins (G3 supersuite) are commonly associated to CCB

(Fig. 3d). The mineralogy consists of quartz (22-45 %), plagioclase (8-24 %), K-feldspar (17-43%), biotite (1-5%), garnet (3-18%) and minor sillimanite (0-5%). Accessory phases include spinel, ilmenite, rutile, apatite, monazite and zircon. The most of the garnet crystals occur as porphyroblasts (Grt_1), with innumerous inclusions of rounded biotite, rounded to lobate quartz and plagioclase (Fig. 3e). Generally, Grt_1 is wrapped by a second generation of garnet (Grt_2) that consists of subhedral to euhedral crystals with inclusions of fine sillimanite needles (Fig. 3f). In these samples, sillimanite inclusions are aligned with foliated matrix sillimanite. Biotite occurs as rounded inclusions in garnet, single lamellae and/or clots defining the foliated matrix and occasionally replacing the poikiloblastic garnet rims (Fig. 3e,f). Microstructural evidence for the former presence of melt is recognized in all samples, including thin films of melt along garnet boundaries, pseudomorphed melt pools in the vicinity of biotite and garnet crystals, and cuspate-lobate quartz and plagioclase among matrix grains (see petrographic details in Melo et al., 2016).

3.2. Nanuque granite (Sample CC12)

The Nanuque granite is light gray, medium to very coarse-grained (Fig. 3g), consisting of quartz (25%), k-feldspar (35%), plagioclase (32%), biotite (5%), and garnet (3%). Ilmenite, zircon, monazite and apatite are common accessory phases. At mesoscopic scale this granite is strongly foliated and show deformation features, such as stretched K-feldspar. Poikiloblastic garnet crystals (Fig. 3h) contain rounded biotite, plagioclase, lobate to rounded quartz, and minor ilmenite, monazite and zircon as inclusions. Matrix biotite defines the regional foliation and retrograde biotite rarely occurs along the boundaries of poikiloblastic garnet crystals.

4. U-Pb GEOCHRONOLOGY

In an attempt to evaluate the metamorphic history from CCB, we carefully investigated the internal structure of the zircons through cathodoluminescence (CL) imaging (Fig. 4). This allowed inherited, magmatic and anatectic domains to be distinguished within the zircon grains. Cores and/or rims of zircon were analyzed in nine representative rock samples (Fig. 2) and U-Pb data of the dated zircons are presented in Supplementary Data (Tables S1and S2) and plotted in Figures 5 to 8.

The common zircon population is represented by light pink to colorless, translucent, short- and long-prismatic grains, exhibiting rounded to subrounded or subhedral to euhedral terminations. The length of individual grains ranges from 90 to 800 µm and their length/width ratios vary between 2:1 and 7:1, with an average of 4:1. Cl-images (Fig. 4) revealed that most of the zircons have unzoned or oscillatory zoned cores with medium to high luminescence, surrounded by structureless dark rim domains. Detailed descriptions of the individual samples is presented in Supplementary Material.

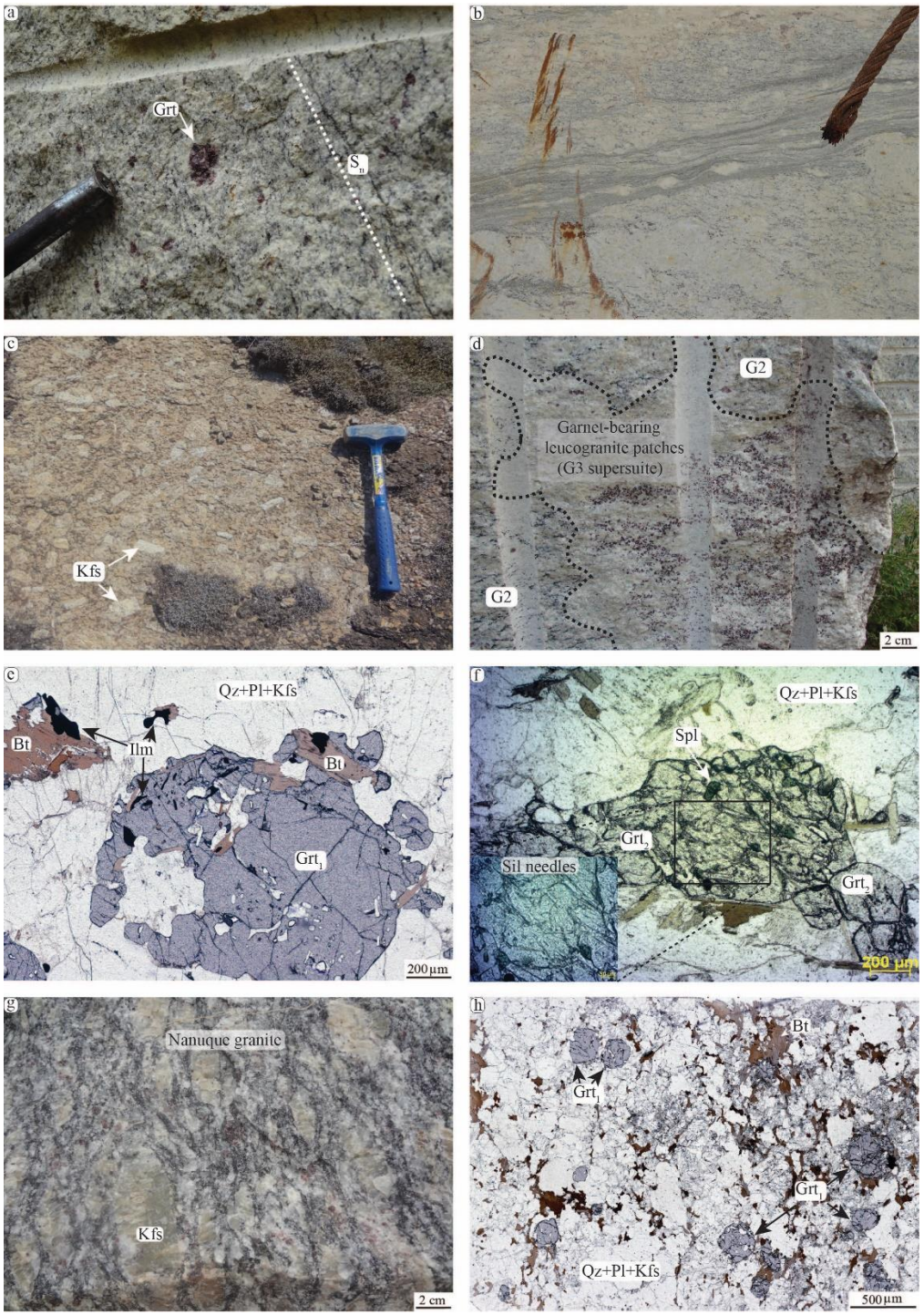

Figure 3. Field photographs and photomicrographs from the Carlos Chagas leucogranite (a-f) and Nanuque granite (g-h). (a) Deformed granite showing garnet crystals from the coarse-grained biotite and sillimanite-bearing quartz-feldspathic matrix (sample CC40). (b) Sigma shape of K-feldspar grains in mylonite. (c) Leucogranite showing euhedral to subhedral garnet crystals. (d) Dashed lined delimited garnet-bearing leucogranite patches (G3 supersuite) associated to Carlos Chagas batholith (G2 supersuite). (e) Well-preserved poikiloblastic garnet showing innumerous inclusions of lobate quartz, plagioclase, biotite and ilmenite. (f) Garnet crystals in the foliated granite, showing sillimanite needles and spinel as inclusions. (g) Typical appearance from the Nanuque granite. (h) Scanned thin section showing the rock texture, with biotite defining the foliation.

Figure 4. Cathodoluminescence images of representative zircon grains from the Carlos Chagas batholith.

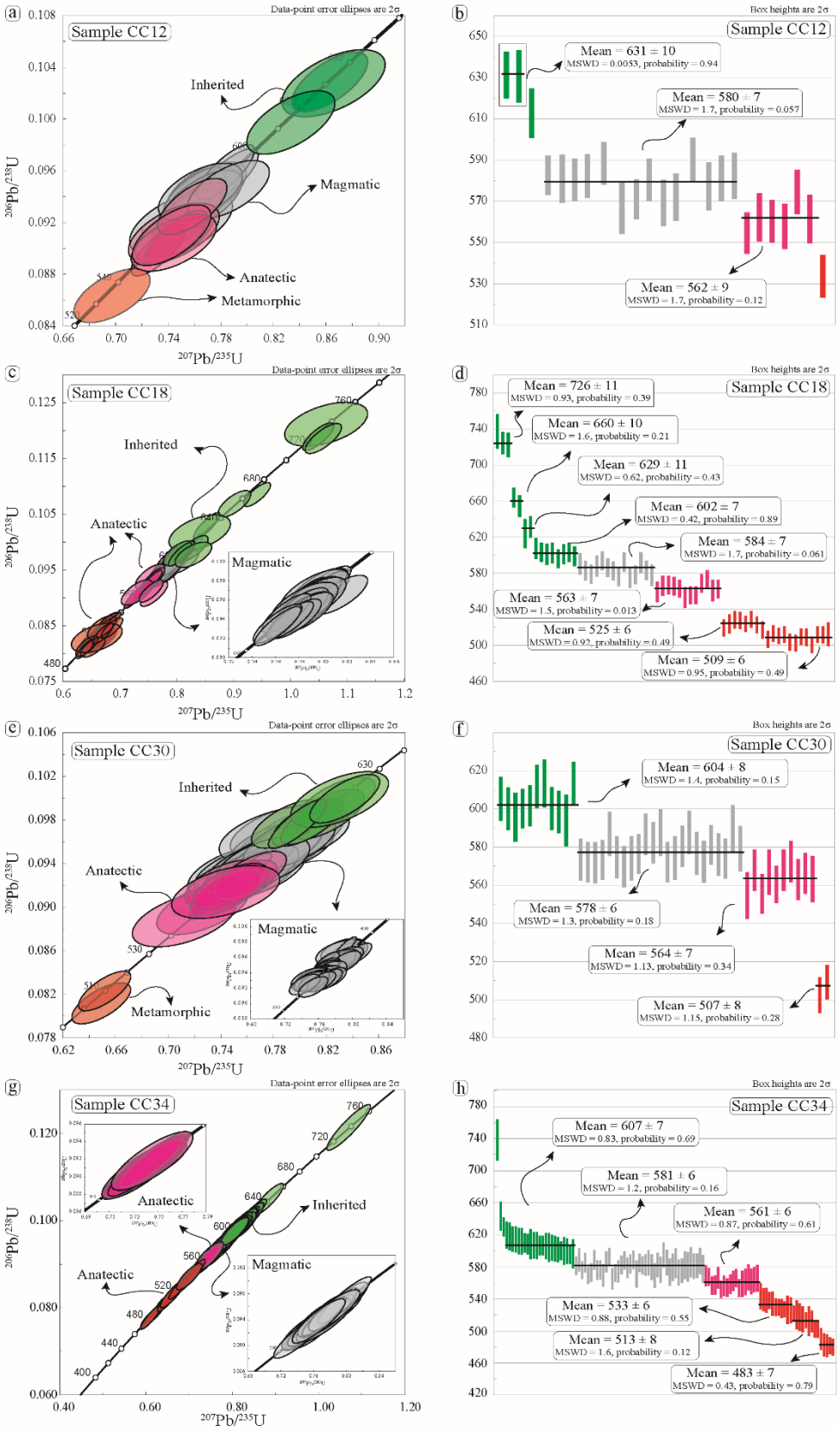

Figure 5. Concordia diagrams and weighted mean $^{206}Pb/^{238}U$ ages calculated from Isoplot 4.15 (Ludwig 2003). Analytical uncertainties are based on the quadratic addition of the average mean error (given by Isoplot) and the 1% error inherent precision of the technique and final ages are quoted at the 95% confidence interval. Individual analysis error are shown in 2σ. (a-b) Sample CC12. (c-d) Sample CC18. (d-e) Sample CC30. (f-g) Sample CC34.

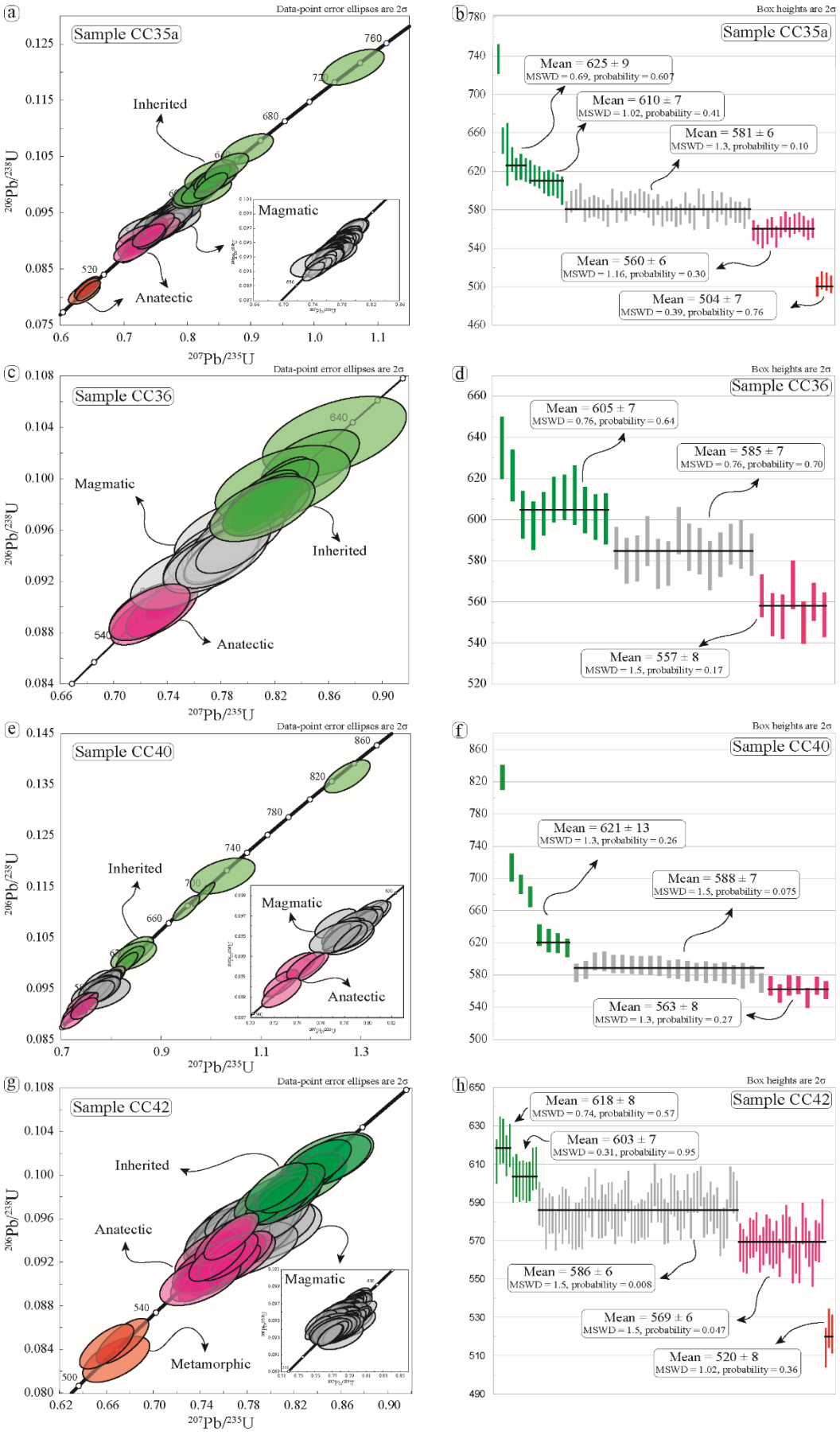

Figure 6. Concordia diagrams and weighted mean $^{206}Pb/^{238}U$ ages calculated from Isoplot 4.15 (Ludwig. 2003). (a-b) Sample CC35a. (c-d) Sample CC36. (d-e) Sample CC40. (f-g) Sample CC42.

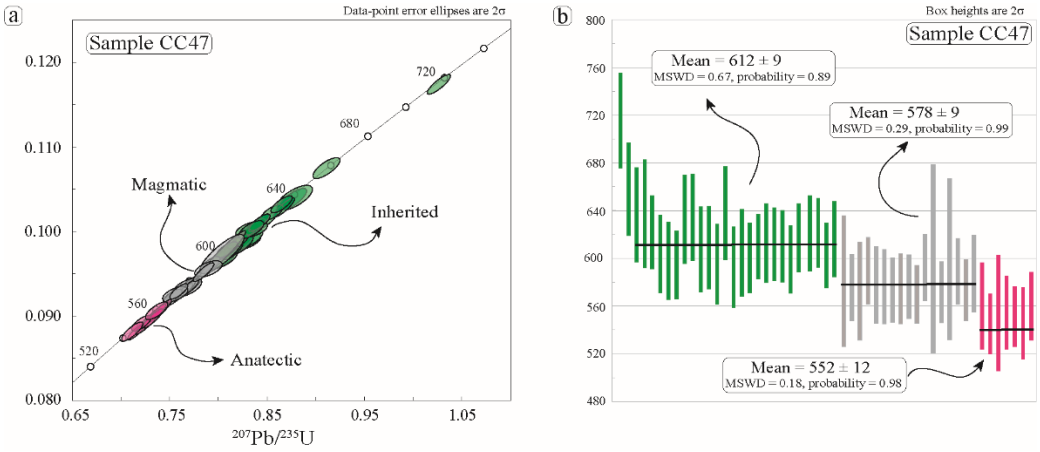

Figure 7. Concordia diagrams and weighted mean $^{206}Pb/^{238}U$ ages calculated from the sample CC47.

All samples show CL-defined inherited cores which are characterized by unzoned or weakly zoned domains with medium to high luminescence (Fig. 4). They have Th/U ratios ranging from 0.01 to 2.24 (Supplementary Data - Tables S1and S2). As illustrated in Figs. 5 to 8, all samples have similar age patterns, with one dominant peak age between 600 and 615 Ma (n = 93, Table 2). Subordinate peaks are recorded at 630-620 Ma (n = 20), 680-635 Ma (n = 7), 740-690 (n = 8) and 826 Ma (n = 1) (Table 2).

Table 2. Main populations of inherited zircons identified in the Carlos Chagas batholith.

Sample	Method	Population ca. 826 Ma	Population ca. 740-690 Ma	Population ca. 680-635 Ma	Population ca. 630-620 Ma	Population ca. 615-600 Ma
CC12	LA-Q-ICP-MS				631 ± 10 (n=2)	613 ± 12 (n=1)
CC18	LA-Q-ICP-MS		726 ± 11 (n=3)	660 ± 10 (n=2)	629 ± 11 (n=2)	602 ± 7 (n=8)
CC30	LA-Q-ICP-MS					604 ± 8 (n=11)
CC34	LA-SF-ICP-MS		739 ± 25 (n=1)	644 ± 17 (n=1)	630 ± 11 (n=1)	607 ± 7 (n=23)
CC35a	LA-Q-ICP-MS		736 ± 16 (n=1)	651 ± 14 (n=1)	625 ± 9 (n=5)	610 ± 7 (n=8)
CC36	LA-Q-ICP-MS			635 ± 8 (n=1)	622 ± 6 (n=1)	605 ± 7 (n=9)
CC40	LA-Q-ICP-MS	826 ± 15 (n=1)	714 ± 17 (n=1); 693 ± 11 (n=1)	678 ± 12 (n=1)	621 ± 13 (n=4)	
CC42	LA-Q-ICP-MS				618 ± 8 (n=5)	603 ± 7 (n=8)
CC47	LA-SF-ICP-MS		716 ± 6 (n=1)	658 ± 12 (n=1)		612 ± 9 (n=25)

Analytical uncertainties on weighted mean ages are based on the quadratic addition of the average mean error (given by Isoplot) and the 1% error inherent precision of the technique and final ages are quoted at the 95% confidence interval. Analytical uncertainties from individual grain are reported as 2σ.

The oscillatory to irregular zoned cores (Fig. 4) with Th/U ratios ranging from 0.02 to 2.29 (Supplementary Data - Tables S1and S2) are interpreted as magmatic origin. U-Pb analysis performed on these grains (n =248) yield weighted mean ages ranging from 578 ± 6 to 588 ± 7 Ma (Figs. 5 to 8; Table 3).

The most of the zircon cores (inherited or magmatic) are enveloped by internally structureless, unzoned and low luminescence domains, interpreted as anatectic rims formed during high-grade metamorphic events. They have variable Th/U ratios between 0.01 and 1.27 (Supplementary Data - Tables S1and S2). Analyses in rim domains (n = 160) indicates distinct populations. The oldest anatectic zircon population is recorded in all

samples and gives weighted mean ages for individual samples that range in age between 552 ± 12 and 569 ± 6 Ma (Figs. 5 to 8; Table 3). Most of the samples also record younger metamorphic populations, with weighted mean ages for individual samples that range in age from 534 ± 10 to 504 ± 7 Ma (Figs. 5 to 8; Table 3).

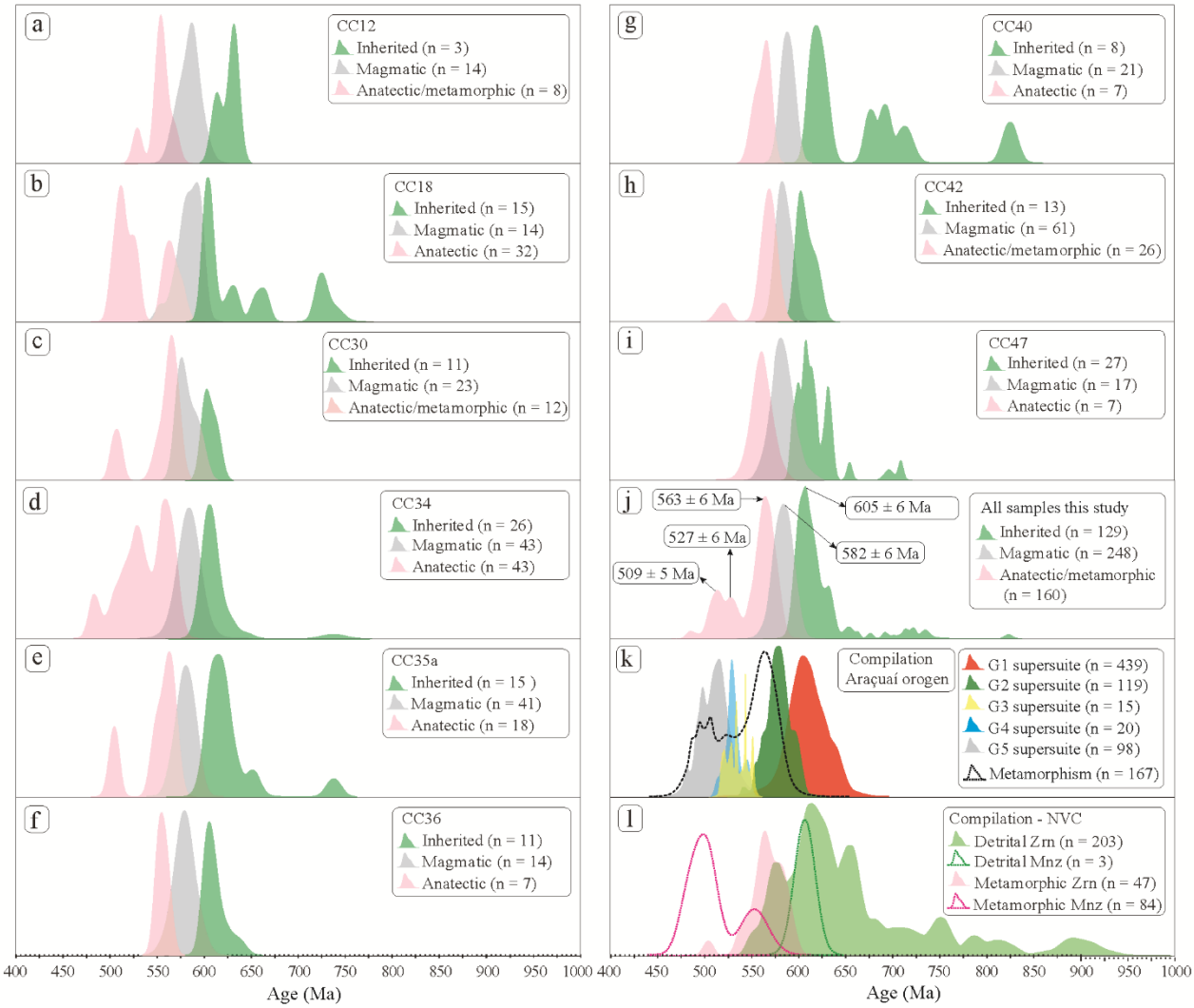

Figure 8. Probability density plots for zircon samples from Carlos Chagas batholith (a-j) Age distribution pattern of zircon and monazite from the G1 to G2 supersuite (k) Nova Venécia complex (l). Compiled data from Vauchez et al. (2007); Petitgirard et al. (2009); Roncato (2009); Novo et al. (2010); Pedrosa-Soares et al. (2011); Mondou et al. (2012); Gonçalves et al. (2014, 2015); Gradim et al. (2014); De Campos et al. (2016); Richter et al. (2016) and Tedeschi et al. (2016).

5. Lu-Hf ISOTOPE ANALYSES

Three hundred analyses were successfully performed on zircon cores and/or rims with concordant ages (Supplementary Data – Table S3). The data indicates that these zircons (inherited, magmatic and anatectic/metamorphic) are highly heterogeneous in Hf isotope composition. A summary with the initial $^{176}Hf/^{177}Hf$ ratios and εHf(t) is presented in Table 4.

Table 3. Summary of U-Pb ages (Ma) for Carlos Chagas batholith from this study and previous data from the literature.

Sample	Method	Mineral	Crystallization magmatic	1st partial melting	2nd partial melting and/or metamorphic recrystallization		Reference
CC12	LA-Q-ICP-MS	Zrn	580 ± 7	562 ± 9	534 ± 10		This study
CC18	LA-Q-ICP-MS	Zrn	584 ± 7	563 ± 7	525 ± 6	509 ± 6	This study
CC21	LA-Q-ICP-MS	Zrn*		564 ± 4			Melo et al. (2016)
CC21	LA-Q-ICP-MS	Mnz*		552 ± 8	515 ± 14		Melo et al. (2016)
CC30	LA-Q-ICP-MS	Zrn	578 ± 6	564 ± 7		507 ± 8	This study
CC31	LA-Q-ICP-MS	Mnz*		560 ± 9			Melo et al. (2016)
CC31	LA-Q-ICP-MS	Zrn*		563 ± 9			Melo et al. (2016)
CC34	LA-SF-ICP-MS	Zrn	581 ± 6	561 ± 6	533 ± 6	513 ± 8	This study
CC35a	LA-Q-ICP-MS	Zrn	581 ± 6	560 ± 6		504 ± 7	This study
CC36	LA-Q-ICP-MS	Zrn	585 ± 7	557 ± 8			This study
CC37	LA-Q-ICP-MS	Mnz*		557 ± 7	528 ± 14		Melo et al. (2016)
CC37	LA-Q-ICP-MS	Zrn	576 ± 3	562 ± 5	530 ± 4		Melo et al. (2016)
CC40	LA-Q-ICP-MS	Zrn	588 ± 7	563 ± 8			This study
CC42	LA-Q-ICP-MS	Zrn	586 ± 6	569 ± 6	520 ± 8		This study
CC47	LA-SF-ICP-MS	Zrn	578 ± 9	552 ± 12			This study
LC48	SHRIMP	Zrn	573 ± 5				Silva et al. (2002)
AR548	SHRIMP	Zrn	575 ± 3				Vauchez et al. (2007)
EP66b	LA-ICP-MS	Zrn	576 ± 5				Roncato (2009)
MP21	SHRIMP	Zrn	576 ± 2				Roncato (2009)
21	SHRIMP	Zrn	576 ± 4				Gradim et al. (2014)
66B	LA-MC-ICP-MS	Zrn	568 ± 5	563 ± 13			Gradim et al. (2014)
472	SHRIMP	Zrn		549 ± 28			Gradim et al. (2014)

In this study, the analytical uncertainties on weighted mean ages are based on the quadratic addition of the average mean error (given by Isoplot) and the 1% error inherent precision of the technique and final ages are quoted at the 95% confidence interval. Analytical uncertainties from individual grain are reported as 2σ. * In situ zircon and monazite dating included in peritectic garnet crystals.

Seventy-one analyses on the ca. 597-826 Ma inherited cores yield initial $^{176}Hf/^{177}Hf$ ratios ranging from 0.282070 to 0.282371, with εHf(t) values between -7.4 and -1.4 (Fig. 9a,b). The distribution of model age (T_{DM}) spans from 1340 to 1830 Ma (Fig. 9c). One hundred and forty-three analyses done on magmatic zircons gives initial $^{176}Hf/^{177}Hf$ ratios ranging from 0.282201 to 0.282386 and εHf(t) between -8.2 and -1.8 (Fig. 9a,b). Eighty-six analyses performed on anatectic/metamorphic domains yield initial $^{176}Hf/^{177}Hf$ ratios between 0.282203 and 0.282381 (Fig. 9a). Although the initial $^{176}Hf/^{177}Hf$ ratios of the all domains (inherited, magmatic, anatectic and metamorphic) appear to be similar (Fig. 9a; Table 4), the anatectic zircons (ca. 570-550 Ma and ca. 535-500 Ma) display higher values compared to those magmatic/inherited cores of individual zircon grains (Fig. 9d,e). In contrast, the metamorphic zircon domains (ca. 535-500 Ma) show similar to slightly lower initial $^{176}Hf/^{177}Hf$ ratios those to the relict domains (magmatic or inherited) (Fig. 9f).

Table 4. Summary of initial $^{176}Hf/^{177}Hf$ ratios and $\varepsilon_{Hf(t)}$ for samples from the Carlos Chagas batholith.

Sample	Inherited (ca. 826-600 Ma)	Magmatic (ca. 588-578 Ma)	Anatectic (ca. 570-550 Ma)	Anatectic and/or metamorphic recrystallization (ca. 535-500 Ma)
Initial $^{176}Hf/^{177}Hf$ ratios				
CC12	0.282284-0.282324	0.282201-0.282386	0.282266-0.282344	0.282285
CC18	0.282204-0.282366	0.282253.282346	0.282211-0.282381	0.282203-0.282318
CC30	0.282281-0.282340	0.282305-0.282377	0.282312-0.282374	0.282354
CC34	0.282245-0.282300	0.282248-0.282309	0.282251-0.282292	0.282278-0.282307
CC35a	0.282268-0.282325	0.282263-0.282345	0.282253-0.282357	0.282284-0.282337
CC36	0.282268-0.282302	0.282228-0.282257	0.282283-0.282305	
CC40	0.282070-0.282327	0.282238-0.282352	0.282273-0.282341	
CC42	0.282250-0.282371	0.282243-0.282345	0.282266-0.282381	0.282294-0.282333
$\varepsilon Hf_{(t)}$				
CC12	- 3.4 to - 4.0	- 1.8 to - 8.2	- 3.7 to - 6.5	- 6.2
CC18	- 2.0 to - 6.7	- 2.9 to - 6.4	- 3.3 to - 7.7	- 5.5 to - 9.4
CC30	- 2.7 to - 4.8	- 2.2 to - 4.6	- 3.0 to - 4.6	- 4.3
CC34	- 3.0 to - 6.2	- 4.5 to - 6.5	- 5.3 to - 6.7	- 5.3 to - 6.6
CC35a	- 1.9 to - 5.2	- 3.2 to - 5.8	- 3.2 to - 6.6	- 5.2 to - 6.7
CC36	- 3.7 to - 5.2	- 6.0 to - 6.9	- 5.2 to - 5.8	
CC40	- 1.4 to - 7.4	- 2.8 to - 6.9	- 3.6 to - 5.9	
CC42	- 1.8 to - 5.3	- 3.0 to - 6.5	- 2.2 to - 6.3	- 3.6 to - 4.9

6. RARE EARTH ELEMENTS IN ZIRCON

Rare earth element (REEs) compositions were determined by LA-ICP-MS on distinct growth domains within individual zircon grains previously dated for U-Pb. REE results from two samples (CC18 and CC30) are presented in Table 5. As can be seen in Fig. 10a-b, trace element data of inherited zircon cores display similar chondrite-normalized (McDonough & Sun, 1995) REE patterns comparable to those of magmatic zircon domains from same sample, with enrichment in heavy (HREE) and depletion in light (LREE). Both domains are characterized by flat HREE patterns (Gd_N/Lu_N = 0.02-0.15) and show broadly similar negative Eu anomalies (Eu/Eu* = 0.03-0.09) (Fig. 10a,b). On the other hand, the chondrite normalized values for most REE show a clear difference between magmatic cores and anatectic/metamorphic rims (Fig. 10c,d,e), except for ca. 510 Ma zircon rims (CC30; Fig.10f) which display similar HREE contents. The measured REE values within anatectic zircon rims (ca. 570-550 Ma) indicate less enrichment in HREE (Gd_N/Lu_N = 0.05-0.20) compared to the magmatic cores and negative Eu anomaly (Eu/Eu* = 0.02-010) (Fig. 10c,d). The ca. 535-500 Ma zircon rims show difference in HREE content between studied samples (Gd_N/Lu_N = 0.05-0.50 for CC18 and 0.15-0.17 for CC30) and moderately negative Eu anomaly (Eu/Eu* = 0.02-0.26) (Fig. 10e,f).

7. Ti-IN-ZIRCON THERMOMETER

Ti-in-zircon thermometry has been commonly applied in petrology as a powerful geochemical tracer to constrain magmatic and metamorphic zircon crystallization temperatures in igneous (e.g., Fu et al., 2008; Moecher et al., 2014) and high-grade metamorphic rocks (e.g., Ewing et al., 2013; Liu et al., 2015). The Ti-

in-zircon calibration performed by Watson et al. (2006) show that the incorporation of Ti into zircon is chiefly controlled by activity of TiO_2 (a_{TiO2}) and temperature. Ferry & Watson (2007) revised this calibration and demonstrated that the solubility of Ti in zircon depend not only on temperature and activity of TiO_2 (a_{TiO2}), but also on the activity of SiO_2 (a_{SiO2}).

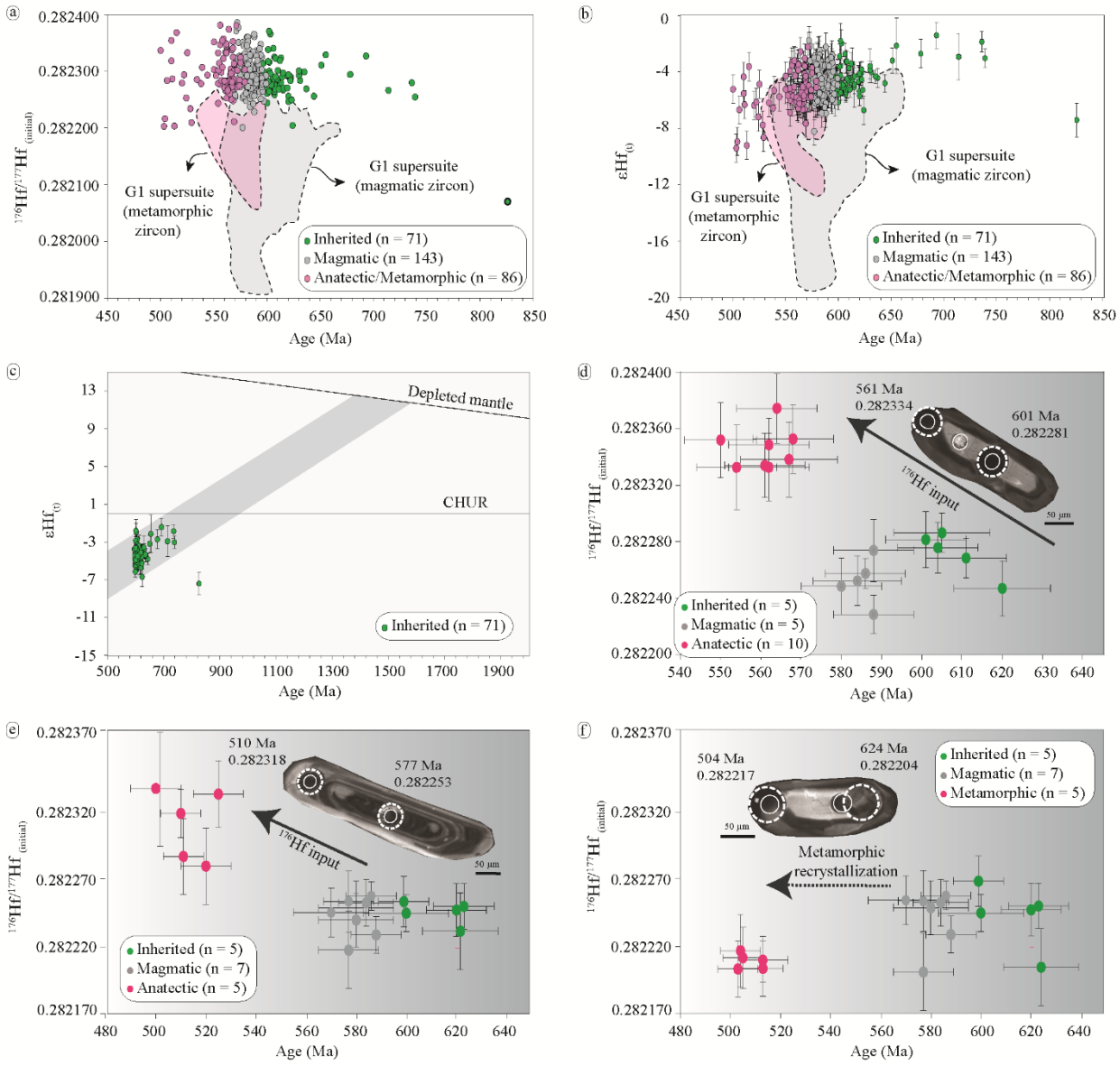

Figure 9. Hf isotopic composition for the Carlos Chagas batholith. (a) Initial $^{176}Hf/^{177}Hf$ ratios of distinct zircon domains from the studied samples plotted against their age. (b) εHf(t)-age plots for zircon this study. Data from the Rio Doce magmatic arc (G1 supersuite) compiled from Gonçalves et al. (2015),Tedeschi et al. (2016) and Narduzzi et al. (in prep.). (c) Isotopic evolution (shaded area) of the inherited zircon population with time (Ma). (d and e) The initial $^{176}Hf/^{177}Hf$ values of the anatectic zircons (ca. 570-550 Ma and ca. 535-500 Ma) are higher than those of the magmatic/inherited cores, indicating ^{176}Hf input in the system. (f) Metamorphic zircons show similar to slightly lower initial $^{176}Hf/^{177}Hf$ values compared to those magmatic and inherited domains.

Table 5. Trace element analyses of zircon (in ppm) from the Carlos Chagas batholith.

Spot nº	Nature	La^{139}	Ce^{140}	Pr^{141}	Nd^{142}	Sm^{152}	Eu^{153}	Gd^{158}	Tb^{159}	Dy^{164}	Ho^{165}	Er^{166}	Tm^{169}	Yb^{174}	Lu^{175}
CC18-028	Inh	0.5	1.3	0.3	1.8	5.8	0.3	43.8	21.5	351.4	133.4	762.6	146.5	1011.3	246.6
CC18-040	Inh	0.3	3.4	0.6	7.0	18.1	0.6	79.7	25.8	351.4	110.0	505.2	89.1	773.6	102.8
CC18-042	Inh	0.2	1.5	0.4	3.4	10.3	0.4	53.6	19.8	274.7	98.3	444.8	97.0	825.9	113.0
CC18-045	Inh	0.6	4.4	0.8	8.9	21.9	1.5	102.9	32.8	493.3	157.8	700.5	152.5	1137.8	201.9
CC18-046	Inh	<0.219	0.9	0.2	2.0	9.4	0.3	53.4	21.6	307.7	108.8	470.4	106.7	923.2	126.5
CC18-048	Inh	<0.225	0.9	0.2	1.9	8.6	0.3	50.8	21.7	305.7	110.1	561.0	113.0	948.7	134.6
CC18-007	Mag	0.2	1.6	0.2	2.0	7.0	0.3	39.2	15.6	220.3	73.3	337.6	74.0	743.4	88.3
CC18-008	Mag	1.2	6.6	1.9	11.8	16.9	0.4	67.9	29.7	312.5	95.8	388.3	80.5	1003.4	120.5
CC18-012	Mag	3.3	0.7	0.1	1.0	4.6	0.2	30.8	14.2	221.8	76.0	384.2	89.3	892.7	123.2
CC18-013	Mag	0.2	1.3	0.2	2.8	8.9	0.3	47.3	18.3	247.4	81.3	400.8	78.4	794.1	93.4
CC18-017	Mag	0.2	0.8	0.1	1.2	5.5	0.2	35.3	15.5	231.0	77.6	372.5	77.8	804.4	99.1
CC18-026	Mag	0.4	2.1	0.5	3.7	7.7	0.3	42.4	17.5	251.3	83.5	386.7	79.9	776.3	96.3
CC18-029	Mag	2.0	4.6	1.4	6.5	8.1	0.8	49.7	24.5	387.9	133.7	643.4	105.6	934.0	145.3
CC18-030	Mag	0.2	0.6	0.1	1.0	4.8	0.2	31.5	14.4	219.2	76.3	361.0	82.0	791.5	105.8
CC18-043	Mag	<0.202	1.0	0.2	2.1	9.3	0.3	52.2	19.6	255.6	80.4	361.9	69.9	709.6	79.5
CC18-049	Mag	<0.230	0.7	0.2	1.7	7.4	0.2	44.8	19.0	283.1	99.8	513.7	102.9	920.0	123.6
CC18-009	Ana	0.3	3.7	0.4	5.5	17.3	0.3	54.1	14.3	139.4	33.6	110.7	21.2	274.4	21.8
CC18-010	Ana	0.2	5.1	0.8	11.4	33.5	0.4	94.8	22.9	207.4	47.8	146.2	26.6	323.1	23.6
CC18-011	Ana	1.1	5.2	1.0	5.6	7.3	0.2	46.4	25.3	430.9	118.6	455.9	64.7	604.9	41.1
CC18-014	Ana	4.1	10.5	1.9	11.7	9.8	1.9	39.7	17.1	217.3	64.9	288.2	62.4	647.1	73.6
CC18-016	Ana	0.4	3.7	0.5	7.2	20.8	0.3	61.0	15.8	143.4	34.2	106.7	19.5	252.2	18.1
CC18-024	Ana	0.2	1.7	0.2	2.1	7.2	0.3	42.6	17.0	236.9	81.1	388.2	82.6	807.4	105.4
CC18-025	Ana	0.2	2.7	0.3	3.9	9.6	0.3	28.1	6.9	60.9	13.1	38.6	6.8	124.3	6.3
CC18-027	Ana	3.8	5.9	1.0	5.9	6.1	0.3	30.6	13.0	198.0	66.5	294.3	69.0	679.8	81.6
CC18-032	Ana	1.3	16.5	2.3	18.2	18.5	1.4	67.4	23.0	342.5	101.8	432.6	80.9	758.0	80.2
CC18-041	Ana	0.4	3.4	0.4	5.7	17.8	0.4	54.2	14.2	128.4	30.8	95.4	18.1	233.3	16.7
CC30-007	Inh	<0.41	18.8	1.2	20.3	36.5	2.4	140.2	38.6	442.8	125.3	504.1	100.0	1193.3	108.7
CC30-025	Inh	0.3	4.3	0.3	4.8	11.6	0.3	55.0	17.2	209.1	62.8	284.2	60.6	657.9	71.5
CC30-039	Inh	0.2	1.7	0.1	1.4	3.8	0.2	22.2	8.7	122.0	39.2	182.6	43.7	543.8	62.2
CC30-041	Inh	<0.131	2.5	0.2	3.1	9.5	0.2	47.2	15.6	197.5	58.6	270.0	59.4	626.0	71.7
CC30-042	Inh	0.4	3.1	0.3	4.4	11.5	0.3	58.1	19.3	243.8	73.8	354.9	74.2	755.4	90.9
CC30-044	Inh	0.2	4.6	0.5	20.3	15.1	0.7	58.4	17.5	218.8	65.9	323.2	68.0	689.2	83.9
CC30-045	Inh	<0.137	2.3	0.3	4.0	12.3	0.3	60.9	19.9	241.4	71.7	394.8	66.4	666.5	78.4
CC30-046	Inh	1.0	5.0	0.8	6.5	8.9	0.3	38.0	15.5	216.8	65.3	312.9	67.8	690.6	81.8
CC30-073	Inh	<0.186	1.5	<0.095	0.9	2.7	<0.128	18.6	7.9	122.6	40.2	193.2	45.8	601.6	55.4
CC30-074	Inh	<0.183	1.2	<0.093	0.8	2.6	<0.126	17.1	7.7	122.6	40.2	197.9	47.1	590.0	59.5
CC30-008	Mag	1.7	13.7	1.2	13.6	18.4	1.0	72.4	21.0	249.4	71.3	305.2	66.3	730.1	74.6
CC30-009	Mag	0.1	10.8	0.7	11.3	20.7	0.8	81.1	22.7	288.8	89.8	339.0	75.7	683.5	79.5
CC30-011	Mag	<0.102	3.5	0.1	3.0	7.8	0.2	43.2	14.8	195.3	60.9	313.2	63.8	694.0	76.2
CC30-012	Mag	<0.102	2.7	0.2	3.2	7.7	0.4	36.5	12.1	154.3	48.6	222.3	54.8	619.2	75.1
CC30-013	Mag	<0.100	2.3	0.1	2.2	5.3	0.2	27.4	9.5	134.4	42.7	200.1	49.0	601.9	66.9
CC30-014	Mag	<0.109	7.7	0.4	8.0	16.4	0.6	75.2	23.0	282.2	82.4	424.4	80.4	776.3	91.3
CC30-024	Mag	0.3	4.3	0.3	4.4	10.8	0.3	52.9	18.3	227.6	69.8	340.3	76.0	686.0	78.3
CC30-026	Mag	<0.114	1.8	0.1	2.1	6.4	0.2	37.4	13.5	184.0	59.4	283.5	60.8	628.2	70.1
CC30-027	Mag	0.24	7.6	0.5	7.9	17.2	0.8	79.2	24.0	300.2	87.3	472.8	80.4	747.5	88.3
CC30-028	Mag	<0.116	6.1	0.4	6.5	14.8	0.7	71.7	22.3	278.6	83.8	461.9	78.5	739.7	88.0
CC30-029	Mag	<0.128	6.3	0.4	6.6	16.5	0.7	74.2	22.4	261.9	78.1	367.6	71.7	696.1	77.1
CC30-030	Mag	1.61	21.8	1.3	17.7	23.1	1.2	85.7	23.9	271.3	77.8	397.6	67.6	653.1	71.8
CC30-031	Mag	0.36	19.9	0.7	15.4	23.7	1.3	93.0	25.3	333.3	93.4	419.4	78.0	714.0	80.5
CC30-032	Mag	0.34	17.9	0.7	13.9	21.6	1.2	82.9	23.5	279.7	81.5	405.1	70.9	683.5	75.6
CC30-055	Mag	0.49	7.6	0.4	5.6	9.7	0.4	46.2	14.6	183.6	55.8	248.2	54.6	586.8	62.9
CC30-056	Mag	<0.148	2.9	0.1	3.0	8.3	0.3	41.8	14.6	187.2	55.9	285.6	55.7	607.0	63.0
CC30-057	Mag	0.27	6.9	0.8	10.5	21.9	1.2	92.3	27.2	382.9	115.6	383.3	99.1	797.2	105.6
CC30-059	Mag	<0.171	5.2	0.4	5.7	12.1	0.7	55.5	17.8	223.1	67.2	327.9	66.0	662.3	77.0
CC30-060	Mag	<0.172	5.8	0.7	9.3	21.1	0.6	84.0	24.8	299.8	88.0	408.7	85.5	786.1	98.6
CC30-061	Mag	<0.175	3.3	0.2	3.4	9.8	0.3	51.8	17.0	215.2	66.1	309.4	67.0	682.5	81.0
CC30-062	Mag	3.76	17.8	2.2	17.8	19.3	0.7	75.6	22.8	273.9	82.9	435.4	79.9	780.5	91.3
CC30-063	Mag	<0.176	3.0	0.1	2.0	5.5	0.2	30.9	11.5	159.8	50.7	241.3	57.2	629.3	70.6
CC30-064	Mag	<0.168	2.1	<0.086	1.9	6.1	0.2	38.5	14.3	197.6	61.7	330.0	68.8	727.7	86.9
CC30-072	Mag	<0.192	2.7	<0.098	1.9	5.9	0.2	34.0	12.2	173.2	53.2	244.4	57.6	600.4	67.5
CC30-010	Ana	5.0	27.3	2.5	25.5	28.3	1.6	92.8	24.6	272.4	78.0	323.2	68.6	827.2	77.9
CC30-016	Ana	<0.109	8.8	0.3	6.4	12.1	0.4	56.4	18.3	228.3	69.2	339.3	69.9	696.2	79.0
CC30-043	Ana	<0.139	3.5	0.1	2.8	7.0	0.2	37.4	12.9	170.9	53.1	229.2	52.5	590.1	61.0
CC30-047	Ana	0.6	3.2	0.3	2.7	3.5	0.2	22.1	8.8	125.2	39.1	173.9	34.1	441.2	53.5
CC30-048	Ana	<0.144	2.1	0.1	1.8	5.0	0.1	29.1	11.1	147.0	44.7	200.8	46.4	505.3	53.6
CC30-071	Ana	<0.191	3.0	0.2	4.0	13.1	0.5	68.4	23.8	348.8	113.0	444.6	99.8	834.0	105.0
CC30-076	Met	0.2	7.3	0.8	11.6	27.9	2.2	117.2	32.0	407.2	110.9	484.3	90.0	813.3	99.6
CC30-077	Met	<0.196	6.8	0.7	10.9	25.0	2.1	106.1	29.1	347.3	98.2	394.1	75.6	684.4	79.2

Notes: Ana = anatectic, Inh = inherited, Mag = magmatic and Met = metamorphic.

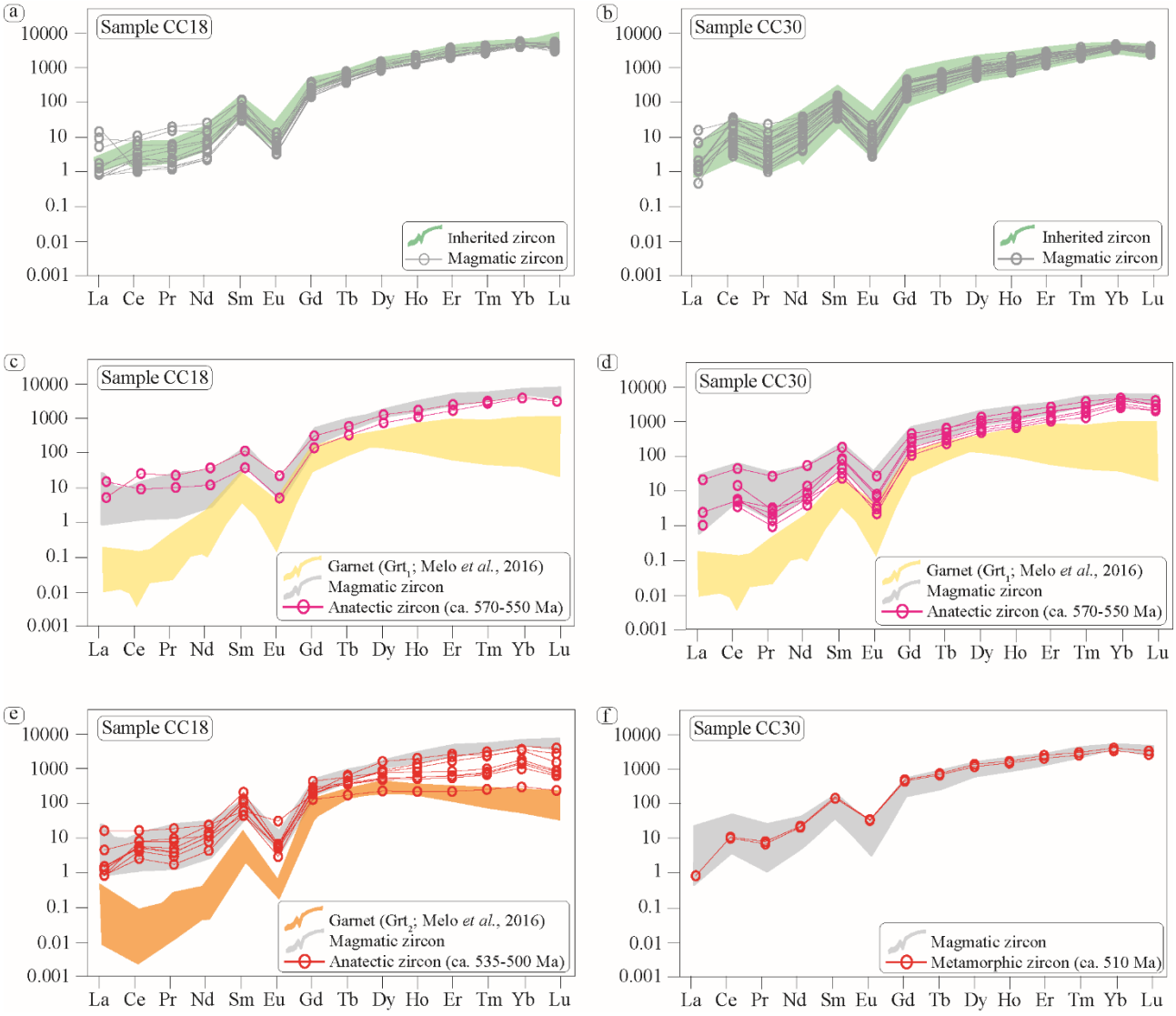

Figure 10. Chondrite-normalized (McDonough & Sun, 1995) REE patterns for different domains within zircon from the Carlos Chagas batholith. (a,b) Magmatic zircon cores chondrite-normalized values are similar those inherited cores (dark gray area). (c,d) REE patterns for anatectic zircon that grew during the first metamorphism event (ca. 550-570 Ma) in the Araçuaí orogen. (e,f) REE patterns for anatectic and/or metamorphic zircons related to a second metamorphism event in orogen. Note that the green area in (c), (d), (e) and (f) refers to magmatic cores, whilst the light gray area in (c), (d) and (e) represents the REE patterns of garnet crystals (Grt_1 and Grt_2) compiled from Melo et al. (2016).

In this study, the Ti-in-zircon temperatures were calculated using the revised calibration of Ferry & Watson (2007). Therefore, for an accurate estimation of zircon crystallization temperature, it is necessary to determine the a_{SiO2} and a_{TiO2} at the time of zircon crystallization (Ferry & Watson, 2007; Fu et al., 2008; Hayden & Watson, 2007). In the CCB, zircon crystals commonly occur as inclusions in biotite and quartz, as well as between plagioclase and quartz crystals in the matrix (Fig. 11a-c). As can seen in backscattered electron (BSE) imaging (Fig. 11d), zircon crystals contain inclusions of quartz. Rutile is more likely to be found as inclusions in quartz and occasionally in quartz boundaries (Fig. 11e-f). This petrographic evidence indicates TiO_2 saturation in the magma at the time of zircon crystallization and may indicate that quartz and zircon

crystallization overlapped. For calculations of Ti-in-zircon temperature, the a_{SiO2} and a_{TiO2} were assumed to be 1.0 due to coexistence of zircon, quartz and rutile in the studied samples. This is in agreement with experimental studies (650-1450 ºC and 1-1.4 GPa) that demonstrate the a_{TiO2} in silicate melts at typical magmatic temperatures are generally between 0.6 and 1 (Watson et al., 2006; Hayden & Watson, 2007). The choice of a_{TiO2} and a_{SiO2} has influence on the temperature estimates. For example, the temperature calculations would be overestimates if we assumed $a_{TiO2} < 1$ and underestimates if $a_{SiO2} < 1$.

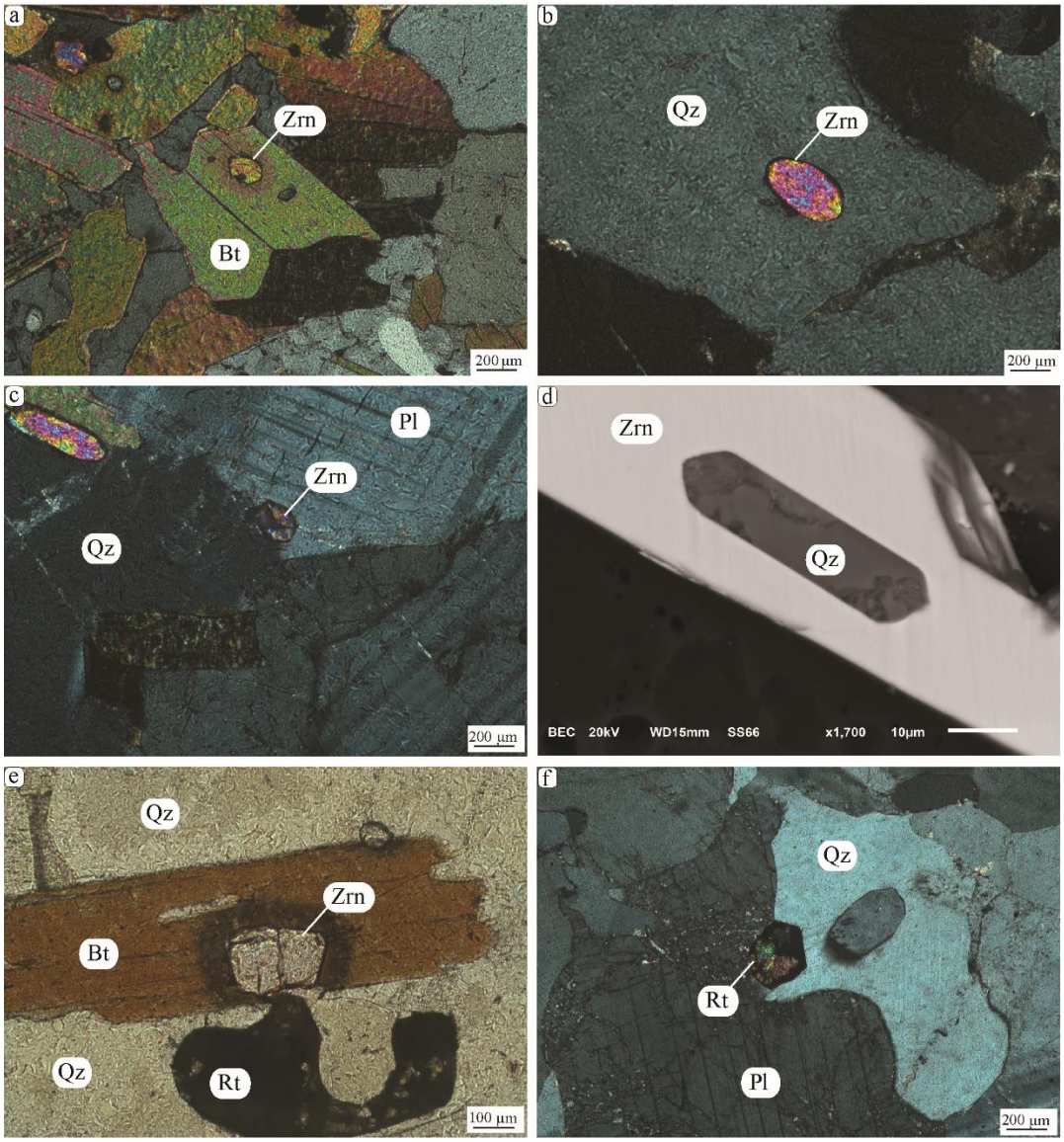

Figure 11. Photomicrographs showing microstructural position of zircon and rutile in the studied samples. Zircon grains are more likely to be found as inclusions in biotite (a,e) and quartz (b) and rarely between plagioclase and quartz in the matrix (c). BSE imaging show quartz inclusions in zircon crystals (d). Rutile occurs as inclusion in quartz (e) and occasionally in quartz boundaries (f).

The Ti contents in zircon and calculated temperatures are listed in Table 6 and are illustrated in Fig. 12. The Ti contents of inherited zircon cores analyzed range from 9 to 61 ppm in sample CC18 and from 7 to 73 ppm in sample CC30. The calculated temperatures for these domains vary from 732 to 949 ºC (average =

844 ± 77 ºC; n = 6; for sample CC18) and from 709 to 997 ºC (average = 863 ± 88 ºC; n = 9; for sample CC30). A single inherited grain (CC30-46; Table 6) have high Ti concentration (143 ppm) corresponding to temperature of 1077 ºC. The measured Ti concentrations in the magmatic core domains are similar in both samples (9-41 ppm for CC18 and 9-48 for CC30) and correspond to temperatures that range from 735 to 898 ºC (average = 790 ± 56 ºC; n = 10) and from 730 to 918 ºC (average = 800 ± 49 ºC; n = 24), respectively. Zircon crystallized as a result of the first anatectic event in the CCB (ca. 570-550 Ma) has relatively high Ti contents of 10-71 ppm, equivalent to the temperatures of 749-970 ºC (average = 824 ± 67 ºC; n = 8). On the other hand, Ti concentrations in most of the youngest anatectic and/or metamorphic zircons (ca. 535-500 Ma) range from 11 to 29 ppm and indicate temperatures of 755-905 ºC (average = 817 ± 45º C; n = 8), except for two metamorphic domains which yield lower temperatures of 681-713ºC (average = 697 ± 16º C; n = 2).

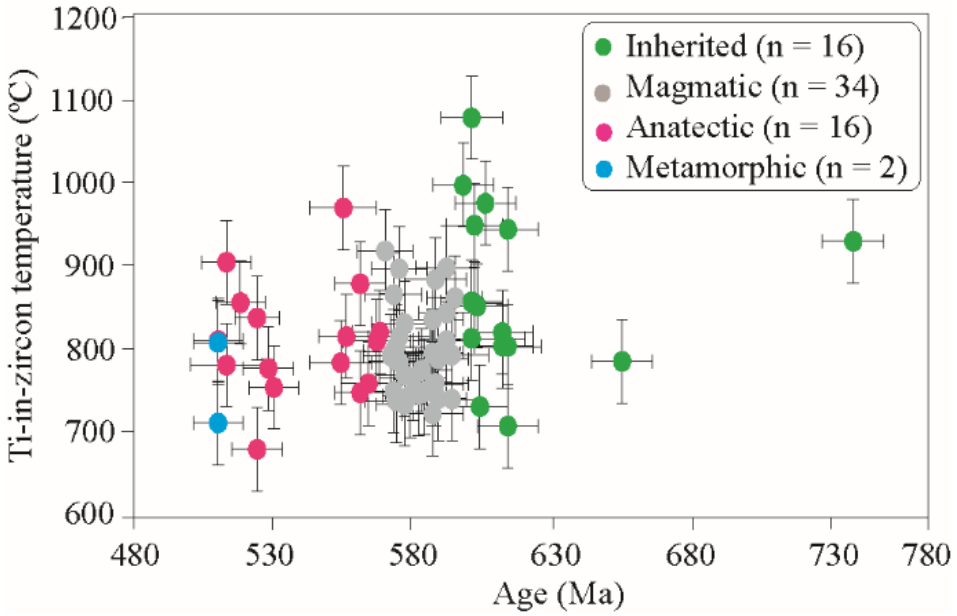

Figure 12. Temperature-time for crystallization of zircon in the Carlos Chagas batholith. Zircon U-Pb ages (Ma) and temperatures (ºC) are listed in Table 6. Temperatures were calculated using the revised calibration of Ferry & Watson (2007), which predicts an uncertainty of ±50 ºC (error bars).

8. DISCUSSION

Although previous studies showed a relatively uniform geochemistry and identical (within error) U-Pb crystallization /magmatic ages for the CCB (Roncato, 2009; Pedrosa-Soares et al., 2011; Gradim et al., 2014), detailed investigation of zircon textures combined with isotope and trace element data suggest a long-lived evolution marked by magmatic crystallization and subsequent anatectic events. This discrimination between inherited, magmatic and anatectic/metamorphic zircon domains was done via detailed cathodoluminescence imaging from hundreds of zircons from several samples of the CCB. Figure 4 shows for example how weakly luminescent areas of anatectic and/or metamorphic zircon are clearly distinguished from

magmatic or inherited cores. The U-Pb geochronological data from the distinct growth zones (see Supplementary Data (Tables S1 and S2) and summary in Table 3) indicate a 10 million year period of magmatic zircon growth between 588 and 578 Ma, followed by at least two distinct periods of new anatectic zircon growth and/or solid-state recrystallization (ca. 570-550 Ma and ca. 535-500 Ma). In addition, the magmatic and anatectic domains are chemically different, showing distinct zircon REE patterns (Fig. 10) and therefore originated from different petrogenetic processes (Fig.13).

Despite variations in trace element data, Ti-in-zircon thermometry from all zircon domains indicate that the events recorded in the CCB samples occurred under similar temperatures (Fig. 12; see also Melo et al., 2016). In fact, the results from the thermometry indicate that the CCB record a remarkably evolution during which temperature of the two metamorphic events exceeded 800 ºC. Such a long-lived and hot evolution has had a major influence on the way zircon crystallized. The petrogenetic processes that occurred during the different episodes of zircon growth can be explained with due consideration of the Hf isotopic compositions and the U-Pb ages. The zircon domains of distinct origin can be grouped according to their initial $^{176}Hf/^{177}Hf$ ratios and U-Pb ages. For instance, the Lu-Hf analyses of the ca. 588-578 Ma magmatic cores (or zircon domains) show similar initial $^{176}Hf/^{177}Hf$ ratios and εHf(t) to those of the ca. 826-600 Ma inherited domains (Fig. 9a,b), but differ quite demonstrably from anatectic rims (Fig. 9d,e; Table S3 – Supplementary data). Our interpretation is that the magmatic zircons (or growth zones) originated by dissolution and re-precipitation of inherited zircons from source rocks, due to the similar Hf isotope composition (Fig. 9). In addition, chondrite-normalized REE patterns of inherited and magmatic zircons from the CCB show similar features, including a rather steeply-rising slope due to significant HREE enrichment relative to LREE and MREE, negative Eu and positive Ce anomalies (Fig. 10a-b). These chemical features are typical of unaltered magmatic zircons (e.g., Belousova et al., 2002; Hoskin & Schaltegger, 2003). The inherited zircon crystals contain high concentration of REE (∑REE = 1032-3018 ppm; Table 5), which is a characteristic feature of granitoid zircons (Belousova et al., 2002), whereas negative Eu anomalies in both inherited and magmatic zircons can indicate feldspar crystallization prior to or during zircon growth. Thus, the Cl-images, REE patterns and Hf isotope compositions of oscillatory to irregular zoned grains attest a magmatic origin and its chemical signature can be interpreted as an inheritance from the source. In fact, the magmatic zircons record a wide range of negative εHf(t) values (from -8.2 to -1.8), indicating that they crystallized from heterogeneous crustal anatectic melts, as observed in some S-type granites (Villaros et al., 2012; Farina et al., 2014).

The Ti thermometry from ca. 738-598 Ma inherited zircons of two samples indicates average zircon crystallization temperatures of 844 ºC and 863 ºC (Fig. 12), except a single grain (CC30-46) that have higher temperature (1077 ºC) which may probably represent small inclusions of Ti-rich mineral phases. The Ti-in-zircon temperatures from inherited grains in combination with chemical signature corroborate the interpretation that the zircons grew within hot granitic magmas.

Table 6. Ti-in-zircon temperatures and U-Pb zircon ages for the Carlos Chagas batholith.

Spot no.	Domain	Nature	Ti (ppm)	1σ (ppm)	T (ºC)	$^{206}Pb/^{238}U$ age (Ma)
CC18-028	core	Inherited	61	7	949	602 ± 10
CC18-040	core	Inherited	28	4	852	603 ± 11
CC18-042	core	Inherited	20	3	814	601 ± 11
CC18-045	core	Inherited	53	8	930	738 ± 19
CC18-046	core	Inherited	15	3	786	655 ± 11
CC18-048	core	Inherited	9	2	732	604 ± 10
CC18-007	core	Magmatic	10	1	749	584 ± 10
CC18-008	core	Magmatic	26	3	844	592 ± 10
CC18-012	core	Magmatic	10	1	745	579 ± 10
CC18-013	core	Magmatic	41	1	898	592 ± 11
CC18-017	core	Magmatic	10	1	741	594 ± 10
CC18-026	core	Magmatic	10	1	742	589 ± 10
CC18-029	core	Magmatic	30	4	862	595 ± 10
CC18-030	core	Magmatic	9	1	735	577 ± 10
CC18-043	core	Magmatic	17	3	796	587 ± 10
CC18-049	core	Magmatic	16	3	789	589 ± 11
CC18-009		Anatectic - new growth	29	3	857	518 ± 9
CC18-010		Anatectic - new growth	14	1	782	513 ± 13
CC18-011		Anatectic - new growth	5	1	681	524 ± 9
CC18-014	rim	Anatectic - overgrowth	11	4	755	530 ± 9
CC18-016	rim	Anatectic - overgrowth	25	2	838	524 ± 8
CC18-024	rim	Anatectic - overgrowth	19	2	811	510 ± 9
CC18-025		Anatectic - new growth	14	2	778	528 ± 9
CC18-027	rim	Anatectic - overgrowth	20	2	816	556 ± 10
CC18-032		Anatectic - new growth	15	2	784	554 ± 11
CC18-041		Anatectic - new growth	43	6	905	513 ± 9
CC30-007	core	Inherited	73	3	975	606 ± 11
CC30-025	core	Inherited	29	1	857	601 ± 11
CC30-039	core	Inherited	29	1	855	602 ± 10
CC30-041	core	Inherited	18	1	805	612 ± 11
CC30-042	core	Inherited	21	1	821	612 ± 11
CC30-044	core	Inherited	18	1	804	614 ± 12
CC30-045	core	Inherited	85	3	997	598 ± 11
CC30-046	core	Inherited	143	5	1077	601 ± 11
CC30-073	core	Inherited	58	2	944	614 ± 11
CC30-074	core	Inherited	7	1	709	614 ± 11
CC30-008	core	Magmatic	9	1	739	574 ± 11
CC30-009	core	Magmatic	31	1	866	573 ± 10
CC30-011	core	Magmatic	16	1	793	572 ± 10
CC30-012	core	Magmatic	15	1	787	574 ± 10
CC30-013	core	Magmatic	18	1	804	574 ± 10
CC30-014	core	Magmatic	8	1	724	587 ± 11
CC30-024	core	Magmatic	19	1	811	592 ± 12
CC30-026	core	Magmatic	23	1	831	577 ± 12
CC30-027	core	Magmatic	20	1	815	575 ± 11
CC30-028	core	Magmatic	15	1	786	575 ± 11
CC30-029	core	Magmatic	48	2	918	570 ± 10
CC30-030	core	Magmatic	24	1	836	587 ± 11
CC30-031	core	Magmatic	17	1	796	587 ± 11
CC30-032	core	Magmatic	12	1	759	587 ± 11
CC30-055	core	Magmatic	12	1	760	588 ± 12
CC30-056	core	Magmatic	14	1	776	583 ± 11
CC30-057	core	Magmatic	11	1	750	573 ± 10
CC30-059	core	Magmatic	16	1	793	594 ± 13
CC30-060	core	Magmatic	36	1	884	588 ± 11
CC30-061	core	Magmatic	17	1	798	573 ± 11
CC30-062	core	Magmatic	10	1	747	582 ± 10
CC30-063	core	Magmatic	12	1	766	580 ± 12
CC30-064	core	Magmatic	13	1	770	577 ± 10
CC30-072	core	Magmatic	41	2	897	575 ± 10
CC30-010	rim	Anatectic - overgrowth	71	2	970	555 ± 12
CC30-016	rim	Anatectic - overgrowth	21	1	821	568 ± 10
CC30-043	rim	Anatectic - overgrowth	19	1	810	567 ± 12
CC30-047	rim	Anatectic - overgrowth	35	1	879	561 ± 9
CC30-048	rim	Anatectic - overgrowth	10	1	749	561 ± 9
CC30-071		Anatectic - overgrowth	12	1	759	564 ± 10
CC30-076	core	Metamorphic - new growth	19	1	809	510 ± 9
CC30-077	rim	Metamorphic - new growth	7	1	713	510 ± 9

Temperature were calculated using the Ferry & Watson (2007) calibration.

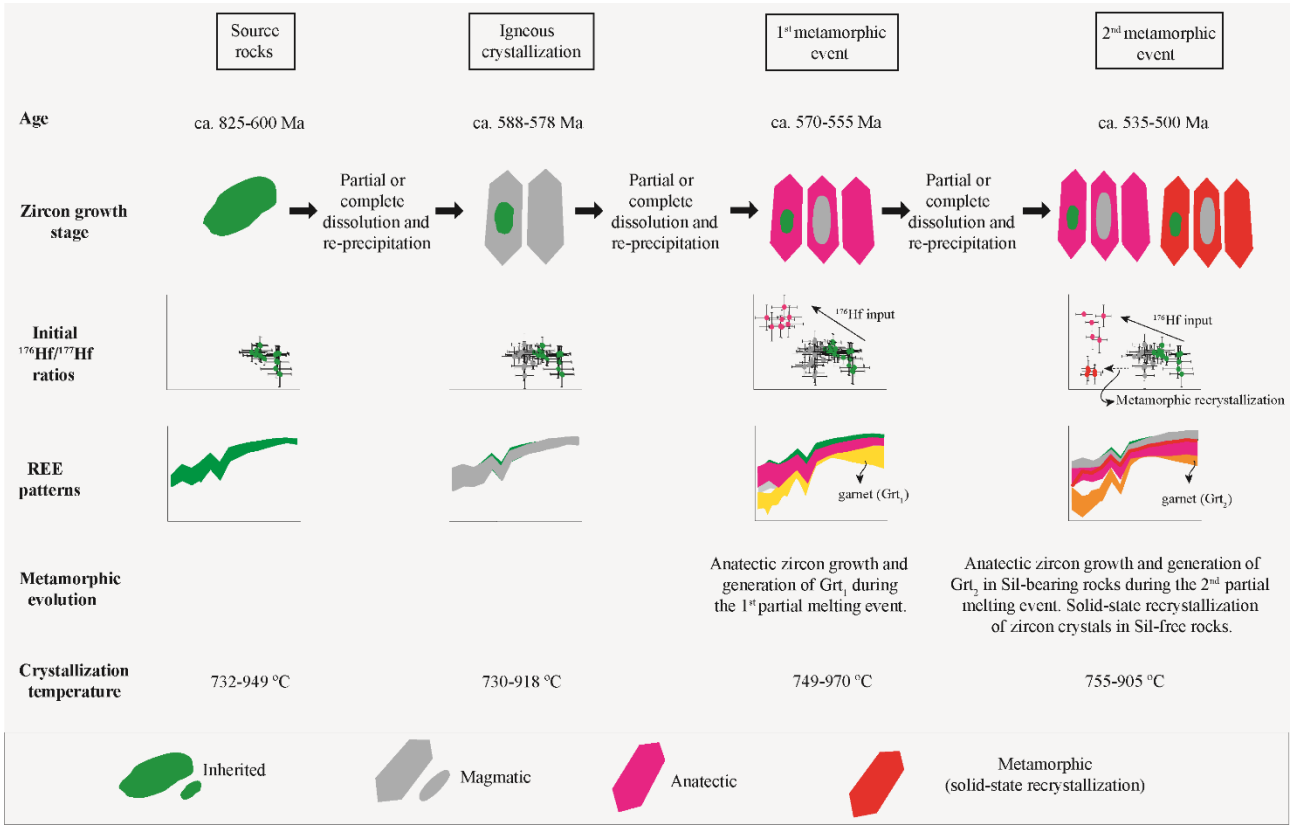

Figure 13. Schematic diagram illustrating the processes of zircon growth from the CCB during the tectono-metamorphic evolution of the Araçuaí orogen.

Magmatic zircons in the CCB (ca. 588-578 Ma) crystallized between 730 ºC and 898 ºC, as indicated by Ti-in-zircon thermometry. These crystallization temperatures indicate that the magmatic zircons crystallized above the granite solidus and therefore the temperature range may reflect the actual temperature range over which zircon crystallized. In granitic magmas produced by crustal melting processes in orogenic systems, high temperatures are required for producing substantial volume of crustal melts under fluid-absent melting conditions (Clemens, 2003).

Anatectic growth and solid-state recrystallization

The initial $^{176}Hf/^{177}Hf$ values of the oldest anatectic zircons (ca. 570-550 Ma) are variable in all samples, but higher than those of the relict cores (magmatic or inherited) of the same analyzed grain (Fig. 4: e.g. CC18-94, CC30-62 and CC40-82). Thus, the anatectic zircon growth is characterized by low $^{176}Lu/^{177}Hf$ values and high $^{176}Hf/^{177}Hf$ ratios (Supplementary data – Table S3), implying ^{176}Hf input in the system at this time (Fig. 9d). Moreover, anatectic zircon hava ε_{Hf} ~ -3 to -9, whereas magmatic zircon have ε_{Hf} ~ -2 to -8, demonstrating a total variation of 7 ε_{Hf} units.

These high $^{176}Hf/^{177}Hf$ values can be linked to new zircon growth (or overgrowth domains) during the high-grade metamorphism and partial melting of the CCB. Several studies relate this fact to volume and

composition of the partial melts, as well as release of Zr of the mineral phases such as garnet, hornblende, biotite, rutile and ilmenite (Vavra et al., 1996; Fraser et al., 1997; Liermann et al., 2002). For instance, biotite of the CCB commonly has zircon as inclusions and its breakdown during the anatexis can release zircon in the system, with subsequent dissolution and growth of new zircon.

In open systems, the higher initial $^{176}Hf/^{177}Hf$ values in zircon compared to the relict cores are generally attributed to melt and/or fluid enriched in Hf (Chen et al., 2015). We suggest that the observed high initial $^{176}Hf/^{177}Hf$ ratios can be caused by dissolution of inherited/magmatic zircon grains, followed by new zircon growth in the presence of melt. The occurrence of peritectic garnet crystals produced by fluid-absent partial melting reactions at granulite facies conditions in this time (Melo et al., 2016), further support the interpretation that anatectic zircon and garnet grew contemporaneously during the first partial melting episode in the CCB. Pseudosection modeling performed by Melo et al. (2016) shows that 12-34 vol.% of melt was produced at peak metamorphic conditions. Considering the Hf analyses between relict core and anatectic rim of individual zircon crystals, an increase of $^{176}Hf/^{177}Hf$ ratios by about 0.0001-0.0002 must be added to the anatectic zircon to achieve the ratio shift that is observed these distinct domains in the studied samples (Fig. 14). As illustrated in Fig. 10c-d, zircon chondrite-normalized REE patterns for the oldest anatectic zircons (ca. 570-550 Ma) display similar characteristics to those zircons that grew contemporaneously with garnet in high-grade metamorphic rocks (Rubatto & Hermann, 2007; Fornelli et al., 2014). The steep REE patterns in the anatectic zircon compared to with the slightly flat REE patterns in the garnet reflect a change in the behavior of REE during the high-grade metamorphism (Fig. 10c-d). Such REE features may indicate zircon growth coeval with garnet, in which HREE are preferentially incorporate into zircon rather than garnet at high temperatures due to increase atomic number of the REE. This interpretation is consistent with experimental studies (e.g., Rubatto & Hermann, 2007) which report greatest enrichment of HREE into zircon compared to garnet at 800-850 ºC. Therefore, the new zircon growths probably occurred in an anatectic melt enriched in Hf.

The average temperature of 824 ± 67 ºC estimated by Ti-in-zircon thermometer for the anatectic domains (ca. 570-550 Ma) is in agreement with reported peak temperatures of 790-820ºC (at 9.5-10.5 kbar) calculated by phase equilibria modelling (Melo et al., 2016). As closure temperature of zircon U-Pb (> 900 ºC; Cherniak & Watson, 2000) is above the crystallization temperature obtained in this study for the anatectic zircon, we can infer that the isotopic system remained closed during the high-grade metamorphism and the U-Pb ages (ca. 550-570 Ma) represent the timing this anatectic event. Moreover, experimental studies carried out in synthetic and natural zircon demonstrate that the closure temperatures for the REEs in zircon must be in excess of 1000 ºC for change your geochemical signature (Cherniak et al., 1997). Therefore, our U-Pb and Hf isotope data associated with trace element composition and thermometry in zircon support that the CCB underwent by fluid-absent partial melting at ca. 570-550 Ma, with coeval zircon and garnet growth at granulite conditions (~ 820 ºC) during the same metamorphic cycle.

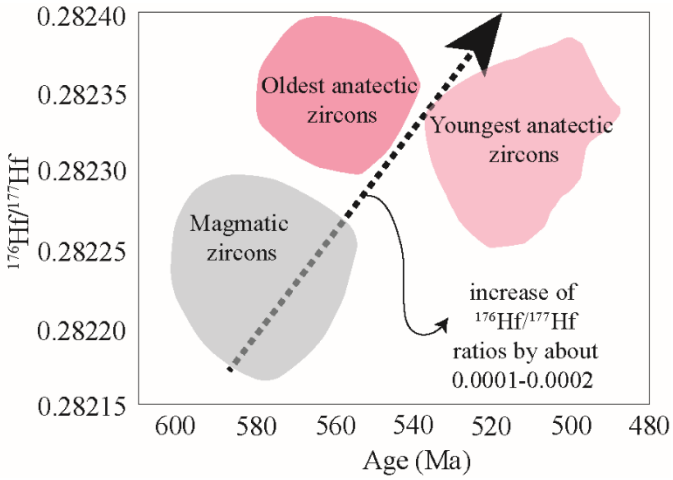

Figure 14. Initial $^{176}Hf/^{177}Hf$ ratios of distinct domains of individual zircon crystals plotted against their age. Note that the increase of Hf isotope composition require an external Hf source that can increase of $^{176}Hf/^{177}Hf$ ratios by about 0.0001-0.0002.

As for the Hf isotopic composition of the youngest anatectic zircon (ca. 535-500 Ma), we observed high initial $^{176}Hf/^{177}Hf$ values relative to the relict cores of the same analyzed grain (Fig. 4: e.g. CC18-94, CC30-62 and CC40-82). The presence of a second generation of peritectic garnet formed by fluid-absent melting reactions (Bt + Qz + Pl + Sil = Grt + Kfs + Melt) in the sillimanite-bearing granites (Fig. 3f) support the interpretation of remelting in the batholith with growth of new zircon at this time. Additionally, Melo et al. (2016) show microstructures that corroborate the presence of melt, such as pseudomorphed thin films of quartz surrounding the garnet crystals in the sillimanite-bearing granites. All these petrographic evidences support that the ca. 535-500 Ma zircons crystallized into anatectic melts. On the other hand, some metamorphic domains yield initial $^{176}Hf/^{177}Hf$ values similar to the relict cores (Fig. 4: e.g. CC18-110), indicating that they might have formed by solid-state recrystallization at high-temperature. In the youngest zircons (ca. 535-500 Ma), the REE patterns are chemically distinct between the analyzed samples (Fig. 10e-f). The anatectic zircon chondrite-normalized REE patterns from sample CC18 are characterized by steep REE patterns, whilst the garnet displays slightly flat REE patterns (Fig. 10e). These chemical features indicate coeval growth of zircon and garnet at this time. This interpretation is coherent with the petrographic evidence, which shows a second generation of garnet in the studied sample (Fig. 3f). In fact, the anatectic zircons have higher initial $^{176}Hf/^{177}Hf$ values than the relict cores (Fig. 4), which is expected for zircon growth in the presence of melt due to fluid-absent partial melting processes. On the other hand, the ca. 510 Ma metamorphic zircon chondrite-normalized REE patterns from sample CC30 are similar those to the magmatic zircon (Fig. 10f). There is no petrographic evidence of a second generation of garnet in the sillimanite-free rocks (e.g., CC12, CC30, CC42 and CC47). Therefore, U-Pb ages, REE patterns and Hf isotope composition of zircon can be used to distinguish anatectic growth from metamorphic recrystallization in zircon (Fig. 13).

Given the analytical uncertainties of the Ti-in-zircon thermometer, the average temperature of 817 ± 45 ºC for these anatectic/metamorphic zircon (ca. 535-500 Ma) is in agreement with peak temperature

documented by phase equilibrium modelling in the CCB (770 ºC and 6.6 kbar; Melo et al., 2016) during the gravitational collapse of the Araçuaí orogen. As studied samples were collected close to intrusions of the G5 supersuite, the high temperatures recorded in the youngest zircons could be related to the contact metamorphism at this time or re-equilibration of Ti in the zircon. However, zircon has very slow diffusivity under geologic conditions (Cherniak & Watson, 2007), indicating that Ti-in-zircon temperatures cannot be a consequence from diffusive resetting. Therefore, the youngest metamorphic zircon must have crystallized at high temperatures as showed by Ti-in-zircon thermometry.

8.1. Regional Implications

The crystallization ages obtained for all samples studied here (Fig 8) are strikingly similar (within error) to the crystallization ages of the youngest G1 granitoids of the magmatic arc of the Araçuaí orogeny. This fact is consistent with the conclusion that the CCB emplacement was contemporaneous with the late G1 magmatism (ca. 574-586 Ma; Gonçalves et al., 2015; Tedeschi et al., 2016) and prior to partial melting episode in the metasediments from the NVC dated by Gradim et al. (2014) and Richter et al. (2016) at ca. 560-575 Ma. Our U-Pb data (Fig. 8j-l; Table 3) indicate that first metamorphic/anatectic event in the CCB take place between 552 ± 12 and 569 ± 6 Ma (Figs. 5, 6 and 7), with a weighted mean age of 563 ± 6 Ma (MSWD = 1.4) (Fig. 8j). This age interval coincide with the peak metamorphism recorded in zircon and monazite from the NVC (ca. 560-575 Ma, Fig. 8l; Gradim et al., 2014; Richter et al., 2016), implying that both units were metamorphosed at essentially the same time. The phase equilibrium modelling performed by Richter et al. (2016) indicates that the NVC was metamorphosed at temperatures of 750-850 ºC and pressures of 5.3-7.5 kbar in depths around of ~ 25 km. On the other hand, the CCB record higher pressure conditions (9.5-10.5 km; Melo et al., 2016), implying that the batholith was at a deeper crustal level (26-29 km) at the time of peak metamorphism. Shear zones developed along the major lithological contacts must have accommodated the differential motion of blocks (Pinto et al., 2001; Castañeda et al., 2006; Queiroga et al., 2012).

As illustrated in Figs. 5 to 8, most of the inherited zircons record a dominant peak of ages that varies from 600 Ma to 615 Ma (Table 2), with a weighted mean of 605 ± 6 Ma (MSWD = 1.5) (Fig. 8j), and four subordinate peaks at ca. 826 Ma, ca. 740-690 Ma, ca. 680-635 Ma and ca. 630-620 Ma (Figs. 5 to 8; Table 2). This spectrum of ages (Fig. 8j) matches well the age distribution of detrital zircon and monazite grains from the surrounding Nova Venécia complex (Fig. 8l), suggesting that both CCB and NVC are somehow linked to the same source rocks. Indeed, the youngest inherited zircons (ca. 630-620 Ma and 615-600 Ma) are consistent (within analytical uncertainties) with the dated rocks from the Rio Doce (ca. 630-580 Ma – G1 supersuite; Silva et al., 2002; Novo et al., 2010; Pedrosa-Soares et al., 2011; Mondou et al., 2012; Gonçalves et al., 2014, 2015; Tedeschi et al., 2016; Fig. 8k) and/or Rio Negro (ca. 635-600 Ma; Tupinambá et al., 2000, 2012; Heilbron & Machado, 2003) arcs.

Although the most of the inherited zircons in the CCB present similar U-Pb ages to the G1 supersuite (Fig. 8j-k), its Hf isotope composition (Supplementary data – Table S3) is significantly distinct (Gonçalves et al., 2015; Tedeschi et al., 2016; Narduzzi et al., in prep.). As can be seen in Fig. 9a-b, the Hf isotope composition of zircon extracted from the granitoids of the Rio Doce magmatic arc displays wide isotopic variability among the samples compared to inherited zircons in the CCB which exhibit a relatively small Hf isotopic variation amongst studied samples (Supplementary data – Table S3). Based on similarities Hf isotope composition of inherited zircons between samples within CCB, we can suggest that source rock was in a restrict region during the pre-collisional stage of the orogeny. The weighted mean age of 602 ± 7 Ma (CC18; Table 2) for inherited zircon grains provide an upper age limit for the burial of the protholiths from the CCB. The protholiths involved during crustal melting for CCB production could be the metasediments similar to the NVC initially buried at a deeper crustal level and that were not exhumed during the development of the orogen. Hf isotope data of the country rocks is still lacking. Therefore, a more extensive study of the granites and their country rocks is requires to fully resolve the origin of the CCB, as well as the composition of the sources involved.

The origin of the oldest inherited population zircon cores (ca. 826 Ma) is uncertain and has been recorded in detrital zircon from NVC (ca. 807-822 Ma, Richter et al., 2016). The inherited zircons belonging to the interval ca. 740-690 Ma may correlate to reported ages of ca. 714-732 Ma (U-Pb titanite) and ca. 696-724 (Pb-Pb zircon) from the Southern Bahia Alkaline Province (Rosa et al., 2007), which is related to the rift episode along the southern part of the São Francisco craton. The age interval (ca. 680-635 Ma) coincides (within analytical uncertainties) with existing U-Pb age of 660 ± 29 Ma (LA-ICP-MS) for magmatic zircons extracted from plagiogranite veins associated with ophiolitic remnants (Queiroga et al., 2007).

ACKNOWLEDGEMENTS

This work was carried out as part of the Brazil-South Africa scientific collaboration and was supported by CNPq (402852/2012-5, 401334/2012-0 and 302058/2015-0), FAPEMIG (APQ-03943, RPQ 0067-10 and RDP 00063-10) and by NRF funding to Gary Stevens via the SARChI programme. This work is part of the doctoral research of the first author.

REFERENCES

Alkmim, F.F., Marshak, S., Pedrosa-Soares, A.C., Peres, G.G., Cruz, S.C.P., Whittingyon, A., 2006. Kinematic evolution of the Araçuaí-West Congo orogen in Brazil and Africa: Nutcraker tectonics during the Neoproterozoic assembly of Gondwana. Precambrian Reserarch 149, 43-64.

Baltazar, O.F., Zuchetti, M., Oliveira, S.A.M., Scandolara J., Silva, L.C., 2010. Folhas São Gabriel da Palha e Linhares. Nota explicativa. Programa Geologia do Brasil, CPRM-BH. 144 p.

Belousova, E.A., Griffin, E.W.L., O'Reilly, S.Y., Fischer, N.I., 2002. Igneous zircon: trace element composition as an indicator of source rock type. Contribution to Mineralogy and Petrology 143, 602-622.

Castañeda, C., Pedrosa-Soares, A.C., Belém, J., Dias, P.H.A., Gradim, D.T., Medeiros, S.R., Oliveira, F.F., 2006. Folha Ecoporanga, SE.24-Y-A-III, escala 1:100.000: nota explicativa. Espírito Santo, UFMG/CPRM. 80 p.

Chen, Y-X., Gao, P., Zheng, Y-F., 2015. The anatectic effect on the zircon Hf isotope composition of migmatites and associated granites. Lithos 238, 174-184.

Cherniak, D.J. & Watson, E.B., 2000. Pb diffusion in zircon. Chemical Geology 172, 5-24.

Cherniak, D.J., Hanchar, J.M., Watson, E.B., 1997. Rare-earth diffusion in zircon. Chemical Geology 134, 289-301.

Clark, C., Collins, A.S., Santosh, M., Taylor, R., Wade, B.P., 2009. The *P-T-t* architecture of a Gondwanan suture: REE, U–Pb and Ti-in-zircon thermometric constraints from the Palghat Cauvery shear system, South India. Precambrian Research 174, 129-144.

Clemens, J.D., 2003. S-type granitic magmas—petrogenetic issues, models and evidence. Earth-Science Reviews 61, 1-18.

Dalziel, I.W.D., 1997. Neoproterozoic-Proterozoic geography and tectonics: review, hypothesis, environmental speculation. The Geological Society of American Bulletin 109, 16-42.

De Campos, C.P., Mendes, J.C., Ludka, I.P., Medeiros, S.R., Moura, J. C., Wallfass, C., 2004. A review of the Brasiliano magmatism in southern Espírito Santo, Brazil, with emphasis on post-collisional magmatism. Journal of the Virtual Explorer 17.

De Campos, C.P., Medeiros, S.R., Mendes, J.C., Pedrosa-Soares, A.C., Dussin, I., Ludka, I.P., Dantas, E.L., 2016. Cambro-Ordovician Magmatism in the Araçuaí Belt (SE Brazil): snapshots from a post-collisional event. Journal of South American Earth Sciences 68, 248-268.

Ewing, T., Hermann, J., Rubatto, D., 2013. The robustness of the Zr-in-rutile and Ti-in-zircon thermometers during high-temperature metamorphism (Ivrea–Verbano Zone, Northern Italy). Contribution to Mineralogy and Petrology 165,757–779.

Farina, F., Stevens, G., Gerdes, A., Frei, D., 2014. Small-scale Hf isotopic variability in the Peninsula pluton (South Africa): the processes that control inheritance of source $^{176}Hf/^{177}Hf$ diversity in S-type granites. Contributions to Mineralogy and Petrology 168, 1065.

Ferry, J.M. & Watson, E.B., 2007. New thermodynamic models and revised calibrations for the Ti-in-zircon and Zr-in-rutile thermometers. Contributions to Mineralogy and Petrology 154, 429-437.

Flowerdew, M., Millar, I., Vaughan, A., Horstwood, M., Fanning, C., 2006. The source of granitic gneisses and migmatites in the Antarctic Peninsula: a combined U–Pb SHRIMP and laser ablation Hf isotope study of complex zircons. Contributions to Mineralogy and Petrology 151, 751-768.

Fornelli, A., Langone, A., Micheletti, F., Pascazio, A., Picarreta, G., 2014. The role of trace element partitioning between garnet, zircon and orthopyroxene on the interpretation of zircon U–Pb ages: an example from high-grade basement in Calabria (Southern Italy). International Journal of Earth Sciences 103, 487-507.

Fraser, G., Ellis, D., Eggins, S., 1997. Zirconium abundance in granulite facies minerals, with implications for zircon geochronology in high-grade rocks. Geology 25, 607-610.

Fu, B., Page, F.Z., Cavosie, A.J., Fournelle, J., Kita, N.T., Lackey, J.S., Wilde, S.A., Valley, J.W., 2008. Ti-in-zircon thermometry: applications and limitations. Contributions to Mineralogy and Petrology 156, 197-215.

Ge, R., Zhu, W., Wu, H., He, J., Zheng, B., 2013a. Zircon U-Pb ages and Lu-Hf isotopes of Paleoproterozoic metasedimentary rocks in the Korla Complex, NW China: Implications for metamorphic zircon formation and geological evolution of the Tarim Craton. Precambrian Research 231, 1-18.

Ge, R., Zhu, W., Wu, H., Zheng, B., He, J., 2013b. Timing and mechanisms of multiple episodes of migmatization in the Korla Complex, northern Tarim Craton, NW China: Constraints from zircon U-Pb-Lu-Hf isotopes and implications for crustal growth. Precambrian Research 231, 136-156.

Geisler, T., Schaltegger, Urs., Tomaschek, F., 2007. Re-equilibration of zircon in aqueous fluids and melts. Elements 3, 43-50.

Gonçalves, L., Farina, F., Lana, C., Pedrosa-Soares, A.C., Alkmim, F., Nalini, Jr.H.A., 2014. New U-Pb ages and lithochemical attributes of the Ediacaran Rio Doce magmatic arc, Araçuaí confined orogen, southeastern Brazil. Journal of South American Earth Sciences 52, 129-148.

Gonçalves, L., Alkmim, F.F., Pedrosa-Soares, A.C., Dussin, I.A., Valeriano, C.M., Lana, C., Tedeschi, M., 2015. Granites of the intracontinental termination of a magmatic arc: An example from the Ediacaran Araçuaí Orogen, Southeastern Brazil. Gondwana Research 36, 439-458 .

Gradim, C.T., Queiroga, G.N., Roncato, J.G., Novo, T.A., Pedrosa-Soares, A.C., 2007. Mapa Geológico da Folha Mantena 1: 100.000. Belo Horizonte, Programa Geologia do Brasil, CPRM-UFMG.

Gradim, C., Roncato, J., Pedrosa-Soares, A.C., Cordani, U., Dussin, I., Alkmim, F.F., Queiroga, G., Jacobssohn, T., Silva, L.C., Babinski, M., 2014. The hot back-arc zone of the Araçuaí orogen, Eastern Brazil: from sedimentation to granite generation. Brazilian Journal of Geology 44, 155-180.

Hayden, L.A. & Watson, E.B., 2007. Rutile saturation in hydrous siliceous melts and its bearing on Ti-thermometry of quartz and zircon. Earth and Planetary Science Letters 258, 561-568.

Harley, S.L., Kelly, N.M., 2007. Zircon tiny but timely. Elements 3, 13-18.

Heilbron, M. & Machado, N., 2003. Timing of terrane accretion in the Neoproterozoic-Eopaleozoic Ribeira Orogen (SE Brazil). Precambrian Research 125, 87–112.

Hoskin, P.W. & Black, L.P., 2000. Metamorphic zircon formation by solid-state recrystallization of protolith igneous zircon. Journal of Metamorphic Geology 18, 423-439.

Hoskin, P.W.O., Schaltegger, U., 2003. The composition of zircon and igneous and metamorphic petrogenesis. Reviews in Mineralogy and Geochemistry. 53, 27-62.

Liermann, H-P., Isachsen, C., Altenberger, U., Oberhänsli, R., 2002. Behavior of zircon during high-pressure, low-temperature metamorphism: Case study from the Internal Unit of the Sesia Zone (Western Italian Alps). European Journal of Mineralogy 14, 61-71.

Liu, Y-C., Deng, L-P., Gu, X-F., Groppo, C., Rolfo, F., 2015. Application of Ti-in-zircon and Zr-in-rutile thermometers to constrain high-temperature metamorphism in eclogites from the Dabie orogen, central China. Gondwana Research 27, 410-423.

Ludwig, K.R., 2003. Mathematical-statistical treatment of data and errors for Th/U geochronology. Reviews in Mineralogy and Geochemistry 52, 631-656.

McDonough, W.F. & Sun, S.S., 1995. The composition of the Earth. Chemical Geology 120, 223-253.

Melo, M.G., Stevens, G., Lana, C., Pedrosa-Soares, A.C., Frei, D., Alkmim, F.F., Alkmin, L.A., 2016. Two cryptic anatectic events within a syn-collisional granitoid from the Araçuaí orogen (southeastern Brazil): evidence from the polymetamorphic Carlos Chagas batholith. Lithos (in press). http://dx.doi.org/10.1016/j.lithos.2016.10.012

Moecher, D.P., McDowell, S.M., Samson, S.D., Miller C.F., 2014. Ti-in-zircon thermometry and crystallization modeling support hot Grenville granite hypothesis. Geology 42, 267-270.

Mondou, M., Egydio-Silva, M., Vauchez, A., Raposo, M.I.B., Bruguier, O., Oliveira, A.F., 2012. Complex, 3D strain patterns in a synkinematic tonalite batholith from the Araçuaí Neoproterozoic orogen (Eastern Brazil): evidence from combined magnetic and isotopic chronology studies. Journal of Structural Geology 39, 158-179.

Nalini, H.A., Machado, R., Bilal, E., 2005. Geoquímica e petrogênese da Suíte Galiléia: Exemplo de magmatismo tipo-I metaluminoso pré-colisional Neoproterozóico da região do Médio Vale do Rio Doce (MG). Revista Brasileira de Geociências 35, 23-34.

Narduzzi, F., Farina, F., Lana, C., Stevens, G., Nalini-Jr., H.A., Geochemical, U-Pb geochronological and Hf isotopic evolution of a large Cordilleran-type batholith: clues from the Galiléia granitoids (Brazil). (in prep.)

Noce, C.M., Macambira, M.J.B., Pedrosa-Soares, A.C., 2000. Chronology of Neoproterozoic-Cambrian granitic magmatism in the Araçuaí Belt, eastern Brazil, based on single zircon evaporation dating. Revista Brasileira de Geociências 30, 25-29.

Noce, C.M., Pedrosa-Soares, A.C., Piuzana, D., Armstrong, R., Laux, J.H., De Campos, C.M., Medeiros, S.R., 2004. Ages of sedimentation of the kinzigitic complex and of a late orogenic thermal episode in the Araçuaí orogen, northern Espírito Santo state, Brazil: Zircon and monazite U-Pb SHRIMP and IDTIMS data. Revista Brasileira de Geociências 34, 587-592.

Novo, T.A., Pedrosa-Soares, A.C., Noce, C.M., Alkmim, F.F., Dussin, I.A., 2010. Rochas charnockíticas do sudeste de Minas Gerais: a raiz granulítica do arco magmático do Orógeno Araçuaí. Revista Brasileira de Geociências 40, 573-592.

Pedrosa-Soares, A.C.; Queiroga, G.N.; Gradim, C.T.; Roncato, J.G.; Novo, T.A.; Jacobsohn, T.; Silva, K.L. 2007. Geologia da Folha Mantena (SE-24-Y-A-VI). Programa Geologia do Brasil, CPRM, 82p. (http://geobank.cprm.gov.br)

Pedrosa-Soares, A.C., De Campos, C.P., Noce, C., Silva, L.C., Novo, T., Roncato, J., Medeiros, S., Castañeda, C., Queiroga, G., Dantas, E., Dussin, I., Alkmim, F., 2011. Late Neoproterozoic–Cambrian granitic magmatism in the Araçuaí orogen (Brazil), the Eastern Brazilian Pegmatite Province and related mineral resources. Geological Society of London, Special Publications 350, 25–51.

Peixoto, E., Pedrosa-Soares, A.C., Alkmim, F.F., Dussin, I.A., 2015. A suture–related accretionary wedge formed in the Neoproterozoic Araçuaí orogen (SE Brazil) during Western Gondwanaland assembly. Gondwana Research 27, 878-896.

Petitgirard, S., Vauches, A., Egydio-Silva, M., Bruguier, O., Camps, P., Monié, P., Babinski, M., Mondou, M., 2009. Conflicting structural and geochronological data from the Ibituruna quartz-syenite (SE Brazil): Effect of protracted “hot” orogeny and slow cooling rate? Tectonophysics 477, 174-196.

Pinto, C.P., Drumond, J.B.V., Féboli, W.L., 2001. Projeto Leste. Belo Horizonte: CPRM/CODEMIG, CD-ROM.

Queiroga, C.N., Pedrosa-Soares, A.C., Noce, C.M., Alkmim, F.F., Pimentel, M.M., Dantas, E., Martins, M., Castañeda, C., Suita, M.T.F., Prichard, H., 2007. Age of the Ribeirão da Folha ophiolite, Araçuaí orogen: The U-Pb zircon (LA-ICPMS) Dating of a plagiogranite. Geonomos 15, 61-65.

Queiroga, G.N., Pedrosa-Soares, A.C., Roncato, J.G., Dias, P.H.A., Guimarães, H.A., Coutinho, M.O.G., Freitas, N.C., Gradim, C.T., Braga, F.C.S., Novo, T.A., 2012. Geologia e recursos mineras da Folha Nova Venécia SE-24-Y-B-IV Escala 1:100.000, Estado do Espírito Santo. Programa Geologia do Brasil, CPRM-UFMG.

Richter, F., Lana, C., Stevens, G., Buick, I., Pedrosa-Soares, A.C., Alkmim, F.F., Cutts, K., 2016. Sedimentation, metamorphism and granite generation in a back-arc region: Records from the Ediacaran Nova Venécia Complex (Araçuaí Orogen, Southeastern Brazil). Precambrian Research 272, 78–100.

Roncato, J.G., 2009. As suítes graníticas tipo-s do norte do Espírito Santo na região das folhas Ecoporanga, Mantena, Montanha e Nova Venécia. Instituto de Geociências, Universidade Federal de Minas Gerais, Minas Gerais, MSc Dissertation 102p.

Roncato, J.G., Pedrosa-Soares, A.C, Mascarenhas, T.F., Fornero, S.A., Galinari, L.M., Gonçalves, L.T., Queiroga, G.N., Braga, F.C.S., Novo, T.A., 2012. Geologia e recursos mineras da Folha Montanha SE-24-Y-B-I Escala 1:100.000, Estado do Espírito Santo. Programa Geologia do Brasil, CPRM-UFMG.

Rosa, M.L.S., Conceição, H., Macambira, M.J.B., Galarza, M.A., Cunha, M.P., Menezes, R.C.L., Marinho, M.M., Filho, B.E.C., Rios, D.C., 2007. Neoproterozoic anorogenic magmatism in the Southern Bahia Alkaline Province of NE Brazil: U-Pb and Pb-Pb ages of the blue sodalite syenites. Lithos 97, 88-97.

Rubatto, D., 2002. Zircon trace element geochemistry: partitioning with garnet and the link between U–Pb ages and metamorphism. Chemical Geology 184, 123-138.

Rubatto, D. & Hermann, J., 2007. Experimental zircon/melt and zircon/garnet trace element partitioning and implications for the geochronology of crustal rocks. Chemical Geology 241, 38-61.

Rubatto, D., Hermann, J., Buick, I., 2006. Temperature and bulk composition control on the growth of monazite and zircon during low-pressure anatexis (Mount Stafford, Central Australia). Journal of Petrology 47, 1973-1996.

Schaltegger, U., Fanning, C.M., Günther, D., Maurin, J.C., Schulmann, K., Gebauer, D., 1999. Growth, annealing and recrystallization of zircon and preservation of monazite in high-grade metamorphism: conventional and in-situ U-Pb isotope, cathodoluminescence and microchemical evidence. Contributions to Mineralogy and Petrology 134, 186-201.

Silva, L.C., Armstrong, R., Noce, C.M., Carneiro, M.A., Pimentel, M., Pedrosa-Soares, A.C., Leite, C.A., Vieira, V.S., Silva, M.A., Paes, V.J.C., Filho, J.M.C., 2002. Reavaliação da evolução geológica em terrenos pré-cambrianos brasileiros com base em novos dados U-Pb SHRIMP, Parte II: Orógeno Araçuaí, Cinturão Mineiro e Cráton São Francisco Meridional. Revista Brasileira de Geociências 32, 513-528.

Silva, L.C., Pedrosa-Soares, A.C., Armstrong, R., Noce, C.M., 2011. Determinando a duração do período colisional do Orógeno Araçuaí com base em geocronologia U–Pb de alta resolução em zircão: uma contribuição para a história da amalgamação do Gondwana Ocidental. Geonomos 19, 180-197.

Sláma, J., Košler, J., Pedersen, R., 2007. Behaviour of zircon in high-grade metamorphic rocks: evidence from Hf isotopes, trace elements and textural studies. Contributions to Mineralogy and Petrology 154, 335-356.

Tang, M., Wang, X-L., Shu, X-J., Wang, D., Yang, T., Gopon, P., 2014. Hafnium isotopic heterogeneity in zircons from granitic rocks: geochemical evaluation and modeling of "zircon effect" in crustal anatexis. Earth and Planetary Science Letters 389, 188-199.

Taylor, R.J.M., Clark, C., Fitzsimons, I.C.W., Santosh, M., Hand, M., Evans, N., McDonald, B., 2014. Post-peak, fluid-mediated modification of granulite facies zircon and monazite in the Trivandrum Block, southern India. Contributions to Mineralogy and Petrology 168, 1044.

Taylor, R.J.M., Harley, S.L., Hinton, R.W., Elphick, S., Clark, C., Kelly, N.M., 2015. Experimental determination of REE partition coefficients between zircon, garnet and melt: a key to understanding high-*T* crustal processes. Journal of Metamorphic Geology 33, 231-248.

Tedeschi, M., Novo, T., Pedrosa-Soares, A.C., Dussin, I., Tassinari, C., Silva, L.C., Gonçalves, L., Alkmim, F., Lana, C., Figueiredo, C., Dantas, E., Medeiros, S., De Campos, C., Corrales, F., Heilbron, M., 2016. The Ediacaran Rio Doce magmatic arc revisited (Araçuaí-Ribeira orogenic system, SE Brazil). Journal of South American Earth Sciences 68, 167-186.

Tupinambá, M., Teixeira, W., Heilbron, M., 2000. Neoproterozoic Western Gondwana assembly and subduction related plutonism: The role of the Rio Negro Complex in the Ribeira belt. Revista Brasileira de Geociências 300, 7-11.

Tupinambá, M., Heilbron, M., Valeriano, C., Júnior, R.P., Dios, F.B., Machado, N., Silva, L.G.E., Almeida, J.C.H., 2012. Juvenile contribution of the Neoproterozoic Rio Negro Magmatic Arc (Ribeira Belt, Brazil): Implications for Western Gondwana amalgamation. Gondwana Research 21, 422-438.

Vauchez, A., Egydio Silva, M., Babinski, M., Tommasi, A., Uhlein, A., Liu, D., 2007. Deformation of a pervasely molten middle crust: insights from the Neoproterozoic Ribeira-Araçuaí orogen (SE Brazil). Terra Nova 19, 278-286.

Vavra, G., Gebauer, D., Schmid, R., 1996. Multiple zircon growth and recrystallization during polyphase Late Carboniferous to Triassic metamorphic in granulites of the Ivrea Zone (Southern Alps): an ion microprobe (SHRIMP) study. Contributions to Mineralogy and Petrology 122, 337-358.

Vavra, G., Schmid, R., Gebauer, D., 1999. Internal morphology, habit and U-Th-Pb microanalysis of amphibolite-to-granulite facies zircons: geochronology of the Ivrea Zone (Southern Alps). Contributions to Mineralogy and Petrology 134, 380-404.

Vieira, V.S., 2007. Significado do Grupo Rio Doce no contexto do Orógeno Araçuaí. Instituto de Geociências, Universidade Federal de Minas Gerais, Belo Horizonte, Thesis, 117p.

Villaros, A., Buick, I.S, Stevens, G., 2012. Isotopic variations in S-type granites: an inheritance from a heterogeneous source? Contributions to Mineralogy and Petrology 163, 243-257.

Watson, E.B., Wark, D.A., Thomas, J.B., 2006. Crystallization thermometers for zircon and rutile. Contributions to Mineralogy and Petrology 151, 413-433.

Whitehouse, M.J. & Platt. J.P., 2003. Dating high-grade metamorphism - constraints from rare-earth elements in zircon and garnet. Contributions to Mineralogy and Petrology 145, 61-74.

Whitney, D.L., & Evans, B.W., 2010. Abbreviations for names of rock-forming minerals. American Mineralogist 95, 185-187.

Williams, I.S., Buick, I.S., Cartwright, I., 1996. An extended episode of early Mesoproterozoic metamorphic fluid flow in the Reynolds Range, central Australia. Journal of Metamorphic Geology 14, 29-47.

Wu, Y.B., Zheng, Y.F., Zhang, S.B., Zhao, Z.F., Wu, F.Y., Liu, X.M., 2007. Zircon U-Pb ages and Hf isotope compositions of Migmatite from the North Dabie Terrane in China: constraints on partial melting. Journal of Metamorphic Geology 25, 991-1009.

Xia, Q-X., Zheng, Y-F., Yuan, H., Wu, F-Y., 2009. Contrasting Lu-Hf and U-Th-Pb isotope systematics between metamorphic growth andrecrystallization of zircon from eclogite-facies metagranites in the Dabie orogen, China. Lithos 112, 477-496.

Zheng, Y.-F., 2009. Fluid regime in continental subduction zones: petrological insights from ultrahigh-pressure metamorphic rocks. Journal of the Geological Society 166, 763-782.

CHAPTER 5

MELT INCLUSIONS IN PERITECTIC GARNET FROM THE CARLOS CHAGAS BATHOLITH

This chapter presents preliminary data about the occurrence of preserved melt inclusions within peritectic garnet crystals from the Carlos Chagas batholith in the Araçuaí orogen (southeastern Brazil). It provides an excellent opportunity for better understanding crustal recycling processes during a long-lived orogeny.

5.1 - INTRODUCTION

Crustal differentiation is an important process for the production and stabilization of the continental crust. Orogenic events drive crustal differentiation by introducing fertile material for the production of granitic magma into the deep crust (Brown, 1994; 2010). Partial melting (> 800 °C) produces granitic magmas by fluid-absent melting reactions involving the breakdown of micas and amphiboles (Clemens, 1992; Stevens & Clemens, 1993). Such reactions produce peritectic phases that provide a textural record of the incongruent melting reaction (e.g., Stevens *et al.*, 2007) and occasionally record the trapping and preservation of primary melt inclusions during their growth (e.g., Cesare *et al.*, 2009; Ferrero *et al.*, 2012; Acosta-Vigil *et al.*, 2016).

The primary melt inclusions can preserve information on the composition of primary anatectic crustal melts. Re-homogenization experiments for melt inclusions hosted in garnet have become a powerful tool for the study of crustal melting (e.g., Ferrero *et al.*, 2012, 2015, 2016; Bartoli *et al.*, 2013a,b). In this study, we report the presence of carbonate melt inclusions into peritectic garnet crystals from the polymetamorphic Carlos Chagas batholith. The investigation of peritectic mineral textures within the batholith provides a unique insight into multiple crustal recycling events during the evolution of the Araçuaí orogen between 580 and 500 Ma.

5.2. PETROGRAPHY

Granites are medium- to very coarse-grained rocks made of abundant to frequent quartz, plagioclase, k-feldspar, garnet, biotite and sillimanite. The accessory phase is dominated by spinel, rutile, ilmenite, zircon, monazite, apatite and sulphides (e.g. pyrite, chalcopyrite and sphalerite). The CCB contains large garnet porphyroblasts (Grt_1; 5-35 mm), which present numerous inclusions (40-380 µm) of rounded Ti-rich biotite, lobate and rounded quartz (Figure 5.1a), as well as the accessory minerals (ilmenite, rutile, apatite, zircon and monazite).

For the first time polyphase inclusions of calcite and rutile have been identified in the peritectic garnet crystals (Grt_1) of the CCB. These inclusions are small (80-180 µm), have a sub-circular shape, low angle terminations and are dark-coloured in transmitted light (Figure 5.1a,b,c,d). Microcracks frequently occur in the garnet crystals, but some polycrystalline inclusions appear to have no association with cracks. Investigation via SEM demonstrated that calcite locally presents euhedral internal faces and rutile occurs commonly as subhedral aggregates or as single crystals surrounded by calcite (Table 5.1; Figure 5.1c-d). Pseudomorphed melt films associated to euhedral rutile crystals occur adjacent to large garnets (Figure 5.1e-f).

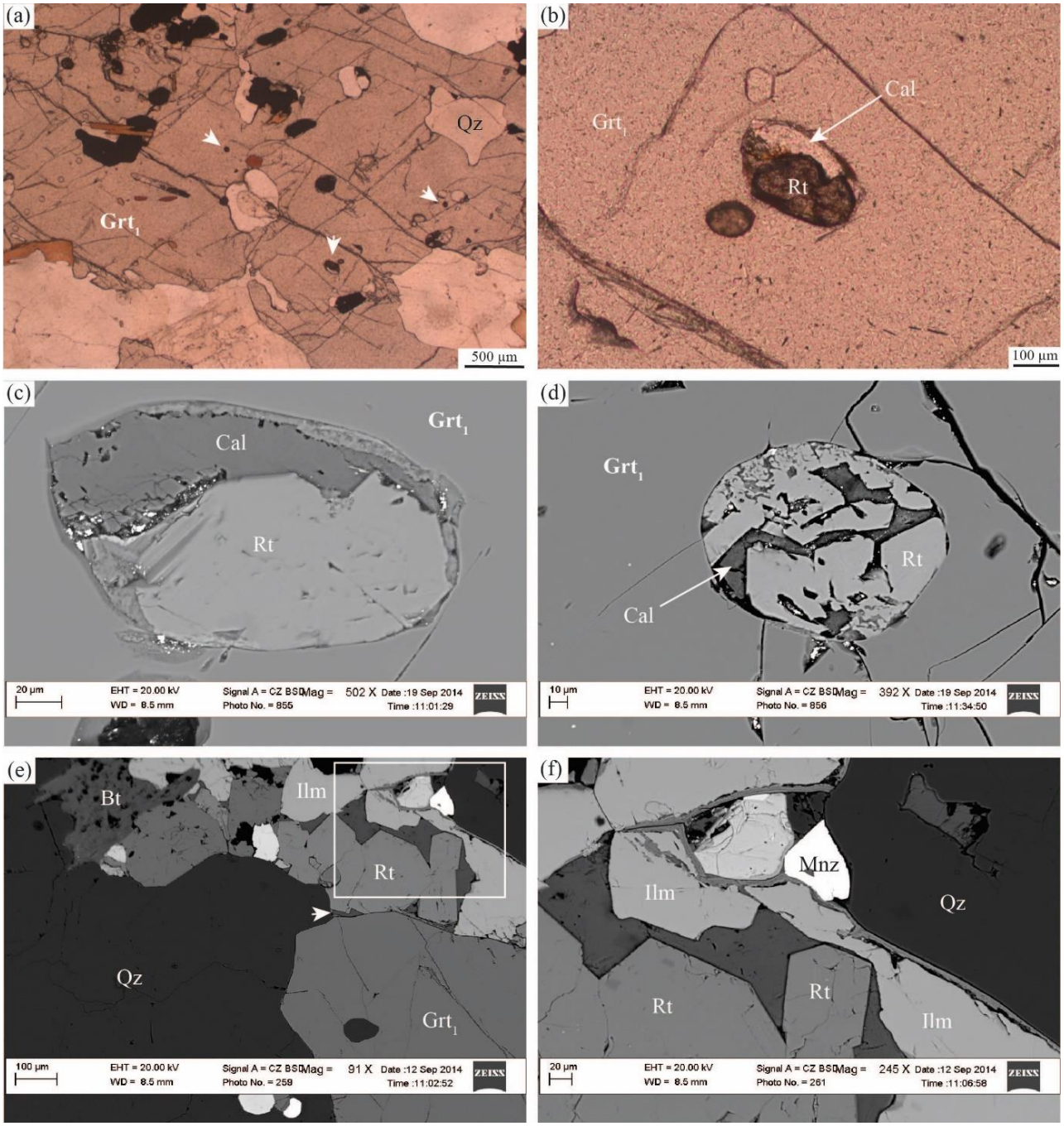

Figure 5.1 – Petrographic photomicrographs from Carlos Chagas batholith. (a) Large garnet showing mineral inclusions of quartz, biotite, ilmenite and melt inclusions (white arrows). (b) Melt inclusion within garnet crystal. (c) and (d) Backscattered electron images of crystallized melt inclusions in garnet of granite. (e) BSE image showing melt film (white arrow) in garnet boundaries and surrounded euhedral rutile crystals. (f) Details from the euhedral rutile crystals.

Table 5.1 - Major element compositions (wt%) and structural formulae of melt inclusions from the sample CC31.

	Calcite	Rutile
Analysis	n = 9	n = 6
SiO_2		0.12 ± 0.29
TiO_2		94.66 ± 2.50
Al_2O_3		0.10 ± 0.26
FeO_t	1.71 ± 0.88	1.10 ± 0.70
MnO	2.66 ± 0.65	0.07 ± 0.17
MgO	0.25 ± 0.18	0.04 ± 0.09
CaO	50.96 ± 1.70	0.06 ± 0.10
Na_2O		
K_2O		
Total	55.59 ± 1.89	96.16 ± 2.29
Si		0.00 ± 0.00
Ti		0.99 ± 0.01
^{IV}Al		0.00 ± 0.00
^{VI}Al		0.00 ± 0.00
Fe^{3+}		
Fe^{2+}	0.05 ± 0.02	0.01 ± 0.01
Mn	0.08 ± 0.02	0.00 ± 0.00
Mg	0.01 ± 0.01	0.00 ± 0.00
Ca	1.82 ± 0.06	0.00 ± 0.00
Na		
K		
Total	1.95 ± 0.06	1.01 ± 0.00

n = number of analyses used to define the average and standard deviations. Analytical method is reported in Appendix A.

5.3. ORIGIN OF THE MELT INCLUSIONS

The garnet crystals are the product of fluid-absent incongruent melting of biotite, which also resulted in a significant volume of granitic melt which has been lost from the system, thereby preserving the peritectic garnet. Petrographic observations show rutile in association with calcite within garnet (Figure 5.1b to d). This microstructural evidence is interpreted to reflect primary Ti-rich carbonatitic melt trapped as inclusions during peritectic garnet growth. In addition, pseudomorphed granitic melt films are represented by quartz and plagioclase developed along the boundaries of both garnet and euhedral rutile crystals in the matrix (Figure 5.1e), attest to the presence of the granitic melt produced by biotite incongruent melting during the growth of garnet and rutile.

The rocks of the CCB record two separate incongruent melting events and the coexistence of immiscible silicate and carbonate melts during the first anatectic event (ca. 570-550 Ma). The carbonate melt is interpreted to reflect anataxis of zones of minor carbonate alteration within the granite, which occurred prior to the first anatexis. Phase equilibrium modelling of the garnet-bearing assemblage via Theriak Domino indicate peak metamorphic conditions of 790-820 °C and 9.5-10.5 kbar, i.e. depth of approximately 30 km (see Chapter 3). These P-T conditions estimated are in agreement with the findings of re-homogenization experiments performed by Ferrero *et al.* (2016) for calcite-bearing inclusions hosted in peritetic garnet of migmatites from Oberpfalz.

REFERENCES

Acosta-Vigil A., Barich A., Bartoli O., Garrido C. J., Cesare B., Remusat L., Raepsaet C. 2016. The composition of nanogranitoids in migmatites overlying the Ronda peridotites (Betic Cordillera, S Spain): the anatectic history of a polymetamorphic basement. Contributions to Mineralogy and Petrology, **171**:24.

Brown M. 1994. The generation, segregation, ascent and emplacement of granite magma: the migmatite-to-crustally-derived granite connection in thickened orogens. *Earth-Science Reviews*, **36:**83-130.

Brown M. 2010. Melting of the continental crust during orogenesis: the thermal, rheological, and compositional consequences of melt transport from lower to upper continental crust. *Canadian Journal of Earth Sciences*, **47:**655-694.

Bartoli O., Cesare B., Poli S., Bodnar R. J., Acosta-Vigil A., Frezzotti M. L., Meli S. 2013a. Recovering the composition of melt and the fluid regime at the onset of crustal anatexis and S-type granite formation. *Geology*, **41**:115-118.

Bartoli O., Cesare B., Poli S., Acosta-Vigil A., Esposito R., Turina A., Bodnar R. J., Angel R. J., Hunter J. 2013b. Nanogranite inclusions in migmatitic garnet: behavior during piston-cylinder remelting experiments. *Geofluids*, **13**:405-420.

Cesare B., Ferrero S., Salvioli-Marian E., Pedron D., Cavallo A. 2009. "Nanogranite" and glassy inclusions: the anatectic melt in migmatites and granulites. *Geology*, **37**(7):627-630.

Clemens J. D. 1992. Partial melting and granulite genesis: a partisan overview. *Precambrian Research*, 55:297-301.

Ferrero S., Bartoli O., Cesare B., Salvioli-Mariani E., Acosta-Vigil A., Cavallo A., Groppo C., Battiston S., 2012. Microstructures of melt inclusions in anatectic metasedimentary rocks. *Journal of Metamorphic Geology*, **30**:303-322.

Ferrero S., Wunder B., Walczak K., O'Brien P. J., Ziemann M. A., 2015. Preserved near ultrahigh-pressure melt from continental crust subducted to mantle depths. *Geology*, **43**:447-450.

Ferrero S., Wunder B., Ziemann M. A., Wälle M., O'Brien P. J. 2016. Carbonatitic and granitic melts produced under conditions of primary immiscibility during anatexis in the lower crust. *Earth and Planetary Science Letters*, **454**:121-131.

Stevens G. & Clemens J. D. 1993. Fluid-absent melting and the roles of fluids in the lithosphere: a slanted summary? *Chemical Geology*, **108:**1-17.

Stevens G., Villaros A., Moyen J-F. 2007. Selective peritectic garnet entrainment as the origin of geochemical diversity in S-type granites. Geology, 35(1):9-12.

CHAPTER 6

CONCLUSIONS

6.1. REPEATED PARTIAL MELTING EVENTS IN THE CARLOS CHAGAS BATHOLITH

The combination of field observations, petrographic investigation, mineral chemistry, metamorphic modelling, monazite and zircon U-Pb ages (LA-ICP-MS), Hf isotope composition and Ti-in-zircon thermometer allowed the following conclusions about the partial melting events recorded in the Carlos Chagas batholith (CCB) during the orogeny:

1) CCB (G2 supersuite) comprises S-type granites formed during the collisional stage of the Araçuaí orogen. Detailed petrographic investigation allowed to characterize three different mineral assemblages within batholith: (1) Qz-Pl-Kfs-Bt-Grt-Ilm-Rt; (2) Qz-Pl-Kfs-Bt-Grt-Ilm-Sil; and (3) Qz-Pl-Kfs-Bt-Grt-Ilm-Sil-Spl. Two generations of garnet (Grt_1 and Grt_2) were identified in mineral assemblages 2 and 3. The well-preserved nature of both generations of garnet indicates substantial melt loss prior to cooling (White & Powell, 2002).

2) According to phase equilibrium modelling on granitic rocks from CCB, the peak metamorphic conditions of first event (M1) were attained at 790-820 ºC and 9.5-10.5 kbar. These P-T conditions have been estimated by rocks of mineral assemblage 1 (Qz-Pl-Kfs-Bt-Grt-Ilm-Rt). Poikiloblastic garnet crystals (Grt_1) were produced by absent-fluid partial melting reactions, which consumed Ti-high biotite, quartz and plagioclase at granulite facies conditions. Thus, the record of first partial melting event in the batholith is characterized by generation of peritectic garnet (Grt_1) and microstructures indicative of the former presence of melt (e.g., films and pools of plagioclase and/or quartz in the matrix and surrounding Grt_1 crystals). After M1 event, part of the batholith was rehydrated along shear zones. The hydration of K-feldspar along the shear fabric to produce an anastomosing muscovite-biotite fabric in rocks from the assemblages 2 and 3. Only these rocks underwent by an anatectic second event (M2), resulting in muscovite breakdown to produce sillimanite. Absent-fluid partial melting reactions involving biotite, sillimanite, plagioclase and quartz produced a second generation of peritectic garnet (Grt_2). Phase equilibrium modelling from mineral assemblage 2 suggests P-T conditions for second anatectic event around 770 ºC and 6.6 kbar.

3) LA-ICP-MS U-Pb dating of zircon and monazite from CCB indicates the time of magmatic crystallization and anatectic/metamorphic events. U-Pb data obtained in magmatic zircon grains yields ages of ca. 588-578 Ma, interpreted as magmatic crystallization age. The first anatectic event has been recorded by development of thin overgrowths on relict cores and also by growth of new anatectic zircon grains, with ages between 570 and 550 Ma. This age interval is consistent with the ages on

monazite and zircon (ca. 569-552 Ma) included in Grt_1, further support the interpretation that the Grt_1 crystals grew during the first anatectic episode. The age this anatectic event coincide with partial melting episode in the metasediments from the Nova Venécia complex (NVC) dated by Gradim *et al.* (2014) and Richter *et al.* (2016) at ca. 560-575 Ma. The second anatectic/metamorphic event took place at ca. 535-500 Ma, being characterized by different ways along batholith. Evidence of new anatectic zircon growth/overgrowth is only recorded in sillimanite-bearing rocks (assemblages 2 and 3), while the resulting rocks (assemblage 1) have zircon grains formed by solid-state recrystallization of pre-existing zircon. This period is similar to the magmatic crystallization of the youngest G3 rocks dated by Silva *et al.* (2002, 2011), Noce *et al.* (2004) and Pedrosa-Soares *et al.* (2011) at ~ 530 Ma. Youngest ages recorded in monazite grains (ca. 480-490 Ma) can be attributed to tectono-thermal event occurred during the orogenic collapse, which led fluid movement through the crust.

4) Regarding to Hf isotope composition and rare earth elements (REEs), both anatectic zircon populations (ca. 570-550 Ma and ca. 535-500 Ma) have higher initial $^{176}Hf/^{177}Hf$ values compared to relict cores and display chondrite-normalized REE patterns typical of zircon that grew contemporaneously with peritectic garnet through fluid-absent partial melting. The processes that might explain a ^{176}Hf input in the system include interaction with fluids and/or melts enriched in Hf. In contrast, metamorphic zircon grains (ca. 535-500 Ma) extracted from free-sillimanite granites (assemblage 1) show initial $^{176}Hf/^{177}Hf$ ratios and chondrite-normalized REE patterns similar to the relict cores, indicating that they might have formed by solid-state recrystallization at high-temperature.

6.2. SOURCE ROCKS OF THE CARLOS CHAGAS BATHOLITH

Some studies have considered the CCB as anatectic product of the paragneisses from NVC (Roncato, 2009; Gradim *et al.*, 2014). However, U-Pb data this study indicate that first metamorphic/anatectic event in the batholith take place at ca. 570-550 Ma, coinciding with the peak granulitic metamorphism recorded in zircon/monazite grains from NVC (ca. 560-575 Ma; Gradim *et al.*, 2014; Richter *et al.*, 2016). Moreover, batholith records higher pressure conditions (9.5-105 kbar; this study) than the paragneisses (5.3-7.5 kbar; Richter *et al.*, 2016), indicating that the currently exposed units in the core of the orogen were buried to varied depths and were differentially exhumed during cooling.

Zircon $\varepsilon Hf_{(t)}$ values of the CCB attest a crustal origin. Spectrum of inherited zircon ages from CCB shows a dominant peak at ca. 605 Ma, with subordinate peaks at ca. 826 Ma, ca. 740-690 Ma, ca. 680-635 Ma and ca. 630-620 Ma. Ages of inherited cores found in the CCB match the age spectrum for detrital zircons of the NVC. Both units have a main peak between 605 and 610 Ma that overlap in age with the rocks from Rio Doce magmatic arc. Richter *et al.* (2016) have suggested the youngest detrital zircons as provenance this arc. However, the Hf isotope composition of inherited zircon from CCB is significantly distinct to those values previously reported for arc-related granitoids in the Araçuaí orogen (Gonçalves *et al.*, 2015; Tedeschi *et al.*,

2016; Narduzzi *et al.*, in prep.). The protholiths involved during crustal melting for CCB production could be the metasediments similar to the NVC initially buried at a deeper crustal level and that were not exhumed during the development of the orogen. Hf isotope data of the country rocks is still lacking. Therefore, a more extensive study of the granites and their country rocks is requires to fully resolve the origin of the CCB, as well as the composition of the sources involved.

REFERENCES

Gonçalves L., Alkmim F. F., Pedrosa-Soares A. C., Dussin I. A., Valeriano C. M., Lana C., Tedeschi M. 2015. Granites of the intracontinental termination of a magmatic arc: An example from the Ediacaran Araçuaí Orogen, Southeastern Brazil. *Gondwana Research*, **36**:439-458.

Gradim C., Roncato J., Pedrosa-Soares A.C., Cordani U., Dussin I., Alkmim F.F., Queiroga G., Jacobssohn T., Silva L.C., Babinski M. 2014. The hot back-arc zone of the Araçuaí orogen, Eastern Brazil: from sedimentation to granite generation. *Brazilian Journal of Geology*, **44**, 155-180.

Narduzzi F., Farina F., Lana C., Stevens G., Nalini-Jr. H.A. Geochemical, U-Pb geochronological and Hf isotopic evolution of a large Cordilleran-type batholith: clues from the Galiléia granitoids (Brazil). (in prep.)

Noce C. M, Pedrosa-Soares A. C., Piuzana D., Armstrong R., Laux J. H. Campos C. M., Medeiros S. R. 2004. Ages of sedimentation of the kinzigitic complex and of a late orogenic thermal episode in the Araçuaí orogen, northern Espírito Santo State, Brazil: Zircon and monazite U-Pb SHRIMP and ID-TIMS data. *Revista Brasileira de Geociências*, **34**:587-592.

Pedrosa-Soares A. C., De Campos C. P., Noce C., Silva L. C., Novo T., Roncato J., Medeiros S., Castañeda C., Queiroga G., Dantas E., Dussin I., Alkmim F. 2011. Late Neoproterozoic–Cambrian granitic magmatism in the Araçuaí orogen (Brazil), the Eastern Brazilian Pegmatite Province and related mineral resources. *Geological Society of London, Special Publications*, **350**:25–51.

Richter F., Lana C., Stevens G., Buick I., Pedrosa-Soares A. C., Alkmim F. F., Cutts K. 2016. Sedimentation, metamorphism and granite generation in a back-arc region: Records from the Ediacaran Nova Venécia Complex (Araçuaí Orogen, Southeastern Brazil). *Precambrian Research*, **272**:78-100.

Roncato J. G. 2009. *As suítes graníticas tipo-S do norte do Espírito Santo na região das folhas Ecoporanga, Mantena, Montanha e Nova Venécia*. Instituto de Geociências, Universidade Federal de Minas Gerais, Minas Gerais, Masters dissertation,102p.

Silva L. C., Armstrong R., Noce C. M., Carneiro M. A., Pimentel M., Pedrosa-Soares A. C., Leite C. A., Vieira V. S., Silva M. A., Paes V. J. C., Filho J. M. C. 2002. Reavaliação da evolução geológica em terrenos Pré-cambrianos brasileiros com base em novos dados U-Pb SHRIMP, parte II: Orógeno Araçuaí, Cinturão Mineiro e Cráton São Francisco Meridional. *Revista Brasileira de Geociências*, **32**(4):513-528.

Silva L. C., Pedrosa-Soares A. C., Armstrong R., Noce C. M. 2011. Determinando a duração do período colisional do Orógeno Araçuaí com base em geocronologia U-Pb de alta resolução em zircão: uma contribuição para a história da amalgamação do Gondwana Ocidental. *Geonomos*, **19**(2):180-197.

Tedeschi M., Novo T., Pedrosa-Soares A. C., Dussin I., Tassinari C., Silva L. C., Gonçalves L., Alkmim F., Lana C., Figueiredo C., Dantas E., Medeiros S., De Campos C., Corrales F., Heilbron M. 2016. The Ediacaran Rio Doce magmatic arc revisited (Araçuaí-Ribeira orogenic system, SE Brazil). *Journal of South American Earth Sciences*, **68**:167-186.

White R. W. & Powell R. 2002. Melt loss and the preservation of granulite facies mineral assemblages. *Journal of Metamorphic Geology*, **20:**621–632.

APPENDIX A

Supplementary material to the article presented in chapter 3

A.1. Mineral chemistry

Mineral compositional analysis was performed using a Leo® 1430VP Scanning Electron Microscope at the Department of Earth Sciences, Stellenbosch University, South Africa. Prior to imaging and analysis, the thin sections were sputter-coated with carbon. Textures were studied in backscattered electron (BSE) mode and mineral compositions quantified by EDX (Energy Dispersive X-ray) analysis using an Oxford Instruments ® 133 keV ED X-ray detector and Oxford INCA software. Beam conditions during the quantitative analyses were 20 KV accelerating voltage and 1.0 A probe current, with a working distance of 16.5 mm and a specimen beam current of −19.0 nA. X-ray counts were typically ~7000 cps, and the counting time was 50s live-time. Analyses were quantified using natural mineral standards and mineral chemical compositions were recalculated to mineral stoichiometries to obtain mineral structural formulae. Estimative of Fe^{3+} concentration was made using the general equation of Droop (1987).

Garnet trace element compositions were analyzed via laser ablation-inductively-coupled-mass spectrometry (LA-ICP-MS) using an Agilent 7500ce quadrupole ICP-MS coupled to a 213 nm New Wave laser at the Department of Earth Sciences, Stellenbosch University, South Africa. In situ sampling on polished thin sections was performed using a 40 μm diameter ablation spot at a fluence of ~7.8 J/cm^2 and a repetition rate of 5Hz. Data was acquired in time resolved mode, which allowed potential contamination from mineral inclusions or fractures to be identified and excluded from the analysis. NIST-612 glass (Pearce *et al*., 1997) was used as a control standard and measured garnet (via EDS) SiO_2 contents were used as an internal standard. Accuracy and reproducibility of multiple analyses was established from the analysis of the secondary standard BHVO 2G, a USGS natural basaltic glass standard. Results were better than 5% relative for most elements. Data was processed using Glitter (Van Achterbergh *et al*., 2001) software and absolute values in ppm, as well as chondrite-normalized trace element values, are reported (McDonough & Sun, 1995).

A.2. XRF Analysis

Whole-rock chemistry analysis was performed at the Department of Earth Sciences, Stellenbosch University, South Africa. Samples were crushed to a fine powder using a jaw crusher and swing mill, and glass disks prepared for XRF analysis using 1.5 g of high purity trace element and REE element free flux ($LiBO_2$ = 80%, $Li_2B_4O_7$ = 20%) mixed with 0.28 g of the rock sample. Whole-rock major element compositions were determined by XRF spectrometry on a Philips 1404Wavelength Dispersive spectrometer. The spectrometer is fitted with an Rh tube, analyzing crystals LIF200, LIF220, LIF420, PE, TLAP and PX1. The instrument is fitted with a gas-flow proportional counter, a scintillation detector. The gas-flow proportional counter uses a 90% Argon, 10% methane gas mixture. Major elements were analyzed on a fused glass disk at 50 kV and

50mA tube operating conditions. Matrix effects in the samples were corrected for by applying theoretical alpha factors and measured line overlap factors to the raw intensities measured with the SuperQ Philips software. Control standards that were used in the calibration procedures for major element analyses were SY-3 (Syenite), SY-2 (Syenite), NIM-S (Syenite), JG-1 (Granodiorite) and NIM-G (Granite).

A.3. LA-ICP-MS U-Pb geochronology

A.3.1. Monazite

Monazite grains were dated in thin section in the Stellenbosch University Central analytical facility (CAF) ICP-MS unit using an Agilent 7500ce quadrupole ICP-MS coupled to a 213 nm New Wave laser. Prior to analysis monazite grains were imaged in BSE (back-scattered electron) mode using a ZEISS EVO MA15VP SEM housed at the Central Analytical Facility (CAF) electron micro-beam unit. Operating conditions for monazite are described in Buick *et al.* (2011) and were optimised to provide maximum sensitivity for the high masses (Pb–U) while inhibiting oxide formation ($ThO^+/Th^+ < 0.5\%$). Ablations occurred in a custom-built small-volume, teardrop-shaped sample cell (cf. Horstwood *et al.*, 2003) in a He carrier gas, and the resulting aerosol was mixed with Ar prior to introduction into the ICP-MS via a signal-smoothing manifold. Initial data reduction used the Glitter software package (Van Achterbergh *et al.*, 2001) to calculate the relevant isotopic ratios ($^{207}Pb/^{206}Pb$, $^{208}Pb/^{206}Pb$, $^{208}Pb/^{232}Th$, $^{206}Pb/^{238}U$ and $^{207}Pb/^{235}U$). ^{235}U was calculated from ^{238}U counts via the natural abundance ratio $^{235}U = {}^{238}U/137.88$ (Jackson *et al.*, 2004). Individual isotopic ratios were displayed in time-resolved mode. Isotopic ratios generated during the first 5-10s of each analysis were not used, and from the remainder of each analysis the integration window was chosen so as to maximise concordance (Jackson *et al.*, 2004). Ablation depth-dependent elemental fractionation was corrected for by tying the integration window for the unknown monazite to the identical integration window of the standard (Jackson *et al.*, 2004).

Instrumental drift was corrected against the monazite standard using linear interpolative fits. The U-Pb data were plotted on a Wetherill concordia diagram using the software Isoplot (Ludwig, 2003). Uncertainties in these were propagated assuming a 1% uncertainty on the age of the standards. ^{204}Pb-based common Pb corrections were not applied because of the well-known contamination of the carrier gases by ^{204}Hg (e.g. Jackson *et al.*, 2004).

The analytical runs involved repeated analysis cycles of the Itambé monazite (Dumond *et al.*, 2008; Gasquet *et al.*, 2010), used as the primary standard, Thompson Mine monazite (Williams *et al.*, 1996), used as a control/secondary standard, and 6-8 analyses of monazite from the thin section. Integration times for U/Pb age determinations were 15 ms for ^{206}Pb, 40 ms for ^{207}Pb, and 10 ms for ^{208}Pb, ^{204}Pb, ^{232}Th and ^{238}U. LA-ICP-MS acquisitions consisted of a 60 second measurement of the gas blank, followed by 40 seconds of

measurement of U, Th and Pb signals during ablation. Laser ablations were performed at a frequency of 4 Hz and an energy density of ~4.5-5 J/cm2, and produced 20 nm diameter wide pits.

A.3.2. Zircon

Prior to analysis, cathodoluminescence (CL) imaging of thin sections and mount were used to determine the microstructural location of zircon as well its internal structures. In zircon U–Pb dating was performed using the Stellenbosch University LA-ICP-MS. A small volume sample cell was employed (Horstwood *et al.*, 2003). Integration times for U/Pb age determinations were 15 ms for ^{206}Pb, 40 ms for ^{207}Pb, and 10 ms for ^{208}Pb, ^{204}Pb, ^{232}Th and ^{238}U. The respective isotopic ratios were displayed in time-resolved mode. The first 5-10s of each analysis was discarded, and from the remainder of each analysis the integration window was chosen so as to maximize its concordance (Jackson *et al.*, 2004). The data were not corrected for common Pb because of an interference of ^{204}Hg on ^{204}Pb. Instead, ^{204}Pb was measured so as to exclude analyses with abnormal concentrations of common Pb. Initial data reduction was performed by the Glitter software package (Van Achterbergh *et al*., 2001) to calculate the relevant isotopic ratios (^{207}Pb/^{206}Pb, ^{208}Pb/^{206}Pb, ^{208}Pb/^{232}Th, ^{206}Pb/^{238}U and ^{207}Pb/^{235}U). ^{235}U was calculated from ^{238}U counts via the natural abundance ratio ^{235}U = ^{238}U/137.88 (Jackson *et al.*, 2004). Errors propagated by the software assume a 1% uncertainty on the age of the standard. The 1% uncertainty in the standard is propagated in quadrature into the uncertainty on each spot age. The U-Pb data were plotted on Concordia diagrams via the software Isoplot (Ludwig, 2003). For detailed information on the long-term reproducibility of U/Pb ages of zircon secondary standards using the Stellenbosch LA-ICP-MS, the reader is referred to Lana *et al.* (2011).

References cited

Droop, G.T.R., 1987. A general equation for estimating $Fe3^{+}$ concentrations in ferromagnesian silicates and oxides from microprobe analyses, using stoichiometric criteria. *Mineralogical Magazine* 51, 431-435.

Dumond, G., McLean, N., Williams, M.L., Jercinovic, M.J., Bowring, S.A., 2008. High-resolution dating of granite petrogenesis and deformation in a lower crustal Shear zone; Athabasca granulite terrane, western Canadian Shield. *Chemical Geology* 254, 197-215.

Gasquet, D., Bertrand, J.M., Paquette, J.L., Lehmann, J., Ratzov, G., Guedes, R.A., Tiepolo, M., Boullier, A.M., 2010. Miocene to Messinian deformation and hydrothermal activity in a pre-Alpine basement massif of the French western Alps: new U-Th-Pb and argon ages from the Lauzière massif. *Bulletin of Geological Society of France* 181, 227-241.

Horstwood, M.S.A., Foster G.L., Parrish R.R., Noble S.R., Nowell G.M., 2003. Common-Pb corrected in situ U?Pb accessory mineral geochronology by LA-MC-ICP-MS. *Journal of Analytical Atomic Spectrometry* 18, 837.

Jackson, S.E., Pearson, N.J., Griffin, W.L., Belousova, E.A. 2004 The application of laser ablation-inductively coupled plasma-mass spectrometry to in situ U-Pb zircon geochronology: *Chemical Geology* 211, 47–69.

Lana, C., Buick, I., Stevens, G., Rossouw, R., De Wet, W., 2011. 3230–3200 Ma postorogenic extension and mid-crustal magmatism along the southeastern margin of the Barberton Greenstone Belt, South Africa. *Journal of Structural Geology* 33, 844–858.

Ludwig, K.R., 2003. Mathematical-statistical treatment of data and errors for Th/U geochronology. *Reviews in Mineralogy and Geochemistry* 52, 631-656.

McDonough, W.F. & Sun, S.S., 1995. The composition of the Earth. *Chemical Geology* 120, 223-253.

Pearce, N.J.G., Perkins, W.T., Westgate, J.A., Gorton, M.P., Jackson, S.E., Neal, C.R., and Chenery, S.P., 1997. A compilation of new and published major and trace element data for NIST SRM 610 and NIST SRM 612 glass reference materials: *Geostandards Newsletter* 21, 115-144.

Van Achterbergh, E., Ryan, C.G., Jackson, S.E., and Griffin, W., 2001. Data reduction software for LA-ICP-MS, in Sylvester, P., ed., Laser ablation-ICPMS in the Earth Science, *Mineralogical Association of Canada* 29, 239-243.

Williams, I.S., Buick, I.S, Cartwright, I.,1996. An extended episode of early Mesoproterozoic metamorphic fluid flow in the Reynolds Range, Central Australia, *Journal of Metamorphic Geology* 14, 29-48.

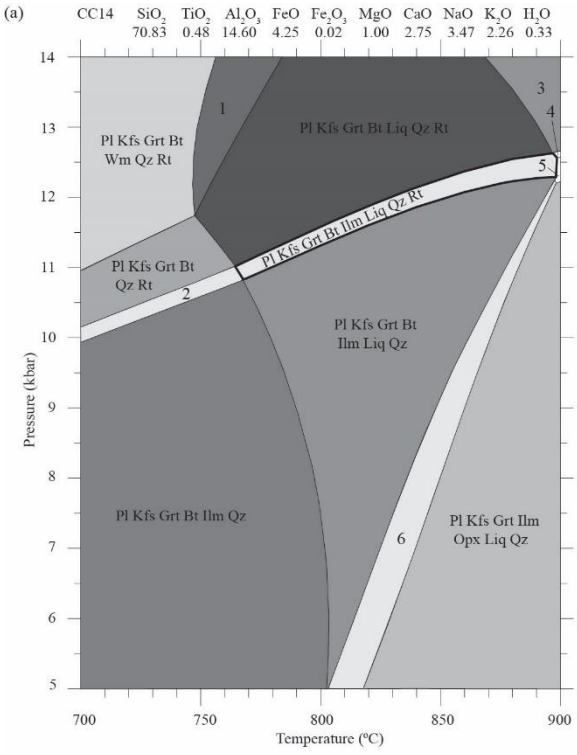

Field labels: 1 - Pl Kfs Grt Bt Wm Liq Qz Rt; 2 - Pl Kfs Grt Bt Ilm Qz Rt; 3 - Pl Ks Grt Liq Qz Rt; 4 - Pl Ks Grt Ilm Liq Qz Rt; 5 - Pl Kfs Grt Ilm Opx Liq Qz Rt; 6 - Pl Kfs Grt Bt Ilm Opx Liq Qz

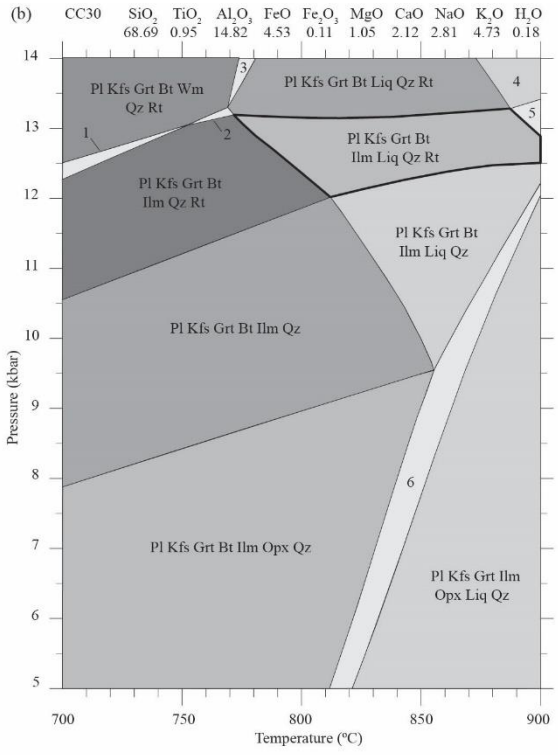

Field labels: 1 - Pl Kfs Grt Bt Wm Ilm Qz Rt; 2 - Pl Kfs Grt Bt Qz Rt; 3 - Pl Kfs Grt Bt Wm Liq Qz Rt; 4 - Pl Kfs Grt Liq Qz Rt; 5 - Pl Kfs Grt Ilm Liq Qz Rt; 6 - Pl Kfs Grt Bt Ilm Opx Liq Qz

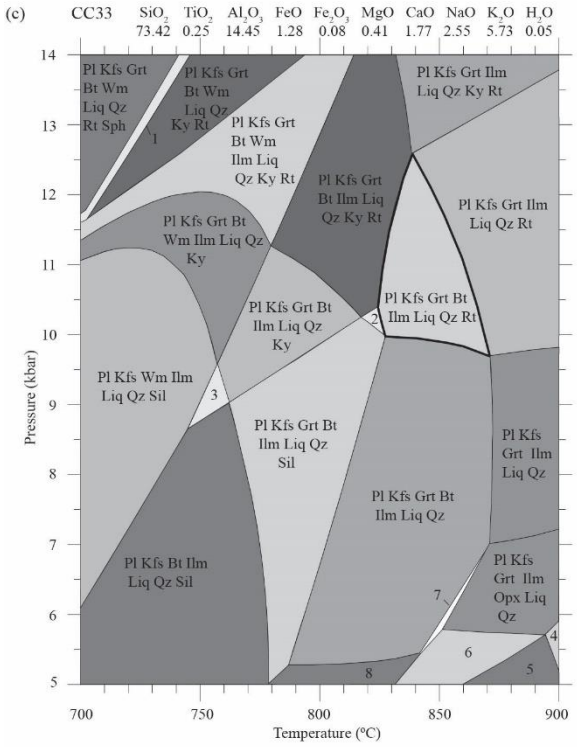

Field labels: 1 - Pl Kfs Grt Bt Wm Liq Qz Sph; 2 - Pl Kfs Grt Bt Ilm Liq Qz Sil Rt; 3 - Pl Kfs Bt Ilm Liq Qz Ky; 4 - Pl Kfs Ilm Opx Liq Qz; 5 - Pl Kfs Ilm Opx Crd Liq Qz; 6 - Pl Kfs Grt Ilm Opx Crd Liq Qz; 7 - Pl Kfs Grt Ilm Opx Liq Qz; 8 - Pl Kfs Grt Bt Ilm Crd Liq Qz

Figure SM1. P-T pseudosection calculated using the bulk composition of three samples from assemblage 1. (a) P-T fields of peak assemblage Pl-Kfs-Grt-Bt-Ilm-Qz-Rt-Liq (bold line) from sample CC14. (b) P-T fields of peak assemblagePl-Kfs-Grt-Bt-Ilm-Qz-Rt-Liq (bold line) from sample CC30. (c) P-T fields of peak assemblage Pl-Kfs-Grt-Bt-Ilm-Qz-Rt-Liq (bold line) from sample CC33.

Table A1 - Major element compositions (wt%) and structural formulae of representative minerals from the Carlos Chagas batholith

Sample CC28 - Assemblage 1

Analysis	Grt_1 n = 34	$Bt_{inclusion}$ n = 16	Bt_{matrix} n = 10	$Bt_{retrograde}$ n = 10	Pl_{matrix} n = 7	Kfs_{matrix} n = 9	$Ilm_{inclusion}$ n = 8	$Rt_{inclusion}$ n = 3
SiO_2	36.83 ± 0.19	36.73 ± 1.03	35.81 ± 1.59	37.64 ± 0.55	58.68 ± 0.26	63.80 ± 046	-	-
TiO_2	0.00 ± 0.00	5.73 ± 0.08	4.26 ± 0.10	3.85 ± 0.06	0.00 ± 0.00	0.00 ± 0.00	52.49 ± 0.31	96.98 ± 0.29
Al_2O_3	21.50 ± 0.15	17.40 ± 0.48	17.67 ± 0.33	18.11 ± 0.31	25.31 ± 0.13	19.75 ± 0.25	-	-
FeO_t	34.31 ± 0.50	15.53 ± 0.24	19.36 ± 0.21	17.48 ± 0.40	0.00 ± 0.00	0.00 ± 0.00	46.50 ± 0.23	1.69 ± 0.09
MnO	0.89 ± 0.00	0.00 ± 0.00	0.00 ± 0.00	0.00 ± 0.00	-	-	0.06 ± 0.05	-
MgO	4.82 ± 0.12	9.97 ± 0.74	9.10 ± 0.08	9.33 ± 0.37	0.00 ± 0.00	0.00 ± 0.00	0.74 ± 0.05	-
CaO	1.69 ± 0.19	0.00 ± 0.00	0.00 ± 0.00	0.00 ± 0.00	5.95 ± 0.36	0.06 ± 0.04	-	-
Na_2O	0.00 ± 0.00	0.50 ± 0.06	0.16 ± 0.09	0.18 ± 0.07	7.99 ± 0.26	2.40 ± 0.80	-	-
K_2O	0.00 ± 0.00	9.41 ± 0.22	9.87 ± 0.18	10.14 ± 0.09	0.20 ± 0.03	12.86 ± 1.07	-	-
Total	100.03 ± 0.58	95.27 ± 1.42	96.23 ± 2.31	96.73 ± 0.88	98.13 ± 0.38	98.87 ± 0.56	99.80 ± 0.30	98.67 ± 0.36
Si	2.93 ± 0.01	5.49 ± 0.07	5.41 ± 0.10	5.59 ± 0.04	2.65 ± 0.01	2.95 ± 0.01	-	-
Ti	0.00 ± 0.00	0.64 ± 0.01	0.48 ± 0.01	0.43 ± 0.01	0.00 ± 0.00	0.00 ± 0.00	0.99 ± 0.01	0.98 ± 0.00
^{IV}Al	0.07 ± 0.01	2.51 ± 0.07	2.59 ± 0.10	2.41 ± 0.04	1.35 ± 0.01	1.08 ± 0.01	-	-
^{VI}Al	1.94 ± 0.02	0.56 ± 0.11	0.56 ± 0.06	0.75 ± 0.06	-	-	-	-
Fe^{3+}	0.13 ± 0.03	-	-	-	-	-	0.02 ± 0.01	-
Fe^{2+}	2.15 ± 0.02	2.02 ± 0.09	2.45 ± 0.06	2.17 ± 0.05	0.00 ± 0.00	0.00 ± 0.00	0.96 ± 0.01	0.02 ± 0.00
Mn	0.06 ± 0.01	0.00 ± 0.00	0.00 ± 0.00	0.00 ± 0.00	-	-	0.00 ± 0.00	-
Mg	0.57 ± 0.01	2.22 ± 0.19	2.05 ± 0.06	2.06 ± 0.08	0.00 ± 0.00	0.00 ± 0.00	0.03 ± 0.00	-
Ca	0.14 ± 0.02	0.00 ± 0.00	0.00 ± 0.00	0.00 ± 0.00	0.29 ± 0.01	0.00 ± 0.00	-	-
Na	0.00 ± 0.00	0.14 ± 0.02	0.05 ± 0.03	0.05 ± 0.02	0.70 ± 0.01	0.21 ± 0.07	-	-
K	0.00 ± 0.00	1.79 ± 0.02	1.90 ± 0.03	1.92 ± 0.01	0.01 ± 0.00	0.76 ± 0.07	-	-
Total	8.00 ± 0.00	15.38 ± 0.07	15.50 ± 0.08	15.39 ± 0.05	5.00 ± 0.00	5.00 ± 0.00	2.00 ± 0.00	1.00 ± 0.00
X_{Alm}	0.73 ± 0.01	-	-	-	-	-	-	-
X_{Spss}	0.02 ± 0.00	-	-	-	-	-	-	-
X_{Py}	0.19 ± 0.01	-	-	-	-	-	-	-
X_{Grs}	0.05 ± 0.01	-	-	-	-	-	-	-
Mg#	0.21 ± 0.01	0.53 ± 0.03	0.45 ± 0.01	0.49 ± 0.01	-	-	-	-
X_{Ab}	-	-	-	-	0.70 ± 0.01	0.22 ± 0.07	-	-
X_{An}	-	-	-	-	0.29 ± 0.01	0.00 ± 0.00	-	-
X_{San}	-	-	-	-	0.01 ± 0.00	0.78 ± 0.07	-	-

n = number of analyses used to define the average and standard deviations

Table A2 - Major element compositions (wt%) and structural formulae of representative minerals from the Carlos Chagas batholith

Sample CC31 - Assemblage 1									
	Grt_1	$Bt_{inclusion}$	Bt_{matrix}	$Bt_{retrograde}$	Pl_{matrix}	Kfs_{matrix}	$Ilm_{inclusion}$	Ilm_{matrix}	$Rt_{inclusion}$
Analysis	n = 72	n = 9	n = 20	n = 13	n = 10	n = 10	n = 11	n = 10	n = 3
SiO_2	38.00 ± 0.37	36.39 ± 0.57	35.30 ± 0.83	35.87 ± 0.68	60.81 ± 0.39	65.24 ± 0.35	-	-	-
TiO_2	0.00 ± 0.00	6.17 ± 0.47	5.06 ± 0.37	4.90 ± 0.23	0.00 ± 0.00	0.00 ± 0.00	52.29 ± 0.28	52.24 ± 0.26	97.28 ± 0.21
Al_2O_3	21.76 ± 0.26	16.41 ± 0.36	16.71 ± 0.49	17.05 ± 0.48	25.27 ± 0.13	18.76 ± 0.11	-	-	-
FeO_t	33.07 ± 0.36	16.44 ± 0.61	20.11 ± 0.35	18.28 ± 0.61	0.00 ± 0.00	0.00 ± 0.00	46.72 ± 0.54	47.51 ± 0.26	1.57 ± 0.52
MnO	0.95 ± 0.08	0.00 ± 0.00	0.00 ± 0.00	0.00 ± 0.00	-	-	0.19 ± 0.08	0.23 ± 0.13	0.14 ± 0.04
MgO	5.47 ± 0.18	11.66 ± 0.55	8.87 ± 0.47	10.16 ± 0.35	0.00 ± 0.00	0.00 ± 0.00	1.02 ± 0.23	0.21 ± 0.12	-
CaO	1.68 ± 0.16	0.00 ± 0.00	0.00 ± 0.00	0.00 ± 0.00	6.69 ± 0.16	0.22 ± 0.04	-	-	-
Na_2O	0.00 ± 0.00	0.40 ± 0.08	0.10 ± 0.11	0.05 ± 0.09	7.80 ± 0.18	1.46 ± 0.22	-	-	-
K_2O	0.00 ± 0.00	8.90 ± 0.22	9.09 ± 0.15	9.12 ± 0.25	0.31 ± 0.08	14.73 ± 0.29	-	-	-
Total	101.13 ± 0.55	96.38 ± 1.34	95.24 ± 1.75	95.43 ± 1.77	100.89 ± 0.34	100.41 ± 0.47	100.21 ± 0.54	100.33 ± 0.49	98.99 ± 0.13
Si	2.98 ± 0.02	5.40 ± 0.02	5.40 ± 0.03	5.42 ± 0.03	2.68 ± 0.01	2.99 ± 0.01	-	-	-
Ti	0.00 ± 0.00	0.69 ± 0.05	0.58 ± 0.05	0.56 ± 0.02	0.00 ± 0.00	0.00 ± 0.00	0.98 ± 0.00	0.99 ± 0.00	0.98 ± 0.00
^{IV}Al	0.02 ± 0.02	2.60 ± 0.02	2.60 ± 0.03	2.58 ± 0.03	1.31 ± 0.01	1.01 ± 0.00	-	-	-
^{VI}Al	1.99 ± 0.02	0.27 ± 0.03	0.42 ± 0.05	0.46 ± 0.03	-	-	-	-	-
Fe^{3+}	0.03 ± 0.03	-	-	-	-	-	0.04 ± 0.01	0.02 ± 0.01	-
Fe^{2+}	2.13 ± 0.03	2.04 ± 0.09	2.58 ± 0.06	2.31 ± 0.06	0.00 ± 0.00	0.00 ± 0.00	0.94 ± 0.01	0.98 ± 0.01	0.02 ± 0.01
Mn	0.06 ± 0.01	0.00 ± 0.00	0.00 ± 0.00	0.00 ± 0.00	-	-	0.00 ± 0.00	0.00 ± 0.00	-
Mg	0.64 ± 0.02	2.58 ± 0.10	2.02 ± 0.08	2.29 ± 0.08	0.00 ± 0.00	0.00 ± 0.00	0.04 ± 0.01	0.01 ± 0.00	-
Ca	0.14 ± 0.01	0.00 ± 0.00	0.00 ± 0.00	0.00 ± 0.00	0.32 ± 0.01	0.01 ± 0.00	-	-	-
Na	0.00 ± 0.00	0.12 ± 0.02	0.03 ± 0.03	0.01 ± 0.03	0.67 ± 0.01	0.13 ± 0.02	-	-	-
K	0.00 ± 0.00	1.69 ± 0.05	1.78 ± 0.02	1.76 ± 0.05	0.02 ± 0.00	0.86 ± 0.02	-	-	-
Total	8.00 ± 0.00	15.38 ± 0.03	15.41 ± 0.05	15.39 ± 0.04	5.00 ± 0.00	5.00 ± 0.00	2.00 ± 0.00	2.00 ± 0.00	1.00 ± 0.00
X_{Alm}	0.71 ± 0.01	-	-	-	-	-	-	-	-
X_{Spss}	0.02 ± 0.00	-	-	-	-	-	-	-	-
X_{Py}	0.22 ± 0.01	-	-	-	-	-	-	-	-
X_{Grs}	0.05 /- 0.01	-	-	-	-	-	-	-	-
Mg#	0.23 ± 0.02	0.57 ± 0.02	0.44 ± 0.01	0.50 ± 0.01	-	-	-	-	-
X_{Ab}	-	-	-	-	0.67 ± 0.01	0.13 ± 0.02	-	-	-
X_{An}	-	-	-	-	0.32 ± 0.01	0.01 ± 0.00	-	-	-
X_{San}	-	-	-	-	0.02 ± 0.00	0.86 ± 0.02	-	-	-

n = number of analyses used to define the average and standard deviations

Table A3 - Major element compositions (wt%) and structural formulae of representative minerals from the Carlos Chagas batholith

Sample CC37 - Assemblage 2

	Grt_1	Grt_2	$Bt_{inclusion}$	Bt_{matrix}	$Bt_{retrograde}$	$Pl_{inclusion\ in\ Grt}$	$Pl_{inclusion\ in\ Sil}$	Pl_{matrix}	Kfs_{matrix}	$Ilm_{inclusion}$	Ilm_{matrix}
Analysis	n = 26	n = 20	n = 11	n = 22	n = 13	n = 8	n = 6	n = 12	n = 11	n = 2	n= 4
SiO_2	36.85 ± 0.32	36.48 ± 0.29	35.07 ± 0.41	34.51 ± 0.69	35.40 ± 0.60	60.17 ± 0.33	61.53 ± 0.85	62.69 ± 0.57	65.71 ± 0.32	-	
TiO_2	0.00 ± 0.00	0.00 ± 0.00	4.60 ± 0.09	3.81 ± 0.51	2.37 ± 0.26	0.00 ± 0.00	0.00 ± 0.00	0.00 ± 0.00	0.00 ± 0.00	49.75 ± 0.71	51.13 ± 0.33
Al_2O_3	21.27 ± 0.18	20.98 ± 0.19	18.52 ± 0.20	17.40 ± 0.29	16.88 ± 0.38	25.54 ± 0.17	23.83 ± 0.49	23.34 ± 0.24	18.04 ± 0.20	-	
FeO_t	35.50 ± 0.35	37.67 ± 1.13	16.41 ± 0.33	20.44 ± 0.46	18.31 ± 0.49	0.00 ± 0.00	0.00 ± 0.00	0.00 ± 0.00	0.00 ± 0.00	47.72 ± 0.46	47.39 ± 1.02
MnO	1.12 ± 0.10	1.33 ± 0.10	0.00 ± 0.00	0.00 ± 0.00	0.00 ± 0.00	-	-	-	-	0.00 ± 0.00	1.18 ± 0.38
MgO	4.07 ± 0.14	3.30 ± 0.25	10.07 ± 0.18	7.86 ± 0.33	10.49 ± 0.38	0.00 ± 0.00	0.00 ± 0.00	0.00 ± 0.00	0.00 ± 0.00	0.67 ± 0.01	015 ± 0.21
CaO	1.07 ± 0.11	0.73 ± 0.05	0.00 ± 0.00	0.00 ± 0.00	0.00 ± 0.00	5.91 ± 0.13	5.50 ± 0.32	5.34 ± 0.09	0.00 ± 0.00	-	-
Na_2O	0.00 ± 0.00	0.00 ± 0.00	0.25 ± 0.24	0.00 ± 0.00	0.00 ± 0.00	8.44 ± 0.16	8.15 ± 0.16	8.43 ± 0.19	1.39 ± 0.33	-	-
K_2O	0.00 ± 0.00	0.00 ± 0.00	9.55 ± 0.10	9.49 ± 0.13	9.69 ± 0.11	0.27 ± 0.05	0.38 ± 0.07	0.37 ± 0.07	14.82 ± 0.47	-	-
Total	99.87 ± 0.50	100.50 ± 0.87	94.47 ± 0.46	93.51 ± 1.19	93.13 ± 1.13	100.33 ± 0.42	99.38 ± 1.42	100.17 ± 0.89	99.96 ± 0.56	98.14 ± 1.18	99.86 ± 0.65
Si	2.95 ± 0.02	2.94 ± 0.02	5.33 ± 0.04	5.41 ± 0.05	5.51 ± 0.03	2.65 ± 0.01	2.75 ± 0.02	2.78 ± 0.01	3.03 ± 0.01	-	
Ti	0.00 ± 0.00	0.00 ± 0.00	0.52 ± 0.01	0.45 ± 0.06	0.28 ± 0.03	0.00 ± 0.00	0.00 ± 0.00	0.00 ± 0.00	0.00 ± 0.00	0.96 ± 0.00	0.97 ± 0.01
^{IV}Al	0.05 ± 0.02	0.06 ± 0.02	2.67 ± 0.04	2.59 ± 0.05	2.49 ± 0.03	1.33 ± 0.01	1.26 ± 0.01	1.22 ± 0.01	0.98 ± 0.01	-	-
^{VI}Al	1.96 ± 0.02	1.94 ± 0.03	0.64 ± 0.03	0.62 ± 0.07	0.61 ± 0.06	-	-	-	-	-	-
Fe^{3+}	0.08 ± 0.04	0.12 ± 0.05	-	-	-	-	-	-	-	0.09 ± 0.00	0.06 ± 0.03
Fe^{2+}	2.30 ± 0.03	2.39 ± 0.03	2.08 ± 0.05	2.68 ± 0.06	2.38 ± 0.06	0.00 ± 0.00	0.00 ± 0.00	0.00 ± 0.00	0.00 ± 0.00	0.93 ± 0.00	0.94 ± 0.02
Mn	0.08 ± 0.01	0.09 ± 0.01	0.00 ± 0.00	0.00 ± 0.00	0.00 ± 0.00	-	-	-	-	0.00 ± 0.00	0.03 ± 0.01
Mg	0.49 ± 0.02	0.40 ± 0.03	2.28 ± 0.04	1.84 ± 0.08	2.43 ± 0.08	0.00 ± 0.00	0.00 ± 0.00	0.00 ± 0.00	0.00 ± 0.00	0.03 ± 0.00	0.01 ± 0.01
Ca	0.09 ± 0.01	0.06 ± 0.00	0.00 ± 0.00	0.00 ± 0.00	0.00 ± 0.00	0.28 ± 0.01	0.26 ± 0.01	0.25 ± 0.00	0.00 ± 0.00	-	-
Na	0.00 ± 0.00	0.00 ± 0.00	0.07 ± 0.07	0.00 ± 0.00	0.00 ± 0.00	0.72 ± 0.01	0.71 ± 0.01	0.73 ± 0.01	0.12 ± 0.03	-	-
K	0.00 ± 0.00	0.00 ± 0.00	1.85 ± 0.02	1.90 ± 0.03	1.92 ± 0.03	0.02 ± 0.01	0.02 ± 0.00	0.02 ± 0.00	0.87 ± 0.03	-	-
Total	8.00 ± 0.00	8.00 ± 0.00	15.45 ± 0.05	15.48 ± 0.06	15.63 ± 0.03	5.00 ± 0.00	5.00 ± 0.00	5.00 ± 0.00	5.00 ± 0.00	2.00 ± 0.00	2.00 ± 0.00
X_{Alm}	0.78 ± 0.01	0.81 ± 0.01	-	-	-	-	-	-	-	-	-
X_{Spss}	0.03 ± 0.00	0.03 ± 0.00	-	-	-	-	-	-	-	-	-
X_{Py}	0.16 ± 0.01	0.13 ± 0.01	-	-	-	-	-	-	-	-	-
X_{Grs}	0.03 ± 0.00	0.02 ± 0.00	-	-	-	-	-	-	-	-	-
Mg#	0.17 ± 0.01	0.15 ± 0.02	0.52 ± 0.01	0.41 ± 0.01	0.50 ± 0.01	-	-	-	-	-	-
X_{Ab}	-	-	-	-	-	0.71 ± 0.01	0.73 ± 0.00	0.73 ± 0.01	0.12 ± 0.03	-	-
X_{An}	-	-	-	-	-	0.27 ± 0.01	0.26 ± 0.00	0.25 ± 0.00	0.00 ± 0.00	-	-
X_{San}	-	-	-	-	-	0.02 ± 0.01	0.01 ± 0.00	0.02 ± 0.00	0.88 ± 0.03	-	-

n = number of analyses used to define the average and standard deviations

Table A4 - Major element compositions (wt%) and structural formulae of representative minerals from the Carlos Chagas batholith

Sample CC21 - Assemblage 3

Analysis	Grt_1 n = 18	Grt_2 n = 13	$Bt_{inclusion}$ n = 4	Bt_{matrix} n = 8	$Bt_{retrograde}$ n = 16	$Pl_{inclusion\ in\ Grt}$ n = 7	Pl_{matrix} n = 13	Kfs_{matrix} n = 5	Spl n = 10
SiO_2	36.42 ± 0.17	36.00 ± 0.32	36.14 ± 0.49	35.03 ± 0.19	35.58 ± 0.32	59.04 ± 2.49	60.75 ± 0.71	63.52 ± 0.64	-
TiO_2	0.00 ± 0.00	0.00 ± 0.00	4.81 ± 0.48	4.65 ± 0.14	3.50 ± 0.29	0.00 ± 0.00	0.00 ± 0.00	0.00 ± 0.00	0.00 ± 0.00
Al_2O_3	22.01 ± 0.21	21.75 ± 0.17	16.49 ± 0.18	16.52 ± 0.23	16.93 ± 0.29	26.29 ± 1.41	24.85 ± 0.59	19.47 ± 0.20	59.02 ± 0.41
Cr_2O_3	0.00 ± 0.00	0.00 ± 0.00	-	-	-	-	-	-	0.09 ± 0.07
FeO_t	34.38 ± 0.58	35.91 ± 0.59	13.57 ± 1.24	18.44 ± 0.21	16.50 ± 0.85	0.00 ± 0.00	0.00 ± 0.00	0.00 ± 0.00	29.24 ± 2.19
MnO	1.35 ± 0.20	1.29 ± 0.06	0.00 ± 0.00	0.00 ± 0.00	0.00 ± 0.00	-	-	-	0.00 ± 0.00
MgO	4.76 ± 0.29	3.84 ± 0.31	14.08 ± 1.12	10.58 ± 0.10	12.23 ± 0.54	0.00 ± 0.00	0.00 ± 0.00	0.00 ± 0.00	3.79 ± 0.31
CaO	0.89 ± 0.09	0.75 ± 0.10	0.02 ± 0.02	0.01 ± 0.01	0.01 ± 0.01	5.59 ± 0.49	5.04 ± 0.46	0.08 ± 0.04	-
ZnO	-	-	-	-	-	-	-	-	7.20 ± 2.44
Na_2O	0.00 ± 0.00	0.00 ± 0.00	0.49 ± 0.07	0.16 ± 0.03	0.18 ± 0.03	8.46 ± 0.36	8.88 ± 0.23	1.41 ± 0.59	-
K_2O	0.00 ± 0.00	0.00 ± 0.00	9.28 ± 0.12	9.46 ± 0.14	9.51 ± 0.08	0.26 ± 0.09	0.24 ± 0.09	14.78 ± 0.71	-
Total	99.81 ± 0.57	99.54 ± 0.59	94.87 ± 0.33	94.86 ± 0.43	94.43 ± 0.45	99.64 ± 1.93	99.76 ± 1.22	99.27 ± 0.73	99.35 ± 0.48
Si	2.90 ± 0.02	2.90 ± 0.03	5.39 ± 0.02	5.36 ± 0.02	5.41 ± 0.02	2.62 ± 0.07	2.71 ± 0.02	2.95 ± 0.01	-
Ti	0.00 ± 0.00	0.00 ± 0.00	0.54 ± 0.06	0.54 ± 0.02	0.40 ± 0.03	0.00 ± 0.00	0.00 ± 0.00	0.00 ± 0.00	0.00 ± 0.00
^{IV}Al	0.10 ± 0.02	0.10 ± 0.03	2.61 ± 0.02	2.64 ± 0.02	2.59 ± 0.02	1.38 ± 0.10	1.30 ± 0.02	1.07 ± 0.01	1.99 ± 0.01
^{VI}Al	1.97 ± 0.02	1.97 ± 0.03	0.29 ± 0.02	0.35 ± 0.03	0.45 ± 0.05	-	-	-	0.00 ± 0.00
Cr	0.00 ± 0.00	0.00 ± 0.00	-	-	-	-	-	-	0.00 ± 0.00
Fe^{3+}	0.13 ± 0.04	0.12 ± 0.05	-	-	-	-	-	-	0.01 ± 0.01
Fe^{2+}	2.17 ± 0.04	2.29 ± 0.06	1.70 ± 0.17	2.36 ± 0.03	2.10 ± 0.11	0.00 ± 0.00	0.00 ± 0.00	0.00 ± 0.00	0.69 ± 0.04
Mn	0.09 ± 0.01	0.09 ± 0.00	0.00 ± 0.00	0.00 ± 0.00	0.00 ± 0.00	-	-	-	0.00 ± 0.00
Mg	0.56 ± 0.04	0.46 ± 0.04	3.13 ± 0.22	2.41 ± 0.02	2.77 ± 0.12	0.00 ± 0.00	0.00 ± 0.00	0.00 ± 0.00	0.16 ± 0.01
Ca	0.08 ± 0.01	0.06 ± 0.01	0.00 ± 0.00	0.00 ± 0.00	0.00 ± 0.00	0.27 ± 0.02	0.24 ± 0.02	0.00 ± 0.00	-
Zn	-	-	-	-	-	-	-	-	0.15 ± 0.05
Na	0.00 ± 0.00	0.00 ± 0.00	0.14 ± 0.02	0.05 ± 0.01	0.05 ± 0.01	0.73 ± 0.02	0.75 ± 0.02	0.13 ± 0.05	-
K	0.00 ± 0.00	0.00 ± 0.00	1.77 ± 0.03	1.85 ± 0.02	1.84 ± 0.02	0.01 ± 0.01	0.01 ± 0.01	0.87 ± 0.05	-
Total	8.00 ± 0.00	8.00 ± 0.00	15.57 ± 0.05	15.56 ± 0.02	15.62 ± 0.03	5.00 ± 0.00	5.00 ± 0.00	5.00 ± 0.01	3.00 ± 0.00
X_{Alm}	0.75 ± 0.01	0.79 ± 0.01	-	-	-	-	-	-	-
X_{Spss}	0.03 ± 0.00	0.03 ± 0.00	-	-	-	-	-	-	-
X_{Py}	0.19 ± 0.01	0.16 ± 0.01	-	-	-	-	-	-	-
X_{Grs}	0.03 ± 0.00	0.02 ± 0.00	-	-	-	-	-	-	-
Mg#	0.21 ± 0.01	0.17 ± 0.01	0.65 ± 0.04	0.51 ± 0.01	0.57 ± 0.02	-	-	-	-
X_{Ab}	-	-	-	-	-	0.73 ± 0.02	0.75 ± 0.02	0.13 ± 0.05	-
X_{An}	-	-	-	-	-	0.27 ± 0.02	0.24 ± 0.02	0.00 ± 0.00	-
X_{San}	-	-	-	-	-	0.01 ± 0.01	0.01 ± 0.01	0.87 ± 0.05	-
X_{Hc}	-	-	-	-	-	-	-	-	0.69 ± 0.04
X_{Ghn}	-	-	-	-	-	-	-	-	0.15 ± 0.05
X_{Spl}	-	-	-	-	-	-	-	-	0.16 ± 0.01

n = number of analyses used to define the average and standard deviations

Table A5 - Rare earth element concentrations (in ppm) of garnets from assemblages 1, 2 and 3.

Element	La	Ce	Pr	Nd	Sm	Eu	Gd	Tb	Dy	Ho	Er	Tm	Yb	Lu
CC31 - Poikiloblastic garnet														
CC31-1-1	0.01	0.03	0.04	0.78	2.84	0.17	18.57	6.08	49.19	11.03	29.93	4.36	29.88	4.81
CC31-1-2	<0.02	<0.01	0.02	0.40	1.91	0.19	16.66	6.25	59.64	16.13	47.26	6.17	41.74	6.47
CC31-1-3	<0.02	0.02	0.01	0.44	2.17	0.16	16.49	6.52	65.88	18.37	57.72	7.42	50.48	7.94
CC31-1-4	0.01	0.03	0.02	0.50	2.82	0.16	19.61	6.85	66.06	17.26	55.97	8.51	58.68	9.45
CC31-1-5	<0.00	0.01	0.02	0.51	2.82	0.13	17.09	6.11	57.18	14.98	53.86	8.59	65.57	10.33
CC31-1-6	<0.01	<0.02	<0.01	0.42	2.46	0.17	19.36	6.67	66.40	19.17	66.54	10.43	76.90	11.74
CC31-1-7	<0.00	0.01	0.01	0.48	2.98	0.05	20.98	8.00	82.19	23.72	84.95	13.42	94.19	14.20
CC31-1-8	<0.02	0.02	0.01	0.41	2.57	0.09	19.03	7.43	80.10	24.62	91.05	14.74	104.23	16.21
CC31-1-9	<0.02	<0.02	0.01	0.40	2.42	0.12	19.17	8.11	89.12	30.15	118.64	19.57	141.94	22.40
CC31-1-10	<0.01	0.02	0.03	0.53	2.28	0.17	19.03	7.89	91.63	31.83	122.52	20.27	150.05	23.28
CC31-1-11	<0.01	<0.01	0.03	0.20	1.83	0.12	16.87	7.14	81.75	28.79	114.00	19.18	138.52	22.21
CC31-1-12	<0.01	<0.01	<0.01	0.26	1.88	0.11	13.61	4.62	44.03	12.86	44.35	7.59	56.95	9.02
CC31-1-13	<0.01	<0.02	<0.02	0.24	1.61	0.11	13.71	5.20	48.69	15.37	57.97	9.40	70.86	11.70
CC31-1-14	<0.01	<0.02	0.01	0.38	1.74	0.10	14.04	5.30	59.33	21.51	93.59	16.62	128.90	22.11
CC31-1-15	<0.00	0.02	<0.01	0.16	1.58	0.11	13.83	5.43	53.00	17.94	74.98	13.71	105.91	18.66
CC31-1-16	0.01	0.01	<0.01	0.08	0.84	0.05	10.22	4.62	48.33	14.61	56.45	9.63	76.10	12.33
CC31-1-17	0.00	0.01	0.00	0.27	1.58	0.09	14.32	5.25	56.99	20.07	85.94	15.34	116.53	19.09
CC31-1-18	<0.01	<0.02	<0.01	0.05	1.27	0.07	13.17	5.16	50.77	15.46	58.79	9.99	75.21	12.58
CC31-1-19	<0.01	<0.01	0.01	0.08	1.01	0.09	12.52	5.00	49.82	13.69	48.76	8.12	63.06	10.65
CC31-1-20	0.01	<0.01	0.01	0.15	1.66	0.09	13.11	5.71	57.82	18.45	71.84	12.51	97.31	16.13
CC31-1-21	<0.01	0.01	0.00	0.32	2.00	0.10	14.61	5.69	60.28	20.19	79.62	13.02	97.14	16.14
CC31-1-22	<0.01	<0.01	<0.01	0.27	1.51	0.10	11.63	4.57	42.51	10.75	32.83	4.87	32.40	5.14
CC31-1-23	<0.01	0.02	0.02	0.44	2.38	0.13	16.32	6.06	53.03	12.43	39.05	5.50	36.89	5.95
CC31-1-24	<0.01	0.03000	0.03	0.53	2.62	0.13	17.02	5.76	51.93	12.58	38.58	5.76	40.76	7.11
CC37 - Poikiloblastic garnet														
CC37-4-1	0.01	0.01	0.02	0.24	1.63	0.03	11.88	6.37	72.34	17.08	43.64	5.67	33.76	3.85
CC37-4-2	0.00	0.02	0.01	0.34	1.28	0.04	6.92	4.83	67.33	21.51	69.32	11.24	72.47	9.57
CC37-4-3	<0.02	0.02	0.01	0.30	1.23	0.03	6.63	4.46	59.56	17.65	58.77	9.08	61.04	8.03
CC37-4-4	<0.02	0.00	0.01	0.29	1.22	0.03	7.60	4.47	59.40	17.50	56.93	9.07	61.34	8.72
CC37-4-5	<0.00	0.01	<0.01	0.31	1.27	0.02	9.21	4.94	50.26	10.87	29.19	4.12	25.41	3.10
CC37-4-6	<0.01	<0.01	<0.01	0.13	1.36	<0.02	10.65	5.69	63.04	15.60	45.54	7.08	48.59	6.25
CC37-4-7	<0.00	0.02	<0.01	0.17	1.48	0.04	10.77	5.75	58.03	14.48	42.01	6.84	48.44	6.61
CC37-4-8	<0.01	<0.01	0.01	0.31	1.49	0.04	11.76	5.96	55.20	11.77	34.83	5.40	39.81	5.38
CC37-4-9	0.01	0.02	0.02	0.17	1.56	0.07	12.97	6.94	71.79	16.83	50.25	8.34	61.86	8.29
CC37-4-10	0.01	<0.01	<0.01	0.12	1.05	<0.03	9.58	5.84	77.43	23.53	84.89	15.26	119.25	18.41
CC37-4-11	0.01	0.01	<0.01	<0.07	1.64	0.05	13.25	6.89	77.83	20.66	65.19	10.46	75.21	10.10
CC37-4-12	<0.01	0.00	<0.01	0.20	1.28	0.03	12.03	6.18	59.89	12.80	32.55	4.68	29.78	3.44
CC37-4-13	<0.00	0.02	0.01	0.13	1.03	<0.02	14.74	7.74	78.23	17.36	45.06	6.03	33.39	3.66
CC37-4-14	0.01	0.01	0.01	0.26	1.23	<0.03	10.63	6.65	82.34	20.67	57.10	8.02	48.78	6.28
CC37-4-15	0.01	0.02	0.01	0.17	0.69	0.03	7.52	5.17	70.04	21.48	72.41	11.37	76.86	10.82
CC37-4-16	<0.01	<0.01	<0.01	0.23	0.7	<0.03	6.04	4.49	59.85	18.24	60.99	9.56	64.11	8.81
CC37-4-17	<0.01	<0.01	0.01	0.33	0.92	<0.02	6.69	4.48	60.68	17.88	56.29	8.43	52.12	6.45
CC37-4-18	<0.00	<0.01	0.01	0.33	2.11	0.02	13.02	6.50	71.15	17.52	46.56	6.50	40.58	5.19
CC37-4-19	<0.01	<0.01	<0.01	0.28	1.82	0.04	12.33	6.93	77.37	20.30	59.99	9.21	59.36	7.79
CC37-4-20	<0.02	0.01	0.01	0.22	1.06	0.04	9.96	5.33	58.37	14.46	40.85	6.56	43.58	5.30
CC37 - Smaller garnet														
CC37-3-1	0.02	0.03	<0.02	0.18	1.32	0.02	17.76	10.09	87.35	14.37	26.58	2.78	14.37	1.37
CC37-3-2	0.08	0.03	0.02	0.23	1.18	<0.02	16.60	10.99	103.61	18.05	35.15	3.60	17.14	1.62
CC37-3-3	0.04	0.06	<0.01	0.17	0.327	<0.02	13.43	11.07	124.63	23.59	47.96	4.98	22.72	2.42
CC37-3-4	0.02	0.02	0.01	0.04	0.53	<0.03	16.38	11.96	125.38	22.54	44.93	4.32	20.63	2.16
CC37-3-5	0.12	0.06	0.02	0.08	0.78	0.03	16.14	11.90	121.46	21.96	41.75	4.26	19.90	2.02
CC21 - Poikiloblastic garnet														
CC21-1-1	0.00	0.02	<0.01	0.12	1.33	0.02	25.32	9.03	65.52	12.04	27.95	3.26	18.65	2.06
CC21-1-2	<0.02	<0.01	0.01	0.17	2	<0.03	27.94	9.05	60.16	11.21	29.59	4.10	25.17	3.26
CC21-1-3	<0.02	<0.02	0.01	0.07	1.85	<0.03	24.20	7.98	59.61	11.85	33.99	4.84	30.00	3.83
CC21-1-4	<0.01	0.02	0.02	0.56	1.61	0.06	6.63	3.50	48.36	15.57	54.16	9.27	62.20	7.89
CC21-1-5	<0.01	<0.02	0.03	0.53	0.87	<0.02	6.87	4.05	47.06	12.76	38.86	6.05	41.90	5.34
CC21-1-6	<0.02	0.01	0.01	0.35	0.8	0.04	9.47	4.58	48.33	10.09	25.22	3.63	25.10	2.82
CC21-1-7	<0.01	<0.02	0.01	0.35	1.33	0.04	11.30	5.09	41.33	6.75	13.91	1.88	12.51	1.23
CC21-1-8	<0.01	0.00	<0.01	0.51	1.57	0.06	14.35	5.73	41.08	5.59	10.19	1.29	7.37	0.61
CC21-1-9	<0.00	<0.01	<0.01	0.37	1.64	0.09	15.80	6.41	49.12	8.36	17.29	2.21	14.99	1.45
CC21-1-10	<0.01	0.01	<0.01	0.38	2.08	0.10	18.69	7.86	64.29	11.22	26.81	4.26	27.20	2.90
CC21-1-11	0.04	<0.02	<0.01	0.27	2.26	0.07	21.19	8.63	74.37	14.81	37.33	5.71	38.35	4.36
CC21-1-12	0.01	0.02	<0.01	0.29	1.63	0.12	18.52	8.21	78.76	16.02	39.18	5.59	36.82	3.86
CC21-1-13	0.00	0.01	0.02	0.12	1.01	0.09	15.04	7.89	90.41	23.54	66.79	9.27	59.46	7.14
CC21-1-14	<0.00	0.02	0.02	0.32	0.9	0.08	12.46	7.09	85.18	22.65	65.84	9.44	59.20	6.84
CC21-1-15	<0.01	0.02	0.02	0.28	1.01	0.05	11.68	6.64	83.86	23.29	71.08	10.60	72.10	8.85
CC21-1-16	<0.01	<0.02	0.02	0.57	0.85	0.04	8.76	5.52	76.40	23.36	78.04	12.85	89.39	11.98
CC21-1-17	<0.00	0.03	<0.01	0.23	1.12	0.03	8.31	5.07	75.14	25.38	86.01	13.77	95.20	12.07
CC21-1-18	<0.01	0.02	0.02	0.45	1.7	0.03	8.28	4.83	70.63	25.24	90.30	14.68	99.11	12.28
CC21-1-19	<0.00	0.01	0.03	0.44	2.41	0.02	8.05	3.87	56.68	22.32	86.62	14.57	97.75	12.41
CC21-1-20	0.01	0.03	0.02	0.45	3.36	0.02	22.16	6.68	47.48	10.47	29.59	4.65	31.19	4.10
CC21-1-21	<0.02	0.09	0.02	0.25	2.31	0.01	23.44	8.32	63.71	13.33	33.72	4.37	27.73	3.10
CC21 - Smaller garnet														
CC21-4-1	<0.01	<0.00	0.01	0.06	1.56	0.02	26.24	11.01	93.47	21.46	58.34	7.86	48.0	6.15
CC21-4-2	<0.01	0.01	<0.01	<0.00	1.41	<0.02	29.16	10.66	92.35	20.59	53.51	7.41	45.9	5.08
CC21-4-3	<0.01	0.00	0.00	0.06	1.43	0.03	27.51	11.22	97.51	21.68	59.94	8.19	50.03	6.63
CC21-5-1	<0.02	0.02	<0.01	0.30	2.62	<0.02	32.01	11.70	97.93	21.65	60.62	8.49	51.01	7.06
CC21-5-2	<0.02	0.01	0.03	0.16	2.49	<0.02	29.39	10.75	89.84	20.00	56.97	7.96	47.49	6.29
CC21-5-3	<0.01	<0.01	<0.01	0.19	2.13	0.03	27.69	10.58	89.82	20.44	54.62	7.87	47.72	6.61

Table A6. Monazite U–Pb data for three samples from Carlos Chagas batholith (CC31, CC37 and CC21). Conc = concordance

Sample-Spot	U [ppm][a]	Pb [ppm][a]	Th [ppm][a]	Th/U[a]	RATIOS							AGES [Ma]						Conc.
					$^{207}Pb/^{235}U$[b]	2σ[d]	$^{206}Pb/^{238}U$[b]	2σ[d]	rho[c]	$^{207}Pb/^{206}Pb$[e]	2σ[d]	$^{207}Pb/^{235}U$	2σ	$^{206}Pb/^{238}U$	2σ	$^{207}Pb/^{206}Pb$	2σ	%
CC31 - Poikiloblastic garnet core																		
CC31-4	127	13	49242	389	0.92704	0.041	0.09873	0.003	0.72	0.06810	0.004	666	29	607	18	872	124	70
CC31-5	108	11	43233	400	0.93353	0.041	0.09861	0.003	0.72	0.06866	0.004	669	29	606	18	889	122	68
CC31-6	437	40	58696	134	0.74887	0.028	0.09190	0.003	0.78	0.05910	0.003	568	21	567	16	571	100	99
CC31-7	160	16	49028	306	0.94444	0.039	0.09826	0.003	0.75	0.06971	0.004	675	28	604	18	920	109	66
CC31-8	924	81	43353	47	0.71985	0.023	0.08816	0.002	0.88	0.05922	0.002	551	18	545	15	575	67	95
CC31-9	1297	109	25826	20	0.66692	0.021	0.08380	0.002	0.89	0.05772	0.002	519	16	519	14	519	62	100
CC31-10	304	29	50342	166	0.85508	0.030	0.09606	0.003	0.83	0.06456	0.003	627	22	591	16	760	82	78
CC31-11	403	37	43574	108	0.75784	0.030	0.09219	0.003	0.73	0.05962	0.003	573	22	569	16	590	114	96
CC31-12	908	83	70836	78	0.74881	0.026	0.09180	0.003	0.83	0.05916	0.002	568	19	566	15	573	83	99
CC31-13	968	90	38498	40	0.75154	0.024	0.09251	0.003	0.89	0.05892	0.002	569	18	570	15	564	61	101
CC31-18	133	13	40799	306	0.82848	0.034	0.09715	0.003	0.74	0.06185	0.003	613	25	598	17	669	116	89
CC31-19	170	17	56080	329	0.87498	0.040	0.09757	0.003	0.67	0.06504	0.004	638	29	600	17	776	139	77
CC31-20	556	49	38179	69	0.72531	0.025	0.08907	0.003	0.84	0.05906	0.002	554	19	550	15	570	80	97
CC31-21	428	43	36190	85	0.85105	0.030	0.10127	0.003	0.83	0.06095	0.002	625	22	622	17	638	82	98
CC31-26	436	39	34134	78	0.73260	0.025	0.09047	0.003	0.84	0.05873	0.002	558	19	558	15	557	78	100
CC31-27	490	49	40841	83	0.82989	0.028	0.09975	0.003	0.85	0.06034	0.002	614	21	613	17	616	76	100
CC31 - Poikiloblastic garnet rim																		
CC31-1	2156	167	59002	27	0.62398	0.021	0.07728	0.002	0.85	0.05856	0.002	492	16	480	13	551	76	87
CC31-2	1746	147	47720	27	0.66918	0.021	0.08423	0.002	0.90	0.05762	0.002	520	16	521	14	515	60	101
CC31-3	1897	159	48184	25	0.67777	0.023	0.08377	0.002	0.84	0.05868	0.002	525	17	519	14	555	78	93
CC31 - Matrix																		
CC31-14	1054	83	39467	37	0.61785	0.020	0.07892	0.002	0.89	0.05678	0.002	488	15	490	13	482	64	102
CC31-15	1098	86	39716	36	0.61185	0.020	0.07814	0.002	0.87	0.05679	0.002	485	16	485	13	483	72	100
CC31-16	1071	88	29341	27	0.66404	0.021	0.08206	0.002	0.89	0.05869	0.002	517	16	508	14	556	61	91
CC31-22	1039	81	41619	40	0.61290	0.020	0.07837	0.002	0.87	0.05672	0.002	485	16	486	13	480	72	101
CC31-23	901	74	38777	43	0.64841	0.021	0.08180	0.002	0.87	0.05749	0.002	507	17	507	14	510	71	99
CC31-24	704	65	42149	60	0.74471	0.025	0.09195	0.003	0.86	0.05874	0.002	565	19	567	15	558	73	102
CC31-25	613	55	37456	61	0.73597	0.024	0.09044	0.003	0.86	0.05902	0.002	560	18	558	15	568	71	98
CC31-28	334	33	32828	98	0.82710	0.029	0.09963	0.003	0.82	0.06021	0.002	612	22	612	17	611	85	100
CC31-29	613	55	61587	100	0.76081	0.027	0.09031	0.003	0.82	0.06110	0.002	574	20	557	15	643	86	87
CC31-30	638	60	59410	93	0.81173	0.028	0.09465	0.003	0.84	0.06220	0.002	603	21	583	16	681	78	86
CC31-31	497	45	60256	121	0.79464	0.028	0.09086	0.003	0.82	0.06343	0.003	594	21	561	16	723	84	78
CC31-32	930	78	62195	67	0.70684	0.025	0.08411	0.002	0.83	0.06095	0.002	543	19	521	14	638	82	82
CC31-33	2039	153	15254	7	0.60247	0.019	0.07522	0.002	0.88	0.05809	0.002	479	15	468	13	533	67	88
CC31-34	1313	104	44744	34	0.64451	0.022	0.07900	0.002	0.85	0.05917	0.002	505	17	490	13	573	78	86
CC31-35	1381	105	45882	33	0.63460	0.022	0.07585	0.002	0.84	0.06068	0.002	499	17	471	13	628	78	75

Continued Table A6. Monazite U–Pb data for three samples from Carlos Chagas batholith (CC31, CC37 and CC21). Conc = concordance

Sample-Spot	U [ppm][a]	Pb [ppm][a]	Th [ppm][a]	Th/U[a]	RATIOS							AGES [Ma]						Conc.
					$^{207}Pb/^{235}U$[b]	2σ[d]	$^{206}Pb/^{238}U$[b]	2σ[d]	rho[c]	$^{207}Pb/^{206}Pb$[e]	2σ[d]	$^{207}Pb/^{235}U$	2σ	$^{206}Pb/^{238}U$	2σ	$^{207}Pb/^{206}Pb$	2σ	%
CC37 - Poikiloblastic garnet core																		
CC37-3	4207	388	70420	17	0.75064	0.022	0.09218	0.003	0.91	0.05906	0.001	569	17	568	15	570	51	100
CC37-4	4999	401	91004	18	0.65108	0.020	0.08028	0.002	0.90	0.05882	0.002	509	15	498	13	561	57	89
CC37-5	4330	389	76618	18	0.72428	0.022	0.08984	0.002	0.91	0.05847	0.001	553	16	555	14	548	54	101
CC37-6	5614	465	66095	12	0.64660	0.019	0.08284	0.002	0.91	0.05661	0.001	506	15	513	13	476	54	108
CC37-7	5171	464	63037	12	0.72458	0.022	0.08977	0.002	0.91	0.05854	0.001	553	16	554	14	550	53	101
CC37-8	4381	392	38083	9	0.71895	0.023	0.08944	0.002	0.87	0.05830	0.002	550	17	552	14	540	70	102
CC37 - Poikiloblastic garnet rim																		
CC37-1	5724	488	88041	15	0.68928	0.021	0.08528	0.002	0.91	0.05862	0.001	532	16	528	14	553	54	95
CC37-2	5981	552	75289	13	0.74970	0.022	0.09233	0.003	0.92	0.05889	0.001	568	17	569	15	563	52	101
CC37 - Matrix																		
CC37-9	7311	656	58481	8	0.72401	0.022	0.08970	0.002	0.90	0.05854	0.002	553	17	554	15	550	57	101
CC37-10	7309	674	80594	11	0.74157	0.022	0.09219	0.003	0.91	0.05834	0.001	563	17	569	15	542	56	105
CC37-11	3991	355	82780	21	0.72038	0.022	0.08884	0.002	0.90	0.05881	0.002	551	17	549	14	560	57	98
CC37-12	4276	392	66486	16	0.74394	0.023	0.09173	0.003	0.90	0.05882	0.002	565	17	566	15	560	57	101
CC37-13	3638	331	74511	20	0.73949	0.023	0.09095	0.003	0.89	0.05897	0.002	562	17	561	15	566	59	99
CC37-14	4198	349	105457	25	0.67559	0.021	0.08302	0.002	0.89	0.05902	0.002	524	16	514	14	568	63	91
CC37-15	1635	151	21946	13	0.75310	0.024	0.09231	0.003	0.87	0.05917	0.002	570	18	569	15	573	68	99
CC37-16	3805	348	63575	17	0.72639	0.024	0.09140	0.003	0.87	0.05764	0.002	554	18	564	15	516	71	109
CC37-17	3512	304	41914	12	0.69601	0.022	0.08666	0.002	0.89	0.05825	0.002	536	17	536	14	539	62	99
CC37-18	1670	110	15762	9	0.51696	0.017	0.06601	0.002	0.89	0.05680	0.002	423	14	412	12	483	64	85
CC37-19	1314	77	10569	8	0.46639	0.015	0.05833	0.002	0.89	0.05799	0.002	389	13	366	10	529	65	69
CC37-20	8616	672	71461	8	0.61011	0.019	0.07800	0.002	0.90	0.05673	0.002	484	15	484	13	481	59	101
CC21 - Poikiloblastic garnet core																		
CC21-13	524	48	42708	81	0.75082	0.040	0.09169	0.003	0.56	0.05939	0.005	569	30	566	16	581	186	97
CC21-14	2929	223	68347	23	0.61986	0.020	0.07621	0.002	0.86	0.05899	0.002	490	16	473	13	567	72	84
CC21-15	1457	126	60823	42	0.70257	0.022	0.08657	0.002	0.88	0.05886	0.002	540	17	535	14	562	64	95
CC21-16	3930	328	58770	15	0.66342	0.021	0.08336	0.002	0.90	0.05772	0.002	517	16	516	14	519	60	99
CC21-17	2905	232	61964	21	0.64461	0.020	0.07989	0.002	0.89	0.05852	0.002	505	16	495	13	549	63	90
CC21-18	2435	218	59383	24	0.72721	0.024	0.08947	0.003	0.86	0.05895	0.002	555	18	552	15	565	71	98
CC21 - Smaller garnet core																		
CC21-4	5274	438	53124	10	0.66063	0.020	0.08314	0.002	0.91	0.05763	0.001	515	16	515	14	516	56	100
CC21-8	3010	219	28724	10	0.59447	0.019	0.07278	0.002	0.86	0.05924	0.002	474	16	453	12	576	73	79
CC21 - Matrix																		
CC21-1	1503	133	56199	37	0.71701	0.024	0.08823	0.003	0.85	0.05894	0.002	549	18	545	15	565	75	96
CC21-2	1656	152	30421	18	0.74395	0.023	0.09156	0.003	0.90	0.05893	0.002	565	18	565	15	565	58	100
CC21-3	939	87	49035	52	0.74913	0.025	0.09226	0.003	0.85	0.05889	0.002	568	19	569	16	563	77	101

Continued Table A6. Monazite U–Pb data for three samples from Carlos Chagas batholith (CC31, CC37 and CC21). Conc = concordance

Sample-Spot	U [ppm][a]	Pb [ppm][a]	Th [ppm][a]	Th/U[a]	RATIOS							AGES [Ma]						Conc.
					$^{207}Pb/^{235}U$[b]	2σ[d]	$^{206}Pb/^{238}U$[b]	2σ[d]	rho[c]	$^{207}Pb/^{206}Pb$[e]	2σ[d]	$^{207}Pb/^{235}U$	2σ	$^{206}Pb/^{238}U$	2σ	$^{207}Pb/^{206}Pb$	2σ	%
CC21-9	4149	325	19936	5	0.61055	0.019	0.07836	0.002	0.90	0.05651	0.002	484	15	486	13	472	59	103
CC21-10	1095	93	106345	97	0.69417	0.023	0.08513	0.002	0.85	0.05914	0.002	535	18	527	14	572	77	92
CC21-11	1113	92	114751	103	0.66793	0.022	0.08233	0.002	0.86	0.05884	0.002	519	17	510	14	561	72	91
CC21-12	1155	106	135160	117	0.75383	0.034	0.09212	0.003	0.64	0.05935	0.004	570	25	568	15	580	145	98
CC21-19	2712	231	53551	20	0.68876	0.022	0.08523	0.002	0.88	0.05861	0.002	532	17	527	14	553	65	95
CC21-20	2137	196	38807	18	0.74557	0.024	0.09176	0.003	0.86	0.05893	0.002	566	18	566	15	564	71	100
CC21-21	2345	198	73500	31	0.68785	0.023	0.08457	0.002	0.85	0.05899	0.002	532	18	523	14	567	74	92
CC21-22	1994	182	57623	29	0.74369	0.024	0.09145	0.003	0.88	0.05898	0.002	565	18	564	15	567	64	100
CC21-23	2588	235	113951	44	0.73553	0.026	0.09091	0.003	0.81	0.05868	0.002	560	20	561	15	555	89	101
CC21-24	3072	277	125122	41	0.72589	0.024	0.09004	0.003	0.86	0.05847	0.002	554	18	556	15	547	72	102
CC21-25	4373	341	110209	25	0.60888	0.020	0.07787	0.002	0.87	0.05671	0.002	483	15	483	13	480	69	101
Itambé monazite - Primary standard																		
A_117	1883	160	51197	27	0.67538	0.021	0.08504	0.002	0.89	0.05760	0.002	524	16	526	14	514	63	102
A_133	2111	176	57102	27	0.66222	0.022	0.08321	0.002	0.85	0.05772	0.002	516	17	515	14	519	76	99
A_100	1858	159	78169	42	0.68177	0.022	0.08543	0.002	0.88	0.05788	0.002	528	17	529	14	525	65	101
A_145	2097	176	74001	35	0.66834	0.020	0.08411	0.002	0.91	0.05763	0.001	520	16	521	14	515	57	101
A_157	1981	167	70056	35	0.67039	0.021	0.08450	0.002	0.91	0.05754	0.001	521	16	523	14	512	56	102
A_171	1872	157	65221	35	0.66824	0.021	0.08385	0.002	0.90	0.05780	0.002	520	16	519	14	522	58	99
A_184	1681	141	57497	34	0.66414	0.021	0.08380	0.002	0.88	0.05748	0.002	517	16	519	14	510	68	102
A_198	1808	149	73228	41	0.65353	0.022	0.08226	0.002	0.84	0.05762	0.002	511	17	510	14	515	78	99
Thompson Mine - Secondary standard																		
A_116	1481	470	66996	45	4.74024	0.14	0.31730	0.009	0.91	0.10835	0.003	1774	54	1777	43	1772	45	100
A_132	1446	456	66923	46	4.68860	0.15	0.31524	0.009	0.89	0.10787	0.003	1765	55	1766	43	1764	51	100
A_144	1510	476	94430	63	4.69248	0.14	0.31553	0.009	0.93	0.10786	0.002	1766	53	1768	43	1764	41	100
A_170	1597	507	84791	53	4.69181	0.14	0.31722	0.009	0.92	0.10727	0.002	1766	53	1776	43	1754	42	101
A_183	1498	478	85233	57	4.73585	0.14	0.31889	0.009	0.92	0.10771	0.003	1774	54	1784	43	1761	44	101
A_197	1355	427	93067	69	4.70121	0.14	0.31492	0.009	0.91	0.10827	0.003	1767	54	1765	43	1770	46	100

[a]U and Pb concentrations and Th/U ratios are calculated relative to reference monazite USGS 44069

[b]Corrected for background and within-run Pb/U fractionation and normalised to reference monazite USGS 44069 (ID-TIMS values/measured value); $^{207}Pb/^{235}U$ calculated using $(^{207}Pb/^{206}Pb)/(^{238}U/^{206}Pb * 1/137.88)$

[c]Rho is the error correlation defined as the quotient of the propagated errors of the $^{206}Pb/^{238}U$ and the $^{207}/^{235}U$ ratio

[d]Quadratic addition of within-run errors (2 SD) and daily reproducibility of reference monazite USGS 44069

[e]Corrected for mass-bias by normalising to GJ-1 reference zircon (~0.6 per atomic mass unit) and common Pb using the model Pb composition of Stacey & Kramers (1975)

Table A 7. Zircon U–Pb data for three samples from Carlos Chagas batholith (CC31, CC37 and CC21). Conc = concordance

Sample-Spot	U [ppm][a]	Pb [ppm][a]	Th/U[a]	RATIOS							AGES [Ma]						Conc.
				$^{207}Pb/^{235}U$[b]	2σ[d]	$^{206}Pb/^{238}U$[b]	2σ[d]	rho[c]	$^{207}Pb/^{206}Pb$[e]	2σ[d]	$^{207}Pb/^{235}U$	2σ	$^{206}Pb/^{238}U$	2σ	$^{207}Pb/^{206}Pb$	2σ	%
CC31 - Poikiloblastic garnet core																	
CC31-4	71	7	2.4	0.78302	0.026	0.09176	0.002	0.70	0.06189	0.003	587	20	566	13	670	101	84
CC31-5	66	6	1.3	0.74200	0.024	0.09146	0.002	0.74	0.05884	0.003	564	18	564	13	561	94	100
CC31-6	58	5	1.5	0.73276	0.060	0.09097	0.002	0.30	0.05842	0.009	558	46	561	13	546	325	103
CC31 - Poikiloblastic garnet rim																	
CC31-7	69	6	1.3	0.69749	0.045	0.08743	0.002	0.39	0.05786	0.007	537	34	540	13	524	249	103
CC31-8	171	15	0.2	0.70928	0.022	0.08810	0.002	0.73	0.05839	0.002	544	17	544	12	544	92	100
CC31 - Matrix - Magmatic zircon																	
CC31-15	47	4	1.76	0.76572	0.079	0.09503	0.002	0.24	0.05844	0.012	577	60	585	14	546	412	107
CC31-16	41	4	0.88	0.76651	0.050	0.09348	0.002	0.36	0.05947	0.007	578	38	576	13	584	254	99
CC31-17	34	3	1.23	0.76603	0.049	0.09415	0.002	0.39	0.05901	0.007	577	37	580	14	568	245	102
CC31-18	54	5	1.14	0.75779	0.028	0.09347	0.002	0.66	0.05880	0.003	573	21	576	13	560	119	103
CC31-19	88	8	1.29	0.76524	0.024	0.09331	0.002	0.74	0.05948	0.003	577	18	575	13	585	91	98
CC31 - Matrix - Metamorphic zircon																	
CC31-1	116	11	1.78	0.74261	0.025	0.09104	0.002	0.67	0.05916	0.003	564	19	562	12	573	107	98
CC31-2	292	27	0.01	0.74862	0.021	0.09173	0.002	0.78	0.05919	0.002	567	16	566	12	574	75	99
CC31-3	56	5	0.70	0.75061	0.034	0.09185	0.002	0.50	0.05927	0.005	569	26	567	12	577	168	98
CC31-10	113	10	1.06	0.69178	0.023	0.08649	0.002	0.70	0.05801	0.003	534	18	535	12	530	104	101
CC31-11	169	15	2.51	0.73409	0.022	0.08998	0.002	0.75	0.05917	0.002	559	17	555	12	574	86	97
CC31-12	115	10	0.46	0.73954	0.021	0.09045	0.002	0.80	0.05930	0.002	562	16	558	12	578	75	97
CC31-13	121	11	0.24	0.74074	0.021	0.09017	0.002	0.80	0.05958	0.002	563	16	557	12	588	74	95
CC31-14	70	6	1.65	0.74239	0.034	0.09143	0.002	0.50	0.05889	0.005	564	26	564	13	563	169	100
CC31-21	45	4	1.10	0.67850	0.045	0.08502	0.002	0.39	0.05788	0.007	526	35	526	13	525	258	100
CC31-22	63	5	1.21	0.67966	0.028	0.08518	0.002	0.62	0.05787	0.004	527	21	527	13	525	138	100
CC31-24	53	5	1.23	0.68082	0.062	0.08534	0.002	0.26	0.05786	0.010	527	48	528	12	524	365	101
CC31-25	104	9	1.53	0.67623	0.032	0.08500	0.002	0.50	0.05770	0.005	524	25	526	12	518	174	102
CC31-26	86	7	0.98	0.64315	0.027	0.07894	0.002	0.59	0.05909	0.004	504	21	490	12	571	145	86
CC31-27	36	3	2.11	0.74950	0.050	0.09136	0.002	0.37	0.05950	0.007	568	38	564	13	586	256	96
CC31-28	46	4	2.35	0.75908	0.040	0.09259	0.002	0.45	0.05946	0.006	573	31	571	13	584	200	98
CC31-29	58	5	1.85	0.73303	0.035	0.09040	0.002	0.49	0.05881	0.005	558	27	558	13	560	178	100
CC21 - Poikiloblastic garnet core																	
CC21-1	309	28	0.07	0.73996	0.021	0.09093	0.002	0.77	0.05902	0.002	562	16	561	12	568	78	99
CC21-2	906	83	0.06	0.76508	0.032	0.09125	0.002	0.53	0.06081	0.004	577	24	563	12	633	149	89
CC21-3	599	55	0.09	0.74559	0.019	0.09184	0.002	0.86	0.05888	0.002	566	14	566	12	563	55	101
CC21-4	1039	96	0.03	0.75096	0.019	0.09247	0.002	0.86	0.05890	0.002	569	15	570	12	564	58	101
CC21-5	421	38	0.07	0.73948	0.020	0.09084	0.002	0.83	0.05904	0.002	562	15	561	12	569	65	99
CC21-6	361	33	0.39	0.74895	0.021	0.09205	0.002	0.78	0.05901	0.002	568	16	568	12	568	76	100

Continued Table A 7. Zircon U–Pb data for three samples from Carlos Chagas batholith (CC31, CC37 and CC21). Conc = concordance

Sample-Spot	U [ppm][a]	Pb [ppm][a]	Th/U[a]	RATIOS							AGES [Ma]						Conc.
				$^{207}Pb/^{235}U$[b]	2σ[d]	$^{206}Pb/^{238}U$[b]	2σ[d]	rho[c]	$^{207}Pb/^{206}Pb$[e]	2σ[d]	$^{207}Pb/^{235}U$	2σ	$^{206}Pb/^{238}U$	2σ	$^{207}Pb/^{206}Pb$	2σ	%
CC21-7	746	69	0.09	0.75202	0.020	0.09210	0.002	0.84	0.05922	0.002	569	15	568	12	575	61	99
CC21-8	1082	97	0.06	0.73494	0.021	0.08960	0.002	0.78	0.05949	0.002	559	16	553	12	585	76	95
CC21-9	1008	66	0.04	0.53798	0.016	0.06561	0.001	0.74	0.05947	0.002	437	13	410	9	585	84	70
CC21 - Poikiloblastic garnet rim																	
CC21-10	825	61	0.03	0.60888	0.018	0.07457	0.002	0.75	0.05922	0.002	483	14	464	10	575	84	81
CC37 - Inherited zircon																	
CC37-1	165	16	0.49	0.81656	0.022	0.09818	0.002	0.83	0.06032	0.002	606	16	604	13	615	65	98
CC37-6	182	15	0.52	0.70884	0.027	0.08252	0.002	0.68	0.06230	0.003	544	20	511	13	684	115	75
CC37-8	434	50	0.10	1.00589	0.028	0.11580	0.003	0.82	0.06300	0.002	707	19	706	15	708	66	100
CC37-18	1568	155	0.03	0.81674	0.020	0.09871	0.002	0.89	0.06001	0.001	606	15	607	13	604	48	101
CC37-22	145	14	0.28	0.80338	0.022	0.09742	0.002	0.82	0.05981	0.002	599	16	599	13	597	68	100
CC37-26	610	60	0.08	0.81133	0.021	0.09773	0.002	0.85	0.06021	0.002	603	16	601	13	611	60	98
CC37-33	487	46	0.27	0.79040	0.029	0.09469	0.002	0.63	0.06054	0.003	591	22	583	13	623	121	94
CC37-36	1143	112	0.06	0.81034	0.020	0.09792	0.002	0.88	0.06002	0.001	603	15	602	13	604	51	100
CC37-38	1501	127	0.10	0.70666	0.019	0.08484	0.002	0.80	0.06041	0.002	543	15	525	11	618	69	85
CC37-43	230	23	0.31	0.81476	0.033	0.09777	0.002	0.55	0.06044	0.004	605	24	601	13	619	143	97
CC37-45	414	41	0.27	0.82390	0.021	0.09926	0.002	0.86	0.06020	0.002	610	16	610	13	611	56	100
CC37-47	1913	176	0.02	0.78767	0.023	0.09217	0.002	0.77	0.06198	0.002	590	17	568	12	673	78	84
CC37-55	249	25	0.10	0.83818	0.022	0.10068	0.002	0.84	0.06038	0.002	618	16	618	13	617	62	100
CC37-58	309	31	0.12	0.83049	0.022	0.09969	0.002	0.84	0.06042	0.002	614	16	613	13	619	61	99
CC37-60	384	38	0.29	0.83371	0.022	0.09932	0.002	0.85	0.06088	0.002	616	16	610	13	635	59	96
CC37-63	1097	110	0.03	0.92775	0.027	0.10007	0.002	0.75	0.06724	0.003	666	20	615	13	845	81	73
CC37 - Magmatic zircon																	
CC37-11	1798	167	0.02	0.75691	0.021	0.09273	0.002	0.80	0.05920	0.002	572	16	572	12	575	70	99
CC37-13	347	32	0.46	0.75886	0.021	0.09300	0.002	0.81	0.05918	0.002	573	16	573	12	574	71	100
CC37-23	405	38	0.43	0.77297	0.021	0.09328	0.002	0.83	0.06010	0.002	581	16	575	12	607	64	95
CC37-30	111	10	0.56	0.76916	0.040	0.09404	0.002	0.43	0.05932	0.006	579	30	579	12	579	196	100
CC37-39	849	79	0.03	0.76059	0.019	0.09293	0.002	0.87	0.05936	0.001	574	14	573	12	580	53	99
CC37-40	289	27	0.06	0.76940	0.020	0.09407	0.002	0.85	0.05932	0.002	579	15	580	12	579	60	100
CC37-41	230	22	0.92	0.77798	0.022	0.09472	0.002	0.78	0.05957	0.002	584	17	583	12	588	77	99
CC37-50	308	29	0.91	0.75345	0.023	0.09251	0.002	0.73	0.05907	0.003	570	18	570	12	570	91	100
CC37-52	282	26	0.28	0.76952	0.020	0.09369	0.002	0.84	0.05957	0.002	579	15	577	12	588	60	98
CC37-53	265	25	0.54	0.76708	0.020	0.09355	0.002	0.84	0.05947	0.002	578	15	577	12	584	61	99
CC37-54	735	68	0.33	0.75767	0.020	0.09298	0.002	0.82	0.05910	0.002	573	15	573	12	571	66	100
CC37-56	2878	206	0.06	0.58863	0.015	0.07151	0.002	0.86	0.05970	0.002	470	12	445	9	593	56	75
CC37-62	804	75	0.06	0.76533	0.019	0.09354	0.002	0.87	0.05934	0.002	577	15	576	12	580	54	99
CC37-65	1683	158	0.03	0.77282	0.020	0.09406	0.002	0.87	0.05959	0.002	581	15	580	12	589	54	98

Continued Table A7. Zircon U–Pb data for three samples from Carlos Chagas batholith (CC31, CC37 and CC21). Conc = concordance

Sample-Spot	U [ppm][a]	Pb [ppm][a]	Th/U[a]	RATIOS							AGES [Ma]						Conc.
				$^{207}Pb/^{235}U$[b]	2σ[d]	$^{206}Pb/^{238}U$[b]	2σ[d]	rho[c]	$^{207}Pb/^{206}Pb$[e]	2σ[d]	$^{207}Pb/^{235}U$	2σ	$^{206}Pb/^{238}U$	2σ	$^{207}Pb/^{206}Pb$	2σ	%
CC37-67	320	30	0.88	0.76766	0.023	0.09362	0.002	0.76	0.05947	0.002	578	17	577	12	584	82	99
CC37-11	1798	167	0.02	0.75691	0.021	0.09273	0.002	0.80	0.05920	0.002	572	16	572	12	575	70	99
CC37 - Metamorphic zircon																	
CC37-2	1640	121	0.03	0.62297	0.017	0.07367	0.002	0.83	0.06133	0.002	492	14	458	10	651	65	70
CC37-3	609	53	0.05	0.72717	0.020	0.08643	0.002	0.79	0.06102	0.002	555	15	534	11	640	73	84
CC37-10	726	66	0.08	0.74306	0.019	0.09108	0.002	0.88	0.05917	0.001	564	14	562	12	574	51	98
CC37-14	1978	147	0.03	0.65970	0.018	0.07433	0.002	0.83	0.06437	0.002	514	14	462	10	754	63	61
CC37-15	5328	409	0.01	0.65757	0.017	0.07681	0.002	0.87	0.06209	0.002	513	13	477	10	677	54	70
CC37-16	1023	88	0.08	0.69253	0.019	0.08636	0.002	0.79	0.05816	0.002	534	15	534	11	535	75	100
CC37-17	4761	340	0.01	0.63755	0.017	0.07149	0.002	0.83	0.06468	0.002	501	13	445	10	764	63	58
CC37-19	1785	153	0.01	0.69936	0.021	0.08581	0.002	0.72	0.05911	0.003	538	16	531	11	571	91	93
CC37-20	3844	300	0.03	0.65349	0.017	0.07812	0.002	0.84	0.06067	0.002	511	13	485	10	628	61	77
CC37-21	1611	125	0.02	0.62332	0.016	0.07749	0.002	0.86	0.05834	0.002	492	13	481	10	543	58	89
CC37-24	388	30	0.04	0.67793	0.025	0.07667	0.002	0.61	0.06413	0.004	526	19	476	10	746	122	64
CC37-25	1626	123	0.08	0.64831	0.018	0.07557	0.002	0.78	0.06222	0.002	507	14	470	10	682	75	69
CC37-27	428	37	0.03	0.68470	0.025	0.08590	0.002	0.59	0.05781	0.003	530	20	531	11	522	128	102
CC37-28	277	24	0.43	0.68928	0.021	0.08566	0.002	0.73	0.05836	0.002	532	16	530	11	544	89	97
CC37-29	322	30	0.14	0.74545	0.019	0.09176	0.002	0.85	0.05892	0.002	566	15	566	12	564	60	100
CC37-31	1053	96	0.06	0.74902	0.021	0.09147	0.002	0.79	0.05939	0.002	568	16	564	12	582	73	97
CC37-32	620	53	0.11	0.69008	0.020	0.08598	0.002	0.76	0.05821	0.002	533	16	532	11	537	84	99
CC37-34	672	62	0.04	0.74770	0.020	0.09199	0.002	0.82	0.05895	0.002	567	15	567	12	565	67	100
CC37-35	1173	82	0.04	0.56996	0.015	0.06951	0.002	0.86	0.05947	0.002	458	12	433	9	585	56	74
CC37-46	1532	130	0.02	0.68012	0.019	0.08490	0.002	0.77	0.05810	0.002	527	15	525	11	533	79	99
CC37-48	2426	216	0.02	0.72143	0.019	0.08906	0.002	0.84	0.05875	0.002	552	14	550	12	558	59	99
CC37-49	474	43	0.14	0.74518	0.022	0.09137	0.002	0.76	0.05915	0.002	565	16	564	12	573	81	98
CC37-51	351	30	0.12	0.68847	0.018	0.08609	0.002	0.84	0.05800	0.002	532	14	532	11	529	64	101
CC37-64	1194	101	0.02	0.68153	0.019	0.08493	0.002	0.77	0.05820	0.002	528	15	526	11	537	80	98
CC37-66	220	19	0.16	0.70086	0.036	0.08636	0.002	0.43	0.05886	0.005	539	28	534	11	562	196	95

[a]U and Pb concentrations and Th/U ratios are calculated relative to GJ-1 reference zircon

[b]Corrected for background and within-run Pb/U fractionation and normalised to reference zircon GJ-1 (ID-TIMS values/measured value); $^{207}Pb/^{235}U$ calculated using $(^{207}Pb/^{206}Pb)/(^{238}U/^{206}Pb * 1/137.88)$

[c]Rho is the error correlation defined as the quotient of the propagated errors of the $^{206}Pb/^{238}U$ and the $^{207}/^{235}U$ ratio

[d]Quadratic addition of within-run errors (2 SD) and daily reproducibility of GJ-1 (2 SD)

[e]Corrected for mass-bias by normalising to GJ-1 reference zircon (~0.6 per atomic mass unit) and common Pb using the model Pb composition of Stacey & Kramers (1975)

APPENDIX B

Supplementary material to the manuscript presented in chapter 4

B.1. U-Pb geochronology

Zircons were separated from nine rock samples at the Department of Geology (DEGEO), Universidade Federal de Ouro Preto, Brazil. The zircon extraction technique makes use of jaw crusher, milling, manual panning, heavy liquids separation, hand-picking under a binocular microscope and mounting on 25 mm epoxy (SpeciFix) mounts. Mounts were polished to expose the grain centers and imaged under SEM-cathodoluminescence (CL) in a JEOL 6510 Scanning Electron Microscope hosted at DEGEO.

U-Pb analysis for seven rock samples were performed using an Agilent 7700x quadrupole ICP-MS coupled to a 213 NdYAG laser (New Wave Research UP-213) at DEGEO. The standard and unknown zircons were ablated in a small volume (tear-drop shape) sample cell, with an insert that holds one 25 mm diameter sample mount and a 7 mm diameter standard mount.

Acquisitions consisted of a 20 s measurement of the gas blank, followed by a 40 s measurement of U, Th and Pb signals during ablation, and 30 s washout (e.g. Lana *et al.*, 2010, 2013; Buick *et al.*, 2011). Samples and standards, as well as sample holders were acid-washed before being analyzed to remove possible surface Pb contamination. Laser ablations were carried out at 30 µm spot size, 6–8 J/cm^2 fluence and 10 Hz repetition rate. Ablations were performed using He as a carrier gas mixed with Ar prior to introduction into the ICP-MS. Integration times were 15 ms for ^{206}Pb and ^{238}U, 40 ms for ^{207}Pb and 10 ms for ^{208}Pb; ^{204}Pb + ^{204}Hg and ^{232}Th. Details of the LA-Q-ICP-MS analytical procedures are described in Takenaka *et al.* (2015). The zircon GJ1 (Jackson *et al.*, 2004) was used as primary reference material and for quality control were used the Plešovice (Sláma *et al.*, 2008) and BB (Santos *et al.*, 2016) zircons as secondary standard. Two hundred and forty analyses of the GJ-1 reference zircon yield a weighted mean ages of 609 ± 7 Ma (^{207}Pb/^{206}Pb, MSWD = 0.52), 609 ± 6 Ma (^{206}Pb/^{238}U, MSWD = 0.83) and 609 ± 6 Ma (^{207}Pb/^{235}U, MSWD = 1.06). Sixty-four analyses of the Plešovice give weighted mean ages of 341 ± 7 Ma (^{207}Pb/^{206}Pb, MSWD = 0.54), 341 ± 2 Ma (^{206}Pb/^{238}U, MSWD = 0.97) and 341 ± 2 Ma (^{207}Pb/^{235}U, MSWD = 1.3). Twenty- three analysis of the BB standard yield weighted mean ages of 560 ± 18 Ma (^{207}Pb/^{206}Pb, MSWD = 0.20), 555 ± 6 Ma (^{206}Pb/^{238}U, MSWD = 1.14) and 555 ± 6 Ma (^{207}Pb/^{235}U, MSWD = 0.68). The results were consistently in good agreement with the published ID-TIMS ages. The data were reduced using the software Glitter (Van Achterbergh et al., 2001) and the weighted mean ^{206}Pb/^{238}U ages and concordia plots, as well as the probability density diagrams were processed using Isoplot 4.15 (Ludwig, 2003). Analytical uncertainties on single spot ages and on weighted mean ages are based on the quadratic addition of the average mean error (given by Isoplot) and the 1% error inherent precision of the technique and final ages are quoted at the 95% confidence interval.

U-Pb analysis for two samples were carried out using a Thermo-Finnigan Element 2 sector field ICP-MS coupled to a CETAC ultraviolet laser system (LA-SF-ICP-MC) housed at DEGEO. Data were acquired in peak jumping mode during 20 s background measurement followed by 20 s sample ablation and spot size of 20 µm. Data were corrected for background signal, common Pb, laser-induced elemental fractionation, instrumental mass discrimination, and time-dependent elemental fractionation of Pb/U using a MS Excel spreadsheet program (Gerdes and Zeh, 2006). The common-Pb correction was based on the Pb composition model (Stacey and Kramers, 1975). Laser-induced elemental fractionation and instrumental mass discrimination were corrected by normalization to the reference zircon GJ-1 (Jackson *et al.*, 2004). Accuracy and reproducibility was checked by repeated analyses of reference zircon Plešovice (Sláma *et al.*, 2008), Blue Berry (Santos *et al.*, 2016) and 91500 (Blichert-Toft, 2008).

B.2. Lu-Hf isotope

Lu-Hf analyses were carried out using a Thermo-Scientific Finnigan Neptune MC-ICP-MS, at the Institut für Petrologie, Geochemie und Lagerstättenkunde, Universität Frankfurt (Germany), following the instrumentation and analytical methods described by Gerdes and Zeh (2006, 2009). Three-hundred Lu–Hf analysis were performed on individual zircons on the same spots originally used for U–Pb analyses.

Data were collected in static mode during 60 s of ablation with a spot size of 50 µm. The isotopes ^{172}Yb, ^{173}Yb and ^{175}Lu were simultaneously monitored during each analysis step to allow the correction of isobaric interferences between ^{176}Lu and ^{176}Yb isotopes. The correction for instrumental mass bias utilized an exponential law and $^{172}Yb/^{173}Yb$ and $^{179}Hf/^{177}Hf$ values of 1.35351 (mean of Chu *et al.*, 2002; Segal *et al.*, 2003) and 0.7325 (Patchett *et al.*, 1981), respectively. The mass bias of Yb (β_{Yb}) isotopes typically differs from that of the Hafnium (β_{Hf}) with an offset of β_{Hf}/β_{Yb}, calculated for each analytical session by averaging the β_{Hf}/β_{Yb} of multiple analyses of the Temora reference material. The mass bias behaviour of Lu was assumed to follow that of Yb. For Yb-rich zircons, the β_{Hf}/β_{Yb} offset factor was determined from the mean β_{Yb} of each analysis. For Yb-poor zircon crystals, the applied correction was calculated using the β_{Hf} of each integration step divided by the average β_{Hf}/β_{Yb} offset factor of the whole analytical session. It is important to note that any under- or over-correction for Yb and Lu interference on mass 176 would result in an apparent correlation of the $^{176}Hf/^{177}Hf$ and $^{176}Yb/^{177}Yb$ ratios. The dataset presented in this study has been examined by plotting $^{176}Hf/^{177}Hf$ against $^{176}Yb/^{177}Yb$ (Fig. S1), and the results show insignificant interference by Yb, testifying of the good quality of the data.

The accuracy and external reproducibility was checked by repeated analyses of the reference zircons GJ-1 (Jackson *et al.*, 2004), Plešovice (Sláma *et al.*, 2008), Temora (Black *et al.*, 2003; Wu *et al.*, 2006), BB (Santos *et al.*, 2016) which yielded $^{176}Hf/^{177}Hf$ of 0.282016 ± 0.000020 (n = 31), 0.282490 ± 0.000017 (n = 18), 0.282683 ± 0.000020 (n = 16), 0.281677 ± 0.000023 (n = 27) respectively (data given as mean with 2 SD

uncertainties).These ratios are in good agreement with the recommended values of 0.282000 ± 0.000005 (GJ-1), 0.282482 ± 0.000013 (Plešovice), 0.282680 ± 0.000031 (Temora) and 0.281674 ± 0.000018 (Blue Berry).

Figure S1. $^{176}Hf/^{177}Hf$ versus $^{176}Yb/^{177}Hf$ for the GJ-1, Temora, Plešovice and BB standards. The apparent lack of correlation for the Temora analyses suggests that accurateYb interference corrections were applied.

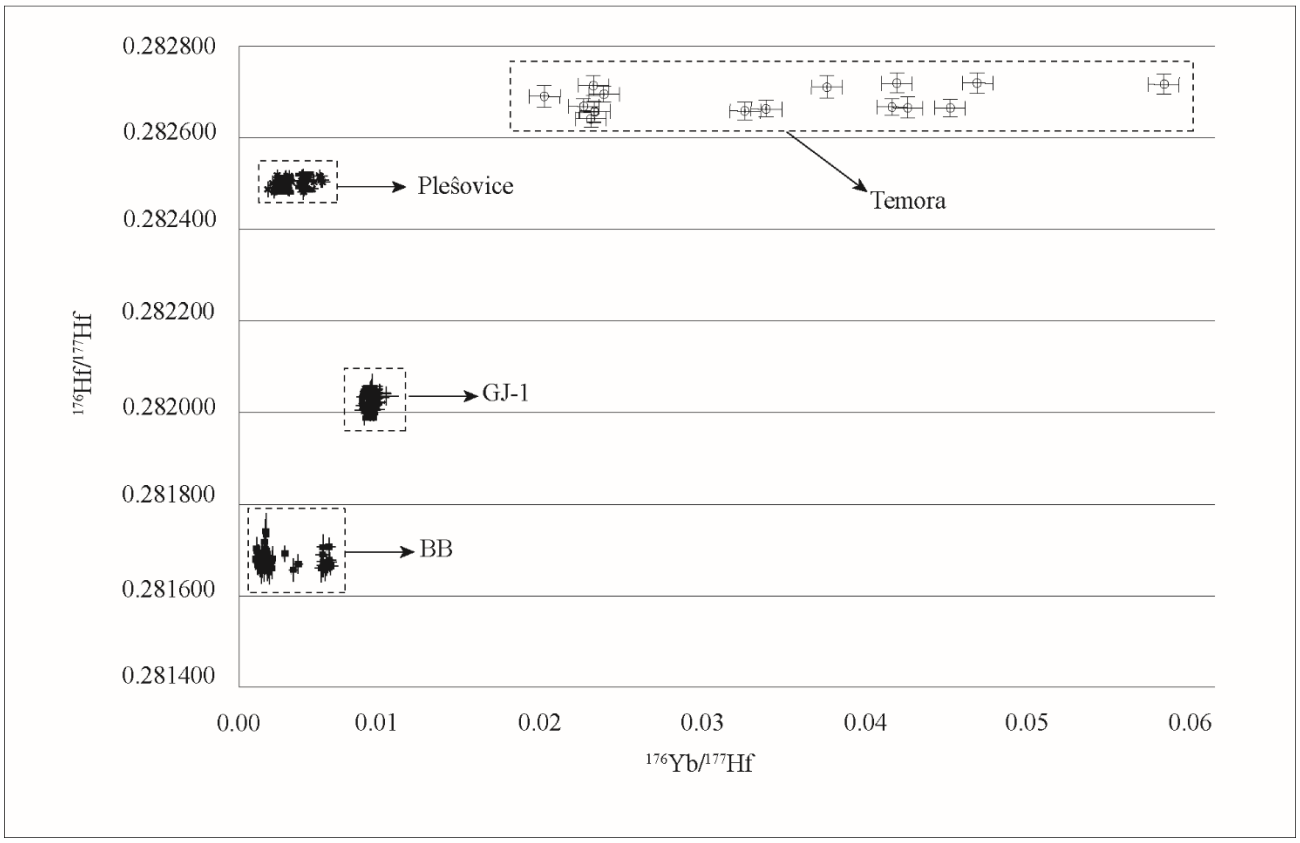

B.3. Trace elements in zircon

Trace element analysis of zircon was performed using a Thermo-Scientific Finnigan Element 2 SF-ICP-MS, at the LOPAG, Universidade Federal de Ouro Preto (Brazil). Acquisitions consisted of a 20 s measurement of the gas blank, followed by a 40 s measurement ^{49}Ti, ^{139}La, ^{140}Ce, ^{141}Pr, ^{142}Nd, ^{147}Sm, ^{153}Eu, ^{157}Gd, ^{159}Tb, ^{163}Dy, ^{165}Ho, ^{166}Er, ^{169}Tm, ^{174}Yb, ^{175}Lu, and 30 s washout (e.g. Lana et al., 2010, 2013; Buick et al., 2011). Samples and standards, as well as sample holders were acid-washed before being analyzed to remove possible surface Pb contamination. Laser ablations were carried out at 30 µm spot size, 6–8 J/cm^2 fluence and 10 Hz repetition rate. Ablations were performed using He as a carrier gas mixed with Ar prior to introduction into the ICP-MS. Data was reduced using Glitter software.

B.4. Sample and zircon description and isotopic results

Sample CC12 (18º45’47’’S/41º7’49.3’’W) was collected from outcrop on MG-381, a few kilometers from east of Mantena (Fig. 2, Table 1). Zircon grains are subhedral to euhedral prismatic, light pink,

translucent, ranging from 150 to 800 µm, with length/width ratios in average of 4:1. CL images of the internal structure of the zircons shows that they have a core with oscillatory-zoned patterns or irregular zoning, which are generally surrounded by low luminescence and structureless rim (Fig. 4). Some inherited cores were identified as unzoned rounded areas that appear luminescent in CL images. Two out of three spot analyses done in these areas give a weighted mean $^{206}Pb/^{238}U$ age of 631 ± 10 Ma (MSWD = 0.0053, Th/U = 0.21-0.28) and one other analysis show a $^{206}Pb/^{238}U$ age of 613 ± 12 Ma (2σ, Th/U = 0.42) (Fig. 5a,b). Fourteen spot analyses on zoning domains yield a weighted mean $^{206}Pb/^{238}U$ age of 580 ± 7 Ma (MSWD = 1.7, Th/U = 0.19-0.85), considered as the crystallization age (Fig. 5a,b). Six out of seven analyses performed on low luminescence rims yield a weighted mean $^{206}Pb/^{238}U$ age of 562 ± 9 Ma (MSWD = 1.7, Th/U = 0.18-0.42) and a single analysis show a $^{206}Pb/^{238}U$ age of 534 ± 10 Ma (2σ, Th/U = 0.26) (Fig. 5a,b), interpreted as anatectic and metamorphic ages, respectively. Two analyses on the ca. 631-613 Ma inherited cores yield initial $^{176}Hf/^{177}Hf$ ratios ranging from 0.282284 to 0.282324, with εHf(t) values between -3.4 and -4.0. The distribution of model age (T_{DM}) spans from 1440 to 1490 Ma. Eight analyses done on magmatic zircons gives initial $^{176}Hf/^{177}Hf$ ratios ranging from 0.282201 to 0.282386 and εHf(t) between -8.2 and -1.8. Six analyses performed on anatectic/metamorphic domains yield initial $^{176}Hf/^{177}Hf$ ratios between 0.282266 and 0.282344.

Sample CC18 (18º41'1.2''S/40º45'44.4''W) was taken from the Stone Mining, southeast of Paulista (Fig. 2, Table 1). The common zircon population is represented by pale pink to colorless, translucent and prismatic grains exhibiting rounded to subrounded, or subhedral to euhedral crystal faces. They range from 90 to 450 µm and have length/width ratios predominantly of 4:1, although lower ratios of 2:1 and 3:1 can be observed. CL imaging shows different internal structures such as strongly luminescent inherited and weakly zoned magmatic cores, frequently truncated by darker structureless overgrowths (Fig 4). The spot analyses plot on the concordia yield $^{206}Pb/^{238}U$ ages ranging from ca. 738 to 501 Ma (Fig. 5c). Based on thirteen spot analyses of the luminescent inherited core, four age populations were identified and yield a weighted mean $^{206}Pb/^{238}U$ ages of: 726 ± 11 Ma (n = 3, MSWD = 0.93, Th/U = 0.01-0.22); 660 ± 10 Ma (n = 2, MSWD = 1.6, Th/U = 0.04-0.09); 629 ± 11 Ma (n = 2, MSWD = 0.62, Th/U = 0.12-2.24); and 602 ± 7 Ma (n = 8, MSWD = 0.42, Th/U =0.07-0.92) (Fig. 5d). Fourteen spot analyses on weak oscillatory zoned domains give a weighted mean $^{206}Pb/^{238}U$ age of 584 ± 7 Ma (MSWD = 1.7, Th/U = 0.08-0.33), indicating the crystallization age (Fig. 5d). Twelve out of thirty-two spot analyses done on the darker and structureless zircon rim yielded a weighted mean $^{206}Pb/^{238}U$ age of 563 ± 7.0 Ma (MSWD = 1.5, Th/U = 0.04-1.27), representing the time of the first anatectic event. Other twenty analyses give younger weighted mean $^{206}Pb/^{238}U$ ages of 525 ± 6 Ma (MSWD = 0.92, Th/U = 0.03-0.71) and 509 ± 6 Ma (MSWD = 0.95, Th/U = 0.04-1.25) (Fig. 5d), corresponds to the time of the other anatectic event recorded in the batholith. Seven analyses on the ca. 597-655 Ma inherited cores yield initial $^{176}Hf/^{177}Hf$ ratios ranging from 0.282204 to 0.282366, with εHf(t) values between -2.1 and -6.7. The distribution of model age (T_{DM}) spans from 1350 to 1630 Ma. Eight analyses done on magmatic zircons gives initial $^{176}Hf/^{177}Hf$ ratios ranging from 0.282253 to 0.282346 and εHf(t) between -6.4 and -2.9. Seventeen analyses performed on anatectic/metamorphic domains yield initial $^{176}Hf/^{177}Hf$ ratios between 0.282203 and 0.282381.

Sample CC30 (18º55'54.4"S/41º45'17.3"W) was extracted from ES-080 road, north of Águia Branca (Fig. 2, Table 1). Zircon grains are light pink to colorless, translucent and prismatic with their terminations rounded or subhedral. The grains range from 100 to 500 µm in length and have variable length/width ratios from 2:1 to 7:1. They dominantly show weak or irregular oscillatory zoning and some grains have homogeneous and high luminescence inherited cores. Most the grains exhibit structureless and low luminescence rims (Fig. 4). Data from eleven spot analyses done on inherited core yield a weighted mean $^{206}Pb/^{238}U$ age of 604 ± 8 Ma (MSWD = 1.4, Th/U = 0.04-2.23) (Fig. 5f). The weighted mean $^{206}Pb/^{238}U$ age of twenty-three spot analyses performed on weakly zoned domains is 578 ± 6 Ma (MSWD = 1.3, Th/U = 0.24-2.29) (Fig. 5f), interpreted as crystallization age. Spot analysis from CL-dark rims give a anatectic age with weighted mean $^{206}Pb/^{238}U$ ages of 564 ± 7 Ma (n = 10, MSWD = 1.13, Th/U = 0.07-1.09) and a metamorphic age of 507 ± 8 Ma (n = 2, MSWD = 1.15, Th/U = 0.42-0.48) (Fig. 5f). Four analyses on the ca. 596-606 Ma inherited cores yield initial $^{176}Hf/^{177}Hf$ ratios ranging from 0.282281 to 0.282340, with εHf(t) values between -2.7 and -4.8. The distribution of model age (T_{DM}) spans from 1400 to 1510 Ma. Fourteen analyses done on magmatic zircons gives initial $^{176}Hf/^{177}Hf$ ratios ranging from 0.282305 to 0.282377 and εHf(t) between -4.6 and -2.2. Seven analyses performed on anatectic/metamorphic domains yield initial $^{176}Hf/^{177}Hf$ ratios between 0.282312 and 0.282374.

Sample CC34 (18º33'17.9''S/40º58'13.6''W) was taken from outcrop exposed on ES-080, near of Água Doce (Fig. 2, Table 1). Zircons from this sample are light pink to colorless, translucent, subhedral to euhedral prismatic and rounded grains with a length from 120 to 530 µm and have length/width ratios ranging from 2:1 to 6:1. The zircon grains generally contain rounded or subhedral prismatic cores showing weak oscillatory zoning or no zoning. The core is commonly surrounded by large unzoned domains that exhibit low luminescence on CL images (Fig. 4). Twenty-three spot analyses performed on inherited core give a weighted mean $^{206}Pb/^{238}U$ age of 607 ± 7 Ma (MSWD = 0.83, Th/U = 0.08-1.20). Three cores measured yield oldest ages of 739 ± 25 Ma (2σ, Th/U = 0.39), 644 ± 17 Ma (2σ, Th/U = 0.13) and 630 ± 11 Ma (2σ, Th/U = 0.08) (Fig. 5h). Other forty-three spot analyses done on the zoned domains yield a weighted mean $^{206}Pb/^{238}U$ age of 581 ± 6 Ma (MSWD = 1.2, Th/U = 0.04-1.55) (Fig. 5h), considered as the crystallization age. Forty-three spot analyses done on low-CL zircon rims do not cluster around a single age. The $^{206}Pb/^{238}U$ ages from individual zircon rims can be grouped in four age populations with weighted mean of 561 ± 6 Ma (n = 18, MSWD = 0.87, Th/U = 0.04-1.23), 533 ± 6 Ma (n = 11, MSWD = 0.88, Th/U = 0.03-0.44), 513 ± 8 Ma (n = 9, MSWD = 1.6, Th/U = 0.01-0.09), and 483 ± 7 Ma (n = 5, MSWD = 0.43, Th/U = 0.02-0.18) (Fig. 5h). Twenty-two analyses on the ca. 597-739 Ma inherited cores yield initial $^{176}Hf/^{177}Hf$ ratios ranging from 0.282245 to 0.282300, with εHf(t) values between -3.0 and -6.2. The distribution of model age (T_{DM}) spans from 1480 to 1580 Ma. Twenty-six analyses done on magmatic zircons gives initial $^{176}Hf/^{177}Hf$ ratios ranging from 0.282248 to 0.282309 and εHf(t) between -4.5 and -6.2. Thirteen analyses performed on anatectic/metamorphic domains yield initial $^{176}Hf/^{177}Hf$ ratios between 0.282251 and 0.282307.

Sample CC35a (18º41'26.4"S/40º54'22.4"W) was collected from granite exposed on ES-080 road a few km from Barra do São Francisco (Fig.2, Table 1). Zircon grains are light pink to colorless, short- and long-prismatic, exhibiting rounded or subhedral to euhedral terminations. They range from 90 to 480 µm in length and have length/width ratios of 2:1 to 4:1 (Fig. 4). In CL-images (Fig. 4), many grains show rounded or subhedral to euhedral cores with oscillatory or no zoning. Inherited cores are generally resorbed by structureless dark rims, whilst the magmatic zircons display subhedral to euhedral faces surrounded by thin CL-dark domains. Spot analyses done on inherited cores yield weighted mean $^{206}Pb/^{238}U$ ages of 625 ± 9 Ma (n = 5, MSWD = 0.69, Th/U = 0.02-0.40) and 610 ± 7 Ma (n = 8, MSWD = 1.02, Th/U = 0.02-0.50). Other two spot analyses have oldest inherited ages of 736 ± 16 Ma (2σ, Th/U = 0.24) and 651 ± 14 Ma (2σ, Th/U = 0.54) (Fig. 6b). Taken into consideration the oscillatory zoned magmatic cores, forty-one spot analyses give a weighted mean $^{206}Pb/^{238}U$ age of 581 ± 6 Ma (MSWD = 1.3, Th/U = 0.10-0.66) (Fig. 6b). The dark-CL rims data show two age populations, with a weighted mean $^{206}Pb/^{238}U$ ages of 560 ± 6 Ma (n = 14, MSWD = 1.16, Th/U = 0.05-0.43) and 504 ± 7 Ma (n = 4, MSWD = 0.39, Th/U = 0.05-0.14) (Fig. 6b), corresponding to the time of the anatectic events. Ten analyses on the ca. 607-736 Ma inherited cores yield initial $^{176}Hf/^{177}Hf$ ratios ranging from 0.282268 to 0.282325, with εHf(t) values between -1.9 and -5.2. The distribution of model age (T_{DM}) spans from 1430 to 1530 Ma. Twenty-five analyses done on magmatic zircons gives initial $^{176}Hf/^{177}Hf$ ratios ranging from 0.282274 to 0.282345 and εHf(t) between -3.2 and -5.8. Twelve analyses performed on anatectic/metamorphic domains yield initial $^{176}Hf/^{177}Hf$ ratios between 0.282253 and 0.282357.

Sample CC36 (18º20'19.3''S/40º47'59.7"W) was extracted from outcrop on ES-320 road between Ecoporanga and Imburana (Fig. 2, Table 1). Zircons are light pink to colorless, translucent, subhedral to euhedral prismatic grains with a length from 90 to 480 µm and length/width ratios less than 5:1. Zircons predominantly display well-developed oscillatory zoning typical of magmatic origin (Fig. 4). Inherited cores commonly exhibit oscillatory and convolute zoning, although structureless and medium luminescence cores can be observed. Thin structureless CL-dark rims are present in some grains. Nine spot analyses performed on inherited core yield a weighted mean $^{206}Pb/^{238}U$ age of 605 ± 7 Ma (MSWD = 0.76, Th/U = 0.04-0.33) and two spots present oldest ages of 635 ± 8 Ma (2σ, Th/U = 0.28) and 622 ± 6 Ma (2σ, Th/U = 0.30) (Fig. 6d). Spot analyses in fourteen oscillatory zoning magmatic crystals give a weighted mean $^{206}Pb/^{238}U$ age of 585 ± 7 Ma (MSWD = 0.76, Th/U = 0.04-0.50) (Fig. 6d). Seven spot analyses obtained in the structureless rim yield a weighted mean $^{206}Pb/^{238}U$ age of 557 ± 8 Ma (MSWD = 1.5, Th/U = 0.03-0.18) (Fig. 6d), indicating the time of the first anatectic event in the batholith. Eight analyses on the ca. 597-635 Ma inherited cores yield initial $^{176}Hf/^{177}Hf$ ratios ranging from 0.282268 to 0.282301, with εHf(t) values between -3.7 and -5.2. The distribution of model age (T_{DM}) spans from 1460 to 1530 Ma. Two analyses done on magmatic zircons gives initial $^{176}Hf/^{177}Hf$ ratios ranging from 0.282228 to 0.282257 and εHf(t) between -6.0 and -6.9. Four analyses performed on anatectic/metamorphic domains yield initial $^{176}Hf/^{177}Hf$ ratios between 0.282283 and 0.282303.

Sample CC40 (18º14'43"S/41º43'47.5"W) was collected in outcrop on ES-320 road between Cotaxé and Imburana (Fig. 2, Table 1). The grains are colorless to light pink, prismatic, and length of individual grains

varies between 100 and 750 µm. Their length/width ratios range from 2:1 to 7:1, with an average of 3:1. Most of the CL-defined cores (Fig. 4) display oscillatory or convolute zoning, whilst a few zircon cores are unzoned and have bright luminescence. These cores are commonly enveloped by internally structureless, unzoned and dark domains. Four out of eight spot analyses performed on CL-defined inherited cores yield a weighted mean $^{206}Pb/^{238}U$ age of 621 ± 13 Ma (MSWD = 1.3, Th/U = 0.11-0.27). Four individual zircon grains give oldest ages of 826 ± 15 (2σ, Th/U = 0.24), 714 ± 17 (2σ, Th/U = 0.04), 693 ± 11 (2σ, Th/U = 0.44) and 678 ± 12 Ma (2σ, Th/U = 0.65) (Fig. 4f). Twenty-one spot analyses yield a weighted mean $^{206}Pb/^{238}U$ age of 588 ± 7 Ma (MSWD = 1.5, Th/U = 0.04-0.86) (Fig. 4f). Analyses in seven rim domains give a weighted mean $^{206}Pb/^{238}U$ age of 563 ± 8 Ma (MSWD = 1.3, Th/U = 0.01-0.49) (Fig. 4f), interpreted as anatectic age. Seven analyses on the ca. 614-826 Ma inherited cores yield initial $^{176}Hf/^{177}Hf$ ratios ranging from 0.282070 to 0.282327, with εHf(t) values between -1.4 and -7.4. The distribution of model age (T_{DM}) spans from 1390 to 1830 Ma. Sixteen analyses done on magmatic zircons gives initial $^{176}Hf/^{177}Hf$ ratios ranging from 0.282238 to 0.282352 and εHf(t) between -6.9 and -2.8. Seven analyses performed on anatectic/metamorphic domains yield initial $^{176}Hf/^{177}Hf$ ratios between 0.282273 and 0.282341.

Sample CC42 (18º3'59"S/40º46'28.8"W) was taken from outcrop near Cotaxé (Fig. 2, Table 1). The zircons are characterized by light pink to colorless, rounded to prismatic grains, ranging from 100 to 750 µm. They have length/width ratios that range from 2:1 to 7:1. Cl-images (Fig. 4) reveal that most of the zircons are complexly zoned, with subrounded to subhedral, unzoned or oscillatory zoned cores. They are frequently truncated by structureless dark overgrowths around the cores. Analyses in inherited cores indicate two distinct age populations with a weighted mean $^{206}Pb/^{238}U$ ages of 618 ± 8 Ma (n = 5, MSWD = 0.74, Th/U = 0.16-0.26) and 603 ± 7 Ma (n = 8, MSWD = 0.31, Th/U = 0.10-0.32) (Fig. 6h). Sixty-one spot analyses done on magmatic cores yield a weighted mean $^{206}Pb/^{238}U$ age of 586 ± 6 Ma (MSWD = 1.5, Th/U = 0.04-0.55) (Fig. 6h). Twenty-nine spot analyses in dark metamorphic overgrowths give a weighted mean $^{206}Pb/^{238}U$ ages of 569 ± 6 Ma (n = 26, MSWD = 1.5, Th/U = 0.01-0.44) and 520 ± 8 Ma (n = 3, MSWD = 1.02, Th/U = 0.02-0.11) (Fig. 6h). Eleven analyses on the ca. 601-623 Ma inherited cores yield initial $^{176}Hf/^{177}Hf$ ratios ranging from 0.282250 to 0.282371, with εHf(t) values between -1.8 and -5.3. The distribution of model age (T_{DM}) spans from 1340 to 1550 Ma. Forty-four analyses done on magmatic zircons gives initial $^{176}Hf/^{177}Hf$ ratios ranging from 0.282243 to 0.282345 and εHf(t) between -6.5 and -3.0. Twenty analyses performed on anatectic/metamorphic domains yield initial $^{176}Hf/^{177}Hf$ ratios between 0.282266 and 0.282381.

Sample CC47 (18º53'4.2"S/40º37'48.3"W) was extracted from outcrop near Invejada Peak, southeast of Barra do São Francisco (Fig. 2, Table 1). Zircons are light pink to colorless, translucent, subhedral to euhedral prismatic grains with a length from 100 to 450 µm and length/width ratios less than 4:1. Zircons predominantly display well-developed oscillatory zoning typical of magmatic origin (Fig. 4). Inherited zircons are characterized by structureless and medium luminescence cores. Thin structureless CL-dark rims are present in some grains. Twenty-five spot analyses performed on inherited core yield a weighted mean $^{206}Pb/^{238}U$ age of 612 ± 9 Ma (MSWD = 0.67, Th/U = 0.04-0.33) and two spot analyses present oldest age of 716 ± 6 Ma (2σ,

Th/U = 0.01) and 658 ± 12 Ma (2σ, Th/U = 0.32) (Fig. 7b). Spot analyses in seventeen oscillatory zoning magmatic crystals give a weighted mean $^{206}Pb/^{238}U$ age of 578 ± 9 Ma (MSWD = 0.29, Th/U = 0.02-0.58) (Fig. 7b). Seven spot analyses obtained in the structureless rim yield a weighted mean $^{206}Pb/^{238}U$ age of 552 ± 12 Ma (MSWD = 0.18, Th/U = 0.04-0.15) (Fig. 7b), indicating the time of the anatectic event.

References cited

Black, L.P., Kamo, S.L., Allen, C.M., Aleinikoff, J.N., Davis, D.W., Korsch, R.J., Foudoulis,C., 2003. TEMORA 1 a new zircon standard for phanerozoic U–Pb geochronology. *Chemical Geology*, 200, 155–170.

Blichert-Toft, J., 2008. The Hf isotopic composition of zircon reference material 91500. *Chemical Geology* 253, 252-257.

Buick, I.S., Lana, C., Gregory, C., 2011. A LA-ICP-MS and SHRIMP U/Pb age constraint on the timing of REE mineralisation associated with Bushveld granites. *South African Journal of Geology* 144, 1–14.

Chu, N.C., Taylor, R.N., Chavagnac, V., Nesbitt, R.W., Boella, R.M., Milton, J.A., German, C.R., Bayon, G., Burton, K., 2002. Hf isotope ratio analysis using multi-collector inductively coupled plasma mass spectrometry: an evaluation of isobaric interference corrections. *Journal of Analytical Atomic Spectrometry* 17, 1567-1574.

Gerdes, A., Zeh, A., 2006. Combined U–Pb and Hf isotope LA-(MC-)ICP-MS analyses of detrital zircons: comparison with SHRIMP and new constraints for the provenance and age of an Armorican metasediment in central Germany. *Earth and Planetary Science Letters* 249, 47–61.

Gerdes, A., Zeh, A., 2009. Zircon formation versus zircon alteration – new insights from combined U–Pb and Lu–Hf in situ LA-ICP-MS analyses, and consequences for the interpretation of Archean zircon from the Limpopo Belt. *Chemical Geology* 261, 230–243.

Jackson, S.E., Pearson, N.J., Griffin, W.L., Belousova, E.A., 2004. The application of laser ablation-inductively coupled plasma-mass spectrometry to in situ U–Pb zircon geochronology. *Chemical Geology* 211, 47–69.

Lana, C., Kisters, A., Stevens, G., 2010. Exhumation of Mesoarchaean TTG gneisses from the middle crust: insights from the Steynsdorp core complex, Barberton granitoid–greenstone terrain South Africa. *Geological Society of America Bulletin* 122, 183-197.

Lana, C., Alkmim, F.F., Armstrong, R., Scholz, R., Romano, R., Nalini Jr., H.A., 2013. The ancestry and magmatic evolution of Archaean TTG rocks of the Quadrilátero Ferrífero province, southeast Brazil. *Precambrian Research* 231, 157-173.

Ludwig, K.R., 2003. Mathematical-statistical treatment of data and errors for Th/U geochronology. *Reviews in Mineralogy and Geochemistry* 52, 631-656.

Patchett, P.J., Kouvo, O., Hedge, C.E., Tatsumoto, M., 1981. Evolution of continental crust and mantle heterogeneity: evidence from Hf isotopes. *Contributions to Mineralogy and Petrology* 78, 279-297.

Santos, M.M., Lana, C., Scholz, R., Buick, I., Kamo, S.L., Gerdes, A., Condon, D.J., Corfu,F., Tohver, E., Storey, C.D., Basei, M.A.S., Krambrock, K., Fantini, C., 2016. BB zircon– a new Sri Lankan reference material for U–Pb and Hf isotopic laser ablation ICP-MS analysis. (submitted for publication).

Segal, I., Halicz, L., Platzner, I.T., 2003. Accurate isotope ratio measurements of ytterbium by multi-collector inductively coupled plasma mass spectrometry applying erbium and hafnium in an improved double external normalisation procedure. *Journal of Analytical Atomic Spectrometry* 18, 1217-1223.

Sláma, J., Kosler, J., Condon, D.J., Crowley, J.L., Gerdes, A., Hanchar, J.M., Horstwood, M.S.A., Morris, G.A., Nasdala, L., Norberg, N., Schaltegger, U., Schoene, B., Tubrett, M.N., Whitehouse, M.J., 2008. Plešovice zircon - a new natural reference material or U-Pb and Hf isotopic microanalysis. *Chemical Geology* 249, 1–35.

Stacey, J.S. & Kramers, J.D., 1975. Approximation of terrestrial lead isotope evolution by a two-stage model. *Earth and Planetary Science Letters* 26, 207–221.

Takenaka, L., Lana, C., Scholz, R., Nalini Jr., H.A., Abreu, A.T., 2015. Optimization of the in-situ U–Pb age dating method via LA-Quadrupole ICP-MS with applications to the timing of U–Zr–Mo mineralization in the Poços de Caldas Alkaline Complex, SE Brazil. *Journal of South American Earth Sciences* 62, 70–79.

van Achterbergh, E., Ryan, C.G., Jackson, S.E., Griffin, W., 2001. Data reduction software for LAICP-MS. In: Sylvester, P. (Ed.), Laser-ablation-ICP-MS in the Earth sciences, principles and applications. Mineralogical Association of Canada. Short Course Series 29, pp. 239–243.

Wu, F.-Y., Yang, Y.-H., Xie, L.-W., Yang, J.-H., Xu, P., 2006. Hf isotopic compositions of the standard zircons and baddeleyites in U–Pb geochronology. *Chemical Geology* 234, 105–126.

LA-Q-ICP-MS U-Pb results - Sample CC12

	PPM			Ratios						Ages (Ma)							
Spot	**^{206}Pb**	**^{238}U**	**Th^{b}/U**	**^{207}Pb/^{206}Pb**	**± 2σ (abs)**	**^{206}Pb^{a}/^{238}U**	**± 2σ (abs)**	**^{207}Pb^{a}/^{235}U**	**± 2σ (abs)**	**^{207}Pb/^{206}Pb**	**± 2σ**	**^{206}Pb/^{238}U**	**± 2σ**	**^{207}Pb/^{235}U**	**± 2σ**	**Rho^{c}**	**Conc.^{d}**
Inherited - Population ca. 630-620 Ma																	
CC12-30	113	246	0.28	0.06084	0.00182	0.10290	0.00188	0.86309	0.02352	634	64	631	11	632	13	0.67	100
CC12-32	94	209	0.21	0.06110	0.00244	0.10279	0.00212	0.86597	0.03210	643	85	631	12	633	17	0.56	100
Average	104	228	0.25	0.06097	0.00213	0.10285	0.00200	0.86453	0.02781	638	74	631	12	633	15	0.61	100
SD	9	19	0.04	0.00013	0.00031	0.00005	0.00012	0.00144	0.00429	5	10	0	1	1	2	0.06	0
RSD%	8.77	8.18	15.03	0.21	14.55	0.05	6.00	0.17	15.43	0.71	13.94	0.05	5.99	0.13	15.32	9.30	0.17
Inherited - Population ca.615-600 Ma																	
CC12-76	247	580	0.42	0.06060	0.00214	0.09975	0.00200	0.83349	0.02738	625	75	613	12	616	15	0.61	100
Magmatic																	
CC12-22	231	536	0.40	0.05897	0.00138	0.09463	0.00158	0.76930	0.01564	566	50	583	9	579	9	0.82	101
CC12-27	134	355	0.32	0.05918	0.00200	0.09433	0.00192	0.76950	0.02442	574	73	581	11	580	14	0.64	100
CC12-28	191	476	0.19	0.05883	0.00152	0.09422	0.00170	0.76423	0.0179	561	56	581	10	576	10	0.77	101
CC12-44	194	449	0.35	0.05883	0.00192	0.09455	0.00174	0.76672	0.02294	561	71	582	10	578	13	0.62	101
CC12-45	181	436	0.49	0.05962	0.00154	0.09562	0.00170	0.78605	0.01838	590	56	589	10	589	10	0.76	100
CC12-51	137	361	0.42	0.05919	0.00268	0.09193	0.00208	0.74989	0.03198	574	97	567	12	568	19	0.53	100
CC12-53	394	985	0.85	0.05916	0.00130	0.09266	0.00160	0.75580	0.01472	573	48	571	9	572	9	0.89	100
CC12-60	196	471	0.61	0.05849	0.00164	0.09424	0.00168	0.75991	0.01924	548	61	581	10	574	11	0.70	101
CC12-70	177	479	0.60	0.05921	0.00182	0.09236	0.00184	0.75392	0.02166	575	66	570	11	571	13	0.69	100
CC12-84	372	1033	0.27	0.05921	0.00184	0.09281	0.00190	0.75759	0.02218	575	67	572	11	573	13	0.70	100
CC12-91	245	609	0.31	0.05927	0.00148	0.09591	0.00174	0.78384	0.01786	577	54	590	10	588	10	0.80	100
CC12-94	216	570	0.22	0.05929	0.00204	0.09371	0.00192	0.76607	0.02474	578	74	577	11	578	14	0.63	100
CC12-98	75	174	0.31	0.05877	0.00218	0.09437	0.00182	0.76467	0.02614	559	80	581	11	577	15	0.56	101
CC12-105	211	513	0.38	0.06027	0.00212	0.09456	0.00184	0.78589	0.02552	613	75	582	11	589	15	0.60	99
Average	211	532	0.41	0.05916	0.00182	0.09399	0.00179	0.76667	0.02167	573	66	579	11	578	12	0.69	100
SD	82	220	0.17	0.00041	0.00036	0.00113	0.00013	0.01120	0.00455	15	13	7	1	6	3	0.10	1
RSD%	38.81	41.40	41.98	0.69	19.88	1.20	7.46	1.46	21.01	2.62	19.52	1.15	7.54	1.11	21.21	14.37	0.55
Anatectic																	
CC12-69	383	1017	0.42	0.05913	0.00152	0.08988	0.00164	0.73281	0.01712	572	55	555	10	558	10	0.78	99
CC12-71	129	333	0.33	0.05923	0.00240	0.09116	0.00192	0.74438	0.02824	575	87	562	11	565	16	0.56	100
CC12-75	198	526	0.21	0.05959	0.00166	0.09084	0.00172	0.74642	0.01926	589	60	561	10	566	11	0.73	99
CC12-92	218	540	0.26	0.05968	0.00230	0.09044	0.00180	0.74430	0.02650	593	81	558	11	565	15	0.56	99
CC12-106	200	507	0.35	0.05899	0.00182	0.09324	0.00178	0.75845	0.02154	567	66	575	11	573	12	0.67	100
CC12-113	160	451	0.18	0.05918	0.00206	0.09103	0.00192	0.74271	0.02446	574	75	562	11	564	14	0.64	100
Average	215	562	0	0	0	0	0	1	0	578	71	562	11	565	13	1	99
SD	81	215	0	0	0	0	0	0	0	9	11	6	1	4	2	0	0
RSD%	34.37	34.81	25.31	0.54	14.41	1.99	5.21	2.28	14.84	2.08	14.05	1.91	5.21	1.77	14.83	11.86	0.41
Metamorphic																	
CC12-93	169	446	0.26	0.05857	0.00216	0.08634	0.00170	0.69733	0.02370	551	79	534	10	537	14	0.58	99

LA-Q-ICP-MS U-Pb results - Sample CC18

Spot	PPM ^{206}Pb	PPM ^{238}U	Th^{b}/U	Ratios $^{207}Pb/^{206}Pb$	± 2σ (abs)	$^{206}Pb^{a}/^{238}U$	± 2σ (abs)	$^{207}Pb^{a}/^{235}U$	± 2σ (abs)	Ages (Ma) $^{207}Pb/^{206}Pb$	± 2σ	$^{206}Pb/^{238}U$	± 2σ	$^{207}Pb/^{235}U$	± 2σ	Rho[c]	Conc.[d]
Inherited - Population ca. 740-690 Ma																	
CC18-88	661	1290	0.01	0.06360	0.00378	0.12121	0.00322	1.06212	0.05952	728	123	738	19	735	29	0.47	100
CC18-118	252	470	0.16	0.06391	0.00156	0.11897	0.00202	1.04836	0.02250	739	51	725	12	728	11	0.79	100
CC18-38	111	224	0.22	0.06464	0.00174	0.11864	0.00220	1.05731	0.02610	763	57	723	13	733	13	0.75	99
Average	341	661	0.13	0.06405	0.00236	0.11961	0.00248	1.05593	0.03604	743	77	728	14	732	18	0.67	100
SD	233	456	0.09	0.00044	0.00101	0.00114	0.00053	0.00570	0.01667	14	33	7	3	3	8	0.14	1
RSD%	68.36	68.96	67.54	0.68	42.66	0.95	21.31	0.54	46.25	1.93	42.65	0.90	21.31	0.38	46.03	20.98	0.69
Inherited - Population ca. 680-635 Ma																	
CC18-16	571	1131	0.04	0.06288	0.00150	0.10856	0.00176	0.94108	0.01922	704	50	664	10	673	10	0.79	99
CC18-63	173	374	0.09	0.06112	0.00174	0.10692	0.00194	0.90111	0.02330	644	61	655	11	652	12	0.70	100
Average	372	753	0.06	0.06200	0.00162	0.10774	0.00185	0.92110	0.02126	674	55	660	11	663	11	0.75	100
SD	199	378	0.03	0.00088	0.00012	0.00082	0.00009	0.01999	0.00204	30	5	5	1	11	1	0.05	1
RSD%	53.46	50.27	43.88	1.42	7.41	0.76	4.86	2.17	9.60	4.50	9.55	0.73	5.00	1.59	10.68	6.16	0.86
Inherited - Population ca. 630-620 Ma																	
CC18-109	95	241	2.24	0.05994	0.00332	0.10170	0.00264	0.84023	0.04408	601	118	624	15	619	24	0.49	101
CC18-142	262	629	0.12	0.06005	0.00144	0.10299	0.00192	0.85260	0.01870	605	51	632	11	626	10	0.85	101
Average	179	435	1.18	0.06000	0.00238	0.10235	0.00228	0.84642	0.03139	603	84	628	13	623	17	0.67	101
SD	83	194	1.06	0.00005	0.00094	0.00065	0.00036	0.00619	0.01269	2	33	4	2	3	7	0.18	0
RSD%	46.58	44.62	89.58	0.09	39.50	0.63	15.79	0.73	40.43	0.32	39.34	0.60	16.09	0.55	40.74	26.41	0.05
Inherited - Population ca. 615-600 Ma																	
CC18-36	105	260	0.42	0.06076	0.00172	0.09891	0.00188	0.82863	0.02154	631	60	608	11	613	12	0.73	99
CC18-53	166	398	0.10	0.05994	0.00134	0.09820	0.00170	0.81158	0.01612	601	48	604	10	603	9	0.87	100
CC18-82	99	227	0.15	0.06150	0.00212	0.09777	0.00186	0.82904	0.02632	657	73	601	11	613	15	0.60	98
CC18-90	173	406	0.92	0.05945	0.00182	0.09806	0.00182	0.80372	0.02244	584	66	603	11	599	13	0.66	101
CC18-107	220	520	0.14	0.05985	0.00142	0.09699	0.00168	0.80023	0.01672	598	51	597	10	597	9	0.83	100
CC18-113	191	459	0.15	0.05973	0.00140	0.09783	0.00172	0.80567	0.01680	594	50	602	10	600	9	0.84	100
CC18-114	252	576	0.07	0.05909	0.00138	0.09818	0.00166	0.79990	0.01634	571	49	604	10	597	9	0.83	101
CC18-123	138	331	0.29	0.05972	0.00148	0.09744	0.00172	0.80238	0.01784	594	53	599	10	598	10	0.79	100
Average	168	397	0.28	0.06001	0.00159	0.09792	0.00176	0.81014	0.01927	604	56	602	10	603	11	0.77	100
SD	50	113	0.26	0.00072	0.00026	0.00053	0.00008	0.01132	0.00350	26	9	3	0	6	2	0.09	1
RSD%	29.76	28.55	94.10	1.20	16.30	0.54	4.55	1.40	18.17	4.26	15.27	0.52	4.58	1.05	17.65	11.69	0.89
Magmatic																	
CC18-37	83	218	0.25	0.05982	0.00184	0.09605	0.00190	0.79222	0.02270	597	66	591	11	592	13	0.69	100
CC18-42	93	231	0.22	0.06015	0.00164	0.09470	0.00172	0.78530	0.01956	609	59	583	10	589	11	0.73	99
CC18-43	115	287	0.23	0.05990	0.00154	0.09406	0.00168	0.77686	0.01812	600	56	580	10	584	10	0.77	99
CC18-52	183	461	0.08	0.05954	0.00190	0.09559	0.00186	0.78470	0.02326	587	69	589	11	588	13	0.66	100
CC18-80	136	312	0.14	0.06121	0.00162	0.09656	0.00166	0.81482	0.01922	647	56	594	10	605	11	0.73	98
CC18-81	142	330	0.18	0.05960	0.00156	0.09527	0.00164	0.78287	0.01824	589	56	587	10	587	10	0.74	100

Continued.... LA-Q-ICP-MS U-Pb results - Sample CC18

	PPM			Ratios							Ages (Ma)					
Spot	**^{206}Pb**	**^{238}U**	**Th^{b}/U**	**^{207}Pb/^{206}Pb**	**± 2σ (abs)**	**^{206}Pb^{a}/^{238}U**	**± 2σ (abs)**	**^{207}Pb^{a}/^{235}U**	**± 2σ (abs)**	**^{207}Pb/^{206}Pb**	**± 2σ**	**^{206}Pb/^{238}U**	**± 2σ**	**^{207}Pb/^{235}U**	**± 2σ**	**Rho^{c}**	**Conc.^{d}**
CC18-87	141	343	0.28	0.05897	0.00144	0.09465	0.00166	0.76957	0.01688	566	54	583	10	580	10	0.80	101
CC18-93	132	332	0.11	0.05910	0.00144	0.09356	0.00166	0.76239	0.01680	571	53	577	10	575	10	0.81	100
CC18-108	259	623	0.15	0.05906	0.00136	0.09633	0.00166	0.78440	0.01598	569	50	593	10	588	9	0.85	101
CC18-122	102	271	0.07	0.05821	0.00176	0.09383	0.00184	0.75298	0.02122	537	67	578	11	570	12	0.70	101
CC18-129	214	548	0.16	0.05928	0.00138	0.09330	0.00166	0.76250	0.01602	577	50	575	10	576	9	0.85	100
CC18-153	208	499	0.23	0.05967	0.00142	0.09390	0.00160	0.77246	0.01626	592	51	579	9	581	9	0.81	100
CC18-166	123	309	0.33	0.05961	0.00166	0.09623	0.00182	0.79088	0.02038	590	60	592	11	592	12	0.73	100
CC18-173	103	251	0.18	0.05999	0.00164	0.09477	0.00172	0.78379	0.01944	603	59	584	10	588	11	0.73	99
Average	145	358	0.19	0.05958	0.00159	0.09491	0.00172	0.77970	0.01886	588	57	585	10	585	11	0.76	100
SD	50	120	0.07	0.00066	0.00016	0.00106	0.00009	0.01486	0.00232	24	6	6	1	8	1	0.06	1
RSD%	34.38	33.61	39.00	1.11	10.28	1.12	5.31	1.91	12.28	4.11	10.25	1.07	5.26	1.45	12.09	7.44	0.77
Anatectic - Population 1																	
CC18-23	394	1151	0.05	0.06078	0.00166	0.09072	0.00182	0.76016	0.01954	631	58	560	11	574	11	0.78	98
CC18-24	148	407	1.04	0.05815	0.00166	0.09187	0.00178	0.73665	0.01946	535	63	567	11	561	11	0.73	101
CC18-58	187	483	0.28	0.05920	0.00132	0.09203	0.00160	0.75117	0.01476	575	48	568	9	569	9	0.88	100
CC18-94	161	408	0.09	0.05883	0.00138	0.09179	0.00160	0.74457	0.01564	561	51	566	9	565	9	0.83	100
CC18-98	334	847	0.04	0.05862	0.00122	0.09133	0.00154	0.73816	0.01334	553	45	563	9	561	8	0.93	100
CC18-102	98	273	1.27	0.05834	0.00202	0.08971	0.00184	0.72154	0.02352	542	76	554	11	552	14	0.63	100
CC18-111	203	530	0.16	0.05847	0.00130	0.09010	0.00158	0.72629	0.01446	547	49	556	9	554	9	0.88	100
CC18-121	226	583	0.04	0.05838	0.00130	0.09008	0.00156	0.72507	0.01432	544	48	556	9	554	8	0.88	100
CC18-135	124	296	0.95	0.05920	0.00176	0.09235	0.00164	0.75381	0.02016	575	64	569	10	570	12	0.66	100
CC18-144	250	623	0.04	0.05894	0.00132	0.09304	0.00160	0.75611	0.01492	565	48	574	9	572	9	0.87	100
CC18-157	176	490	0.27	0.05823	0.00190	0.09097	0.00186	0.73008	0.02246	538	72	561	11	557	13	0.66	101
CC18-174	135	342	0.17	0.06001	0.00152	0.09124	0.00162	0.75496	0.01734	604	55	563	10	571	10	0.77	99
Average	203	536	0.37	0.05893	0.00153	0.09127	0.00167	0.74155	0.01749	564	56	563	10	563	10	0.79	100
SD	84	239	0.43	0.00075	0.00025	0.00096	0.00011	0.01311	0.00329	28	10	6	1	8	2	0.10	1
RSD%	41.25	44.63	116.91	1.28	16.62	1.05	6.80	1.77	18.83	4.91	17.49	1.01	6.85	1.36	19.05	12.30	0.95
Anatectic - Population 2																	
CC18-103	128	363	0.64	0.05763	0.00156	0.08398	0.00154	0.66728	0.01640	515	59	520	9	519	10	0.75	100
CC18-120	93	277	0.23	0.05723	0.00188	0.08473	0.00170	0.66847	0.02056	500	71	524	10	520	13	0.65	101
CC18-124	100	269	0.50	0.05768	0.00156	0.08553	0.00154	0.68018	0.01676	518	60	529	9	527	10	0.73	100
CC18-125	103	282	0.71	0.05764	0.00152	0.08538	0.00154	0.67849	0.01620	516	58	528	9	526	10	0.76	100
CC18-138	255	660	0.43	0.05778	0.00140	0.08471	0.00142	0.67483	0.01442	521	53	524	8	524	9	0.78	100
CC18-152	282	773	0.09	0.05816	0.00124	0.08563	0.00148	0.68660	0.01296	535	47	530	9	531	8	0.92	100
CC18-160	712	1964	0.03	0.05884	0.00146	0.08459	0.00150	0.68618	0.01538	561	54	524	9	531	9	0.79	99
CC18-169	296	849	0.39	0.05813	0.00140	0.08358	0.00152	0.66981	0.01476	534	54	518	9	521	9	0.83	99
Average	246	680	0.38	0.05789	0.00150	0.08477	0.00153	0.67648	0.01593	525	57	525	9	525	10	0.78	100
SD	194	533	0.23	0.00045	0.00017	0.00069	0.00007	0.00716	0.00210	17	7	4	0	4	1	0.07	1
RSD%	78.77	78.48	60.67	0.79	11.56	0.81	4.89	1.06	13.17	3.28	11.56	0.77	5.09	0.83	13.44	9.22	0.64

Continued... LA-Q-ICP-MS U-Pb results - Sample CC18

	PPM			Ratios								Ages (Ma)					
Spot	**^{206}Pb**	**^{238}U**	**Th^{b}/U**	**^{207}Pb/^{206}Pb ± 2σ (abs)**		**^{206}Pb^{a}/^{238}U ± 2σ (abs)**		**^{207}Pb^{a}/^{235}U ± 2σ (abs)**		**^{207}Pb/^{206}Pb**	**± 2σ**	**^{206}Pb/^{238}U**	**± 2σ**	**^{207}Pb/^{235}U**	**± 2σ**	**Rho^{c}**	**Conc.^{d}**
Anatectic - Population 3																	
CC18-25	380	1149	0.04	0.05855	0.00130	0.08186	0.00148	0.66083	0.01336	550	48	507	9	515	8	0.89	98
CC18-77	132	359	0.05	0.05877	0.00150	0.08296	0.00142	0.67224	0.01522	559	55	514	9	522	9	0.76	98
CC18-79	142	404	0.05	0.05781	0.00136	0.08252	0.00144	0.65769	0.01374	522	51	511	9	513	8	0.84	100
CC18-92	170	482	0.28	0.05767	0.00130	0.08278	0.00144	0.65818	0.01320	517	48	513	9	514	8	0.87	100
CC18-110	121	352	0.52	0.05723	0.00156	0.08136	0.00150	0.64198	0.01608	500	60	504	9	504	10	0.74	100
CC18-134	92	255	1.25	0.05833	0.00174	0.08117	0.00146	0.65280	0.01768	542	66	503	9	510	11	0.66	99
CC18-137	105	292	0.16	0.05715	0.00156	0.08237	0.00148	0.64903	0.01598	497	60	510	9	508	10	0.73	100
CC18-149	180	522	0.40	0.05751	0.00162	0.08224	0.00154	0.65200	0.01690	511	61	510	9	510	10	0.72	100
CC18-150	272	787	0.45	0.05737	0.00134	0.08087	0.00142	0.63969	0.01330	505	51	501	8	502	8	0.84	100
CC18-154	244	662	0.10	0.05930	0.00146	0.08275	0.00142	0.67660	0.01478	578	53	513	8	525	9	0.79	98
CC18-158	112	320	0.76	0.05752	0.00150	0.08270	0.00150	0.65578	0.01562	511	56	512	9	512	10	0.76	100
CC18-168	255	738	0.44	0.05778	0.00336	0.08284	0.00214	0.65955	0.03646	521	125	513	13	514	22	0.47	100
Average	184	527	0.37	0.05792	0.00163	0.08220	0.00152	0.65636	0.01686	526	61	509	9	512	10	0.76	99
SD	83	252	0.34	0.00064	0.00054	0.00069	0.00019	0.01028	0.00607	24	20	4	1	6	4	0.11	1
RSD%	45.42	47.90	91.57	1.11	32.84	0.84	12.53	1.57	36.03	4.65	32.67	0.81	12.40	1.23	35.97	14.33	0.84

LA-Q-ICP-MS U-Pb results - Sample CC30

	PPM			Ratios							Ages (Ma)						
Spot	**^{206}Pb**	**^{238}U**	**Th[b]/U**	**^{207}Pb/^{206}Pb ± 2σ (abs)**		**^{206}Pb[a]/^{238}U ± 2σ (abs)**		**^{207}Pb[a]/^{235}U ± 2σ (abs)**		**^{207}Pb/^{206}Pb**	**± 2σ**	**^{206}Pb/^{238}U**	**± 2σ**	**^{207}Pb/^{235}U**	**± 2σ**	**Rho[c]**	**Conc.[d]**
Inherited- Population ca. 615-600 Ma																	
CC30-16	57	138	2.03	0.06031	0.00190	0.09852	0.00188	0.81915	0.02384	615	67	606	11	608	13	0.66	100
CC30-37	58	139	0.86	0.05878	0.00186	0.09765	0.00182	0.79124	0.02308	559	69	601	11	592	13	0.64	99
CC30-38	23	54	1.45	0.05906	0.00274	0.09689	0.00210	0.78893	0.03432	569	99	596	12	591	19	0.50	99
CC30-45	126	286	0.25	0.05969	0.00172	0.09767	0.00170	0.80380	0.02068	593	61	601	10	599	12	0.68	100
CC30-46	98	231	0.18	0.05995	0.00162	0.09789	0.00174	0.80910	0.01960	602	58	602	10	602	11	0.73	100
CC30-48	51	120	0.46	0.06022	0.00192	0.09962	0.00188	0.82703	0.02422	611	68	612	11	612	13	0.64	100
CC30-57	62	149	0.58	0.06024	0.00236	0.09990	0.00208	0.82962	0.03026	612	83	614	12	613	17	0.57	100
CC30-60	308	803	0.04	0.05927	0.00144	0.09765	0.00184	0.79783	0.01796	577	52	601	11	596	10	0.84	99
CC30-61	245	638	0.07	0.05903	0.00138	0.09733	0.00182	0.79201	0.01704	568	51	599	11	592	10	0.87	99
CC30-74	33	74	2.23	0.05915	0.00322	0.09661	0.00224	0.78774	0.04018	573	116	595	13	590	23	0.45	99
CC30-92	94	218	0.27	0.06048	0.00172	0.09996	0.00182	0.83352	0.02162	621	61	614	11	616	12	0.70	100
Average	105	259	0.77	0.05965	0.00199	0.09815	0.00190	0.80727	0.02480	591	71	604	11	601	14	0.66	100
SD	87	230	0.75	0.00059	0.00054	0.00113	0.00016	0.01660	0.00689	21	19	7	1	9	4	0.12	1
RSD%	82.47	88.65	98.26	0.98	27.11	1.15	8.35	2.06	27.79	3.62	27.24	1.10	8.27	1.55	28.19	18.19	0.57
Magmatic																	
CC30-15	85	222	2.16	0.06011	0.00190	0.09311	0.00180	0.77141	0.02262	608	68	574	11	581	13	0.66	101
CC30-17	57	139	2.29	0.05901	0.00198	0.09289	0.00174	0.75558	0.02334	567	72	573	10	572	14	0.61	100
CC30-18	54	137	0.86	0.05966	0.00192	0.09285	0.00176	0.76361	0.02252	591	69	572	10	576	13	0.64	101
CC30-20	69	167	0.24	0.05882	0.00194	0.09310	0.00172	0.75491	0.02280	560	70	574	10	571	13	0.61	100
CC30-22	55	139	0.91	0.06017	0.00208	0.09540	0.00190	0.79128	0.02532	610	74	587	11	592	14	0.62	101
CC30-36	49	126	0.63	0.06023	0.00202	0.09332	0.00182	0.77483	0.02408	612	72	575	11	583	14	0.63	101
CC30-39	45	113	0.57	0.05837	0.00204	0.09248	0.00178	0.74416	0.02390	544	75	570	10	565	14	0.60	99
CC30-41	44	108	2.04	0.05834	0.00238	0.09322	0.00192	0.74962	0.02858	542	90	575	11	568	17	0.54	99
CC30-42	74	176	0.47	0.05896	0.00190	0.09362	0.00172	0.76098	0.02232	566	69	577	10	575	13	0.63	100
CC30-44	83	215	1.49	0.05856	0.00162	0.09536	0.00180	0.76985	0.01964	551	60	587	11	580	11	0.74	99
CC30-66	55	135	0.61	0.05893	0.00192	0.09461	0.00178	0.76875	0.02306	565	70	583	11	579	13	0.63	99
CC30-68	48	113	1.72	0.05967	0.00266	0.09552	0.00204	0.78569	0.03272	592	95	588	12	589	19	0.51	100
CC30-69	65	157	1.39	0.05844	0.00196	0.09288	0.00172	0.74836	0.02292	546	72	573	10	567	13	0.60	99
CC30-70	39	95	1.41	0.05858	0.00230	0.09326	0.00188	0.75322	0.02754	552	85	575	11	570	16	0.55	99
CC30-75	73	178	0.39	0.05894	0.00194	0.09432	0.00178	0.76642	0.02316	565	71	581	10	578	13	0.62	99
CC30-76	56	136	1.13	0.05966	0.00206	0.09552	0.00184	0.78568	0.02500	591	74	588	11	589	14	0.61	100
CC30-78	43	109	1.29	0.05876	0.00208	0.09366	0.00184	0.75884	0.02490	558	76	577	11	573	14	0.60	99
CC30-80	54	138	0.93	0.05889	0.00198	0.09292	0.00182	0.75442	0.02360	563	73	573	11	571	14	0.63	100
CC30-82	94	229	0.91	0.05917	0.00172	0.09442	0.00172	0.77022	0.02040	573	63	582	10	580	12	0.69	100
CC30-87	54	133	0.56	0.05953	0.00212	0.09356	0.00182	0.76787	0.02524	586	76	577	11	579	15	0.59	100
CC30-91	73	183	0.41	0.05929	0.00180	0.09320	0.00172	0.76193	0.02114	578	65	575	10	575	12	0.67	100
CC30-95	46	116	0.64	0.05988	0.00230	0.09591	0.00198	0.79177	0.02834	599	82	590	12	592	16	0.58	100

Continued... LA-Q-ICP-MS U-Pb results - Sample CC30

	PPM			Ratios							Ages (Ma)					
Spot	**^{206}Pb**	**^{238}U**	**Th^{b}/U**	**^{207}Pb/^{206}Pb**	**± 2σ (abs)**	**^{206}Pb^{a}/^{238}U**	**± 2σ (abs)**	**^{207}Pb^{a}/^{235}U**	**± 2σ (abs)**	**^{207}Pb/^{206}Pb**	**± 2σ**	**^{206}Pb/^{238}U**	**± 2σ**	**^{207}Pb/^{235}U**	**± 2σ**	**Rho^{c}**	**Conc.^{d}**
CC30-96	55	138	0.59	0.05949	0.00240	0.09407	0.00196	0.77160	0.02894	585	86	580	12	581	17	0.56	100
Average	60	148	1.03	0.05919	0.00204	0.09388	0.00182	0.76613	0.02444	574	74	578	11	578	14	0.61	100
SD	15	37	0.58	0.00058	0.00023	0.00102	0.00009	0.01310	0.00299	21	8	6	1	8	2	0.05	1
RSD%	24.37	24.73	56.80	0.97	11.23	1.09	4.86	1.71	12.23	3.68	11.18	1.04	4.76	1.30	11.98	7.84	0.69
Anatectic																	
CC30-13	108	310	0.51	0.05857	0.00242	0.08993	0.00200	0.72608	0.02842	551	88	555	12	554	17	0.57	100
CC30-19	51	130	1.09	0.05935	0.00196	0.09218	0.00176	0.75416	0.02286	580	71	568	10	571	13	0.63	100
CC30-40	56	143	0.83	0.05874	0.00198	0.09008	0.00170	0.72948	0.02260	557	73	556	10	556	13	0.61	100
CC30-47	49	115	1.01	0.05845	0.00274	0.09202	0.00194	0.74150	0.03228	547	101	567	12	563	19	0.48	99
CC30-62	212	551	0.07	0.05849	0.00132	0.09091	0.00158	0.73307	0.01464	548	49	561	9	558	9	0.87	100
CC30-81	57	138	0.89	0.05843	0.00210	0.09219	0.00176	0.74257	0.02458	546	78	569	10	564	14	0.58	99
CC30-83	91	237	0.39	0.05948	0.00188	0.09295	0.00178	0.76228	0.02218	585	68	573	11	575	13	0.66	100
CC30-89	60	155	0.78	0.05905	0.00190	0.09135	0.00172	0.74371	0.02202	569	69	564	10	565	13	0.64	100
CC30-90	60	149	0.36	0.05900	0.00202	0.09189	0.00174	0.74753	0.02344	567	73	567	10	567	14	0.60	100
CC30-97	48	113	0.65	0.05901	0.00286	0.09140	0.00198	0.74348	0.03344	567	104	564	12	564	19	0.48	100
Average	79	204	0.66	0.05886	0.00212	0.09149	0.00180	0.74239	0.02465	562	77	564	11	564	14	0.61	100
SD	48	129	0.31	0.00036	0.00043	0.00091	0.00013	0.01041	0.00521	13	15	5	1	6	3	0.10	0
RSD%	60.53	63.45	46.43	0.61	20.16	1.00	7.13	1.40	21.15	2.37	20.03	0.96	7.10	1.07	21.23	16.85	0.41
Metamorphic																	
CC30-23	139	409	0.48	0.05803	0.00178	0.08117	0.00154	0.64925	0.01822	531	67	503	9	508	11	0.68	101
CC30-98	112	317	0.42	0.05744	0.00158	0.08231	0.00148	0.65183	0.01614	508	59	510	9	510	10	0.73	100
Average	125	363	0.45	0.05774	0.00168	0.08174	0.00151	0.65054	0.01718	519	63	507	9	509	11	0.70	100
SD	13	46	0.03	0.00030	0.00010	0.00057	0.00003	0.00129	0.00104	11	4	3	0	1	1	0.03	1
RSD%	10.57	12.63	6.56	0.51	5.95	0.70	1.99	0.20	6.05	2.18	6.20	0.67	2.01	0.16	6.15	3.57	0.51

LA-Q-ICP-MS U-Pb results - Sample CC35a

Spot	PPM			Ratios							Ages (Ma)				Rho[c]	Conc.[d]
	^{206}Pb	^{238}U	Th^{b}/U	$^{207}Pb/^{206}Pb$	± 2σ (abs)	$^{206}Pb^{a}/^{238}U$	± 2σ (abs)	$^{207}Pb^{a}/^{235}U$	± 2σ (abs)	$^{207}Pb/^{206}Pb$	± 2σ	$^{206}Pb/^{238}U$	± 2σ	$^{207}Pb/^{235}U$	± 2σ		
Inherited - Population ca. 740-690 Ma																	
CC35a-a41	100	194	0.24	0.06366	0.00256	0.12091	0.00260	1.06100	0.04000	731	84	736	15	734	20	0.57	100
Inherited - Population ca. 680-635 Ma																	
CC35a-a31	69	149	0.54	0.06104	0.00244	0.10631	0.00224	0.89455	0.03336	641	85	651	13	649	18	0.57	100
Inherited - Population ca. 630-620 Ma																	
CC35a-a55	117	270	0.40	0.05964	0.00250	0.10171	0.00222	0.83595	0.03296	590	90	624	13	617	18	0.55	101
CC35a-b20	144	319	0.19	0.06060	0.00218	0.10112	0.00204	0.84488	0.02836	625	77	621	12	622	16	0.60	100
CC35a-b21	107	236	0.14	0.06031	0.00170	0.10122	0.00188	0.84162	0.02176	615	60	622	11	620	12	0.72	100
CC35a-b35	129	260	0.16	0.06300	0.00958	0.10392	0.00546	0.87040	0.12382	708	308	637	32	636	67	0.37	100
CC35a-b45	147	335	0.02	0.06068	0.00212	0.10302	0.00212	0.86195	0.02806	628	74	632	12	631	15	0.63	100
Average	129	284	0.18	0.06085	0.00362	0.10220	0.00274	0.85096	0.04699	633	122	627	16	625	26	0.57	100
SD	15	37	0.12	0.00114	0.00299	0.00110	0.00136	0.01302	0.03858	40	94	6	8	7	21	0.12	0
RSD%	11.97	13.08	67.35	1.87	82.77	1.07	49.66	1.53	82.10	6.27	76.74	1.02	49.67	1.14	81.31	20.17	0.46
Inherited - Population ca. 615-600 Ma																	
CC35a-a16	79	176	0.25	0.05994	0.00226	0.09870	0.00196	0.81556	0.02846	602	81	607	12	606	16	0.57	100
CC35a-a20	272	593	0.15	0.05999	0.00174	0.10015	0.00180	0.82823	0.02162	603	62	615	11	613	12	0.69	100
CC35a-a42	77	180	0.32	0.05988	0.00230	0.09831	0.00204	0.81150	0.02906	599	82	605	12	603	16	0.58	100
CC35a-a52	44	99	0.16	0.06046	0.00292	0.09883	0.00222	0.82388	0.03724	620	103	608	13	610	21	0.50	100
CC35a-a59	73	162	0.20	0.06047	0.00226	0.10079	0.00202	0.84029	0.02914	620	80	619	12	619	16	0.58	100
CC35a-a63	134	307	0.50	0.06012	0.00192	0.09895	0.00188	0.82014	0.02408	608	69	608	11	608	13	0.65	100
CC35a-b80	67	143	0.18	0.05994	0.00356	0.09751	0.00242	0.80528	0.04486	601	126	600	14	600	25	0.45	100
CC35a-b131	136	318	0.02	0.06080	0.00170	0.09985	0.00186	0.83701	0.02140	632	60	614	11	618	12	0.73	99
Average	110	247	0.22	0.06020	0.00233	0.09914	0.00203	0.82274	0.02948	611	83	609	12	610	16	0.59	100
SD	68	149	0.13	0.00031	0.00059	0.00099	0.00019	0.01136	0.00754	11	21	6	1	6	4	0.09	0
RSD%	61.85	60.31	59.69	0.52	25.29	1.00	9.52	1.38	25.56	1.84	25.12	0.96	9.68	1.04	25.98	14.93	0.33
Magmatic																	
CC35a-a17	117	298	0.58	0.05960	0.00182	0.09375	0.00184	0.77030	0.02178	589	65	578	11	580	13	0.69	100
CC35a-a21	75	180	0.19	0.05982	0.00192	0.09553	0.00184	0.78788	0.02338	597	69	588	11	590	13	0.65	100
CC35a-a23	112	274	0.11	0.05978	0.00162	0.09590	0.00180	0.79038	0.01964	595	59	590	11	591	11	0.76	100
CC35a-a27	69	177	0.16	0.05964	0.00230	0.09661	0.00210	0.79437	0.02880	590	82	595	12	594	16	0.60	100
CC35a-a32	63	160	0.37	0.05920	0.00212	0.09397	0.00192	0.76695	0.02578	575	77	579	11	578	15	0.61	100
CC35a-a35	163	377	0.25	0.05922	0.00188	0.09459	0.00176	0.77223	0.02242	575	68	583	10	581	13	0.64	100
CC35a-a37	74	182	0.66	0.05967	0.00184	0.09479	0.00184	0.77993	0.02222	592	66	584	11	585	13	0.68	100
CC35a-a39	87	208	0.21	0.05902	0.00192	0.09445	0.00182	0.76863	0.02312	568	70	582	11	579	13	0.64	100
CC35a-a40	95	231	0.21	0.05933	0.00180	0.09405	0.00178	0.76941	0.02152	579	65	579	11	579	12	0.68	100
CC35a-a43	102	251	0.31	0.05945	0.00216	0.09307	0.00188	0.76271	0.02586	584	78	574	11	576	15	0.60	100
CC35a-a47	93	218	0.33	0.05957	0.00194	0.09594	0.00182	0.78793	0.02358	588	70	591	11	590	13	0.63	100
CC35a-a48	108	271	0.24	0.05946	0.00196	0.09378	0.00186	0.76874	0.02348	584	71	578	11	579	13	0.65	100

Continued ... LA-Q-ICP-MS U-Pb results - Sample CC35a

	PPM			Ratios							Ages (Ma)						
Spot	**^{206}Pb**	**^{238}U**	**Th[b]/U**	**^{207}Pb/^{206}Pb**	**± 2σ (abs)**	**^{206}Pb[a]/^{238}U**	**± 2σ (abs)**	**^{207}Pb[a]/^{235}U**	**± 2σ (abs)**	**^{207}Pb/^{206}Pb**	**± 2σ**	**^{206}Pb/^{238}U**	**± 2σ**	**^{207}Pb/^{235}U**	**± 2σ**	**Rho[c]**	**Conc.[d]**
CC35a-a54	103	254	0.25	0.05925	0.00176	0.09546	0.00182	0.77993	0.02146	577	64	588	11	585	12	0.69	100
CC35a-a56	74	172	0.25	0.05945	0.00246	0.09420	0.00194	0.77210	0.02966	584	89	580	11	581	17	0.54	100
CC35a-a57	90	223	0.11	0.05988	0.00224	0.09546	0.00198	0.78809	0.02760	599	80	588	12	590	16	0.59	100
CC35a-a58	82	195	0.14	0.05929	0.00208	0.09510	0.00186	0.77734	0.02518	578	75	586	11	584	14	0.60	100
CC35a-a66	93	217	0.25	0.05967	0.00222	0.09583	0.00190	0.78834	0.02704	592	79	590	11	590	15	0.58	100
CC35a-a67	99	241	0.10	0.05938	0.00192	0.09548	0.00186	0.78170	0.02336	581	69	588	11	587	13	0.65	100
CC35a-a69	208	487	0.13	0.05949	0.00250	0.09485	0.00198	0.77813	0.03038	585	90	584	12	584	17	0.53	100
CC35a-b22	78	171	0.36	0.05981	0.00334	0.09361	0.00224	0.77136	0.04046	597	119	577	13	581	23	0.46	99
CC35a-b26	153	363	0.21	0.05993	0.00154	0.09503	0.00174	0.78510	0.01844	601	55	585	10	588	10	0.78	99
CC35a-b42	96	234	0.25	0.05965	0.00170	0.09303	0.00174	0.76511	0.02010	591	61	573	10	577	12	0.71	99
CC35a-b51	128	303	0.35	0.05925	0.00168	0.09388	0.00172	0.76684	0.01980	576	61	578	10	578	11	0.71	100
CC35a-b54	71	163	0.11	0.05925	0.00236	0.09406	0.00190	0.76820	0.02842	576	85	580	11	579	16	0.55	100
CC35a-b73	97	236	0.23	0.05973	0.00176	0.09288	0.00174	0.76496	0.02068	594	63	573	10	577	12	0.69	99
CC35a-b74	62	150	0.47	0.05921	0.00200	0.09335	0.00182	0.76207	0.02388	575	73	575	11	575	14	0.62	100
CC35a-b75	104	249	0.31	0.05930	0.00208	0.09526	0.00190	0.77880	0.02526	578	75	587	11	585	14	0.61	100
CC35a-b79	175	414	0.24	0.05967	0.00162	0.09351	0.00168	0.76930	0.01884	592	58	576	10	579	11	0.73	99
CC35a-b83	117	266	0.18	0.05922	0.00292	0.09275	0.00206	0.75707	0.03482	575	105	572	12	572	20	0.48	100
CC35a-b84	93	220	0.11	0.05976	0.00180	0.09599	0.00180	0.79095	0.02184	595	65	591	11	592	12	0.68	100
CC35a-b85	64	153	0.27	0.06009	0.00204	0.09492	0.00186	0.78638	0.02482	607	73	585	11	589	14	0.62	99
CC35a-b96	67	154	0.26	0.05967	0.00226	0.09689	0.00194	0.79699	0.02794	592	81	596	11	595	16	0.57	100
CC35a-b98	69	162	0.23	0.05972	0.00218	0.09552	0.00188	0.78654	0.02646	594	78	588	11	589	15	0.59	100
CC35a-b105	92	223	0.33	0.05998	0.00186	0.09385	0.00178	0.77615	0.02218	603	67	578	10	583	13	0.66	99
CC35a-b108	63	149	0.24	0.06008	0.00228	0.09525	0.00192	0.78901	0.02784	606	81	587	11	591	16	0.57	99
CC35a-b110	136	346	0.18	0.05944	0.00196	0.09337	0.00184	0.76519	0.02348	583	71	575	11	577	14	0.64	100
CC35a-b111	117	279	0.22	0.05964	0.00180	0.09448	0.00176	0.77700	0.02150	591	65	582	10	584	12	0.67	100
CC35a-b113	78	189	0.33	0.05987	0.00198	0.09372	0.00182	0.77374	0.02360	599	71	578	11	582	14	0.64	99
CC35a-b120	95	233	0.33	0.06039	0.00192	0.09369	0.00178	0.78016	0.02270	618	68	577	11	586	13	0.65	99
CC35a-b121	73	180	0.21	0.05994	0.00210	0.09274	0.00182	0.76645	0.02484	601	75	572	11	578	14	0.61	99
CC35a-b122	128	310	0.20	0.06016	0.00182	0.09432	0.00176	0.78242	0.02160	610	65	581	10	587	12	0.68	99
Average	99	238	0.26	0.05961	0.00204	0.09451	0.00186	0.77670	0.02453	589	73	582	11	584	14	0.63	100
SD	32	76	0.12	0.00031	0.00034	0.00107	0.00011	0.00996	0.00422	11	12	6	1	6	2	0.07	0
RSD%	32.20	31.74	45.64	0.51	16.64	1.13	5.70	1.28	17.19	1.89	16.40	1.08	5.70	0.97	17.25	10.54	0.43
Anatectic - Population 1																	
CC35a-a18	92	240	0.43	0.05837	0.00170	0.09052	0.00174	0.72840	0.01972	544	63	559	10	556	12	0.71	101
CC35a-a24	119	309	0.14	0.05835	0.00158	0.08977	0.00166	0.72228	0.01792	543	59	554	10	552	11	0.75	100
CC35a-a25	232	581	0.21	0.05863	0.00152	0.08899	0.00158	0.71931	0.01682	554	56	550	9	550	10	0.76	100
CC35a-a26	87	247	0.05	0.05838	0.00272	0.09032	0.00216	0.72699	0.03228	544	100	557	13	555	19	0.54	100
CC35a-a33	102	257	0.21	0.05889	0.00178	0.09102	0.00172	0.73907	0.02052	563	64	562	10	562	12	0.68	100

Continued ... LA-Q-ICP-MS U-Pb results - Sample CC35a

	PPM			Ratios							Ages (Ma)						
Spot	**^{206}Pb**	**^{238}U**	**Th^{b}/U**	**^{207}Pb/^{206}Pb**	**± 2σ (abs)**	**^{206}Pb^{a}/^{238}U**	**± 2σ (abs)**	**^{207}Pb^{a}/^{235}U**	**± 2σ (abs)**	**^{207}Pb/^{206}Pb**	**± 2σ**	**^{206}Pb/^{238}U**	**± 2σ**	**^{207}Pb/^{235}U**	**± 2σ**	**Rho^{c}**	**Conc.^{d}**
CC35a-a49	113	305	0.33	0.05840	0.00202	0.08936	0.00182	0.71945	0.02322	545	74	552	11	550	14	0.63	100
CC35a-a53	82	211	0.13	0.05904	0.00196	0.09114	0.00180	0.74191	0.02286	569	71	562	11	564	13	0.64	100
CC35a-b23	122	289	0.12	0.06016	0.00178	0.09201	0.00170	0.76308	0.02064	609	63	567	10	576	12	0.68	99
CC35a-b29	89	221	0.41	0.05916	0.00174	0.09103	0.00172	0.74251	0.02016	573	63	562	10	564	12	0.70	100
CC35a-b31	103	252	0.10	0.05894	0.00170	0.09167	0.00170	0.74487	0.01964	565	61	565	10	565	11	0.70	100
CC35a-b56	118	289	0.15	0.05872	0.00164	0.09195	0.00170	0.74446	0.01888	557	60	567	10	565	11	0.73	100
CC35a-b77	89	220	0.29	0.05909	0.00182	0.09123	0.00172	0.74329	0.02096	570	66	563	10	564	12	0.67	100
CC35a-b91	119	300	0.10	0.05953	0.00168	0.09058	0.00166	0.74354	0.01902	587	60	559	10	565	11	0.72	99
CC35a-b106	156	376	0.18	0.05895	0.00186	0.09096	0.00168	0.73917	0.02116	565	68	561	10	562	12	0.65	100
Average	116	293	0.20	0.05890	0.00182	0.09075	0.00174	0.73702	0.02099	563	66	560	10	561	12	0.68	100
SD	37	91	0.11	0.00049	0.00028	0.00087	0.00013	0.01182	0.00354	18	11	5	1	7	2	0.05	1
RSD%	32.12	31.05	56.36	0.83	15.45	0.96	7.44	1.60	16.88	3.19	15.84	0.92	7.52	1.23	17.07	7.95	0.54
Anatectic - Population 2																	
CC35a-b28	135	391	0.05	0.05731	0.00198	0.08072	0.00162	0.63786	0.02052	503	74	500	10	501	13	0.62	100
CC35a-b50	427	116	0.07	0.05692	0.00156	0.08183	0.00148	0.64220	0.01592	488	60	507	9	504	10	0.73	101
CC35a-b53	116	328	0.06	0.05703	0.00154	0.08157	0.00150	0.64145	0.01582	492	60	506	9	503	10	0.75	100
CC35a-b95	167	474	0.14	0.05762	0.00150	0.08114	0.00148	0.64457	0.01520	515	57	503	9	505	9	0.77	100
Average	211	328	0.08	0.05722	0.00165	0.08132	0.00152	0.64152	0.01687	500	63	504	9	503	10	0.72	100
SD	126	133	0.03	0.00027	0.00019	0.00042	0.00006	0.00241	0.00213	10	7	3	0	1	1	0.06	0
RSD%	59.55	40.46	42.26	0.47	11.83	0.52	3.84	0.38	12.62	2.10	10.79	0.50	3.95	0.29	12.79	7.89	0.44

LA-Q-ICP-MS U-Pb results - Sample CC36

	PPM			Ratios							Ages (Ma)					
Spot	^{206}Pb	^{238}U	Th^{b}/U	$^{207}Pb/^{206}Pb$ ± 2σ (abs)		$^{206}Pb^{a}/^{238}U$ ± 2σ (abs)		$^{207}Pb^{a}/^{235}U$ ± 2σ (abs)		$^{207}Pb/^{206}Pb$	± 2σ	$^{206}Pb/^{238}U$	± 2σ	$^{207}Pb/^{235}U$	± 2σ	Rho^{c}	$Conc.^{d}$
Inherited - Population ca. 680-635 Ma																	
CC36-a39	72	151	0.28	0.06095	0.00332	0.10355	0.00258	0.86984	0.04390	638	115	635	15	636	24	0.49	100
Inherited - Population ca. 630-620 Ma																	
CC36-a43	91	201	0.30	0.06065	0.00236	0.10126	0.00210	0.84646	0.03012	627	83	622	12	623	17	0.58	100
Inherited - Population ca. 615-600 Ma																	
CC36-a26	111	253	0.18	0.05996	0.00228	0.09710	0.00198	0.80230	0.02772	602	81	597	12	598	16	0.59	100
CC36-a38	115	273	0.13	0.06008	0.00200	0.09801	0.00196	0.81155	0.02452	607	71	603	11	603	14	0.66	100
CC36-a40	334	785	0.04	0.06003	0.00158	0.09807	0.00178	0.81141	0.01894	605	56	603	10	603	11	0.78	100
CC36-a41	193	436	0.24	0.06030	0.00186	0.09926	0.00186	0.82493	0.02276	614	66	610	11	611	13	0.68	100
CC36-a46	198	460	0.24	0.05992	0.00168	0.09945	0.00184	0.82133	0.02054	601	60	611	11	609	11	0.74	100
CC36-a61	104	221	0.33	0.06016	0.00326	0.09962	0.00244	0.82602	0.04118	609	115	612	14	611	23	0.49	100
CC36-a70	142	334	0.09	0.05979	0.00186	0.09839	0.00188	0.81090	0.02274	596	67	605	11	603	13	0.68	100
CC36-b13	129	280	0.13	0.06038	0.00222	0.09779	0.00186	0.81374	0.02656	617	78	602	11	605	15	0.58	99
CC36-b14	140	307	0.07	0.06025	0.00264	0.09765	0.00208	0.81095	0.03206	613	93	601	12	603	18	0.54	100
Average	163	372	0.16	0.06010	0.00215	0.09837	0.00196	0.81479	0.02634	607	76	605	12	605	15	0.64	100
SD	68	164	0.09	0.00018	0.00050	0.00083	0.00019	0.00731	0.00643	7	17	5	1	4	4	0.09	0
RSD%	41.99	44.18	55.16	0.30	23.12	0.84	9.57	0.90	24.42	1.08	22.64	0.81	9.60	0.68	24.26	13.89	0.28
Magmatic																	
CC36-a30	334	796	0.04	0.05998	0.00158	0.09523	0.00172	0.78731	0.01820	603	56	586	10	590	10	0.78	99
CC36-a65	234	577	0.06	0.06022	0.00200	0.09419	0.00186	0.78167	0.02338	611	71	580	11	586	13	0.66	99
CC36-a89	194	478	0.39	0.05916	0.00202	0.09439	0.00186	0.76962	0.02368	573	73	581	11	580	14	0.64	100
CC36-a91	97	233	0.16	0.05908	0.00236	0.09580	0.00202	0.78011	0.02846	570	86	590	12	586	16	0.58	101
CC36-a95	112	289	0.20	0.06029	0.00238	0.09397	0.00204	0.78082	0.02828	614	84	579	12	586	16	0.60	99
CC36-a107	129	315	0.44	0.06024	0.00198	0.09396	0.00180	0.78027	0.02288	612	70	579	11	586	13	0.65	99
CC36-a110	127	301	0.12	0.06016	0.00216	0.09669	0.00192	0.80174	0.02600	609	77	595	11	598	15	0.61	100
CC36-a111	128	316	0.20	0.06003	0.00210	0.09531	0.00192	0.78872	0.02516	605	75	587	11	590	14	0.63	99
CC36-a114	108	261	0.11	0.06001	0.00214	0.09499	0.00186	0.78580	0.02520	604	76	585	11	589	14	0.61	99
CC36-a116	102	258	0.10	0.05970	0.00240	0.09378	0.00200	0.77176	0.02842	593	85	578	12	581	16	0.58	100
CC36-b30	164	408	0.11	0.05964	0.00192	0.09471	0.00182	0.77851	0.02256	591	69	583	11	585	13	0.66	100
CC36-b36	572	1378	0.25	0.05944	0.00156	0.09557	0.00164	0.78288	0.01756	583	56	588	10	587	10	0.77	100
CC36-b49	103	251	0.50	0.06021	0.00236	0.09554	0.00198	0.79279	0.02824	611	84	588	12	593	16	0.58	99
CC36-b57	159	360	0.30	0.06047	0.00202	0.09471	0.00170	0.78933	0.02292	621	71	583	10	591	13	0.62	99
Average	183	444	0.21	0.05990	0.00207	0.09492	0.00187	0.78367	0.02435	600	74	585	11	588	14	0.64	99
SD	125	299	0.14	0.00042	0.00026	0.00080	0.00012	0.00796	0.00339	15	9	5	1	5	2	0.06	1
RSD%	68.22	67.24	64.87	0.70	12.44	0.84	6.36	1.02	13.92	2.52	12.30	0.81	6.33	0.77	13.94	9.46	0.58
Anatectic																	
CC36-a48	360	938	0.03	0.05931	0.00162	0.09132	0.00172	0.74652	0.01844	579	59	563	10	566	11	0.76	99
CC36-a93	126	323	0.12	0.05947	0.00196	0.08975	0.00174	0.73574	0.02194	584	71	554	10	560	13	0.65	99

Continued.. LA-Q-ICP-MS U-Pb results - Sample CC36

	PPM			Ratios							Ages (Ma)					
Spot	**^{206}Pb**	**^{238}U**	**Th[b]/U**	**^{207}Pb/^{206}Pb**	**± 2σ (abs)**	**^{206}Pb[a]/^{238}U**	**± 2σ (abs)**	**^{207}Pb[a]/^{235}U**	**± 2σ (abs)**	**^{207}Pb/^{206}Pb**	**± 2σ**	**^{206}Pb/^{238}U**	**± 2σ**	**^{207}Pb/^{235}U**	**± 2σ**	**Rho[c]**	**Conc.[d]**
CC36-a115	114	290	0.12	0.05884	0.00222	0.08959	0.00180	0.72670	0.02472	561	81	553	11	555	15	0.59	100
CC36-b16	77	186	0.18	0.05897	0.00260	0.09222	0.00198	0.74948	0.03010	566	95	569	12	568	17	0.53	100
CC36-b50	95	243	0.11	0.05899	0.00198	0.08910	0.00168	0.72438	0.02174	567	73	550	10	553	13	0.63	99
CC36-b51	382	934	0.06	0.05947	0.00162	0.09078	0.00154	0.74402	0.01730	584	59	560	9	565	10	0.73	99
CC36-b52	78	202	0.07	0.05884	0.00226	0.08974	0.00182	0.72770	0.02534	561	83	554	11	555	15	0.58	100
Average	176	445	0.10	0.05913	0.00204	0.09036	0.00175	0.73636	0.02280	572	74	558	10	560	13	0.64	100
SD	125	313	0.05	0.00026	0.00033	0.00103	0.00013	0.00961	0.00405	10	12	6	1	6	2	0.08	0
RSD%	70.79	70.43	47.37	0.44	16.14	1.15	7.15	1.30	17.74	1.68	16.22	1.10	7.16	1.00	17.68	11.84	0.36

LA-Q-ICP-MS U-Pb results - Sample CC40

	PPM			Ratios							Ages (Ma)					
Spot	^{206}Pb	^{238}U	Th^{b}/U	$^{207}Pb/^{206}Pb$	± 2σ (abs)	$^{206}Pb^{a}/^{238}U$	± 2σ (abs)	$^{207}Pb^{a}/^{235}U$	± 2σ (abs)	$^{207}Pb/^{206}Pb$	± 2σ	$^{206}Pb/^{238}U$	± 2σ	$^{207}Pb/^{235}U$	± 2σ	Rho^{c}	$Conc.^{d}$
Inherited - Population ca. 826 Ma																	
CC40-106	67	112	0.24	0.06756	0.00216	0.13667	0.00264	1.27302	0.03746	855	66	826	15	834	17	0.66	99
Inherited - Population ca. 740-690 Ma																	
CC40-57	210	407	0.04	0.06338	0.00346	0.11712	0.00288	1.02330	0.05316	721	114	714	17	716	27	0.47	100
CC40-59	572	1125	0.44	0.06296	0.00136	0.11353	0.00190	0.98558	0.01834	707	45	693	11	697	9	0.90	100
Inherited - Population ca. 680-635 Ma																	
CC40-96	128	271	0.65	0.06222	0.00158	0.11083	0.00202	0.95085	0.02200	682	54	678	12	679	11	0.79	100
Inherited - Population ca. 630-620 Ma																	
CC40-24	157	363	0.16	0.06007	0.00220	0.10266	0.00210	0.85004	0.02888	606	78	630	12	625	16	0.60	101
CC40-65	155	350	0.27	0.06040	0.00284	0.10151	0.00228	0.84524	0.03724	618	100	623	13	622	21	0.51	100
CC40-81	237	567	0.11	0.06022	0.00180	0.10095	0.00196	0.83811	0.02328	612	64	620	11	618	13	0.70	100
CC40-61	120	277	0.14	0.06021	0.00156	0.09994	0.00180	0.82968	0.01952	611	56	614	11	613	11	0.77	100
Average	167	389	0.17	0.06023	0.00210	0.10127	0.00204	0.84077	0.02723	612	74	622	12	620	15	0.64	100
SD	43	108	0.06	0.00012	0.00048	0.00098	0.00018	0.00768	0.00667	4	17	6	1	4	4	0.10	0
RSD%	25.66	27.62	35.95	0.19	23.07	0.97	8.69	0.91	24.50	0.67	22.50	0.92	8.69	0.69	24.26	15.04	0.29
Magmatic																	
CC40-15	129	319	0.10	0.05970	0.00162	0.09467	0.00174	0.77912	0.01934	593	57	583	10	585	11	0.74	100
CC40-16	279	713	0.07	0.05945	0.00136	0.09531	0.00176	0.78117	0.01646	584	50	587	10	586	9	0.88	100
CC40-19	72	172	0.38	0.05981	0.00172	0.09658	0.00178	0.79647	0.02092	597	62	594	11	595	12	0.70	100
CC40-22	228	566	0.12	0.05908	0.00136	0.09495	0.00170	0.77337	0.01606	570	49	585	10	582	9	0.86	101
CC40-25	87	206	0.18	0.06009	0.00164	0.09711	0.00176	0.80455	0.01994	607	58	598	10	599	11	0.73	100
CC40-27	139	360	0.21	0.05911	0.00180	0.09541	0.00188	0.77756	0.02214	571	66	588	11	584	13	0.69	101
CC40-28	59	147	0.50	0.05923	0.00266	0.09490	0.00210	0.77488	0.03260	576	96	584	12	583	19	0.53	100
CC40-35	70	176	0.86	0.05946	0.00210	0.09617	0.00196	0.78843	0.02594	584	76	592	12	590	15	0.62	100
CC40-36	69	169	0.15	0.05822	0.00190	0.09626	0.00188	0.77269	0.02350	538	72	592	11	581	13	0.64	102
CC40-38	104	252	0.20	0.05942	0.00150	0.09656	0.00174	0.79102	0.01806	582	54	594	10	592	10	0.79	100
CC40-46	497	1243	0.04	0.05988	0.00134	0.09480	0.00170	0.78261	0.01576	599	48	584	10	587	9	0.89	99
CC40-47	113	279	0.65	0.05985	0.00156	0.09437	0.00170	0.77870	0.01832	598	56	581	10	585	10	0.77	99
CC40-54	161	397	0.12	0.05960	0.00142	0.09544	0.00172	0.78432	0.01696	589	51	588	10	588	10	0.83	100
CC40-56	157	372	0.06	0.05954	0.00226	0.09427	0.00188	0.77379	0.02716	587	81	581	11	582	16	0.57	100
CC40-63	246	595	0.07	0.05973	0.00142	0.09641	0.00172	0.79396	0.01698	594	51	593	10	593	10	0.83	100
CC40-86	205	541	0.28	0.05877	0.00196	0.09257	0.00188	0.75007	0.02342	559	72	571	11	568	14	0.65	100
CC40-87	148	393	0.24	0.06001	0.00232	0.09475	0.00206	0.78370	0.02856	604	82	584	12	588	16	0.60	99
CC40-93	162	395	0.25	0.06015	0.00392	0.09405	0.00256	0.77965	0.04800	609	138	580	15	585	27	0.44	99
CC40-94	300	744	0.06	0.05979	0.00230	0.09504	0.00198	0.78327	0.02802	596	82	585	12	587	16	0.58	100
CC40-108	187	466	0.06	0.05977	0.00180	0.09709	0.00190	0.80012	0.02234	595	65	597	11	597	13	0.70	100
CC40-112	94	226	0.48	0.06007	0.00170	0.09630	0.00178	0.79753	0.02072	606	61	593	10	595	12	0.71	100
Average	167	416	0.24	0.05956	0.00189	0.09538	0.00187	0.78319	0.02291	587	68	587	11	587	13	0.70	100

Continued... LA-Q-ICP-MS U-Pb results - Sample CC40

	PPM			Ratios							Ages (Ma)						
Spot	**^{206}Pb**	**^{238}U**	**Th^{b}/U**	**^{207}Pb/^{206}Pb ± 2σ (abs)**		**^{206}Pb^{a}/^{238}U ± 2σ (abs)**		**^{207}Pb^{a}/^{235}U ± 2σ (abs)**		**^{207}Pb/^{206}Pb**	**± 2σ**	**^{206}Pb/^{238}U**	**± 2σ**	**^{207}Pb/^{235}U**	**± 2σ**	**Rho^{c}**	**Conc.^{d}**
SD	98	247	0.21	0.00045	0.00057	0.00108	0.00019	0.01144	0.00706	17	20	6	1	7	4	0.12	1
RSD%	58.77	59.49	86.47	0.76	29.95	1.13	10.17	1.46	30.79	2.83	29.09	1.08	10.32	1.11	30.95	16.49	0.58
Anatectic																	
CC40-62	240	660	0.06	0.05825	0.00166	0.09038	0.00176	0.72585	0.01928	539	63	558	10	554	11	0.73	101
CC40-78	138	380	0.22	0.05885	0.00204	0.09208	0.00194	0.74705	0.02454	561	75	568	11	567	14	0.64	100
CC40-92	160	412	0.38	0.05881	0.00180	0.09209	0.00178	0.74673	0.02120	560	67	568	10	566	12	0.68	100
CC40-82	1275	3734	0.03	0.05893	0.00188	0.08944	0.00190	0.72631	0.02212	564	69	552	11	554	13	0.70	100
CC40-40	431	1177	0.03	0.05942	0.00142	0.09200	0.00176	0.75367	0.01680	582	52	567	10	570	10	0.86	99
CC40-105	120	299	0.49	0.05944	0.00192	0.09108	0.00172	0.74643	0.02216	583	69	562	10	566	13	0.64	99
CC40-107	810	2212	0.01	0.05826	0.00188	0.09196	0.00188	0.73855	0.02258	539	71	567	11	562	13	0.67	101
Average	453	1268	0.17	0.05885	0.00180	0.09129	0.00182	0.74066	0.02124	561	67	563	11	563	12	0.70	100
SD	405	1184	0.18	0.00045	0.00019	0.00096	0.00008	0.01007	0.00233	17	7	6	0	6	1	0.07	1
RSD%	89.23	93.39	103.65	0.76	10.47	1.06	4.32	1.36	10.95	2.98	10.54	1.01	4.26	1.05	11.00	10.06	0.60

LA-Q-ICP-MS U-Pb results - Sample CC42

Spot	PPM			Ratios						Ages (Ma)						Rho[c]	Conc.[d]
	^{206}Pb	^{238}U	Th^{b}/U	$^{207}Pb/^{206}Pb$	± 2σ (abs)	$^{206}Pb^{a}/^{238}U$	± 2σ (abs)	$^{207}Pb^{a}/^{235}U$	± 2σ (abs)	$^{207}Pb/^{206}Pb$	± 2σ	$^{206}Pb/^{238}U$	± 2σ	$^{207}Pb/^{235}U$	± 2σ		
Inherited - Population ca. 630-620 Ma																	
CC42-a72	43	96	0.16	0.06068	0.00248	0.10141	0.00208	0.84840	0.03228	628	87	623	12	624	18	0.54	100
CC42-a93	76	165	0.20	0.06090	0.00222	0.10133	0.00196	0.85083	0.02846	636	77	622	11	625	16	0.58	100
CC42-b32	119	261	0.21	0.06039	0.00180	0.10002	0.00178	0.83277	0.02230	618	64	615	10	615	12	0.66	100
CC42-a33	70	156	0.26	0.06047	0.00228	0.09953	0.00194	0.82974	0.02868	620	80	612	11	614	16	0.56	100
CC42-b113	76	173	0.17	0.06026	0.00194	0.10094	0.00190	0.83857	0.02470	613	69	620	11	618	14	0.64	100
Average	77	170	0.20	0.06054	0.00214	0.10065	0.00193	0.84006	0.02728	623	75	618	11	619	15	0.60	100
SD	24	53	0.04	0.00023	0.00024	0.00075	0.00010	0.00834	0.00346	8	8	4	1	5	2	0.05	0
RSD%	31.59	31.13	18.04	0.37	11.37	0.74	5.01	0.99	12.68	1.30	11.09	0.71	5.01	0.74	12.44	7.91	0.24
Inherited - Population ca. 615-600 Ma																	
CC42-a35	157	368	0.19	0.05976	0.00242	0.09786	0.00202	0.80620	0.03036	595	87	602	12	600	17	0.55	100
CC42-a74	85	199	0.10	0.06018	0.00198	0.09825	0.00186	0.81522	0.02468	610	70	604	11	605	14	0.63	100
CC42-b49	96	228	0.29	0.05959	0.00164	0.09771	0.00176	0.80274	0.02010	589	59	601	10	598	11	0.72	100
CC42-b18	153	365	0.21	0.06043	0.00150	0.09783	0.00174	0.81512	0.01820	619	53	602	10	605	10	0.80	99
CC42-b79	94	224	0.27	0.06031	0.00166	0.09764	0.00176	0.81184	0.02016	615	59	601	10	604	11	0.73	100
CC42-b81	158	375	0.32	0.05974	0.00146	0.09775	0.00172	0.80518	0.01754	594	53	601	10	600	10	0.81	100
CC42-b101	73	171	0.21	0.05998	0.00190	0.09882	0.00186	0.81722	0.02384	603	68	608	11	607	13	0.65	100
CC42-b115	104	244	0.11	0.05903	0.00174	0.09891	0.00182	0.80500	0.02164	568	63	608	11	600	12	0.68	101
Average	115	272	0.21	0.05988	0.00179	0.09810	0.00182	0.80982	0.02207	599	64	603	11	602	12	0.69	100
SD	33	78	0.07	0.00042	0.00029	0.00048	0.00009	0.00529	0.00390	15	11	3	1	3	2	0.08	1
RSD%	28.61	28.77	34.60	0.71	16.31	0.49	5.03	0.65	17.69	2.56	16.52	0.46	4.99	0.49	17.69	11.79	0.58
Magmatic																	
CC42-a16	91	223	0.30	0.06004	0.00212	0.09576	0.00188	0.79269	0.02596	605	76	590	11	593	15	0.60	99
CC42-a17	111	269	0.09	0.05960	0.00162	0.09542	0.00170	0.78411	0.01922	589	59	588	10	588	11	0.73	100
CC42-a20	180	498	0.05	0.05996	0.00288	0.09401	0.00224	0.77690	0.03526	602	102	579	13	584	20	0.52	99
CC42-a22	224	582	0.44	0.05985	0.00158	0.09489	0.00176	0.78299	0.01896	598	57	584	10	587	11	0.77	100
CC42-a23	231	543	0.46	0.06035	0.00148	0.09477	0.00160	0.78859	0.01688	616	52	584	9	590	10	0.79	99
CC42-a24	83	209	0.27	0.05968	0.00164	0.09334	0.00168	0.76802	0.01922	593	58	575	10	579	11	0.72	99
CC42-a26	183	442	0.32	0.06008	0.00158	0.09485	0.00166	0.78564	0.01840	606	56	584	10	589	10	0.75	99
CC42-a27	98	229	0.27	0.06020	0.00382	0.09473	0.00250	0.78604	0.04694	611	134	583	15	589	27	0.44	99
CC42-a32	120	271	0.14	0.05964	0.00216	0.09524	0.00180	0.78309	0.02604	590	78	587	11	587	15	0.57	100
CC42-a37	115	279	0.07	0.05903	0.00274	0.09435	0.00206	0.76770	0.03328	568	99	581	12	578	19	0.50	100
CC42-a38	164	384	0.55	0.05972	0.00174	0.09337	0.00164	0.76877	0.02014	594	62	576	10	579	12	0.67	99
CC42-a42	115	290	0.21	0.05953	0.00266	0.09376	0.00204	0.76950	0.03220	587	96	578	12	580	18	0.52	100
CC42-a47	110	274	0.08	0.05937	0.00234	0.09387	0.00192	0.76835	0.02808	581	84	578	11	579	16	0.56	100
CC42-a48	98	239	0.06	0.05957	0.00308	0.09397	0.00218	0.77151	0.03734	588	110	579	13	581	21	0.48	100
CC42-a52	85	191	0.20	0.05949	0.00254	0.09527	0.00194	0.78136	0.03074	585	91	587	11	586	18	0.52	100
CC42-a55	79	189	0.16	0.05957	0.00182	0.09633	0.00178	0.79109	0.02198	588	65	593	10	592	12	0.67	100
CC42-a57	103	250	0.51	0.05962	0.00174	0.09453	0.00172	0.77697	0.02068	590	63	582	10	584	12	0.68	100

Continued... LA-Q-ICP-MS U-Pb results - Sample CC42

	PPM			Ratios						Ages (Ma)							
Spot	^{206}Pb	^{238}U	Th^{b}/U	^{207}Pb/^{206}Pb	± 2σ (abs)	^{206}Pb^{a}/^{238}U	± 2σ (abs)	^{207}Pb^{a}/^{235}U	± 2σ (abs)	^{207}Pb/^{206}Pb	± 2σ	^{206}Pb/^{238}U	± 2σ	^{207}Pb/^{235}U	± 2σ	Rho^{c}	Conc.^{d}
CC42-a60	114	265	0.19	0.05960	0.00200	0.09700	0.00184	0.79693	0.02464	589	72	597	11	595	14	0.61	100
CC42-a68	87	212	0.10	0.05924	0.00170	0.09441	0.00172	0.77105	0.02006	576	62	582	10	580	12	0.70	100
CC42-a71	43	103	0.21	0.05998	0.00340	0.09509	0.00234	0.78631	0.04202	603	121	586	14	589	24	0.46	99
CC42-a73	193	497	0.04	0.05989	0.00172	0.09474	0.00180	0.78203	0.02066	600	61	584	11	587	12	0.72	99
CC42-a75	143	342	0.07	0.05943	0.00154	0.09592	0.00168	0.78593	0.01838	583	56	590	10	589	10	0.75	100
CC42-a76	101	243	0.39	0.05880	0.00258	0.09559	0.00204	0.77486	0.03176	560	94	589	12	583	18	0.52	101
CC42-a77	90	223	0.19	0.05925	0.00172	0.09395	0.00172	0.76741	0.02040	576	63	579	10	578	12	0.69	100
CC42-a80	108	275	0.10	0.06013	0.00206	0.09478	0.00190	0.78557	0.02514	608	73	584	11	589	14	0.63	99
CC42-a85	142	376	0.06	0.05880	0.00226	0.09494	0.00204	0.76925	0.02778	560	82	585	12	579	16	0.59	101
CC42-a88	83	200	0.20	0.05953	0.00176	0.09601	0.00176	0.78796	0.02132	587	64	591	10	590	12	0.68	100
CC42-a91	64	153	0.12	0.05988	0.00196	0.09682	0.00184	0.79929	0.02404	599	70	596	11	596	14	0.63	100
CC42-b22	128	339	0.30	0.05806	0.00168	0.09417	0.00182	0.75385	0.02022	532	63	580	11	571	12	0.72	102
CC42-b24	147	368	0.25	0.05908	0.00138	0.09393	0.00164	0.76513	0.01592	570	49	579	10	577	9	0.84	100
CC42-b34	204	462	0.09	0.05967	0.00178	0.09411	0.00164	0.77420	0.02070	592	64	580	10	582	12	0.65	100
CC42-b36	145	361	0.09	0.05908	0.00140	0.09447	0.00166	0.76945	0.01642	570	50	582	10	579	9	0.82	100
CC42-b37	116	283	0.24	0.05932	0.00174	0.09431	0.00172	0.77129	0.02066	579	63	581	10	581	12	0.68	100
CC42-b46	84	224	0.10	0.05798	0.00202	0.09478	0.00196	0.75761	0.02468	529	76	584	12	573	14	0.63	102
CC42-b47	190	419	0.40	0.05970	0.00196	0.09580	0.00172	0.78861	0.02350	593	70	590	10	590	13	0.60	100
CC42-b54	117	293	0.16	0.05944	0.00176	0.09745	0.00188	0.79859	0.02186	583	64	599	11	596	12	0.70	101
CC42-b55	159	376	0.11	0.05913	0.00164	0.09584	0.00170	0.78130	0.01948	572	60	590	10	586	11	0.71	101
CC42-b56	73	163	0.19	0.05901	0.00248	0.09605	0.00194	0.78138	0.03042	567	90	591	11	586	17	0.52	101
CC42-b57	140	372	0.12	0.06070	0.00216	0.09416	0.00196	0.78802	0.02640	629	76	580	12	590	15	0.62	98
CC42-b60	73	181	0.16	0.06029	0.00178	0.09405	0.00176	0.78186	0.02108	614	63	580	10	587	12	0.69	99
CC42-b61	86	207	0.21	0.05912	0.00168	0.09664	0.00178	0.78770	0.02032	571	61	595	10	590	12	0.71	101
CC42-b75	63	150	0.13	0.05940	0.00184	0.09648	0.00180	0.79006	0.02236	582	66	594	11	591	13	0.66	100
CC42-b76	81	197	0.37	0.05890	0.00168	0.09516	0.00174	0.77276	0.02004	563	61	586	10	581	11	0.71	101
CC42-b77	131	331	0.21	0.05993	0.00158	0.09428	0.00172	0.77897	0.01868	601	57	581	10	585	11	0.76	99
CC42-b80	150	365	0.17	0.06101	0.00150	0.09524	0.00168	0.80118	0.01768	640	53	587	10	598	10	0.80	98
CC42-b82	156	373	0.14	0.05962	0.00146	0.09668	0.00170	0.79474	0.01752	590	53	595	10	594	10	0.80	100
CC42-b83	220	571	0.07	0.06037	0.00158	0.09448	0.00178	0.78636	0.01884	617	56	582	10	589	11	0.79	99
CC42-b84	114	272	0.04	0.05919	0.00158	0.09672	0.00174	0.78938	0.01910	574	58	595	10	591	11	0.74	101
CC42-b85	109	246	0.05	0.05953	0.00216	0.09683	0.00186	0.79476	0.02656	587	78	596	11	594	15	0.57	100
CC42-b89	107	254	0.18	0.05919	0.00160	0.09731	0.00176	0.79412	0.01954	574	59	599	10	594	11	0.74	101
CC42-b90	133	332	0.06	0.06005	0.00164	0.09454	0.00174	0.78273	0.01946	605	58	582	10	587	11	0.74	99
CC42-b91	100	251	0.11	0.06067	0.00180	0.09492	0.00180	0.79393	0.02174	628	64	585	11	593	12	0.69	99
CC42-b92	112	271	0.13	0.05847	0.00160	0.09597	0.00172	0.77358	0.01908	547	59	591	10	582	11	0.73	102
CC42-b93	130	319	0.26	0.06007	0.00156	0.09480	0.00170	0.78514	0.01848	606	56	584	10	588	11	0.76	99
CC42-b98	90	218	0.41	0.06089	0.00176	0.09539	0.00176	0.80073	0.02108	635	62	587	10	597	12	0.70	98
CC42-b99	126	300	0.22	0.06072	0.00294	0.09321	0.00208	0.78029	0.03520	629	102	575	12	586	20	0.49	98

Continued.. LA-Q-ICP-MS U-Pb results - Sample CC42

	PPM			Ratios						Ages (Ma)							
Spot	**^{206}Pb**	**^{238}U**	**Th^{b}/U**	**^{207}Pb/^{206}Pb**	**± 2σ (abs)**	**^{206}Pb^{a}/^{238}U**	**± 2σ (abs)**	**^{207}Pb^{a}/^{235}U**	**± 2σ (abs)**	**^{207}Pb/^{206}Pb**	**± 2σ**	**^{206}Pb/^{238}U**	**± 2σ**	**^{207}Pb/^{235}U**	**± 2σ**	**Rho^{c}**	**Conc.^{d}**
CC42-b100	139	355	0.23	0.06001	0.00170	0.09363	0.00176	0.77460	0.02022	604	61	577	10	582	12	0.72	99
CC42-b108	111	272	0.21	0.05903	0.00166	0.09438	0.00172	0.76819	0.01952	568	60	581	10	579	11	0.72	100
CC42-b109	80	191	0.20	0.05974	0.00178	0.09722	0.00180	0.80067	0.02180	594	64	598	11	597	12	0.68	100
CC42-b110	74	176	0.14	0.05956	0.00182	0.09675	0.00180	0.79447	0.02210	588	65	595	11	594	13	0.67	100
CC42-b116	101	243	0.14	0.06094	0.00178	0.09599	0.00178	0.80652	0.02158	637	63	591	10	601	12	0.69	98
Average	120	295	0.19	0.05963	0.00195	0.09514	0.00183	0.78217	0.02344	590	70	586	11	587	13	0.66	100
SD	41	105	0.12	0.00062	0.00050	0.00110	0.00017	0.01138	0.00630	23	18	6	1	6	4	0.10	1
RSD%	34.35	35.52	62.83	1.05	25.65	1.15	9.52	1.45	26.87	3.86	25.17	1.10	9.61	1.11	26.95	14.32	0.86
Anatectic																	
CC42-a34	156	400	0.22	0.05906	0.00150	0.09231	0.00164	0.75161	0.01716	569	55	569	10	569	10	0.78	100
CC42-a41	215	605	0.09	0.06036	0.00190	0.09161	0.00186	0.76223	0.02260	616	68	565	11	575	13	0.68	98
CC42-a50	122	305	0.17	0.05903	0.00156	0.09122	0.00160	0.74234	0.01770	568	57	563	9	564	10	0.74	100
CC42-a51	128	296	0.44	0.05962	0.00222	0.09272	0.00176	0.76213	0.02602	590	80	572	10	575	15	0.56	99
CC42-a53	173	406	0.05	0.05863	0.00174	0.09267	0.00162	0.74909	0.01990	553	64	571	10	568	12	0.66	101
CC42-a56	89	224	0.10	0.05923	0.00168	0.09326	0.00172	0.76155	0.01974	576	61	575	10	575	11	0.71	100
CC42-a59	140	346	0.29	0.05873	0.00158	0.09134	0.00160	0.73952	0.01786	557	58	563	9	562	10	0.73	100
CC42-a69	88	221	0.19	0.05941	0.00170	0.09201	0.00166	0.75366	0.01960	582	62	567	10	570	11	0.69	99
CC42-a70	97	241	0.19	0.05888	0.00162	0.09309	0.00168	0.75571	0.01894	563	61	574	10	572	11	0.72	100
CC42-a78	105	289	0.06	0.06042	0.00234	0.09239	0.00200	0.76951	0.02814	619	83	570	12	580	16	0.59	98
CC42-a79	134	329	0.08	0.05890	0.00164	0.09168	0.00162	0.74448	0.01858	563	60	566	10	565	11	0.71	100
CC42-a86	101	272	0.08	0.06022	0.00202	0.09235	0.00188	0.76669	0.02398	612	71	569	11	578	14	0.65	99
CC42-a87	185	465	0.24	0.06025	0.00174	0.09095	0.00166	0.75539	0.01978	612	62	561	10	571	11	0.70	98
CC42-a90	174	430	0.23	0.05886	0.00150	0.09310	0.00164	0.75549	0.01722	562	55	574	10	571	10	0.77	100
CC42-b20	140	343	0.05	0.05885	0.00154	0.09395	0.00166	0.76226	0.01782	562	56	579	10	575	10	0.76	101
CC42-b25	153	396	0.16	0.05828	0.00186	0.09277	0.00180	0.74538	0.02202	540	70	572	11	566	13	0.66	101
CC42-b35	119	321	0.09	0.05965	0.00162	0.09046	0.00170	0.74396	0.01858	591	58	558	10	565	11	0.75	99
CC42-b50	426	1228	0.01	0.05938	0.00230	0.09164	0.00204	0.75007	0.02764	581	83	565	12	568	16	0.60	99
CC42-b51	105	275	0.10	0.05941	0.00192	0.09055	0.00176	0.74159	0.02210	582	69	559	10	563	13	0.65	99
CC42-b53	107	276	0.12	0.05876	0.00176	0.09398	0.00182	0.76142	0.02120	558	65	579	11	575	12	0.70	101
CC42-b74	55	138	0.18	0.06059	0.00184	0.09274	0.00176	0.77465	0.02166	625	65	572	10	582	12	0.68	98
CC42-b96	257	614	0.04	0.06084	0.00158	0.09177	0.00156	0.76983	0.01760	634	55	566	9	580	10	0.74	98
CC42-b97	270	696	0.27	0.05942	0.00242	0.09036	0.00190	0.73991	0.02820	583	87	558	11	562	16	0.55	99
CC42-b102	143	374	0.15	0.05989	0.00176	0.09251	0.00178	0.76382	0.02074	600	63	570	10	576	12	0.71	99
CC42-b107	106	264	0.09	0.05926	0.00170	0.09232	0.00168	0.75423	0.01966	577	62	569	10	571	11	0.70	100
CC42-b111	230	585	0.03	0.05891	0.00160	0.09438	0.00176	0.76644	0.01908	564	59	581	10	578	11	0.75	101
Average	154	398	0.14	0.05942	0.00179	0.09224	0.00174	0.75550	0.02090	582	65	569	10	571	12	0.69	100
SD	75	213	0.10	0.00067	0.00026	0.00105	0.00012	0.01000	0.00331	24	9	6	1	6	2	0	1
RSD%	48.69	53.46	67.03	1.12	14.49	1.14	6.95	1.32	15.84	4.18	13.87	1.09	6.95	1.01	15.80	8.72	0.94

Continued.. LA-Q-ICP-MS U-Pb results - Sample CC42

	PPM			Ratios						Ages (Ma)							
Spot	**^{206}Pb**	**^{238}U**	**Th^{b}/U**	**^{207}Pb/^{206}Pb**	**± 2σ (abs)**	**^{206}Pb^{a}/^{238}U**	**± 2σ (abs)**	**^{207}Pb^{a}/^{235}U**	**± 2σ (abs)**	**^{207}Pb/^{206}Pb**	**± 2σ**	**^{206}Pb/^{238}U**	**± 2σ**	**^{207}Pb/^{235}U**	**± 2σ**	**Rho^{c}**	**Conc.^{d}**
Metamorphic																	
CC42-b19	359	1054	0.02	0.05838	0.00218	0.08309	0.00172	0.66817	0.02332	544	81	515	10	520	14	0.59	99
CC42-b31	243	744	0.03	0.05764	0.00166	0.08477	0.00170	0.67343	0.01832	516	63	525	10	523	11	0.74	100
CC42-b112	131	393	0.11	0.05681	0.00174	0.08427	0.00168	0.66000	0.01886	483	67	522	10	515	12	0.70	101
Average	244	730	0.05	0.05761	0.00186	0.08404	0.00170	0.66720	0.02017	514	70	520	10	519	12	0.68	100
SD	93	270	0.04	0.00064	0.00023	0.00070	0.00002	0.00553	0.00224	25	7	4	0	3	1	0.06	1
RSD%	38.01	36.94	85.51	1.11	12.29	0.84	0.96	0.83	11.11	4.81	10.39	0.81	1.13	0.65	11.10	8.99	0.96

LA-Q-ICP-MS U-Pb results (GJ-1 zircon, primary standard)

	PPM			Ratios							Ages (Ma)					
Standards	^{206}Pb	^{238}U	Th^{b}/U	$^{207}Pb/^{206}Pb$	± 2σ (abs)	$^{206}Pb^{a}/^{238}U$	± 2σ (abs)	$^{207}Pb^{a}/^{235}U$	± 2σ (abs)	$^{207}Pb/^{206}Pb$	± 2σ	$^{206}Pb/^{238}U$	± 2σ	$^{207}Pb/^{235}U$	± 2σ	Rho^{c}	$Conc.^{d}$
GJ-1																	
GJ-1-2	142	334	0.02	0.06003	0.00140	0.09967	0.00176	0.82487	0.01730	605	50	613	10	611	10	0.84	100
GJ-1-3	135	312	0.02	0.06093	0.00148	0.09956	0.00174	0.83638	0.01804	637	52	612	10	617	10	0.81	99
GJ-1-5	137	319	0.02	0.06085	0.00144	0.09985	0.00174	0.83773	0.01768	634	51	614	10	618	10	0.83	99
GJ-1-14	133	309	0.02	0.06008	0.00146	0.09934	0.00174	0.82292	0.01776	607	52	611	10	610	10	0.81	100
GJ-1-15	132	311	0.02	0.05979	0.00146	0.09805	0.00172	0.80828	0.01760	596	52	603	10	602	10	0.81	100
GJ-1-16	140	326	0.02	0.05983	0.00144	0.09852	0.00172	0.81264	0.01736	597	52	606	10	604	10	0.82	100
GJ-1-34	138	322	0.02	0.06060	0.00148	0.09856	0.00172	0.82348	0.01798	625	52	606	10	610	10	0.80	99
GJ-1-35	141	327	0.02	0.05953	0.00144	0.09935	0.00174	0.81547	0.01768	587	52	611	10	606	10	0.81	101
GJ-1-41	138	321	0.02	0.05979	0.00146	0.09861	0.00172	0.81280	0.01762	595	53	606	10	604	10	0.80	100
GJ-1-42	139	323	0.02	0.06047	0.00146	0.09871	0.00172	0.82298	0.01764	621	52	607	10	610	10	0.81	100
GJ-1-43	139	322	0.02	0.06044	0.00146	0.09853	0.00172	0.82100	0.01776	619	52	606	10	609	10	0.81	100
GJ-1-56	140	322	0.02	0.05994	0.00150	0.09829	0.00170	0.81219	0.01818	601	54	604	10	604	10	0.77	100
GJ-1-57	140	329	0.02	0.06009	0.00144	0.09869	0.00174	0.81765	0.01764	607	52	607	10	607	10	0.82	100
GJ-1-58	140	332	0.02	0.06076	0.00144	0.09870	0.00174	0.82681	0.01768	631	51	607	10	612	10	0.82	99
GJ-1-72	139	326	0.02	0.06053	0.00150	0.09839	0.00174	0.82108	0.01814	623	53	605	10	609	10	0.80	99
GJ-1-73	138	327	0.02	0.06049	0.00154	0.09893	0.00178	0.82497	0.01892	621	54	608	10	611	11	0.78	100
GJ-1-74	138	334	0.02	0.06097	0.00160	0.09875	0.00182	0.83013	0.01976	638	56	607	11	614	11	0.77	99
GJ-1-85	137	320	0.02	0.06068	0.00152	0.09891	0.00176	0.82753	0.01866	628	54	608	10	612	10	0.79	99
GJ-1-87	137	320	0.02	0.06121	0.00152	0.09945	0.00176	0.83928	0.01868	647	53	611	10	619	10	0.80	99
GJ-1-88	137	324	0.02	0.06007	0.00150	0.09906	0.00176	0.82038	0.01842	606	53	609	10	608	10	0.79	100
GJ-1-102	137	317	0.02	0.06042	0.00156	0.09940	0.00178	0.82810	0.01926	619	55	611	10	613	11	0.77	100
GJ-1-103	138	307	0.02	0.06000	0.00168	0.10005	0.00178	0.82769	0.02100	604	60	615	10	612	12	0.70	100
GJ-1-104	137	314	0.02	0.05930	0.00154	0.09981	0.00178	0.81592	0.01916	578	56	613	10	606	11	0.76	101
GJ-1-1	137	321	0.02	0.06020	0.00142	0.09807	0.00168	0.81403	0.01694	611	51	603	10	605	9	0.82	100
GJ-1-2	135	318	0.02	0.05930	0.00136	0.10015	0.00174	0.81889	0.01672	578	50	615	10	607	9	0.85	101
GJ-1-3	138	318	0.02	0.05954	0.00140	0.10036	0.00172	0.82393	0.01708	587	51	617	10	610	10	0.83	101
GJ-1-4	138	318	0.02	0.05998	0.00140	0.10028	0.00172	0.82932	0.01722	603	50	616	10	613	10	0.83	100
GJ-1-12	135	314	0.02	0.06060	0.00142	0.09953	0.00170	0.83152	0.01718	625	50	612	10	615	10	0.83	100
GJ-1-13	135	317	0.02	0.06013	0.00142	0.09880	0.00170	0.81905	0.01708	608	51	607	10	608	10	0.83	100
GJ-1-14	135	320	0.02	0.05967	0.00142	0.09761	0.00168	0.80295	0.01680	592	51	600	10	599	9	0.82	100
GJ-1-26	138	320	0.02	0.06070	0.00144	0.09924	0.00170	0.83055	0.01736	629	51	610	10	614	10	0.82	99
GJ-1-27	139	323	0.02	0.05992	0.00142	0.09930	0.00170	0.82035	0.01724	601	51	610	10	608	10	0.81	100
GJ-1-28	139	323	0.02	0.06076	0.00144	0.09963	0.00172	0.83457	0.01744	631	50	612	10	616	10	0.83	99
GJ-1-29	140	325	0.02	0.06021	0.00142	0.09919	0.00170	0.82346	0.01722	611	51	610	10	610	10	0.82	100
GJ-1-33	140	329	0.02	0.06025	0.00142	0.09848	0.00170	0.81807	0.01708	613	51	606	10	607	10	0.83	100
GJ-1-34	140	329	0.02	0.06125	0.00144	0.09835	0.00170	0.83063	0.01716	648	50	605	10	614	10	0.84	99
GJ-1-49	139	326	0.02	0.05975	0.00142	0.09861	0.00170	0.81235	0.01716	594	52	606	10	604	10	0.82	100
GJ-1-50	139	326	0.02	0.06031	0.00144	0.09844	0.00170	0.81857	0.01726	615	51	605	10	607	10	0.82	100

Continued ... LA-Q-ICP-MS U-Pb results (GJ-1 zircon, primary standard)

	PPM			Ratios						Ages (Ma)							
Standards	^{206}Pb	^{238}U	Th[b]/U	^{207}Pb/^{206}Pb	± 2σ (abs)	^{206}Pb[a]/^{238}U	± 2σ (abs)	^{207}Pb[a]/^{235}U	± 2σ (abs)	^{207}Pb/^{206}Pb	± 2σ	^{206}Pb/^{238}U	± 2σ	^{207}Pb/^{235}U	± 2σ	Rho[c]	Conc.[d]
GJ-1-51	140	327	0.02	0.06018	0.00142	0.09934	0.00172	0.82431	0.01734	610	51	611	10	611	10	0.82	100
GJ-1-65	139	325	0.02	0.06103	0.00146	0.09925	0.00172	0.83511	0.01776	640	51	610	10	616	10	0.81	99
GJ-1-66	138	325	0.02	0.06084	0.00146	0.09867	0.00172	0.82765	0.01754	634	51	607	10	612	10	0.82	99
GJ-1-67	139	327	0.02	0.06110	0.00146	0.09865	0.00172	0.83105	0.01762	643	51	607	10	614	10	0.82	99
GJ-1-84	139	324	0.02	0.05893	0.00142	0.09950	0.00174	0.80846	0.01748	565	52	612	10	602	10	0.81	102
GJ-1-85	139	325	0.02	0.05974	0.00144	0.09905	0.00172	0.81580	0.01764	594	52	609	10	606	10	0.80	101
GJ-1-86	139	325	0.02	0.05969	0.00146	0.09885	0.00172	0.81349	0.01764	593	51	608	10	604	10	0.80	101
GJ-1-99	138	321	0.02	0.05985	0.00146	0.09939	0.00174	0.82014	0.01786	598	52	611	10	608	10	0.80	100
GJ-1-100	138	323	0.02	0.06066	0.00148	0.09909	0.00174	0.82872	0.01796	627	52	609	10	613	10	0.81	99
GJ-1-101	138	324	0.02	0.05963	0.00146	0.09852	0.00172	0.80998	0.01766	590	52	606	10	602	10	0.80	101
GJ-1-115	138	319	0.02	0.05930	0.00146	0.09974	0.00176	0.81538	0.01800	578	53	613	10	606	10	0.80	101
GJ-1-116	139	322	0.02	0.06053	0.00148	0.09970	0.00174	0.83201	0.01818	623	52	613	10	615	10	0.80	100
GJ-1-117	138	323	0.02	0.05982	0.00148	0.09880	0.00174	0.81485	0.01792	597	53	607	10	605	10	0.80	100
GJ-1-131	138	322	0.02	0.06041	0.00150	0.09921	0.00174	0.82637	0.01828	618	53	610	10	612	10	0.79	100
GJ-1-132	138	322	0.02	0.05916	0.00148	0.09933	0.00174	0.81016	0.01808	573	54	611	10	603	10	0.78	101
GJ-1-133	138	322	0.02	0.06001	0.00148	0.09864	0.00174	0.81612	0.01814	604	53	607	10	606	10	0.79	100
GJ-1-146	138	320	0.02	0.06080	0.00152	0.09951	0.00176	0.83415	0.01864	632	53	612	10	616	10	0.79	99
GJ-1-147	137	320	0.02	0.06016	0.00150	0.09934	0.00176	0.82393	0.01852	609	54	611	10	610	10	0.79	100
GJ-1-148	136	321	0.02	0.06096	0.00154	0.09739	0.00172	0.81859	0.01844	638	54	599	10	607	10	0.78	99
GJ-1-161	137	320	0.02	0.06010	0.00152	0.09921	0.00176	0.82204	0.01864	607	54	610	10	609	10	0.78	100
GJ-1-162	137	318	0.02	0.05962	0.00150	0.09977	0.00176	0.82015	0.01868	590	54	613	10	608	10	0.77	101
GJ-1-163	138	323	0.02	0.06083	0.00152	0.09917	0.00176	0.83171	0.01882	633	54	610	10	615	10	0.78	99
GJ-1-177	136	317	0.02	0.06012	0.00154	0.09963	0.00178	0.82587	0.01904	608	55	612	10	611	11	0.77	100
GJ-1-178	138	322	0.02	0.06070	0.00154	0.09915	0.00176	0.82971	0.01908	629	54	609	10	614	11	0.77	99
GJ-1-179	136	318	0.02	0.06154	0.00156	0.09874	0.00176	0.83772	0.01924	658	54	607	10	618	11	0.78	98
GJ-1-2	136	325	0.02	0.05979	0.00136	0.09809	0.00170	0.80860	0.01630	596	49	603	10	602	9	0.86	100
GJ-1-3	138	329	0.02	0.06028	0.00136	0.09798	0.00170	0.81433	0.01632	614	49	603	10	605	9	0.87	100
GJ-1-4	139	328	0.02	0.06089	0.00142	0.09799	0.00168	0.82255	0.01692	635	50	603	10	610	9	0.83	101
GJ-1-10	138	325	0.02	0.05942	0.00140	0.09806	0.00168	0.80332	0.01664	583	50	603	10	599	9	0.83	99
GJ-1-11	138	325	0.02	0.06074	0.00142	0.09814	0.00168	0.82180	0.01698	630	50	604	10	609	9	0.83	101
GJ-1-12	137	322	0.02	0.05987	0.00140	0.09843	0.00170	0.81241	0.01682	599	50	605	10	604	9	0.83	100
GJ-1-27	139	316	0.02	0.06015	0.00142	0.10171	0.00176	0.84345	0.01756	609	50	624	10	621	10	0.83	99
GJ-1-29	138	315	0.02	0.05984	0.00140	0.10134	0.00174	0.83605	0.01742	598	51	622	10	617	10	0.82	99
GJ-1-31	135	312	0.02	0.06028	0.00142	0.09985	0.00172	0.82981	0.01732	614	51	614	10	614	10	0.83	100
GJ-1-32	135	310	0.02	0.06048	0.00142	0.10062	0.00174	0.83901	0.01740	621	50	618	10	619	10	0.83	100
GJ-1-33	138	318	0.02	0.06012	0.00140	0.10031	0.00172	0.83136	0.01720	608	50	616	10	614	10	0.83	100
GJ-1-34	138	316	0.02	0.05962	0.00140	0.10111	0.00174	0.83100	0.01720	590	50	621	10	614	10	0.83	99
GJ-1-35	137	314	0.02	0.06006	0.00142	0.10058	0.00172	0.83290	0.01740	606	51	618	10	615	10	0.82	100
GJ-1-49	139	327	0.02	0.05988	0.00144	0.09889	0.00172	0.81636	0.01752	599	52	608	10	606	10	0.81	100

Continued ... LA-Q-ICP-MS U-Pb results (GJ-1 zircon, primary standard)

	PPM			Ratios						Ages (Ma)							
Standards	^{206}Pb	^{238}U	Th[b]/U	^{207}Pb/^{206}Pb	± 2σ (abs)	^{206}Pb[a]/^{238}U	± 2σ (abs)	^{207}Pb[a]/^{235}U	± 2σ (abs)	^{207}Pb/^{206}Pb	± 2σ	^{206}Pb/^{238}U	± 2σ	^{207}Pb/^{235}U	± 2σ	Rho[c]	Conc.[d]
GJ-1-50	139	327	0.02	0.06002	0.00146	0.09856	0.00172	0.81553	0.01752	604	52	606	10	606	10	0.81	100
GJ-1-51	139	326	0.02	0.05964	0.00144	0.09836	0.00170	0.80872	0.01742	590	52	605	10	602	10	0.80	99
GJ-1-52	138	323	0.02	0.06028	0.00146	0.09901	0.00172	0.82278	0.01766	614	52	609	10	610	10	0.81	100
GJ-1-53	141	329	0.02	0.06034	0.00146	0.09871	0.00172	0.82115	0.01766	616	52	607	10	609	10	0.81	100
GJ-1-54	138	327	0.02	0.05984	0.00144	0.09791	0.00170	0.80780	0.01736	598	52	602	10	601	10	0.81	100
GJ-1-71	137	321	0.02	0.06016	0.00148	0.09864	0.00172	0.81814	0.01804	609	53	606	10	607	10	0.79	100
GJ-1-72	137	323	0.02	0.06113	0.00150	0.09815	0.00172	0.82718	0.01818	644	53	604	10	612	10	0.80	101
GJ-1-73	139	324	0.02	0.05931	0.00148	0.09877	0.00172	0.80763	0.01788	578	53	607	10	601	10	0.79	99
GJ-1-84	138	326	0.02	0.06087	0.00150	0.09866	0.00174	0.82794	0.01830	635	53	607	10	613	10	0.80	101
GJ-1-85	139	321	0.02	0.06047	0.00158	0.09798	0.00170	0.81684	0.01894	620	56	603	10	606	11	0.75	101
GJ-1-86	138	326	0.02	0.06085	0.00150	0.09843	0.00172	0.82577	0.01820	634	53	605	10	611	10	0.79	101
GJ-1-99	138	325	0.02	0.06005	0.00152	0.09825	0.00172	0.81344	0.01836	605	54	604	10	604	10	0.78	100
GJ-1-101	138	324	0.02	0.05973	0.00152	0.09874	0.00174	0.81312	0.01850	594	54	607	10	604	10	0.77	100
GJ-1-105	136	321	0.02	0.05976	0.00152	0.09864	0.00174	0.81274	0.01848	595	55	606	10	604	10	0.78	100
GJ-1-106	137	320	0.02	0.06038	0.00154	0.09932	0.00176	0.82685	0.01882	617	54	610	10	612	10	0.78	100
GJ-1-107	138	320	0.02	0.06076	0.00154	0.10020	0.00176	0.83948	0.01914	631	54	616	10	619	11	0.77	101
GJ-1-99b	140	316	0.02	0.05977	0.00164	0.10195	0.00188	0.84016	0.02104	595	60	626	11	619	12	0.74	101
GJ-1-13a	138	323	0.02	0.06056	0.00228	0.10051	0.00210	0.83896	0.02958	624	80	617	12	619	16	0.59	100
GJ-1-16b	138	321	0.02	0.06008	0.00164	0.10041	0.00192	0.83176	0.02106	607	59	617	11	615	12	0.76	100
GJ-1-86b	140	321	0.02	0.06093	0.00166	0.10030	0.00186	0.84255	0.02090	637	58	616	11	621	12	0.75	99
GJ-1-33b	141	323	0.02	0.05941	0.00154	0.10029	0.00186	0.82144	0.01952	582	56	616	11	609	11	0.78	101
GJ-1-4a	138	320	0.02	0.05987	0.00154	0.10029	0.00184	0.82786	0.01954	599	55	616	11	612	11	0.78	101
GJ-1-100b	138	319	0.02	0.05965	0.00164	0.10013	0.00186	0.82351	0.02072	591	59	615	11	610	12	0.74	101
GJ-1-15a	138	313	0.02	0.05991	0.00164	0.10009	0.00184	0.82667	0.02050	600	58	615	11	612	11	0.74	101
GJ-1-71b	139	319	0.02	0.06039	0.00162	0.10005	0.00186	0.83303	0.02054	618	58	615	11	615	11	0.75	100
GJ-1-61a	139	328	0.02	0.06027	0.00176	0.09988	0.00192	0.83002	0.02248	613	63	614	11	614	12	0.71	100
GJ-1-6a	139	323	0.02	0.05931	0.00154	0.09986	0.00184	0.81655	0.01930	579	56	614	11	606	11	0.78	101
GJ-1-44a	138	323	0.02	0.06049	0.00164	0.09980	0.00186	0.83226	0.02066	621	58	613	11	615	11	0.75	100
GJ-1-18b	137	322	0.02	0.06010	0.00166	0.09968	0.00192	0.82602	0.02118	607	59	613	11	611	12	0.75	100
GJ-1-87b	138	318	0.02	0.06104	0.00168	0.09966	0.00184	0.83876	0.02116	641	59	612	11	619	12	0.73	99
GJ-1-2b	136	318	0.02	0.05907	0.00160	0.09950	0.00190	0.81037	0.02044	570	59	612	11	603	11	0.76	101
GJ-1-5a	138	321	0.02	0.06113	0.00158	0.09948	0.00184	0.83843	0.01970	644	55	611	11	618	11	0.79	99
GJ-1-32b	139	321	0.02	0.05988	0.00156	0.09946	0.00184	0.82111	0.01956	599	56	611	11	609	11	0.78	100
GJ-1-30a	138	318	0.02	0.06026	0.00164	0.09939	0.00184	0.82580	0.02064	613	59	611	11	611	11	0.74	100
GJ-1-70b	140	322	0.02	0.06119	0.00164	0.09937	0.00184	0.83828	0.02060	646	57	611	11	618	11	0.75	99
GJ-1-1b	137	317	0.02	0.06030	0.00156	0.09933	0.00186	0.82571	0.01970	614	56	611	11	611	11	0.78	100
GJ-1-15b	137	322	0.02	0.06109	0.00166	0.09929	0.00190	0.83624	0.02108	642	58	610	11	617	12	0.76	99
GJ-1-101b	138	321	0.02	0.05916	0.00164	0.09929	0.00184	0.80989	0.02060	573	60	610	11	602	12	0.73	101
GJ-1-45a	138	320	0.02	0.06066	0.00170	0.09928	0.00184	0.83035	0.02140	627	60	610	11	614	12	0.72	99

Continued... LA-Q-ICP-MS U-Pb results (GJ-1 zircon, primary standard)

	PPM			Ratios						Ages (Ma)							
Standards	^{206}Pb	^{238}U	Th[b]/U	^{207}Pb/^{206}Pb	± 2σ (abs)	^{206}Pb[a]/^{238}U	± 2σ (abs)	^{207}Pb[a]/^{235}U	± 2σ (abs)	^{207}Pb/^{206}Pb	± 2σ	^{206}Pb/^{238}U	± 2σ	^{207}Pb/^{235}U	± 2σ	Rho[c]	Conc.[d]
GJ-1-46b	139	323	0.02	0.06070	0.00158	0.09924	0.00184	0.83050	0.01970	629	55	610	11	614	11	0.78	99
GJ-1-4b	138	323	0.02	0.05964	0.00162	0.09921	0.00190	0.81575	0.02056	590	58	610	11	606	12	0.76	101
GJ-1-72b	138	318	0.02	0.06059	0.00166	0.09921	0.00184	0.82881	0.02070	625	58	610	11	613	12	0.74	99
GJ-1-28a	137	322	0.02	0.05959	0.00158	0.09919	0.00184	0.81498	0.01972	589	57	610	11	605	11	0.77	101
GJ-1-88b	137	318	0.02	0.06034	0.00166	0.09915	0.00184	0.82488	0.02078	616	59	609	11	611	12	0.74	100
GJ-1-34b	140	325	0.02	0.05947	0.00154	0.09906	0.00184	0.81224	0.01938	585	56	609	11	604	11	0.78	101
GJ-1-115b	139	326	0.02	0.05971	0.00166	0.09904	0.00184	0.81534	0.02064	593	59	609	11	605	12	0.73	101
GJ-1-29a	137	325	0.02	0.05983	0.00158	0.09886	0.00184	0.81556	0.01962	598	56	608	11	606	11	0.77	100
GJ-1-14a	136	317	0.02	0.05985	0.00158	0.09878	0.00182	0.81515	0.01968	598	57	607	11	605	11	0.76	100
GJ-1-3b	136	320	0.02	0.06095	0.00166	0.09877	0.00190	0.83001	0.02088	638	58	607	11	614	12	0.76	99
GJ-1-2a	139	328	0.02	0.05996	0.00154	0.09869	0.00182	0.81584	0.01908	602	55	607	11	606	11	0.79	100
GJ-1-3a	138	325	0.02	0.06036	0.00156	0.09853	0.00182	0.81994	0.01928	616	55	606	11	608	11	0.79	100
GJ-1-60a	138	328	0.02	0.06074	0.00174	0.09850	0.00186	0.82494	0.02166	630	61	606	11	611	12	0.72	99
GJ-1-46a	137	309	0.02	0.05991	0.00194	0.09848	0.00186	0.81346	0.02422	600	70	606	11	604	14	0.63	100
GJ-1-47b	139	327	0.02	0.05945	0.00154	0.09841	0.00182	0.80666	0.01922	584	56	605	11	601	11	0.78	101
GJ-1-130b	135	320	0.02	0.06025	0.00170	0.09837	0.00184	0.81720	0.02114	613	60	605	11	607	12	0.72	100
GJ-1-62b	138	325	0.02	0.06045	0.00158	0.09830	0.00182	0.81919	0.01968	620	56	604	11	608	11	0.77	99
GJ-1-60b	139	327	0.02	0.05942	0.00156	0.09815	0.00182	0.80407	0.01924	582	56	604	11	599	11	0.77	101
GJ-1-114b	136	321	0.02	0.06062	0.00168	0.09814	0.00182	0.82019	0.02078	626	59	604	11	608	12	0.73	99
GJ-1-6b	137	325	0.02	0.05913	0.00164	0.09795	0.00188	0.79854	0.02044	572	60	602	11	596	12	0.75	101
GJ-1-129b	136	324	0.02	0.06040	0.00170	0.09794	0.00182	0.81562	0.02092	618	60	602	11	606	12	0.72	99
GJ-1-62a	138	321	0.02	0.05998	0.00186	0.09779	0.00184	0.80875	0.02310	603	67	601	11	602	13	0.66	100
GJ-1-1a	138	328	0.02	0.06026	0.00154	0.09725	0.00180	0.80800	0.01892	613	55	598	11	601	11	0.79	100
GJ-1-5b	134	321	0.02	0.05999	0.00166	0.09693	0.00186	0.80166	0.02054	603	59	596	11	598	12	0.75	100
GJ-1-116b	134	324	0.02	0.06005	0.00168	0.09626	0.00178	0.79702	0.02030	605	60	593	11	595	11	0.73	100
GJ-1-a2	137	315	0.02	0.05908	0.00188	0.09913	0.00192	0.80714	0.02316	570	68	609	11	601	13	0.68	101
GJ-1-a5	136	317	0.02	0.05964	0.00188	0.09770	0.00188	0.80301	0.02288	591	68	601	11	599	13	0.68	100
GJ-1-a6	138	322	0.02	0.05944	0.00186	0.09754	0.00188	0.79905	0.02254	583	67	600	11	596	13	0.68	101
GJ-1-a7	138	321	0.02	0.06069	0.00190	0.09771	0.00188	0.81725	0.02308	628	67	601	11	607	13	0.68	99
GJ-1-a18	139	319	0.02	0.05907	0.00188	0.09851	0.00190	0.80190	0.02296	570	68	606	11	598	13	0.67	101
GJ-1-a19	138	321	0.02	0.06088	0.00192	0.09767	0.00188	0.81950	0.02318	635	67	601	11	608	13	0.68	99
GJ-1-a20	139	316	0.02	0.06013	0.00194	0.09871	0.00190	0.81795	0.02384	608	69	607	11	607	13	0.66	100
GJ-1-a22	140	326	0.02	0.05982	0.00180	0.09922	0.00190	0.81805	0.02222	597	64	610	11	607	12	0.71	100
GJ-1-a35	139	324	0.02	0.05867	0.00176	0.09847	0.00188	0.79627	0.02166	555	65	606	11	595	12	0.70	102
GJ-1-a52	140	329	0.02	0.05950	0.00182	0.09782	0.00186	0.80227	0.02208	586	66	602	11	598	12	0.69	101
GJ-1-a53	143	314	0.02	0.06016	0.00204	0.09997	0.00192	0.82886	0.02514	609	72	614	11	613	14	0.63	100
GJ-1-a58	136	347	0.02	0.05968	0.00262	0.09759	0.00230	0.80266	0.03290	592	94	600	14	598	19	0.57	100
GJ-1-a72	139	326	0.02	0.06102	0.00188	0.09793	0.00186	0.82369	0.02272	640	66	602	11	610	13	0.69	99
GJ-1-a73	137	345	0.02	0.06025	0.00234	0.09851	0.00218	0.81806	0.02960	612	83	606	13	607	17	0.61	100

Continued ... LA-Q-ICP-MS U-Pb results (GJ-1 zircon, primary standard)

	PPM			Ratios						Ages (Ma)							
Standards	^{206}Pb	^{238}U	Th[b]/U	^{207}Pb/^{206}Pb	± 2σ (abs)	^{206}Pb[a]/^{238}U	± 2σ (abs)	^{207}Pb[a]/^{235}U	± 2σ (abs)	^{207}Pb/^{206}Pb	± 2σ	^{206}Pb/^{238}U	± 2σ	^{207}Pb/^{235}U	± 2σ	Rho[c]	Conc.[d]
GJ-1-a75	140	318	0.02	0.06036	0.00198	0.09802	0.00186	0.81564	0.02394	617	70	603	11	606	13	0.65	100
GJ-1-a76	139	322	0.02	0.06031	0.00192	0.09922	0.00190	0.82488	0.02346	615	68	610	11	611	13	0.67	100
GJ-1-a77	138	321	0.02	0.06058	0.00194	0.09818	0.00188	0.81983	0.02358	624	68	604	11	608	13	0.67	99
GJ-1-a78	137	333	0.02	0.05978	0.00204	0.09767	0.00196	0.80486	0.02512	595	74	601	12	600	14	0.64	100
GJ-1-a83	139	318	0.02	0.05961	0.00188	0.09937	0.00188	0.81650	0.02304	590	68	611	11	606	13	0.67	101
GJ-1-a85	138	321	0.02	0.06096	0.00188	0.09936	0.00188	0.83488	0.02310	638	66	611	11	616	13	0.68	99
GJ-1-a86	138	324	0.02	0.05952	0.00188	0.09835	0.00188	0.80698	0.02290	586	68	605	11	601	13	0.67	101
GJ-1-a98	142	304	0.02	0.05990	0.00226	0.09940	0.00194	0.82068	0.02740	600	80	611	11	608	15	0.58	100
GJ-1-a101	139	318	0.02	0.05997	0.00194	0.09777	0.00184	0.80820	0.02318	603	69	601	11	601	13	0.66	100
GJ-1-a124	139	313	0.02	0.06086	0.00210	0.09850	0.00188	0.82636	0.02518	634	73	606	11	612	14	0.63	99
GJ-1-b1	139	320	0.02	0.05983	0.00180	0.09911	0.00182	0.81728	0.02186	598	65	609	11	607	12	0.69	100
GJ-1-b26	138	312	0.02	0.06048	0.00192	0.09851	0.00180	0.82108	0.02302	621	68	606	11	609	13	0.65	100
GJ-1-b3	140	315	0.02	0.06021	0.00186	0.09937	0.00180	0.82460	0.02226	611	66	611	11	611	12	0.67	100
GJ-1-b4	138	333	0.02	0.05878	0.00194	0.09923	0.00196	0.80395	0.02414	559	71	610	11	599	14	0.66	102
GJ-1-b62	144	304	0.02	0.05971	0.00312	0.09967	0.00236	0.81997	0.03900	593	111	613	14	608	22	0.50	101
GJ-1-b63	141	328	0.02	0.05989	0.00200	0.09878	0.00186	0.81523	0.02410	600	71	607	11	605	13	0.64	100
GJ-1-b68	138	315	0.02	0.05966	0.00200	0.09792	0.00182	0.80503	0.02386	591	72	602	11	600	13	0.63	100
GJ-1-b69	143	286	0.02	0.06009	0.00324	0.09862	0.00234	0.81627	0.03972	607	115	606	14	606	22	0.49	100
GJ-1-b70	135	315	0.02	0.06013	0.00196	0.09772	0.00182	0.80966	0.02330	608	70	601	11	602	13	0.65	100
GJ-1-b71	134	318	0.02	0.06041	0.00212	0.09756	0.00190	0.81216	0.02558	618	75	600	11	604	14	0.62	99
GJ-1-1	135	317	0.02	0.06041	0.00144	0.09821	0.00174	0.81806	0.01756	618	51	604	10	607	10	0.83	99
GJ-1-2	135	315	0.02	0.06007	0.00144	0.09871	0.00174	0.81760	0.01762	606	52	607	10	607	10	0.82	100
GJ-1-3	136	316	0.02	0.06113	0.00146	0.09932	0.00176	0.83715	0.01790	644	51	610	10	618	10	0.83	99
GJ-1-4	139	322	0.02	0.05955	0.00142	0.09940	0.00174	0.81608	0.01750	587	52	611	10	606	10	0.82	101
GJ-1-12	138	327	0.02	0.05938	0.00140	0.09883	0.00176	0.80914	0.01706	581	51	608	10	602	10	0.84	101
GJ-1-13	139	325	0.02	0.06079	0.00146	0.09893	0.00174	0.82913	0.01772	632	51	608	10	613	10	0.82	99
GJ-1-14	137	318	0.02	0.06079	0.00146	0.09931	0.00176	0.83233	0.01786	632	51	610	10	615	10	0.83	99
GJ-1-31	138	320	0.02	0.05955	0.00146	0.09921	0.00176	0.81463	0.01780	587	52	610	10	605	10	0.81	101
GJ-1-32	140	326	0.02	0.06000	0.00142	0.10007	0.00178	0.82783	0.01766	603	51	615	10	612	10	0.83	100
GJ-1-33	139	329	0.02	0.05925	0.00140	0.09894	0.00176	0.80823	0.01728	576	51	608	10	602	10	0.83	101
GJ-1-49	140	325	0.02	0.05907	0.00144	0.09981	0.00178	0.81286	0.01782	570	51	613	10	604	10	0.81	102
GJ-1-50	143	308	0.02	0.05961	0.00340	0.09900	0.00242	0.81332	0.04352	589	121	609	14	604	24	0.46	101
GJ-1-51	141	327	0.02	0.06060	0.00144	0.10073	0.00180	0.84164	0.01798	625	51	619	11	620	10	0.84	100
GJ-1-52	140	325	0.02	0.06012	0.00146	0.09927	0.00176	0.82282	0.01800	608	52	610	10	610	10	0.81	100
GJ-1-53	138	323	0.02	0.05993	0.00146	0.09872	0.00176	0.81577	0.01794	601	53	607	10	606	10	0.81	100
GJ-1-66	138	324	0.02	0.06037	0.00150	0.09871	0.00176	0.82171	0.01826	617	53	607	10	609	10	0.80	100
GJ-1-67	138	327	0.02	0.05956	0.00152	0.09817	0.00176	0.80618	0.01860	588	55	604	10	600	10	0.78	101
GJ-1-68	139	317	0.02	0.06060	0.00162	0.09919	0.00176	0.82880	0.01986	625	57	610	10	613	11	0.74	99
GJ-1-75	137	327	0.02	0.06008	0.00150	0.09732	0.00174	0.80617	0.01800	607	53	599	10	600	10	0.80	100
GJ-1-76	140	329	0.02	0.06019	0.00148	0.09834	0.00176	0.81612	0.01818	611	53	605	10	606	10	0.80	100
GJ-1-89	137	319	0.02	0.06037	0.00152	0.09986	0.00180	0.83122	0.01894	617	54	614	11	614	11	0.79	100

Continued ... LA-Q-ICP-MS U-Pb results (GJ-1 zircon, primary standard)

	PPM			Ratios						Ages (Ma)							
Standards	^{206}Pb	^{238}U	Th^{b}/U	$^{207}Pb/^{206}Pb$	± 2σ (abs)	$^{206}Pb^{a}/^{238}U$	± 2σ (abs)	$^{207}Pb^{a}/^{235}U$	± 2σ (abs)	$^{207}Pb/^{206}Pb$	± 2σ	$^{206}Pb/^{238}U$	± 2σ	$^{207}Pb/^{235}U$	± 2σ	Rho^{c}	$Conc.^{d}$
GJ-1-90	137	322	0.02	0.06012	0.00152	0.09905	0.00178	0.82109	0.01872	608	54	609	10	609	10	0.79	100
GJ-1-91	135	319	0.02	0.06006	0.00152	0.09811	0.00176	0.81234	0.01858	606	54	603	10	604	10	0.78	100
GJ-1-102	137	316	0.02	0.06027	0.00158	0.09893	0.00178	0.82206	0.01952	613	56	608	10	609	11	0.76	100
GJ-1-103	138	320	0.02	0.06030	0.00158	0.09881	0.00178	0.82149	0.01952	614	56	607	10	609	11	0.76	100
GJ-1-104	139	321	0.02	0.06036	0.00154	0.10009	0.00180	0.83294	0.01924	616	55	615	11	615	11	0.78	100
GJ-1-115	139	314	0.02	0.05983	0.00176	0.09968	0.00182	0.82240	0.02206	598	63	613	11	609	12	0.68	101
GJ-1-116	135	321	0.02	0.06068	0.00154	0.09839	0.00178	0.82313	0.01898	628	54	605	10	610	11	0.78	99
GJ-1-117	138	325	0.02	0.06003	0.00152	0.09990	0.00182	0.82685	0.01894	605	54	614	11	612	11	0.80	100
GJ-1-2a	139	328	0.02	0.05910	0.00138	0.09842	0.00168	0.80203	0.01660	571	51	605	10	598	9	0.82	101
GJ-1-3a	137	321	0.02	0.06006	0.00140	0.09939	0.00170	0.82298	0.01702	606	50	611	10	610	9	0.83	100
GJ-1-4a	135	317	0.02	0.06178	0.00144	0.09911	0.00170	0.84420	0.01734	666	49	609	10	622	10	0.84	98
GJ-1-5a	134	316	0.02	0.06078	0.00142	0.09890	0.00170	0.82877	0.01710	631	50	608	10	613	10	0.83	99
GJ-1-6a	136	312	0.02	0.05992	0.00144	0.09925	0.00170	0.82000	0.01744	601	52	610	10	608	10	0.81	100
GJ-1-13a	139	318	0.02	0.06101	0.00148	0.09953	0.00170	0.83723	0.01804	640	52	612	10	618	10	0.79	99
GJ-1-14a	138	323	0.02	0.06029	0.00142	0.09943	0.00172	0.82647	0.01730	614	51	611	10	612	10	0.83	100
GJ-1-15a	139	324	0.02	0.06010	0.00142	0.09908	0.00170	0.82102	0.01714	607	51	609	10	609	10	0.82	100
GJ-1-28a	142	334	0.02	0.06005	0.00144	0.09817	0.00170	0.81277	0.01722	605	51	604	10	604	10	0.82	100
GJ-1-29a	142	320	0.02	0.05984	0.00166	0.09852	0.00170	0.81285	0.02004	598	59	606	10	604	11	0.70	100
GJ-1-30a	142	332	0.02	0.05962	0.00138	0.10016	0.00174	0.82333	0.01700	590	50	615	10	610	9	0.84	101
GJ-1-44a	142	328	0.02	0.06021	0.00156	0.09889	0.00174	0.82093	0.01912	611	56	608	10	609	11	0.76	100
GJ-1-45a	139	327	0.02	0.06011	0.00150	0.09944	0.00176	0.82405	0.01838	608	53	611	10	610	10	0.79	100
GJ-1-46a	143	332	0.02	0.06009	0.00144	0.09946	0.00172	0.82408	0.01764	607	52	611	10	610	10	0.81	100
GJ-1-61a	137	335	0.02	0.06044	0.00170	0.09949	0.00188	0.82886	0.02152	619	60	611	11	613	12	0.73	100
GJ-1-62a	139	323	0.02	0.06011	0.00150	0.09962	0.00174	0.82561	0.01832	608	53	612	10	611	10	0.79	100
GJ-1-63a	137	324	0.02	0.06040	0.00148	0.09876	0.00174	0.82234	0.01806	618	52	607	10	609	10	0.80	100
GJ-1-82a	136	299	0.02	0.05953	0.00196	0.09858	0.00180	0.80905	0.02430	586	71	606	11	602	14	0.61	101
GJ-1-83a	134	321	0.02	0.06076	0.00156	0.09789	0.00176	0.82001	0.01900	631	55	602	10	608	11	0.78	99
GJ-1-84a	136	310	0.02	0.05996	0.00158	0.10065	0.00178	0.83198	0.01984	602	57	618	10	615	11	0.74	101
GJ-1-29b	140	330	0.02	0.05923	0.00148	0.09955	0.00178	0.81301	0.01832	576	54	612	10	604	10	0.79	101
GJ-1-42b	140	324	0.02	0.05952	0.00148	0.09936	0.00174	0.81531	0.01812	586	54	611	10	605	10	0.79	101
GJ-1-43b	139	329	0.02	0.06072	0.00148	0.09846	0.00174	0.82420	0.01794	629	52	605	10	610	10	0.81	99
GJ-1-44b	139	326	0.02	0.05991	0.00148	0.09843	0.00172	0.81298	0.01790	600	53	605	10	604	10	0.79	100
GJ-1-62b	137	307	0.02	0.06045	0.00166	0.09824	0.00172	0.81878	0.02022	620	59	604	10	607	11	0.71	99
GJ-1-63b	138	321	0.02	0.06066	0.00152	0.09953	0.00176	0.83249	0.01868	627	54	612	10	615	10	0.79	99
GJ-1-64b	136	316	0.02	0.05956	0.00150	0.09976	0.00176	0.81915	0.01860	588	54	613	10	608	10	0.78	101
GJ-1-71b	139	323	0.02	0.05999	0.00150	0.09942	0.00176	0.82232	0.01852	603	54	611	10	609	10	0.79	100
GJ-1-72b	137	324	0.02	0.06059	0.00152	0.09791	0.00174	0.81798	0.01832	625	53	602	10	607	10	0.79	99
GJ-1-73b	141	327	0.02	0.05874	0.00148	0.09933	0.00176	0.80450	0.01818	558	54	611	10	599	10	0.78	102
GJ-1-86b	139	317	0.02	0.06023	0.00162	0.09954	0.00176	0.82652	0.02010	612	58	612	10	612	11	0.73	100
GJ-1-87b	138	323	0.02	0.06104	0.00154	0.09904	0.00176	0.83350	0.01884	641	54	609	10	616	10	0.79	99
GJ-1-88b	135	320	0.02	0.05949	0.00154	0.09852	0.00176	0.80808	0.01880	585	55	606	10	601	11	0.77	101

Continued... LA-Q-ICP-MS U-Pb results (GJ-1 zircon, primary standard)

	PPM			Ratios						Ages (Ma)							
Standards	**^{206}Pb**	**^{238}U**	**Th^{b}/U**	**^{207}Pb/^{206}Pb**	**± 2σ (abs)**	**^{206}Pb^{a}/^{238}U**	**± 2σ (abs)**	**^{207}Pb^{a}/^{235}U**	**± 2σ (abs)**	**^{207}Pb/^{206}Pb**	**± 2σ**	**^{206}Pb/^{238}U**	**± 2σ**	**^{207}Pb/^{235}U**	**± 2σ**	**Rho^{c}**	**Conc.^{d}**
GJ-1-103b	137	321	0.02	0.06043	0.00158	0.09930	0.00178	0.82736	0.01940	619	56	610	10	612	11	0.76	100
GJ-1-104b	139	327	0.02	0.06099	0.00156	0.09903	0.00178	0.83276	0.01928	639	55	609	10	615	11	0.78	99
GJ-1-105b	137	320	0.02	0.06053	0.00158	0.09950	0.00178	0.83035	0.01944	623	56	612	10	614	11	0.76	100
Average	138	322	0.02	0.06014	0.00160	0.09900	0.00179	0.82086	0.01969	609	57	609	11	609	11	0.77	100
SD	2	6	0.00	0.00055	0.00027	0.00082	0.00010	0.00996	0.00343	20	10	5	1	6	2	0.07	1
RSD%	1.31	2.00	1.10	0.92	16.77	0.83	5.79	1.21	17.44	3.27	16.74	0.79	5.77	0.91	17.54	8.76	0.72

LA-Q-ICP-MS U-Pb results - (Plešovice and Blue Berry zircons - secondary standard)																	
	PPM		Ratios							Ages (Ma)							
Standards	^{206}Pb	^{238}U	Th^{b}/U	$^{207}Pb/^{206}Pb$	$\pm 2\sigma$ (abs)	$^{206}Pb^{a}/^{238}U$	$\pm 2\sigma$ (abs)	$^{207}Pb^{a}/^{235}U$	$\pm 2\sigma$ (abs)	$^{207}Pb/^{206}Pb$	$\pm 2\sigma$	$^{206}Pb/^{238}U$	$\pm 2\sigma$	$^{207}Pb/^{235}U$	$\pm 2\sigma$	Rho^{c}	$Conc.^{d}$
Plešovice																	
Ples-6	155	657	0.06	0.05277	0.00126	0.05448	0.00094	0.39638	0.00836	319	53	342	6	339	6	0.82	101
Ples-7	155	655	0.06	0.05308	0.00124	0.05446	0.00094	0.39852	0.00832	332	53	342	6	341	6	0.83	100
Ples-9	153	648	0.06	0.05289	0.00124	0.05430	0.00094	0.39597	0.00824	324	53	341	6	339	6	0.83	101
Ples-11	149	631	0.06	0.05261	0.00124	0.05417	0.00092	0.39289	0.00828	312	54	340	6	337	6	0.81	101
Ples-12	153	652	0.06	0.05382	0.00126	0.05398	0.00092	0.40054	0.00832	363	52	339	6	342	6	0.82	99
Ples-36	150	646	0.06	0.05304	0.00128	0.05349	0.00092	0.39113	0.00848	330	55	336	6	335	6	0.79	100
Ples-37	148	625	0.06	0.05284	0.00128	0.05376	0.00092	0.39164	0.00850	322	55	338	6	336	6	0.79	101
Ples-38	147	633	0.06	0.05283	0.00132	0.05335	0.00092	0.38861	0.00866	321	56	335	6	333	6	0.77	101
Ples-39	147	618	0.06	0.05264	0.00128	0.05394	0.00092	0.39154	0.00852	314	55	339	6	336	6	0.78	101
Ples-5	162	692	0.06	0.05242	0.00118	0.05486	0.00094	0.39657	0.00790	304	51	344	6	339	6	0.86	102
Ples-6	153	678	0.06	0.05361	0.00124	0.05435	0.00096	0.40177	0.00832	355	51	341	6	343	6	0.85	100
Ples-7	157	675	0.06	0.05320	0.00120	0.05486	0.00094	0.40247	0.00798	337	50	344	6	343	6	0.86	100
Ples-8	151	653	0.06	0.05249	0.00118	0.05457	0.00094	0.39498	0.00790	307	51	343	6	338	6	0.86	101
Ples-9	147	661	0.06	0.05380	0.00130	0.05451	0.00098	0.40441	0.00882	363	54	342	6	345	6	0.82	99
Ples-10	153	666	0.06	0.05414	0.00120	0.05436	0.00094	0.40578	0.00800	377	50	341	6	346	6	0.88	99
Ples-11	161	694	0.06	0.05305	0.00118	0.05475	0.00094	0.40049	0.00786	331	50	344	6	342	6	0.87	100
Ples-30	146	637	0.06	0.05325	0.00124	0.05422	0.00094	0.39807	0.00826	340	52	340	6	340	6	0.84	100
Ples-31	145	631	0.06	0.05299	0.00124	0.05420	0.00094	0.39602	0.00826	329	52	340	6	339	6	0.83	100
Ples-32	144	576	0.06	0.05365	0.00166	0.05411	0.00094	0.40017	0.01118	356	69	340	6	342	8	0.62	99
Ples-47	147	608	0.06	0.05252	0.00132	0.05495	0.00094	0.39787	0.00888	308	57	345	6	340	6	0.77	101
Ples-48	148	664	0.06	0.05352	0.00132	0.05423	0.00098	0.40018	0.00906	351	55	340	6	342	7	0.80	100
Ples-5	143	617	0.06	0.05366	0.00126	0.05446	0.00094	0.40289	0.00842	357	53	342	6	344	6	0.83	101
Ples-6	139	592	0.06	0.05343	0.00132	0.05404	0.00094	0.39807	0.00876	347	55	339	6	340	6	0.79	100
Ples-7	136	583	0.06	0.05388	0.00134	0.05373	0.00092	0.39908	0.00880	366	56	337	6	341	6	0.78	101
Ples-8	135	578	0.06	0.05331	0.00134	0.05393	0.00094	0.39632	0.00884	342	56	339	6	339	6	0.78	100
Ples-102	149	637	0.06	0.05399	0.00136	0.05439	0.00096	0.40492	0.00920	371	57	341	6	345	7	0.78	101
Ples-103	148	645	0.06	0.05283	0.00130	0.05423	0.00096	0.39500	0.00878	322	55	340	6	338	6	0.80	99
Ples-104	146	625	0.06	0.05349	0.00138	0.05426	0.00096	0.40012	0.00930	349	58	341	6	342	7	0.76	100
Ples-8a	171	717	0.07	0.05296	0.00128	0.05526	0.00100	0.40348	0.00886	327	54	347	6	344	6	0.82	101
Ples-9a	171	740	0.07	0.05293	0.00132	0.05429	0.00100	0.39618	0.00908	326	56	341	6	339	7	0.80	101
Ples-10a	161	689	0.07	0.05356	0.00134	0.05450	0.00100	0.40248	0.00916	353	56	342	6	343	7	0.81	100
Ples-11a	144	620	0.07	0.05372	0.00138	0.05320	0.00096	0.39408	0.00926	359	58	334	6	337	7	0.77	99
Ples-12a	151	644	0.07	0.05364	0.00132	0.05465	0.00100	0.40421	0.00904	356	55	343	6	345	7	0.82	100
Ples-8b	164	691	0.06	0.05283	0.00140	0.05364	0.00098	0.39075	0.00956	322	60	337	6	335	7	0.75	101
Ples-9b	160	685	0.06	0.05281	0.00138	0.05346	0.00098	0.38926	0.00940	321	59	336	6	334	7	0.76	101
Ples-10b	157	684	0.06	0.05270	0.00152	0.05351	0.00102	0.38883	0.01048	316	65	336	6	334	8	0.71	101
Ples-11b	156	645	0.06	0.05251	0.00148	0.05366	0.00098	0.38844	0.00998	308	63	337	6	333	7	0.71	101

Continued ....LA-Q-ICP-MS U-Pb results - (Plešovice and Blue Berry zircons - secondary standard)

	PPM			Ratios							Ages (Ma)							
Standards	**^{206}Pb**	**^{238}U**	**Th^{b}/U**	**^{207}Pb/^{206}Pb**	**± 2σ (abs)**	**^{206}Pb^{a}/^{238}U**	**± 2σ (abs)**	**^{207}Pb^{a}/^{235}U**	**± 2σ (abs)**	**^{207}Pb/^{206}Pb**	**± 2σ**	**^{206}Pb/^{238}U**	**± 2σ**	**^{207}Pb/^{235}U**	**± 2σ**	**Rho^{c}**	**Conc.^{d}**
Ples-12b	155	647	0.06	0.05330	0.00138	0.05431	0.00100	0.39907	0.00952	341	58	341	6	341	7	0.77	100
Ples-13b	151	639	0.06	0.05350	0.00142	0.05381	0.00100	0.39692	0.00976	350	60	338	6	339	7	0.76	100
Ples-14b	157	660	0.06	0.05315	0.00136	0.05432	0.00100	0.39809	0.00940	335	58	341	6	340	7	0.78	100
Ples-64b	163	690	0.06	0.05322	0.00134	0.05382	0.00096	0.39498	0.00908	338	57	338	6	338	7	0.78	100
Ples-65b	168	706	0.07	0.05407	0.00136	0.05437	0.00098	0.40531	0.00922	374	56	341	6	346	7	0.79	99
Ples-68b	161	668	0.08	0.05373	0.00136	0.05518	0.00100	0.40880	0.00942	360	57	346	6	348	7	0.79	99
Ples-69b	157	663	0.07	0.05301	0.00136	0.05414	0.00098	0.39568	0.00922	329	57	340	6	339	7	0.78	100
Ples-5	162	704	0.06	0.05366	0.00124	0.05383	0.00094	0.39830	0.00830	357	52	338	6	340	6	0.84	99
Ples-6	160	725	0.06	0.05332	0.00146	0.05427	0.00104	0.39894	0.01016	342	61	341	6	341	7	0.75	100
Ples-7	161	725	0.07	0.05359	0.00140	0.05374	0.00100	0.39705	0.00956	354	58	337	6	340	7	0.77	99
Ples-8	160	742	0.07	0.05434	0.00164	0.05416	0.00108	0.40585	0.01154	385	67	340	7	346	8	0.70	98
Ples-9	162	736	0.07	0.05297	0.00150	0.05411	0.00104	0.39520	0.01038	328	63	340	6	338	8	0.73	100
Ples-10	179	751	0.08	0.05298	0.00126	0.05422	0.00094	0.39607	0.00846	328	54	340	6	339	6	0.81	100
Ples-11	108	461	0.06	0.05369	0.00138	0.05462	0.00098	0.40432	0.00940	358	57	343	6	345	7	0.77	99
Ples-70	121	514	0.06	0.05397	0.00146	0.05432	0.00098	0.40419	0.00998	370	61	341	6	345	7	0.73	99
Ples-71	94	406	0.06	0.05282	0.00182	0.05395	0.00104	0.39286	0.01256	321	77	339	6	337	9	0.60	101
Ples-72	100	428	0.06	0.05294	0.00150	0.05396	0.00098	0.39389	0.01020	326	64	339	6	337	7	0.70	100
Ples-73	181	806	0.08	0.05439	0.00134	0.05393	0.00098	0.40440	0.00910	387	55	339	6	345	7	0.81	98
Ples-74	130	573	0.06	0.05332	0.00142	0.05392	0.00100	0.39643	0.00966	343	59	339	6	339	7	0.76	100
Ples-7a	156	665	0.06	0.05349	0.00120	0.05516	0.00094	0.40676	0.00804	349	50	346	6	347	6	0.86	100
Ples-9a	149	662	0.06	0.05241	0.00140	0.05415	0.00098	0.39125	0.00946	303	60	340	6	335	7	0.75	101
Ples-10a	148	630	0.06	0.05323	0.00122	0.05503	0.00094	0.40380	0.00814	338	51	345	6	344	6	0.85	100
Ples-11a	159	682	0.06	0.05319	0.00118	0.05479	0.00094	0.40174	0.00790	337	50	344	6	343	6	0.87	100
Ples-12a	163	694	0.06	0.05337	0.00118	0.05533	0.00094	0.40711	0.00798	344	50	347	6	347	6	0.87	100
Ples-8b	154	653	0.06	0.05306	0.00130	0.05433	0.00094	0.39746	0.00866	331	55	341	6	340	6	0.79	100
Ples-13b	159	657	0.06	0.05378	0.00134	0.05503	0.00094	0.40805	0.00910	362	56	345	6	348	7	0.77	99
Ples-66b	152	628	0.06	0.05410	0.00146	0.05438	0.00094	0.40568	0.00990	375	61	341	6	346	7	0.71	99
Average	151	649	0.06	0.05328	0.00134	0.05425	0.00096	0.39857	0.00905	341	56	341	6	341	7	0.79	100
SD	15	68	0.00	0.00049	0.00012	0.00047	0.00003	0.00522	0.00091	21	5	3	0	4	1	0.05	1
RSD%	10.02	10.43	7.75	0.92	8.96	0.87	3.60	1.31	10.01	6.07	8.88	0.84	3.45	1.11	10.07	6.92	0.77
Blue Berry																	
BB-a10	102	260	0.10	0.05874	0.00212	0.09106	0.00188	0.73710	0.02450	558	78	562	11	561	14	0.62	100
BB-a11	103	261	0.10	0.05871	0.00244	0.09091	0.00200	0.73562	0.02822	556	90	561	12	560	17	0.57	100
BB-a12	103	251	0.10	0.05881	0.00256	0.09096	0.00200	0.73711	0.02946	560	93	561	12	561	17	0.55	100
BB-a121	97	248	0.10	0.05975	0.00218	0.08948	0.00178	0.73695	0.02422	594	78	553	11	561	14	0.61	99
BB-a123	94	254	0.10	0.05849	0.00240	0.08828	0.00190	0.71167	0.02684	548	90	545	11	546	16	0.57	100
BB-a14	101	252	0.10	0.05919	0.00208	0.09124	0.00184	0.74429	0.02378	574	75	563	11	565	14	0.63	100
BB-a16	100	252	0.10	0.05855	0.00308	0.09075	0.00226	0.73207	0.03572	550	113	560	13	558	21	0.51	100

Continued ....LA-Q-ICP-MS U-Pb results - (Plešovice and Blue Berry zircons - secondary standard)

	PPM			Ratios						Ages (Ma)							
Standards	^{206}Pb	^{238}U	Th^{b}/U	^{207}Pb/^{206}Pb	± 2σ (abs)	^{206}Pb^{a}/^{238}U	± 2σ (abs)	^{207}Pb^{a}/^{235}U	± 2σ (abs)	^{207}Pb/^{206}Pb	± 2σ	^{206}Pb/^{238}U	± 2σ	^{207}Pb/^{235}U	± 2σ	Rho^{c}	Conc.^{d}
BB-a17	98	258	0.10	0.05766	0.00214	0.08886	0.00184	0.70604	0.02404	516	81	549	11	542	14	0.61	101
BB-a54	101	258	0.10	0.05835	0.00202	0.08996	0.00178	0.72360	0.02270	543	74	555	11	553	13	0.63	100
BB-a55	100	248	0.10	0.05801	0.00222	0.08956	0.00180	0.71607	0.02504	530	84	553	11	548	15	0.57	101
BB-a56	97	262	0.10	0.05868	0.00232	0.08854	0.00192	0.71618	0.02624	555	85	547	11	548	16	0.59	100
BB-a79	100	259	0.10	0.05963	0.00212	0.08905	0.00178	0.73191	0.02362	590	76	550	11	558	14	0.62	99
BB-a80	101	266	0.10	0.05898	0.00212	0.08838	0.00178	0.71857	0.02348	567	77	546	11	550	14	0.62	99
BB-a81	103	264	0.10	0.05878	0.00200	0.08941	0.00176	0.72444	0.02236	559	72	552	10	553	13	0.64	100
BB-a82	96	263	0.10	0.05861	0.00252	0.08941	0.00204	0.72228	0.02878	553	92	552	12	552	17	0.57	100
BB-b27	95	242	0.10	0.05844	0.00244	0.09087	0.00194	0.73185	0.02792	546	90	561	11	558	16	0.56	101
BB-b28	97	250	0.10	0.05939	0.00200	0.08877	0.00168	0.72659	0.02194	581	72	548	10	555	13	0.63	99
BB-b29	101	249	0.10	0.05885	0.00204	0.09026	0.00170	0.73217	0.02272	562	75	557	10	558	13	0.61	100
BB-b5	100	255	0.10	0.05904	0.00208	0.09179	0.00182	0.74696	0.02380	569	76	566	11	567	14	0.62	100
BB-b6	98	268	0.10	0.05891	0.00258	0.09059	0.00206	0.73553	0.02990	564	94	559	12	560	18	0.56	100
BB-b7	97	244	0.10	0.05913	0.00210	0.08983	0.00174	0.73214	0.02346	572	77	555	10	558	14	0.60	99
BB-b65	99	235	0.10	0.05858	0.00244	0.08945	0.00178	0.72205	0.02684	551	89	552	11	552	16	0.54	100
BB-b66	98	256	0.10	0.05851	0.00218	0.08964	0.00178	0.72278	0.02438	549	81	553	11	552	14	0.59	100
Average	99	255	0.10	0.05877	0.00227	0.08987	0.00186	0.72800	0.02565	559	83	555	11	555	15	0.59	100
SD	3	8	0.00	0.00046	0.00025	0.00098	0.00013	0.01003	0.00316	17	9	6	1	6	2	0.03	1
RSD%	2.56	3.12	1.19	0.79	11.14	1.09	7.17	1.38	12.30	3.07	11.33	1.04	7.17	1.06	12.24	5.62	0.63

[a]corrected for background, within-run Pb/U fractionation (in case of ^{206}Pb/^{238}U) and common Pb using Stacy and Kramers (1975) model Pb composition and subsequently normalised to GJ-1 (ID-TIMS value/measured value); ^{207}Pb/^{235}U calculated using ^{207}Pb/^{206}Pb/(^{238}U/^{206}Pb*1/137.88)

[b] U and Pb content and Th/U ratio were calculated relative to GJ-1 reference zircon.

[c] Rho is the ^{207}Pb/^{235}U/^{206}Pb/^{238}U error correlation coefficient.

[d] Concordance: 1 + ((^{206}Pb/^{238}U - ^{207}Pb/^{235}U)/ ^{206}Pb/^{238}U))*100

LA-SF-ICP-MS U-Pb results - Sample CC34

Spot	PPM			Ratios								Ages (Ma)				Rho[c]	Conc.[d]
	^{206}Pb	^{238}U	Th^{b}/U	$^{207}Pb/^{206}Pb$	± 2σ	$^{206}Pb^{a}/^{238}U$	± 2σ	$^{207}Pb^{a}/^{235}U$	± 2σ	$^{207}Pb/^{206}Pb$	± 2σ	$^{206}Pb/^{238}U$	± 2σ	$^{207}Pb/^{235}U$	± 2σ		
Inherited - Population ca. 740-690 Ma																	
CC34-a100	19	151	0.39	0.06378	1.55224	0.12145	3.52936	1.06805	3.85562	734	33	739	25	738	20	0.92	100
Inherited - Population ca. 680-635 Ma																	
CC34-b98	10	103	0.13	0.06099	1.57148	0.10500	2.79294	0.88299	3.20469	639	34	644	17	643	15	0.87	100
Inherited - Population ca. 630-620 Ma																	
CC34-a152	31	318	0.08	0.06042	1.23221	0.10270	1.81512	0.85552	2.19386	619	27	630	11	628	10	0.83	100
Inherited - Population ca. 615-600 Ma																	
CC34-a97	23	249	0.10	0.06018	1.47038	0.09907	2.10015	0.82202	2.56372	610	32	609	12	609	12	0.82	100
CC34-a114	20	221	0.09	0.05988	1.45259	0.09768	1.91726	0.80642	2.40539	599	31	601	11	600	11	0.80	100
CC34-a127	14	157	0.12	0.05906	1.95906	0.09674	1.83211	0.78779	2.68226	569	43	595	10	590	12	0.68	101
CC34-a128	11	112	0.16	0.06024	2.06600	0.09928	1.90646	0.82458	2.81121	612	45	610	11	611	13	0.68	100
CC34-a133	12	131	0.09	0.06019	1.84466	0.09876	1.95892	0.81957	2.69075	610	40	607	11	608	12	0.73	100
CC34-a154	17	182	0.14	0.05995	1.52513	0.09877	1.92266	0.81642	2.45410	602	33	607	11	606	11	0.78	100
CC34-b53	12	122	0.20	0.06014	1.63952	0.09970	2.66639	0.82675	3.13012	609	35	613	16	612	14	0.85	100
CC34-b55	18	197	0.09	0.05977	1.30206	0.09828	2.60396	0.80999	2.91135	595	28	604	15	602	13	0.89	100
CC34-b59	16	159	0.44	0.05985	1.53131	0.09866	2.68697	0.81425	3.09269	598	33	607	16	605	14	0.87	100
CC34-b74	13	137	0.16	0.06000	1.73665	0.09809	2.64234	0.81149	3.16194	604	38	603	15	603	14	0.84	100
CC34-b75	11	114	0.13	0.06006	1.83069	0.09964	2.72312	0.82519	3.28128	606	40	612	16	611	15	0.83	100
CC34-b79	9	98	0.11	0.05982	1.82729	0.09755	2.68188	0.80459	3.24522	597	40	600	15	599	15	0.83	100
CC34-b82	9	95	0.19	0.05998	1.82537	0.09906	3.08392	0.81926	3.58365	603	40	609	18	608	17	0.86	100
CC34-b83	29	305	0.08	0.06015	1.13276	0.10009	2.57320	0.83008	2.81150	609	24	615	15	614	13	0.92	100
CC34-b84	10	101	0.14	0.05963	2.01352	0.09761	2.87561	0.80247	3.51047	590	44	600	17	598	16	0.82	100
CC34-b86	9	95	0.15	0.05979	1.91077	0.09784	2.58108	0.80663	3.21139	596	41	602	15	601	15	0.80	100
CC34-b97	7	69	0.15	0.06016	1.69217	0.10004	2.69825	0.82978	3.18497	609	37	615	16	613	15	0.85	100
CC34-b99	4	36	0.18	0.06007	2.30883	0.09878	2.74016	0.81819	3.58318	606	50	607	16	607	17	0.76	100
CC34-b102	14	107	1.20	0.06041	1.65555	0.10072	2.78160	0.83892	3.23699	618	36	619	16	619	15	0.86	100
CC34-b104	10	101	0.39	0.06003	1.87031	0.09879	2.72636	0.81772	3.30622	605	40	607	16	607	15	0.82	100
CC34-b107	15	164	0.12	0.05965	1.37976	0.09702	3.04618	0.79794	3.34410	591	30	597	17	596	15	0.91	100
CC34-b108	18	192	0.09	0.06027	1.45283	0.10098	2.68208	0.83910	3.05028	613	31	620	16	619	14	0.88	100
CC34-b110	12	129	0.09	0.05979	1.63138	0.09837	2.99761	0.81092	3.41278	596	35	605	17	603	16	0.88	100
Average	14	142	0.20	0.05996	1.69820	0.09876	2.54036	0.81652	3.07242	602	37	607	15	606	14	0.82	100
SD	6	60	0.23	0.00028	0.26718	0.00108	0.38242	0.01230	0.33940	10	6	6	2	7	2	0.06	0
RSD%	40	42	114	0	16	1	15	2	11	2	16	1	15	1	11	8	0
Magmatic																	
CC34-a93	15	166	0.20	0.05951	1.58291	0.09446	1.94001	0.77503	2.50384	586	34	582	11	583	11	0.77	100
CC34-a96	23	218	0.52	0.05994	1.73357	0.09566	2.42094	0.79054	2.97762	601	38	589	14	591	13	0.81	100
CC34-a98	24	276	0.04	0.05930	1.27186	0.09351	1.84542	0.76455	2.24125	578	28	576	10	577	10	0.82	100
CC34-a101	18	198	0.10	0.05939	1.58461	0.09515	2.03741	0.77913	2.58109	581	34	586	11	585	12	0.79	100

Continued ... LA-SF-ICP-MS U-Pb results - Sample CC34

	PPM			Ratios								Ages (Ma)					
Spot	^{206}Pb	^{238}U	Th^{b}/U	$^{207}Pb/^{206}Pb$	± 2σ	$^{206}Pb^{a}/^{238}U$	± 2σ	$^{207}Pb^{a}/^{235}U$	± 2σ	$^{207}Pb/^{206}Pb$	± 2σ	$^{206}Pb/^{238}U$	± 2σ	$^{207}Pb/^{235}U$	± 2σ	Rho^{c}	$Conc.^{d}$
CC34-a103	19	213	0.12	0.05925	1.58541	0.09240	1.85760	0.75486	2.44217	576	34	570	10	571	11	0.76	100
CC34-a104	17	189	0.15	0.05903	1.49351	0.09298	2.00579	0.75673	2.50076	568	33	573	11	572	11	0.80	100
CC34-a105	27	250	0.70	0.05918	1.45515	0.09572	1.95459	0.78108	2.43678	574	32	589	11	586	11	0.80	101
CC34-a107	29	312	0.18	0.05933	1.12918	0.09354	2.10687	0.76525	2.39039	579	25	577	12	577	11	0.88	100
CC34-a108	25	274	0.17	0.05931	1.26341	0.09361	2.05958	0.76544	2.41621	578	27	577	11	577	11	0.85	100
CC34-a109	11	126	0.14	0.05912	1.83061	0.09242	2.42983	0.75329	3.04224	571	40	570	13	570	13	0.80	100
CC34-a112	17	184	0.11	0.05956	1.71930	0.09528	2.19013	0.78235	2.78436	587	37	587	12	587	12	0.79	100
CC34-a113	20	221	0.12	0.05975	1.60759	0.09643	1.73519	0.79451	2.36542	595	35	594	10	594	11	0.73	100
CC34-a121	25	192	1.55	0.05910	1.52056	0.09176	2.24963	0.74768	2.71532	571	33	566	12	567	12	0.83	100
CC34-a132	30	341	0.46	0.05915	1.03986	0.09296	1.84792	0.75809	2.12040	573	23	573	10	573	9	0.87	100
CC34-a135	11	123	0.98	0.05921	1.52052	0.09327	2.39717	0.76136	2.83873	575	33	575	13	575	13	0.84	100
CC34-a140	5	58	0.15	0.05948	1.87452	0.09465	1.91703	0.77616	2.68120	585	41	583	11	583	12	0.71	100
CC34-a141	17	180	0.17	0.05959	1.55329	0.09560	1.86672	0.78553	2.42845	589	34	589	11	589	11	0.77	100
CC34-a143	13	142	0.14	0.05942	1.75828	0.09397	2.16246	0.76985	2.78708	582	38	579	12	580	12	0.78	100
CC34-a146	17	187	0.14	0.05953	1.50095	0.09484	2.04699	0.77850	2.53831	587	33	584	11	585	11	0.81	100
CC34-a148	16	176	0.11	0.05952	1.66789	0.09572	1.93839	0.78562	2.55718	586	36	589	11	589	11	0.76	100
CC34-a149	15	175	0.08	0.05923	1.68163	0.09271	2.88254	0.75708	3.33721	575	37	572	16	572	15	0.86	100
CC34-a157	30	301	0.37	0.05970	1.56433	0.09512	1.89301	0.78302	2.45573	593	34	586	11	587	11	0.77	100
CC34-a158	19	167	0.88	0.05966	1.90178	0.09451	1.90396	0.77752	2.69106	591	41	582	11	584	12	0.71	100
CC34-a159	15	145	0.67	0.05957	1.91296	0.09460	2.24310	0.77705	2.94804	588	42	583	13	584	13	0.76	100
CC34-b57	17	189	0.11	0.05945	1.43147	0.09510	2.65970	0.77947	3.02045	584	31	586	15	585	14	0.88	100
CC34-b60	12	130	0.12	0.05921	1.69898	0.09415	2.72298	0.76865	3.20955	575	37	580	15	579	14	0.85	100
CC34-b63	10	113	0.21	0.05905	1.99911	0.09241	2.71379	0.75239	3.37062	569	44	570	15	570	15	0.81	100
CC34-b66	19	209	0.70	0.05931	1.37789	0.09465	2.60392	0.77403	2.94601	579	30	583	15	582	13	0.88	100
CC34-b68	15	167	0.75	0.05927	1.59697	0.09356	2.80028	0.76457	3.22364	577	35	577	15	577	14	0.87	100
CC34-b70	19	160	1.17	0.05974	1.59332	0.09669	2.63245	0.79643	3.07709	594	35	595	15	595	14	0.86	100
CC34-b73	24	258	0.24	0.05946	1.25792	0.09514	2.70921	0.77998	2.98700	584	27	586	15	585	13	0.91	100
CC34-b76	15	175	0.07	0.05926	1.85145	0.09311	2.91598	0.76079	3.45410	577	40	574	16	574	15	0.84	100
CC34-b78	20	223	0.44	0.05924	1.43188	0.09415	2.90672	0.76901	3.24026	576	31	580	16	579	14	0.90	100
CC34-b80	12	126	0.30	0.05945	1.57057	0.09500	3.11066	0.77864	3.48467	583	34	585	17	585	16	0.89	100
CC34-b85	14	159	0.09	0.05910	1.61954	0.09304	2.76083	0.75816	3.20080	571	35	573	15	573	14	0.86	100
CC34-b87	15	146	0.59	0.05947	2.24218	0.09344	2.62427	0.76622	3.45169	584	49	576	14	578	15	0.76	100
CC34-b90	10	97	0.43	0.05939	1.87422	0.09459	2.96892	0.77459	3.51101	582	41	583	17	582	16	0.85	100
CC34-b95	59	662	0.12	0.05966	2.12620	0.09420	3.13826	0.77493	3.79070	591	46	580	17	583	17	0.83	100
CC34-b103	17	177	0.20	0.05947	1.51206	0.09522	3.16865	0.78073	3.51094	584	33	586	18	586	16	0.90	100
CC34-b105	8	88	0.18	0.05938	2.12590	0.09440	2.64169	0.77292	3.39087	581	46	581	15	581	15	0.78	100
CC34-b109	26	293	0.12	0.05932	1.26804	0.09451	2.58151	0.77300	2.87613	579	28	582	14	581	13	0.90	100
CC34-b112	14	124	0.85	0.05966	1.80364	0.09546	2.72427	0.78524	3.26722	591	39	588	15	588	15	0.83	100

Continued... LA-SF-ICP-MS U-Pb results - Sample CC34

	PPM			Ratios						Ages (Ma)							
Spot	**^{206}Pb**	**^{238}U**	**Th^{b}/U**	**^{207}Pb/^{206}Pb**	**± 2σ**	**^{206}Pb^{a}/^{238}U**	**± 2σ**	**^{207}Pb^{a}/^{235}U**	**± 2σ**	**^{207}Pb/^{206}Pb**	**± 2σ**	**^{206}Pb/^{238}U**	**± 2σ**	**^{207}Pb/^{235}U**	**± 2σ**	**Rho^{c}**	**Conc.^{d}**
CC34-b116	9	104	0.11	0.05926	1.71960	0.09380	2.99057	0.76642	3.44971	577	37	578	17	578	15	0.87	100
Average	18	196	0.35	0.05939	1.62453	0.09427	2.40249	0.77201	2.91263	582	35	581	13	581	13	0.82	100
SD	9	95	0.34	0.00021	0.25731	0.00114	0.42651	0.01154	0.41918	8	6	7	2	7	2	0.05	0
RSD%	47	49	97	0	16	1	18	1	14	1	16	1	18	1	14	6	0
Anatectic - Population 1																	
CC34-a94	22	255	0.09	0.75193	2.57129	0.09232	2.25628	0.75193	2.57129	570	27	569	12	569	11	0.88	100
CC34-a144	21	245	0.10	0.75158	2.39156	0.09211	1.88122	0.75158	2.39156	574	32	568	10	569	10	0.79	100
CC34-a110	26	300	0.10	0.73147	2.42114	0.09028	1.99690	0.73147	2.42114	558	30	557	11	557	10	0.82	100
CC34-a122	51	608	0.04	0.73327	2.34602	0.09043	2.09236	0.73327	2.34602	560	23	558	11	558	10	0.89	100
CC34-a125	9	102	0.25	0.05923	2.18982	0.09192	2.33223	0.75065	3.19916	575	48	567	13	569	14	0.73	100
CC34-a126	40	482	0.06	0.72427	2.15689	0.08948	1.84365	0.72427	2.15689	556	24	552	10	553	9	0.85	100
CC34-a136	12	137	0.12	0.73056	2.63048	0.09023	2.17977	0.73056	2.63048	557	32	557	12	557	11	0.83	100
CC34-a137	15	177	0.06	0.72731	2.45368	0.08991	2.02092	0.72731	2.45368	555	30	555	11	555	11	0.82	100
CC34-a138	10	95	0.76	0.73761	2.61023	0.09056	2.11464	0.73761	2.61023	570	33	559	11	561	11	0.81	100
CC34-a139	9	87	0.59	0.74305	2.85514	0.09131	2.16539	0.74305	2.85514	568	41	563	12	564	12	0.76	100
CC34-a142	13	137	0.27	0.74942	2.71459	0.09186	1.97153	0.74942	2.71459	573	41	567	11	568	12	0.73	100
CC34-a145	15	175	0.14	0.72795	2.46930	0.08973	1.96108	0.72795	2.46930	561	33	554	10	555	11	0.79	100
CC34-b106	8	92	0.14	0.73549	3.46066	0.09068	2.86204	0.73549	3.46066	561	42	560	15	560	15	0.83	100
CC34-b77	14	167	0.08	0.73908	3.29301	0.09107	2.92946	0.73908	3.29301	562	33	562	16	562	14	0.89	100
CC34-b81	15	171	0.12	0.74768	3.08415	0.09199	2.80135	0.74768	3.08415	565	28	567	15	567	13	0.91	100
CC34-b89	27	225	1.23	0.05893	1.60957	0.09115	2.78963	0.74063	3.22068	564	35	562	15	563	14	0.87	100
CC34-b91	13	147	0.11	0.74423	3.22850	0.09157	2.77005	0.74423	3.22850	565	36	565	15	565	14	0.86	100
CC34-b93	7	76	0.15	0.74570	3.68220	0.09182	2.96970	0.74570	3.68220	563	47	566	16	566	16	0.81	100
Average	18	204	0.24	0.66327	2.67601	0.09102	2.32990	0.73955	2.82159	564	34	562	13	562	12	0.83	100
SD	11	136	0.30	0.21377	0.50120	0.00087	0.39056	0.00876	0.43056	6	7	5	2	5	2	0.05	0
RSD%	63	67	123	32	19	1	17	1	15	1	20	1	17	1	16	6	0
Anatectic - Population 2																	
CC34-a115	26	320	0.07	0.68724	2.41713	0.08571	2.01314	0.68724	2.41713	536	29	530	10	531	10	0.83	100
CC34-a123	18	229	0.07	0.68418	2.64958	0.08545	2.14448	0.68418	2.64958	533	34	529	11	529	11	0.81	100
CC34-a134	23	291	0.03	0.68262	2.08916	0.08528	1.78581	0.68262	2.08916	532	24	528	9	528	9	0.85	100
CC34-a151	15	186	0.12	0.68628	2.42670	0.08569	1.86666	0.68628	2.42670	533	34	530	10	531	10	0.77	100
CC34-a156	23	250	0.04	0.70081	2.29892	0.08711	1.85560	0.70081	2.29892	543	30	538	10	539	10	0.81	100
CC34-b56	25	315	0.03	0.69301	3.02224	0.08648	2.73876	0.69301	3.02224	534	28	535	14	535	13	0.91	100
CC34-b69	27	325	0.07	0.70035	2.87586	0.08727	2.64135	0.70035	2.87586	537	25	539	14	539	12	0.92	100
CC34-b92	25	311	0.04	0.67972	3.28379	0.08514	3.03327	0.67972	3.28379	526	28	527	15	527	14	0.92	100
CC34-b94	16	166	0.44	0.70880	3.22220	0.08802	2.92981	0.70880	3.22220	545	29	544	15	544	14	0.91	100
CC34-b96	7	82	0.13	0.69972	3.42505	0.08717	2.84643	0.69972	3.42505	538	42	539	15	539	14	0.83	100
CC34-b101	12	148	0.04	0.68008	3.54960	0.08516	3.30657	0.68008	3.54960	527	28	527	17	527	15	0.93	100

Continued ... LA-SF-ICP-MS U-Pb results - Sample CC34

	PPM			Ratios						Ages (Ma)							
Spot	**^{206}Pb**	**^{238}U**	**Th^{b}/U**	**^{207}Pb/^{206}Pb**	**± 2σ**	**^{206}Pb^{a}/^{238}U**	**± 2σ**	**^{207}Pb^{a}/^{235}U**	**± 2σ**	**^{207}Pb/^{206}Pb**	**± 2σ**	**^{206}Pb/^{238}U**	**± 2σ**	**^{207}Pb/^{235}U**	**± 2σ**	**Rho^{c}**	**Conc.^{d}**
Average	20	239	0.10	0.69116	2.84184	0.08622	2.46926	0.69116	2.84184	535	30	533	13	533	12	0.86	100
SD	6	79	0.11	0.00944	0.47345	0.00098	0.52190	0.00944	0.47345	6	5	6	3	6	2	0.05	0
RSD%	32	33	114	1	17	1	21	1	17	1	16	1	21	1	17	6	0
Anatectic - Population 3																	
CC34-a106	18	213	0.04	0.64237	2.62383	0.08116	2.08720	0.64237	2.62383	507	35	503	10	504	10	0.80	100
CC34-a111	33	427	0.06	0.65844	2.99091	0.08275	2.60493	0.65844	2.99091	519	32	512	13	514	12	0.87	100
CC34-a130	20	261	0.06	0.64250	2.47437	0.08121	2.05083	0.64250	2.47437	506	30	503	10	504	10	0.83	100
CC34-a153	43	551	0.01	0.67163	2.16247	0.08441	1.87353	0.67163	2.16247	519	24	522	9	522	9	0.87	100
CC34-a155	36	472	0.02	0.66084	2.19105	0.08302	1.86522	0.66084	2.19105	519	25	514	9	515	9	0.85	100
CC34-b64	50	630	0.07	0.66581	3.43748	0.08366	3.25132	0.66581	3.43748	519	24	518	16	518	14	0.95	100
CC34-b67	16	201	0.09	0.65751	3.89159	0.08281	3.59631	0.65751	3.89159	514	33	513	18	513	16	0.92	100
CC34-b72	15	196	0.06	0.66143	3.51980	0.08318	3.10379	0.66143	3.51980	517	36	515	15	515	14	0.88	100
CC34-b100	15	195	0.05	0.66989	3.68959	0.08407	3.44077	0.66989	3.68959	522	29	520	17	521	15	0.93	100
Average	27	350	0.05	0.65894	2.99790	0.08292	2.65265	0.65894	2.99790	516	30	514	13	514	12	0.88	100
SD	13	162	0.02	0.00992	0.62412	0.00107	0.66540	0.00992	0.62412	5	4	6	3	6	3	0.05	0
RSD%	46	46	45	2	21	1	25	2	21	1	15	1	26	1	21	5	0
Anatectic - Population 4																	
CC34-a124	21	297	0.04	0.60901	2.57178	0.07767	2.11955	0.60901	2.57178	487	32	482	10	483	10	0.82	100
CC34-a129	19	263	0.06	0.60652	2.51246	0.07739	2.07729	0.60652	2.51246	485	31	481	10	481	10	0.83	100
CC34-a147	20	276	0.05	0.62377	3.03233	0.07908	2.69971	0.62377	3.03233	500	30	491	13	492	12	0.89	100
CC34-b54	42	586	0.02	0.61106	3.20252	0.07785	2.91245	0.61106	3.20252	489	29	483	14	484	12	0.91	100
CC34-b88	15	193	0.18	0.05829	1.40605	0.07767	2.85443	0.62427	3.18194	541	31	482	13	493	12	0.90	98
Average	24	323	0.07	0.50173	2.54503	0.07793	2.53269	0.61493	2.90021	500	31	484	12	487	11	0.87	99
SD	10	136	0.06	0.22180	0.62751	0.00059	0.36158	0.00757	0.29881	21	1	4	2	5	1	0.04	1
RSD%	41	42	80	44	25	1	14	1	10	4	3	1	15	1	11	4	1

LA-SF-ICP-MS U-Pb results - Sample CC47

	PPM			Ratios								Ages (Ma)					
Spot	^{206}Pb	^{238}U	Th^{b}/U	$^{207}Pb/^{206}Pb$	± 2σ	$^{206}Pb^{a}/^{238}U$	± 2σ	$^{207}Pb^{a}/^{235}U$	± 2σ	$^{207}Pb/^{206}Pb$	± 2σ	$^{206}Pb/^{238}U$	± 2σ	$^{207}Pb/^{235}U$	± 2σ	Rho[c]	Conc.[d]
Inherited - Population ca. 740-690 Ma																	
CC47-041	19	174	0.01	0.06344	0.49468	0.11743	0.81236	1.02714	0.95113	723	10	716	6	717	5	0.85	99
Inherited - Population ca. 680-635 Ma																	
CC47-150	17	148	0.32	0.06148	0.82534	0.10753	0.93622	0.91152	1.24808	656	18	658	6	658	6	0.75	100
Inherited - Population ca. 630-600 Ma																	
CC47-032	22	223	0.07	0.06125	0.86197	0.10383	1.01671	0.87690	1.33293	648	19	637	6	639	6	0.76	98
CC47-033	22	224	0.07	0.06129	1.24175	0.10401	1.15843	0.87893	1.69821	649	27	638	7	640	8	0.68	98
CC47-035	23	237	0.07	0.06090	0.51240	0.10134	0.82011	0.85088	0.96702	636	11	622	5	625	5	0.85	98
CC47-037	11	105	0.33	0.06045	0.92586	0.09825	0.92237	0.81892	1.30690	620	20	604	5	607	6	0.71	97
CC47-040	28	303	0.04	0.06024	3.28548	0.09726	0.93385	0.80780	3.41562	612	71	598	5	601	16	0.27	98
CC47-067	22	238	0.07	0.06027	1.06089	0.09668	0.82552	0.80338	1.34423	613	23	595	5	599	6	0.61	97
CC47-068	27	280	0.05	0.06128	3.97141	0.10318	0.96201	0.87183	4.08627	649	85	633	6	637	20	0.24	98
CC47-069	25	259	0.06	0.06135	3.81969	0.10351	0.93669	0.87558	3.93286	651	82	635	6	639	19	0.24	97
CC47-070	21	216	0.08	0.06066	0.61533	0.09888	1.00135	0.82702	1.17530	627	13	608	6	612	5	0.85	97
CC47-072	19	196	0.09	0.06081	1.10040	0.09916	0.97214	0.83140	1.46831	633	24	609	6	614	7	0.66	96
CC47-073	18	198	0.07	0.06034	1.16701	0.09678	0.98369	0.80518	1.52629	616	25	596	6	600	7	0.64	97
CC47-076	32	317	0.09	0.06146	5.13439	0.10408	0.99899	0.88204	5.23067	655	110	638	6	642	25	0.19	97
CC47-078	15	164	0.08	0.06024	4.48760	0.09636	0.99855	0.80034	4.59735	612	97	593	6	597	21	0.22	97
CC47-079	13	137	0.07	0.06056	1.04871	0.09838	1.03206	0.82147	1.47137	624	23	605	6	609	7	0.70	97
CC47-080	40	428	0.07	0.06058	0.53084	0.09768	0.83184	0.81592	0.98679	624	11	601	5	606	5	0.84	96
CC47-114	48	492	0.10	0.06022	0.52809	0.09931	0.75423	0.82450	0.92073	611	11	610	4	611	4	0.82	100
CC47-115	46	470	0.09	0.06030	0.52092	0.09979	0.91684	0.82974	1.05449	614	11	613	5	613	5	0.87	100
CC47-147	37	374	0.12	0.06030	0.55760	0.09965	0.84360	0.82841	1.01123	614	12	612	5	613	5	0.83	100
CC47-149	25	261	0.09	0.06021	2.02289	0.09936	0.83317	0.82489	2.18775	611	44	611	5	611	10	0.38	100
CC47-151	19	201	0.11	0.05993	0.60510	0.09744	0.81128	0.80520	1.01209	601	13	599	5	600	5	0.80	100
CC47-153	22	205	0.30	0.06045	0.67931	0.10058	0.77830	0.83824	1.03306	620	15	618	5	618	5	0.75	100
CC47-154	45	473	0.04	0.06046	0.56491	0.10105	0.85368	0.84230	1.02366	620	12	621	5	620	5	0.83	100
CC47-155	47	494	0.04	0.06049	0.66595	0.10110	0.77702	0.84314	1.02335	621	14	621	5	621	5	0.76	100
CC47-156	17	176	0.09	0.06000	0.79613	0.09786	0.77391	0.80958	1.11029	603	17	602	4	602	5	0.70	100
CC47-159	16	168	0.07	0.06036	0.93302	0.10023	0.86076	0.83422	1.26942	617	20	616	5	616	6	0.68	100
Average	26	274	0.09	0.06058	1.50551	0.09983	0.90388	0.83391	1.84745	624	32	613	5	616	9	0.64	98
SD	11	114	0.07	0.00043	1.38426	0.00237	0.09989	0.02513	1.26358	15	30	14	1	14	6	0.23	1
RSD%	41	42	73	1	92	2	11	3	68	2	92	2	12	2	70	36	1
Magmatic																	
CC47-027	45	513	0.03	0.05978	0.45934	0.09424	1.68953	0.77678	1.75086	596	10	581	9	584	8	0.96	97
CC47-028	17	188	0.13	0.05965	0.56985	0.09331	0.85766	0.76746	1.02971	591	12	575	5	578	5	0.83	97
CC47-030	36	413	0.03	0.05955	0.47504	0.09283	1.29296	0.76212	1.37746	587	10	572	7	575	6	0.94	97
CC47-031	33	371	0.03	0.06000	0.49038	0.09569	0.82324	0.79163	0.95823	604	11	589	5	592	4	0.86	98

Continued ... LA-SF-ICP-MS U-Pb results - Sample CC47

	PPM			Ratios						Ages (Ma)							
Spot	**^{206}Pb**	**^{238}U**	**Th^{b}/U**	**^{207}Pb/^{206}Pb**	**± 2σ**	**^{206}Pb^{a}/^{238}U**	**± 2σ**	**^{207}Pb^{a}/^{235}U**	**± 2σ**	**^{207}Pb/^{206}Pb**	**± 2σ**	**^{206}Pb/^{238}U**	**± 2σ**	**^{207}Pb/^{235}U**	**± 2σ**	**Rho^{c}**	**Conc.^{d}**
CC47-036	13	106	0.58	0.05972	0.78595	0.09371	0.98708	0.77170	1.26176	594	17	577	5	581	6	0.78	97
CC47-039	21	226	0.11	0.05964	1.28738	0.09343	0.96791	0.76831	1.61065	591	28	576	5	579	7	0.60	97
CC47-066	15	166	0.07	0.05970	0.48067	0.09295	0.83818	0.76511	0.96622	593	10	573	5	577	4	0.87	97
CC47-071	41	470	0.03	0.05973	0.48052	0.09313	0.91481	0.76693	1.03334	594	10	574	5	578	5	0.89	97
CC47-077	21	236	0.06	0.05981	0.59375	0.09343	0.82631	0.77052	1.01751	597	13	576	5	580	5	0.81	96
CC47-107	16	178	0.07	0.05915	0.72039	0.09236	0.76372	0.75330	1.04987	573	16	569	4	570	5	0.73	99
CC47-108	25	236	0.28	0.05972	0.69353	0.09615	0.81320	0.79170	1.06878	593	15	592	5	592	5	0.76	100
CC47-109	58	611	0.08	0.05994	0.67592	0.09742	2.28843	0.80508	2.38616	601	15	599	13	600	11	0.96	100
CC47-110	55	600	0.13	0.05921	1.16043	0.09262	0.80153	0.75620	1.41034	575	25	571	4	572	6	0.57	99
CC47-117	98	1074	0.03	0.05989	1.24747	0.09738	1.94750	0.80414	2.31278	600	27	599	11	599	11	0.84	100
CC47-146	14	153	0.10	0.05993	1.20637	0.09563	0.81232	0.79021	1.45437	601	26	589	5	591	7	0.56	98
CC47-158	35	365	0.17	0.05928	0.62443	0.09298	0.79389	0.75988	1.01003	577	14	573	4	574	4	0.79	99
CC47-160	29	332	0.02	0.05980	0.56064	0.09525	0.96239	0.78532	1.11378	596	12	586	5	589	5	0.86	98
Average	34	367	0.12	0.05968	0.73600	0.09426	1.08122	0.77567	1.34187	592	16	581	6	583	6	0.80	98
SD	21	233	0.13	0.00024	0.28714	0.00160	0.44275	0.01564	0.43426	9	6	9	3	9	2	0.12	1
RSD%	63	64	116	0	39	2	41	2	32	1	39	2	43	2	33	15	1
Anatectic																	
CC47-026	23	264	0.06	0.05923	0.52412	0.09069	1.19718	0.74061	1.30688	575	11	560	6	563	6	0.92	97
CC47-029	24	285	0.04	0.05889	0.49604	0.08816	0.87281	0.71588	1.00392	563	11	545	5	548	4	0.87	97
CC47-038	18	204	0.09	0.05911	0.57089	0.08967	1.63073	0.73088	1.72777	571	12	554	9	557	7	0.94	97
CC47-075	16	186	0.06	0.05923	0.53436	0.08977	1.03322	0.73312	1.16322	576	12	554	5	558	5	0.89	96
CC47-106	26	311	0.05	0.05866	0.77782	0.08921	0.84619	0.72150	1.14937	554	17	551	4	552	5	0.74	99
CC47-113	24	264	0.15	0.05853	0.71945	0.08823	1.03503	0.71198	1.26052	550	16	545	5	546	5	0.82	99
CC47-118	19	222	0.06	0.05895	0.85332	0.09067	0.93892	0.73701	1.26875	565	19	560	5	561	5	0.74	99
Average	21	248	0.07	0.05894	0.63943	0.08949	1.07916	0.72728	1.26863	565	14	552	6	555	5	0.84	98
SD	3	42	0.03	0.00025	0.13142	0.00096	0.25035	0.01012	0.20967	9	3	6	1	6	1	0.08	1
RSD%	16	17	47	0	21	1	23	1	17	2	21	1	23	1	17	9	1

[a]corrected for background, within-run Pb/U fractionation (in case of ^{206}Pb/^{238}U) and common Pb using Stacy and Kramers (1975) model Pb composition and subsequently normalised to GJ-1 (ID-TIMS value/measured value); ^{207}Pb/^{235}U calculated using ^{207}Pb/^{206}Pb/(^{238}U/^{206}Pb*1/137.88)

[b] U and Pb content and Th/U ratio were calculated relative to GJ-1 reference zircon.

[c] Rho is the ^{207}Pb/^{235}U/^{206}Pb/^{238}U error correlation coefficient.

d Concordance: 1 + ((^{206}Pb/^{238}U - ^{207}Pb/^{235}U)/ ^{206}Pb/^{238}U))*100

LA-Q-ICP-MS U-Pb results (GJ-1 zircon, primary standard)

	PPM			Ratios							Ages (Ma)					
Standards	^{206}Pb	^{238}U	Th^{b}/U	$^{207}Pb/^{206}Pb$	± 2σ	$^{206}Pb^{a}/^{238}U$	± 2σ	$^{207}Pb^{a}/^{235}U$	± 2σ	$^{207}Pb/^{206}Pb$	± 2σ	$^{206}Pb/^{238}U$	± 2σ	$^{207}Pb/^{235}U$	± 2σ	Rho^{c}	$Conc.^{d}$
GJ-1-021	34	368	0.01	0.06051	0.47182	0.09881	0.88905	0.82436	1.00650	622	10	607	5	610	5	0.88	98
GJ-1-022	33	357	0.02	0.06052	0.45794	0.09862	0.84351	0.82292	0.95980	622	10	606	5	610	4	0.88	97
GJ-1-023	33	357	0.02	0.06054	0.46532	0.09882	0.88112	0.82489	0.99644	623	10	607	5	611	5	0.88	98
GJ-1-024	33	364	0.02	0.06039	0.72846	0.09794	1.38114	0.81546	1.56147	617	16	602	8	606	7	0.88	98
GJ-1-025	30	332	0.01	0.06047	0.47302	0.09817	0.83098	0.81849	0.95618	620	10	604	5	607	4	0.87	97
GJ-1-041	32	350	0.01	0.06041	0.45643	0.09784	0.80156	0.81490	0.92240	618	10	602	5	605	4	0.87	97
GJ-1-042	33	365	0.01	0.06047	0.46249	0.09837	0.84169	0.82014	0.96038	620	10	605	5	608	4	0.88	98
GJ-1-043	31	339	0.01	0.06040	0.46854	0.09802	0.83207	0.81633	0.95492	618	10	603	5	606	4	0.87	98
GJ-1-044	31	334	0.01	0.06067	0.47737	0.09889	0.79237	0.82718	0.92506	627	10	608	5	612	4	0.86	97
GJ-1-045	29	321	0.01	0.06039	0.54950	0.09792	0.80214	0.81534	0.97230	618	12	602	5	605	4	0.82	98
GJ-1-061	28	307	0.01	0.06056	0.52005	0.09797	0.81407	0.81809	0.96601	624	11	602	5	607	4	0.84	97
GJ-1-062	29	322	0.01	0.06060	0.63908	0.09846	0.82879	0.82276	1.04657	625	14	605	5	610	5	0.79	97
GJ-1-063	29	318	0.01	0.06066	0.47356	0.09870	0.79315	0.82550	0.92377	627	10	607	5	611	4	0.86	97
GJ-1-064	29	313	0.01	0.06063	0.45928	0.09857	0.83556	0.82405	0.95347	626	10	606	5	610	4	0.88	97
GJ-1-065	27	290	0.01	0.06067	0.51853	0.09884	0.79891	0.82676	0.95243	627	11	608	5	612	4	0.84	97
GJ-1-081	25	269	0.02	0.06004	0.62894	0.09853	0.93774	0.81575	1.12912	605	14	606	5	606	5	0.83	100
GJ-1-082	23	249	0.02	0.06004	0.47369	0.09840	1.06075	0.81456	1.16171	605	10	605	6	605	5	0.91	100
GJ-1-083	24	262	0.02	0.06010	0.75954	0.09888	0.88838	0.81941	1.16881	607	16	608	5	608	5	0.76	100
GJ-1-084	24	267	0.02	0.06004	1.11181	0.09841	0.88219	0.81464	1.41929	605	24	605	5	605	6	0.62	100
GJ-1-101	31	344	0.02	0.06015	0.88454	0.09862	0.87897	0.81793	1.24700	609	19	606	5	607	6	0.70	100
GJ-1-102	38	421	0.02	0.06037	0.53419	0.09741	0.83733	0.81088	0.99322	617	12	599	5	603	5	0.84	97
GJ-1-103	31	338	0.01	0.06016	0.52071	0.09868	0.86794	0.81852	1.01215	609	11	607	5	607	5	0.86	100
GJ-1-104	30	333	0.01	0.06003	0.50072	0.09786	0.87020	0.80997	1.00398	605	11	602	5	602	5	0.87	100
GJ-1-105	31	341	0.02	0.06020	0.48186	0.09895	0.90111	0.82139	1.02185	611	10	608	5	609	5	0.88	100
GJ-1-141	29	319	0.01	0.05998	0.51394	0.09750	0.85443	0.80627	0.99709	603	11	600	5	600	5	0.86	100
GJ-1-142	29	321	0.01	0.06012	0.61449	0.09846	0.89219	0.81615	1.08333	608	13	605	5	606	5	0.82	100
GJ-1-143	28	307	0.02	0.06000	0.62044	0.09762	0.88774	0.80763	1.08306	604	13	600	5	601	5	0.82	99
GJ-1-144	28	315	0.01	0.05997	0.58572	0.09754	0.84257	0.80653	1.02616	603	13	600	5	601	5	0.82	100
GJ-1-145	30	330	0.02	0.05995	1.01140	0.09747	0.86690	0.80570	1.33209	602	22	600	5	600	6	0.65	100
GJ-1-161	30	331	0.01	0.06004	0.46974	0.09810	0.80734	0.81211	0.93406	605	10	603	5	604	4	0.86	100
GJ-1-162	29	320	0.01	0.06000	0.53962	0.09782	0.78111	0.80923	0.94938	604	12	602	4	602	4	0.82	100
GJ-1-163	31	337	0.01	0.06001	0.51758	0.09810	0.93943	0.81167	1.07258	604	11	603	5	603	5	0.88	100
GJ-1-164	31	339	0.01	0.06012	0.49713	0.09840	1.19423	0.81568	1.29357	608	11	605	7	606	6	0.92	100
GJ-1-182	30	332	0.01	0.06004	0.46974	0.09807	0.80734	0.81189	0.93406	605	10	603	5	604	4	0.86	100
GJ-1-183	29	321	0.01	0.06000	0.53962	0.09779	0.78111	0.80901	0.94938	604	12	601	4	602	4	0.82	100
GJ-1-184	31	337	0.01	0.06001	0.51758	0.09807	0.93943	0.81145	1.07258	604	11	603	5	603	5	0.88	100
GJ-1-185	31	340	0.01	0.06012	0.49713	0.09837	1.19423	0.81546	1.29357	608	11	605	7	606	6	0.92	99
Average	30	327	0.01	0.06025	0.56418	0.09825	0.88409	0.81622	1.05581	613	12	604	5	606	5	0.84	99
SD	3	31	0.00	0.00025	0.14743	0.00050	0.12304	0.00657	0.14845	9	3	3	1	4	1	0.06	1
RSD%	9	10	1	0	26	1	14	1	14	1	26	0	14	1	14	7	1

LA-Q-ICP-MS U-Pb results (Plešovice, 91500, Peixe zircon - secondary standard)

		PPM		Ratios						Ages (Ma)							
Standards	^{206}Pb	^{238}U	Th[b]/U	^{207}Pb/^{206}Pb	± 2σ	^{206}Pb[a]/^{238}U	± 2σ	^{207}Pb[a]/^{235}U	± 2σ	^{207}Pb/^{206}Pb	± 2σ	^{206}Pb/^{238}U	± 2σ	^{207}Pb/^{235}U	± 2σ	Rho[c]	Conc.[d]
Plešovice																	
Ples-006	49	972	0.05	0.05369	0.44896	0.05384	0.85166	0.39860	0.96275	358	10	338	3	341	3	0.88	94
Ples-007	50	969	0.05	0.05378	0.44858	0.05445	0.86472	0.40376	0.97415	362	10	342	3	344	3	0.89	94
Ples-008	63	1237	0.05	0.05393	0.42820	0.05385	0.80118	0.40037	0.90843	368	10	338	3	342	3	0.88	92
Ples-009	60	1172	0.05	0.05374	0.42892	0.05455	0.85390	0.40422	0.95557	360	10	342	3	345	3	0.89	95
Ples-010	55	1070	0.05	0.05379	0.47501	0.05479	0.78202	0.40639	0.91498	362	11	344	3	346	3	0.85	95
Ples-046	42	844	0.04	0.05361	0.45065	0.05353	0.88861	0.39569	0.99635	355	10	336	3	339	3	0.89	95
Ples-047	45	898	0.04	0.05361	0.43896	0.05353	1.24299	0.39569	1.31822	355	10	336	4	339	4	0.94	95
Ples-048	65	1281	0.04	0.05366	0.43324	0.05388	0.81804	0.39864	0.92568	357	10	338	3	341	3	0.88	95
Ples-049	36	704	0.04	0.05375	0.58457	0.05458	0.83585	0.40450	1.01998	361	13	343	3	345	3	0.82	95
Ples-050	63	1232	0.04	0.05373	0.41825	0.05441	1.16500	0.40303	1.23780	360	9	342	4	344	4	0.94	95
Ples-086	47	942	0.05	0.05315	0.69184	0.05333	1.91372	0.39081	2.03494	335	16	335	6	335	6	0.94	100
Ples-087	39	755	0.06	0.05332	0.43967	0.05474	0.83563	0.40246	0.94424	343	10	344	3	343	3	0.88	100
Ples-088	42	823	0.05	0.05328	0.44003	0.05436	0.81203	0.39937	0.92359	341	10	341	3	341	3	0.88	100
Ples-089	43	840	0.05	0.05330	0.42100	0.05447	0.84209	0.40033	0.94146	342	10	342	3	342	3	0.89	100
Ples-090	42	827	0.05	0.05324	0.44251	0.05403	1.79411	0.39659	1.84787	339	10	339	6	339	5	0.97	100
Ples-127	42	832	0.05	0.05330	0.76854	0.05394	0.85253	0.39645	1.14780	342	17	339	3	339	3	0.74	99
Ples-128	46	897	0.05	0.05328	0.54675	0.05383	1.02049	0.39547	1.15773	341	12	338	3	338	3	0.88	99
Ples-129	45	906	0.05	0.05312	0.50614	0.05312	1.01723	0.38903	1.13619	334	11	334	3	334	3	0.90	100
Ples-130	46	908	0.05	0.05326	0.47825	0.05381	0.78089	0.39517	0.91570	340	11	338	3	338	3	0.85	99
Ples-166	43	840	0.04	0.05346	0.48207	0.05485	1.00035	0.40436	1.11045	349	11	344	3	345	3	0.90	99
Ples-167	50	937	0.05	0.05357	0.53917	0.05606	1.30403	0.41408	1.41110	353	12	352	4	352	4	0.92	100
Ples-168	49	961	0.06	0.05332	0.52099	0.05398	0.90089	0.39687	1.04069	343	12	339	3	339	3	0.87	99
Ples-169	51	969	0.06	0.05352	1.96520	0.05503	1.18431	0.40613	2.29448	351	44	345	4	346	7	0.52	98
Ples-170	54	1063	0.07	0.05324	1.00982	0.05373	1.06753	0.39442	1.46948	339	23	337	4	338	4	0.73	100
Average	49	953	0.05	0.05349	0.57530	0.05420	1.01791	0.39968	1.19123	349	13	340	3	341	3	0.9	97
SD	8	150	0.01	0.00023	0.31897	0.00063	0.29324	0.00546	0.36852	10	7	4	1	4	1	0.1	3
RSD%	16	16	15	0	55	1	29	1	31	3	55	1	29	1	31	10	3
Peixe																	
Peixe-020	3	30	0.12	0.06045	1.34309	0.09819	0.92446	0.81840	1.63050	620	29	604	5	607	7	0.57	97
Peixe-099	3	30	0.12	0.05948	2.27967	0.09459	0.89567	0.77576	2.44931	585	49	583	5	583	11	0.37	100
Peixe-137	3	30	0.12	0.05997	1.94233	0.09722	0.89778	0.80389	2.13978	603	42	598	5	599	10	0.42	99
Peixe-138	3	30	0.12	0.06000	1.20851	0.09782	1.22722	0.80928	1.72237	604	26	602	7	602	8	0.71	100
Peixe-139	3	31	0.12	0.05997	1.39696	0.09783	0.88563	0.80901	1.65404	603	30	602	5	602	8	0.54	100
Peixe-140	3	30	0.12	0.05996	1.55433	0.09729	0.88358	0.80431	1.78792	602	34	599	5	599	8	0.49	99
Peixe-176	3	32	0.12	0.06041	2.37110	0.09790	0.84191	0.81537	2.51613	618	51	602	5	605	12	0.33	97
Peixe-177	3	32	0.12	0.05999	1.37090	0.09833	0.86327	0.81331	1.62007	603	30	605	5	604	7	0.53	100
Peixe-178	3	31	0.12	0.06062	2.42308	0.09911	0.85899	0.82832	2.57083	626	52	609	5	613	12	0.33	97

Continued ... LA-Q-ICP-MS U-Pb results (Plešovice, 91500, Peixe zircon - secondary standard)

	PPM			Ratios							Ages (Ma)					
Standards	**^{206}Pb**	**^{238}U**	**Th^{b}/U**	**^{207}Pb/^{206}Pb**	**± 2σ**	**^{206}Pb^{a}/^{238}U**	**± 2σ**	**^{207}Pb^{a}/^{235}U**	**± 2σ**	**^{207}Pb/^{206}Pb**	**± 2σ**	**^{206}Pb/^{238}U**	**± 2σ**	**^{207}Pb/^{235}U**	**± 2σ**	**Rho^{c}**	**Conc.^{d}**
Peixe-179	3	31	0.12	0.06018	1.16471	0.09784	0.86589	0.81187	1.45132	610	25	602	5	604	7	0.60	99
Peixe-180	3	32	0.12	0.05982	1.40201	0.09656	0.88348	0.79648	1.65716	597	30	594	5	595	7	0.53	100
Average	3	31	0.12	0.06008	1.67788	0.09752	0.91162	0.80782	1.92722	606	36	600	5	601	9	0	99
SD	0	1	0.00	0.00029	0.44047	0.00107	0.09769	0.01233	0.37601	11	10	6	1	7	2	0	1
RSD%	3	3	1	0	26	1	11	2	20	2	26	1	11	1	20	22	1
91500																	
91500-011	13	71	0.16	0.07529	0.50756	0.18004	0.84445	1.86905	0.98525	1076	10	1067	8	1070	7	0.86	99
91500-012	13	73	0.16	0.07545	0.62696	0.18054	0.90525	1.87819	1.10116	1081	13	1070	9	1073	7	0.82	99
91500-013	13	73	0.16	0.07523	0.56219	0.17951	0.85666	1.86197	1.02466	1075	11	1064	8	1068	7	0.84	99
91500-014	13	71	0.16	0.07552	0.58948	0.18112	0.83322	1.88597	1.02066	1082	12	1073	8	1076	7	0.82	99
91500-015	14	75	0.16	0.07543	0.63063	0.18031	0.81206	1.87531	1.02817	1080	13	1069	8	1072	7	0.79	99
91500-051	12	63	0.15	0.07530	0.96859	0.17987	0.84247	1.86734	1.28371	1076	19	1066	8	1070	9	0.66	99
91500-052	13	71	0.16	0.07538	0.68998	0.18018	0.85698	1.87280	1.10022	1079	14	1068	8	1072	7	0.78	99
91500-054	14	76	0.16	0.07533	0.69456	0.17997	0.82770	1.86918	1.08051	1077	14	1067	8	1070	7	0.77	99
91500-055	11	62	0.15	0.07536	0.74203	0.17987	0.82954	1.86882	1.11299	1078	15	1066	8	1070	7	0.75	99
91500-091	10	56	0.16	0.07538	1.01028	0.17897	1.03852	1.86013	1.44886	1079	20	1061	10	1067	10	0.72	98
91500-092	10	52	0.16	0.07548	0.95331	0.17942	1.05494	1.86731	1.42187	1081	19	1064	10	1070	9	0.74	98
91500-093	10	55	0.16	0.07569	1.30128	0.17997	0.87625	1.87831	1.56880	1087	26	1067	9	1073	10	0.56	98
91500-094	10	55	0.17	0.07541	0.85389	0.17926	1.08259	1.86380	1.37882	1079	17	1063	11	1068	9	0.79	98
91500-095	10	55	0.16	0.07502	0.73178	0.17855	1.01649	1.84685	1.25250	1069	15	1059	10	1062	8	0.81	99
91500-133	15	85	0.16	0.07455	0.88328	0.17753	0.91395	1.82490	1.27102	1056	18	1053	9	1054	8	0.72	100
91500-135	14	78	0.16	0.07434	1.68819	0.17658	1.01036	1.80997	1.96744	1051	34	1048	10	1049	13	0.51	100
91500-172	15	83	0.16	0.07430	0.88170	0.17640	0.87470	1.80724	1.24197	1050	18	1047	8	1048	8	0.70	100
91500-173	13	73	0.16	0.07433	1.45644	0.17562	1.00833	1.79997	1.77143	1051	29	1043	10	1045	12	0.57	99
91500-174	14	78	0.16	0.07413	1.55884	0.17509	0.94997	1.78953	1.82549	1045	31	1040	9	1042	12	0.52	100
91500-175	13	72	0.16	0.07478	1.26132	0.17632	0.96144	1.81791	1.58597	1063	25	1047	9	1052	10	0.61	99
Average	13	69	0.16	0.07509	0.92961	0.17876	0.91979	1.85073	1.32357	1071	19	1060	9	1064	9	0.72	99
SD	2	10	0.00	0.00048	0.34005	0.00177	0.08555	0.02951	0.28514	13	7	10	1	11	2	0.11	0
RSD%	14	14	2	1	37	1	9	2	22	1	37	1	9	1	21	15	0

Hf isotopes results determined by LA-ICP-MS - Sample CC12

Spot	$^{176}Yb/^{177}Hf$	±2σ	$^{176}Lu/^{177}Hf$ [a]	±2σ	$^{178}Hf/^{177}Hf$	$^{180}Hf/^{177}Hf$	Sig_{Hf} [b]	$^{176}Hf/^{177}Hf$	±2σ [c]	$^{176}Hf/^{177}Hf(t)$ [d]	εHf(t) [d]	±2σ [c]	T_{DM} [e]	age [f]	±2σ
Sample CC12															
Inherited															
CC12-32	0.02593	25	0.00084	7	1.46721	1.88706	10	0.282284	22	0.282274	-4.0	0.8	1.49	631	12
CC12-76	0.05741	55	0.00192	14	1.46716	1.88579	13	0.282324	32	0.282302	-3.4	1.1	1.44	613	12
Magmatic															
CC12-28	0.07761	68	0.00244	17	1.46721	1.88695	9	0.282281	21	0.282255	-5.8	0.8	1.54	581	10
CC12-53	0.17763	144	0.00570	35	1.46726	1.88710	11	0.282371	29	0.282310	-4.1	1.0	1.44	571	10
CC12-70	0.03786	32	0.00119	8	1.46723	1.88697	7	0.282274	36	0.282262	-5.8	1.3	1.53	570	10
CC12-84	0.03389	32	0.00113	9	1.46710	1.88482	9	0.282386	62	0.282374	-1.8	2.2	1.32	572	12
CC12-91	0.05168	53	0.00166	13	1.46708	1.88580	10	0.282314	31	0.282296	-4.1	1.1	1.46	590	10
CC12-94	0.03324	29	0.00109	7	1.46719	1.88733	7	0.282201	69	0.282189	-8.2	2.4	1.67	577	12
CC12-98	0.04016	56	0.00129	17	1.46718	1.88645	14	0.282273	40	0.282259	-5.6	1.4	1.54	581	10
CC12-105	0.02752	50	0.00092	16	1.46713	1.88563	8	0.282316	53	0.282306	-4.0	1.9	1.44	582	10
Anatectic and/or metamorphic															
CC12-69	0.09771	84	0.00289	25	1.46713	1.88656	10	0.282314	55	0.282284	-5.3	2.0	1.50	555	10
CC12-71	0.03384	30	0.00103	7	1.46720	1.88722	13	0.282277	25	0.282266	-5.8	0.9	1.53	562	12
CC12-75	0.04970	41	0.00158	10	1.46720	1.88703	10	0.282266	27	0.282249	-6.5	1.0	1.56	561	10
CC12-93	0.03570	32	0.00118	8	1.46711	1.88642	10	0.282285	38	0.282274	-6.2	1.3	1.53	534	10
CC12-106	0.02179	43	0.00068	13	1.46715	1.88626	8	0.282325	45	0.282317	-3.7	1.6	1.42	575	10
CC12-113	0.06695	62	0.00218	16	1.46714	1.88644	10	0.282344	24	0.282321	-3.9	0.9	1.42	562	12

Hf isotopes results determined by LA-ICP-MS - Sample CC18

Spot	$^{176}Yb/^{177}Hf$	±2σ	$^{176}Lu/^{177}Hf$ [a]	±2σ	$^{178}Hf/^{177}Hf$	$^{180}Hf/^{177}Hf$	Sig_{Hf} [b]	$^{176}Hf/^{177}Hf$	±2σ [c]	$^{76}Hf/^{177}Hf(t)$	εHf(t) [d]	±2σ [c]	T_{DM} [e]	age [f]	±2σ
Inherited															
CC18-53	0.04690	40	0.00133	10	1.46713	1.88681	8	0.282277	19	0.282262	-5.0	0.7	1.52	604	10
CC18-63	0.04632	38	0.00149	9	1.46711	1.88591	10	0.282329	56	0.282311	-2.1	2.0	1.40	655	12
CC18-90	0.05160	45	0.00152	11	1.46714	1.88625	11	0.282366	27	0.282349	-2.0	1.0	1.35	603	10
CC18-107	0.02598	23	0.00074	5	1.46716	1.88650	9	0.282280	20	0.282272	-4.8	0.7	1.50	597	10
CC18-109	0.00759	7	0.00022	2	1.46721	1.88661	11	0.282204	29	0.282202	-6.7	1.0	1.63	624	16
CC18-113	0.04616	40	0.00137	10	1.46710	1.88623	11	0.282300	32	0.282285	-4.3	1.1	1.48	602	10
CC18-123	0.03578	36	0.00110	11	1.46717	1.88679	6	0.282268	19	0.282256	-5.4	0.7	1.53	599	10
Magmatic															
CC18-37	0.03683	31	0.00107	7	1.46721	1.88682	13	0.282267	50	0.282255	-5.6	1.8	1.54	591	12
CC18-42	0.03464	38	0.00109	10	1.46713	1.88598	11	0.282306	43	0.282294	-4.4	1.5	1.47	583	10
CC18-43	0.02821	23	0.00092	6	1.46725	1.88618	9	0.282346	49	0.282336	-2.9	1.7	1.39	580	10
CC18-52	0.03688	30	0.00109	7	1.46721	1.88641	10	0.282308	29	0.282295	-4.2	1.0	1.46	589	10
CC18-87	0.06295	69	0.00192	18	1.46713	1.88657	7	0.282311	28	0.282290	-4.5	1.0	1.47	583	10
CC18-93	0.03602	30	0.00119	8	1.46719	1.88665	11	0.282253	23	0.282240	-6.4	0.8	1.57	577	10
CC18-108	0.03019	29	0.00089	8	1.46717	1.88660	11	0.282276	21	0.282267	-5.1	0.7	1.52	593	10
CC18-129	0.03992	45	0.00115	13	1.46719	1.88666	0	0.282273	17	0.282260	-5.7	0.6	1.54	575	10
Anatectic and/or metamorphic															
CC18-92	0.00791	7	0.00021	1	1.46715	1.88670	9	0.282203	21	0.282201	-9.2	0.7	1.67	513	8
CC18-102	0.00757	14	0.00022	4	1.46713	1.88605	16	0.282244	35	0.282241	-6.9	1.2	1.58	554	10
CC18-103	0.00730	7	0.00021	2	1.46716	1.88575	13	0.282279	28	0.282277	-6.4	1.0	1.52	520	10
CC18-110	0.00628	6	0.00018	2	1.46711	1.88618	10	0.282217	27	0.282215	-8.9	1.0	1.65	504	8
CC18-111	0.04381	38	0.00147	10	1.46712	1.88612	11	0.282277	28	0.282262	-6.1	1.0	1.54	556	10
CC18-120	0.00576	5	0.00016	1	1.46714	1.88629	8	0.282253	23	0.282251	-7.2	0.8	1.57	524	10
CC18-121	0.12814	137	0.00391	36	1.46724	1.88659	9	0.282381	25	0.282341	-3.3	0.9	1.39	556	10
CC18-124	0.00839	10	0.00023	3	1.46719	1.88642	13	0.282210	18	0.282207	-8.6	0.6	1.66	529	10
CC18-125	0.00613	6	0.00017	1	1.46723	1.88676	0	0.282234	22	0.282233	-7.8	0.8	1.61	528	10
CC18-134	0.00389	6	0.00010	1	1.46715	1.88690	12	0.282203	21	0.282202	-9.4	0.7	1.68	503	8
CC18-135	0.00488	7	0.00014	2	1.46718	1.88662	11	0.282211	23	0.282210	-7.7	0.8	1.64	569	10
CC18-137	0.03778	32	0.00119	8	1.46715	1.88649	9	0.282318	18	0.282307	-5.5	0.6	1.47	510	8
CC18-144	0.04335	38	0.00122	8	1.46721	1.88675	13	0.282275	23	0.282262	-5.7	0.8	1.53	574	10
CC18-58	0.04054	48	0.00081	9	1.46714	1.88638	10	0.282248	15	0.282239	-6.6	0.5	1.58	568	10
CC18-79	0.00776	7	0.00024	2	1.46714	1.88573	9	0.282287	28	0.282284	-6.3	1.0	1.51	511	8
CC18-94	0.04961	40	0.00159	10	1.46723	1.88662	10	0.282304	22	0.282287	-5.0	0.8	1.49	566	10
CC18-98	0.01884	16	0.00040	2	1.46719	1.88642	8	0.282264	22	0.282259	-6.0	0.8	1.54	563	10

Hf isotopes results determined by LA-ICP-MS - Sample CC30

Spot	$^{176}Yb/^{177}Hf$	±2σ	$^{176}Lu/^{177}Hf$	±2σ	$^{178}Hf/^{177}Hf$	$^{180}Hf/^{177}Hf$	Sig_{Hf} [b]	$^{176}Hf/^{177}Hf$	±2σ [c]	$^{176}Hf/^{177}Hf(t)$	εHf(t) [d]	±2σ [c]	T_{DM} [e]	age [f]	±2σ
Inherited															
CC30-16	0.04229	37	0.00132	9	1.46721	1.88667	15	0.282340	22	0.282325	-2.7	0.8	1.40	606	12
CC30-38	0.03207	28	0.00099	7	1.46717	1.88654	10	0.282314	27	0.282303	-3.8	1.0	1.44	596	12
CC30-45	0.03918	37	0.00125	10	1.46725	1.88655	11	0.282338	24	0.282324	-2.9	0.9	1.40	601	10
CC30-60	0.03407	28	0.00105	7	1.46722	1.88644	10	0.282281	20	0.282269	-4.8	0.7	1.51	601	10
Magmatic															
CC30-17	0.05576	60	0.00167	16	1.46720	1.88646	15	0.282351	27	0.282333	-3.2	1.0	1.39	573	10
CC30-18	0.03485	29	0.00114	7	1.46721	1.88684	11	0.282305	20	0.282293	-4.6	0.7	1.47	572	10
CC30-20	0.03191	29	0.00099	8	1.46719	1.88648	11	0.282327	18	0.282316	-3.8	0.6	1.43	574	10
CC30-39	0.03748	31	0.00119	8	1.46725	1.88673	12	0.282323	23	0.282310	-4.1	0.8	1.44	570	10
CC30-42	0.04402	43	0.00134	11	1.46713	1.88639	7	0.282351	19	0.282336	-3.0	0.7	1.39	577	10
CC30-66	0.03616	31	0.00113	8	1.46715	1.88620	8	0.282338	22	0.282325	-3.3	0.8	1.41	583	10
CC30-68	0.03048	29	0.00094	7	1.46717	1.88643	10	0.282361	22	0.282351	-2.2	0.8	1.35	588	12
CC30-69	0.05029	60	0.00146	15	1.46718	1.88631	11	0.282377	25	0.282362	-2.2	0.9	1.34	573	10
CC30-74	0.04887	50	0.00138	11	1.46713	1.88679	12	0.282325	22	0.282310	-3.5	0.8	1.43	595	14
CC30-75	0.03768	32	0.00118	8	1.46721	1.88644	8	0.282360	24	0.282347	-2.5	0.9	1.36	581	10
CC30-76	0.04148	36	0.00132	8	1.46714	1.88612	8	0.282365	34	0.282351	-2.2	1.2	1.35	588	10
CC30-78	0.03977	33	0.00122	8	1.46718	1.88659	10	0.282322	25	0.282309	-4.0	0.9	1.44	577	10
CC30-80	0.04068	34	0.00125	8	1.46715	1.88663	11	0.282315	25	0.282301	-4.3	0.9	1.46	573	10
CC30-82	0.03631	32	0.00111	7	1.46719	1.88576	10	0.282360	25	0.282348	-2.5	0.9	1.36	582	10
Anatectic and/or metamorphic															
CC30-19	0.03432	29	0.00109	7	1.46716	1.88647	10	0.282353	24	0.282341	-3.0	0.9	1.38	568	10
CC30-40	0.03858	32	0.00121	8	1.46719	1.88636	10	0.282347	23	0.282334	-3.5	0.8	1.40	556	14
CC30-47	0.03142	26	0.00094	6	1.46716	1.88654	11	0.282338	27	0.282328	-3.5	0.9	1.41	567	12
CC30-62	0.02320	20	0.00076	5	1.46715	1.88636	8	0.282334	23	0.282326	-3.7	0.8	1.41	561	10
CC30-81	0.04542	39	0.00141	10	1.46716	1.88662	10	0.282312	24	0.282297	-4.6	0.9	1.47	569	10
CC30-89	0.05238	44	0.00163	10	1.46719	1.88667	12	0.282374	25	0.282357	-2.6	0.9	1.35	564	10
CC30-98	0.04550	47	0.00144	12	1.46721	1.88672	9	0.282354	23	0.282341	-4.3	0.8	1.41	510	8

Hf isotopes results determined by LA-ICP-MS - Sample CC34

Spot	$^{176}Yb/^{177}Hf$	±2σ	$^{176}Lu/^{177}Hf$	±2σ	$^{178}Hf/^{177}Hf$	$^{180}Hf/^{177}Hf$	Sig_{Hf} [b]	$^{176}Hf/^{177}Hf$	±2σ [c]	$^{176}Hf/^{177}Hf(t)$	εHf(t) [d]	±2σ [c]	T_{DM} [e]	age [f]	±2σ
Inherited															
CC34-b84	0.03167	25	0.00106	6	1.46726	1.88680	21	0.282245	14	0.282233	-6.2	0.6	1.58	600	17
CC34-a100	0.04622	37	0.00159	10	1.46726	1.88697	13	0.282255	17	0.282233	-3.0	0.7	1.52	739	25
CC34-b98	0.03253	33	0.00109	9	1.46725	1.88662	17	0.282256	17	0.282243	-4.8	0.6	1.54	644	17
CC34-b107	0.03587	35	0.00125	11	1.46728	1.88635	16	0.282300	20	0.282286	-4.3	0.6	1.48	597	17
CC34-b108	0.03652	36	0.00125	10	1.46726	1.88647	18	0.282256	24	0.282242	-5.4	0.5	1.55	620	16
CC34-b99	0.03888	35	0.00132	10	1.46728	1.88633	17	0.282259	26	0.282244	-5.6	0.5	1.55	607	16
CC34-a133	0.02420	20	0.00086	5	1.46724	1.88637	15	0.282259	20	0.282249	-5.4	0.6	1.54	607	11
CC34-b79	0.03109	25	0.00108	7	1.46728	1.88641	18	0.282261	14	0.282249	-5.6	0.5	1.55	600	15
CC34-b104	0.04022	33	0.00140	8	1.46728	1.88666	15	0.282264	22	0.282248	-5.5	0.6	1.55	607	16
CC34-b59	0.02943	24	0.00100	6	1.46731	1.88594	19	0.282265	22	0.282253	-5.3	0.6	1.54	607	16
CC34-b86	0.03571	29	0.00121	7	1.46727	1.88635	17	0.282265	14	0.282251	-5.5	0.5	1.54	602	15
CC34-b97	0.03374	27	0.00117	7	1.46721	1.88661	18	0.282267	19	0.282254	-5.1	0.5	1.53	615	16
CC34-b75	0.02827	23	0.00096	6	1.46726	1.88688	16	0.282275	20	0.282264	-4.8	0.5	1.51	612	16
CC34-a154	0.03587	29	0.00124	8	1.46727	1.88641	20	0.282276	16	0.282262	-4.9	0.5	1.52	607	11
CC34-b55	0.04643	37	0.00159	10	1.46725	1.88627	20	0.282277	24	0.282259	-5.1	0.5	1.53	604	15
CC34-b53	0.02844	23	0.00097	6	1.46728	1.88627	19	0.282280	19	0.282269	-4.6	0.6	1.50	613	16
CC34-b74	0.03661	29	0.00125	8	1.46724	1.88596	16	0.282281	16	0.282267	-4.9	0.5	1.51	603	15
CC34-b110	0.05360	44	0.00184	12	1.46726	1.88656	16	0.282281	21	0.282260	-5.1	0.6	1.52	605	17
CC34-a128	0.02947	25	0.00098	6	1.46726	1.88648	16	0.282285	18	0.282274	-4.5	0.5	1.49	610	11
CC34-b82	0.04196	34	0.00144	9	1.46728	1.88632	17	0.282287	14	0.282271	-4.6	0.5	1.50	609	18
CC34-b102	0.04195	37	0.00144	10	1.46729	1.88655	15	0.282292	21	0.282275	-4.2	0.7	1.49	619	16
CC34-a152	0.03761	30	0.00124	7	1.46727	1.88618	19	0.282293	18	0.282279	-3.9	0.6	1.48	630	11
Magmatic															
CC34-b60	0.01442	12	0.00049	3	1.46724	1.88646	21	0.282248	20	0.282243	-6.2	0.5	1.57	580	15
CC34-a146	0.02967	33	0.00096	8	1.46723	1.88643	21	0.282252	17	0.282242	-6.2	0.5	1.57	584	11
CC34-b63	0.03276	27	0.00110	7	1.46728	1.88645	19	0.282254	18	0.282242	-6.5	0.5	1.57	570	15
CC34-a109	0.03524	28	0.00119	7	1.46718	1.88641	10	0.282258	19	0.282245	-6.4	0.8	1.57	570	13
CC34-a158	0.03413	28	0.00115	7	1.46728	1.88579	18	0.282260	14	0.282247	-6.0	0.5	1.56	582	11
CC34-b57	0.03793	30	0.00127	8	1.46727	1.88628	19	0.282262	20	0.282248	-5.9	0.4	1.55	586	15
CC34-a148	0.01924	15	0.00061	4	1.46724	1.88641	19	0.282264	16	0.282257	-5.5	0.6	1.54	589	11
CC34-b109	0.03540	29	0.00121	8	1.46725	1.88659	16	0.282268	16	0.282255	-5.8	0.6	1.54	582	14
CC34-b90	0.03037	24	0.00104	6	1.46730	1.88632	16	0.282269	13	0.282257	-5.7	0.6	1.54	583	17

Continued ... Hf isotopes results determined by LA-ICP-MS - Sample CC34

Spot	$^{176}Yb/^{177}Hf$	±2σ	$^{176}Lu/^{177}Hf$	±2σ	$^{178}Hf/^{177}Hf$	$^{180}Hf/^{177}Hf$	Sig_{Hf} [b]	$^{176}Hf/^{177}Hf$	±2σ [c]	$^{176}Hf/^{177}Hf(t)$	εHf(t) [d]	±2σ [c]	T_{DM} [e]	age [f]	±2σ
CC34-a141	0.03682	30	0.00126	8	1.46724	1.88651	15	0.282271	20	0.282257	-5.5	0.6	1.54	589	11
CC34-b73	0.04164	33	0.00134	8	1.46724	1.88634	18	0.282272	17	0.282257	-5.6	0.5	1.54	586	15
CC34-b105	0.02732	24	0.00093	7	1.46729	1.88668	16	0.282273	18	0.282263	-5.5	0.5	1.53	582	15
CC34-a113	0.03817	31	0.00127	8	1.46723	1.88652	10	0.282275	18	0.282261	-5.3	0.8	1.53	594	10
CC34-a108	0.04406	36	0.00153	9	1.46722	1.88671	9	0.282275	15	0.282258	-5.8	0.7	1.54	577	11
CC34-a159	0.03094	25	0.00107	6	1.46732	1.88557	17	0.282280	19	0.282268	-5.3	0.6	1.52	583	13
CC34-b80	0.05228	51	0.00182	15	1.46728	1.88638	16	0.282281	24	0.282261	-5.5	0.5	1.53	585	17
CC34-a112	0.04125	33	0.00138	8	1.46725	1.88629	11	0.282282	20	0.282267	-5.2	0.6	1.52	587	12
CC34-a140	0.03703	30	0.00124	7	1.46729	1.88642	18	0.282283	18	0.282269	-5.2	0.5	1.51	583	11
CC34-a107	0.04978	40	0.00167	10	1.46737	1.88583	14	0.282287	11	0.282269	-5.4	0.8	1.52	577	12
CC34-a143	0.03646	29	0.00120	7	1.46725	1.88624	18	0.282289	18	0.282276	-5.1	0.5	1.50	579	12
CC34-b70	0.03264	27	0.00110	7	1.46725	1.88625	19	0.282290	17	0.282278	-4.7	0.4	1.49	595	15
CC34-b112	0.02238	19	0.00077	5	1.46723	1.88660	14	0.282292	21	0.282283	-4.6	0.6	1.49	588	15
CC34-a104	0.02058	17	0.00070	4	1.46724	1.88635	10	0.282301	13	0.282293	-4.6	0.8	1.47	573	11
CC34-a121	0.03974	32	0.00133	8	1.46725	1.88695	9	0.282302	18	0.282288	-5.0	0.7	1.49	566	12
CC34-b103	0.04944	43	0.00167	11	1.46728	1.88638	14	0.282304	23	0.282286	-4.6	0.6	1.48	586	18
CC34-a103	0.03161	26	0.00103	6	1.46728	1.88645	10	0.282309	13	0.282298	-4.5	0.7	1.46	570	10
Anatectic and/or metamorphic															
CC34-b93	0.03036	30	0.00104	9	1.46722	1.88659	16	0.282251	12	0.282240	-6.7	0.5	1.58	566	16
CC34-b81	0.04083	33	0.00139	8	1.46726	1.88652	17	0.282274	14	0.282259	-6.0	0.5	1.54	567	15
CC34-b106	0.02961	26	0.00101	7	1.46722	1.88667	17	0.282271	22	0.282260	-6.1	0.5	1.54	560	15
CC34-a125	0.03976	32	0.00133	8	1.46728	1.88679	16	0.282267	15	0.282253	-6.2	0.5	1.55	567	13
CC34-a156	0.05243	42	0.00178	11	1.46722	1.88628	19	0.282278	15	0.282260	-6.6	0.5	1.55	538	10
CC34-a145	0.03579	29	0.00117	7	1.46728	1.88625	18	0.282279	17	0.282266	-6.0	0.5	1.53	554	10
CC34-a139	0.04282	35	0.00138	8	1.46731	1.88657	17	0.282283	17	0.282268	-5.7	0.5	1.52	563	12
CC34-a142	0.03648	29	0.00123	7	1.46726	1.88662	17	0.282283	17	0.282270	-5.6	0.5	1.52	567	11
CC34-a136	0.03247	26	0.00110	7	1.46724	1.88665	16	0.282284	20	0.282272	-5.7	0.6	1.52	557	12
CC34-b89	0.03726	30	0.00120	7	1.46726	1.88655	15	0.282282	14	0.282269	-5.7	0.6	1.52	562	15
CC34-b91	0.03511	29	0.00120	7	1.46730	1.88669	17	0.282292	11	0.282280	-5.3	0.5	1.50	565	15
CC34-b94	0.04065	33	0.00139	8	1.46727	1.88664	16	0.282293	16	0.282279	-5.8	0.5	1.51	544	15
CC34-b96	0.03466	28	0.00120	8	1.46726	1.88664	15	0.282307	19	0.282295	-5.3	0.6	1.48	539	15

Hf isotopes results determined by LA-ICP-MS - Sample CC35a

Spot	$^{176}Yb/^{177}Hf$	±2σ	$^{176}Lu/^{177}Hf$ [a]	±2σ	$^{178}Hf/^{177}Hf$	$^{180}Hf/^{177}Hf$	Sig_{Hf} [b]	$^{176}Hf/^{177}Hf$	±2σ [c]	$^{176}Hf/^{177}Hf(t)$	εHf(t) [d]	±2σ [c]	T_{DM} [e]	age [f]	±2σ
Inherited															
CC35a-a16	0.04412	36	0.00136	8	1.46718	1.88646	9	0.282325	23	0.282310	-3.3	0.8	1.43	607	12
CC35a-a20	0.03366	35	0.00102	10	1.46713	1.88646	9	0.282270	45	0.282259	-4.9	1.6	1.52	615	10
CC35a-a31	0.07426	79	0.00223	21	1.46715	1.88663	8	0.282311	25	0.282284	-3.2	0.9	1.46	651	14
CC35a-a41	0.03004	27	0.00091	7	1.46717	1.88637	10	0.282280	20	0.282267	-1.9	0.7	1.46	736	16
CC35a-a52	0.03747	33	0.00111	8	1.46719	1.88640	15	0.282268	20	0.282256	-5.2	0.7	1.53	608	14
CC35a-a59	0.02673	22	0.00073	5	1.46715	1.88605	8	0.282271	20	0.282262	-4.7	0.7	1.51	619	12
CC35a-b35	0.03064	29	0.00094	7	1.46717	1.88668	10	0.282269	20	0.282258	-4.4	0.7	1.51	637	16
CC35a-a63	0.04045	38	0.00119	9	1.46719	1.88646	11	0.282323	21	0.282309	-3.3	0.8	1.43	608	12
CC35a-b20	0.04072	33	0.00126	8	1.46712	1.88634	8	0.282291	23	0.282276	-4.1	0.8	1.49	621	12
CC35a-b21	0.03117	27	0.00095	7	1.46721	1.88654	10	0.282289	21	0.282278	-4.0	0.7	1.48	622	12
Magmatic															
CC35a-a21	0.03878	40	0.00120	11	1.46721	1.88639	9	0.282295	20	0.282282	-4.7	0.7	1.49	588	10
CC35a-a17	0.06081	67	0.00184	16	1.46720	1.88651	9	0.282345	27	0.282325	-3.4	1.0	1.41	578	10
CC35a-a23	0.04020	45	0.00128	12	1.46715	1.88619	9	0.282337	26	0.282322	-3.2	0.9	1.41	590	10
CC35a-a32	0.04665	51	0.00142	13	1.46721	1.88641	8	0.282304	20	0.282288	-4.7	0.7	1.48	579	12
CC35a-a37	0.04725	47	0.00133	11	1.46718	1.88648	8	0.282325	23	0.282311	-3.8	0.8	1.43	584	10
CC35a-a39	0.04856	42	0.00151	11	1.46714	1.88649	9	0.282310	23	0.282293	-4.4	0.8	1.47	582	10
CC35a-a40	0.03439	36	0.00098	10	1.46713	1.88643	9	0.282291	22	0.282280	-5.0	0.8	1.50	579	10
CC35a-a43	0.04573	51	0.00138	13	1.46714	1.88613	19	0.282307	19	0.282292	-4.6	0.7	1.47	574	12
CC35a-a47	0.03025	31	0.00092	8	1.46714	1.88658	12	0.282310	33	0.282300	-4.0	1.2	1.45	591	10
CC35a-a48	0.03640	34	0.00116	9	1.46718	1.88600	12	0.282329	23	0.282317	-3.7	0.8	1.42	578	10
CC35a-a54	0.04802	45	0.00141	11	1.46718	1.88622	13	0.282301	28	0.282285	-4.6	1.0	1.48	588	10
CC35a-a56	0.03925	47	0.00119	13	1.46714	1.88656	10	0.282284	19	0.282271	-5.3	0.7	1.51	580	12
CC35a-a57	0.03469	45	0.00109	14	1.46716	1.88604	10	0.282294	24	0.282282	-4.7	0.8	1.49	588	12
CC35a-a58	0.02637	22	0.00074	5	1.46721	1.88656	11	0.282287	22	0.282279	-4.8	0.8	1.49	586	10
CC35a-a66	0.03280	33	0.00100	9	1.46724	1.88646	9	0.282294	17	0.282283	-4.6	0.6	1.49	590	12
CC35a-a67	0.02565	35	0.00075	10	1.46717	1.88654	6	0.282274	22	0.282265	-5.3	0.8	1.52	588	10
CC35a-a69	0.03021	32	0.00091	9	1.46713	1.88613	11	0.282308	18	0.282298	-4.2	0.6	1.46	584	12
CC35a-b22	0.03080	31	0.00090	7	1.46722	1.88666	13	0.282290	18	0.282281	-5.0	0.6	1.49	577	14
CC35a-b26	0.03122	31	0.00100	8	1.46719	1.88648	11	0.282263	22	0.282252	-5.8	0.8	1.55	585	10
CC35a-b42	0.03687	38	0.00116	11	1.46720	1.88602	15	0.282287	30	0.282275	-5.3	1.1	1.51	573	10
CC35a-b51	0.04379	38	0.00131	9	1.46716	1.88661	10	0.282281	29	0.282267	-5.4	1.0	1.52	578	10

Hf isotopes results determined by LA-ICP-MS - Sample CC35a

Spot	$^{176}Yb/^{177}Hf$	±2σ	$^{176}Lu/^{177}Hf$ [a]	±2σ	$^{178}Hf/^{177}Hf$	$^{180}Hf/^{177}Hf$	Sig_{Hf} [b]	$^{176}Hf/^{177}Hf$	±2σ [c]	$^{176}Hf/^{177}Hf(t)$	εHf(t) [d]	±2σ [c]	T_{DM} [e]	age [f]	±2σ
CC35a-b54	0.08033	149	0.00247	44	1.46731	1.88655	8	0.282315	37	0.282288	-4.6	1.3	1.48	580	12
CC35a-b73	0.04248	41	0.00133	11	1.46714	1.88665	10	0.282277	16	0.282262	-5.7	0.6	1.53	573	10
CC35a-b75	0.03866	36	0.00125	10	1.46718	1.88681	10	0.282305	24	0.282291	-4.4	0.8	1.47	587	12
CC35a-b79	0.06551	57	0.00194	13	1.46723	1.88662	17	0.282315	20	0.282294	-4.5	0.7	1.47	576	10
Anatectic and/or metamorphic															
CC35a-a18	0.04803	45	0.00152	11	1.46710	1.88608	10	0.282357	21	0.282341	-3.2	0.8	1.38	559	10
CC35a-a24	0.02690	33	0.00080	10	1.46708	1.88608	8	0.282332	30	0.282324	-3.9	1.1	1.42	554	10
CC35a-a25	0.11372	175	0.00340	49	1.46716	1.88638	11	0.282352	27	0.282317	-4.3	0.9	1.44	550	10
CC35a-a26	0.03937	49	0.00122	14	1.46716	1.88614	9	0.282298	18	0.282286	-5.2	0.6	1.49	557	12
CC35a-a33	0.03548	41	0.00106	11	1.46718	1.88619	8	0.282345	30	0.282334	-3.4	1.0	1.40	562	10
CC35a-a49	0.03529	49	0.00110	15	1.46720	1.88618	10	0.282302	24	0.282290	-5.2	0.8	1.49	552	10
CC35a-a53	0.02845	27	0.00084	7	1.46721	1.88678	11	0.282253	20	0.282244	-6.6	0.7	1.57	562	10
CC35a-b28	0.05189	72	0.00159	21	1.46708	1.88612	10	0.282337	43	0.282322	-5.2	1.5	1.45	500	10
CC35a-b29	0.05129	49	0.00157	13	1.46723	1.88653	8	0.282348	19	0.282332	-3.5	0.7	1.40	562	10
CC35a-b31	0.02871	25	0.00085	7	1.46720	1.88662	11	0.282260	19	0.282251	-6.3	0.7	1.56	565	10
CC35a-b53	0.02435	26	0.00072	7	1.46725	1.88657	11	0.282284	21	0.282277	-6.7	0.7	1.53	506	10
CC35a-b56	0.04350	38	0.00136	10	1.46716	1.88667	12	0.282286	21	0.282272	-5.5	0.8	1.52	567	10

Hf isotopes results determined by LA-ICP-MS - Sample CC36

Spot	$^{176}Yb/^{177}Hf$	±2σ	$^{176}Lu/^{177}Hf$	±2σ	$^{178}Hf/^{177}Hf$	$^{180}Hf/^{177}Hf$	Sig_{Hf} [b]	$^{176}Hf/^{177}Hf$	±2σ [c]	$^{176}Hf/^{177}Hf(t)$	εHf(t) [d]	±2σ [c]	T_{DM} [e]	age [f]	±2σ
Inherited															
CC36-a26	0.02356	19	0.00076	5	1.46729	1.88541	17	0.282281	13	0.282272	-4.5	0.5	1.50	597	12
CC36-a38	0.05544	45	0.00181	11	1.46719	1.88658	12	0.282296	12	0.282276	-4.8	0.8	1.50	603	12
CC36-a39	0.03713	30	0.00119	7	1.46724	1.88686	16	0.282299	14	0.282286	-4.3	0.5	1.48	635	12
CC36-a41	0.03577	34	0.00120	9	1.46722	1.88675	18	0.282302	14	0.282288	-3.7	0.5	1.46	610	10
CC36-a43	0.02817	23	0.00095	6	1.46731	1.88615	15	0.282289	14	0.282278	-3.8	0.6	1.48	622	12
CC36-a46	0.03503	28	0.00109	7	1.46725	1.88721	19	0.282268	14	0.282256	-5.2	0.6	1.53	611	10
CC36-a70	0.06146	50	0.00205	12	1.46722	1.88639	16	0.282286	14	0.282263	-5.1	0.6	1.52	605	12
CC36-b13	0.03464	28	0.00113	7	1.46723	1.88736	17	0.282282	13	0.282269	-4.8	0.6	1.51	602	10
Magmatic															
CC36-a30	0.03860	31	0.00124	7	1.46725	1.88656	18	0.282257	11	0.282244	-6.0	0.5	1.56	586	10
CC36-b36	0.04079	33	0.00093	6	1.46732	1.88579	19	0.282228	14	0.282218	-6.9	0.6	1.61	588	10
Anatectic and/or metamorphic															
CC36-b16	0.03407	28	0.00110	7	1.46727	1.88694	16	0.282285	13	0.282273	-5.4	0.5	1.51	569	12
CC36-b50	0.03859	31	0.00129	8	1.46724	1.88685	14	0.282303	14	0.282290	-5.3	0.6	1.49	550	10
CC36-b51	0.04470	36	0.00144	9	1.46722	1.88667	20	0.282283	16	0.282268	-5.8	0.5	1.53	560	10
CC36-b52	0.03221	26	0.00110	7	1.46725	1.88662	16	0.282301	15	0.282290	-5.2	0.6	1.49	554	10

Hf isotopes results determined by LA-ICP-MS - Sample CC40

Spot	$^{176}Yb/^{177}Hf$	±2σ	$^{176}Lu/^{177}Hf$	±2σ	$^{178}Hf/^{177}Hf$	$^{180}Hf/^{177}Hf$	Sig_{Hf} [b]	$^{176}Hf/^{177}Hf$	±2σ [c]	$^{176}Hf/^{177}Hf(t)$	εHf(t) [d]	±2σ [c]	T_{DM} [e]	age [f]	±2σ
Inherited															
CC40-24	0.04086	35	0.00123	8	1.46712	1.88626	10	0.282301	34	0.282286	-3.6	1.2	1.46	630	12
CC40-57	0.04054	39	0.00113	9	1.46724	1.88682	12	0.282267	46	0.282251	-2.9	1.6	1.50	714	16
CC40-59	0.04621	37	0.00150	9	1.46718	1.88647	10	0.282327	26	0.282308	-1.4	0.9	1.39	693	12
CC40-61	0.04507	46	0.00142	13	1.46719	1.88667	12	0.282290	20	0.282274	-4.4	0.7	1.49	614	10
CC40-81	0.04584	38	0.00124	8	1.46722	1.88650	16	0.282247	20	0.282232	-5.7	0.7	1.57	620	12
CC40-96	0.03510	39	0.00111	11	1.46714	1.88641	11	0.282295	29	0.282281	-2.7	1.0	1.45	678	12
CC40-106	0.03371	41	0.00107	12	1.46717	1.88654	10	0.282070	34	0.282053	-7.4	1.2	1.83	826	14
Magmatic															
CC40-15	0.04114	50	0.00124	12	1.46722	1.88688	9	0.282276	29	0.282263	-5.5	1.0	1.53	583	10
CC40-16	0.06134	60	0.00170	14	1.46718	1.88659	12	0.282273	21	0.282254	-5.7	0.7	1.54	587	10
CC40-19	0.04148	38	0.00117	8	1.46715	1.88650	11	0.282329	24	0.282316	-3.4	0.8	1.42	594	10
CC40-25	0.04104	34	0.00128	8	1.46718	1.88660	13	0.282291	20	0.282276	-4.6	0.7	1.49	598	10
CC40-22	0.04821	44	0.00150	12	1.46720	1.88642	9	0.282311	25	0.282295	-4.3	0.9	1.46	585	10
CC40-27	0.04239	36	0.00128	9	1.46711	1.88599	11	0.282292	25	0.282278	-4.8	0.9	1.50	588	12
CC40-28	0.04802	41	0.00155	11	1.46716	1.88689	8	0.282238	38	0.282221	-6.9	1.3	1.61	584	12
CC40-35	0.04757	40	0.00141	9	1.46720	1.88663	12	0.282312	22	0.282296	-4.1	0.8	1.46	592	12
CC40-38	0.04981	44	0.00149	12	1.46714	1.88635	9	0.282348	23	0.282331	-2.8	0.8	1.39	594	10
CC40-46	0.06229	51	0.00187	12	1.46722	1.88662	13	0.282277	18	0.282257	-5.7	0.6	1.54	584	10
CC40-56	0.03979	37	0.00128	10	1.46715	1.88583	10	0.282352	23	0.282338	-2.8	0.8	1.38	582	16
CC40-63	0.04931	41	0.00145	9	1.46716	1.88653	13	0.282264	23	0.282248	-5.8	0.8	1.55	593	10
CC40-93	0.04221	47	0.00132	13	1.46722	1.88661	10	0.282278	31	0.282264	-5.5	1.1	1.53	580	16
CC40-94	0.04054	42	0.00124	12	1.46713	1.88508	11	0.282330	53	0.282317	-3.5	1.9	1.42	585	12
CC40-108	0.03586	47	0.00110	14	1.46702	1.88591	11	0.282248	39	0.282235	-6.1	1.4	1.58	597	12
CC40-112	0.03409	30	0.00101	7	1.46718	1.88630	11	0.282302	31	0.282291	-4.3	1.1	1.47	593	10
Anatectic and/or metamorphic															
CC40-40	0.04502	43	0.00114	9	1.46715	1.88645	13	0.282273	26	0.282261	-5.9	0.9	1.54	567	10
CC40-62	0.04969	40	0.00159	10	1.46716	1.88662	13	0.282307	22	0.282290	-5.1	0.8	1.48	558	10
CC40-78	0.04608	42	0.00141	10	1.46725	1.88667	9	0.282325	30	0.282310	-4.1	1.1	1.44	568	12
CC40-82	0.05237	45	0.00153	10	1.46714	1.88644	10	0.282292	23	0.282277	-5.7	0.8	1.51	552	10
CC40-92	0.04633	85	0.00148	25	1.46709	1.88618	6	0.282341	51	0.282325	-3.6	1.8	1.41	568	10
CC40-105	0.03764	34	0.00111	9	1.46714	1.88624	11	0.282333	24	0.282321	-3.9	0.8	1.42	562	10
CC40-107	0.03638	32	0.00112	8	1.46712	1.88604	15	0.282295	20	0.282283	-5.1	0.7	1.49	567	12

Hf isotopes results determined by LA-ICP-MS - Sample CC42

Spot	$^{176}Yb/^{177}Hf$	±2σ	$^{176}Lu/^{177}Hf$	±2σ	$^{178}Hf/^{177}Hf$	$^{180}Hf/^{177}Hf$	Sig_{Hf} [b]	$^{176}Hf/^{177}Hf$	±2σ [c]	$^{176}Hf/^{177}Hf(t)$	εHf(t) [d]	±2σ [c]	T_{DM} [e]	age [f]	±2σ
Inherited															
CC42-a33	0.04715	44	0.00142	10	1.46715	1.88661	11	0.282319	22	0.282303	-3.4	0.8	1.44	612	12
CC42-a35	0.03278	52	0.00105	15	1.46721	1.88608	9	0.282316	32	0.282304	-3.6	1.1	1.44	602	12
CC42-a72	0.01915	19	0.00060	6	1.46717	1.88659	12	0.282250	17	0.282243	-5.3	0.6	1.55	623	12
CC42-a74	0.03196	27	0.00101	7	1.46717	1.88639	11	0.282276	18	0.282264	-4.9	0.6	1.52	604	10
CC42-a93	0.05370	71	0.00163	20	1.46719	1.88673	12	0.282284	24	0.282264	-4.5	0.8	1.51	622	12
CC42-b18	0.04417	61	0.00143	17	1.46714	1.88556	14	0.282371	34	0.282355	-1.8	1.2	1.34	602	10
CC42-b32	0.06025	63	0.00190	18	1.46717	1.88646	10	0.282297	18	0.282275	-4.3	0.6	1.49	615	10
CC42-b49	0.04051	35	0.00128	9	1.46717	1.88650	11	0.282317	21	0.282303	-3.6	0.7	1.44	601	10
CC42-b81	0.04328	37	0.00134	9	1.46713	1.88606	10	0.282282	22	0.282267	-4.9	0.8	1.51	601	10
CC42-b101	0.04364	39	0.00143	10	1.46728	1.88645	8	0.282290	38	0.282274	-4.5	1.3	1.49	608	10
CC42-b113	0.05084	43	0.00143	9	1.46715	1.88640	11	0.282294	22	0.282277	-4.1	0.8	1.48	620	12
Magmatic															
CC42-a17	0.05787	53	0.00167	13	1.46721	1.88661	10	0.282257	24	0.282238	-6.2	0.9	1.57	588	10
CC42-a22	0.02859	31	0.00093	9	1.46714	1.88599	10	0.282287	28	0.282277	-5.0	1.0	1.50	584	10
CC42-a24	0.02788	23	0.00090	6	1.46714	1.88616	9	0.282295	28	0.282285	-4.9	1.0	1.49	575	10
CC42-a26	0.04533	51	0.00147	14	1.46701	1.88577	9	0.282299	22	0.282283	-4.7	0.8	1.49	584	10
CC42-a27	0.05464	93	0.00168	27	1.46713	1.88597	9	0.282320	30	0.282301	-4.1	1.1	1.45	583	14
CC42-a32	0.05345	44	0.00187	12	1.46722	1.88601	5	0.282335	25	0.282314	-3.6	0.9	1.43	587	10
CC42-a37	0.03332	29	0.00111	8	1.46698	1.88495	4	0.282345	45	0.282333	-3.0	1.6	1.39	581	12
CC42-a38	0.04530	44	0.00139	11	1.46720	1.88643	10	0.282323	26	0.282308	-4.0	0.9	1.44	576	10
CC42-a42	0.03122	35	0.00098	9	1.46715	1.88627	13	0.282256	26	0.282246	-6.2	0.9	1.56	578	12
CC42-a47	0.01690	22	0.00058	6	1.46716	1.88611	6	0.282302	47	0.282295	-4.4	1.7	1.47	578	12
CC42-a48	0.00966	15	0.00030	4	1.46711	1.88627	11	0.282279	61	0.282275	-5.1	2.2	1.50	579	12
CC42-a52	0.03573	54	0.00106	15	1.46718	1.88683	12	0.282243	23	0.282231	-6.5	0.8	1.59	587	12
CC42-a55	0.04017	58	0.00120	17	1.46717	1.88647	9	0.282340	27	0.282327	-3.0	1.0	1.40	593	10
CC42-a57	0.03334	29	0.00105	7	1.46717	1.88628	11	0.282300	20	0.282289	-4.6	0.7	1.48	582	10
CC42-a71	0.02591	23	0.00079	6	1.46716	1.88677	11	0.282278	24	0.282269	-5.2	0.9	1.51	586	14
CC42-a73	0.04086	37	0.00126	9	1.46720	1.88651	11	0.282271	23	0.282258	-5.6	0.8	1.54	584	10
CC42-a75	0.03275	27	0.00102	7	1.46718	1.88673	13	0.282279	21	0.282268	-5.1	0.7	1.51	590	10
CC42-a77	0.02642	23	0.00086	6	1.46710	1.88591	15	0.282331	28	0.282322	-3.5	1.0	1.41	579	10
CC42-a80	0.02187	20	0.00065	5	1.46718	1.88653	11	0.282281	25	0.282274	-5.1	0.9	1.50	584	12
CC42-a85	0.04090	36	0.00124	9	1.46715	1.88646	10	0.282270	21	0.282256	-5.7	0.8	1.54	585	12

Continued... Hf isotopes results determined by LA-ICP-MS - Sample CC42

Spot	$^{176}Yb/^{177}Hf$	±2σ	$^{176}Lu/^{177}Hf$ [a]	±2σ	$^{178}Hf/^{177}Hf$	$^{180}Hf/^{177}Hf$	Sig_{Hf} [b]	$^{176}Hf/^{177}Hf$	±2σ [c]	$^{76}Hf/^{177}Hf(t)$	εHf(t) [d]	±2σ [c]	T_{DM} [e]	age [f]	±2σ
CC42-a91	0.04050	38	0.00121	10	1.46717	1.88647	10	0.282265	20	0.282251	-5.6	0.7	1.54	596	10
CC42-b108	0.03660	30	0.00113	7	1.46720	1.88651	10	0.282275	21	0.282263	-5.5	0.7	1.53	581	10
CC42-b109	0.02181	24	0.00069	7	1.46715	1.88637	9	0.282280	25	0.282272	-4.8	0.9	1.50	598	10
CC42-b110	0.01984	19	0.00065	5	1.46714	1.88626	10	0.282272	26	0.282265	-5.1	0.9	1.52	595	10
CC42-b22	0.04453	50	0.00139	14	1.46716	1.88630	11	0.282325	22	0.282310	-3.9	0.8	1.44	580	10
CC42-b24	0.04515	41	0.00142	11	1.46716	1.88621	10	0.282299	28	0.282283	-4.8	1.0	1.49	579	10
CC42-b34	0.03917	36	0.00122	9	1.46720	1.88659	11	0.282261	24	0.282248	-6.1	0.9	1.56	580	10
CC42-b36	0.03833	33	0.00124	8	1.46714	1.88614	12	0.282312	20	0.282298	-4.2	0.7	1.46	582	10
CC42-b37	0.04624	55	0.00149	16	1.46718	1.88624	8	0.282292	25	0.282276	-5.0	0.9	1.50	581	10
CC42-b47	0.04035	42	0.00127	12	1.46714	1.88623	10	0.282327	21	0.282313	-3.5	0.8	1.43	590	10
CC42-b54	0.03076	26	0.00102	7	1.46719	1.88613	9	0.282292	25	0.282281	-4.5	0.9	1.49	599	12
CC42-b55	0.03736	47	0.00123	14	1.46719	1.88602	9	0.282286	26	0.282272	-5.0	0.9	1.51	590	10
CC42-b56	0.02791	28	0.00085	7	1.46710	1.88596	10	0.282320	20	0.282310	-3.6	0.7	1.43	591	12
CC42-b61	0.03178	28	0.00091	6	1.46718	1.88659	11	0.282288	28	0.282278	-4.7	1.0	1.49	595	10
CC42-b75	0.02808	27	0.00086	7	1.46716	1.88664	11	0.282251	20	0.282242	-6.0	0.7	1.56	594	10
CC42-b76	0.03212	27	0.00101	7	1.46723	1.88615	11	0.282292	18	0.282281	-4.8	0.6	1.49	586	10
CC42-b82	0.03687	30	0.00109	7	1.46717	1.88644	9	0.282277	20	0.282265	-5.1	0.7	1.52	595	10
CC42-b84	0.01392	13	0.00047	4	1.46716	1.88616	10	0.282303	25	0.282298	-4.0	0.9	1.45	595	10
CC42-b85	0.01586	16	0.00053	5	1.46724	1.88654	11	0.282279	27	0.282273	-4.8	1.0	1.50	596	10
CC42-b89	0.02885	25	0.00095	7	1.46715	1.88601	10	0.282279	22	0.282268	-4.9	0.8	1.51	599	10
CC42-b90	0.02944	26	0.00099	7	1.46717	1.88629	9	0.282273	21	0.282262	-5.5	0.7	1.53	582	10
CC42-b93	0.06428	73	0.00200	19	1.46719	1.88658	14	0.282303	16	0.282282	-4.8	0.6	1.49	584	10
CC42-b93-2	0.12446	225	0.00360	62	1.46717	1.88635	12	0.282329	25	0.282289	-4.5	0.9	1.47	584	10
CC42-b100	0.01827	19	0.00061	6	1.46713	1.88636	13	0.282278	30	0.282272	-5.3	1.1	1.51	577	10
Anatectic and/or metamorphic															
CC42-b107	0.03384	31	0.00108	8	1.46718	1.88639	11	0.282301	20	0.282289	-4.8	0.7	1.48	569	10
CC42-b112	0.03834	44	0.00121	13	1.46715	1.88639	11	0.282294	17	0.282282	-6.2	0.6	1.51	522	10
CC42-b19	0.03242	35	0.00109	10	1.46707	1.88521	14	0.282368	61	0.282358	-3.6	2.1	1.37	515	10
CC42-b31	0.05195	68	0.00168	20	1.46719	1.88604	8	0.282333	25	0.282316	-4.9	0.9	1.45	525	10
CC42-b20	0.04222	46	0.00138	13	1.46724	1.88637	11	0.282303	21	0.282288	-4.7	0.8	1.48	579	10
CC42-b25	0.05289	60	0.00173	17	1.46718	1.88627	8	0.282302	29	0.282283	-5.0	1.0	1.49	572	10
CC42-b50	0.02663	35	0.00085	11	1.46710	1.88653	10	0.282282	19	0.282273	-5.5	0.7	1.51	565	12
CC42-b53	0.01650	14	0.00053	4	1.46713	1.88643	12	0.282281	30	0.282275	-5.1	1.1	1.50	579	10

Continued... Hf isotopes results determined by LA-ICP-MS - Sample CC42

Spot	$^{176}Yb/^{177}Hf$	±2σ	$^{176}Lu/^{177}Hf$ [a]	±2σ	$^{178}Hf/^{177}Hf$	$^{180}Hf/^{177}Hf$	Sig_{Hf} [b]	$^{176}Hf/^{177}Hf$	±2σ [c]	$^{176}Hf/^{177}Hf(t)$	εHf(t) [d]	±2σ [c]	T_{DM} [e]	age [f]	±2σ
CC42-b51	0.03313	33	0.00104	9	1.46713	1.88618	10	0.282323	21	0.282312	-4.3	0.7	1.44	559	10
CC42-b97	0.03418	47	0.00110	14	1.46712	1.88579	9	0.282354	33	0.282343	-3.2	1.2	1.38	558	12
CC42-a34	0.02850	42	0.00085	11	1.46718	1.88620	10	0.282314	24	0.282305	-4.3	0.8	1.45	569	10
CC42-a50	0.02684	32	0.00083	9	1.46716	1.88639	12	0.282269	20	0.282260	-6.0	0.7	1.54	563	10
CC42-a51	0.03955	53	0.00120	14	1.46721	1.88658	12	0.282272	20	0.282259	-5.8	0.7	1.54	572	10
CC42-a53	0.05686	76	0.00175	22	1.46720	1.88644	9	0.282381	22	0.282362	-2.2	0.8	1.34	571	10
CC42-a56	0.02510	27	0.00075	7	1.46720	1.88645	10	0.282315	19	0.282307	-4.1	0.7	1.44	575	10
CC42-a59	0.04224	45	0.00125	12	1.46720	1.88643	12	0.282266	19	0.282253	-6.3	0.7	1.55	563	10
CC42-a69	0.04320	46	0.00137	13	1.46715	1.88645	13	0.282281	25	0.282267	-5.7	0.9	1.53	567	10
CC42-a70	0.03238	28	0.00098	7	1.46720	1.88660	12	0.282284	23	0.282274	-5.3	0.8	1.51	574	10
CC42-a79	0.03315	29	0.00106	7	1.46715	1.88631	15	0.282296	18	0.282285	-5.1	0.6	1.49	566	10
CC42-a90	0.04279	44	0.00131	12	1.46721	1.88642	11	0.282275	22	0.282260	-5.8	0.8	1.54	574	10

(a) $^{176}Yb/^{177}Hf = (^{176}Yb/^{173}Yb)_{true} \times (^{173}Yb/^{177}Hf)_{measured} \times (m_{173(Yb)}/m_{177(Hf)})^{b(Hf)}$, $b(Hf) = \ln(^{179}Hf/^{177}Hf_{true} / {}^{179}Hf/^{177}Hf_{measured}) / \ln(m_{179(Hf)}/m_{177(Hf)})$;
m=mass of respective isotope. The $^{176}Lu/^{177}Hf$ were calculated in a similar way by using the $^{175}Lu/^{177}Hf$ and b(Yb);

(b) Mean Hf signal in volt;

(c) Uncertainties are quadratic additions of the within-run precision and the reproducibility of the standard zircons GJ-1. Uncertainties for the standars are quoted at 2SD (2 standard deviation);

(d) Initial $^{176}Hf/^{177}Hf$ and εHf calculated using the estimated Pb-Pb ages of respective zircon domains, and the CHUR parameters:
$^{176}Lu/^{177}Hf = 0.0336$, and $^{176}Hf/^{177}Hf = 0.282785$ (Bouvier et al., 2008);

(e) two stage model age in billion years using the measured $^{176}Lu/^{177}Lu$ of each spot (first stage = age of zircon), a value of 0.0113 for the average continental crust (second stage), and a average MORB (DM) $^{176}Lu/^{177}Hf$ and $^{176}Hf/^{177}Hf$ of 0.0384 and 0.28314.

(f) Age determined by LA-ICP-MS

Hf isotopes results determined by LA-ICP-MS - Primary and secondary standards

Standards	$^{176}Yb/^{177}Hf$	±2σ	$^{176}Lu/^{177}Hf$ [a]	±2σ	$^{178}Hf/^{177}Hf$	$^{180}Hf/^{177}Hf$	Sig_{Hf} [b]	$^{176}Hf/^{177}Hf$	±2σ [c]	$^{176}Hf/^{177}Hf(t)$ [d]	εHf(t) [d]	±2σ [c]	age
GJ-1													
GJ-2	0.00824	7	0.00028	2	1.467252	1.88678	9	0.282008	21	0.282019	-14.0	0.7	608
GJ-3	0.00800	6	0.00027	2	1.467186	1.88633	9	0.282027	21	0.282008	-13.4	0.6	608
GJ-4	0.00790	6	0.00027	2	1.467186	1.88645	10	0.281994	21	0.282011	-14.5	0.8	608
GJ-1	0.00786	6	0.00027	2	1.467183	1.88657	9	0.282006	24	0.282016	-14.1	0.7	608
GJ-2	0.00802	6	0.00026	2	1.467196	1.88643	9	0.282014	24	0.282006	-13.8	0.9	608
GJ-3	0.00808	7	0.00026	2	1.467186	1.88649	9	0.282035	22	0.281988	-13.1	0.8	608
GJ-4	0.00801	7	0.00026	2	1.467266	1.88662	8	0.282025	17	0.282008	-13.4	0.8	608
GJ-5	0.00795	6	0.00027	2	1.467179	1.88647	9	0.282019	18	0.282460	-13.6	0.7	608
GJ-6	0.00801	6	0.00027	2	1.467140	1.88648	9	0.282034	14	0.282466	-13.1	0.8	608
GJ-7	0.00804	7	0.00026	2	1.467192	1.88669	8	0.282002	16	0.282480	-14.2	0.8	608
GJ-9	0.00819	7	0.00026	2	1.467172	1.88644	8	0.282007	22	0.282651	-14.1	0.8	608
GJ-10	0.00811	7	0.00026	2	1.467172	1.88644	8	0.282020	22	0.282649	-13.6	0.8	608
GJ-11	0.00806	6	0.00026	2	1.467222	1.88648	8	0.282037	17	0.282664	-13.0	0.8	608
GJ-12	0.00780	6	0.00027	2	1.467199	1.88662	9	0.282001	19	0.282656	-14.3	0.8	608
GJ-13	0.00794	6	0.00026	2	1.467177	1.88644	9	0.282031	16	0.282657	-13.2	0.7	608
GJ-14	0.00802	6	0.00026	2	1.467234	1.88658	9	0.282004	16	0.282665	-14.2	0.8	608
GJ-1	0.00894	7	0.00028	2	1.467206	1.88680	20	0.282023	22	0.282645	-13.5	0.5	608
GJ-1	0.00655	5	0.00024	1	1.467124	1.88625	11	0.282019	22	0.282016	-13.7	0.8	608
GJ-2	0.00609	5	0.00022	1	1.467169	1.88630	12	0.282021	19	0.282019	-13.6	0.7	608
GJ-5	0.00605	5	0.00022	1	1.467205	1.88643	10	0.282022	21	0.282019	-13.5	0.7	608
GJ-6	0.00649	5	0.00024	1	1.467154	1.88640	10	0.282017	20	0.282014	-13.7	0.7	608
GJ-7	0.00628	5	0.00023	1	1.467128	1.88624	10	0.282012	22	0.282009	-13.9	0.8	608
GJ-8	0.00640	5	0.00024	1	1.467227	1.88637	9	0.282011	21	0.282008	-13.9	0.7	608
GJ-9	0.00640	5	0.00024	1	1.467106	1.88628	9	0.282014	21	0.282011	-13.8	0.7	608
GJ-11	0.00643	5	0.00023	1	1.467149	1.88645	10	0.282018	24	0.282016	-13.7	0.8	608
GJ-12	0.00611	5	0.00023	1	1.467172	1.88638	9	0.281998	16	0.281995	-14.4	0.6	608
GJ-13	0.00647	5	0.00024	1	1.467160	1.88632	10	0.282031	27	0.282028	-13.2	0.9	608
GJ-14	0.00616	5	0.00023	1	1.467157	1.88637	9	0.282009	24	0.282006	-14.0	0.9	608
GJ-15	0.00603	5	0.00022	1	1.467125	1.88631	9	0.281990	22	0.281988	-14.6	0.8	608
GJ-4	0.00665	5	0.00025	1	1.467176	1.88648	10	0.282034	16	0.282031	-13.1	0.6	608
GJ-3	0.00637	5	0.00023	1	1.467145	1.88628	13	0.282010	17	0.282008	-13.9	0.6	608
Mean	0.00728	6	0.00025	2	1.467179	1.88645	10	0.282016	20	0.282201	-13.8	0.7	608
SD	0.00090	1	0.00002	0	0.000037	0.00014	2	0.000012	3	0.000280	0.4	0.1	0
RSD%	12.3	12.5	7.2	7.5	0.0	0.0	22.1	0.0	15.2	0.1	-3.1	13.4	0.0

Continued ... Hf isotopes results determined by LA-ICP-MS - Primary and secondary standards

Standards	$^{176}Yb/^{177}Hf$	±2σ	$^{176}Lu/^{177}Hf$ [a]	±2σ	$^{178}Hf/^{177}Hf$	$^{180}Hf/^{177}Hf$	Sig_{Hf} [b]	$^{176}Hf/^{177}Hf$	±2σ [c]	$^{176}Hf/^{177}Hf(t)$ [d]	εHf(t) [d]	±2σ [c]	age
Plesovice													
Ples-1	0.00391	3	0.00010	1	1.467107	1.88646	17	0.282507	14	0.282506	-2.3	0.5	337
Ples-2	0.00292	2	0.00007	0	1.467178	1.88653	14	0.282499	17	0.282498	-2.6	0.6	337
Ples-3	0.00266	2	0.00007	0	1.467160	1.88641	14	0.282500	17	0.282499	-2.6	0.6	337
Ples-4	0.00281	2	0.00007	0	1.467178	1.88658	14	0.282486	16	0.282486	-3.1	0.6	337
Ples-5	0.00290	2	0.00007	0	1.467190	1.88661	15	0.282486	17	0.282485	-3.1	0.6	337
Ples-6	0.00477	4	0.00012	1	1.467183	1.88668	16	0.282521	16	0.282521	-1.8	0.6	337
Ples-7	0.00520	4	0.00013	1	1.467150	1.88664	16	0.282508	17	0.282507	-2.3	0.6	337
Ples-8	0.00414	3	0.00010	1	1.467161	1.88660	15	0.282504	18	0.282503	-2.4	0.6	337
Ples-9	0.00360	3	0.00009	1	1.467174	1.88665	15	0.282500	16	0.282500	-2.6	0.6	337
Ples-10	0.00362	3	0.00009	1	1.467175	1.88666	14	0.282496	17	0.282496	-2.7	0.6	337
Ples-11	0.00456	4	0.00011	1	1.467112	1.88624	15	0.282507	18	0.282507	-2.3	0.6	337
Ples-1	0.00358	3	0.00009	1	1.467109	1.88662	15	0.282466	17	0.282465	-3.8	0.6	337
Ples-2	0.00501	4	0.00013	1	1.467160	1.88708	13	0.282461	18	0.282460	-4.0	0.6	337
Ples-3	0.00417	3	0.00010	1	1.467158	1.88668	13	0.282467	14	0.282466	-3.8	0.5	337
Ples-4	0.00401	3	0.00010	1	1.467168	1.88671	14	0.282476	19	0.282475	-3.4	0.7	337
Ples-5	0.00350	3	0.00009	1	1.467223	1.88659	14	0.282481	16	0.282480	-3.3	0.6	337
Ples-6	0.00433	3	0.00011	1	1.467173	1.88659	14	0.282490	20	0.282489	-2.9	0.7	337
Ples-7	0.00372	3	0.00009	1	1.467144	1.88659	14	0.282466	16	0.282466	-3.8	0.6	337
Mean	0.00386	3	0.00010	1	1.46716	1.88661	14	0.282490	17	0.28249	-2.9	0.6	337
SD	0.00073	0.6	0.00002	0.1	0.00003	0.00016	1.0	0.00002	1.4	0.00002	0.6	0.1	0
RSD%	18.9	18.9	18.6	18.6	0.0	0.0	7.1	0.0	8.6	0.0	-20.6	8.6	0.0
Temora													
TEM-1	0.05689	57	0.00198	16	1.467194	1.88679	10	0.282718	22	0.282703	6.4	0.8	417
TEM-2	0.04047	32	0.00143	9	1.467199	1.88667	10	0.282721	21	0.282710	6.6	0.8	417
TEM-3	0.04539	37	0.00155	10	1.467193	1.88684	10	0.282720	22	0.282708	6.6	0.8	417
TEM-4	0.02179	17	0.00084	5	1.467229	1.88671	9	0.282715	22	0.282709	6.6	0.8	417
TEM-5	0.02243	18	0.00087	5	1.467196	1.88668	10	0.282696	17	0.282689	5.9	0.6	417
TEM-6	0.03615	29	0.00132	8	1.467161	1.88671	8	0.282712	24	0.282702	6.3	0.9	417
TEM-7	0.01878	16	0.00070	5	1.467218	1.88666	11	0.282692	24	0.282686	5.8	0.9	417
TEM-1	0.03111	28	0.00115	8	1.467186	1.88703	12	0.282660	20	0.282651	4.5	0.7	417

Continued ... Hf isotopes results determined by LA-ICP-MS - Primary and secondary standards

Standards	$^{176}Yb/^{177}Hf$	±2σ	$^{176}Lu/^{177}Hf$ [a]	±2σ	$^{178}Hf/^{177}Hf$	$^{180}Hf/^{177}Hf$	Sig_{Hf} [b]	$^{176}Hf/^{177}Hf$	±2σ [c]	$^{176}Hf/^{177}Hf(t)$ [d]	εHf(t) [d]	±2σ [c]	age
TEM-2	0.02185	18	0.00085	5	1.467175	1.88653	8	0.282658	22	0.282651	4.6	0.8	417
TEM-2	0.02185	18	0.00085	5	1.467175	1.88653	8	0.282656	22	0.282649	4.5	0.8	417
TEM-4	0.03242	26	0.00116	7	1.467136	1.88654	15	0.282665	18	0.282656	4.7	0.6	417
TEM-5	0.04017	33	0.00143	9	1.467123	1.88659	15	0.282668	18	0.282657	4.8	0.6	417
TEM-6	0.04374	35	0.00153	9	1.467140	1.88658	13	0.282665	18	0.282653	4.6	0.7	417
TEM-7	0.02118	20	0.00075	5	1.467136	1.88650	15	0.282671	15	0.282665	5.0	0.5	417
TEM-8	0.04114	33	0.00145	9	1.467147	1.88694	11	0.282667	23	0.282656	4.7	0.8	417
TEM-9	0.02166	18	0.00076	5	1.467192	1.88690	14	0.282641	16	0.282635	4.0	0.6	417
Mean	0.03231	27	0.00116	8	1.467175	1.88670	11	0.282683	20	0.282674	5.4	0.7	417
SD	0.01111	10	0.00037	3	0.000030	0.00016	2	0.000026	3	0.000025	0.9	0.1	0
RSD%	34.4	38.5	31.4	38.0	0.0	0.0	20.6	0.0	13.7	0.0	16.8	13.7	0.0
Blue Berry													
BB1-1	0.00096	1	0.00003	0	1.467198	1.88657	10	0.281696	20	0.281695	-26.1	0.9	560
BB1-1	0.00096	1	0.00003	0	1.467202	1.88669	10	0.281690	29	0.281690	-26.3	0.9	560
BB1-2	0.00091	1	0.00003	0	1.467228	1.88666	10	0.281673	19	0.281673	-26.9	0.7	560
BB1-3	0.00106	2	0.00003	1	1.467183	1.88661	10	0.281662	24	0.281662	-27.3	0.8	560
BB1-4	0.00089	1	0.00003	0	1.467157	1.88666	10	0.281676	21	0.281675	-26.8	0.9	560
BB1-5	0.00119	1	0.00004	0	1.467167	1.88657	10	0.281658	22	0.281658	-27.4	0.8	560
BB1-6	0.00101	1	0.00003	0	1.467203	1.88660	10	0.281662	17	0.281661	-27.3	0.7	560
BB1-7	0.00131	1	0.00004	0	1.467208	1.88673	10	0.281660	22	0.281659	-27.4	0.8	560
BB2-1	0.00544	5	0.00016	1	1.467225	1.88671	9	0.281670	35	0.281668	-27.0	0.7	560
BB2-2	0.00542	4	0.00016	1	1.467249	1.88657	10	0.281698	21	0.281696	-26.0	0.7	560
BB2-3	0.00527	4	0.00016	1	1.467167	1.88654	10	0.281660	28	0.281659	-27.4	0.8	560
BB2-4	0.00546	4	0.00016	1	1.467184	1.88669	10	0.281666	23	0.281664	-27.2	0.7	560
BB2-5	0.00553	5	0.00016	1	1.467195	1.88652	11	0.281657	21	0.281655	-27.5	0.7	560
BB3-1	0.00352	3	0.00011	1	1.467219	1.88672	8	0.281662	19	0.281661	-27.3	0.7	560
BB3-2	0.00321	3	0.00010	1	1.467200	1.88685	8	0.281651	18	0.281650	-27.7	0.9	560
BB3-3	0.00271	4	0.00008	1	1.467229	1.88662	8	0.281685	19	0.281684	-26.5	0.6	560
BB3-4	0.00191	2	0.00006	0	1.467133	1.88678	9	0.281654	17	0.281654	-27.6	0.8	560
BB3-5	0.00192	2	0.00005	0	1.467214	1.88679	10	0.281670	21	0.281669	-27.0	0.8	560
BB3-6	0.00182	1	0.00006	0	1.467174	1.88658	10	0.281663	22	0.281662	-27.3	0.7	560
BB3-7	0.00195	2	0.00006	0	1.467202	1.88653	8	0.281675	17	0.281674	-26.8	0.9	560
BB4-1	0.00106	1	0.00003	0	1.467204	1.88657	10	0.281682	22	0.281682	-26.5	0.8	560

Continued ... Hf isotopes results determined by LA-ICP-MS - Primary and secondary standards

Standards	$^{176}Yb/^{177}Hf$	±2σ	$^{176}Lu/^{177}Hf$ [a]	±2σ	$^{178}Hf/^{177}Hf$	$^{180}Hf/^{177}Hf$	Sig_{Hf} [b]	$^{176}Hf/^{177}Hf$	±2σ [c]	$^{176}Hf/^{177}Hf(t)$ [d]	εHf(t) [d]	±2σ [c]	age
BB4-2	0.00109	1	0.00003	0	1.467252	1.88684	10	0.281678	34	0.281677	-26.7	0.9	560
BB4-3	0.00108	1	0.00003	0	1.467210	1.88667	9	0.281678	21	0.281677	-26.7	0.8	560
BB4-4	0.00152	1	0.00005	0	1.467074	1.88537	7	0.281732	28	0.281732	-24.8	0.9	560
BB4-5	0.00154	1	0.00005	0	1.467134	1.88539	6	0.281726	21	0.281725	-25.0	1.6	560
BB4-6	0.00146	1	0.00004	0	1.467162	1.88642	9	0.281710	29	0.281709	-25.6	1.0	560
BB4-7	0.00142	1	0.00004	0	1.467169	1.88626	10	0.281697	19	0.281696	-26.0	0.6	560
Mean	0.00228	2	0.00007	0	1.46719	1.88654	9	0.281677	23	0.28168	-26.7	0.8	560
SD	0.00163	1	0.00005	0	0.00004	0.00035	1	0.000021	5	0.00002	0.7	0.2	0
RSD%	71.6	68.8	69.6	65.4	0.0	0.0	12.1	0.0	20.8	0.0	-2.8	22.7	0.0

(a) $^{176}Yb/^{177}Hf = (^{176}Yb/^{173}Yb)_{true} \times (^{173}Yb/^{177}Hf)_{measured} \times (m_{173(Yb)}/m_{177(Hf)})^{b(Hf)}$, $b(Hf) = \ln(^{179}Hf/^{177}Hf_{true} / {}^{179}Hf/^{177}Hf_{measured}) / \ln(m_{179(Hf)}/m_{177(Hf)})$;

m=mass of respective isotope. The $^{176}Lu/^{177}Hf$ were calculated in a similar way by using the $^{175}Lu/^{177}Hf$ and b(Yb);

(b) Mean Hf signal in volt;

(c) Uncertainties are quadratic additions of the within-run precision and the reproducibility of the standard zircons GJ-1. Uncertainties for standars are 2S.D.;

(d) Initial $^{176}Hf/^{177}Hf$ and eHf calculated using the estimated Pb-Pb ages of respective zircon domains, and the CHUR parameters:

$^{176}Lu/^{177}Hf = 0.0336$, and $^{176}Hf/^{177}Hf = 0.282785$ (Bouvier et al., 2008).;

Trace element results determined by LA-ICP-MS - NIST 610

Element	Ti49	La139	Ce140	Pr141	Nd142	Sm152	Eu153	Gd158	Tb159	Dy164	Ho165	Er166	Tm169	Yb174	Lu175
NIST610-001	443.1	504.2	487.0	455.6	436.6	483.1	468.0	431.2	457.9	440.2	480.3	438.8	419.0	470.1	426.6
NIST610-002	432.4	442.0	434.6	418.6	431.2	447.3	464.0	431.7	448.3	433.1	450.1	429.2	428.5	469.9	449.9
NIST610-003	449.5	469.4	429.3	449.8	449.1	462.3	488.7	422.4	455.5	440.0	479.5	455.3	466.6	486.5	478.8
NIST610-018	431.8	421.7	479.5	422.3	410.8	415.6	429.2	401.2	414.4	405.6	434.2	397.8	379.0	441.1	413.9
NIST610-019	451.9	452.0	500.1	510.7	469.8	490.7	498.5	470.0	450.2	475.2	509.2	484.5	445.1	510.0	472.6
NIST610-020	392.2	435.8	423.3	380.0	401.0	414.5	426.1	386.2	417.5	382.3	383.9	376.3	378.0	409.1	380.5
NIST610-034	488.1	476.8	489.7	497.3	471.9	515.0	489.8	476.2	486.8	477.7	504.8	478.6	458.4	525.7	494.0
NIST610-035	422.9	489.7	473.1	439.8	441.7	464.5	477.7	428.5	461.9	426.5	460.6	440.4	427.9	481.2	468.9
NIST610-036	437.9	483.5	434.8	438.6	421.7	449.6	459.1	410.8	434.6	449.2	470.0	429.0	449.5	459.1	433.4
NIST610-050	441.9	428.6	426.5	455.4	435.6	445.9	474.7	409.7	429.1	412.7	457.9	411.0	392.8	438.4	412.3
NIST610-051	452.4	464.9	459.8	429.2	449.8	468.9	480.7	427.4	458.7	441.4	486.9	457.9	476.1	497.5	463.4
NIST610-052	427.8	486.2	427.6	433.3	445.4	471.9	485.7	455.7	495.8	450.1	483.2	472.3	458.2	506.9	504.7
NIST610-001	431.8	459.3	448.7	428.0	431.2	447.2	464.6	419.1	441.2	426.6	448.1	425.6	419.5	457.8	434.6
NIST610-002	434.3	421.0	451.7	400.3	412.3	432.4	451.2	399.4	408.7	409.4	393.3	396.3	377.6	432.7	414.5
NIST610-003	431.5	411.1	417.4	375.3	400.4	412.6	424.8	390.8	432.9	399.9	424.0	386.2	383.7	420.3	392.5
NIST610-017	443.8	417.3	445.9	394.8	402.4	416.1	402.4	403.4	417.5	396.9	420.6	386.7	385.3	428.7	399.5
NIST610-018	432.7	439.3	448.7	429.7	422.1	454.8	448.7	422.2	424.4	430.6	425.6	416.2	398.2	454.4	433.9
NIST610-019	415.1	406.7	450.3	390.4	403.5	417.9	448.4	383.3	407.1	381.9	406.7	386.4	402.2	427.5	396.8
NIST610-033	427.3	430.9	456.8	416.1	415.9	438.0	418.7	417.6	443.5	421.3	426.3	409.8	391.1	446.0	430.5
NIST610-034	410.7	403.1	426.9	389.0	396.9	393.2	401.1	384.2	400.4	387.4	407.5	381.5	398.9	415.8	381.7
NIST610-035	434.0	430.1	440.6	404.2	398.9	413.8	428.2	397.6	406.6	392.1	408.7	384.7	362.2	418.8	397.1
NIST610-049	431.3	411.3	443.4	404.3	401.6	404.5	393.1	393.3	404.3	389.4	402.4	375.8	385.2	427.4	417.0
NIST610-050	434.8	422.2	439.3	386.0	420.8	429.1	417.0	398.0	436.5	393.8	422.8	388.2	403.7	423.1	420.0
NIST610-051	418.4	384.3	424.1	396.6	395.7	398.4	410.4	383.2	387.5	383.4	386.4	377.7	356.2	403.0	381.0
NIST610-065	428.3	449.3	458.0	408.7	427.6	438.5	449.6	411.0	455.6	404.3	447.8	405.2	381.9	440.7	409.3
NIST610-066	429.0	413.0	431.0	374.6	409.0	422.2	430.0	395.9	404.5	393.2	403.4	387.1	375.8	421.1	409.4
NIST610-067	426.8	450.9	455.3	426.5	389.3	400.7	391.6	387.8	425.7	390.6	411.4	384.1	388.8	423.9	401.4
NIST610-078	422.9	416.0	437.5	378.0	397.9	414.0	432.2	407.2	424.4	396.1	432.5	392.8	385.8	430.1	398.2
NIST610-079	426.9	437.0	440.4	398.2	426.9	437.8	451.6	416.4	425.9	409.0	419.3	405.1	405.2	450.6	429.0
NIST610-080	439.1	449.9	444.4	437.4	429.4	462.1	448.7	422.7	449.4	426.3	454.6	427.4	422.5	475.0	435.0
Mean	433.0	440.3	447.5	419.0	421.5	438.8	445.1	412.8	433.6	415.5	438.1	412.9	406.8	449.7	426.0
SD	15.8	28.7	20.6	32.8	21.5	29.2	30.0	23.5	25.0	26.3	34.1	31.7	31.5	31.8	32.6
RSD%	3.6	6.5	4.6	7.8	5.1	6.7	6.7	5.7	5.8	6.3	7.8	7.7	7.8	7.1	7.7

Trace element results determined by LA-ICP-MS - NIST 612

Element	Ti49	La139	Ce140	Pr141	Nd142	Sm152	Eu153	Gd158	Tb159	Dy164	Ho165	Er166	Tm169	Yb174	Lu175
NIST612-004	48.9	31.9	37.0	32.3	36.3	36.1	33.6	31.5	31.0	34.5	33.4	32.0	30.7	37.0	32.9
NIST612-005	38.4	30.3	32.2	33.6	34.3	32.1	33.3	30.4	31.9	32.0	32.3	33.2	29.1	34.7	32.1
NIST612-006	43.2	32.1	34.7	32.6	38.0	37.8	34.9	32.9	32.0	31.7	32.5	31.7	29.0	36.6	32.3
NIST612-037	34.2	27.5	31.6	28.9	31.1	30.1	30.5	28.1	26.0	27.2	28.8	29.2	27.6	31.5	29.6
NIST612-038	43.1	30.8	32.7	30.9	33.6	33.8	33.3	29.3	29.2	28.1	30.3	30.7	28.4	33.0	30.4
NIST612-039	41.4	26.1	29.6	28.2	30.5	30.8	30.9	27.0	26.2	24.8	26.9	26.4	25.8	28.8	27.9
Mean	41.5	29.8	33.0	31.1	33.9	33.4	32.7	29.9	29.4	29.7	30.7	30.6	28.4	33.6	30.9
SD	4.5	2.2	2.4	2.0	2.6	2.8	1.5	2.0	2.5	3.3	2.3	2.2	1.5	2.9	1.8
RSD%	10.9	7.5	7.1	6.3	7.8	8.3	4.7	6.6	8.5	11.1	7.4	7.2	5.3	8.6	5.7

Trace element results determined by LA-ICP-MS - GJ-1

Element	Ti47	La139	Ce140	Pr141	Nd143	Sm147	Eu153	Gd157	Tb159	Dy163	Ho165	Er166	Tm169	Yb172	Lu175
GJ-1-041	3238.4		10.1			1.5	0.9	4.3		19.8	26.4	7.2	85.0	9.9	4024.3
GJ-1-042	3287.0		10.6		0.5	1.4	0.9	4.2		20.3	28.0	7.5	89.1	10.4	4003.4
GJ-1-043	3266.5		10.3		0.4	1.4	0.9	4.3		20.7	27.0	7.4	92.1	10.6	3906.0
GJ-1-044	3385.5		11.1		0.7	1.4	1.0	3.9		21.5	28.3	7.7	92.1	10.6	3970.9
GJ-1-045	3223.8		9.9		0.7	1.5	0.9	3.8		20.1	27.1	7.1	88.2	10.1	4141.5
Mean	3280.2		10.4		0.6	1.4	0.9	4.1		20.5	27.4	7.4	89.3	10.3	4009.2
SD	57.0		0.4		0.1	0.1	0.0	0.2		0.6	0.7	0.2	2.7	0.3	77.3
RSD%	1.7		3.8		22.9	3.5	5.2	5.4		2.9	2.5	3.1	3.0	2.6	1.9

Trace element results determined by LA-ICP-MS - 91500

Element	Ti47	La139	Ce140	Pr141	Nd143	Sm147	Eu153	Gd157	Tb159	Dy163	Ho165	Er166	Tm169	Yb172	Lu175
91500-046	3204.6		0.8				0.1			3.4	6.3	1.9	24.6	3.1	3468.5
91500-047	3104.4		0.9	0.1			0.1			2.8	5.8	1.9	24.5	2.9	3423.0
91500-048	2965.7		0.7		1.2	0.4	0.1			2.6	5.8	1.9	24.3	2.8	3400.3
91500-049	2908.4		0.6		0.7					2.4	5.6	1.7	22.8	2.8	3232.4
91500-050	3024.2		0.7		0.6	0.4	0.1			2.4	5.1	1.8	23.5	2.7	3160.5
Mean	2966.1		0.7		0.9	0.4	0.1			2.5	5.5	1.8	23.5	2.8	3264.4
SD	104.2		0.1	0.0	0.3	0.0	0.0			0.4	0.4	0.1	0.7	0.1	119.0
RSD%	3.5		14.3		33.0	6.1	33.5			15.4	7.4	4.5	3.0	5.0	3.6

Trace element results determined by LA-ICP-MS - Plesovice

Element	Ti47	La139	Ce140	Pr141	Nd143	Sm147	Eu153	Gd157	Tb159	Dy163	Ho165	Er166	Tm169	Yb172	Lu175
Ples-054	3007.7		2.4	0.3	5.0	7.1	1.7	15.6		68.2	53.4	11.1	95.5	7.3	5918.8
Ples-055	3107.7		2.2	0.3	4.6	7.3	1.6	15.4		67.3	54.0	11.1	94.0	7.3	6168.8
Ples-056	2870.4		2.3	0.3	5.1	7.4	1.7	16.6		67.6	54.0	11.1	94.3	7.3	6077.3
Ples-057	2982.5		2.4	0.3	4.7	7.1	1.5	14.7		66.2	53.4	11.0	91.8	7.1	5909.7
Ples-058	3057.7		2.5	0.4	5.0	7.3	1.8	15.3		69.3	55.2	11.2	95.2	7.5	6222.2
Mean	3005.2		2.4	0.3	4.9	7.3	1.6	15.5		67.7	54.0	11.1	94.2	7.3	6059.4
SD	79.9		0.1	0.0	0.2	0.1	0.1	0.6		1.0	0.7	0.1	1.3	0.1	127.2
RSD%	2.7		3.6	11.2	4.2	1.8	5.0	4.0		1.5	1.3	0.6	1.4	1.5	2.1

APPENDIX C
ABSRACTS TO CONFERENCES

List of communications:

I. Melo M.G., Stevens G., Lana C., Gerdes A. 2014. The granulite facies history of the Carlos Chaga batholiths, Araçuaí orogen, SE Brazil. 6th Igneous and Metamorphic Study Group 2014, Rhodes, South Africa. (presentation)

II. Melo M.G., Stevens G., C. Lana, Pedrosa-Soares A.C., Frei D., Alkmim F.F. 2015. Two granulite-facies anatectic episodes in the Carlos Chagas batholith (Brazil). The 8th Hutton Symposium on Granites and Related Rocks 2015, Florianópolis, Brazil. (poster)

III. Melo M.G., Stevens G., C. Lana. 2016. Carbonatitic melt inclusions in peritectic garnet from Carlos Chagas batholith: Implications for crustal melting in the Araçuaí orogen, Brazil. 35th International Geological Congress 2016, Cape Town, South Africa. (presentation)

IV. Melo M.G., Stevens G., Lana C., Pedrosa-Soares A.C., Frei D., Alkmim F.F., Alkmin L.A., Oliveira R., Alves T., Schuch C.S., Mazoz A., Ribeiro T. 2016. Repeated partial melting events in the Araçuaí orogen (southeastern Brazil): evidence from the polymetamorphic Carlos Chagas batholiths. 48º Congresso Brasileiro de Geologia 2016, Porto Alegre, Brazil. (presentation)

V. Melo M.G., Lana C., Stevens G., Alkmin L.A., Gerdes A., Nalini Jr H.A., Gonçalves G.O., Alkmim F.F., Teixeira L., Silva J.P, Silveira G., Fadul C. 2016. U-Pb ages and Hf isotopic record of zircons from Carlos Chagas batholiths: implications for tectono-metamorphic evolution of the Araçuaí orogen (southeastern Brazil). 48º Congresso Brasileiro de Geologia 2016, Porto Alegre, Brazil. (presentation)

VI. Melo M.G, Lana C., Stevens G., Alkmin L.A., Gerdes A., Alkmim F.F., Nalini-Jr H.A. 2016. Assessing the isotopic evolution of S-type granites of the Carlos Chagas Batholith, SE Brazil: clues from U-Pb, Hf isotopes, Ti geothermometry and the trace element composition of zircon. Primer Simposio de Tectónica Sudamericana 2016, Santiago, Chile. (presentation)

THE GRANULITE FACIES HISTORY OF THE CARLOS CHAGAS BATHOLITH, ARAÇUAÍ OROGEN, SE BRAZIL

M.G. Melo[1], G. Stevens[1], C. Lana[2] & A. Gerdes[3]
[1]Centre for Crustal Petrology, Earth Science Department, University of Stellenbosch, South Africa. marilanegonzaga@hotmail.com, gs@sun.ac.za
[2]Department of Geology, University of Ouro Preto, Brazil. cristianodeclana@gmail.com
[3]Institut für Petrologie, Geochemie und Lagerstättenkunde, Universität Frankfurt, Germany. gerdes@em.uni-frankfurt.de

The Late Neoproterozoic–Cambrian Araçuaí orogeny encompasses the entire region between the São Francisco craton and the Atlantic continental margin in eastern Brazil. The crystalline core consists of high-grade rocks and granites exposed in eastern Minas Gerais and Espirito Santo and represents the internal part of the orogen. The granitic supersuites (G1 to G5) originated during the pre- to pos-collisional phase of the orogen (630-480 Ma) (Pedrosa-Soares *et al.* 2011). The G2 supersuite mostly consists of S-type granites formed during the syn-collisional stage (c. 585–560 Ma), and includes the Carlos Chagas batholith, Ataléia and Urucum suites and the Nanuque and Montanha plutons. The Carlos Chagas batholith is one of the largest S-type granites in the world with an area around 14000 km2. The main feature of the Carlos Chagas granite is the large and variable concentration of garnet (5 to 10 vol %) in the rocks. The main objective of this study is to understand the origin of the garnet crystals by studying their compositional and textural characteristics. To date, all studies that have examined the Carlos Chagas granite have assumed that the garnet crystals are of igneous origin. The Carlos Chagas granite is characterized by a medium- to coarse-grained matrix consisting of platy biotite, quartz, plagioclase, perthitic K-feldspar, garnet, ±sillimanite with minor apatite, monazite, zircon, ilmenite, rutile and hercenitic (and gahnitic) spinel as accessory phases. At least two different textural varieties of garnet occur within the granite. The oldest of these consists of large poikiloblastic garnet crystals (10-30 mm) which contain many rounded to lobate quartz inclusions, round ilmenite, biotite, chlorite, plagioclase, monazite and spinel inclusions. The biotite inclusions contain high Ti^{4+} concentrations and are Na-rich compared to the biotite in the matrix. The major element composition of the poikiloblastic garnet crystals is homogeneous and is iron rich with minor grossular and spessartine components ($Alm_{76–89}Py_{6–18}Gro_{1-4}Sps_{2–4}$). A second generation of garnet occurs as smaller euhedral crystals (0.1-0.6 mm) that are similar in composition to the large crystals ($Alm_{79–89}Py_{5-15}Gro_{1-2}Sps_{3–4}$) and that are also unzoned. These crystals contain fine sillimanite needles as inclusions that are aligned with foliated matrix sillimanite. This second generation of garnet also occurs as overgrowths on the large poikiloblastic crystals. The large poikiloblastic garnet crystals are interpreted to arise by reactions that consume biotite, quartz and plagioclase, as is indicated by the fact that these minerals occur as common inclusions. Consequently, the garnet crystals are interpreted to be metamorphic in origin as, in cooling granite magmas, garnet of this composition would always tend to be replaced by biotite. This interpretation is consistent with the unzoned character of the crystals. The second generation of garnet is interpreted to arise through a similar reaction that consumed both biotite and sillimanite. Consequently, the Carlos Chagas batholith has acquired its garnet rich character as a consequence of a previously unrecognized granulite facies metamorphic event. The U-Pb age data obtained from zircons through LA-ICP-MS constrains the magmatic crystallization age of Carlos Chagas granite to between 583.9 ± 1.3 Ma and 574.5 ± 2.7 Ma. An age of 569.1 ±9.4 to 558.3 ± 3.1 is indicated for the granulite facies event that produced the garnet. In this case the zircons are characterized by low in Th/U ratios. All samples analyzed show inherited zircons grains with U-Pb ages between 594 and 630 Ma. Older inherited zircons are also recognized (1735-1400 Ma; 1133-1037 Ma; 855-800 Ma; 739-700 Ma). Lu–Hf analysis results of zircons from the granite yielded initial $^{176}Hf/^{177}Hf$ ratios from 0.282203 to 0.282388 and $\varepsilon_{Hf(t)}$ values from −6.9 to −1.8.

References

Pedrosa-Soares A. C., De Campos C. P., Noce C., Silva L. C., Novo T., Roncato J., Medeiros S., Castañeda C., Queiroga G., Dantas E., Dussin I., Alkmim F. 2011. Late Neoproterozoic–Cambrian granitic magmatism in the Araçuaí orogen (Brazil), the Eastern Brazilian Pegmatite Province and related mineral resources. Geological Society of London, Special Publications, 350:25–51.

PT.032

Two granulite-facies anatectic episodes in the Carlos Chagas Batholith (Brazil)

Melo MG[1,2], Stevens G[2], Lana C[1], Pedrosa-Soares AC[3], Frei D[2], Alkmim FF[1]

[1]Universidade Federal de Ouro Preto - Departamento de Geologia
[2]University of Stellenbosch - Department of Earth Sciences
[3]Universidade Federal de Minas Gerais - Instituto de Geociências

The Carlos Chagas batholith (CCB) is a large body (exposed area = 14,000 km^2) of peraluminous granitoid rocks formed during the syn-collisional period (585-560 Ma) of the Araçuaí orogeny (Brazil). A dominant feature of this batholith is its garnet-rich and biotite-poor character. No previous studies have investigated the origin of the mineralogy of the CCB in detail. In this study, we present new petrographic and mineral chemical evidence which documents garnet growth during two separate partial melting episodes. *In situ* U-Pb monazite and zircon dating, allow the timing of the partial melting events to be accurately constrained.

Three different domains within CCB can be differentiated based on the occurrence of the mineral assemblages: (1) Qz+Pl+Kfs+Bt+Grt+Ilm±Rt, (2) Qz+Pl+Kfs+Bt+Grt+Ilm+Sil±Crd, (3) Qz+Pl+Kfs+Bt+Grt+Ilm+Sil+Spl. In all three domains garnet occurs as large poikiloblastic crystals which include rounded biotite crystals with higher TiO_2 contents than the matrix biotite. In domains 2 and 3 a sillimanite fabric wraps around the large garnet crystals and a second generation of garnet occurs as smaller euhedral crystals that overgrow both the sillimanite fabric and the large garnet crystals. This 2nd generation of garnet contains sillimanite inclusions. Both generations of garnet are unzoned in terms of major element ($Alm_{70-80}Py_{15-23}Sps_{2-4}Grs_{2-6}$ and $Alm_{71–83}Py_{12-23}Sps_{2–4}Gro_{2-6}$ respectively) and HREE (Gd_N/Lu_N=0.08-0.60 and 0.51-1.60 respectively).

Textural evidence for the presence of melt at the peak of metamorphism is recognized in all domains on all scales, from the formation of garnet-bearing neosome to melt inclusions within garnet. Phase equilibria modelling using melt-depleted bulk compositions allows that P-T conditions of the last melting event to be constrained in each domain. Domain 1 records the conditions of the 1st metamorphic event to be 807-905 ºC and 12.4-12.8 kbar, whilst Domains 2 and 3 record the conditions of equilibration during the 2nd metamorphic event to be: 765-835 ºC and 5.1-9.5 kbar; and 765-819 ºC and 5.0-10.2 kbar respectively.

The CCB crystallized as a K-feldspar megacrystic biotite granite at 587-572 Ma and the 1st granulite facies event occurred at 560-552 Ma, producing poikiloblastic garnet (1-15%) in neosomes around phenocrysts via biotite fluid-absent melting. The Nova Venécia complex, which forms the country rocks around the CCB, records conditions of 750-850 ºC and 5.3-7.5 Kbar at this time.

Reheating related to asthenosphere ascent during the extensional thinning and gravitational collapse of the orogen promoted sufficient heat to allow for a 2nd anatectic event in the CCB, where rehydration had allowed for the formation of retrograde muscovite. This 2nd granulite event is recorded in the zircon and monazite geochronology of all domains at 528-515 Ma, but a new generation of garnet is only identified in the rocks of Domains 2 and 3. In these rocks sillimanite is produced by muscovite dehydration melting followed by biotite melting in the sillimanite-bearing rocks and generation of the 2nd generation of garnet. Juxtaposition of the CCB with the Nova Venécia complex was probably accomplished during this extensional episode.

Carbonatitic melt inclusions in peritectic garnet from Carlos Chagas batholith: Implications for crustal melting in the Araçuaí orogen, Brazil

Melo, M.G.[1,2], Stevens, G.[2] and Lana, C.[3]

[1]Departamento de Geologia, Universidade Federal de Ouro Preto, Morro do Cruzeiro, 35400-000, Ouro Preto, MG, Brazil. marilanegonzaga@hotmail.com
[2]Department of Earth Sciences, Stellenbosch University, Private Bag X1, Matieland 7602, South Africa
[3]Departamento de Geologia, Universidade Federal de Ouro Preto, Morro do Cruzeiro, 35400-000, Ouro Preto, MG, Brazil

---

Crustal differentiation is an important process for the production and stabilization of the continental crust. Orogenic events drive crustal differentiation by introducing fertile material for the production of granitic magma into the deep crust. Partial melting (> 800 °C) produces granitic magmas by fluid-absent melting reactions involving the breakdown of micas and amphiboles. Such reactions produce peritectic phases that can trap primary melt inclusions during their growth. The investigation of preserved melt inclusions within peritectic phases provides an excellent opportunity for better understanding of the crustal recycling processes during an orogeny. We report the presence of melt inclusions in garnet from the polymetamorphic Carlos Chagas batholith (CCB), which is a very large body (14,000 km^2) of peraluminous, S-type granite formed during the collisional stage (ca. 585-545 Ma) of the Araçuaí orogeny (ca. 630-480 Ma). The CCB contains large garnet porphyroblasts (5-35 mm), which present numerous inclusions (40-380 µm) of rounded Ti-high biotite, lobate and rounded quartz as well as the accessory minerals ilmenite, rutile, apatite, zircon and monazite. These garnet crystals are the product of fluid-absent incongruent melting of biotite, which also resulted in a significant volume of granitic melt which has been lost from the system, thereby preserving the peritectic garnet. Phase equilibrium modelling of the garnet-bearing assemblage via Theriak Domino indicate peak metamorphic conditions of 790-820 °C and 9.5-10.5 kbar, i.e. depth of approximately 30 km. For the first time polyphase inclusions of calcite and rutile have been identified in the peritectic garnet crystals of the CCB.

These inclusions are small (80-180 µm), have a sub-circular shape, low angle terminations and are dark-coloured in transmitted light. Microcracks frequently occur in the garnet crystals, but some polycrystalline inclusions appear to have no association with cracks. Investigation via SEM demonstrated that calcite locally presents euhedral internal faces and rutile occurs commonly as subhedral aggregates or as single crystals surrounded by calcite. This microstructural evidence is interpreted to reflect primary Ti-rich carbonatitic melt trapped as inclusions during peritectic garnet growth. In addition, pseudomorphed granitic melt films are represented by quartz and plagioclase developed along the boundaries of both garnet and euhedral rutile crystals in the matrix, attest to the presence of the granitic melt produced by biotite incongruent melting during the growth of garnet and rutile.

In combination, this evidence from the CCB appears to record the coexistence of immiscible silicate and carbonate melts during fluid-absent melting of biotite. The carbonate melt is interpreted to reflect anataxis of a carbonate fraction within the metasediments, possibly originating a carbonate cement between grains in the protolith. In addition, the P-T conditions estimated in this study are in agreement with the findings of re-homogenization experiments perfomed by Ferrero et al. [1] for calcite-bearing inclusions hosted in peritetic garnet of migmatites from Oberpfalz.

References:

[1] Ferrero S et al. (2016) In: *35th International Geological Congress*, abstract

REPEATED PARTIAL MELTING EVENTS IN THE ARAÇUAÍ OROGEN (SOUTHEASTERN BRAZIL): EVIDENCE FROM THE POLYMETAMORPHIC CARLOS CHAGAS BATHOLITH

Melo, M.G.[1,2]; Stevens, G.[2]; Lana, C.[1]; Pedrosa-Soares, A.C.[3]; Frei, D.[2]; Alkmim, F.F.[1]; Alkmin, L.A.[1], Oliveira, R.[1]; Alves, T.[1], Schuch, C.S.[1]; Mazoz, A.[1]; Ribeiro, T.[1]

[1]Universidade Federal de Ouro Preto; [2]Stellenbosch University; [3]Universidade Federal de Minas Gerais

The Carlos Chagas batholith (CCB) is the largest (~14,000 km2) granitic body ascribed to the collisional G2 supersuite (ca. 585-545 Ma) of the Araçuaí orogen (AO), southeastern Brazil. The CCB includes a dominant granite richer in garnet than in biotite (the Carlos Chagas leucogranite) and lithotypes with generally prevalent biotite (Montanha and Nanuque granites). Our work focuses on the Carlos Chagas leucogranite, cropping out in the CCB central to southern region, with a view to better understanding crustal recycling during a long-lived orogeny. Three major mineral associations within CCB can be identified: A1) Qz+Pl+Kfs+Bt+Grt+Ilm±Rt; A2) Qz+Pl+Kfs+Bt+Grt+Ilm+Sil; and A3) Qz+Pl+Kfs+Bt+Grt+Ilm+Sil +Spl. Textural evidence for the presence of former melt, recognized in all studied samples, includes: silicate melt inclusions in poikiloblastic garnet, pseudomorphed thin films of melt surrounding the two generations of garnet, pseudomorphed melt pools adjacent to garnet and biotite, and plagioclase and quartz with cuspate-lobate shapes occurring among matrix grains.Two generations of garnet (Grt_1 and Grt_2) are identified within CCB and both are unzoned in terms of major element concentration, both contain small rounded inclusions of Ti-rich biotite and, in addition, the Grt_2 crystals also contains inclusions of remnant sillimanite needles. This microstructural evidence, in combination with the mineral chemistry, indicates that the garnet crystals grew during two distinct partial melting events, assisted by fluid-absent reactions consuming biotite. P-T pseudosections calculated via Theriak Domino in combination with (LA-ICP-MS) *in situ* U-Pb monazite and zircon dating provide new constraints on the thermal evolution of the AO. Data from A1 records P-T conditions of the first granulite-facies metamorphic event (M1) at 790-820 ºC and 9.5-10.5 kbar in depths of 29-32 km, whilst A2 records P-T conditions of the second granulite-facies metamorphism (M2) at 770 ºC and 6.6 kbar corresponding to depths of 20 km. These metamorphism events are recorded in monazites and zircons in all associations, with peak at ca. 564-552 and ca. 530-515 Ma, respectively. The evidence described in this work indicates three episodes of crustal recycling in the Araçuaí orogeny. In the first event source rocks with a volume substantially larger than that of the CCB melted to produce a hydrous, peraluminous granitic melt that intruded at presumably higher crustal level within the orogenic belt at ca. 576-577 Ma. At least part of the water in this hydrous magma was trapped due to biotite crystallization producing significant fertility for the generation of melt from the resultant granite. Thickening and further evolution of the orogen introduced the CCB into the deep crust producing a second process of crustal differentiation, some 20 Ma after the first. This produced an almost completely anhydrous rock, infertile for the production of granitic melt. The third and final episode of recycling occurred only where hydration due to shearing had refertilized the CCB for melt generation and produced relatively minor melt volumes, which were lost leaving the CCB dry and refractory.

PALAVRAS-CHAVE: MULTIPLE ANATECTIC EVENT, MONAZITE AND ZIRCON DATING, ARAÇUAÍ OROGEN

U-PB AGES AND HF ISOTOPIC RECORD OF ZIRCONS FROM CARLOS CHAGAS BATHOLITH: IMPLICATIONS FOR TECTONO-METAMORPHIC EVOLUTION OF THE ARAÇUAÍ OROGEN (SOUTHEASTERN BRAZIL)

Melo, M.G.[1]; Lana, C.[1]; Stevens, G.[2]; Alkmin, L.A.[1]; Gerdes. A.[3]; Nalini Jr, H.A.[1]; Gonçalves, G.O.[1]; Alkmim, F.F.[1]; Teixeira, L.[1]; Silva, J.P[1]; Silveira, G.[1]; Fadul, C.[1]

[1]Universidade Federal de Ouro Preto; [2]Stellenbosch University; [3]Goethe-Universität Frankfurt

The Carlos Chagas batholith (CCB), focus of this study, represents one of the most significant expressions of the G2 supersuite formed during the collisional stage (ca. 585-545 Ma) of the Araçuaí orogen (AO). The CCB rocks correspond to S-type granites which generally contain K-feldspar megacrysts and variable content of garnet and biotite. In this work, we carried out a detailed geochronological and Hf isotopic study by LA-ICP-MS in zircons from the CCB in order to evaluate the tectono-metamorphic evolution of the AO. In addition, analysis of rare earth elements (REEs) and Ti were performed on distinct domains of zircon for a better understanding of the petrologic conditions that affected the batholith during the high-grade metamorphic events. All samples show CL-defined inherited cores and have similar age patterns, with dominant peak between 600 and 637 Ma. Subordinate peaks are recorded at 644-678 Ma, 693-739 Ma and 826 Ma. The U-Pb analysis performed on magmatic zircon grains yield a weighted mean age of 583 ± 6 Ma. Analyses in rim domains indicate two distinct metamorphic populations, with weighted mean ages of 562 ± 6 Ma and 515 ± 6 Ma. The inherited cores yield initial $^{176}Hf/^{177}Hf$ ratios ranging from 0.282233 to 0.282366, with εHf(t) values between -6.7 and -1.8. The distribution of model age (T_{DM}) spans from 1350 to 1580 Ma. Spot analyses done on magmatic zircons gave initial $^{176}Hf/^{177}Hf$ ratios ranging from 0.282201 to 0.282386 and εHf(t) between -8.2 and -1.8, while analyses performed on metamorphic domains yield initial $^{176}Hf/^{177}Hf$ ratios between 0.282203 and 0.282381. Regarding REEs, zircon grains presented lower HREE in the metamorphic rims (Gd_N/Lu_N = 0.05-0.50) than in the inherited/magmatic cores (Gd_N/Lu_N = 0.02-0.10). Both domains display negative Eu anomaly, with Eu/Eu* = 0.03-0.09 (inherited and magmatic) and 0.02-0.52 (metamorphic). Inherited cores have 9-143 ppm Ti, corresponding to Ti-in-zircon temperatures of 732-975 ºC. Magmatic cores and metamorphic rims gave Ti contents of 8-85 ppm (724-918ºC) and 11-71 ppm (755-970ºC), respectively. Based on the main age peak of the inherited zircons, we infer that these minerals are from Rio Doce and/or Rio Negro magmatic arcs. The abundant occurrence of inherited zircon cores in the CCB may indicates Zr saturation in the melt and/or that melt generation and extraction from the source was fast enough to limit the dissolution of these inherited grains. Most of the inherited and magmatic zircons have homogenous Hf isotopic composition and similar enrichment in HREE patterns. Petrological and geochronological data show that the metamorphic zircon grew at granulite-facies conditions in equilibrium with peritectic garnet. The U-Pb ages and initial $^{176}Hf/^{177}Hf$ ratios from distinct domains indicate a complex metamorphic history during the Araçuaí orogeny, associated to the zircon formation by different mechanisms of metamorphic recrystallization and growth/overgrowth at high temperatures, as indicated by Ti-in-zircon thermometer. The authors acknowledge FAPEMIG for providing financial resources for the foment of this abstract.

PALAVRAS-CHAVE: U-PB, LU-HF, ARAÇUAÍ OROGEN

Assessing the isotopic evolution of S-type granites of the Carlos Chagas Batholith, SE Brazil: clues from U-Pb, Hf isotopes, Ti geothermometry and the trace element composition of zircon

Melo, M.G; Lana, C., Stevens, G.; Alkmin, L.A.; Gerdes, A.; Alkmim, F.F.; Nalini-Jr, H.A.

The Araçuaí orogen (AO), located in the southeastern Brazil, and its African counterpart, the West Congo belt, is part of the Pan-African-Brasiliano orogenic system developed between the Congo and São Francisco paleocontinents. The orogenic magmatism in the AO is characterized by the G1 to G5 granitic supersuites formed from pre- to post collisional stages (ca. 630-480 Ma). The Carlos Chagas batholith (CCB) is the largest (~14,000 km^2) S-type granitic body ascribed to the collisional G2 supersuite of the AO. In this study, we report U-Pb and Lu-Hf isotopic data by LA-ICP-MS of zircons from the CCB in order to evaluate the magmatic-metamorphic processes that took place during the evolution of the AO. In addition, analyses of rare earth elements (REEs) were carried out in zircon and garnet for better understanding the petrological conditions of the formation of these minerals during a long-lived orogeny. All samples present CL-defined inherited zircon cores with a dominant age peak at 605 ± 6 Ma. The U-Pb analyses carried out on magmatic zircon cores yield a crystallization age of 582 ± 6 Ma, whilst the analyses in metamorphic rim domains display ages of 563 ± 6 Ma and 509 ± 5 Ma. The inherited cores yield initial $^{176}Hf/^{177}Hf$ ratios ranging from 0.282233 to 0.282366, with $\varepsilon_{Hf(t)}$ values between -6.7 and -1.8. Spot analyses on magmatic zircons give initial $^{176}Hf/^{177}Hf$ ratios ranging from 0.282201 to 0.282386 and $\varepsilon_{Hf(t)}$ between -8.2 and -1.8, while analyses on metamorphic domains yield initial $^{176}Hf/^{177}Hf$ ratios between 0.282203 and 0.282381. The chondrite-normalized REE patterns of inherited and magmatic zircons from the CCB show similar negative Eu anomaly (Eu/Eu* = 0.03-0.09) and HREE enrichment (Gd_N/Lu_N = 0.02-0.10). Metamorphic zircons present higher HREE (Gd_N/Lu_N = 0.05-0.50) than the peritectic garnet (Gd_N/Lu_N = 0.09-1.60) and both have negative Eu anomaly (Eu/Eu* = 0.02-0.52 and 0.01-0.07, respectively). Based on Hf isotope composition and REE patterns, the magmatic zircons from the CCB may be formed from dissolution of pre-existing zircons in the source rock. Initial $^{176}Hf/^{177}Hf$ ratios indicate zircon formation by different mechanisms of metamorphic recrystallization and anatectic growth/overgrowth. HREE were preferentially assimilated into metamorphic zircon instead of garnet at granulite-facies conditions.